Transactions of the ASME®

Journal of Fluids Engineering

Published Quarterly by The American Society of Mechanical Engineers

VOLUME 111 • NUMBER 4 • DECEMBER 1989

(Contents continued on page 419)

Transactions of the ASME, Journal of Fluids Engineering (ISSN 0098-2202) is published quarterly (Mar., June, Sept., Dec.) for $100 per year by The American Society of Mechanical Engineers, 345 East 47th Street, New York, NY 10017. Second class postage paid at New York, NY and additional mailing offices. POSTMASTER: Send address changes to Transactions of the ASME, Journal of Fluids Engineering, c/o THE AMERICAN SOCIETY OF MECHANICAL ENGINEERS, 22 Law Drive, Box 2300, Fairfield, NJ 07007-2300.
CHANGES OF ADDRESS must be received at Society headquarters seven weeks before they are to be effective. Please send old label and new address.
PRICES: To members, $29.00, annually; to nonmembers, $100. Add $15.00 for postage to countries outside the United States and Canada.
STATEMENT from By-Laws. The Society shall not be responsible for statements or opinions advanced in papers or . . . printed in its publications (B7.1, Par. 3).

INDEXED by Applied Mechanics Reviews and Engineering Information, Inc.

Contents (continued)

Hot-Wire Measurements Inside a Centrifugal Fan Impeller

A. Kjörk
Research Assistant.

L. Löfdahl
Associate Professor.

Department of Applied Thermodynamics and Fluid Mechanics,
Chalmers University of Technology,
412 96 Göteborg, Sweden

Measurements of the three mean velocity components and five of the Reynolds stresses have been carried out in the blade passage of a centrifugal fan impeller. The impeller was of ordinary design, with nine backward curved blades, and all measurements were carried out at the design flow rate. The mean velocity measurements show that the flow can be characterized as an attached flow with almost linearly distributed velocity profiles. However, in a region near the suction side close to the shroud a low velocity region is created. From the turbulence measurements it can be concluded that relatively low values of the turbulent stresses are predominating in the center region of the channel. Closer to the walls higher values of the normal as well as shear stresses are noted.

Introduction

The flow fields in a centrifugal impeller can probably be considered as one of the most complex and important flow cases in turbo machinery applications. The complexity is caused partly by the geometry, and partly by the rotation, i.e., the influence on the velocity field from centrifugal and Coriolis forces together with pressure gradients. To enable development, improvement and testing of turbulence models in rotating impellers, it is necessary to obtain experimental data, which include profiles of both the three mean velocity components and the complete turbulent stress tensor (Reynolds' stresses).

Quite a large number of experimental investigations have been carried out in which the flow field of centrifugal impellers have been measured. However, in most of the investigations only the mean velocity field has been determined and in very few cases turbulence measurements have been performed. Examples where the turbulence intensity has been considered are the rotating divergent channel which was investigated by Moore [1], and the fan impeller investigated by Goulas and Mealing [2]. In recent years a number of experiments using laser technique have been reported. For example Eckardt [3], investigated a centrifugal compressor and determined among other quantities also the kinetic energy of the turbulence. In spite of the large number of experimental investigations on centrifugal impellers, there still seems to be quite a large need for well defined test cases in which all Reynolds stresses are determined.

In the present investigation, the mean velocity field and five of the six Reynolds stresses have been determined in a blade passage of a rotating centrifugal impeller using a hot-wire measurement technique. The purpose of these measurements is to obtain an overall picture of the flow field, which means that the measuring points are almost equally spaced in the blade passage. No detailed boundary layer measurements on the side walls are reported here.

Contributed by the Fluids Engineering Division for publication in the JOURNAL OF FLUIDS ENGINEERING. Manuscript received by the Fluids Engineering Division January 5, 1988.

Apparatus and Experimental Method

The test rig, shown in Fig. 1, is composed of an ordinary low pressure centrifugal fan to which an outlet side test airway is connected. At the inlet, the fan is fitted with a bellmouth which can be adjusted in order to obtain a well defined inlet clearance. The width of the collector is 2.6 times the width of the impeller, and it has a log-spiral profile. The fan is driven by an electrical motor, which is connected to a frequency converter so the rotational speed can be adjusted gradually between zero and maximum speed.

The Impeller and the Coordinate System. In Fig. 2, the dimensions of the impeller and the location of the measuring positions are given. The impeller has nine backward curved blades, which were manufactured from 2.5 mm sheet metal. Each blade is curved as an arc with a radius r_s, and arranged so that the center of this arc falls on a circle with a radius r_o

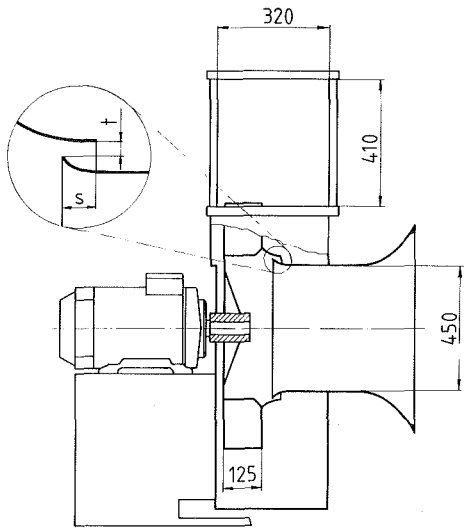

Fig. 1 Test fan (all dimensions in mm)

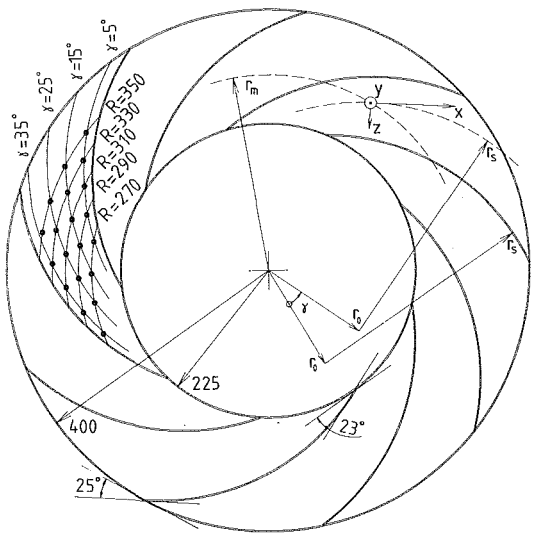

Fig. 2 Test impeller with measuring positions and the reference coordinate system

measured from the center of the impeller. The outer diameter, D_y, and the inner diameter, D_i, of the impeller are 800 mm and 450 mm, respectively, and the width, b, 125 mm. Thus the blade angles can be determined using standard geometry.

As is shown in Fig. 2 each measuring position is defined as the point of intersection between two arcs, one of which is given by a constant value of the angle γ and the other by the radius r_m. The arc defined by the angle γ coincides with the pressure side of the blade if $\gamma = 0$ deg and with the suction side if $\gamma = 40$ deg. A local reference coordinate system is defined by assuming the x-direction to point in the tangential direction of an arc given by γ (positive values in the radial direction). The y-direction is in the hub to shroud direction, and the z-direction is determined by the right-hand rule. U, V, and W are the velocities in the x, y, and z directions, respectively. The positions selected for the detailed hot-wire measurements are located along four different "streamlines" i.e., four different values of γ, and at five different radii. At each position the measurements have been carried out at seven different planes, which are equally spaced between the hub and the shroud. The spacing between the measured points have been chosen as to enable formation of gradients in the different directions, and this means that a total of 140 different points of measurements in the flow field have been investigated.

Fan Performance. For the determination of the fan performance an outlet test airway is connected to the fan. This airway is designed according to British Standard [4], and incorporates a standardized flow straightener together with a set of four wall tappings. The flow straightener, positioned before the wall tappings, is designed as to dissipate any swirl energy at the fan outlet. At the end of the airway a swivel damper is located, which make it possible to control the flow rate. The static pressure is measured as the mean value of the pressure at the wall tappings, and the fan total pressure can then be calculated in accordance with the British Standard [4]. The flow rate is measured in the rearmost part of the airway using a Pitot-static tube which was traversed across the tube. The measured fan characteristic is given in Fig. 3.

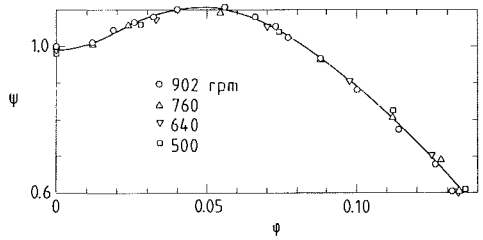

Fig. 3 Fan characteristic. (Uncertainty according to reference [4])

Hot-Wire Technique. For the hot-wire measurements, the probe was mounted in the impeller and connected to a stationary positioned Dantec 56C16 anemometer through a mercury rotary contact. Using a mercury rotary contact for the signal transfer, and including it as a part of the probe cable might be a source of measuring errors. However, this problem was carefully studied, and it could be verified that the noise generation of the rotary contact was insignificant (always considerably smaller than 3mV which was used as the maximum accepted noise level of the whole experiment). The frequency response of the system was determined to 6 kHz, according to a criterion suggested by Freymuth [5]. This upper break frequency must be considered to be satisfactory, since no turbulent kinetic energy content was expected in the frequencies above 5 kHz. Later, spectral analysis of the hot-wire signal also confirmed this assumption, in fact also that turbulent kinetic energy above 4 kHz could be neglected in the present case.

The hot-wire method used was a single rotating technique, which was originally used by Löfdahl [6] in a thick three-dimensional boundary layer. The technique is based on the assumption that the effective cooling velocity of the wire depends on the magnitude and the direction of the flow.

An effective cooling velocity of the hot-wire can thus be expressed, as suggested by Jørgensen [7].

$$U_e^2 = U_N^2 + H * U_B^2 + K * U_T^2 \tag{1}$$

U_N, U_B, and U_T are wire oriented velocity components normal, binormal and parallel to the probe. K and H are angularity coefficients describing the response of the sensor to tangential and binormal velocity components, respectively. The relation between the effective cooling velocity U_e and the electrical output voltage of the anemometer, E, is given by an extended version of King's law:

$$E^2 = A + B * U_e^C \tag{2}$$

Nomenclature

D = impeller diameter, inner and outer
b = impeller width
k = turbulent kinetic energy: $\frac{1}{2}(\overline{u^2} + \overline{v^2} + \overline{w^2})$
p_{tF} = fan total pressure (Pa)
Q = flow rate (m^3/s)
r = radius
U, V, W = instantaneously velocity components
$\bar{U}, \bar{V}, \bar{W}$ = mean velocity components
u, v, w = fluctuating velocity components
u_p = blade tip velocity
$\rho\overline{uv}, \rho\overline{uv}$ = Reynolds shear stresses[1] (N/m^2)
$\rho\overline{u^2}, \rho\overline{v^2}, \rho\overline{w^2}$ = Reynolds normal stresses[1] (N/m^2)
x, y, z = reference coordinate system
γ = angle defined in Fig. 2
φ = flow coefficient $4Q/(\pi D_y^2 \cdot u_p)$
ψ = pressure coefficient $2P_{tF}/(\rho u_p^2)$

[1]In the interest of compactness ρ has been excluded in the discussion.

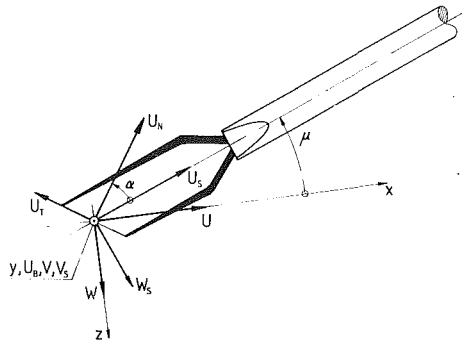

Fig. 4 Velocity components of the wire-fixed (U_N, U_T, U_B), the probe-fixed (U_S, V_S, W_S) and the reference coordinate system (U, V, W). For definition of the axes x, y, and z, see Fig. 2.

A, B, and C are constants with values which must be determined by calibration in a relevant velocity range. When measurements are performed in a rotating frame of reference the probe ought to be calibrated in a rotating mode. However, it has been shown by Hah and Lakshminarayana [8], for the rotational speed and centrifugal acceleration of the present case, that the rotation has a negligible effect on the calibration constants. Therefore the probes were calibrated in a wind tunnel.

In the present investigation a method for correction of the resistance due to the mercury rotary contact and different probe cables, derived by Kjörk [9], was used together with a temperature correction method, derived by Bearman [10]. Pitch factor, H, and yaw factor, K, occurring in equation (1), were determined by calibration using the method suggested by Bruun and Tropea [11], and the constants A, B, and C were calculated in accordance with the method suggested by Swaminatham et al. [12].

In equation (1) the effective cooling velocity is expressed in a wire-fixed coordinate system. Figure 4 shows the relation between the wire-fixed (U_N, U_T, U_B), the probe-fixed (U_S, V_S, W_S), and the reference coordinate system of the impeller (U, V, W). A transformation to the probe-fixed coordinate system gives:

$$U_e^2 = S_1U_S^2 + S_2V_S^2 + S_3W_S^2 + S_4U_SV_S + S_5U_SW_S + S_6V_SW_S \quad (3)$$

where the coefficients $S_1, \ldots, S_6$ are functions of K, H, and the probe orientation. The velocity components in this equation are separated into mean velocities and fluctuating components, then the expression is expanded into a binomial series and time-averaged in the conventional way. In the series expression U_e is expanded about the mean velocity component $\bar{U}_S$ and terms of the second order are included. In this way an equation which expresses $\bar{U}_e$ as a function of the mean velocities and the turbulent components is obtained. This expression is finally squared to yield:

$$\bar{U}_e^2 = S_1\bar{U}_S^2 + S_2\bar{V}_S^2 + S_3\bar{W}_S^2 + S_4\bar{U}_S\bar{V}_S + S_5\bar{U}_S\bar{W}_S + S_6\bar{V}_S\bar{W}_S + \left[S_2 - \frac{S_4 \cdot S_4}{4S_1}\right]\overline{v_S^2} + \left[S_3 - \frac{S_5 \cdot S_5}{4S_1}\right]\overline{w_S^2} + \left[S_6 - \frac{S_4 \cdot S_5}{4S_1}\right]\overline{v_S w_S} \quad (4)$$

An equation for the turbulent stresses is calculated from the expression:

$$\overline{u_e^2} = \overline{U_e^2} - \bar{U}_e^2 \quad (5)$$

where $\overline{U_e^2}$ is obtained from the time averaged version of equation (3) and $\bar{U}_e^2$ from equation (4). Thus, the equation for the turbulent stresses is as follows:

$$\overline{u_e^2} = S_1\overline{u_S^2} + \frac{S_4 \cdot S_4}{4S_1}\overline{v_S^2} + \frac{S_5 \cdot S_5}{4S_1}\overline{w_S^2} + S_4\overline{u_S v_S} + S_5\overline{u_S w_S} + \frac{S_4 \cdot S_5}{2S_1}\overline{v_S w_S} \quad (6)$$

Since the coefficients in equations (4) and (6) are functions of the probe angles, two systems of equations are obtained if measurements are performed at a number of different angle settings of the probe.

In the present investigation the anemometer signals was analogue-to-digital converted and evaluated by a computer (VAX 750) for one setting of a straight probe, and for four different angle settings of a 45 deg slanted probe. A sampling frequency of 2.5 kHz and an integration time of order 100 seconds was used. For each signal the probability density distribution was determined, and by applying equation (2) the mean value $\bar{U}_e$ and the mean squared value u_e^2 were calculated. The mean velocity components were calculated by solving the overdetermined system of equations given by equation (4) for the four measurements performed by the slanted probe. From the straight probe measurements $\bar{U}$ was also calculated and compared with the value calculated from the slanted probe measurements. By solving the linear system of equations given by equation (6) the turbulent quantities u_S^2, v_S^2, w_S^2, $\overline{u_S v_S}$ and $\overline{u_S w_S}$ were determined. The final step in the calculation was to transform the calculated values from the probe-fixed coordinate system to the reference coordinate system of the impeller. For a full account of the test rig and the measuring technique, including the calibration procedure and the data acquisition, see the more comprehensive work of Kjörk [9].

Experimental Results and Discussion

All measurements were carried out at the design point of the fan, which corresponds to an impeller speed of 890 rpm and a blade tip velocity, u_p, of 37 m/s. The flow coefficient was kept constant at $\varphi = 0.10$, which corresponds to a flow rate of 1.9 m^3/s and a fan total pressure of 730 Pa.

Mean Velocity Components. The results of the mean velocity measurements in the impeller passage are shown in Fig. 5. In this figure, the variation of the mean velocity components in the hub to shroud direction is given at different radii. The mean velocities are made dimensionless with the blade tip velocity, u_p, and the dotted lines in the figures are drawn for visualization purpose only. As can be seen in the figure, the components of $\bar{V}$ and $\bar{W}$ are small compared with the $\bar{U}$ component. This implies that the flow behaves fairly well and it can be characterized as an attached flow.

Considering Fig. 5 in more detail, the following may be observed. At the inlet section of the impeller channel the flow has just been turned from the axial to the radial direction. At the smaller radii the largest velocity can be noted close to the shroud, while at the larger radii a more uniform flow could be observed. The increase of the $\bar{U}$ component in the hub region is reflected in the $\bar{V}$ component. This effect may be observed at $\gamma = 15$ deg at the three largest radii, and at $\gamma = 5$ deg at the four largest radii. To notice any tendency in the $\bar{W}$ component is more difficult, due to the blade divergence in this direction.

The velocity profiles along the line given by $\gamma = 35$ deg show quite a different behavior as compared with the other profiles, especially at small radii, i.e., near the inlet. At the radius $r = 270$ mm a peak in the velocity profile can be observed which probably is caused by the leading edge of the blade. In the whole region close to the suction side the flow is very unstable and time averaged turbulence intensities will therefore be at a high level (as will be shown in the next section).

Another conclusion which can be drawn from Fig. 5 is that the main flow velocity is decreasing in the flow direction. This decrease is most probably caused by the weak divergence of the channel in the radial direction. An increase in the absolute value of the $\bar{W}$ component may also be noted, fairly clear at $\gamma = 5$ deg and $\gamma = 25$ deg.

In the upstream half of the impeller, outside the boundary

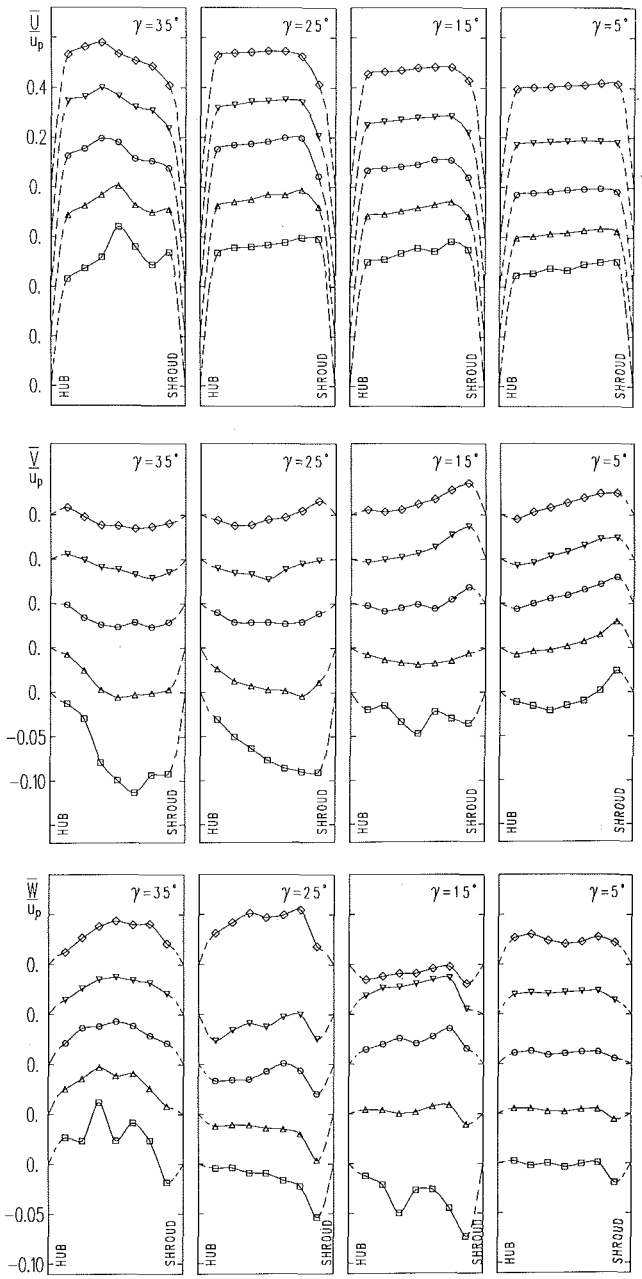

Fig. 5 Profiles of the three mean velocity components across the passage, at different radii (□ r_m = 270 mm, Δ r_m = 290 mm, ○ r_m = 310 mm, ▽ r_m = 330 mm, ◇ r_m = 350 mm) (Uncertainty in $\bar{U}/u_p$ = ±0.006, $\bar{V}/u_p$ = ±0.01 and $\bar{W}/u_p$ = ±0.01, in passage distance ±0.1 percent)

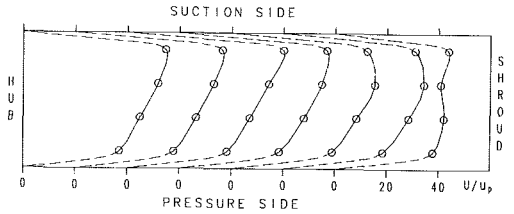

Fig. 6 Mean velocity profiles at the radius R = 330 mm. Direction from the pressure side to the suction side. The seven different profiles are equally spaced in planes between the hub and the shroud. (Uncertainty; see Fig. 5)

layers, the velocity seems to be almost constant in the hub to shroud direction. Considering the variation in the direction from the pressure to the suction side, an increase in the velocity toward the suction side can be observed. This increase is fully in agreement with potential flow calculations, see for example Krain [13]. To show this observation more clearly some velocity profiles in the suction to pressure side direction are given in Fig. 6. As can be seen in this figure, the main flow velocity in the middle of the channel has an almost linearly distributed profile, and a low velocity region is created near the suction side in the region close to the shroud. A very similar development of the flow field, in a pump impeller with almost the same blade angles, has been noted by Murakami et al. [14]. They suggested that the slower flow region is attributed to a wake caused by the rapid change of flow direction at the channel inlet, and it is plausible that this conclusion also is true in the present case.

Reynolds Stresses. The results of the turbulence measurements are given in Figs. 7, 8, and 9. The normal stresses are made dimensionless with the blade tip velocity, u_p, and presented as turbulence intensities in Fig. 7. The shear stresses are also made dimensionless in a similar way and are given in Fig. 8. Also in these figures the dotted lines between the measuring points and the side walls are drawn for visualization purpose only, i.e., the dotted lines in the region close to the walls should not be interpreted as boundary layer measurements. Since the kinetic energy of turbulence, k, is a parameter of interest in computation, it has been computed from the measured normal stresses, and is shown in Fig. 8, also in a dimensionless way.

Examining the turbulence intensities of Fig. 7 the scattering of the points along the line γ = 35 deg is large, and therefore attention should be first directed to the other points of measurements. At the other "streamlines" a fairly low turbulence level is found in all directions. This is due to the scaling against the blade tip velocity. (Scaling against local mean velocity would result in an approximately twice as high a level.) The normal stress component in the flow direction seems to be the dominant component. It reveals a clear minimum at the center of the channel and increasing values toward the hub and the shroud respectively. Peak values as high as 7 percent can be noted. As expected, closer to the walls the turbulence intensities decrease and approach a zero value.

A general tendency concerning the other two normal stresses is that the intensity in the hub to shroud direction is slightly larger than the component in the pressure to suction direction. This may be explained by the geometry of the channel. In the hub to shroud direction the channel width is constant while a slight divergence is present in the other direction. (See also the mean velocity discussion.) The points measured along the "streamline" given by γ = 35 deg show a quite different behavior from the other points. An explanation to this might be, as mentioned in the mean velocity discussion, that instabilities of the flow forms small eddies at the leading edge of the blade and that these eddies are transported downstreams. If the abovementioned figures are studied in more detail, it is obvious that the irregular points are located in the center region of the channel, and that the points near the hub or the shroud, along "streamline" γ = 35 deg, are in better agreement with the earlier discussion. In order to check the repeatability of the data, some of these irregular points have been remeasured, however, the same results were obtained. For some of the irregular points the calculated normal stresses, $\overline{v^2}$ and $\overline{w^2}$ are zero, which of course is not correct, and an explanation to this might be the very irregular flow at these points.

The shear stresses, shown in Fig. 8, all reveal fairly small numerical values through the investigated region as can be expected in a slightly three dimensional flow. The abovementioned irregularities along "streamline" γ = 35 deg can also be observed in these figures. Considering first the other points,

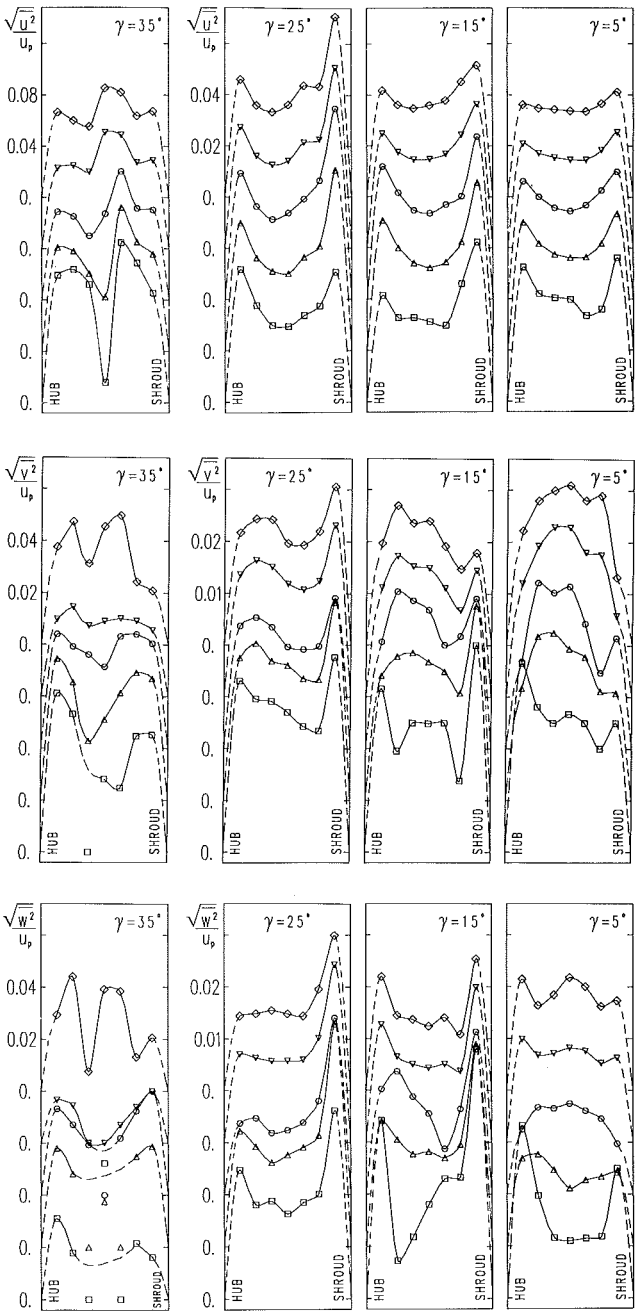

Fig. 7 Normal stresses (for legend see Fig. 5). (Uncertainty in $\sqrt{u^2}/u_p$ = ±2 percent, $\sqrt{v^2}/u_p$ = ±6 percent, $\sqrt{w^2}/u_p$ = ±6 percent, same uncertainty in passage distance as in Fig. 5)

the values are fairly low, and any clear general tendency seems difficult to find. However, the $\overline{uw}$-shear stress appears always to have larger values than the $\overline{uv}$-shear stress, which possibly also can be interpreted as to the "activities" due to the divergence of the channel. An increase of the shear stresses in the hub and the shroud region can be noted similar to what was found in the normal stresses.

Considering the normal as well as the shear stresses, a plateau like behavior of the stresses can be noted. In the center region between the hub and the shroud all stresses have fairly low values, and closer to the hub and the shroud the numerical values increase.

From Fig. 9, it can be noted that the turbulent kinetic energy seems to be almost constant in the flow direction.

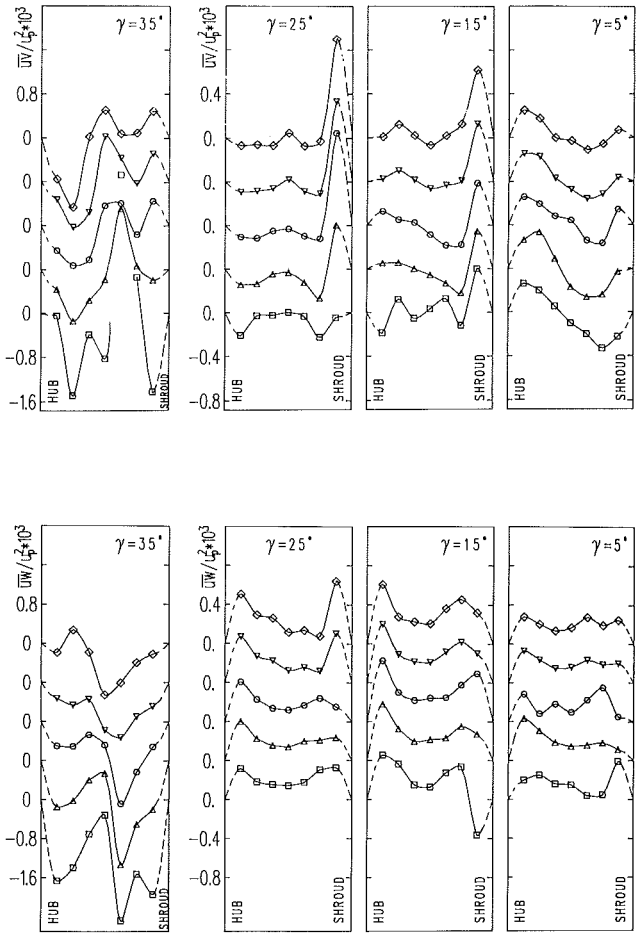

Fig. 8 Shear stresses (for legend see Fig. 5). (Uncertainty in $\overline{uv}/u_p \cdot 10^3$ = ±8 percent and $\overline{uw}/u_p \cdot 10^3$ = ±8 percent, same uncertainty in passage distance as in Fig. 5)

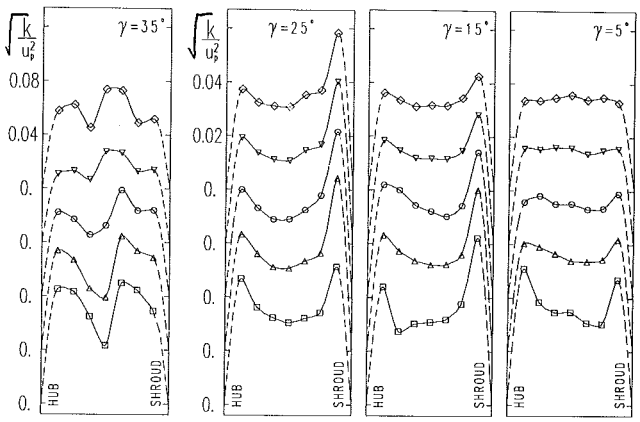

Fig. 9 Kinetic energy of turbulence (for legend see Fig. 5). (Uncertainty slightly higher than the normal stress in the x-direction)

Conclusions

The flow field in the rotating blade passage of a backward curved centrifugal fan impeller at the design flow rate has been determined using a hot-wire probe rotating with the impeller. The major conclusions drawn from the measurements can be summarized as follows:

* In the hub to shroud direction near the inlet the velocity profiles have positive gradients toward the shroud, while at larger radii the profiles becomes more uniform.

* An almost linear increase in the velocity profiles are found in the direction from the pressure side toward the suction side. However, a low velocity region is created near the suction side in the region close to the shroud.
* Due to a weak divergence of the channel the main flow velocity decreases in the flow direction.
* The kinetic energy of turbulence in the middle of the passage is almost constant in the flow direction.
* The normal as well as the shear stresses show a plateau like behavior, with low values in the middle of the channel and values increasing toward the hub and the shroud, respectively.
* Concerning the normal stresses the component in the streamwise direction is dominant, and the component in the hub to shroud direction is slightly larger than the component in the pressure to suction side direction.
* The flow in the vicinity of the suction side is rather unsteady, and time averaged turbulence intensities are therefore high in this part of the passage.

Acknowledgment

This work has been sponsored by the Swedish Board for Technical Development in cooperation with Swedish Industries within the turbomachinery field.

References

1 Moore, J., "A Wake and an Eddy in a Rotating, Radial-Flow Passage, Part 1: Experimental Observations," ASME *Journal of Engineering for Power*, July 1973, pp. 205–212.

2 Goulas, A., and Mealing, B., "Flow at the Tip of a Forward Curved Centrifugal Fan," ASME Paper No. 84-GT-222.

3 Eckardt, D., "Detailed Flow Investigations Within a High-Speed Centrifugal Compressor Impeller," ASME *Journal of Engineering for Power*, Sept. 1976, pp. 390–402.

4 British Standard Institution, BS 848: Part 1, 1980 Fans for General Purposes, Methods of Testing Performance.

5 Freymuth, P., "Nonlinear Control Theory for Constant-Temperature Hot-Wire Anemometers," *The Review of Scientific Instruments*, Vol. 40, No. 2, Feb. 1969, pp. 258–262.

6 Löfdahl, L., "Turbulence Measurements Near the Stern of a Ship Model," *Journal of Ship Research*, Vol. 28, Sept. 1984, pp. 186–201.

7 Jørgensen, F. E., "Directional Sensitivity of Wire and Fiber-film Probes," *DISA Information*, No. 11, May 1971, pp. 31–37.

8 Hah, C., and Lakshminarayana, B., "Effect of Rotation on a Rotating Hot-wire Sensor," *J. Phys. E.: Sci. Instrum.*, Vol. 11, 1978, pp. 999–1001.

9 Kjörk, A., "Hot-wire Measurements in the Impeller Passage of a Centrifugal Fan Impeller," Thesis for the degree of Licentiate of Engineering, Department of Applied Thermodynamics and Fluid Mechanics, Chalmers University of Technology, Göteborg, 1987.

10 Bearman, P. W., "Correction for the Effect of Ambient Temperature Drift on Hot-wire Measurements in Incompressible Flow," *DISA Information No. 11*, May 1971, pp. 25–30.

11 Bruun, H. H., and Tropea, C., "The Calibration of Inclined Hot-wire Probes," *J. Phys. E.: Sci. Instrum.*, Vol. 18, 1985, pp. 405–413.

12 Swaminatham, M. K., Bacic, R., Rankin, G. W., and Sridhar, K., "Improved Calibration of Hot-wire Anemometers," *J. Phys. E.: Sci. Instrum.*, Vol. 16, 1983, pp. 335–338.

13 Krain, H., "Experimental Observation of the Flow in Impellers and Diffusers," *Flow in Centrifugal Compressors*, Lecture Series 1984-07, von Karman Institute for Fluid Dynamics.

14 Murakami, M., Kikuyama, K., and Asakure, E., "Velocity and Pressure Distributions in the Impeller Passages of a Centrifugal Pump," ASME JOURNAL OF FLUIDS ENGINEERING, Vol. 102, Dec. 1980, pp. 427–445.

Secondary Flows in a Transonic Cascade: Comparison Between Experimental and Numerical Results

F. Bassi
Ist. di Macchine,
Universitá di Catania,
95125 Catania, Italy

C. Osnaghi
Dip. di Energetica,
Politecnico di Milano,
20133 Milano, Italy

A. Perdichizzi
Dip. di Ingegneria Meccanica,
Universitá di Brescia,
25060 Brescia, Italy

M. Savini
CNPM - CNR,
20068 Peschiera Borromeo (MI), Italy

The paper presents a comparison between numerical results and experimental data about the secondary flow development in a linear transonic turbine cascade. Computations are carried out by using a three-dimensional inviscid Euler code, based on a Runge-Kutta explicit finite volume method. The experimental inlet total pressure distribution is imposed as inlet boundary condition to simulate the incoming endwall boundary layer. The comparison is made in four planes downstream of the cascade where detailed experimental data obtained in a transonic wind tunnel are available. For each of these planes secondary velocities and streamwise vorticity contour plots are presented and discussed. Moreover pitchwise mass averaged flow angle distributions showing overturning and underturning regions are shown. The comparison shows that an Euler code can predict the essential features of secondary flow phenomena like passage vortex location and intensity but a certain disagreement is found in the overturning and underturning angles evaluation. Numerical results also allow for the investigation of the development of secondary flows inside the blade channel. The investigation is carried out for three different Mach numbers: M_{2is} = 0.5, 1.02, 1.38, in order to show the influence of compressibility on the flow vortex structure.

Introduction

One of the most challenging tasks in cascade aerodynamics is to get a better understanding of the mechanism governing the development of secondary flows together with their influence on blade rows performance. Up to now, most of the experimental and theoretical work in this field refers to subsonic flows and the influence of compressibility and/or shock waves on secondary flows is not yet fully clear. The present authors started a research program two years ago, both theoretical and experimental, to study the development of secondary flows in turbine cascades, particularly in the transonic regime. A substantial effort has been devoted to setting up a suitable test rig in order to obtain reliable measurements of the three-dimensional flow field downstream of a transonic turbine cascade.

The theoretical approach for secondary flow solution, up to few years ago, was based on the classical secondary flow theory originally developed by Hawthorne (1955) solving the secondary flow vorticity equation separately from the primary flow field. Recently the development of modern computers made possible the direct solution of the fully three-dimensional flow equations, thus removing the uncertainties built in any model of secondary effects. Following this approach, a numerical code was developed for the prediction of three-dimensional flows in turbomachinery cascades; the numerical results thus obtained are discussed here and compared with the experimental data. It must be pointed out that, for the moment, the comparison is limited to the use of an inviscid code. Anyway some important features of secondary flows are essentially inviscid phenomena (mainly the passage vortex and the two branches of the horseshoe vortex) and Euler codes can supply informations about the formation and the evolution of these vortices as well as their extent and position, provided that the inlet vorticity is significant compared with that produced by the shear stress inside the blade channel. If large velocity ratios occur between inlet and outlet of the cascade, the vorticity production is important. Even in this case, however, the secondary flow pattern can be slightly affected by the shear stress; this is an important question that will be clarified in the following.

Thus the aim of this work is twofold:

- to make a contribution toward a better understanding of the complex three-dimensional phenomena occurring, with particular attention to the influence of the Mach number.
- to show the limits of an inviscid approach in describing the flow structure, especially downstream of the trailing edge.

Contributed by the Fluids Engineering Division and presented at the Winter Annual Meeting, Chicago, Ill., November 27–December 2, 1988, of THE AMERICAN SOCIETY OF MECHANICAL ENGINEERS. Manuscript received by the Fluids Engineering Division September 20, 1988.

Since the initial results are encouraging, in the early future additional data will be obtained and compared to viscous turbulent computations.

Computations

Governing Equations and Numerical Solution. The integral form of the Euler equations in a cartesian coordinate system x, y, z can be written as

$$\frac{\partial}{\partial t}\int_V W\,dV + \oint_{\partial V}(fn_x + gn_y + hn_z)\,ds = 0 \qquad (1)$$

where

$$W = [\rho, \rho u, \rho v, \rho E]^T$$
$$f = [\rho u, \rho u^2 + p, \rho uv, \rho uH]^T$$
$$g = [\rho v, \rho vu, \rho v^2 + p, \rho vH]^T$$
$$p = (\gamma - 1)\rho e$$
$$E = e + \frac{1}{2}(u^2 + v^2)$$
$$H = E + \frac{p}{\rho}$$

and n_x, n_y, n_z are the components of the unit vector normal to the surface enclosing V, u, v, w are the velocity components, ρ, p, e are, respectively, the density, pressure and internal energy. The ratio of the specific heats γ is assumed constant and equal to 1.4.

The numerical solution of equation (1) is based on the scheme originally proposed by Jameson et al. (1981), i.e., a finite volume method with central spatial differences and explicit adaptive dissipation; the time integration is performed with the following three stage Runge-Kutta scheme:

$$W^{(0)} = W^n$$
$$W^{(k)} = W^{(0)} - \alpha_k \frac{\Delta t}{V}\left(C(W^{(k-1)}) - D(W^{(0)})\right) \quad k = 1,2,3 \qquad (2)$$
$$W^{n+1} = W^{(3)}$$

where C and D are, respectively, the net inviscid flux and the adaptive dissipation term and $\alpha_1 = \alpha_2 = 0.6$, $\alpha_3 = 1$. Observe that for computational efficiency the adaptive dissipation is computed only at the first stage of the Runge-Kutta cycle.

In the present application convergence to steady state is enhanced by using local time stepping, enthalpy damping and a multigrid algorithm.

Boundary Conditions. In order to preserve the computational efficiency, physical and numerical boundary conditions are set or calculated in "phantom cells" all around the computational domain.

Inflow Boundary. The flow at the inlet is subsonic, so four independent variables have to be specified; the last one is computed using the Riemann invariant associated with the characteristic running from inside the domain, assuming the flow to be locally one-dimensional in the axial direction. This inlet condition is well suited for blade row computations since the axial velocity is always incoming, no matter what the boundary values are. Specifying total enthalpy, entropy and two flow angles, the variables in the "phantom cells" are determined by means of the following relations:

$$\frac{q^2}{2} + \frac{c^2}{\gamma - 1} = H_1$$
$$u - \frac{2c}{\gamma - 1} = u_e - \frac{2c_e}{\gamma - 1}$$
$$v = u \tan \beta_1$$
$$w = u\frac{\tan \delta_1}{\cos \beta_1}$$
$$\rho = \left(\frac{c^2}{\gamma s_1}\right)^{\frac{1}{\gamma - 1}}$$

where the subscript 1 and e indicate, respectively, the assigned boundary values and the values extrapolated from the interior.

Outflow Boundary. The pressure is the physical boundary condition specified at the outflow (subscript 2), where the flow is subsonic in the axial direction; the numerical boundary conditions are computed by extrapolating from the interior the characteristic variables of the flow, assumed locally one-dimensionality in the axial direction (subscript e):

$$p = p_2$$
$$u + \frac{2c}{\gamma - 1} = u_e + \frac{2c_e}{\gamma - 1}$$
$$v = v_e$$
$$w = w_e$$
$$s = s_e$$

Periodic and Symmetry Boundaries. At the periodic boundary the variables are set equal to those stored one pitch above or below, and at the midspan symmetry is enforced along the z direction.

Solid Wall Boundary. The density in the phantom cells is extrapolated from the interior, and a reflection condition for the velocity is used. The normal momentum equation is solved for the pressure gradient at the wall, and this is used to obtain the pressure in the phantom cells.

Grid Generation. The three-dimensional grid is obtained by stacking the same two-dimensional mesh in the z direction. In a previous work (Bassi and Savini, 1986), two of the authors used an O type mesh in the blade to blade section that generally is well suited for blade rows computations. However, in the present study, it was found inconvenient to use an O type mesh, since, going far downstream of the trailing edge, as

Nomenclature

b = axial chord
c = chord
h = blade height
i = incidence angle
M = Mach number
$\mathbf{q}$ = velocity
s = pitch
SKE = secondary kinetic energy
u = velocity component along x
v = velocity component along y
w = velocity component along z
x = axial coordinate
y = pitchwise coordinate
z = spanwise coordinate
β = flow angle in the $x - y$ plane with respect to x
β' = blade angle
δ = flow angle with respect to the $x - y$ plane
γ = stagger angle
Ω = vorticity

Subscripts

1 = inlet
2 = outlet
is = isentropic
s = streamwise
S = secondary
t = total

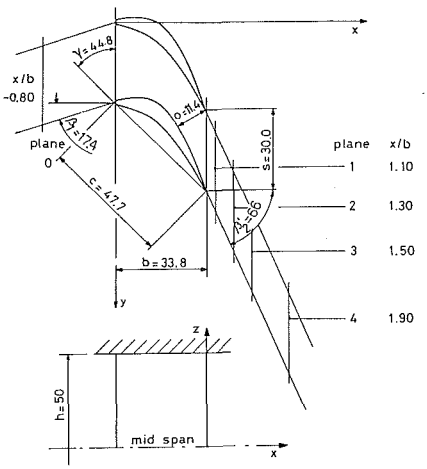

chord length	c	= 47.7 mm.
pitch to chord	s/c	= 0.63
aspect ratio	h/c	= 1.05
inlet blade angle	β_1'	= -2.6 deg.
outlet blade angle	β_2'	= 66. deg.
incidence angle	i	= 20. deg.
stagger angle	γ	= 44.8 deg.
number of blades	z	= 12

Fig. 1 Cascade geometry and measuring plane location

needed for comparison with experiments, the reduced number of grid points in the pitchwise direction results in grid-induced diffusion which smears out the secondary flow effects. Therefore, a C type grid generation method was developed which avoids the previous inconvenience and allows to satisfy some desirable requirements: the mesh is orthogonal at the body surface and along the wake; the skewness of the grid, induced by the periodicity constraint, is confined in a relatively small region of the computational domain; the mesh lines across periodic boundaries have continuous derivative.

The C grid generation procedure is of elliptic type: the two families of coordinate lines are determined by solving the Laplacian of two functions ψ and ϕ with two different sets of boundary conditions. The numerical solution of ψ and ϕ is obtained in the physical plane on a base grid algebraically generated; the space differentiation is based on a finite volume approach and the iterative line Gauss-Seidel method is used for the numerical solution. The convergence rate of the iterative procedure (enhanced by a multigrid technique) is very high for Dirichlet boundary conditions (usually employed for the family of lines which wrap around the blade and the wake), but it is slower when Neumann boundary conditions are used on some boundaries (as it usually happens for the family of lines which intersect the blade and the wake). Compared with the elliptic grid generation techniques in transformed coordinates, this procedure has the advantage that the partial differential equations to be solved are linear and uncoupled. The obvious disadvantage is that the numerical solution of ψ and ϕ requires a grid itself. The final mesh is obtained by interpolating with prescribed ψ and ϕ values the ψ and ϕ solutions on the base grid.

Experiments

Figure 1 shows the blade profile, the cascade arrangement, and the measuring planes downstream of the trailing edge; the blade profile is the mean diameter section of a transonic steam turbine rotor developed by F. Tosi Industriale s.p.a.

The cascade was tested in the CNPM (Centro Nazionale per Ricerche sulla propulsione e sull' Energetica, Milano) transonic

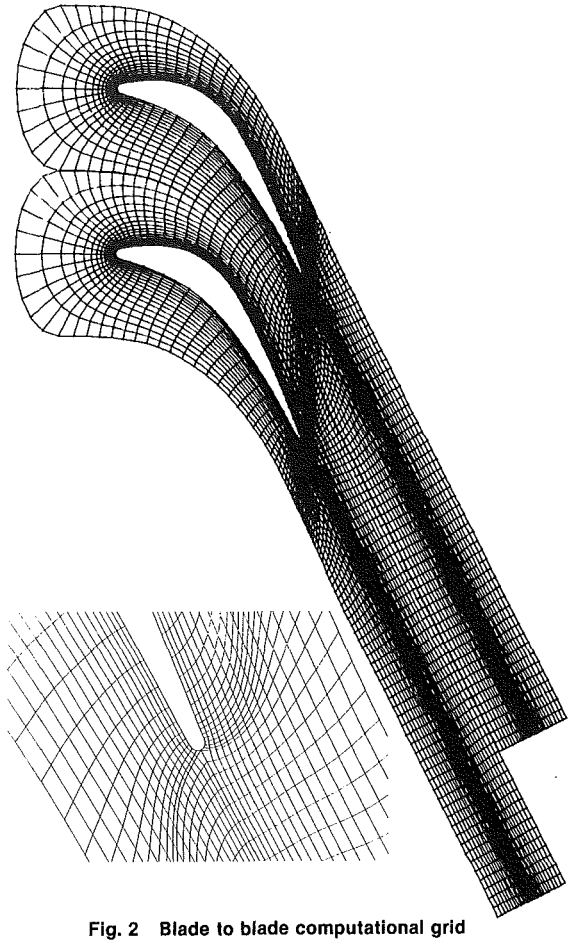

Fig. 2 Blade to blade computational grid

wind tunnel facility at the following isentropic outlet Mach number: M_{2is} = 0.5, 1.02, 1.38; complete measurements were taken in the five planes shown in Fig. 1. The first plane is located upstream of the leading edge and a three hole cobra probe was used to determine the inlet boundary layer profile; the other planes, located at x/b = 1.1, 1.3, 1.5, 1.9 were traversed by means of a miniaturized five hole probe (10 pitchwise traverses at different spanwise locations with 16 points per traverse) providing a detailed three-dimensional picture of the flow field downstream of the cascade. More informations about the experimental apparatus and about the performed tests can be found in Bassi and Perdichizzi (1987).

Results and Discussion

Preliminary Considerations. All of the computations have been carried out on the same C type mesh (192 × 16 × 20 cells), shown in Fig. 2; the large number of cells along the wake has been chosen so as to minimize the numerical diffusion downstream of the trailing edge. Mesh points are properly clustered near the endwall where a good resolution of the entropy gradient is required.

In general, in an inviscid code there is no physical way to impose the Kutta condition for a rounded trailing edge. From a computational point of view this situation can be handled either by modifying the trailing edge geometry or by letting the numerical viscosity to simulate, in some sense, the role of the physical viscosity; the second approach was followed since it yielded the best comparison between the numerical and experimental data. In any event, it was found that the spurious entropy productions at the trailing edge are rather localized and do not seem to disturb the development of secondary vortices.

In transonic nozzles, viscous effects may be important be-

cause of the strong acceleration of the flow throughout the blade channel. The order of magnitude of the viscous contribution to the vorticity can be appreciated by considering a plane accelerating channel with a given velocity profile $u = u(y)$ at each section, neglecting the transverse velocity v. We consider that the total vorticity associated to the boundary layer of thickness δ is

$$\int_0^{\delta} \Omega dl dy$$

where $dl = udt$ is the streamwise displacement of the particle in the time dt. In inviscid flow we can easily evaluate the downstream velocity distribution and verify that the total vorticity remains constant. If viscous effects are taken into account, $u_{wall} = 0$ and we can roughly assume that the velocity profile remains similar as the free stream accelerates; since u and dl are proportional to the free stream velocity, the total vorticity is strongly increased. Note that the local vorticity may be even higher because of the reduction of the boundary layer thickness. However, many experiments (Marchal and Sieverding, 1977) suggest that the secondary flow pattern depends essentially on the inlet total vorticity. So, in a blade row, if the velocity increases strongly, the total vorticity may become very large if compared with the inlet one; however this vorticity is produced near and after the throat, where most of the flow turning has already been experienced and so can not modify the secondary flows. In the turbine cascade discussed here, the whole deflection is accomplished in the entrance region, where the mean velocity is slowly varying and an Euler computation seem therefore meaningful to predict the general flow pattern.

As pointed out by several authors, e.g., Holmes and Warren (1985), this kind of numerical investigations poses severe requirements on the code used; namely:

- the Euler equations must be solved accurately; i.e., the code must exhibit low numerical diffusion and satisfy the physical laws of conservation.
- the mesh-induced errors must be minimized adopting a grid with a smooth variation of the spacing in the logical directions and not too far from being orthogonal.
- as a large number of mesh points have to be used, the code must be computationally efficient.

All the computations were performed on a 32-bit supermini (Gould 67), in single precision, with a peak computing speed slightly lower than 1 Mflops. The three-dimensional computations started from the converged two-dimensional solution at midspan; it took about 60 hours of CPU time for each case to reach a satisfactory level of convergence (RMS(dp/dt) = O (10^{-4})). All the graphic subroutines needed to provide a meaningful representation of the results were developed by the authors.

The comparison between numerical and experimental results refers to three outlet isentropic Mach numbers, namely M_{2is} = 0.5, 1.02, 1.38. The inlet boundary conditions for the computations include the spanwise entropy distribution which produces the experimental inlet velocity profile, shown in Fig. 3.

The main experimental and numerical results are presented in terms of secondary velocities and streamwise vorticity plots. The secondary velocity is defined as the projection of the velocity vector onto a plane normal to the velocity vector at midspan for a given tangential position; the velocity vector at midspan defines the primary velocity direction. The streamwise vorticity Ω_s, i.e., the component of $\nabla \times \mathbf{q}$ in the primary velocity direction, may be evaluated from Ω_x and Ω_y, being Ω_x perpendicular to the primary velocity direction in a linear cascade. The experimental results on each measuring plane allow a direct

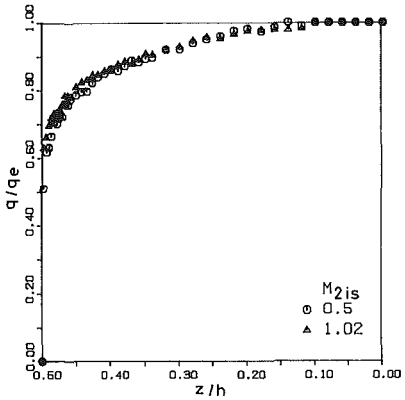

Fig. 3 Inlet boundary layer profile

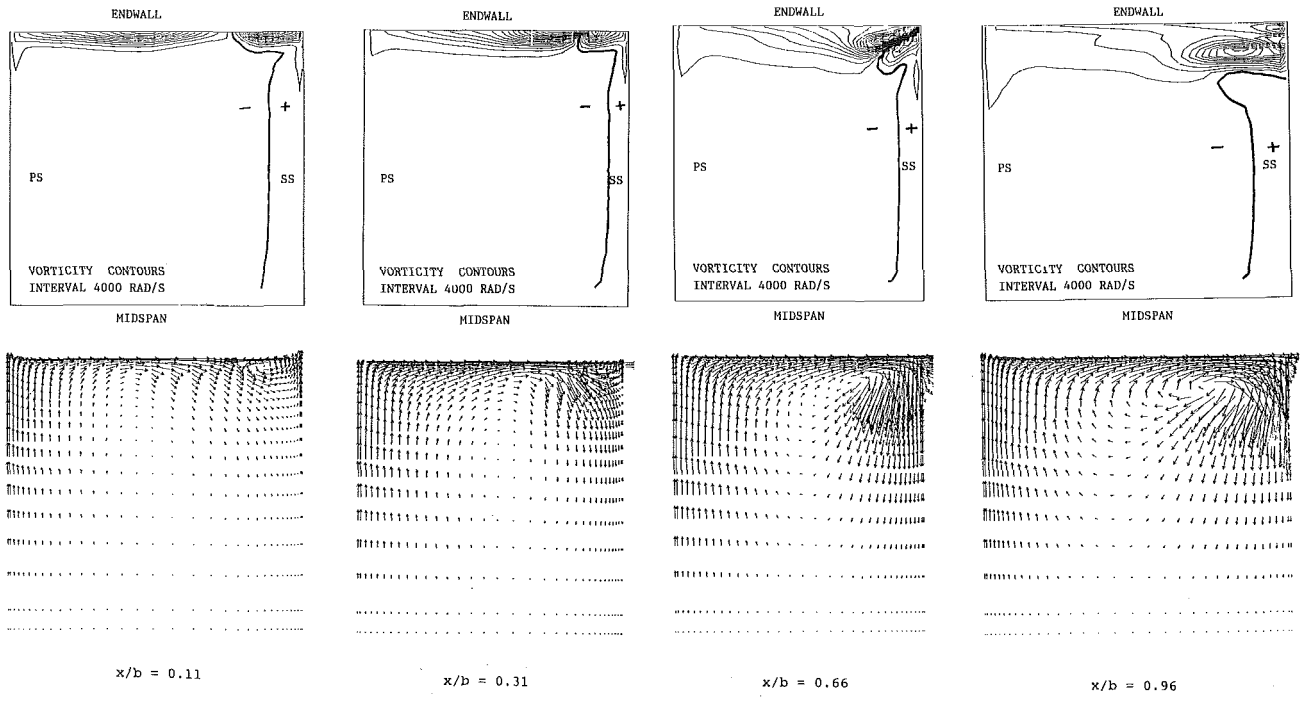

Fig. 4 Secondary flow field and streamwise vorticity inside the blade channel at different axial coordinates

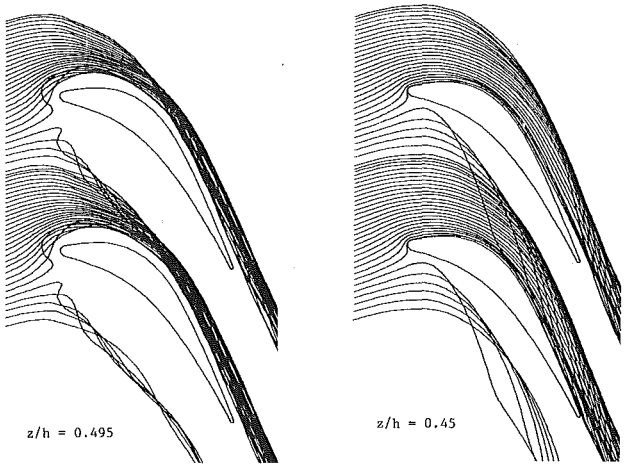

Fig. 5 Projection on $x-y$ planes of the streamlines starting at z constant

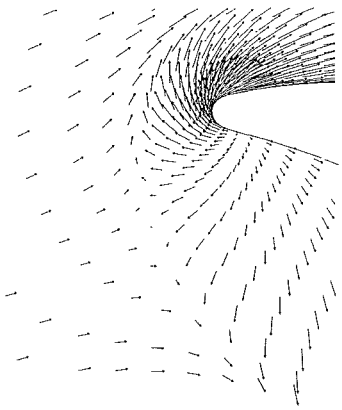

Fig. 6 Enlargement of the blade to blade velocity field close to the endwall

estimation of Ω_x, but Ω_y must be evaluated in an indirect way; following the indications of Gregory-Smith et al. (1987), use has been made of the z component of the Crocco relation with the assumption of constant total enthalpy:

$$\Omega_y = \frac{1}{u}\left(v\Omega_x + \frac{c^2}{\gamma}\frac{\partial(\ln p_t)}{\partial z}\right)$$

The computational results in the measuring planes downstream of the trailing edge are presented with the same discretization of the experimental data and the streamwise vorticity is calculated as for the experimental results.

The test case at $M_{2is} = 1.02$ has been chosen as the most representative for a detailed discussion.

Numerical and Experimental Results: $M_{2is} = 1.02$. Inside the blade channel only computational results are available because, in transonic regimes, meaningful measurements within the blade passage can not be obtained by using mechanical probes which would induce large blockage effects. Figure 4 shows the onset and the development of secondary flows in tangential planes at 11, 33, 66, and 96 percent of the chord from the leading edge. From the secondary velocity vectors and from the streamwise vorticity contour plots, it appears clearly that the passage vortex is dominant and merges together with the pressure branch of the horseshoe vortex. Moving under the influence of the pressure gradient, this lump of fluid progressively overcomes the suction side branch of the horseshoe vortex.

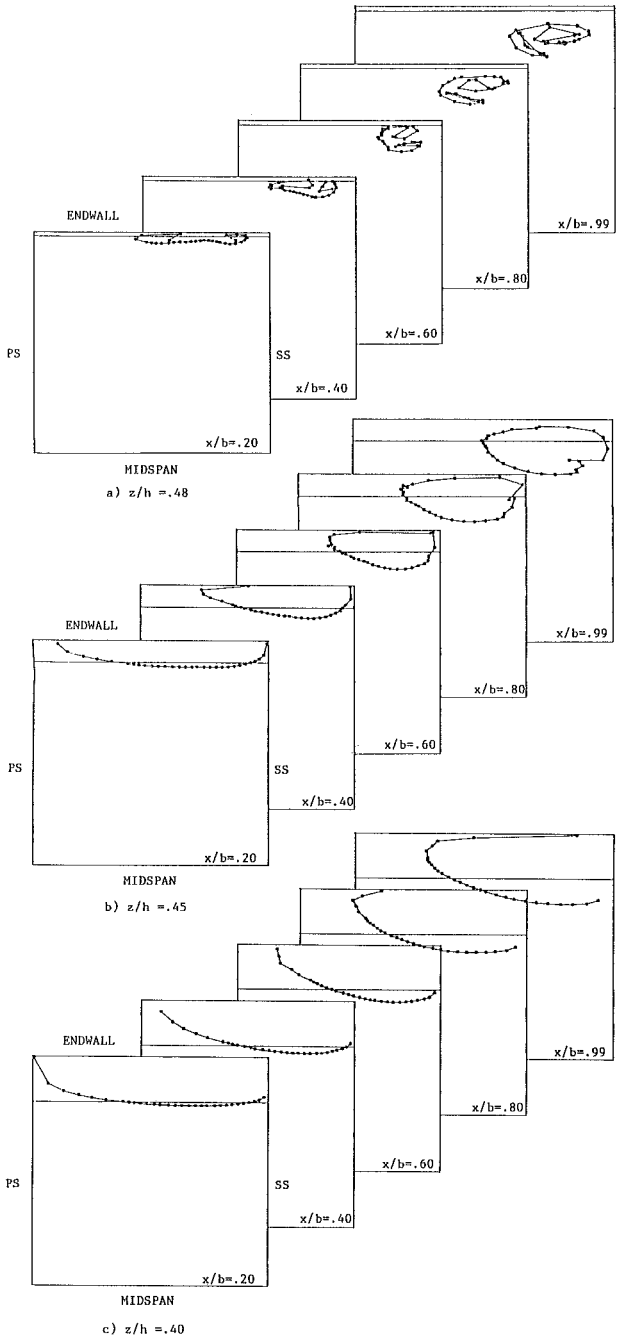

Fig. 7 Evolution of the blade to blade surfaces inside the blade channel for different inlet spanwise positions

Figures 5 and 7 are very interesting pictures which show how some Bernoulli surfaces are influenced by the vortical motion and roll up moving from the inlet toward the throat. In situations like these, it appears questionable to use a theoretical approach which supposes that the Bernoulli surfaces remain flat or that the distortion of the so called s_1 surfaces is limited. In Fig. 6 are shown the velocity vectors near the leading edge at the endwall ($z/h = 0.495$); one can easily note the typical saddle point and separation line.

Streamwise vorticity vectors at the endwall, plotted in Fig. 8, confirm what suggested in the previous section, i.e., that streamwise vorticity is mainly produced in the entrance region.

In Figs. 9 and 10 are presented the secondary velocity vectors and the streamwise vorticity distribution in the planes down-

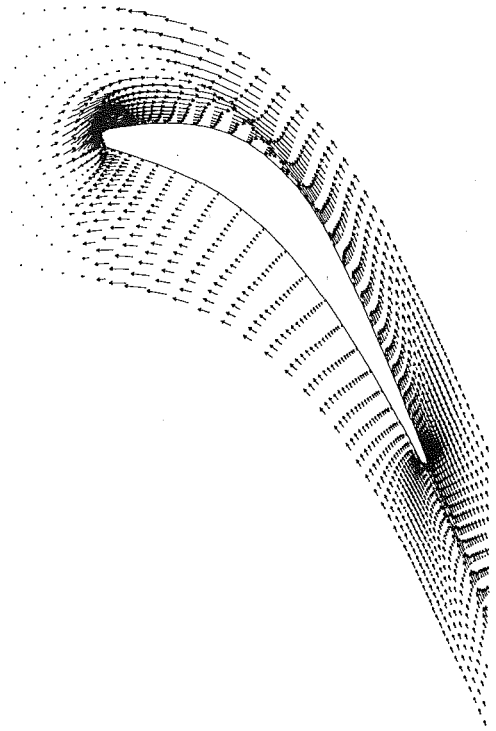

Fig. 8 Streamwise vorticity vectors at the endwall

stream of the trailing edge, respectively, for the experimental and numerical cases.

The measured secondary velocities show the typical vortex configuration, and the following features can be clearly detected:

- the large clockwise flow rotation on the suction side of the wake corresponds to the passage vortex.
- the counter-clockwise rotation across the wake reveals the presence of the trailing shed vortex.
- in the upper part of the wake, close to the endwall, the corner vortex can be noticed as well.

The location of the above vortices is also indicated by the vorticity plots: the peak of negative vorticity is related to the passage vortex, while the two other peaks of positive vorticity correspond to shed and corner vortices. From the development of the above plots downstream of the trailing edge one can detect the following trends:

- both passage and shed vortices reduce their intensity because of shear stresses.
- the passage vortex is stretched in pitchwise direction under the action of endwall crossflow and shed vortex.
- the shed vortex widens considerably in pitchwise direction.
- the corner vortex is also stretched by the endwall crossflow.

The effects of the viscosity on the streamwise vorticity (see Fig. 9) are clear: going downstream, gradients and peak values become smaller, both for positive and negative cores.

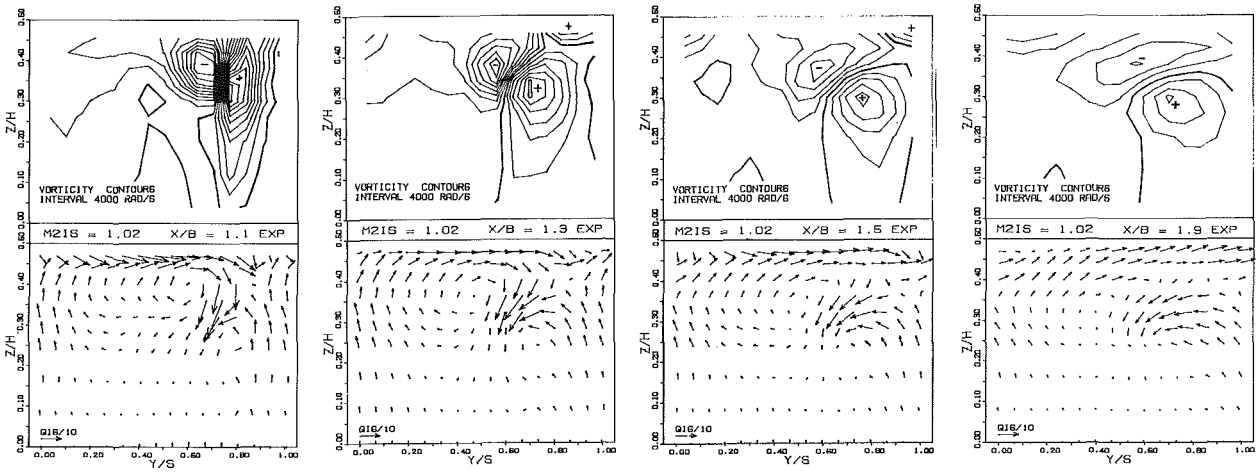

Fig. 9 Secondary velocities and vorticities downstream of the trailing edge. Experimental results for M_{2is} = 1.02.

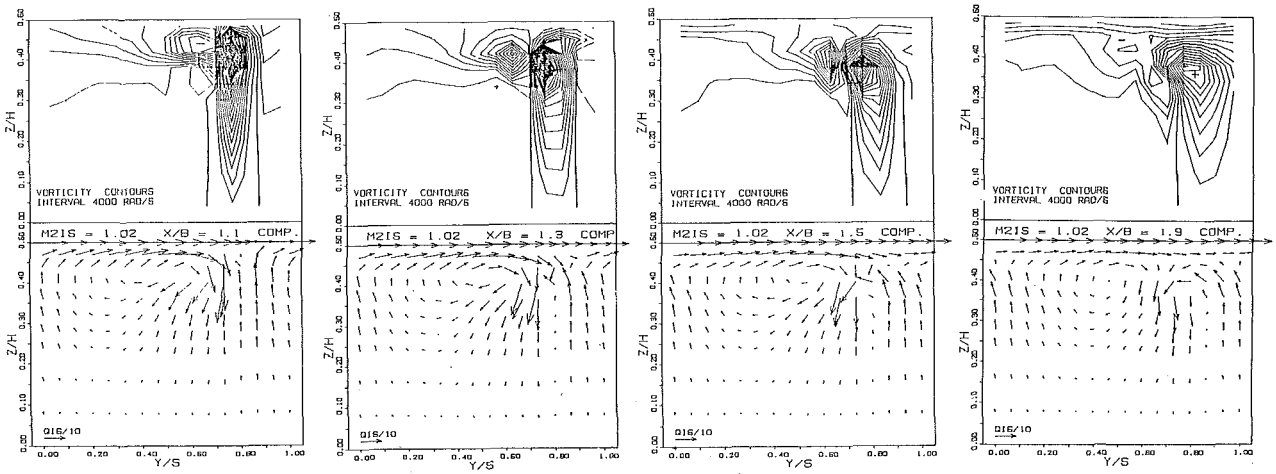

Fig. 10 Secondary velocities and vorticities downstream of the trailing edge. Computed results for M_{2is} = 1.02.

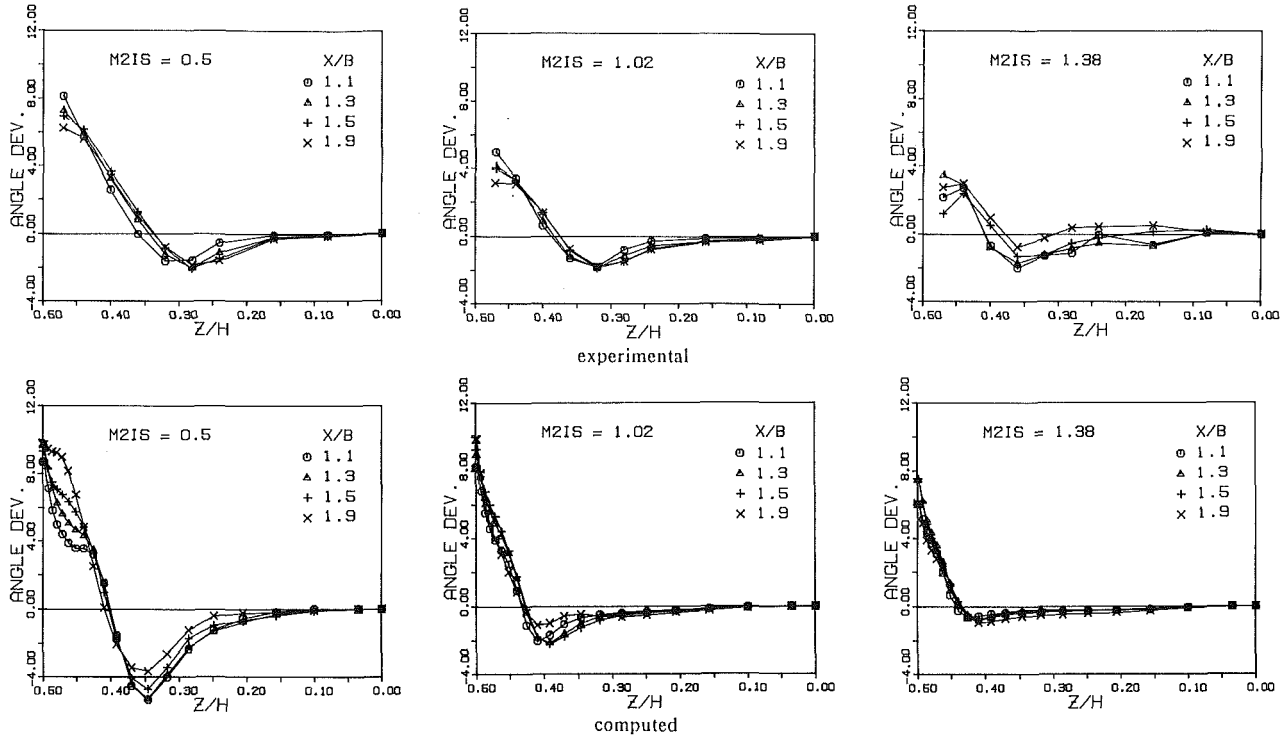

Fig. 11 Experimental and computed deviation angles for different Mach numbers and different axial positions downstream of the trailing edge

Let us now compare the numerical results with the experimental ones in the first plane downstream of the cascade (x/b = 1.1). The numerical results show, as expected by an inviscid calculation, only the presence of the predominant flow rotation connected with the passage vortex, and the trailing filament vortices along the wake extent; no corner vortex is present since, as well known, it is due to the interaction of endwall and blade suction side boundary layers.

The secondary velocity vectors give a picture of the secondary flow field very similar to the experimental ones everywhere but near the endwall, where the corner vortex takes place and viscosity effects are important. As shown by the vorticity distributions, the passage vortex intensity is in good agreement with experiments, but the location of the related vorticity core is found to be closer to the endwall (z/h = 0.43 against z/h = 0.38). Larger vorticity values are found in the computation, especially in the region where passage and shed vortices interact producing high secondary velocities; this difference is also related to the presence of shear stresses that in the real fluid contribute to reduce such secondary velocities.

Moving downstream, the passage vortex shifts toward the midspan in agreement with experiments; this shows that this well-known feature (Moore and Adhye, 1985) is mainly an inviscid effect. Nevertheless the passage vortex does not appear to be stretched in pitchwise direction as in the real fluid flow. A clear diffusion of vorticity is also evident, but it is much lower than in the experimental case; this is right in an inviscid calculation since, except for a certain amount of numerical diffusion, no mechanism of reduction of the overall streamwise vorticity is present.

Pitchwise mass averaged secondary flow angle deviations are presented in Fig. 11; the maximum of the underturning angle, in the numerical case, is found to be nearer the endwall, consistent with the passage vortex location; moreover it is quite close to the experimental value in all of the considered planes but for x/b = 1.9, where the solution is probably affected by the imposition of the boundary conditions. Going downstream, the measured overturning at the wall decreases because of the action of the corner vortex and of the endwall crossflow decay (as shown in Fig. 9); the numerical results show instead the maximum overturning at the wall since the above effects can not be taken into account by an Euler code.

Table 1 Secondary kinetic energy downstream of the trailing edge

x/b		1.1	1.3	1.5	1.9
SKE exp.	0.50	.0041	.0033	.0029	.0020
	1.02	.0023	.0016	.0014	.0010
	1.38	.0038	.0036	.0016	.0014
SKE comp.	0.50	.0068	.0058	.0049	.0043
	1.02	.0027	.0025	.0022	.0017
	1.38	.0016	.0015	.0014	.0013

The mass averaged overall secondary kinetic energy, defined as

$$\mathrm{SKE} = \frac{\frac{v_S^2}{2} + \frac{w_S^2}{2}}{\frac{q_{2is}^2}{2}}$$

is evaluated in the considered planes (see Table 1). In the first plane the computed value of SKE is of the same order of the measured one, confirming that actually secondary flows originate mainly from the incoming vorticity. More surprising is the decay of the computed SKE in the downstream planes; indeed in absence of viscosity secondary kinetic energy can be reduced only by the numerical diffusion and by the downstream boundary condition.

Mach Number Influence. Let us now see which effects arise varying the expansion ratio. In the sequence of Figs. 12 and 13 some plots, as in the above discussion, are shown for M_{2is} = 0.5, 1.38. The main features of the vortex structure and of the development downstream of the cascade are similar; nevertheless some differences are worth pointing out. As the Mach number increases, the secondary flow phenomena appear very clearly to be confined nearer the endwall; the calculated vorticity core in the last plane (x/b = 1.9) is located at z/h = 0.28 for the low Mach number and at z/h = 0.41 for the

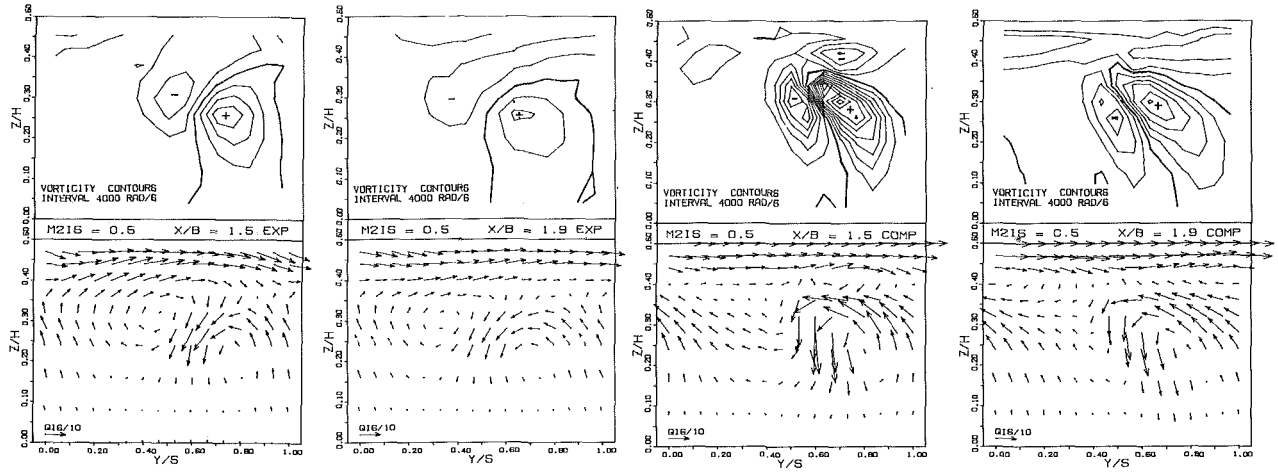

Fig. 12 Secondary velocities and vorticities downstream of the trailing edge. Experimental and computed results for M_{2is} = 0.5.

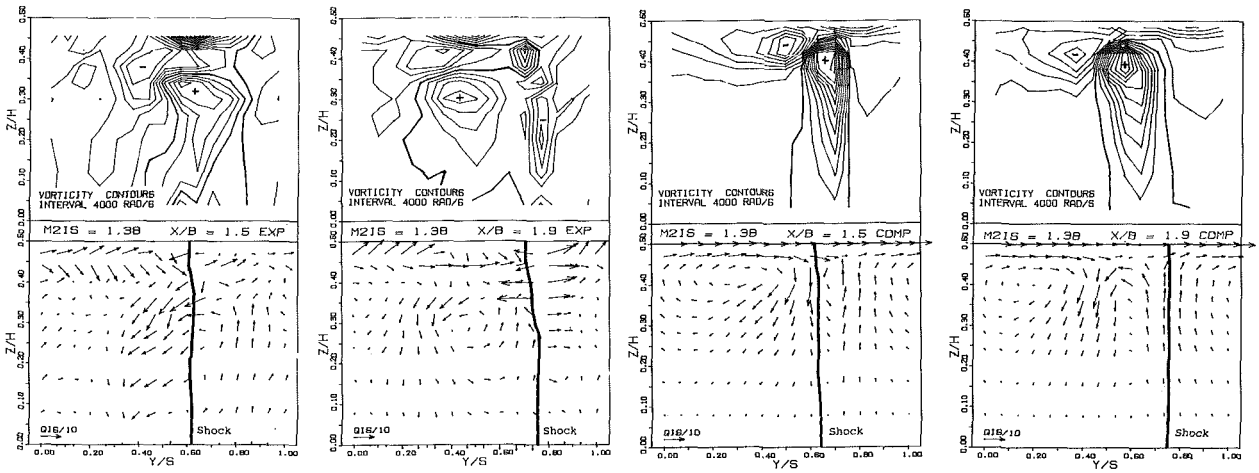

Fig. 13 Secondary velocities and vorticities downstream of the trailing edge. Experimental and computed results for M_{2is} = 1.38.

highest Mach number. This seems to be the main effect produced by the flow compressibility and it is interesting to notice that it is found both in the experimental and theoretical results. Even if in the numerical case this trend is much more emphasized, these results prove that this is essentially a convection dominated phenomenon and that an inviscid computation, at least from a qualitative point of view, can predict this flow behavior. This feature is related to a different primary velocity distribution along the span at the outlet: increasing the Mach number results in smaller primary velocity differences between midspan and endwall.

In the experimental part of Fig. 13 one can notice that the shock is not purely two-dimensional, but it bends slightly in tangential direction approaching the endwall. This explains the sudden appearance of larger tangential secondary velocities. The bending of the shock might be related to the shed vortex and its interaction with the endwall boundary layer as it turns in agreement with the underturning deviation angle. No definitive comment can be made about the influence of the shock on the vorticity patterns.

Analyzing the numerical results for the subsonic case one can notice that the computed secondary velocity plots are dominated by the shed vortex which extends over a wider region if compared with the experiments; higher secondary velocities take place in the interaction region of the two vortices and the passage vortex appears heavily distorted. This appreciable discrepancy with experiments, not observed in the case at M_{2is} = 1.02, might be related to the artificial viscosity dissipation produced in the trailing edge region.

In the supersonic case, computations show a secondary velocity field similar to that at M_{2is} = 1.02, but the passage vortex locates farther from the suction side of the wake causing generally lower vorticity values. Notice that the flow field is mainly influenced by the presence of the passage vortex, while in the real fluid flow most of the vorticity is related to shed and corner vortices. In the last plane the passage vortex has almost disappeared and can not be easily identified, so we can presume that the viscosity at high expansion ratios might play an important role in the passage vortex decay and in the larger importance assumed by the shed vortex.

Increasing the Mach number leads to a decrease in the passage vortex strength but this is due only to the fact that the velocities are normalized with respect to the isentropic outlet condition; the variation of the latter is large, while at the same time the inlet vorticity undergoes small changes (not at all for choked flows). In a nutshell, secondary velocities and kinetic energy, in absence of viscosity, are governed by the incoming boundary layer and do not vary together with the primary flow.

According to this behavior, in the numerical case there is a clear reduction of the deviation angles, both overturning and underturning (see Fig. 11), when the expansion ratio is raised. Referring to the measurements, two points are worth mentioning:

- the above trend is found only for the overturning angles, while the underturning ones appear almost independent from the Mach number.

- the overturning near the wall decreases much more at high Mach numbers.

The first effect may be explained with the already noticed importance gained by the shed vortex; for the second one the same consideration applies to the corner vortex.

The secondary kinetic energy reduces at the highest expansion ratios as it is referred to the outlet dynamic head, but it remains almost constant if referred to the inlet kinetic energy. For $M_{2is} = 1.38$ the experimental data show larger values of SKE because of the shock induced distortion of the secondary flow field.

Finally, no appreciable difference occurs with the separation line and the saddle point position, as should be expected.

Concluding Remarks

From the above mentioned results, the following conclusions can be drawn:

- Euler codes may be useful in understanding most of the secondary flow phenomena, at least up to the investigated expansion ratios.
- the Mach number strongly influences the spanwise location of the passage vortex and the magnitude of the overturning and underturning angles.
- to obtain good quantitative agreement with measurements, especially downstream of the blade channel, one must turn to viscous turbulent computations as believed by Povinelli (1984).

Acknowledgments

The research was supported by C.N.R., under PFE-2 Grant No. 86.00758.59. The authors wish to thank Franco Tosi Industriale s.p.a. which provided the blade cascade.

References

Arts, T., 1985, "Effects of Tip Endwall Contouring on the Three-Dimensional Flow Field in an Annular Turbine Nozzle Guide Vane: Part 2—Numerical Investigation," ASME Paper 85-GT-108.

Bassi, F., and Perdichizzi, A., 1985, "Influenza del Numero di Mach sui Flussi Secondari a Valle di una Schiera ad Alta Deflessione," *Proceedings 50th ATI Congress.*

Bassi, F., and Perdichizzi, A., 1987, "Secondary Flow Development Downstream of a Transonic Cascade," *Proceedings 1987 Tokio Gas Turbine Congress.*

Bassi, F., and Savini, M., 1986, "Transonic Three-Dimensional Inviscid Calculations in Turbomachines," *Transonic and Supersonic Phenomena in Turbomachines*, AGARD CP 401.

Gregory-Smith, D. G., Graves, C. P., and Walsh, J. A., 1987, "Growth of Secondary Losses and Vorticity in an Axial Turbine Cascade," ASME Paper 87-GT-114.

Hawthorne, W. R., 1955, "Rotational Flow Through Cascades," *Jour. Mech. & Appl. Math.*, Vol. 3.

Holmes, D. G., and Warren, R. E., 1985, "Detailed Studies of Inviscid Secondary Flows," *Three Dimensional Flow Phenomena in Fluid Machinery*, ASME FED, Vol. 32.

Jameson, A., Schmidt, W., and Turkel, E., 1981, "Numerical Solutions of the Euler Equations by Finite Volume Methods Using Runge-Kutta Time-Stepping Schemes," AIAA Paper 81-1259.

Langston, L. S., Nice, M. L., and Hooper, R. M., 1977, "Three Dimensional Flow Within a Turbine Blade Passage," ASME *Journal of Engineering for Power*, Vol. 99, No. 1.

Marchal, P., and Sieverding, C. H., 1977, "Secondary Flows Within Turbomachinery Bladings," *Secondary Flows in Turbomachines*, AGARD CP 214.

Moore, J., and Adhye, R. Y., 1985, "Secondary Flows and Losses Downstream of a Turbine Cascade," ASME Paper 85-GT-64.

Moore, J., and Moore, J. G., 1985, "Performance Evaluation of Linear Turbine Cascades Using a Three-Dimensional Viscous Flow Calculation," ASME Paper 85-GT-65.

Povinelli, L. A., 1984, "Assessment of Three-Dimensional Inviscid Codes and Loss Calculations for Turbine Aerodynamic Computations," ASME Paper 84-GT-187.

Sieverding, C. H., 1984, "Recent Progress in the Understanding of Basic Aspects of Secondary Flows in Turbine Blade Passages," ASME Paper 84-GT-78.

Yamamoto, A., and Yanagi, R., 1985, "Production and Development of Secondary Flows and Losses Within a Three Dimensional Turbine Stator Cascade," ASME Paper 85-GT-217.

J. S. Ervin[1]
Graduate Student.

N. V. Suryanarayana
Professor.

Hon Chai Ng
Graduate Student.

Mechanical Engineering,
Engineering Mechanics Department,
Michigan Technological University,
Houghton, MI 49931

Radial, Turbulent Flow of a Fluid Between Two Coaxial Disks

An experimental study to determine the flow characteristics of an incompressible fluid in turbulent, radially outward flow between two coaxial, stationary disks was conducted employing a split film anemometer probe. Instantaneous velocity components in the radial and axial directions were measured; from these measurements, average velocity profiles, turbulence intensities, Reynolds stresses, energy spectra and probability density functions for the fluctuating components were computed. It is observed that the law of the wall may not be applicable everywhere. A criterion established earlier for reverse transition to laminar flow may be valid with a value of the constant smaller than suggested. A few other aspects of the flow are also discussed.

Introduction

Radial, outward flow of a fluid between stationary or rotating coaxial disks has many industrial and scientific applications such as in radial diffusers, centrifugal compressors and rotating heat exchangers. Such flows are quite complex. The pressure gradient may be either positive (for small values of the radius) or negative depending on the radial location. A positive pressure gradient, resulting from a decrease in the velocity with increasing radius, may lead to separation and secondary flows. Further, a flow that starts as turbulent flow may revert to laminar flow at some distance downstream. If one or both the disks are rotating, the radial velocity decreases with radius but the tangential velocity increases and in such a case, the conditions under which the flow will be turbulent or laminar have not been established. It is, therefore, clear that such a flow has many interesting and fascinating flow aspects. This paper is an attempt to partially understand such flows and presents experimental results of fluid flow measurements made with a split film anemometer probe.

Background

There have been many studies dealing with laminar flows—for example, references [1-10]. But there are very few studies dealing with turbulent flows. Moller [7] obtained approximate solutions for the turbulent and laminar radial pressure distribution using integral methods; he suggested that reverse transition to laminar flow would occur at a critical Reynolds number ($\mathrm{Re} = \dot{m}/\pi\, r\, \mu$) of 2000. In an analytical study, Peube [9] concluded that for recirculation to occur, the velocity profile should have a point of inflection. Kreith [10] and Patrat [11] have attempted to define the criteria to determine the reverse transition to laminar flow. One of the conclusions is that if the laminar velocity profile has a point of inflection, the flow will be turbulent. From his experimental results, Garcia [12] concluded that the radial flow is inherently oscillating. More recent studies by Mochizuki and Yang [13] confirm the oscillating nature of the flow due to the possibility of vortex shedding. Tabatabai and Pollard [14] have reported experimental results of mean velocity profiles and other quantities of interest in turbulent flows; their measurements were at larger values of radius than in our studies. Their results are briefly discussed under results and discussions.

From the brief review given, it is clear that there have been a fair number of studies on laminar flows but very few, analytical or experimental, on turbulent flows. The purpose of this paper is to present the experimental results of a study to determine some of the fluid mechanical aspects of such a flow.

To describe the turbulent flow, the instantaneous velocity components in the radial and axial directions of a fluid in radial, outward flow between two stationary, coaxial disks were measured. From these measurements, velocity profiles, turbulence intensity, turbulent stresses, energy spectra and probability density functions of the fluctuating components were obtained. Hot wire anemometer probes in the X-configuration have been successfully used to measure turbulence quantities. But with a gap of 6 mm between the disks, the finite dimensions of such probes precluded their use as a meaningful spatial resolution would not be possible. It was decided to employ a split film anemometer probe for the study. A brief description of the operation of the split film sensor is given in the Appendix.

Experimental Apparatus and Procedure

Figure 1 is a schematic of the experimental set up. Compressed air from the building supply line passed through a pressure regulator (1) to an air reservoir (2) through a second pressure regulator, an orifice flow meter (3) and entered the upper disk through a 1.52 m long, 25 mm diameter tube. This tube ensured that the velocity profile was fully developed before the air entered the upper disk. The pressure regulators at the inlet and exit to the air reservoir minimized the variation in the exit pressure such that the difference in the pressure across the orifice plate for any given flow rate in the range considered was less than one percent of the average pressure difference for that flow rate. The pressure difference across

[1] Present address: Department of Mechanical Engineering, The University of Michigan, Ann Arbor, MI 48109.

Contributed by the Fluids Engineering Division for publication in the JOURNAL OF FLUIDS ENGINEERING. Manuscript received by the Fluids Engineering Division July 6, 1987.

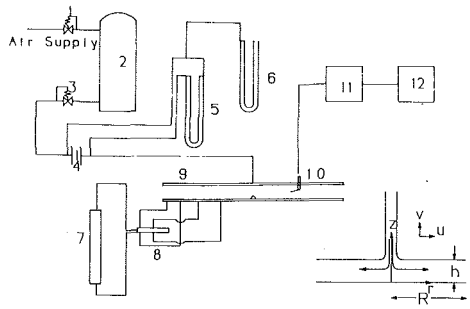

1,3 Pressure regulators
2 Air reservoir
4 Orifice meter
5,6,7 Manometers
8 Valve chest
9 Coaxial disks
10 Anemometer probe
11 Anemometer
12 Norland oscilloscope

Fig. 1 Schematic of apparatus

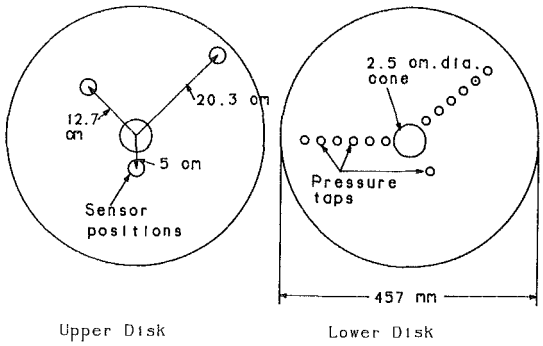

Fig. 2 Coaxial disks

the orifice plate was measured by a Wallace Tiernan manometer (5).

The 25 mm tube supplying the air was flared to 50 mm diameter in the upper disk. The upper disk was made of 13 mm thick steel plate, ground to a smooth finish. Three 6.4 mm diameter holes, 120 deg apart permitted probe insertion between the disks. These openings were at radii of 51, 127, and 203 mm. Only one probe was used at a time, and the two openings not in use were closed with smooth plugs.

The lower disk was made of 10 mm thick aluminum plate lined with 10 mm thick plexiglass. The low thermal conductivity plexiglass was used to reduce the uncertainty resulting from the near wall corrections for the probes [15]. Sixteen 1.6 mm diameter pressure taps were provided in the lower disk; their locations are shown in Fig. 2. A circular cone, 25.4 mm base diameter and 5 mm height, whose position could be adjusted, was placed at the center of the disk. Uniform flow around the periphery of the disks was obtained by adjusting the position of this cone. The gap between the disks was maintained at 6.1 ± 0.3 mm.

The static pressure before the orifice plate was measured by a U-tube mercury manometer (6) and the differential pressure by the Wallace and Tiernan manometer (5). A micromanometer (7) with a liquid of 0.827 specific gravity was used to measure the radial pressure differences in the disks.

The velocities were measured by a TSI model 1287 AF split film probe which was inserted in one of the holes in the upper disk and attached to a micrometer traversing mechanism. The signal from the probe was processed through a TSI model 1054B constant temperature anemometer (11) and model 1057 signal conditioner. A Norland 3001 multichannel digital oscilloscope (12) digitized the anemometer output. Because of the construction of the 1287 AF probe (Fig. 1A in the Appendix), the sensor could be traversed only through the lower half of the gap. A traverse through the entire gap (by horizontal penetration), close to the exit from the disks, was made utilizing a model 1288 CG split film anemometer probe; when this probe was used the upper disk was also lined with a 10 mm thick plexiglass disk. The split film sensor was cylindrical with a diameter of 0.006 inch and a length of 0.19 in.

Prior to acquisition of experimental data, the orifice plate was calibrated by computing the mass flow rates simultaneously from measurements across the orifice plate and from velocity profiles (obtained through a split film probe) at the end of a 2 m long, 25 mm diameter tube. The average difference in the mass flow rates computed by the two methods was 3.3 percent with a maximum of 5 percent. The calibration of the probes used to acquire data was checked prior to their use. The change in calibration was less than 0.8 percent for any of the mass flow rates for any of the angles between two consecutive testing days. Azimuthal uniformity of the flow was ensured by measuring the maximum velocity of the air around the periphery of the disks with a TSI 1650 portable anemometer. The position of the cone located at the center of the lower disk was adjusted to minimize the variation in the maximum velocities; they were within ± 4 percent of the average maximum with a few differing by as much as 7 percent.

Nomenclature

E_1, E_2 = voltages across probe films one and two
h = spacing between the disks
k = E_1/E_2
$\dot{m}$ = mass flow rate
P = pressure
R = radius of the disks
r = coordinate in the radial direction
r_c = critical radius for reverse transition to laminar flow
r^+ = dimensionless radius, r/R
Re = Reynolds number at exit, $h\ U_{exit}/\nu$
Re_d = local Reynolds number, $h\ U/\nu = Re/r^+$
$R(\tau)$ = autocorrelation functon
t = time
U = average velocity $= \dfrac{\dot{m}}{\rho\ 2\ \pi r h}$
U_τ = friction velocity
U_n = fluid velocity normal to sensor
u^+ = dimensionless velocity, $\tilde{u}/\tilde{u}_{max}$ or $\tilde{u}/U_\tau$
u = instantaneous radial velocity component
$\tilde{u}$ = time averaged radial velocity component
u_{max} = time averaged maximum radial velocity
$\overline{u'v'}/\tilde{u}^2_{max}$ = normalized Reynolds stress
y^+ = dimensionless wall coordinate, zU_τ/ν
z = axial distance from the disk of impact
z^+ = dimensionless axial distance, z/h
μ = dynamic viscosity
ν = kinematic viscosity
ρ = density
θ = angle between the plane of the split and the normal velocity vector
τ = time lag, shear stress

When the adjustments were completed, the location of the 1287 AF probe (with a protecting pin) relative to the lower disk was determined by lowering the probe on to a precision 0.1 mm thick steel shim stock laid flat on the lower disk. Contact between the protecting pin and the shim stock was indicated by the sudden drop in the electrical resistance between the probe support and the shim stock. This established the position of the protecting pin and in turn that of the sensor which was 0.13 mm from the tip of the pin. The probe holder was attached to a traversing mechanism with a micrometer which was used to determine the sensor location thereafter. The 1288 CG probe was used in the two outer radial positions. As this probe is straight, it could be inserted in the gap horizontally and traverse the entire gap. A light behind the probe permitted a view of the distance between the plate and the probe. The probe was lowered till this light was no longer visible. This position of the probe defined the location of the sensor relative to the lower disk.

After defining the location of the probe, the flow was started and checked for azimuthal uniformity. Velocity measurements were made:

- at four radial locations of 38.9 mm, 115.1 mm, 212.6 mm, and 228.6 mm corresponding to dimensionless radii of 0.17, 0.5, 0.93, and 1.0, respectively.
- at five mass flow rates of 0.00488 kg/s, 0.0072 kg/s, 0.00886 kg/s, 0.0106 kg/s and 0.0118 kg/s corresponding to R_e of 365, 538, 662, 792, and 881.

Data Reduction

The instantaneous velocity component normal to the axis of the probe U_n and the angle between this vector and the plane of the split were determined from:

$$U_N = (((E_1^2 + E_2^2 k^2) - A)/B)^{1/m} \quad (1)$$

$$\theta = \sin^{-1}((E_1^2 - k^2 E_2^2)/C\ U_N^n) \quad (2)$$

where A, B, C, m, n, and K are constants determined from calibration. If θ and U_N are determined, then the instantaneous velocity components in the radial and axial directions are given by $U_N \cos\theta$ and $U_N \sin\theta$, respectively. From these instantaneous values, the time averaged velocity components and the instantaneous fluctuations can be determined.

For a meaningful interpretation of the average and fluctuating components, a prerequisite is the establishment of an appropriate averaging time and sampling interval. The Norland oscilloscope was capable of storing 32,000 digitized signals per channel (in two channels) with a minimum sampling interval of 10 micro-seconds. From an energy spectrum it was concluded that the frequencies were significantly less than 1000 Hz. A sampling frequency of 2000 Hz was adequate for the study.

The averaging time was established from the running average value of the velocity. It was found that a minimum of 7000 data points were required at smaller radii, decreasing to about 3000 data points at exit. In the experiments 20,480 data points with a sampling interval of 500 μs were processed for each run. Stationarity was tested by taking the average of 20 equal segments of 32,000 data points and comparing them to the average of the entire set [16]. The test showed that stationarity can be accepted at the 95 percent confidence level.

The uncertainties associated with the variables were estimated by the method suggested by Kline and McClintock [21]. The uncertainties associated with the radial mean, instantaneous and fluctuating components were four percent, those related to axial velocity components were much higher of the order of 20 percent. Mass flow rates are within 3.5 percent and Reynolds numbers within 5.3 percent. The uncertainty due to the effect of the solid wall on the signals is not known.

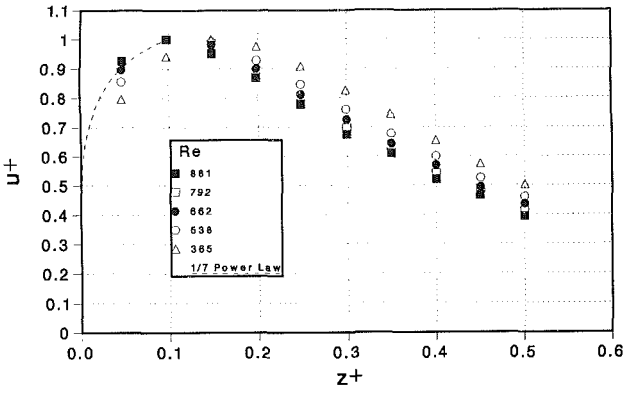

Fig. 3 Radial velocity profile $r^+ = 0.17$

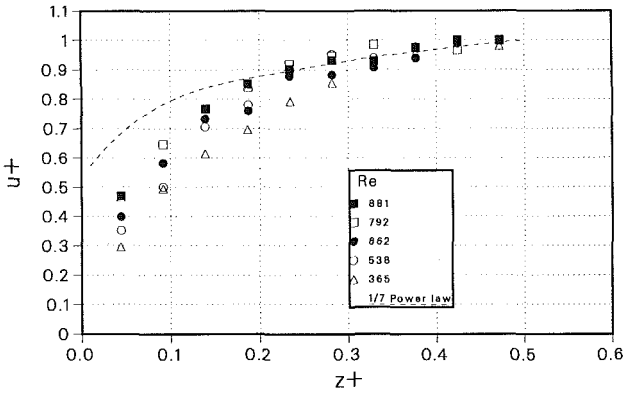

Fig. 4 Radial velocity profile $r^+ = 0.5$

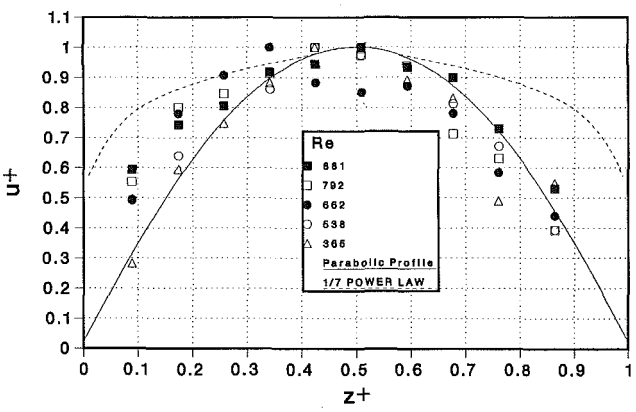

Fig. 5 Radial velocity profile $r^+ = 1$

Results and Discussion

The minimum Reynolds number with the diameter of the inlet tube as the characteristic length was 13,250. With a length/diameter ratio of 60, the flow at entry to the disks may be assumed to be turbulent with a fully developed turbulent velocity profile.

The radial time averaged velocity profiles are shown in Figs. 3–5 at different radii. The 1/7 power law velocity profile is shown superimposed. The skewness of the velocity profile near the entrance, toward the lower disk may be expected from the velocity profile at inlet and the pressure gradient associated with the change in the direction of flow. Close to the exit from the disks, at lower Reynolds number, the velocity profile departs from the 1/7th power law and approaches a parabolic velocity profile. Tabatabai and Pollard [14] have reported results of a similar study. Their measurements were

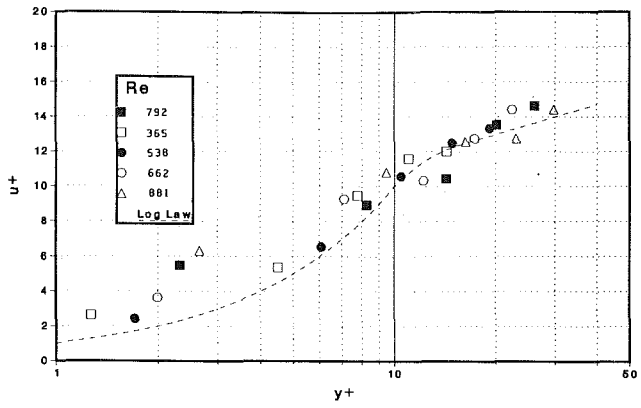

Fig. 6 Universal velocity profile $r^+ = 0.93$

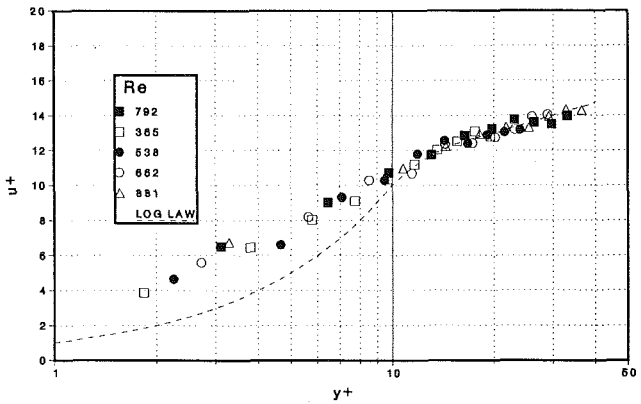

Fig. 7 Universal velocity profile $r^+ = 0.5$

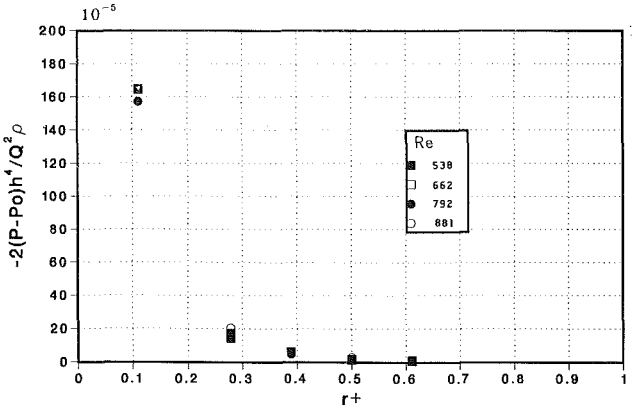

Fig. 8 Radial pressure distribution

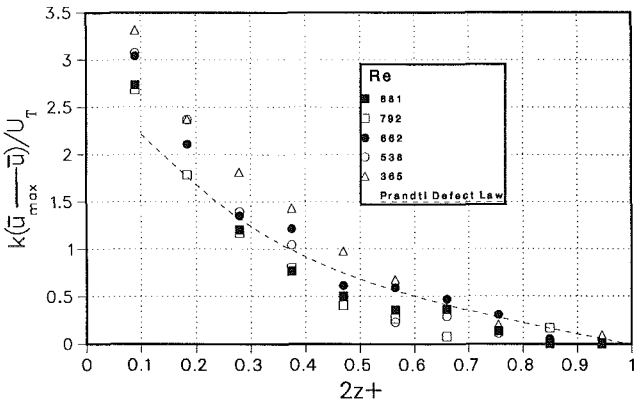

Fig. 9 Velocity defect profile $r^+ = 0.5$

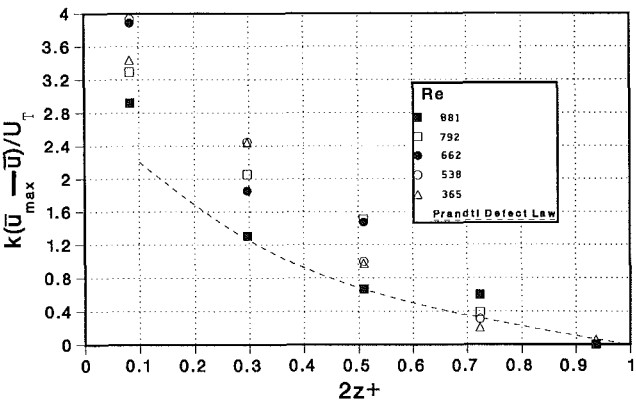

Fig. 10 Velocity defect profile $r^+ = 0.93$

at radii from 300 mm to 600 mm with a gap of 10 mm, compared with radii from 38 mm to 225 mm with a gap of 6 mm in our study. The local Reynolds number (Re_d) were between 284 and 4876 compared with the range of 365 to 5180 in our study. The mean velocity profile of Tabatabai and Pollard also followed the 1/7th power law at high Reynolds numbers and closer to the parabolic velocity profile at lower Reynolds numbers. As they measured the velocity profiles at larger radii, farther away from the inlet than in our study, their velocity profiles do not show any skewness but are symmetric about the center plane.

Figures 6 and 7 compare the velocity profiles with the two-layer universal velocity profile.

$$u^+ = y^+ \qquad y^+ < 11.5$$

$$u^+ = 2.5 \ln y^+ + 5.5 \qquad y^+ > 11.5$$

Shear stresses were not measured; the friction velocity, that best fits the data, was determined from a nonlinear regression analysis for each run. The figures indicate that the law of the wall may be a reasonable representation for larger values of the radius. The universal velocity profile used in the comparison are valid for zero pressure gradient, a condition approximately satisfied at large radii. But at small radii, there is a significant pressure gradient as shown in Fig. 8. Measurements reported in [14] confirm these trends. The mean velocity profiles show reasonable agreement with Prandtl's velocity defect law expressed by:

$$K \frac{\bar{u}_{\max} - \bar{u}}{U_\tau} = -\ln(2\, z^+)$$

Figures 9 and 10 show comparison of the velocity defect law at a dimensionless radii of 0.5 with the constant K set at 0.36. The friction velocity computed for the law of the wall was also used for the velocity defect law. These figures show that the velocity profiles follow the velocity defect law for radii larger than 0.5. But at $r^+ = 0.93$, except at the highest Reynolds number, the departure from the defect law is quite significant. It may be, as discussed later in the paper, that at lower mass flow rates, there is a trend towards relaminarization. This possible relaminarization may be the explanation for the departure from the defect law. It is also seen from Fig. 10 that the velocity profiles are closer to the velocity defect law at higher Reynolds numbers. Figure 5 shows a parabolic velocity profile at exit from the disks. As the Reynolds number is decreased, the parabolic velocity profile is a better representation; this is to be expected if the flow is laminar and hence there is an indication that at low Reynolds numbers employed in this case $R_e = 365$, the flow is tending to be laminar at exit.

There are two strong indications that reverse transition to

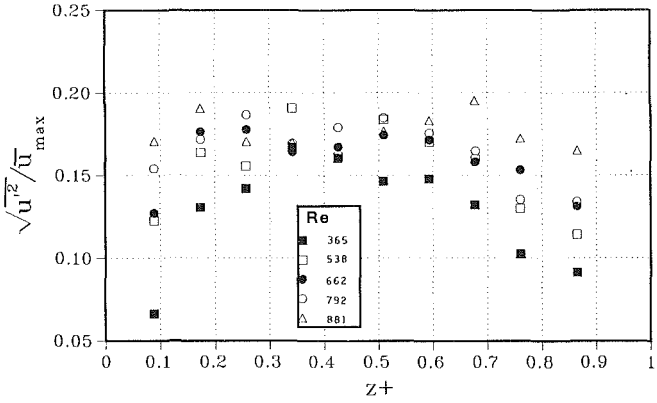

Fig. 11 Turbulence intensity $r^+ = 1.0$

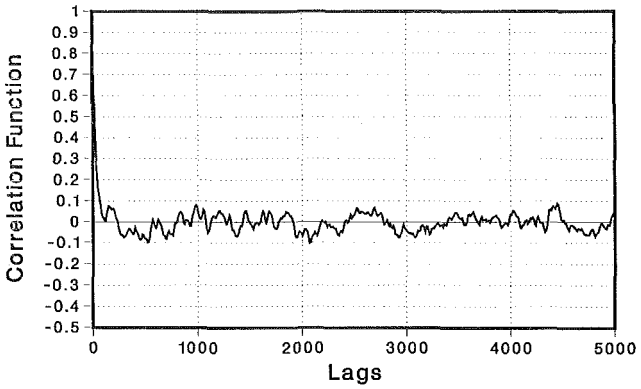

Fig. 13 Autocorrelation function $r^+ = 0.5$ Re = 365

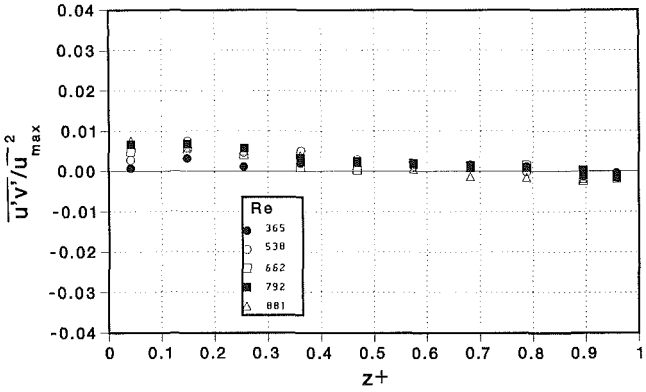

Fig. 12 Reynolds stress profile $r^+ = 0.93$

laminar flow has been initiated at $r^+ < 0.93$. The radial velocity distribution at r^+ values of 0.93 and 1.0 were found to be nearly parabolic and turbulent shear stresses at these locations were very small. Lower energies at higher frequencies are also an indication of reduced turbulence. Kreith [10] suggested the following criterion for reverse transition:

$$\frac{2\,r_c}{h} = K\left(\frac{2\,\dot{m}}{\mu\,h}\right)^{0.5}$$

where K is an empirical constant with an average value of 0.28 and r_c is the critical radius at which transition would take place. If this value of K is used in estimating the location of transition to laminar regime (it may be added that transition does not take place at a given location but is gradual), even at the smallest flow rates employed in this study, reverse transition is predicted outside of the disks—at a radius of about 0.25 m, corresponding to a dimensionless radius of 1.1. For the present case, it appears that a smaller value for K is appropriate. A value of 0.215 which is associated with an inflection point at the laminar velocity profile according to an analysis by Peube [9] appears to fit the data better. If this value is used, for the lowest flow rate, $r_c = 0.192$ m which corresponds to $r^+ = 0.84$. Patel and Head [18] have suggested that the criterion for reverse transition is a dimensionless shear stress gradient falling below a critical value. However, in the present study, the uncertainties associated with approximating the shear stress gradient are considered too large for a meaningful conclusion. Figures 11 and 12 show the turbulence intensity and the tangential Reynolds stress at exit of the disks. At the exit the velocity profile, being parabolic, resembles that in laminar flow. The magnitude of the Reynolds stress is also small lending credence to the conjecture that laminarization has begun prior to the exit from the disks. However, the turbulence intensity is quite high, of the order of 15 percent. Similar trends of high turbulence intensity of the order of 10 to 15 percent and low turbulence shear stress at low Reynolds number were also observed by Tabatabai and Pollard [14]. From the high levels of turbulence intensity but low turbulent shear stress, it may be concluded that though relaminarization has been initiated, there is a persistence of turbulence; turbulence decay is a gradual process. Similar conclusions have been arrived at in reference [14]. This aspect of the flow, where the turbulence shear stress is low but the intensity is high needs further study.

Figure 13 shows the autocorrelation function for Re_d of 365 at $r^+ = 0.5$ corresponding to a local Reynolds number, Re, of 730. The autocorrelation function was determined numerically from

$$R(\tau) = \frac{1}{N-j}\sum_{n=1}^{N-j} g(n)\; g(n+j) \text{ for}$$

$$j = 0,\ 1,\ 2,\ \ldots\ldots\ldots\ m$$

where N is the total number of points and $\tau = j\,\Delta t$, Δt = time interval between two consecutive data points. In a stationary flow the autocorrelation function should approach zero as τ increases. But Fig. 13 shows that it approaches an oscillating function as τ is increased. An oscillation of the function is to be expected if there is some low frequency oscillation in the flow itself. Such a periodic flow was also observed by Garcia [12] and Mochizuki and Yang [13]. From their visual observation and experimental results of heat transfer, Mochizuki and Yao [17] conjecture that such an oscillation is the result of periodic laminar flow separation. Wolf [20] found that radial flows with strong low frequency oscillation existed when the flow also contained swirling components; he felt that flow separation and vortex generation were involved in the generation of such low frequency oscillations.

Conclusions

Some of the turbulent characteristics of radial, outward flow of an incompressible fluid between two stationary coaxial disks were experimentally determined, using a split film anemometer probe. From the results of this study the following conclusions may be drawn:

- The universal velocity profile is not applicable at small radii, near the inlet. However, it appears to be satisfactory far away from the inlet.
- The flow considered weakly stationary, becomes more unsteady, particularly, near the inlet; this inherent unsteadiness observed by other workers, may be due to vortex shedding or swirl in the flow. This aspect needs further investigation.

- The criterion for reverse transition as given by Kreith [10] with a somewhat smaller value for the constant in the equation appears to be satisfactory.
- At exit from the disks, turbulence intensities are quite high—of the order of 10 to 20 percent—but the Reynolds stresses are negligibly small and the velocity profiles resemble that of laminar flow. This aspect of decay of turbulence needs further study.

It is appropriate to mention that this study appears to be the first to utilize a split film anemometer sensor to determine the turbulent variables in a flow. The uncertainties associated with the use of such a probe, particularly near solid boundaries have not been established. Hence, some of the measurements in the present study may be subject to uncertainties which cannot be quantified at present.

Another source of uncertainty is in regard to the frequency response of the split film probe. There is only one paper by Spencer and Jones [22], which deals with the frequency response of a split film probe Their conclusion is that these probes have good frequency response to around 1000 Hz but the response at frequencies higher than this values will be a fraction of the true response and that this fraction is reasonably constant at around 0.4. From an examination of the energy spectra it was concluded that, in the situation studied, there was no significant amount of energy at frequencies higher than around 800 and hence the values presented in this paper may be taken to be a reasonable representation of the true values in so far as the frequency response is concerned. This particular flow has many interesting characteristics. It would be appropriate to employ a noninvasive, well established technique, such as an LDV, for a more accurate determination of the experimental measurements.

Acknowledgment

The first author would like to thank the Mechanical Engineering—Engineering Mechanics Department of Michigan Technological University for providing the financial assistance in the form of fellowship which permitted him to pursue his graduate education.

References

1 Livesey, J. L., "Inertia Effects in Viscous Flows," *Int. J. Mech. Sc.*, Vol. 1, 1960, pp. 84–88.

2 Morgan, P. G., and Saunders, A., "Experimental Investigation of Inertia Effects Inviscous Flow," *Int. J. Mech. Sc.*, Vol. 2, 1960, pp. 8–12.

3 Benenson, D., and Bott, J. F., "Two Dimensional Laminar Boundary Layer Flow Within a Radial Diffuser," ASME Paper No. 67-WA-193, Winter Annual Meeting, 1961.

4 Hagiwara, T., "Studies on the Characteristics of Radial Flow Nozzles (1st Report, Theoretical Analysis of Outward Flow)," *Bull. JSME*, Vol. 5, 1962, pp. 656–663.

5 Hagiwara, T., "Studies on the Characteristics of Radial Flow Nozzles (3rd Report, Experimental Results)," *Bull. JSME*, Vol. 5, 1962, pp. 668–675.

6 Savage, S. B., "Laminar Radial Flow Between Parallel Plates," *Trans. ASME*, Vol. 86, 1964, pp. 594–596.

7 Moller, P. S., "Radial Flow Without Swirl Between Disks," M. S. thesis, Department of Mechanical Engineering, McGill University, 1963.

8 Raal, J. D., "Radial Source Flow Between Parallel Disks," *J. Fluid Mech.*, Vol. 85, No. 3, 1978, pp. 401–416.

9 Peube, J. L., "Sur L'Ecoulement radial permanent d-un fluide viszuex incompressible entre deux plans paralleles fixes," *J. De Mecanique*, Vol. 2, No. 4, 1963, pp. 377–395.

10 Kreith, F., "Reverse Transition in Radial Source Flow Between Two Parallel Planes," *Phys. Fluids*, Vol. 8, No. 6, 1965, pp. 1189–1190.

11 Patrat, J. C., "Contribution a l'etude des pressions dans un ecoulement radial divergent," *J. De Mecanique*, Vol. 14, No. 3, 1975, pp. 505–522.

12 Garcia, C. E., "Unsteady Air Flow Between Two Discs at Low Velocity," *Proc. Inst. Mech. Engrs.*, Vol. 184, No. 1, 1969, pp. 913–926.

13 Mochizuki, S., and Yang, Wen-Jei, "Self Sustained Radial Oscillating Flows Between Parallel Disks," *J. Fluid Mech.*, Vol. 154, 1985, pp. 377–397.

14 Tabatabai, M., and Pollard, A., "Turbulence in Radial Flow Between Parallel Disks at Medium and Low Reynolds Numbers," *J. Fluid Mechanics*, Vol. 185, 1987, pp. 483–502.

15 Bhatia, J. C., Durst, F., and Jovanovic, J., "Corrections of Hot Wire Anemometer Measurements Near Walls," *J. Fluid Mech.*, Vol. 22, 1982, pp. 411–431.

16 Bendat, J., and Pierson, A. G., *Random Data: Analysis and Measurement Procedures*, Wiley, New York, 1971.

17 Mochizuki, S., and Yao, M., "Flow Separation and Heat Transfer in Radial Flows between two Parallel Disks," *Heat Tr. Jap. Res.*, Vol. 12, 1983, pp. 84–88.

18 Patel, V. C., and Head, M. R., "Reversion of Turbulent to Laminar Flows," *J. Fluid Mech.*, Vol. 34, No. 2, 1968, pp. 371–392.

19 Ervin, J. S., "Turbulent, Radial Outflow of an Incompressible Fluid Between Two Coaxial Disks—an Experimental Study," M.S. thesis, Mechanical Engineering and Engineering Mechanics Department, Michigan Technological University, Houghton, 1985.

20 Wolf, L. from the communciation section in reference [12].

21 Kline, S. J., and McClintock, F. A., "The Description of Uncertainties in Single Sample Experiments," *Mech. Eng.*, Vol. 75, 1953.

22 Spencer, Bruce W., and Jones, Barclay, G., "Turbulence Measurements with the Split-Film Anemometer Probe," *Proc. Symp. Turbulence in Liquids*, Rolla, 1971.

APPENDIX

The split film probe, Fig. 1A, is similar to the cylindrical quartz sensor except that it has two semi-cylindrical sensors which are insulated from each other. The total heat transfer rate from the sensor (when operated at constant surface temperature) is dependent on the magnitude of the velocity perpendicular to the axis of the probe. The difference between the heat transfer rates from the two films is a function of the magnitude of the velocity perpendicular to the plane of the split.

Expressing the convective heat transfer coefficient as a function of a power of the Reynolds number, the voltages across the two films can be related to the magnitude of the velocity as:

$$E_1^2 + k^2\ E_2^2 = A + B\ U_N^m \tag{1}$$

where $k = E_1/E_2$ and represents the effect of the difference in the resistances of the two films. Employing a relation suggested by TSI ["TSI split film sensor; calibration and application," Technical Bulletin TB 20, TSI, St. Paul, Minnesota] for the difference between the heat transfer rates from the two halves of the film,

$$E_1^2 - k^2\ E_2^2 = C\ U_N^n \sin\theta \tag{2}$$

The constants A, B, C, k, m, and n in equations (1) and (2) were determined from calibration under steady state conditions. The values of E_1 and E_2 were measured for various values of U_N and θ and the constants determined from a regression analysis. Details related to measurements by the split film anemometer are available in reference [19].

After determining the instantaneous magnitude and direction of the velocity, the instantaneous components of the velocity in the radial and axial directions were computed. From the computed values of the velocity components, the mean velocity, the turbulence intensity and shear stress were computed.

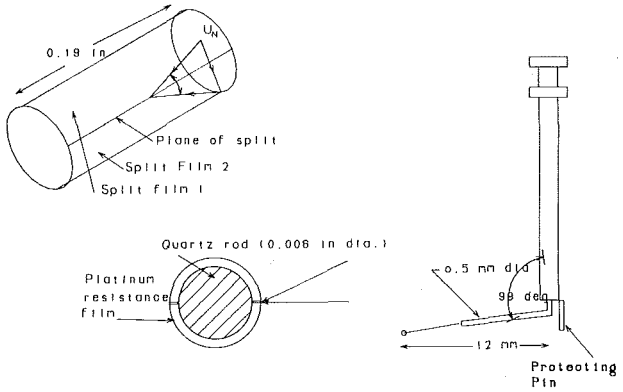

Fig. 1A Split film probe

Three-Dimensional Particle Tracking Velocimetry Based on Automated Digital Image Processing

Koichi Nishino
Graduate Student.

Nobuhide Kasagi
Associate Professor.
Mem. ASME

Masaru Hirata
Professor.

Department of Mechanical Engineering,
The University of Tokyo,
Tokyo 113, Japan

A three-dimensional particle tracking velocimeter for measuring an instantaneous distribution of all the three velocity components in a liquid flow is developed using an automated digital image processing technique. The measurement system consists of three TV cameras, a digital image processor, a laser disk recorder and a 16-bit microcomputer. Motions of neutrally buoyant tracer particles introduced into the flow field are observed by the cameras, and the three-dimensional displacement of each particle is calculated from consecutive TV frames recorded on the laser disk. Instantaneous velocity profiles in an unsteady laminar Couette flow between two concentric cylinders are measured. The results are in good agreement with predictions within the measurement uncertainties evaluated systematically. Furthermore, the measurement of a decaying turbulence in a stirred water tank demonstrates that the present technique is applicable to turbulent flows.

1 Introduction

Knowledge of instantaneous distributions of all the three velocity components is quite important in understanding physical natures of various complex flows. Particularly in turbulent flows, spatial information of the flow field is key to revealing primary mechanisms of Reynolds stress and turbulence energy production. However, conventional measurement techniques, such as hot-wire/film and laser-doppler anemometers, provide velocity signals at a single point in the flow field. These techniques also encounter serious difficulties in simultaneous measurement of three velocity components: the hot-wire/film techniques require time-consuming construction and calibration of a multi-component probe with fine fragile wires, while the laser-doppler anemometry demands quite delicate adjustment of an optical system.

In contrast to the above techniques, a particle tracking velocimeter (PTV) can readily provide instantaneous velocity distributions over a large area or space in the flow field. While most of the existing PTVs (see, e.g., Adrian, 1986) track particles' motions two-dimensionally, simultaneous acquisition of multiple images from different viewing directions allows 3-D particle tracking, thus realizing 3-D whole field measurement. In addition, recent development of micro-electronic equipment for high-speed digital image processing has unburdened researchers of tedious work required in image data analysis.

Up to the present, several studies have been made to develop 3-D PTVs based on automated digital image processing. Chang and Tatterson (1983), and Chang et al. (1984, 1985a, 1985b) first constructed a practical velocimeter based on stereoscopic photogrammetry using a 16 mm motion camera equipped with a Bolex stereoscopic lens. It was demonstrated that the velocimeter was quite useful for measuring a highly 3-D turbulent flow in an agitated water tank. A major disadvantage was limited accuracy in the direction of the depth of scene features; it arose from the fact that images were taken at a small viewing angles in the stereoscopic photogrammetry.

To improve the accuracy, it is desirable to observe the flow field from widely separated points. Viewing the flow field from two perpendicular directions has the advantage of simplifying the procedure of calculating 3-D particles' positions. Hence, this viewing geometry was employed by Yamakawa et al. (1986), Racca and Dewey (1988), and Adamczyk and Rimai (1988) in their velocimeters. However, the advantage is curved by this particular viewing configuration that seriously limits accessible flow geometry. Thus, a velocimeter which permits arbitrary viewing configurations should be developed to make measurement in complex flow geometry.

In this study, a 3-D PTV satisfying the above requirement is developed using a digital image processing technique. Measurement uncertainties associated with the technique are systematically evaluated. An unsteady laminar Couette flow between two concentric cylinders is measured and compared with the exact solutions to examine applicability of the present technique and validity of the uncertainty analysis. Furthermore, a decaying turbulence in a stirred water tank is measured to demonstrate that the present technique is applicable to turbulent flows.

2 Measurement Techniques

Three velocity components are measured by tracking 3-D

Contributed by the Fluids Engineering Division for publication in the JOURNAL OF FLUIDS ENGINEERING. Manuscript received by the Fluids Engineering Division July 19, 1988.

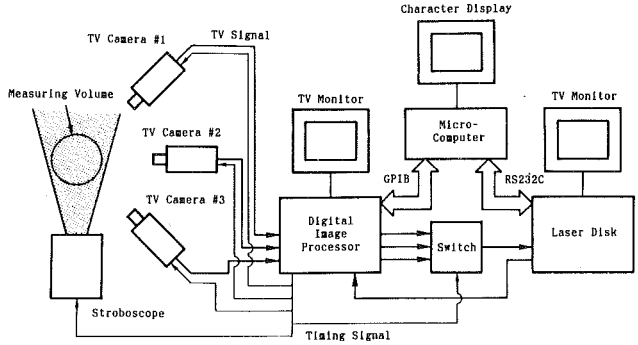

Fig. 1 Digital image processing system

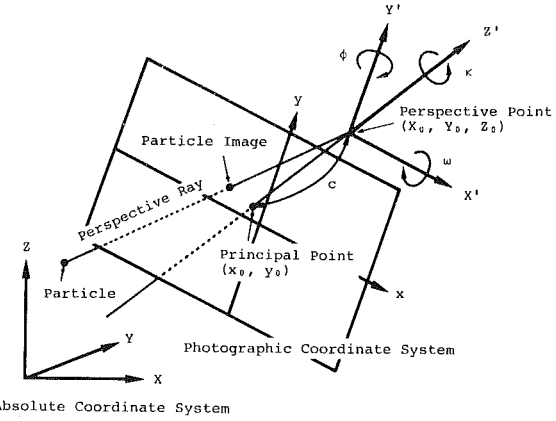

Fig. 2 Relationship between absolute and photographic coordinate systems

motions of the tracer particles suspended homogeneously in the flow field. The particles' motions are observed from arbitrary viewing directions by two or three TV cameras simultaneously, and consecutive sets of TV frames are stored at a given time interval. By processing the TV frames, instantaneous 3-D positions of the tracer particles are reconstructed, and then the displacement of each tracer particle over the time interval is calculated.

2.1 Digital Image Processing System. The digital image processing system is shown in Fig. 1. This system consists of three TV cameras (490×384 pixels), an image processor (512×480 pixels, 256 gray levels), a laser disk recorder, a 16-bit microcomputer, a stroboscope and a switching unit. The motions of tracer particles are simultaneously observed by the TV cameras. TV frames are first stored in the image processor and then successively transferred through the switching unit to the laser disk recorder in real time. The cameras and the switching unit are synchronized with the image processor. Since this image taking procedure is repeated at 10 Hz, consecutive sets of the TV frames are recorded at a 0.1 s interval.

The fluid motion is visualized by fine tracer particles suspended in the flow field. The tracer particles are made of nylon 12, whose specific density is 1.02. The average diameter of the tracer particles is less than 280 μm in the present work. The measuring volume is illuminated by the stroboscope whose flash is triggered at 30 Hz by the timing signal from the camera. Since the duration of the flash is 20 μs, images taken by the cameras are virtually instantaneous.

At the data reduction stage, the TV frames stored on the laser disk are replayed and sent to the image processor, where further data reduction is carried out. The laser disk recorder and the image processor are interfaced with the microcomputer, and both image acquisition and reduction are executed automatically by the original computer programs. About 5–10 minutes were required for processing image data to obtain an instantaneous 3-D velocity distribution.

2.2 Camera Parameters. For the reconstruction of particles' 3-D positions, camera parameters of each TV camera must be determined. Figure 2 shows the relationship between absolute and photographic coordinate systems. Murai et al. (1980) derived the following equations:

$$x = -c\,\frac{a_{11}(X-X_0)+a_{12}(Y-Y_0)+a_{13}(Z-Z_0)}{a_{31}(X-X_0)+a_{32}(Y-Y_0)+a_{33}(Z-Z_0)}+\Delta x \qquad (1)$$

$$y = -c\,\frac{a_{21}(X-X_0)+a_{22}(Y-Y_0)+a_{23}(Z-Z_0)}{a_{31}(X-X_0)+a_{32}(Y-Y_0)+a_{33}(Z-Z_0)}+\Delta y \qquad (2)$$

where

$$\begin{aligned}
a_{11} &= \cos\phi\cos\kappa\\
a_{21} &= \cos\omega\sin\kappa+\sin\omega\sin\phi\cos\kappa\\
a_{31} &= \sin\omega\sin\kappa-\cos\omega\sin\phi\cos\kappa\\
a_{12} &= -\cos\phi\sin\kappa\\
a_{22} &= \cos\omega\cos\kappa-\sin\omega\sin\phi\sin\kappa\\
a_{32} &= \sin\omega\cos\kappa+\cos\omega\sin\phi\sin\kappa\\
a_{13} &= \sin\phi\\
a_{23} &= -\sin\omega\cos\phi\\
a_{33} &= \cos\omega\cos\phi\\
\Delta x &= x_0+(x-x_0)(k_1r^2+k_2r^4)\\
\Delta y &= y_0+(y-y_0)(k_1r^2+k_2r^4)\\
r^2 &= ((x-x_0)^2+(y-y_0)^2)/c^2
\end{aligned}$$

Nomenclature

a_{ij} = elements of rotational matrix
B = bias limit
c = principal distance
d = particle diameter
k_i = correction coefficients for lens distortion
Re = Reynolds number $= r_0^2\omega/\nu$
r = distance from principal point
r_i, r_0 = radii of inner and outer cylinders
r^* = dimensionless distance $=(r-r_i)/(r_0-r_i)$
r, θ, z = cylindrical coordinates
S = precision index
t = time or student t value
t^* = dimensionless time $= t\nu/r_i^2$
u, v, w = velocity components in the x-, y- and z-directions
u^*, v^*, w^* = velocity components nondimensionalized by outer cylinder's speed
X, Y, Z = absolute coordinates
X', Y', Z' = camera coordinates
X_0, Y_0, Z_0 = absolute coordinates of perspective point
x, y = photographic coordinates
x_0, y_0 = photographic coordinates of principal point
$\Delta x, \Delta y$ = corrections for lens distortion
γ = specific density
ν = kinematic viscosity
ρ = density
ω, ϕ, κ = camera attitudes
ω = angular velocity

Superscripts

$(\bar{\ })$ = mean value
$(\ )'$ = fluctuating component unless otherwise denoted

Subscripts

f = fluid
p = particle

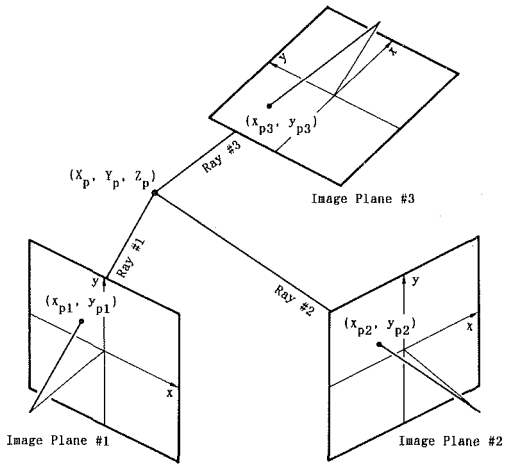

Fig. 3 Schematic of reconstruction of a particle's 3-D position

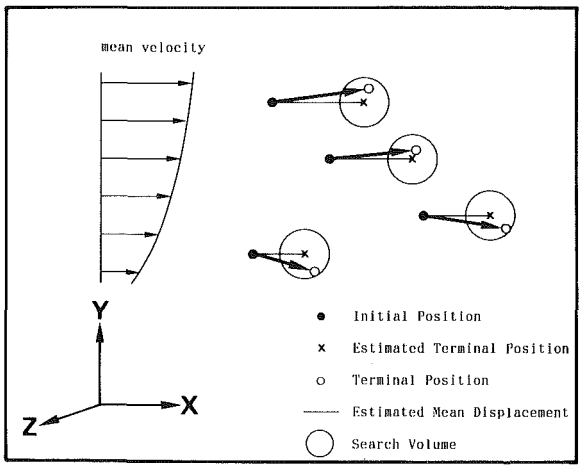

Fig. 4 Schematic of tracer particle tracking

Equations (1) and (2) have eleven unknown camera parameters: the absolute coordinates of the perspective point (X_0, Y_0, Z_0), the attitudes of the camera (ω, ϕ, κ), the principal distance c, the photographic coordinates of the principal point (x_0, y_0), and the correction coefficients for the lens distortion k_1 and k_2. It is noted that the first terms in the right-hand sides of equations (1) and (2) are uniquely derived from the geometrical relationship between the absolute and photographic coordinate systems, and that the second terms are introduced by Murai et al. (1980) to correct for the lens distortion. These parameters are determined by equations (1) and (2) with the data of absolute and photographic coordinates of calibration points. Procedures for obtaining these calibration data will be described in 3.1. The successive approximation method is used to determine the camera parameters because equations (1) and (2) are nonlinear with respect to them.

2.3 Identification of Tracer Particle Images. Photographic coordinates of each tracer particle are determined as a centroid of the tracer-particle's image in the digital image. This procedure is accomplished by converting the TV frame into a digital image, binarizing it with an appropriate threshold, labeling tracer particle images, and calculating the position of each centroid. This procedure is also applied to the photographic coordinates of the calibration points.

2.4 Reconstruction of Tracer Particles' 3-D Positions. After the camera parameters and the photographic coordinates of the tracer particle images are known, 3-D positions of the tracer particles can be reconstructed in a straightforward manner based on geometrical consideration. This is schematically shown in Fig. 3. For each tracer particle image, a perspective ray, i.e., a line passing through the perspective point of the camera and the centroid of the particle image, is calculated by substituting the photographic coordinates (x_p, y_p) into equations (1) and (2). When three TV cameras are used, the 3-D position of the tracer particles is obtained as an intersection of the three perspective rays as shown in Fig. 3.

In reality, many tracer particles are observed at the same time in the measuring volume, and a number of perspective rays are calculated for each image plane. Hence, correct correspondence of the perspective rays must be established. This procedure is made by finding out a set of the rays which intersect each other at the same point in the prescribed measuring volume. To avoid mis-correspondence, rays which have more than one intersection are discarded.

Owing to the measurement uncertainties, perspective rays do not intersect in a mathematically strict sense. Thus, the intersection is recognized when the rays go through the same minute volume. The size of this volume is optimized by taking account of the measurement uncertainties. In the case three camers are used, the 3-D position of a tracer particle is finally defined as the centroid of the triangle formed by the three points, each of which is the middle point of the shortest segment between the rays.

2.5 Tracking of Tracer Particles. In order to obtain the 3-D displacement of a tracer particle, the identical tracer particle must be tracked between the time interval. This tracking, which is schematically shown in Fig. 4, is done as follows:

[1] Estimate the particle's mean displacement during the time interval,

[2] estimate the terminal position of the particle by adding the estimated displacement to its initial position,

[3] search a volume around the estimated terminal position for the tracer,

[4] complete tracking if only one tracer particle is found and one-to-one correspondence is established.

The particle's mean displacement in step [1] is estimated from the mean velocity of the flow field. The size of the search volume in step [3] is determined by considering both the velocity fluctuations and the time interval. If the mean velocity is not known, however, the mean displacement is tentatively assumed to be zero, and the size of the search volume is determined so that it covers the particle's maximum displacement caused by both the mean and the fluctuating velocity components. Then, all the image data are processed to obtain preliminary knowledge of the mean velocity field, with which the data reduction is repeated to obtain the final results.

The above algorithm requires that the average distance between the tracer particles is sufficiently large compared to the unpredictable displacement during the time interval so as not to generate mis-correspondence. Hence, the number of particles introduced into the flow field must be carefully adjusted to satisfy this requirement.

3 Experimental Procedures

Figure 5 summarizes experimental procedures, which can be classified into the camera calibration and the tracer particle tracking.

3.1 Camera Calibration. Determination of the camera parameters requires at least six calibration points which provides the data sets of absolute and photographic coordinates. To do this, white circular marks of 1.5 mm in diameter are pasted on a calibration plate in a grid-like pattern. The 2-D position of the center of each mark is accurately measured us-

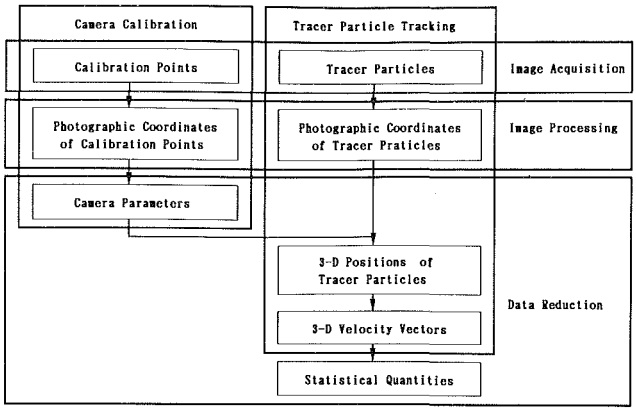

Fig. 5 Experimental procedures

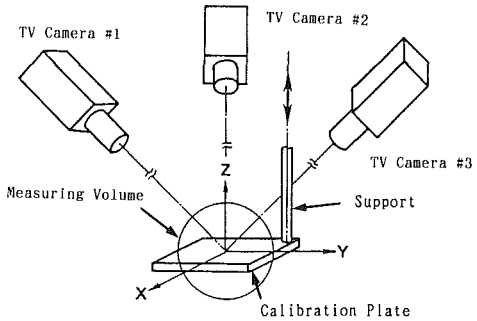

Fig. 6 Schematic of camera calibration

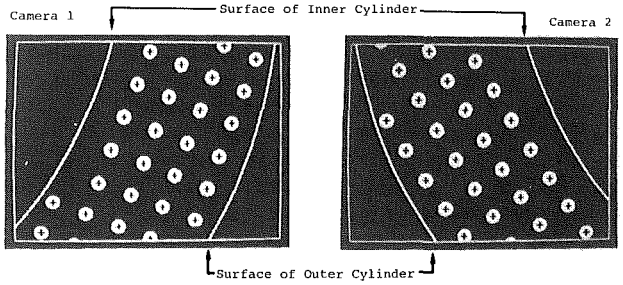

Fig. 7 Images of the calibration plate in the laminar Couette flow measurement; surface of inner and outer cylinders are superimposed on the original images

ing a traversing microscope whose resolution is 5 μm. In the experiment, the calibration plate is traversed in the direction normal to the plate to cover the whole measuring volume as shown in Fig. 6. This is done with a precise traversing mechanism whose resolution is 50 μm. Thus, the absolute cordinates of the centers of calibration points can be measured.

The images of the plate are taken by the cameras and recorded on the laser disk at each location of the plate, typically at eleven locations in total. Examples of the plate images in the laminar Couette flow measurement described later are shown in Fig. 7, where two TV cameras are used. The centers of the calibration points obtained by the procedure described in 2.3 are indicated by cross symbols. These positions provide the photographic coordinates of the calibration points which are used to determine the camera parameters.

3.2 Tracer Particle Tracking. After the calibration plate is removed from the measuring volume, the tracer particles are introduced into the flow field and their motions are recorded on the laser disk. Note that positions and orientations of the cameras are kept unchanged throughout the experiment. Typical images are shown in Fig. 8, where each particle image occupies 7.5 pixels on average. From the camera parameters and the photographic coordinates of the particle images, the

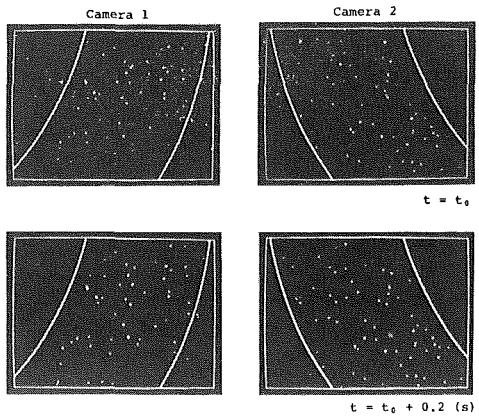

Fig. 8 Images of tracer particles in the laminar Couette flow measurement; surfaces of inner and outer cylinders are superimposed on the original images

Table 1 Uncertainties of 3-D position measurement of tracer particle

Error Sources			Precision Index	Bias Limit	Degrees of Freedom
Camera Parameters	3-D Positions of Calibration Points	X	±22 μm	±2.5 μm	12
		Y	±22 μm	±2.5 μm	12
		Z	±28 μm	±25 μm	>30
	Image Reproduction of Optical Disk Recorder	x	±0.13 pixel	0 pixel	>30
		y	±0.06 pixel	0 pixel	>30
	Thresholding	x	±0.18 pixel	±0.10 pixel	>30
		y	±0.18 pixel	±0.10 pixel	>30
Photographic Positions of Tracer Particles	Image Reproduction of Optical Disk Recorder	x	±0.13 pixel	0 pixel	>30
		y	±0.06 pixel	0 pixel	>30
	Thresholding	x	±0.30 pixel	±0.20 pixel	>30
		y	±0.20 pixel	±0.20 pixel	>30
3-D Positions of Tracer Particles		X	±24.0 μm	±26.4 μm	>30
		Y	±20.5 μm	±24.0 μm	>30
		Z	±50.7 μm	±70.1 μm	>30

3-D positions of the tracer particles are reconstructed. The three velocity components are finally obtained by dividing the 3-D displacement of the particle by the time interval.

4 Uncertainty Analysis

Measurement uncertainties associated with the present technique are systematically evaluated according to the method described in ANSI/ASME PTC 19.1-1985 (1986). The uncertainty interval at 95 percent coverage, U_{RSS}, is calculated as:

$$U_{RSS} = (B^2 + (tS)^2)^{1/2} \tag{3}$$

where B, S, and t denote the bias limit, the precision index and the student t value for the 95 percent confidence level, respectively. Possible elemental error sources of the present technique are listed below:

[1] 3-D position measurement,
[2] time interval between successive frames,
[3] traceability of the particle to the fluid motion,
[4] pathline averaging effect,
[5] spurious vectors arising from mistracking of tracer particles.

Table 1 summarizes the uncertainties associated with the 3-D position measurement of the tracer particle under the condition of the decaying turbulence measurement described later. Since the uncertainties depend on the viewing directions, the quantities listed in this table would change in a different experiment.

The uncertainty involved in the time interval between two successive frames is found to be negligibly small compared to other elemental uncertainties.

Traceability of the particle to the local fluid motion is ex-

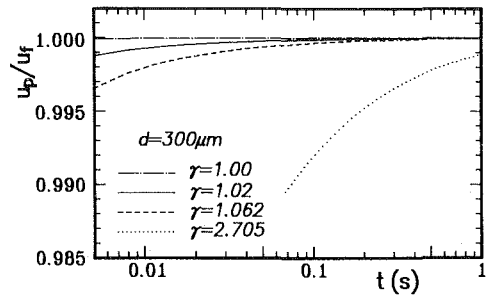

Fig. 9 Particle's traceability to impulsive change in fluid velocity

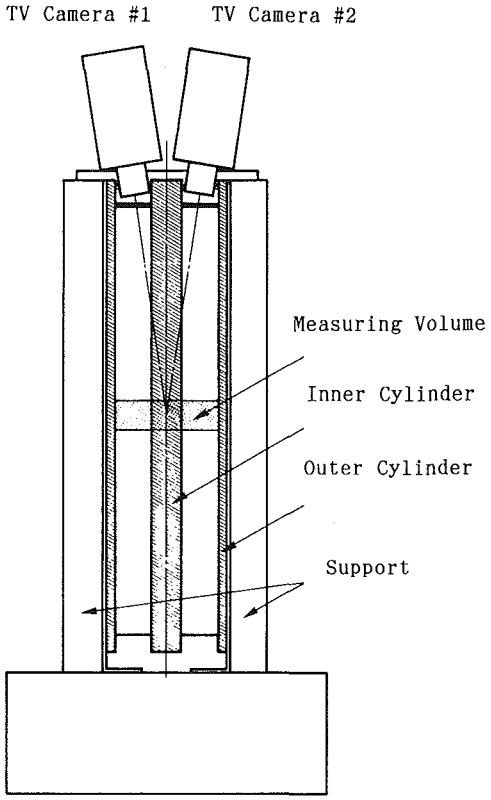

Fig. 10 Experimental apparatus for the laminar Couette flow measurement

amined for both periodic and impulsive changes in the fluid velocity. The motion of a spherical particle in a fluid is expressed by the following equation (Hinze, 1975):

$$\frac{\pi d^3}{6}\rho_p\frac{du_p}{dt}=3\pi\nu\rho_f d(u_f-u_p)+\frac{\pi d^3}{6}\rho_f\frac{du_p}{dt}$$
$$+\frac{1}{2}\frac{\pi d^3}{6}\rho_f\left(\frac{du_f}{dt}-\frac{du_p}{dt}\right)$$
$$+\frac{3}{2}d^2\rho_f\sqrt{\pi\nu}\int_{t_0}^{t}d\xi\left(\frac{du_f}{dt}-\frac{du_p}{dt}\right)\Big/\sqrt{t-\xi} \qquad (4)$$

where d, t_0, u, ρ, and ν are the particle diameter, the initial time, the velocity, the density and the kinematic viscosity of the fluid, respectively. The subscripts of f and p denote the fluid and the particle, respectively. According to Hjelmfelt and Mockros (1966) who solved this equation for the periodic fluid motion, traceability of a particle, 300 μm in diameter with a specific density of 1.02, is sufficiently good: the relative amplitude and the phase lag of the particle's motion are about 99.5 percent and -0.2 degree, respectively, when the fluid oscillates at 50 Hz which is five times the present image sampling frequency. For the impulsive velocity change, equation (4) was numerically solved. Figure 9 shows the results of the particle velocity relative to that of the fluid. The 300 μm particle attains about 99.9 percent of the fluid velocity within 0.005 s, and thus it can follow the impulsive fluid motion sufficiently well.

Table 2 Simulation results of spurious vector occurrence; the lighted zone of 6^3 cm^3 and the measuring volume of about 5^3 cm^3 are assumed

Particle Concentration (cm^{-3})	Number of Particles	Turbulence Energy ($\times10^{-4}m^2/s^2$)	Total Number of Vectors Obtained	Number of Spurious Vectors	Mistracking Ratio (%)
1	216	7.5	56	0	0.0
		30.0	65	0	0.0
		67.5	50	3	6.0
2	432	7.5	120	1	0.8
		30.0	110	2	1.8
		67.5	81	7	8.6
3	648	7.5	165	1	0.6
		30.0	133	6	4.5
		67.5	64	9	14.1
4	864	7.5	176	7	4.0
		30.0	143	9	6.3
		67.5	73	29	39.7

A pathline averaging effect arises because the fluid velocity is calculated from the tracer particle's displacement averaged over a given time interval. Schraub et al. (1965) showed that the uncertainty caused by this effect would reach about ±1 percent of the mean velocity in their investigation of turbulent flows. By the same analysis, the uncertainty interval is estimated to be as small as $\pm4.7\times10^{-4}$ mm/s for the decaying turbulence measurement.

The number of spurious vectors, which are produced by mistracking of tracer particles, increases eventually to an unacceptable level as the number of tracer particles and/or the velocity fluctuations are increased. To obtain a statistical estimate, a computer simulation was carried out of the measurement of an isotropic turbulence. The number of spurious vectors are counted under several conditions of particle concentration and turbulence energy as shown in Table 2. In the decaying turbulence measurement, the number of particle images is about 600, and the turbulence energy is 7.5×10^{-4} m^2/s^2 at most. Thus, occurrence of spurious vectors is considered to be less than 0.6 percent.

Among the error sources, the uncertainties ascociated with the 3-D position measurement are found to be dominant. The uncertainty intervals of three velocity components at 95 percent coverage are evaluated as follows:

For laminar Couette flow measurement:

$$U_{RSS-u}=\pm0.38 \text{ mm/s}$$
$$U_{RSS-v}=\pm0.34 \text{ mm/s}$$
$$U_{RSS-w}=\pm2.89 \text{ mm/s}$$

For decaying turbulence measurement:

$$U_{RSS-u}=\pm0.77 \text{ mm/s}$$
$$U_{RSS-v}=\pm0.67 \text{ mm/s}$$
$$U_{RSS-w}=\pm1.75 \text{ mm/s}$$

Dynamic range of a velocimeter is generally defined as a ratio of the maximum to minimum velocities that can be accurately measured. For the present technique, this ratio is equivalent to that of the maximum to minimum displacement of the tracer particle in the digital image. The minimum displacement is limited by the uncertainties of the particle position in the digital image, and is roughly estimated to be 1 pixel. On the other hand, the maximum displacement is estimated to be about 200 pixels considering the size of the whole digital image. Hence, the dynamic range of the present technique is evaluated to be about 46 dB.

5 Measurement of Laminar Couette Flow

A schematic view of the experimental apparatus is shown in Fig. 10. An inner cylinder of 100 mm in diameter is at rest,

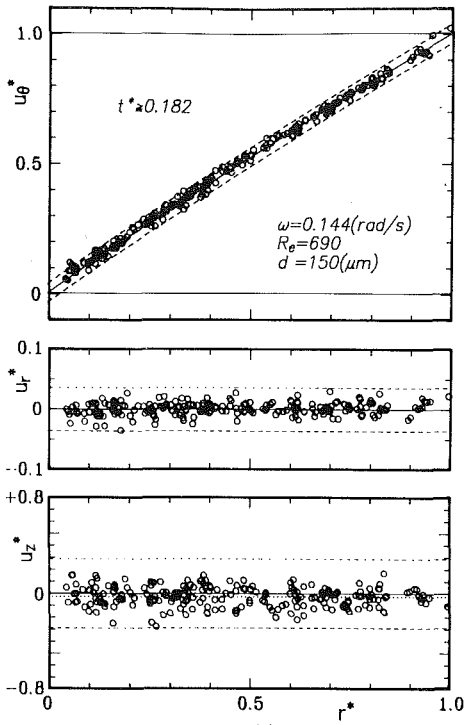

Fig. 11(a)

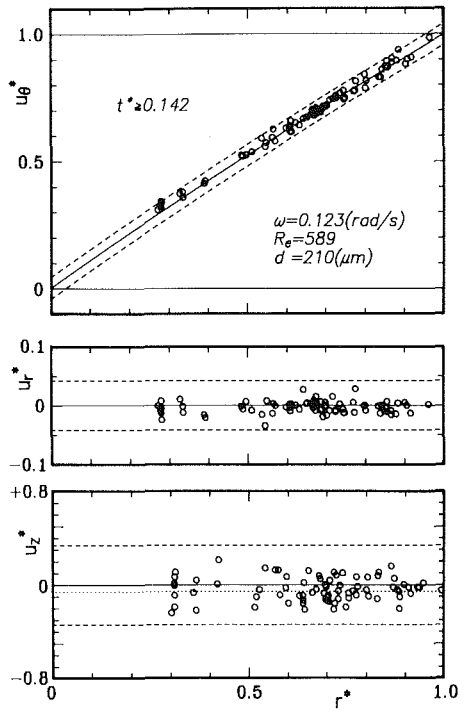

Fig. 11(b)

Fig. 11 Steady state distributions of the three velocity components in laminar Couette flows: (a) Re = 690, d = 150 μm, (b) Re = 556, d = 210 μm

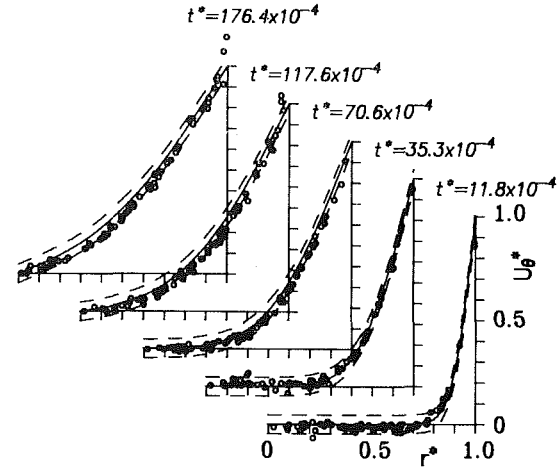

Fig. 12(a)

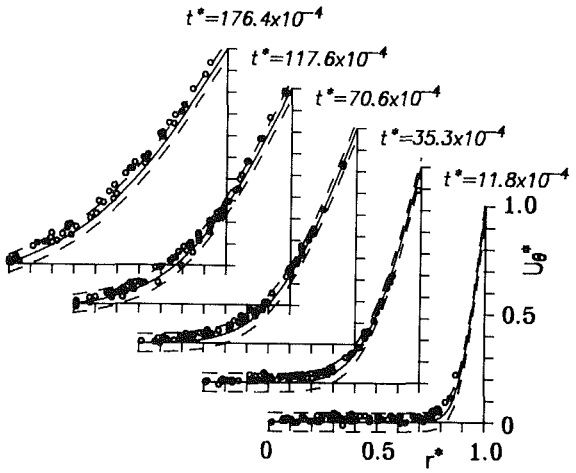

Fig. 12(b)

Fig. 12 Unsteady distributions of the circumferential velocity component: (a) Re = 690, d = 150 μm, (b) Re = 556, d = 210 μm

while an outer cylinder of 140 mm in diameter is driven to rotate impulsively by an AC motor. An unsteady laminar Couette flow is developed in the gap, 20 mm wide and 630 mm high, and is observed by two TV cameras as shown in Fig. 10. The cameras are equipped with zoom lenses and extension tubes so that magnified images can be obtained. To remove both refraction and flicker of the image at the water surface, the front of each lens, to which a water-proof optical filter is attached, is dipped into the water.

TV frames are stored for about 5 minutes from the onset of rotation until the circumferential velocity distribution fully develops. In this measurement, the image acquisition is repeated at a 0.2 s interval, and velocities are calculated from the displacement during this time interval. For tracking the tracer particles, mean displacement in both radial and axial directions is assumed to be zero. On the other hand, circumferential displacement is estimated by assuming a linear velocity profile between the gap. The search region is defined to be 2 and 1.2 times of the uncertainty intervals in the position measurement in the radial and axial directions, respectively. In the circumferential direction, it was defined to be 1.5 times of the mean displacement estimated above.

The measured steady state distributions of three velocity components, u_θ, u_r and u_z, are shown for two different particle diameters in Figs. 11(a) and 11(b), where the ordinate and the abscissa are nondimensionalized by the outer cylinder's speed and the gap width. Note that the analytical solutions of u_θ^* are indicated by the solid lines, and those of u_r^* and u_z^* are zero regardless of the radial position. Dashed lines indicate the uncertainty intervals for each velocity component. Dotted lines in the u_z^* distributions show the estimated buoyancy-induced velocity components due to a small density difference; they are negligibly small compared to the u_θ^* velocity component. These figures clearly demonstrate that the experimental results of three velocity components are in good agreement with the predictions, and that scatters of the experimental data are well within the estimated uncertainty intervals.

In Figs. 12(a) and 12(b), the unsteady distributions of the

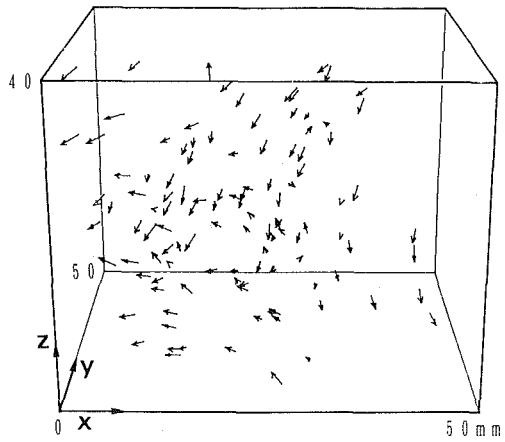

Fig. 13 Three-dimensional representation of an instantaneous velocity distribution in a stirred water tank

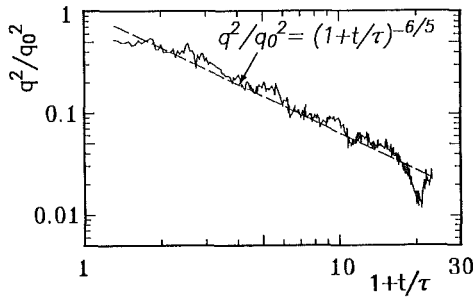

Fig. 14 Decay of turbulence energy in a stirred water tank

circumferential velocity component are shown along with the numerical solutions (solid lines) and the uncertainty intervals (dashed lines). Agreement between the experimental data and the predictions is again quite good. Thus, the present technique is applicable to the 3-D velocity measurement of steady and unsteady laminar shear flows.

6 Measurement of Decaying Turbulence

In order to examine applicability of the present technique to turbulent flows, a decaying turbulence generated in a stirred water tank was measured. The water in the $42 \times 27 \times 27$ cm^3 tank was stirred manually with a slender rod as randomly as possible. Three TV cameras are used to observe the measuring volume of about $5 \times 5 \times 5$ cm^3 at the center of the tank. Consecutive sets of TV frames are recorded at a 0.1 s interval for about 50 s after the water is stirred.

For tracking the tracer particles, the mean velocities are assumed to be zero in all the directions. On the other hand, determination of the search volume is not straightforward because no information of the velocity fluctuations is available. In this study, a spherical search volume is employed, and its radius is determined so that the number of vectors obtained is maximized. As a result, the specified radius is about half the average distance between the tracer particles, and this situation satisfies the requirement of the tracer particle tracking mentioned previously.

An example of 3-D representation of an instantaneous velocity distribution is shown in Fig. 13. In the present measurement, only about 100 vectors on average are obtained from about 600 particle images taken by each camera. This is mainly because many particles outside the specified measuring volume are included in these 600 particles and 3-D reconstruction cannot be made for those particles.

Figure 14 shows the decay of the turbulence energy, $\frac{1}{2}(\overline{u'^2} + \overline{v'^2} + \overline{w'^2})$, with time. The velocity fluctuations are calculated on the basis of the mean velocities which are defined as averages of all the instantaneous velocities obtained in the measuring volume. For comparison, a prediction of the decay of turbulence energy obtained by a simple turbulence model (see, e.g., Reynolds, 1978) is also presented in Fig. 14. Note that two constants, q_0^2 and τ, are determined to be 4.1×10^{-4} m^2/s^2 and 2.17 s, respectively, by the least square method. Since the sample size of the present measurement is not large enough to calculate turbulence statistics, the comparison presented here should be interpreted qualitatively.

It is finally noted that the present technique has already been applied to several other turbulent flows in separate investigations: a turbulent round free jet by Kasagi et al. (1988), a fully developed two-dimensional turbulent channel flow by Nishino and Kasagi (1989), and a separated and reattaching flow over a backward-facing step by Itoh and Kasagi (1989). These measurements present fairly reasonable results of turbulence statistics, thus demonstrating that the present technique is also applicable to various turbulent flows.

7 Conclusions

(1) A three-dimensional particle tracking velocimeter for measuring laminar and turbulent liquid flows is developed. The system is fully automated for data acquisition and reduction so that a large number of image data can be processed efficiently. This is very advantageous for the measurements of complex three-dimensional turbulent flows, in which large sample sizes are required.

(2) Measurement uncertainties associated with the present technique are systematically evaluated by taking into account possible error sources including 3-D position measurement, traceability of the particle, pathline averaging effect and occurrence of spurious vectors.

(3) Laminar Couette flows are measured by the present technique. Good agreement between the experimental results and the predictions demonstrates that the present technique can be applied to the measurement of steady and unsteady laminar shear flows within the estimated uncertainty intervals.

(4) The present technique is successfully applied to a simple turbulent flow; about 100 instantaneous velocity vectors are obtained in a decaying turbulence in a stirred water tank.

Acknowledgments

This work was supported through the Grant-in-Aids for General Scientific Research (No. 61460103) and for Encouragement of Young Scientists (No. 62790196) by the Ministry of Education, Science and Culture, and also by the Mitsubishi Foundation. The assistance of Messrs. N. Ninomiya and Y. Sata in developing computer programs is gratefully acknowledged.

References

Adamczyk, A. A., and Rimai, L., 1988, "Reconstruction of a 3-Dimensional Flow Field from Orthogonal Views of Seed Track Video Images," *Exp. Fluids*, Vol. 6, pp. 380–386.

Adrian, R. J., 1986, "Multi-Point Optical Measurements of Simultaneous Vectors in Unsteady Flow—A Review," *Int'l. J. Heat and Fluid Flow*, Vol. 7, No. 2, pp. 127–145.

ANSI/ASME PTC 19.1-1985, 1986, "Measurement Uncertainty, Supplement on Instruments and Apparatus, Part 1."

Reynolds, W. C., 1978, *Turbulence, Topics in Appl. Phys.*, Bradshaw, P. ed., Vol. 12, Springer-Verlag Berlin, pp. 197–201.

Chang, T. P., and Tatterson, G. B., 1983, "An Automated Analysis Method for Complex Three Dimensional Mean Flow Fields," *Proc. 3rd Int'l. Symp. on Flow Visualization*, pp. 266–273.

Chang, T. P., Wilcox, N. A., and Tatterson, G. B., 1984, "Application of Image Processing to the Analysis of Three-Dimensional Flow Fields," *Optical Eng.*, Vol. 23, No. 3, pp. 283–287.

Chang, T. P. K., Watson, A. T., and Tatterson, G. B., 1985a, "Image Processing of Tracer Particle Motions as Applied to Mixing and Turbulent Flow-I. The Technique," *Chem. Eng. Sci.*, Vol. 40, No. 2, pp. 269–275.

Chang, T. P. K., Watson, A. T., and Tatterson, G. B., 1985b, "Image Processing of Tracer Particle Motions as Applied to Mixing and Turbulent Flow-II. Results and Discussion," *Chem. Eng. Sci.*, Vol. 40, No. 2, pp. 277–285.

Hinze, J. O., 1975, *Turbulence*, McGraw-Hill, 2nd ed., pp. 460–471.

Hjelmfelt, A. T., and Mockros, L. F., 1966, "Motion of Discrete Particles in a Turbulent Fluid," *Appl. Sci. Res.*, Vol. 16, pp. 149–161.

Itoh, N., and Kasagi, N., 1989, "Turbulence Measurement in a Separated and Reattaching Flow over a Backward-Facing Step with the Three-Dimensional Particle Tracing Velocimeter" (in Japanese), *J. Flow Visualization Society of Japan*, Vol. 9, No. 34, pp. 245–248.

Kasagi, N., Ninomiya, N., and Hirata, M., 1988, "Three-Dimensional Velocity Measurement in a Turbulent Jet by Digital Image Processing," *Proc. 1st World Conf. on Experimental Heat Transfer, Fluid Mechanics and Thermodynamics*, Dubrovnik, Yugoslavia, pp. 1502–1509.

Murai, S., Nakamura, H., and Suzuki, Y., 1980, "Analytical Orientation for Non-Metric Camera in the Application to Terrestrial Photogrammetry," *Int'l. Arch. Photogrammetry XXIII*, Commission V, pp. 516–525.

Nishino, K., and Kasagi, N., 1989, "Turbulence Statistics Measurement in a Two-Dimensional Channel Flow Using a Three-Dimensional Particle Tracking Velocimeter," Proc. 7th Symp. on Turbulent Shear Flows, Stanford, Vol. 2, pp. 22.1.1–22.1.6.

Racca, R. G., and Dewey, J. M., 1988, "A Method for Automatic Particle Tracking in a Three-Dimensional Flow Field," *Exp. Fluids*, Vol. 6, pp. 25–32.

Schraub, F. A., Kline, S. J., Henry, J., Runstadler, P. W., and Littell, A., 1965, "Use of Hydrogen Bubbles for Quantitative Determination of Time-Dependent Velocity Fields in Low-Speed Water Flows," ASME *Journal of Basic Engineering*, Vol. 87, pp. 429–444.

Yamakawa, M., Iwashige, K., and Kobayashi, T., 1986, "On-Line Three-Dimensional Velocity Distribution Measuring System Using TV Cameras," (in Japanese), *J. Flow Visualization Society of Japan*, Vol. 6, No. 22, pp. 273–278.

Aerodynamic Torque Characteristics of Butterfly Valves in Compressible Flow[1]

M. J. Morris
Research Scientist,
McDonnell Douglas Research Laboratories,
McDonnell Douglas Corporation,
St. Louis, MO 63166

J. C. Dutton
Associate Professor,
Department of Mechanical and Industrial Engineering,
University of Illinois at Urbana-Champaign,
Urbana, IL 61801

The results of an experimental investigation of the aerodynamic torque characteristics of butterfly valves under compressible flow conditions are reported. Both three-dimensional prototype valves and two-dimensional planar models have been studied at choked and unchoked operating points. Other parameters investigated include the operating pressure ratio across the valve, the valve disk angle, and the disk shape. The results demonstrate the importance of flow separation and reattachment phenomena on the valve aerodynamic torque characteristics, the importance of disk shape at intermediate angles, and the sensitivity of the torque to the valve disk geometry near the leading and trailing edges where extreme pressure gradients can occur.

Introduction

Butterfly valves are widely used piping components for both regulation and on/off flow control. A butterfly valve is a simple compact device that is easily coupled with actuators. In general, it consists of three main parts: the body, the shaft, and the valve disk. In a fully open position, butterfly valves provide a relatively large mass flowrate capacity and minimal obstruction to the flow. When compared to various valve designs of comparable size, butterfly valves are relatively lightweight.

One example of a common butterfly valve use is for nuclear containment purge valves. Butterfly valves provide a relatively fast closing time for containment with a typical stroking speed of three to five seconds. During an accident, the butterfly valve must be able to close against an increasing pressure drop, with containment pressures climbing rapidly to over four atmospheres. Under these conditions, the compressibility of the air must be considered since the flow through the valves will exhibit phenomena such as supersonic velocities, shock systems, expansion waves, and choking. In turn, these phenomena determine both the forces acting on the valve surfaces and the valve capacity. A good understanding of compressible flow through butterfly valves and the related operating characteristics is therefore essential for this application.

Ultimately, a butterfly valve and its components must be designed with sufficient strength to resist pressure forces, shear forces, and torsional forces on the shaft. The butterfly valve must be coupled with an actuator capable of closing and controlling the valve under these design conditions. A good understanding of the operating characteristics of butterfly valves allows a designer to properly size a valve to minimize cost and improve reliability. Kurkjian [1] has observed that most problems related to butterfly valves result from misapplication rather than mechanical or structural problems. Unfortunately, information detailing the operating characteristics of butterfly valves is limited and generally dated. As noted by Cohn [2] in a review of previous butterfly valve research, the information available lacks uniformity and, as a result, is difficult to use for design purposes. The information is often specific to a particular valve or application. General information focusing on compressible flow phenomena through butterfly valves and the related operating characteristics is extremely limited.

The torque characteristics of a butterfly valve consist of contributions from aerodynamic phenomena, the frictional effects of seals and packings, preload from the packing, and preload from the seat. In general, for on/off applications the packing and preload contributions are principal design considerations. More recently, the aerodynamic torque has received attention for on/off applications in which closure is essential, such as the nuclear containment application, and also for applications in which butterfly valves are used for flow control. An understanding of the aerodynamic torque characteristics is essential for an effective control system in these situations. This discussion focuses on the fluid dynamic contribution to the torque.

The aerodynamic torque is primarily a function of the valve disk angle, the operating pressure ratio, the valve disk geometry, and the local piping geometry, with Reynolds number being a secondary effect. The mean aerodynamic torque characteristics of typical butterfly valves with small or no shaft offset have been documented in the available literature for a basic application, a butterfly valve located in a straight section of pipe, and are generically described as follows. In a fully open position, (a valve angle of $\alpha = 0$ deg by present convention), the aerodynamic torque on a butterfly valve is generally small. The aerodynamic forces on the disk are relatively small and generally well balanced. In a nearly

[1]This research was conducted as unfunded independent research at the University of Illinois at Urbana-Champaign prior to the employment of M. J. Morris at McDonnell Douglas Research Laboratories.

Contributed by the Fluids Engineering Division and presented at the Winter Annual Meeting, Chicago, Ill, November 27–December 3, 1988, of THE AMERICAN SOCIETY OF MECHANICAL ENGINEERS. Manuscript received by the Fluids Engineering Division July 22, 1988.

closed position, the net aerodynamic torque on the valve disk is also generally small. In this position, however, the fluid dynamic forces on the disk are large, but they are well balanced with respect to the valve axis of rotation. At an intermediate angle, generally in a range of 10 to 30 deg from fully open, butterfly valves typically exhibit a peak aerodynamic torque. In general, the aerodynamic torque on butterfly valves with geometries similar to those reported herein is in the direction of valve closure. In addition, for a given valve disk angle, the absolute torque and the corresponding pressure forces increase with an increase in the pressure drop across the valve. The pressure on the upstream surface, which contributes to the aerodynamic torque, has been determined to be closely related to the upstream stagnation pressure by Hicks et al. [3]. In addition, Hicks stated that the pressure on the downstream disk surface was at a level between the system back pressure and the pressure at the minimum cross sectional flow area at the valve disk periphery. Furthermore, the pressure on the downstream surface of the disk was approximated by Addy et al. [4] for large valve disk angles (i.e., near a fully closed position) using a one-dimensional, sudden enlargement analytical model. However, the aerodynamic torque characteristics of butterfly valves in typical applications are not so easily generalized. In contrast to the previous generalizations, the absolute level of the torque does not necessarily decrease with closure. This would only be true if the pressure drop across the valve remained constant as the valve was closed. Valve closure often leads to a larger pressure drop across the valve, with the resulting change in the operating conditions increasing the aerodynamic torque.

The analytical prediction of fluid dynamic torque for an incompressible butterfly valve flow was the topic of work by Sarpkaya [5, 6]. Sarpkaya modeled the butterfly valve as a two-dimensional plane lamina bounded by two parallel walls. Sarpkaya predicted the contraction coefficient and the hydrodynamic torque as part of his investigation. These characteristics compared favorably to experimental results of three-dimensional prototype butterfly valves. The general torque characteristics of butterfly valves were presented in the results and featured small torques near both fully open and fully closed positions with a peak torque near a valve disk angle of $\alpha = 20$ deg. Unfortunately, the restrictions of the free streamline model used by Sarpkaya limit the application of this method, particularly in compressible flows. A basic assumption of the model requires that the flow separates from the edges of the valve disk and does not reattach to the downstream surface, thereby implying that the downstream surface is always bounded by a relatively constant pressure wake region. In general, the present investigation will show that the flow does separate from the edges of the valve disk for compressible flows, but that it frequently reattaches to the downstream surface of the disk as a function of both the valve disk angle and operating pressure conditions.

An experimental and analytical investigation of the torque characteristics of a butterfly valve for compressible flow was presented by Sylvester [7]. Sylvester analytically modeled the pressure distribution on the valve disk surface and used this result to calculate an aerodynamic torque. He determined the streamwise pressure distribution using a one-dimensional analysis based on the cross-sectional areas of the flow bounding both the upstream and downstream surfaces of the valve disk. This analysis included locating the position of shock waves resulting from the converging-diverging passage bounded by the downstream surface of the disk. The calculations were used to produce a family of curves predicting the valve aerodynamic torque characteristics. These curves did not accurately model the torque characteristics of typical butterfly valve over a range of operating conditions. Sylvester reasoned that the deviation resulted from the oversimplification inherent in the one-dimensional model. Sylvester did not consider the effects of separation and reattachment on the local flowfield and the related pressure distributions. The results of the present investigation demonstrate that flow separation and the related flowfield phenomena are dominant mechanisms in the determination of the aerodynamic torque of butterfly valves.

Experimental Results

This investigation is part of an extensive study of compressible flow through butterfly valves [8] that include both two- and three-dimensional models of butterfly valves located in straight, constant area ducts. The experiments included a range of valve disk angles and operating pressure ratios, P_b/P_0. The three-dimensional model (nominal diameter = 76.2 mm) was a geometrically similar scale model of a prototype butterfly valve. The valve shaft of the three-dimensional model was supported using ball bearings and sealed with labyrinth seals. The resulting bearing and seal resistance torque was insignificant in comparison to the aerodynamic torque which was measured using a Lebow torque transducer with a capacity of 7.06 N-m. The two-dimensional, planar models (nominally 101.6 mm high by 38.1 mm wide) were included to simplify instrumentation for detailed pressure measurements and to allow optical access for Schlieren flow visualization. The shape of one two-dimensional model ("flat plate") was a streamwise cross-section at mid-plane of the three-dimensional model. A second two-dimensional model, with a bi-convex, circular arc profile, was used to investigate the influences of valve disk shape. The operating pressure ratio was varied between an unchoked operating condition of $P_b/P_0 = 0.85$ to a choked operating ratio of $P_b/P_0 = 0.20$. The valve disk angle was varied in a range from fully open, $\alpha = 0$ deg, to a nearly closed position, $\alpha = 70$ deg. For this range of operating conditions the Mach number of the inlet duct flow approaching the valve disk varied over the range $0.04 \leq M \leq 0.64$ while the inlet duct Reynolds number varied through the range $1.3 \times 10^5 \leq \mathrm{Re} \leq 5.2 \times 10^6$. Detailed pressure distributions were measured on all of the test section surfaces for the two-dimensional models.

Nomenclature

C_T = dimensionless torque coefficient
D = diameter or duct height
M = Mach number
P = pressure
Re = Reynolds number
t = valve disk thickness
T = aerodynamic torque or temperature
w = mass flowrate
x = chordwise coordinate measured from the center of rotation
α = valve disk angle measured from the fully open position

Subscripts

b = back
d = downstream
or = orifice
u = upstream
0 = stagnation conditions
1,2 = locations upstream and downstream of the valve, respectively

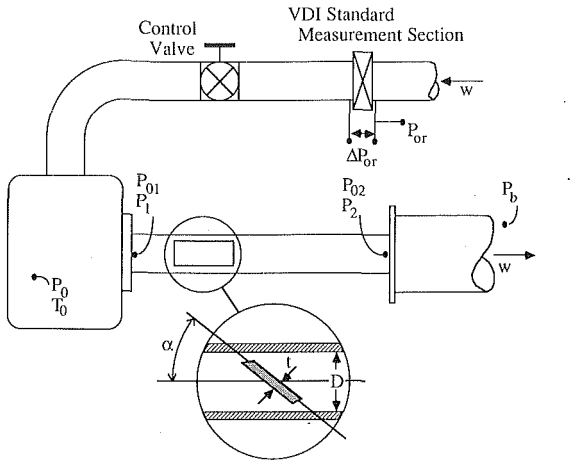

Fig. 1 Schematic of experimental apparatus and nomenclature for model valve experiments

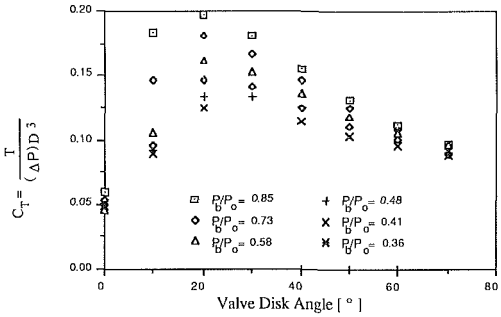

Fig. 2 Aerodynamic torque characteristics for the three-dimensional prototype valve. (Uncertainty in $C_T = \pm 0.02$, in $\alpha = \pm 0.5$ deg, and in $P_b/P_0 = \pm 0.01$.)

The static pressure was measured along the chord on both sides of the valve disk at intervals of 3 percent of the chord length. In addition, the pressure distribution of the entire flowfield bounding the valve disk was measured with approximately 400 static pressure taps on the four test section side walls. The flowfield bounding the models was also visualized using both still and movie Schlieren photography. Regions of separation and reattachment were identified using oil streak surface flow visualization. A schematic of the experimental configuration and the experimental variables is shown in Fig. 1.

Three-Dimensional Model. The torque characteristics measured for the three-dimensional model are typical of prototype butterfly valves and are shown in Fig. 2. The torque coefficient, defined as the aerodynamic torque divided by the product of the pressure difference across the valve and the cube of the diameter, is small at the fully open position for all of the included operating pressure ratios. The small positive value for the torque coefficient at $\alpha = 0$ deg is due to the asymmetry of the leading edge profile of the valve disk, as shown qualitatively in the inset to Fig. 1. The torque coefficient is also small for angles near a closed position for all operating pressure ratios. At an intermediate valve disk angle, $\alpha = 20$ deg, the torque coefficient reaches a maximum value. As will be discussed below and as is mentioned in reference [9], this peak torque phenomenon has been shown to be related to the transition from a flowfield attached to the downstream side of the valve disk to a flowfield entirely separated from the downstream side of the disk. The torque coefficient is also seen to be a function of the operating pressure ratio with the greatest variation near the peak torque angle. These torque characteristics can be qualitatively explained by relating them to the results of the experiments utilizing the two-dimensional models.

Two-Dimensional Models. An indication of the torque characteristics of a two-dimensional model can be determined by integration of the pressure forces on the valve disk surface (assuming that the contribution of the viscous shear forces to the torque is negligible), provided that a sufficiently detailed pressure distribution is measured. As mentioned previously, the pressure distributions on the two-dimensional models of this investigation were determined with pressure taps spaced at 3 percent of the chord length. This spacing was limited by the size of the tubulations and the physical constraints of fabrication. Prior to the experiments and reduction of the results and based on the limited data available, this spacing was believed sufficient. As will be discussed subsequently, the valve disk surface under certain operating conditions is bounded by regions of extreme pressure gradients, particularly near the valve disk leading and trailing edges. As a result, the pressure distributions near these edges could not be sufficiently defined. Compounding this difficulty, the moment arm of the pressure-area force is largest near the valve disk edges, thereby amplifying the uncertainty of the pressure distribution in the net torque calculations. Attempts to extrapolate the pressure distribution from the available data resulted in variations in the net torque of over 100 percent. This uncertainty prevents a more quantitative discussion of the aerodynamic torque on these models; however, it also clearly points out the sensitivity of the net torque in both two- and three-dimensional models to the surface pressure distribution near the valve disk leading and trailing edges.

A qualitative discussion of the local moment distributions and the related pressure distributions on the valve disk surface provides insight into the torque characteristics of butterfly valves. Selected data on the flat plate disk and the circular arc disk are presented herein. A more complete collection of data spanning the entire range of operating variables can be found in references [8 and 10]. In combination with Schlieren flow visualization, surface oil flow visualization, and the moment distributions, these selected pressure distributions demonstrate the importance of separation and reattachment of the flow on the torque characteristics of butterfly valves.

Small Valve Disk Angles. The net torque is relatively small for typical butterfly valves for valve angles near a fully open position. The valve disk surface pressure distributions for the range of operating pressure ratios on both the circular arc and the flat plate disks are shown in Figs. 3 and 4 for the fully open position, $\alpha = 0$ deg. For this and succeeding plots, the surface static pressure has been normalized with the upstream stagnation pressure, P_0, and the disk chord coordinate with respect to the duct height, D. The pressure distributions on each side of the circular arc disk are seen to be identical for all of the operating pressure ratios at $\alpha = 0$ deg. The slight asymmetry of the flat plate disk profile results in a slight asymmetry in the pressure distributions on opposing sides of the disk, particularly at the low operating pressure ratios. This asymmetry at the low pressure ratios was found to be the result of the shock pattern resulting from the asymmetric valve disk geometry. However, in general the pressure-area forces on both models are well balanced across the valve disk and, as shown in the moment distributions of the circular arc model, Fig. 5, the resulting moments are small. The dimensionless local moment on the valve disk is defined here as the local pressure difference across the disk multiplied by the moment arm about the axis divided by the product of the upstream stagnation pressure and the duct height. A similar moment distribution resulted for the flat plate model. This result is in good agreement with the findings for the three-dimensional

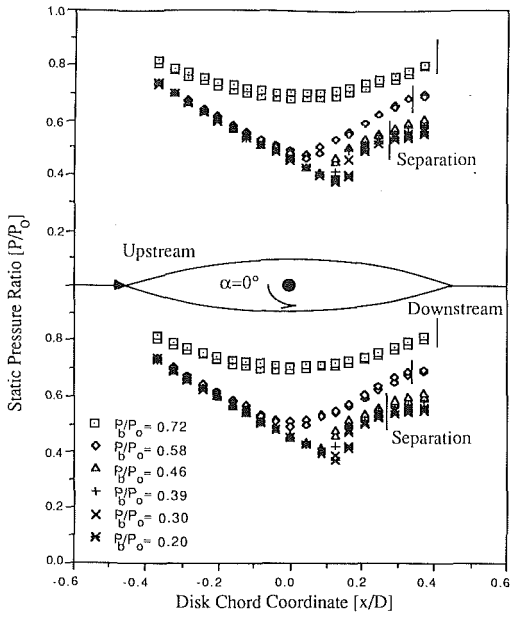

Fig. 3 Surface pressure distributions for the circular arc valve disk at $\alpha = 0$ deg. (Uncertainty in $P/P_0 = \pm 0.01$, in $x/D = \pm 0.002$, and in $P_b/P_0 = \pm 0.01$.)

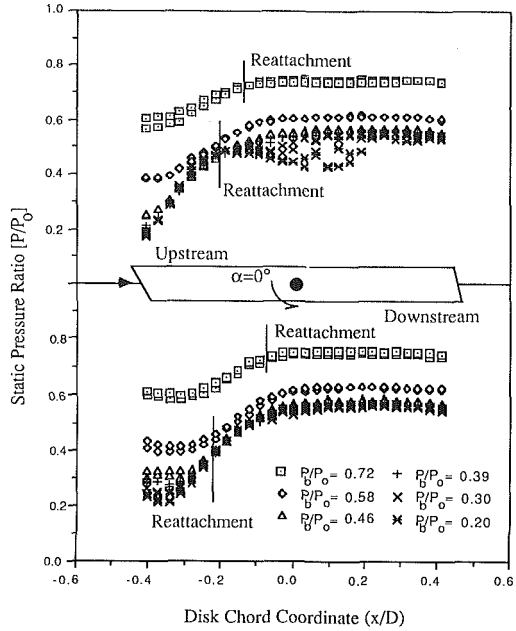

Fig. 4 Surface pressure distributions for the flat plate valve disk at $\alpha = 0$ deg. (Uncertainties same as Fig. 3.)

model experiments and for prototype butterfly valves in general.

For both the circular arc and flat plate disks in the fully open position, the flow through the valves was unchoked for $P_b/P_0 = 0.72$ and choked for all lower operating pressure ratios. In Fig. 3, the solid vertical lines mark the locations at which the flow separates from the downstream portion of the circular arc disk, as determined by surface oil flow visualization. For the flat plate disk of Fig. 4, the blunt nature of the leading edge causes local separation on each side of the disk; in this case, the solid vertical line marks the location of reattachment near the leading edge.

The reported pressure distributions are time-mean values and, as a result, correspond to mean moments. The Schlieren flow visualization also revealed that, upon choking, unsteady shock systems were present for both models as was previously reported in reference [11]. The shock systems for each model possess distinct characteristics that ultimately affect the pressure distributions and contribute to unsteady torque characteristics. Due to the limits of the available instrumentation, the effect of the unsteady shock wave motion on the complete pressure distribution and the resulting net torque of a fully open butterfly valve was beyond the scope of this investigation. However, these fluctuations could be an important operating characteristic of a fully open butterfly valve.

Intermediate Valve Disk Angles. As the valve disk is moved from a fully open position, the similarity of the pressure distributions on the upstream and the downstream valve disk surfaces diminishes for both models. Figure 6 shows the pressure distribution on the circular arc model at a disk angle of 15 deg. The surface oil flow visualization identified a stagnation point on the upstream surface of the valve disk near the leading edge. The flow accelerates away from the stagnation point towards the leading edge where it then separates. Following separation, the flow rapidly accelerates through an aerodynamic throat. At low operating pressure ratios, the flow further accelerates to supersonic velocities and subsequently reattaches to the downstream side of the valve disk. At the point of reattachment the flow turns through an oblique shock to realign itself with the valve disk surface. This reattachment shock was not anticipated by the present investigators nor reported by previous workers. The leading edge and the reattachment location bound a low pressure recirculation region. This low pressure region on the downstream disk surface is opposed by the stagnation region on the upstream side, as indicated by the large spacing between the two pressure distribution curves of Fig. 6, resulting in a relatively large pressure area force at a large moment arm. After reattachment on the downstream surface of the valve disk, the flow recompresses through an oblique shock and then reaccelerates along the valve disk. The flow terminally separates from the downstream surface in a shock wave/boundary layer interaction, as hypothesized by both Hicks [3] and Sylvester [7]. Downstream of this separation the valve disk surface is bounded by a constant pressure wake region. Also, as expected, the pressure distribution on the upstream surface of the valve disk is monotonically decreasing, corresponding to that of a converging nozzle. The dimensionless pressure distribution on the upstream surface of the valve disk for choked operating conditions, $P_b/P_0 < 0.70$, was found to be insensitive to the operating pressure ratio for the length of the disk. In contrast, the pressure distribution on the downstream surface is independent of the operating pressure ratio only up to the terminal separation point.

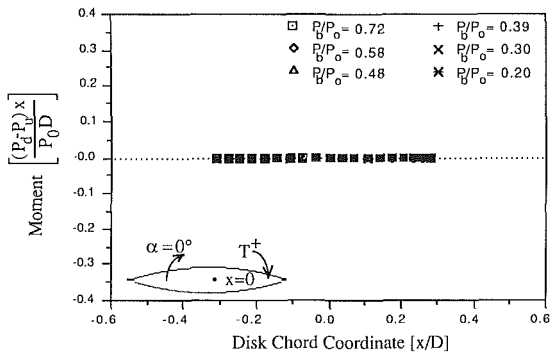

Fig. 5 Local moment distributions for the circular arc valve disk at $\alpha = 0$ deg. (Uncertainty in $(P_d - P_u)x/P_0D = \pm 0.02$, in $x/D = \pm 0.002$, and in $P_b/P_0 = \pm 0.01$.)

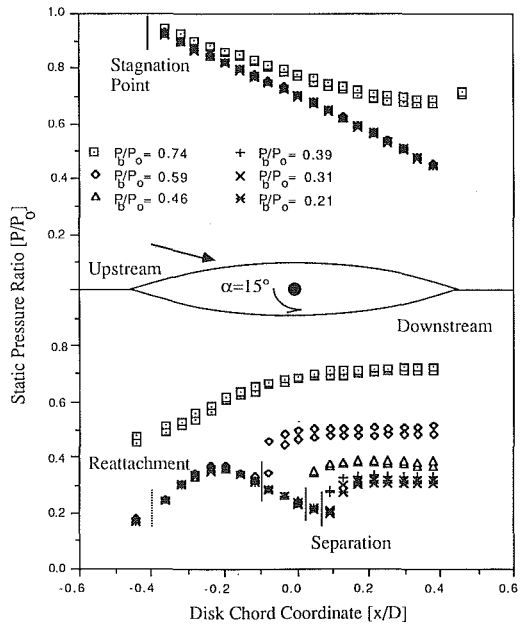

Fig. 6 Surface pressure distributions for the circular arc valve disk at $\alpha = 15$ deg. (Uncertainties same as Fig. 3.)

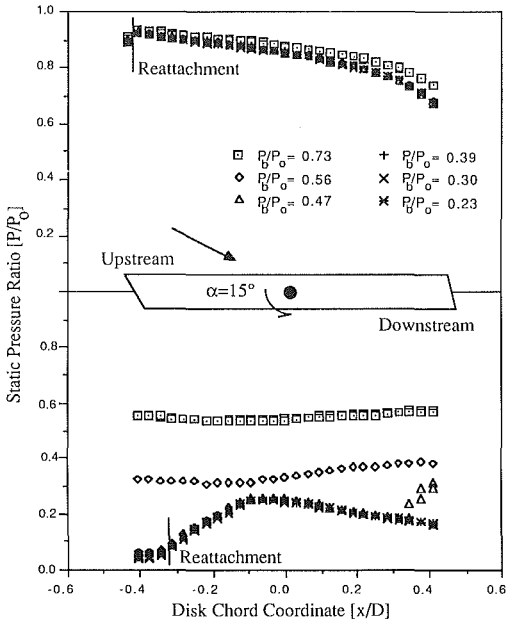

Fig. 8 Surface pressure distributions for the flat plate valve disk at $\alpha = 15$ deg. (Uncertainties same as Fig. 3.)

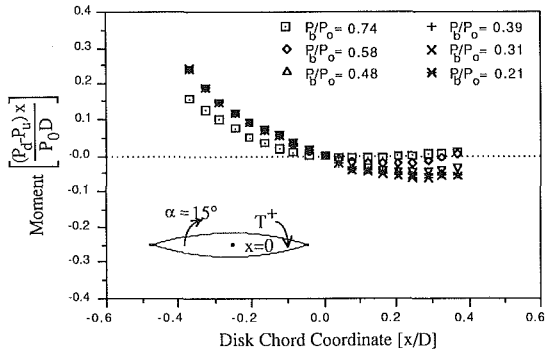

Fig. 7 Local moment distributions for the circular arc valve disk at $\alpha = 15$ deg. (Uncertainties same as Fig. 5.)

At operating pressure ratios for which the flow did not choke, $P_b/P_0 = 0.74$, the flowfield bounding both the upstream and downstream surfaces remains subsonic. The flow adjacent to the upstream surface of the valve disk experiences a decreasing streamwise cross-sectional area and accelerates. The corresponding pressure distribution gradually decreases in the streamwise direction, reaching a minimum near the trailing edge at a level roughly equal to the operating pressure ratio. As for the choked cases, the flow separates at the leading edge and similarly reattaches to the downstream surface of the valve disk. However, because of the subsonic velocities, no shock is associated with the reattachment. Downstream of reattachment, the flow is also subsonic and decelerates with the streamwise increasing flow area. The flow then finally separates from the downstream surface. For this unchoked condition, the pressure distribution on the downstream surface increases from the point of reattachment to the point of terminal separation. The portion of the valve disk surface bounded by the separated wake region is at a relatively constant pressure.

Figure 7 shows the moment distribution for the circular arc model at a valve disk angle of 15 deg. Upstream of the axis of rotation, $x/D < 0$, the pressure-area forces result in relatively large positive closing moments due to relatively large pressure differences across the valve disk at locations with large moment arms. Downstream of midchord, $x/D > 0$, the pressure difference across the valve is small, again as indicated by the spacing of the pressure distribution curves of Fig. 6, due to the abrupt increase caused by the shock/boundary layer interaction at separation on the downstream surface and the streamwise decrease along the upstream surface. At locations with large moment arms near the trailing edge, the pressure difference across the valve disk is small and, as a result, the moments are small. The result is an asymmetric moment distribution about the axis of rotation that causes a relatively large net closing torque. This corresponds to the peak torque phenomenon exhibited by butterfly valves.

Whereas the differences in the valve disk geometrical profiles did not strongly influence the general characteristics of the flowfield for the two disks in a fully open position, the separation characteristics for the two valve disks are quite different at a disk angle of $\alpha = 15$ deg. At this angle, the flow reattaches to the downstream side of the circular arc model after separation from the leading edge for all of the operating pressure ratios. On the other hand, at an operating pressure ratio of $P_b/P_0 = 0.73$, the flow did not attach to the downstream side of the flat plate model after separation from the leading edge. As a result, the entire downstream surface of the valve disk at this pressure ratio is bounded by a relatively constant pressure recirculation region as shown in Fig. 8. For this condition, the pressure distribution on the upstream surface of the valve disk effectively determines the net torque on the model. At lower pressure ratios, the flow patterns are similar to those for the circular arc model; the flow separates from the leading edge, accelerates through an aerodynamic throat to supersonic velocities, and reattaches to the downstream side of the valve disk. At the point of reattachment, the flow realigns to the downstream side of the disk through an oblique shock. Again, an extremely low pressure recirculation region is located near the leading edge of the valve disk on the downstream side. The flow recompresses through the reattachment shock and then reaccelerates to higher supersonic velocities with a corresponding decrease in the static pressure, as indicated by the pressure distributions of Fig. 8. At intermediate operating pressure ratios, the flow separates from the downstream side of the valve disk in a shock wave/boundary layer interaction as discussed above for the circular arc disk. However, for the flat plate model and at

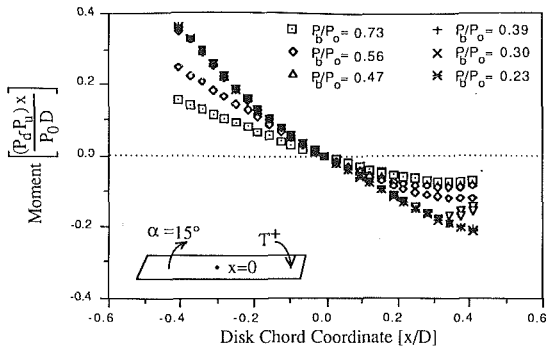

Fig. 9 Local moment distributions for the flat plate valve disk at $\alpha = 15$ deg. (Uncertainties same as Fig. 5.)

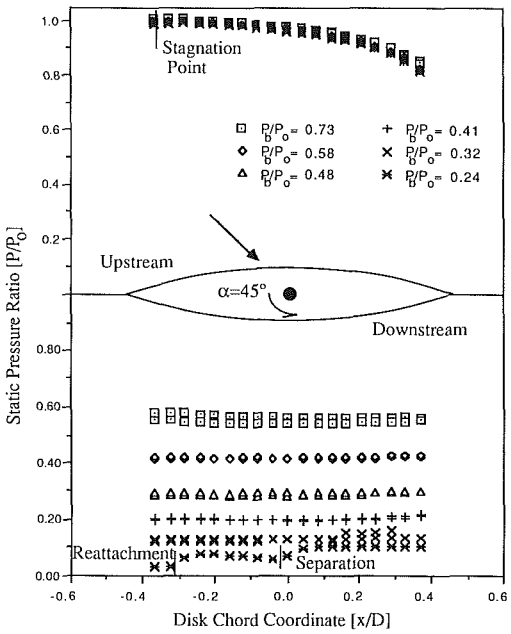

Fig. 10 Surface pressure distributions for the circular arc valve disk at $\alpha = 45$ deg. (Uncertainties same as Fig. 3.)

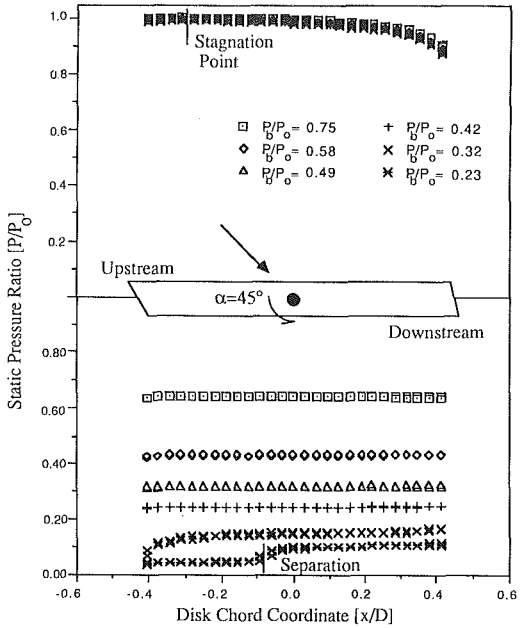

Fig. 11 Surface pressure distributions for the flat plate valve disk at $\alpha = 45$ deg. (Uncertainties same as Fig. 3.)

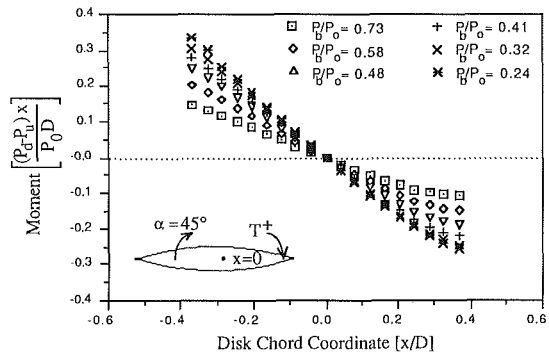

Fig. 12 Local moment distributions for the circular arc valve disk at $\alpha = 45$ deg. (Uncertainties same as Fig. 5.)

operating pressure ratios $P_b/P_0 < 0.40$, the flow does not separate from the downstream side of the valve disk. Rather, the flow separates from the opposing test section wall at the impingement point of the reattachment shock. This finding is in contrast to the flowfields hypothesized by Hicks [3] and Sylvester [7]. Because the flow remains attached to the downstream side of the valve disk, the pressure on the downstream side is sustained at a low level for the length of the disk. The resulting opening moments of the trailing edge region thereby counterbalance the closing moments generated near the leading edge and reduce the net torque. The moment distributions for the flat plate disk at $\alpha = 15$ deg are shown in Fig. 9. Clearly, they are more symmetric about the axis of rotation, and therefore the net torque is smaller, than for the circular arc disk under the same conditions (see Fig. 7).

Large Valve Disk Angles. At larger valve disk angles the pressure distributions and, as a result, the torque characteristics of the two valve disk models again become more similar. The pressure distributions for the circular arc and the flat plate models at $\alpha = 45$ deg are shown in Figs. 10 and 11, respectively. For both models, a stagnation point is located on the upstream surface of the valve disk. The flow gradually accelerates along the upstream valve disk surface and separates at the leading and trailing edges. A large portion of the upstream surface of the valve disk is bounded by a low velocity flow at a relatively constant pressure level approximately equal to the upstream stagnation pressure. The flow accelerates rapidly near both the leading and trailing edges, resulting in large pressure gradients near the valve disk periphery, and then separates from the valve disk leading and trailing edges. At operating conditions for which choking occurs, the flow accelerates through an aerodynamic throat located near the leading edge on the downstream side to supersonic velocities. At all but very low pressure ratios, the flow does not reattach to the downstream surface of the valve disk for $\alpha = 45$ deg. When the flow does not reattach, the entire downstream surface is bounded by a constant pressure wake region. As before for such cases, the moment distributions are principally determined by the pressure distribution on the upstream surface of the disk. The pressure distribution associated with the converging streamwise flow area bounded by the upstream surface of the valve disk causes the net torque to be a closing torque. The moment distributions for the circular arc model, Fig. 12, are seen to be nearly linear and symmetric about the axis of rotation, indicating a small net torque. As shown by Addy et al. [4], the wake pressure for these cases is closely related to the sudden enlargement losses of the flow around the valve disk. The lower the operating pressure ratio, the greater the losses and the lower the wake pressure. As a result, the pressure difference across the valve

disk is larger at lower operating pressure ratios. Further, the larger the pressure difference, the larger the local moments at a given chord position. However, because both the upstream and downstream surfaces of the valve disk are bounded by regions of relatively constant pressure, the moments are well balanced and, as a result, the net torque is small.

At low operating pressure ratios, $P_b/P_0 < 0.3$, the flow reattaches to the downstream surface of both the circular arc and the flat plate valve disk models at a disk angle of $\alpha = 45$ deg. The flow separates from the leading edge, accelerates through the aerodynamic throat, and expands to high supersonic velocities. The results of the flow visualization experiments clearly show the flow reattaching to the downstream surface of the valve disk and separating from the opposing test section wall. The flow accelerates along the downstream surface of the disk after reattachment until separating in a shock wave/boundary layer interaction. As a result, the pressure distribution remains relatively constant at a low level over the length of the downstream surface of both valve disks. The pressure-area forces across the valve disk are large and approximately equal for the entire length of the disk for these reattaching cases. Therefore, the moment distributions for these pressures ratios are similar to those at higher operating pressure ratio levels, i.e., they are nearly linear and symmetric about the axis, indicating a small net torque.

At a valve disk angle of $\alpha = 60$ deg, the flow does not reattach to the downstream side of the valve disk at any of the operating pressure ratios of this investigation. As a result, for all cases of both valve models the downstream surface of the valve disk is bounded by a relatively constant pressure wake region. In addition, nearly all of the upstream valve disk surface is adjacent to a region of very low velocity and a pressure roughly equal to the upstream stagnation pressure. The pressure distributions for both models at $\alpha = 60$ deg are similar and, as a result, only the chordwise pressure profiles for the circular arc model are presented here, Fig. 13. As can be seen, the pressure difference across the valve disk is relatively large, but as before the pressure-area forces are well balanced with respect to the axis of rotation. The moment distributions for this valve angle are essentially linear and symmetric with respect to the axis. For this reason, the net resultant force on the valve disk models is large, but the net torque is small.

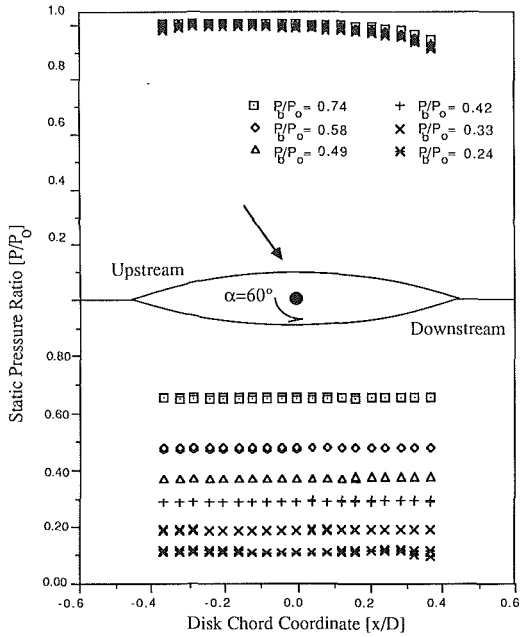

Fig. 13 Surface pressure distributions for the circular arc valve disk at $\alpha = 60$ deg. (Uncertainties same as Fig. 3.)

Conclusions

The two-dimensional models investigated herein provide insight into the local flowfield bounding butterfly valve disks and reveal the significance of separation and reattachment on the aerodynamic torque characteristics of butterfly valves. The experimental measurements obtained with these models qualitatively agree with the results of three-dimensional model valve experiments, such as those by Keller and Salzmann [12], and generally accepted operating characteristics of actual prototype butterfly valves. However, it is recognized that a three-dimensional prototype valve flowfield is different from that of a two-dimensional model flowfield. For example, both separation and reattachment are three-dimensional in nature for prototype valves. Yet, experiments by Keller and Salzmann have indicated that the pressure distributions remain two-dimensional in nature when normalized with the streamwise chord dimension. In addition, Sarpkaya [5] provides an analytical argument for the two-dimensionality of the flow bounding a butterfly valve disk. The characteristics of the flowfield for a prototype valve should therefore be generically similar and the effects of these characteristics on the net torque should be in qualitative agreement with those of the two-dimensional models.

The aerodynamic torque characteristics of butterfly valves are determined by the distribution of pressure-area forces exerted by the local flowfield on the valve disk. In turn, the pressure distribution on the disk is a function of the local piping geometry, the valve disk shape, the valve disk angle, and the operating pressure ratio. Compressibility does not alter the overall qualitative torque characteristics of butterfly valves, featuring relatively small torques at both large and small valve disk angles and a peak torque at an intermediate valve angle. However, effects of compressibility including supersonic velocities, expansion waves, and shock waves contribute to the complexity of the local flowfield and the resulting local pressure distributions.

The valve disk shape is an important design constraint. Flow separation and the corresponding influence on the valve disk pressure distribution strongly influences the unique aerodynamic torque characteristics of butterfly valves. The peak torque phenomenon is directly related to the separation/reattachment characteristics of the flow bounding the butterfly valve disk. The details of the disk shape can alter the magnitude of the peak torque and the angle at which it occurs by inducing or retarding reattachment to the downstream side of the valve disk. The disk geometry is particularly important near both the leading and trailing edges. In particular, separation and reattachment occurring near the leading edge determine the pressure distribution at the maximum moment arm and, as a result, strongly influence the aerodynamic torque. However, at valve disk angles both near a fully open or fully closed position, the influence of disk shape for valves similar to those reported herein is minimal due to the balance of aerodynamic forces.

Considering the apparent influence of separation and reattachment on the torque characteristics of butterfly valves, common techniques in controlling these phenomena could enhance the operating characteristics of these valves. Passive methods might include modification of disk and/or valve body geometries. Valve disk shapes have been shown to influence the location of stagnation points, to influence the local acceleration of the flow, and to influence the separation/reattachment characteristics of the flow. Active methods might include localized suction to retard separation or possibly to enhance flow reattachment. Conversely, transverse blowing might be used to cause separation or inhibit reattachment.

References

1 Kurkjian, G. A., "Follow These Simple Rules to Get Long Life from Your Large Butterfly Valves," *Power*, Vol. 118, July 1974, pp. 42–44.

2 Cohn, S. D., "Performance Analysis of Butterfly Valves," *Instruments*, Vol. 24, 1951, pp. 880–884.

3 Hicks, H. H., Garby, L. C., Stohrer, A., and Reid, F. A., "Flow and Torque Characteristics of Butterfly Valves at Subcritical and Supercritical Pressure Ratios," Project M932 Report for Sverdrup and Parcel, Inc., Engineering Research Institute, University of Michigan, Ann Arbor, Oct. 1952.

4 Addy, A. L., Morris, M. J., and Dutton, J. C., "An Investigation of Compressible Flow Characteristics of Butterfly Valves," ASME JOURNAL OF FLUIDS ENGINEERING, Vol. 107, Dec. 1985, pp. 512–517.

5 Sarpkaya, T., "Torque and Cavitation Characteristics of Butterfly Valves," ASME *Journal of Applied Mechanics*, Vol. 28, Dec. 1961, pp. 511–518.

6 Sarpkaya, T., "Oblique Impact of a Bounded Stream on a Plane Lamina," *Journal of the Franklin Institute*, Vol. 267, 1959, pp. 229–242.

7 Sylvester, R. S., "Torque Induced by a Butterfly Valve Carrying a Compressible Flow," *Institution of Mechanical Engineers Proceedings*, Vol. 196, 1982, pp. 229–237.

8 Morris, M. J., "An Investigation of Compressible Flow Through Butterfly Valves," Ph.D. thesis, Department of Mechanical and Industrial Engineering, University of Illinois at Urbana-Champaign, Urbana, Ill., Apr. 1987.

9 Morris, M. J., Dutton, J. C., and Addy, A. L., "Peak Torque Characteristics of Butterfly Valves," *Proceedings of the Forum on Industrial Applications of Fluid Mechanics*, ASME FED-Vol. 54, Dec. 1987, pp. 63–66.

10 Morris, M. J., Dutton, J. C., and Addy, A. L., "An Investigation of Compressible Flow Through Butterfly Valves," Department of Mechanical and Industrial Engineering, University of Illinois at Urbana-Champaign, Report No. UILU-ENG-87-4007, July 1987.

11 Morris, M. J., Dutton, J. C., and Addy, A. L., "Unsteady Flow Characteristics of Fully Open Butterfly Valves," *Proceedings of the Forum on Unsteady Flow*, ASME FED-Vol. 39, Dec. 1986, pp. 25–27.

12 Keller, C., and Salzmann, F., "Aerodynamic Model Tests on Butterfly Valves," *Escher Wyss News*, Zurich, Vol. IX, No. 1, Jan.–Mar. 1936.

Compressible Flowfield Characteristics of Butterfly Valves[1]

M. J. Morris
Research Scientist,
McDonnell Douglas Research Laboratories,
McDonnell Douglas Corporation,
St. Louis, MO 63166

J. C. Dutton
Associate Professor,
Department of Mechanical
and Industrial Engineering,
University of Illinois at Urbana-Champaign,
Urbana, IL 61801

The results of an experimental investigation into the flowfield characteristics of butterfly valves under compressible flow operating conditions are reported. The experimental results include Schlieren and surface flow visualizations and flowfield static pressure distributions. Two valve disk shapes have been studied in a planar, two-dimensional test section: a generic biconvex circular arc profile and the midplane cross-section of a prototype butterfly valve. The valve disk angle and operating pressure ratio have also been varied in these experiments. The results demonstrate that under certain conditions of operation the butterfly valve flowfield can be extremely complex with oblique shock waves, expansion fans, and regions of flow separation and reattachment. In addition, the sensitivity of the valve disk surface pressure distributions to the local geometry near the leading and trailing edges and the relation of the aerodynamic torque to flow separation and reattachment on the disk are shown.

Introduction

The operating characteristics of butterfly valves, principally the torque and the flowrate capacity, are generally determined empirically for a given design. Anomalies of the operating characteristics are typically identified experimentally and avoided in practice. For example, aerodynamic torque reversals have been avoided by blocking the valve disk rotation such that the valve will not open fully, thereby assuring a closing torque. Unfortunately, this solution reduces the valve capacity and introduces unnecessary losses into the piping system. As a result, valve sizes and subsequently costs are increased.

Little attention has been focused on the actual flowfield within a butterfly valve and the influence of the corresponding flow phenomena on the operating characteristics of the valve. An understanding of these influences would be useful in designing valves to improve their operating characteristics and possibly to eliminate anomalies. As a result, a detailed experimental investigation has been conducted, part of which focused on identifying the features of the flowfield within a butterfly valve [1]. These experiments were performed with planar, two-dimensional valve models mounted in a rectangular wind tunnel test section of 101.6 mm (4 in.) height and 38.1 mm (1.5 in.) width, Fig. 1. The wind tunnel was designed to represent a fundamental butterfly valve system, specifically a butterfly valve in a short, straight section of pipe with a uniform inlet velocity profile for a range of operating pressure ratios. These two-dimensional models were employed to facilitate optical access for flow visualization and instrumentation access for detailed pressure measurements, under the assumption that the two-dimensional model flowfields would be qualitatively similar to those for three-dimensional valve prototypes. Two basic valve disk shapes, shown in Fig. 1, were selected for these experiments, an 18 percent thick biconvex circular arc profile and a 12 percent thick flat plate profile. The circular arc profile was chosen because of its simple geometry with sharp leading and trailing edges and because it has been the subject of previous experimental and numerical airfoil studies [2–5]. The flat plate profile is the midplane cross-section of a prototype butterfly valve that has been the subject of extensive modeling and experimental study [6, 7].

The test section was equipped with two types of side wall panels, both sets supporting the test valve models. One pair of side wall panels was designed to facilitate static pressure measurements on both the side walls and valve disks. For these side walls, an extensive grid of static pressure taps was located on all four walls of the wind tunnel test section, as well as on

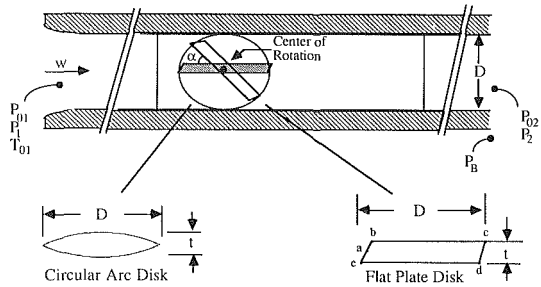

Fig. 1 Schematic of the two-dimensional wind tunnel test section used in the butterfly valve flowfield studies

[1]This research was conducted as unfunded independent research at the University of Illinois at Urbana-Champaign prior to the employment of M. J. Morris at McDonnell Douglas Research Laboratories.

Contributed by the Fluids Engineering Division and presented at the Winter Annual Meeting, Chicago, Ill., November 27-December 2, 1988 of THE AMERICAN SOCIETY OF MECHANICAL ENGINEERS. Manuscript received by the Fluids Engineering Division August 26, 1988.

the valve disk surfaces, thereby allowing the static pressure field in the vicinity of the disk to be completely mapped. The second pair of side wall panels was designed with 19 mm (3/4 in.) thick Pyrex observation windows. These side walls were designed to be streamwise reversible, permitting a view of approximately 60 percent of the upstream or downstream portion of the model chord length. Subsequent Schlieren photographs of similar operating conditions were overlapped and mounted to reveal the entire flowfield. In addition to mean static pressure measurements and Schlieren photographs and movies, surface flow visualization methods have been used to identify features of the flow near the model surfaces, notably separation and reattachment phenomena. The surface flow visualization was accomplished using a mixture of oil and lamp black. The resulting streaklines were observed through the side wall windows during formation and the results were recorded both photographically and by freehand sketches.

The primary independent variables investigated in these experiments are the valve disk angle and the back pressure ratio, which varied over the ranges: 0 deg (fully open) $\leq \alpha \leq 60$ deg (nearly closed) and 0.25 (choked) $\leq P_B/P_{01} \leq 0.75$ (unchoked), respectively. For these flow conditions, the Reynolds number and Mach number, based on the disk chord length and test section flow conditions approaching the valve, varied over the approximate ranges $1.3 \times 10^5 \leq \mathrm{Re} \leq 5.2 \times 10^6$ and $0.04 \leq \mathrm{M} \leq 0.64$, respectively. Because of its closer resemblance to actual prototype valves, the results reported here will primarily focus on the results for the flat plate disk profile. However, in addition, typical results from the circular arc model will be included to identify the influence, or lack thereof, of the valve disk shape on the flowfield details.

Experimental Results

In order to document the flowfield characteristics over a range of operating conditions, the discussion of results is divided into sections according to the magnitude of the valve disk angle: fully open, intermediate angles, and large angles.

Flowfield Description for a Fully Open Valve Disk. Butterfly valves generally exhibit maximum flow capacity and minimum losses when the valve disk is in a fully open position. Thus, this is a common and important operating condition that bears careful consideration. Figures 2(*a*)-(*c*) are Schlieren photographs of the fully open two-dimensional flat plate valve disk at back pressure ratios of $P_B/P_{01} = 0.72$, 0.50, and 0.25 respectively. (Note: The curved lines extending from the lower left to the upper right of this and subsequent Schlieren photographs are striae in the Pyrex glass windows of the test section and are not related to the flow. In addition, the vertical line that intersects the valve disk slightly upstream of midchord is the merger line of the corresponding upstream and downstream Schlieren photographs discussed previously. Finally, the flow direction is from left to right in all of the Schlieren photographs to be presented.) For $P_B/P_{01} = 0.72$, Fig. 2(*a*), the flow past the disk is not choked. The surface visualization experiments, in addition to the Schlieren photograph, identify a stagnation point on the oblique leading surface slightly off center towards the lower disk surface

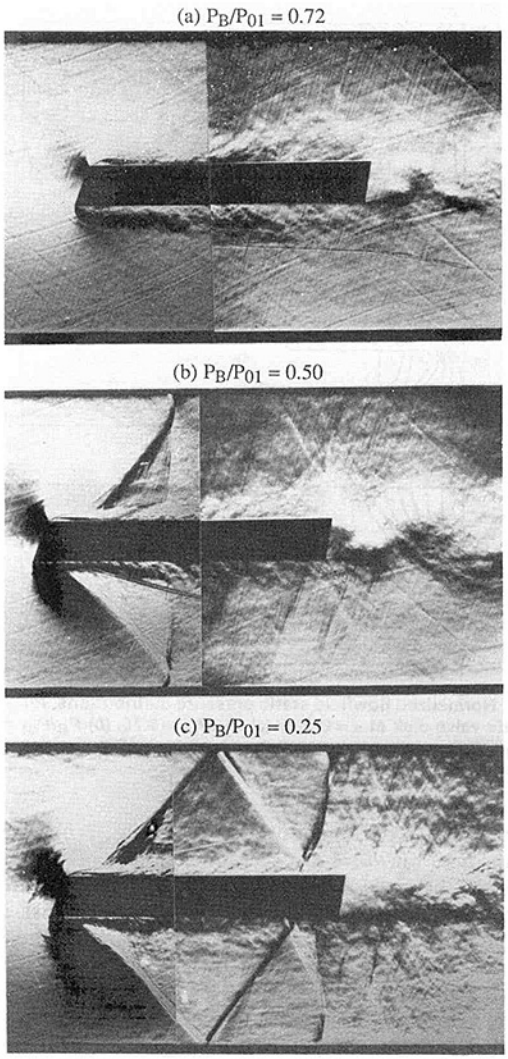

Fig. 2 Schlieren photographs of the flowfield for the flat plate valve disk at $\alpha = 0$ deg: (*a*) $P_B/P_{01} = 0.72$, (*b*) $P_B/P_{01} = 0.50$, (*c*) $P_B/P_{01} = 0.25$

(point "a" of Fig. 1). The flow accelerates away from this stagnation point and separates at the leading edge of both the upper and lower parallel surfaces. A relatively low pressure, separated flow region bounds the leading edge region of both disk surfaces and is evident in both Fig. 2(*a*) and in the flowfield pressure distribution presented in Fig. 3(*a*). The recirculation region formed by the separation of the flow near the leading edge bounds a vena contracta that effectively functions as an aerodynamic minimum flow area. The surface visualization experiments identified the point of flow reattachment on both the upper and lower valve disk surfaces as slightly upstream of midchord for this case. At the downstream periphery, the flow separates at the sharp trailing edges of the disk surfaces, thereby forming a recirculating wake region bounded by two free shear layers.

Nomenclature

D = duct height of the two-dimensional wind tunnel
M = Mach number
P = pressure
Re = Reynolds number
t = valve disk thickness
T = temperature
w = mass flowrate
α = valve disk angle (0 deg is fully open)

Subscripts

01 = stagnation properties upstream of the test section
02 = stagnation properties downstream of the test section
1 = static properties at the inlet to the test section
2 = static properties downstream of the test section
B = back

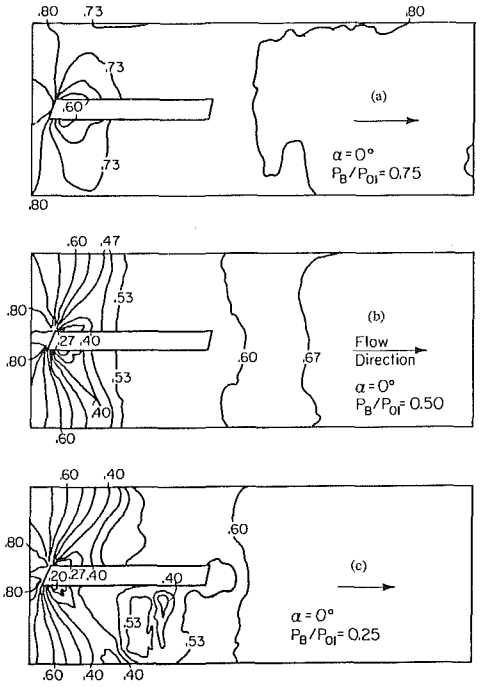

Fig. 3 Normalized flowfield static pressure distributions, P/P_{01}, for the flat plate valve disk at $\alpha = 0$ deg: (a) $P_B/P_{01} = 0.75$, (b) $P_B/P_{01} = 0.50$, (c) $P_B/P_{01} = 0.25$. (Uncertainty in $P/P_{01} = \pm 0.01$ and in the contour positions, x/D and $y/D = \pm 0.005$.)

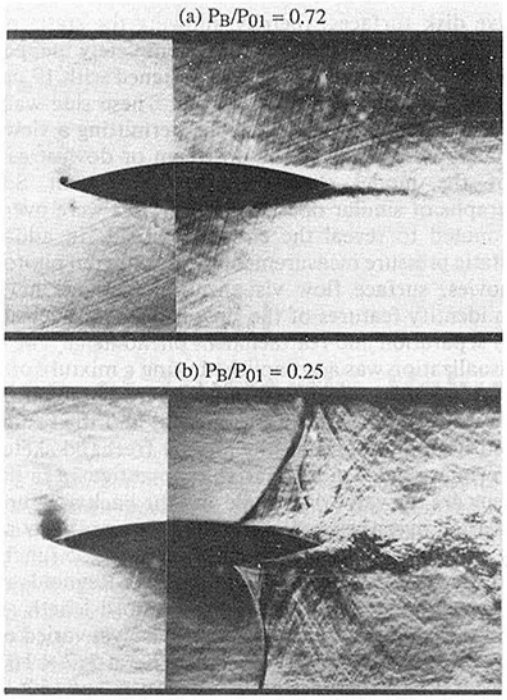

Fig. 4 Schlieren photographs of the flowfield for the circular arc valve disk at $\alpha = 0$ deg: (a) $P_B/P_{01} = 0.72$, (b) $P_B/P_{01} = 0.25$

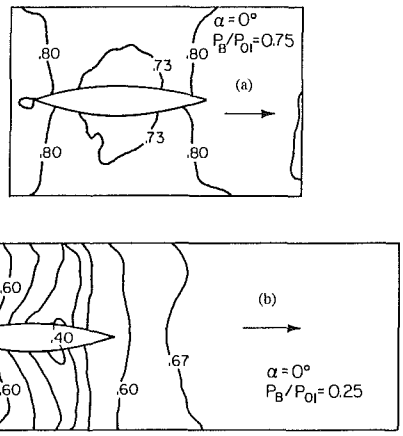

Fig. 5 Normalized flowfield static pressure distributions, P/P_{01}, for the circular arc valve disk at $\alpha = 0$ deg: (a) $P_B/P_{01} = 0.75$, (b) $P_B/P_{01} = 0.25$. (Uncertainties same as Fig. 3.)

For the lower back pressure ratios of Figs. 2(*b*) and (*c*), the flow through the valve test section is choked. Due to the formation of the previously mentioned aerodynamic throat, the region of sonic velocities for the flat plate valve disk is at the aerodynamic minimum flow area, very near the leading edge for these cases, as can be seen in the Schlieren pictures. For operating pressure ratios below $P_B/P_{01} = 0.60$, the flow accelerates through the vena contracta and reattaches to the valve disk supersonically, thereby isolating the upstream recirculation region from downstream influences. An oblique shock, shown in Figs. 2(*b*) and (*c*) for nominal operating pressure ratios of $P_B/P_{01} = 0.50$ and 0.25, respectively, is located at the point of reattachment in order to turn the flow in a direction parallel to the valve disk. In addition, for $P_B/P_{01} = 0.25$ this reattachment shock reflects from the test section walls, impinges on the valve disk near the trailing edge where it reflects again, before terminating at the test section walls.

Flowfield static pressure contours, normalized with respect to the upstream stagnation pressure, P/P_{01}, are presented in Figs. 3(*a*)–(*c*). For each of the back pressure ratios investigated, a strong acceleration of the flow occurs from the oblique leading surface to a minimum pressure located in the recirculation region near the leading edge. The convergence of the isobars also indicates the existence of large pressure gradients in this leading edge region. Downstream of the reattachment point (located by surface visualization) for the nominal operating pressure ratio of $P_B/P_{01} = 0.75$, the pressure distribution is relatively constant over the remainder of the valve disk at a level approximately equal to the back pressure ratio. For the choked operating conditions, Figs. 3(*b*) and (*c*) for $P_B/P_{01} = 0.50$ and 0.25, respectively, areas of low pressure corresponding to supersonic velocities span the duct from the valve disk to the opposing wall and are followed downstream by recompression due to the reattachment shock. For these conditions, $P_B/P_{01} \leq 0.60$, the flow recompresses through the reattachment shock downstream to a location at approximately midchord, as indicated by the increasing pressure distribution. The downstream half of the valve disk is at a relatively constant pressure. Nearly all of the large pressure gradients and the related flow phenomena are located near the leading edge for these cases.

In a fully open position, the local duct geometry of the circular arc model is symmetric with respect to the axis of rotation. Figures 4(*a*) and (*b*) show Schlieren photographs of an unchoked and a choked operating condition typical of this model, $P_B/P_{01} = 0.72$ and 0.25, respectively. Unlike the flat plate valve disk, the minimum flow area occurs near midchord for the circular arc disk. A stagnation point is located at the sharp leading edge. The flow does not separate near the leading edge in this case but rather accelerates subsonically past the forward half of the valve disk. For the unchoked case, the flow then decelerates over the rear half of the valve disk, separating near the trailing edge. For the choked case, the flow continues to accelerate to supersonic velocities and finally recompresses through a shock system to the downstream pressure level. The flowfield pressure distributions corresponding to the two cases shown in Figs. 4(*a*) and (*b*) are presented in Figs. 5(*a*) and (*b*), respectively. The pressure

distributions on both sides of the valve disk are nearly identical, resulting in negligible force imbalance. The low pressure regions and the abrupt pressure rise across the recompression shock for the choked case are not near the valve periphery, as was the case for the flat plate model, but rather are slightly downstream of midchord.

The choked flowfields of neither the flat plate nor the circular arc model in a fully open position were steady. The oblique reattachment shock originating near the leading edge of the flat plate model was relatively steady, as was the flowfield upstream of the reattachment shock, but the flow downstream of this shock was not steady over a range of operating pressure ratios. In particular, the reflected shock systems occurring for $P_B/P_{01} \leq 0.50$ were found to translate and rotate in an unsteady manner. In order to investigate this phenomenon, color Schlieren movies were made for the flowfields with nominal back pressure ratios of $P_B/P_{01} = 0.50$, 0.33, and 0.25. The reflected shock wave systems of the fully open flat plate model were found to be unsteady, moving upstream and downstream on each side of the valve disk approximately in phase. The boundary layers on the valve disk were observed to separate abruptly from the blunt trailing edges of the disk. The resulting free shear layers generate a vortex pair that is shed for these cases at a frequency of approximately 600 Hz, as determined from the movie film timing marks. This vortex shedding results in the stretching and collapse of the recirculation region downstream of the valve disk. The collapse of the recirculation region, in turn, generates unsteady, planar Mach waves that are observed to travel upstream and interact with the shock wave system. For very low back pressure ratios, $P_B/P_{01} \leq 0.20$, the flowfield of the flat plate model became relatively steady.

The shock system for the circular arc model was also unsteady under choked operating conditions. A recompression shock moved upstream and downstream on both sides of the valve disk. In contrast to the flat plate model, the shock motion on opposing sides of the circular arc valve disk was approximately 180 deg out of phase. However, similar to the flat plate model, for low back pressure ratios, the shock system became relatively steady.

This shock wave motion for the flat plate and circular arc valve disks was also verified and quantified in a series of experiments that used relatively high speed pressure transducers located on and near the surface of the disks. Whereas typical pressure fluctuations for the flat plate disk were comparable in amplitude to those for the circular arc disk, no dominant frequency component was easily identified for the flat plate model. In contrast, the shock wave motion for the circular arc model was nearly periodic with a dominant frequency in the range of 560-650 Hz, depending on the operating pressure ratio. Clearly, this unsteady shock wave motion, with its associated pressure fields, can lead to aerodynamic torque fluctuations on the valve disk. Further details concerning the unsteady nature of the flowfields of the flat plate and circular arc disks in the fully open position may be found in references [1] and [8]. In addition, McDevitt et al. [2], Levy [4], and Seegmiller et al. [5] identified similar unsteady shock wave motion for circular arc airfoils in unbounded external flows.

Flowfield Description for Intermediate Valve Disk Angles. When the valve disk is positioned at any angle other than fully open, the test section geometry is asymmetric with respect to the test section centerline. The flow bounding the upstream-facing (lower) side of the disk, in general, encounters a converging geometry which results in a favorable pressure gradient. The flow bounding this side of the disk is generally at relatively low speed and the features tend to vary little over the range of operating conditions. In contrast, the flow bounding the downstream-facing (upper) side of the disk encounters first a rapidly converging then a diverging

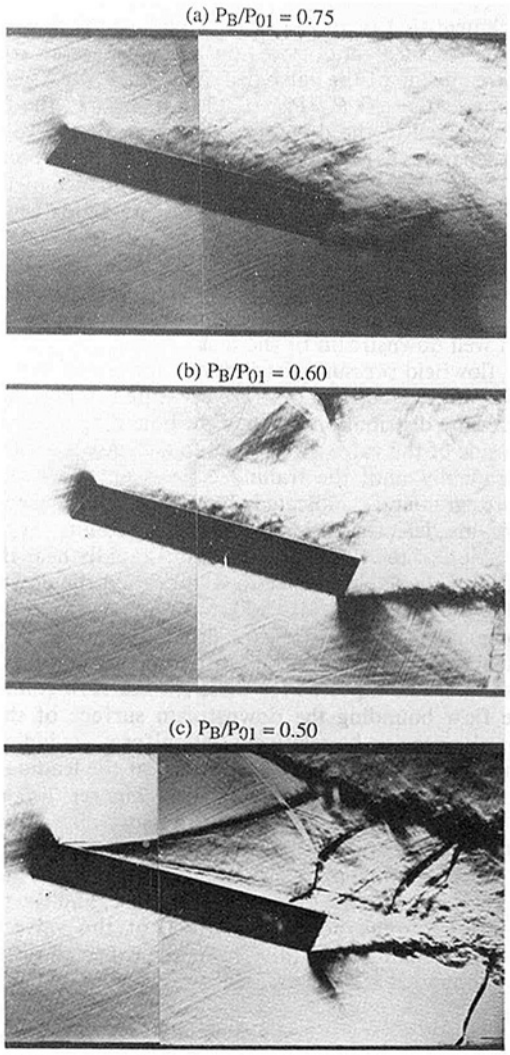

Fig. 6 Schlieren photographs of the flowfield for the flat plate valve disk at $\alpha = 15$ deg: (a) $P_B/P_{01} = 0.75$, (b) $P_B/P_{01} = 0.60$, (c) $P_B/P_{01} = 0.50$

geometry. The resulting flowfield is strongly dependent on both the valve disk angle and the operating pressure ratio and can be generally characterized as either attached or fully separated from the downstream side of the valve disk.

Schlieren photographs of the flowfield for a flat plate valve disk angle of $\alpha = 15$ deg, which is typical of intermediate angles, and back pressure ratios of $P_B/P_{01} = 0.75$, 0.60, and 0.50 are shown in Figs. 6(*a*)–(*c*). For $P_B/P_{01} = 0.75$, the valve flow is unchoked and the upstream stagnation point is located, within the accuracy of the surface flow method, at the leading edge of the upstream valve disk surface (point "e," Fig. 1). The flow accelerates from this stagnation point in the streamwise direction along the upstream surface of the disk and along the oblique leading surface where it separates at the leading edge of the downstream surface (point "b," Fig. 1). As can be seen in Fig. 6(*a*), the flow does not reattach to the downstream surface of the valve disk under these conditions.

For the remaining operating pressure ratios of Figs. 6(*b*) and (*c*), the flow past the model valve disk is choked. At $P_B/P_{01} = 0.60$, Fig. 6(*b*), the flow separates from the leading edge of the downstream disk surface, but does not reattach to this surface. An oblique shock structure can be observed near the wall opposing the downstream disk surface, but this structure does not extend to the disk. In contrast, for $P_B/P_{01} = 0.50$ (Fig. 6(*c*)), the flow separates from the leading edge and then reattaches to the downstream side of the valve disk very near the leading edge. An oblique shock is located at the point of

reattachment that turns the flow parallel to the disk surface. For this pressure ratio, the flow then separates from the downstream side of the valve disk in a shock wave/boundary layer interaction. At $P_B/P_{01} = 0.33$ (not shown), the flow remains attached to the downstream surface of the valve disk until it separates at the downstream disk periphery (point "c," Fig. 1). The flow bounding the upstream surface of the disk for each of the choked operating pressure ratios accelerates and remains attached for the length of the valve disk, separating at the trailing edge. This flow is observed to expand to supersonic velocities through a Prandtl-Meyer expansion at the trailing edge and finally recompresses through a shock system well downstream of the disk.

The flowfield pressure distributions for $\alpha = 15$ deg and for $P_B/P_{01} = 0.75$, 0.50, and 0.25 are presented in Figs. 7(*a*)-(*c*). The pressure distribution for the flow bounding the upstream-facing side of the valve disk is seen to decrease monotonically and gradually until the trailing edge is approached. Large pressure gradients, indicated by the convergence of the isobars, are detected in this region. These results suggest that this portion of the flowfield accelerates rapidly near the trailing edge of the valve surface to well beyond the downstream periphery of the disk. In addition, for $P_B/P_{01} \leq 0.60$ the upstream disk surface pressure distributions are essentially identical when scaled with the upstream stagnation pressure, P_{01}, as would be expected for these choked flow conditions.

The flow bounding the downstream surface of the valve disk is also seen to be relatively nonuniform, as indicated by the curvature of the isobars, but is so near the leading, rather than the trailing, edge of the surface. Figures 7(*a*)-(*c*) also show that the downstream surface pressure distributions are strongly dependent on the operating pressure ratio across the valve. For a nominal pressure ratio of $P_B/P_{01} = 0.75$, the flow does not reattach to the downstream surface, and the pressure distribution on the downstream face of the valve disk is relatively constant, Fig. 7(*a*). This is the expected result for a surface bounded by a separated wake region. At operating pressure ratios less than $P_B/P_{01} = 0.56$, the flow reattaches supersonically to the downstream surface of the disk, and the pressure distribution reflects a significant change, Figs. 7(*b*) and (*c*). Extremely low pressures are detected near the leading edge in the recirculation region for these cases, and the pressure gradients are also very large in this region. Downstream of the reattachment point, the flow recompresses through an oblique shock wave as indicated by a pressure rise, and then re-expands, accelerating along the downstream surface. The flow bounding the downstream surface and upstream of the reattachment shock is characterized by relatively low pressure ratios which are indicative of supersonic flow. The location of the previously discussed reattachment oblique shock wave is indicated by an increase in the static pressure ratio and agrees well with the Schlieren photographs. Also in agreement with the Schlieren photograph of the nominal $P_B/P_{01} = 0.50$, case, Fig 6(*c*), the pressure distribution on the downstream surface, Fig. 7(*b*), increases abruptly at a location corresponding to flow separation due to the shock/boundary layer interaction near the trailing edge. At lower back pressure ratios, Fig. 7(*c*), the disk pressure distributions suggest that the flow accelerates for the length of the downstream surface of the valve disk and separates from the trailing edge (corresponding Schlieren photograph not shown in Fig. 6). The relative insensitivity of the upstream disk surface pressure profiles, coupled with the strong sensitivity of the downstream surface pressure distributions to the operating pressure ratio, clearly leads to the conclusion that the aerodynamic torque on the valve disk is a strong function of whether or not the flow attaches to the downstream disk surface. In turn, this reattached/fully separated phenomenon may help to explain why a peak aerodynamic torque occurs for three-dimensional prototype butterfly valves at intermediate valve angles [7, 9].

The flowfield bounding the circular arc model at intermediate valve disk angles exhibits similarities to the flat plate model, yet also retains several distinguishing characteristics. Figures 8(*a*) and (*b*) for $P_B/P_{01} = 0.75$ (unchoked) and 0.33 (choked) are Schlieren photographs of the circular arc model with the flow separated from and attached

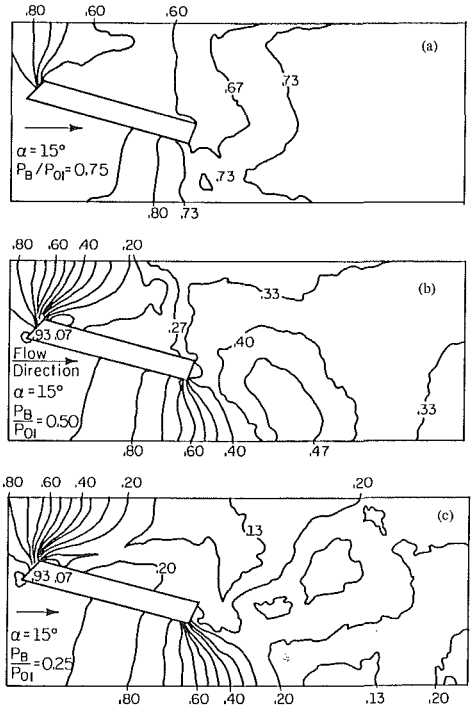

Fig. 7 Normalized flowfield static pressure distributions, P/P_{01}, for the flat plate valve disk at $\alpha = 15$ deg: (*a*) $P_B/P_{01} = 0.75$, (*b*) $P_B/P_{01} = 0.50$, (*c*) $P_B/P_{01} = 0.25$. (Uncertainties same as Fig. 3.)

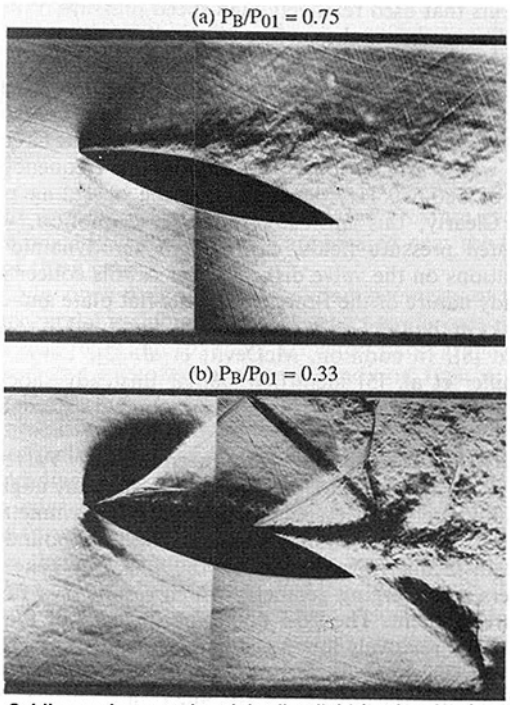

Fig. 8 Schlieren photographs of the flowfield for the circular arc valve disk at $\alpha = 15$ deg: (*a*) $P_B/P_{01} = 0.75$, (*b*) $P_B/P_{01} = 0.33$

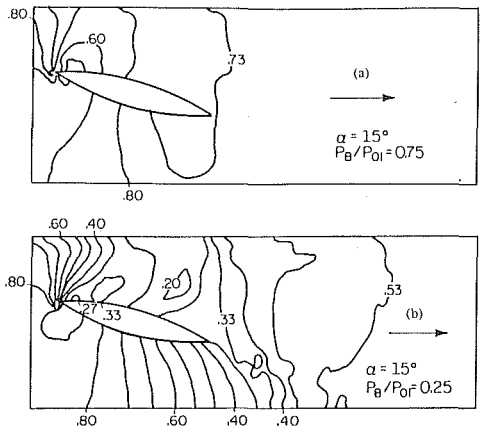

Fig. 9 Normalized flowfield static pressure distributions, P/P_{01}, for the circular arc valve disk at $\alpha = 15$ deg: (a) $P_B/P_{01} = 0.75$, (b) $P_B/P_{01} = 0.25$. (Uncertainties same as Fig. 3.)

to the downstream side of the valve disk, respectively. The flowfield static pressure distributions for similar cases are presented in Figs. 9(*a*) and (*b*). The flow reattaches to the downstream surface of the valve disk at a higher operating pressure ratio for the circular arc model, and thereby alters the valve disk pressure distribution, relative to the flat plate model for a similar case. However, for the reattached cases the pressure distributions on the downstream surface, Fig. 9(*b*), are consistent with those of the flat plate model. A low pressure recirculation region can be identified near the leading edge followed by a supersonic reattachment to the valve disk. At the reattachment point the flow compresses through an oblique shock. Downstream of the shock, the flow accelerates along the valve disk and finally separates in a shock wave/boundary layer interaction. Due to the sharp trailing edge, the flow always separates from the downstream surface of the circular arc valve disk in this type of interaction for reattached operating conditions.

Flowfield Description for Large Valve Disk Angles. As the valve disk angle is increased from the fully open position, the losses across the valve increase and the mass flowrate for a given operating pressure ratio correspondingly decreases. Although the transition from flowfields characteristic of intermediate angles to those characteristic of large angles is a continuous one, results are presented here for the case of $\alpha = 45$ deg as being representative of large valve disk angle flows. The differences in valve disk shapes have less of an effect at relatively large disk angles than at small angles. In addition, at these large angles the stagnation point is located on the upstream surface of the valve disk, with the surface flow visualization experiments indicating that as the valve angle increases, the stagnation point is located nearer to midchord. Also, the operating pressure ratio required for the flow to reattach to the downstream surface of the valve disk decreases as the valve angle increases.

Schlieren photographs of the flat plate disk flowfields for $\alpha = 45$ deg and $P_B/P_{01} = 0.75$, 0.50, and 0.25, are shown in Figs. 10(*a*)–(*c*), respectively. For each of these cases, the flow separates from the leading and trailing edges of the upstream-facing disk surface (points "d" and "e" in Fig. 1). Furthermore, for the unchoked back pressure ratio of $P_B/P_{01} = 0.75$ Fig. 10(*a*), the flow does not reattach to the downstream surface of the disk, but rather remains attached to the test section walls in a subsonic "wall jet" configuration with the downstream disk surface bounded by a separated wake region. The results for $P_B/P_{01} = 0.50$ (choked), Fig. 10(*b*), are quite similar except that the flow expands to supersonic velocities downstream of the valve disk along both test section walls. These jets remain attached to the walls and recompress

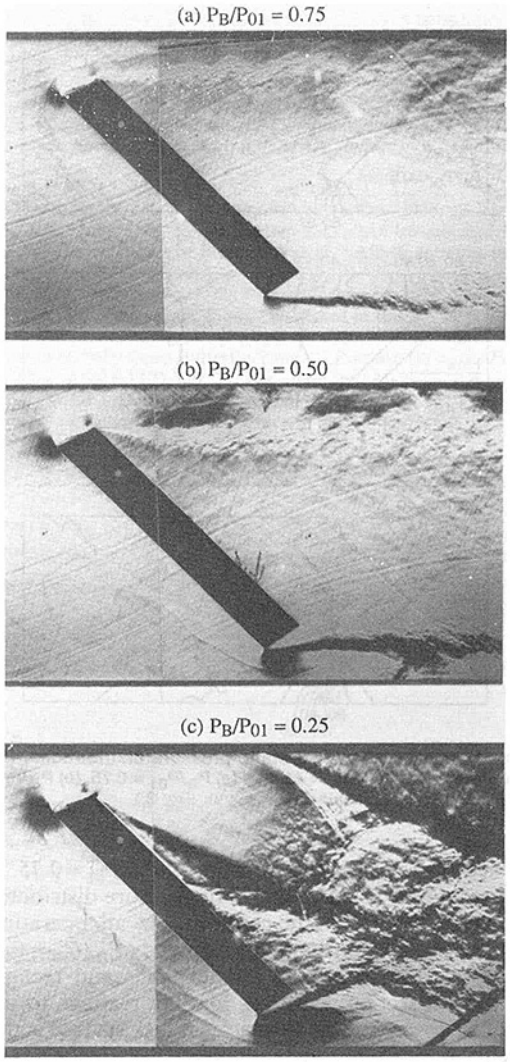

Fig. 10 Schlieren photographs of the flowfield for the flat plate valve disk at $\alpha = 45$: (a) $P_B/P_{01} = 0.75$, (b) $P_B/P_{01} = 0.50$, (c) $P_B/P_{01} = 0.25$

through a shock system to the local pressure conditions downstream of the disk. The flow expands to higher supersonic velocities for an operating pressure ratio of $P_B/P_{01} = 0.33$ (not shown) and briefly attaches to the downstream surface of the valve disk near the leading edge. The flow separates from the downstream surface immediately downstream of reattachment. The jet flows issuing from both the leading and trailing edges for this case separate from the test section walls at shock wave/boundary layer interactions. Finally, at an operating pressure ratio of $P_B/P_{01} = 0.25$, Fig. 10(*c*), the flow is also observed to attach to the downstream surface of the valve disk. In this case the flow separates from the downstream surface near midchord. Similar to the previous result at $P_B/P_{01} = 0.33$, the flow separates from both test section walls downstream of the valve disk at shock/boundary layer interactions.

The flowfield static pressure distributions for the flat plate valve disk at an angle of $\alpha = 45$ deg are given in Figs. 11(*a*)–(*c*) for operating pressure ratios of $P_B/P_{01} = 0.75$, 0.50, and 0.25, respectively. These distributions show that the upstream surface of the disk bounds a large region of low speed flow at a pressure level approximately equal to the upstream stagnation pressure. Relatively large pressure gradients are detected near both valve disk edges, as indicated by the convergence of the isobars. The normalized pressure distributions on the upstream disk surface for the chocked conditions are independent of back pressure ratio and nearly identical to that at the

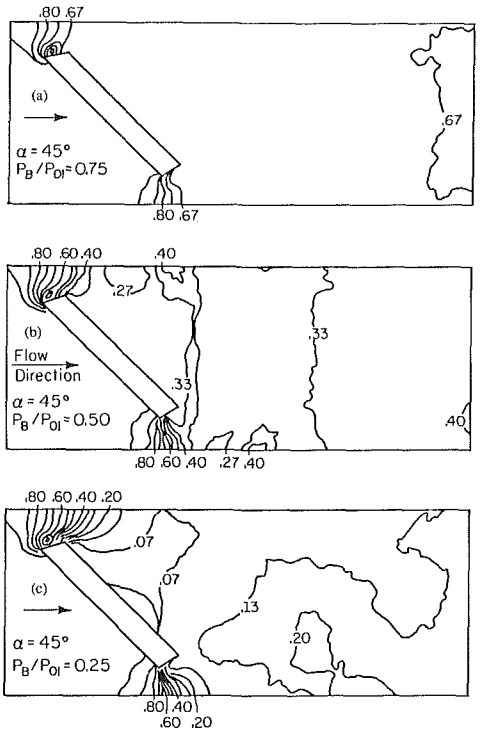

Fig. 11 Normalized flowfield static pressure distributions, P/P_{01}, for the flat plate valve disk at $\alpha = 45$ deg: (a) $P_B/P_{01} = 0.75$, (b) $P_B/P_{01} = 0.50$, (c) $P_B/P_{01} = 0.25$. (Uncertainties same as Fig. 3.)

unchoked operating pressure ratio of $P_B/P_{0l} = 0.75$. On the downstream disk surface, the static pressure distributions are observed to be essentially constant for all operating back pressure ratios greater than approximately $P_B/P_{0l} = 0.40$. The flow downstream from the disk expands and recompresses along the test section walls but does not reattach to the valve disk for these cases. The downstream disk surface is therefore adjacent to a large constant pressure wake region. These results are in agreement with the Schlieren photographs. For $P_B/P_{0l} = 0.25$, the pressure distributions on the downstream disk surface indicate that the flow reattaches and suggest that it may reattach for $P_B/P_{0l} = 0.32$ (not shown), again in agreement with the Schlieren photographs. For $P_B/P_{0l} = 0.25$, the increase in pressure on the downstream disk surface at the separation point near midchord is also clearly evident in Fig. 11(*c*).

For these cases, the flow rapidly accelerates around the valve disk periphery. Since they may be associated with relatively large moment arms, the strong pressure gradients near the leading and trailing disk edges at intermediate and large angles are especially significant in determining the aerodynamic torque on the valve disk. Thus, the valve disk periphery design should take into account aerodynamic torque considerations as well as sealing requirements.

At large angles the differences in the flowfield and the related fluid dynamic phenomena between the circular arc and the flat plate models begin to diminish. Schlieren photographs of the flowfield bounding the circular arc model are shown in Figs. 12(*a*) and (*b*) for a separated (unchoked, $P_B/P_{0l} = 0.75$) and an attached (choked, $P_B/P_{0l} = 0.33$) flowfield, respectively. Flowfield pressure distributions for $P_B/P_{0l} = 0.75$ and 0.25 are shown in Figs. 13(*a*) and (*b*). In all cases the upstream valve disk surfaces are bounded by regions of relatively constant pressure. The flow rapidly accelerates around the valve disk periphery as indicated by the relatively large pressure gradients. Similar to the flat plate model, for operating pressure ratios of $P_B/P_{0l} > 0.33$ the flow does not reattach to the downstream surface of the valve disk but rather remains at-

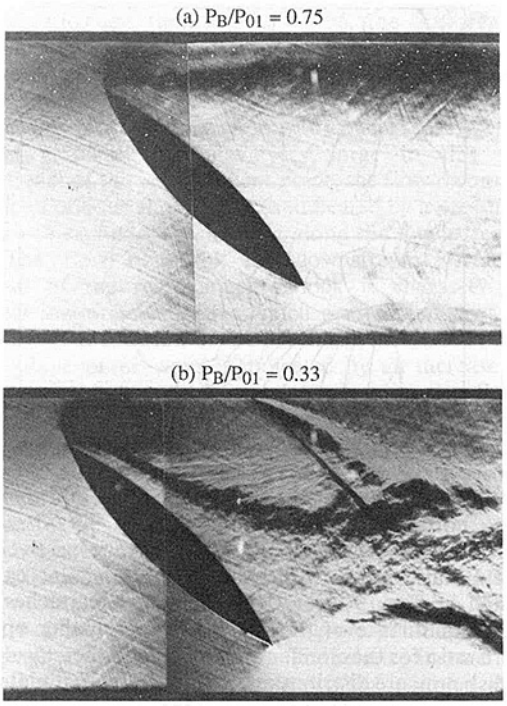

Fig. 12 Schlieren photographs of the flowfield for the circular arc valve disk at $\alpha = 45$ deg: (a) $P_B/P_{01} = 0.75$, (b) $P_B/P_{01} = 0.33$

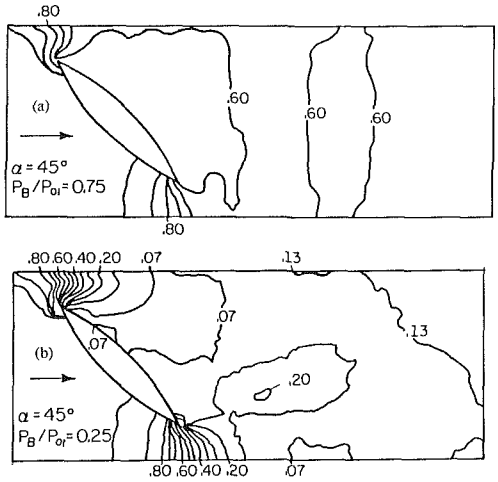

Fig. 13 Normalized flowfield static pressure distributions, P/P_{01}, for the circular arc valve disk at $\alpha = 45$ deg: (a) $P_B/P_{01} = 0.75$, (b) $P_B/P_{01} = 0.25$. (Uncertainties same as Fig. 3.)

tached to the test section walls. At lower operating pressure ratios, the flow supersonically reattaches to the downstream surface of the valve disk and separates from the opposing test section wall in a manner similar to the flat plate model.

Conclusions

An experimental investigation of the compressible flowfield characteristics of butterfly valves has been described herein. The experimental studies have clearly shown that the flowfield through butterfly valves is extremely complex and dependent upon the valve disk design, the operating pressure conditions, and the valve disk angle. The flowfields may consist of regions of strong pressure gradients, flow separation and reattachment, oblique shock waves, and expansion fans. The aerodynamic torque on the valve disk is particularly sensitive to the local flowfield details in the regions of the valve disk

leading and trailing edges and is generally a closing torque due primarily to the nature of the pressure distributions on the upstream and downstream surfaces of the disk. It appears that the peak torque phenomenon may be closely related to the transition of the local flowfield from one attached to the downstream side of the valve disk to one totally separated from the downstream side of the disk with their related pressure distributions. Because of the strong pressure gradients demonstrated to exist near the valve disk edges, the design of the disk periphery can have a strong influence on the aerodynamic torque characteristics of a butterfly valve.

References

1 Morris, M. J., "An Investigation of Compressible Flow Through Butterfly Valves," Ph.D. thesis, Department of Mechanical and Industrial Engineering, University of Illinois at Urbana-Champaign, Urbana, Illinois, Apr. 1987.

2 McDevitt, J. B., Levy, L. L., Jr., and Deiwert, G. S., "Transonic Flow About a Thick Circular-Arc Airfoil," *AIAA Journal*, Vol. 14, May 1976, pp. 606–613.

3 Deiwert, G. S., "Computation of Separated Transonic Turbulent Flows," *AIAA Journal*, Vol. 14, June 1976, pp. 735–740.

4 Levy, L. L., Jr., "Experimental and Computational Steady and Unsteady Transonic Flows about a Thick Airfoil," *AIAA Journal*, Vol. 16, June 1978, pp. 564–572.

5 Seegmiller, H. L., Marvin, J. G., and Levy, L. L., Jr., "Steady and Unsteady Transonic Flow," *AIAA Journal*, Vol. 16, Dec. 1978, pp. 1262–1270.

6 Addy, A. L., Morris, M. J., and Dutton, J. C., "An Investigation of Compressible Flow Characteristics of Butterfly Valves," ASME JOURNAL OF FLUIDS ENGINEERING, Vol. 107, Dec. 1985, pp. 512–517.

7 Morris, M. J., and Dutton, J. C., "Aerodynamic Torque Characeristics of Butterfly Valves in Compressible Flow," published in this issue pp. 392–399.

8 Morris, M. J., Dutton, J. C., and Addy, A. L., "Unsteady Flow Characteristics of Fully Open Butterfly Valves," *Proceedings of the Forum on Unsteady Flow*, ASME FED-Vol. 39, Dec. 1986, pp. 25–27.

9 Morris, M. J., Dutton, J. C., and Addy, A. L., "Peak Torque Characteristics of Butterfly Valves," *Proceedings of the Forum on Industrial Applications of Fluid Mechanics*, ASME FED-Vol. 54, Dec. 1987, pp. 63–66.

Bistable Flow Patterns in a Free Surface Water Channel

E. W. Adams[1]

A. I. Stamou[2]

Sonderforschungsbereich 210,
University of Karlsruhe,
Karlsruhe, Federal Republic of Germany

A series of experiments is reported on a free surface water tunnel with a slot inlet centered at mid-depth in which the flow exhibited equally probable bistable flow patterns. The two flow fields are strongly asymmetric even when the geometry is symmetric and consists of a long stall on one side of the inlet and a short stall on the opposite side. Flow visualization and laser-Doppler velocimetry were performed to examine the flow structure of both stable states in detail. Results showed that the mean flow and turbulence structure of the two bistable states are largely mirror images of each other within the separation zone. The effect of the wall on the flow is minor, only very close to the wall/free surface did the difference in wall constraints cause the two flow patterns to diverge. After reattachment both flows relax to free-surface channel flow. It is shown that the bistable flow pattern results from the interaction of the free shear layers and that only strong disturbances in the free shear layers can cause the flow in one stable state to switch to the other stable state. Bistable flow exists for geometries with asymmetry up to 10 percent for the expansion ratio studied.

Introduction

The high Reynolds number flow through a symmetric sudden expansion (Fig. 1) is known to exhibit two nonsymmetric stable flow patterns in which the separation on one wall is significantly longer than that on the other wall [1]. Each of the two flow patterns is stable to small disturbances, but larger disruptions may lead to a change from one flow pattern to the other one, that is the long stall may change sides. As an application of this and similar phenomenon in fluidic devices, the state of the flow is controlled to perform a useful function. Bistable flows can be laminar as well as turbulent [2]. In laminar flows, the bistable flow patterns are observed only above a certain Reynolds number which is a function of the expansion ratio (ER). In turbulent flows, the phenomenon is not observed when the expansion ratio is below 1.5 [1]. Heat transfer data are also available for turbulent flow in a range of ER between 2.1 and 3.1 [3].

For turbulent bistable flows, detailed velocity and turbulence data within the separation region are largely lacking. One of the objectives of this report is to present detailed laser-Doppler anemometry (LDA) profiles for both stable states and compared these data to each other. Such information is of value in better understanding the physics of bistable flow fields and eventually render a deeper understanding of which variables affect the process by which the flow field charges from one state to the other.

Although it may seem physically plausible that two bistable asymmetric flow patterns exist within a symmetric geometry, the effect of geometric asymmetry on the flow has not previously been discussed. In addition to practical information useful for establishing the geometric tolerances of devices using this flow phenomenon, the degree of asymmetry allowable while maintaining bistable flow structure is a measure of the "stability" of the bistable flow pattern. Finally, in the present experiment a further asymmetry was investigated as part of a series of hydraulic experiments, the bistable phenomenon was observed in turbulent flow when one of the two "walls" was not a wall at all but rather a free surface. That is, the long stall, short stall pattern existed in two stable flow fields, one in which the long stall was on the free surface and one in which the long stall was on the bottom wall. Since the constraints imposed upon the flow at a free surface are substantially dif-

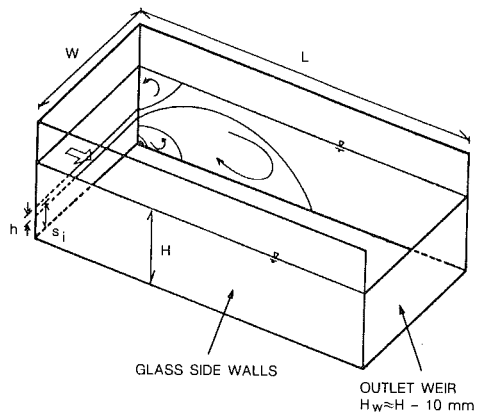

Fig. 1 Geometry of the sudden expansion experiment, L = 2.5 m, s = 10 cm, W = 91 cm, h = 2 cm, $ER = H/h$, $S = s/H$

[1]Current address: United Technologies Research Center, East Hartford, CT.

[2]On leave from: Civil Engineering Dept., The National Technical University of Athens, Athens, Greece.

Contributed by the Fluids Engineering Division for publication in the JOURNAL OF FLUIDS ENGINEERING. Manuscript received by the Fluids Engineering Division May 5, 1987.

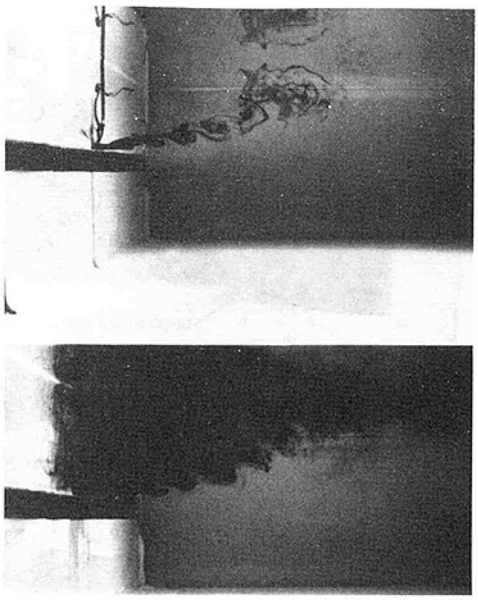

Fig. 2 Upper recirculation region and the free shear layer visualized using dye.
(*a*) Side view. Dye injected in laminar portion of the free shear layer.
(*b*) Side view. Dye injected into small separation.

ferent than those associated with a solid wall, the observance of the bistable flow phenomenon in this asymmetric situation suggested that details of the near wall flow and wall friction play a minor role in the establishment of the dynamics of the bistable structure. Using flow visualization, a series of qualitative experiments were performed to examine the control variables which affect the bistable pattern and to investigate how one state could be made to change to the second bistable state. This investigation also addressed the important practical question of the probability of the initial establishment of a given flow pattern and the effect of flow history on the phenomenon.

Experiment

All the experiments were performed in the open-surface water channel shown in Fig. 1. The test section was 2.5 m long, the inlet slot was 2 cm wide centered 10 cm from the test section floor and the depth within the test section could be varied from 10 cm to 30 cm using the outlet weir. Thus, simply by varying the flow depth, the geometric asymmetry of the test section could be changed. The sides of the test section were made of glass for optical access. In the closed circuit operation normally used, a pump supplied water to a constant heat tank upstream of the inlet. The flow then passed through a porous stone dam which made up one side of the constant head tank, two fiber mats, a honeycomb and three screens. The flow entered the channel through a two stage 10:1 contraction ratio nozzle.

The channel had a width of 91 cm, so that the aspect ratio of the channel width to the step height below the inlet was greater than the 10:1 for the baseline depth of 20 cm. Tests were then performed to examine the two-dimensionality. Dye measurements of the primary reattachment distance both on the free surface and the bottom wall showed these distances to be constant to within the experimental uncertainty in the middle 80 percent of the channel. The mass balance performed based on the LDA measurements also indicated that the channel was two-dimensional to within the experimental uncertainty (+/− 10 percent of the mass flow).

The geometry of the sudden expansion is defined here by two nondimensional parameters (see Fig. 1) the expansion ratio, ER and the nondimensional height of the inlet, S. The

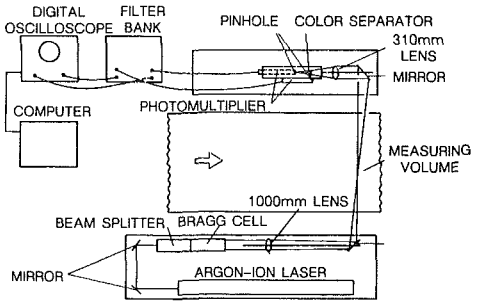

Fig. 3 Laser-Doppler anemometer system used

symmetric expansion has S = 0.5. The Reynolds number based on depth and average fluid velocity U, RE_H, could be varied from 700 to 4000. At all Reynolds numbers, the inlet flow was characterized by thin laminar boundary layers. Transition occurred in the free shear layer about 5 to 7 cm after separation from the lip of the slot (Fig. 2). The flow pattern in Fig. 2 was visualized by injecting dye into the upper separation region near the slot inlet and waiting until this dye was entrained by the free shear layer. The pattern of vortex roll-up shown in Fig. 2 is very similar to the classic pictures of the free shear layer at these Reynolds numbers [4]. Figure 2 also clearly shows that the reattachment region is fully turbulent. Other visual evidence indicated that the flow in the recirculation region and the region downstream of reattachment was turbulent.

Flow visualization was the primary method used to establish the reattachment position. For these measurements, dye was injected slowly from a hand held tube, positioned so that the effect of the injected-dye momentum would be minimized. The accuracy of this method was judged to be about +/− 15 cm for the long reattachment position, about 10 percent of the separation length in each case.

Detailed measurements were performed with the single component LDA system shown in Fig. 3. The focusing optics consisted of a beam splitter, a Bragg cell, and a 1000 mm focusing lens. The receiving optics were used in the forward scatter orientation. Further details of the physical hardware of the system are given by [5]. The burst frequency was evaluated by a transient recorder-computer combination in which the Doppler burst itself is digitized and then passed to the computer (HP-310) through the data interface (IEEE-488). Once inside the computer, software routines evaluate the burst frequency in a manner similar to that accomplished in hardware by counter-processors. The system was designed following that of [6] but uses the frequency evaluation algorithm of [7].

Because of the long processing times required for the evaluation of burst frequency (0.1 s) and the high availability of Doppler bursts in water with a 2W laser, many more bursts were available for processing than could actually be processed. By arming the transient recorder at 0.25 s intervals, the data were taken at almost equal time intervals. Mean velocity statistics were generated using simple averages following the logic of [8] and [9] who showed that this data reduction method is bias free. The uncertainty of the mean velocity measurements was estimated at 1 percent of U_{ref}, the inlet jet velocity.

Results

Figure 4 shows the reattachament lengths as a function of the Reynolds number for both stable flow patterns. Qualitatively, the length of the long stall increases significantly with Reynolds number until a Reynolds number of 1700–2000 is reached. Above this Reynolds number, the pattern stabilizes. When impulsively starting the flow, each pattern existed with a probability near 0.5. When the flow was started and the water level raised slowly to S = 0.5, the probability of the

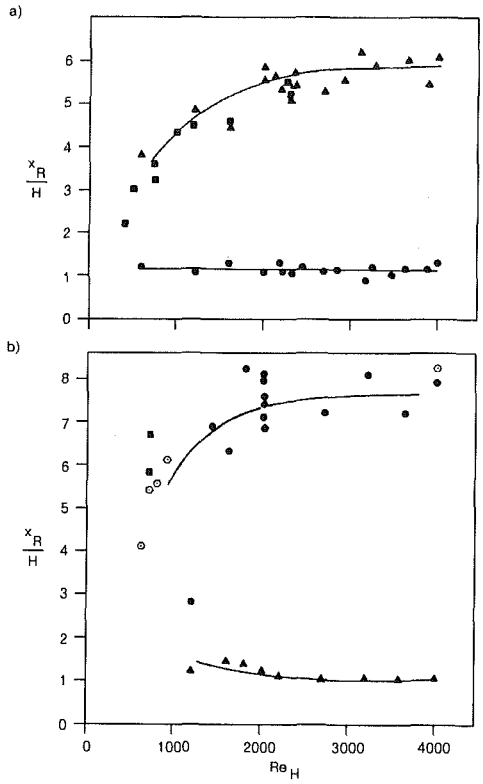

Fig. 4 Reattachment length as a function of Reynolds number for S = 0.5 (*a*) long separation on the free surface, (*b*) long separation on the bottom wall. ▲ free surface; ● bottom wall; ■ experiment of Stamou; ⊙ results for S = 0.59.

long stall being on the bottom wall was considerably greater than 0.5.

Upon careful examination of Fig. 4, it appears that the separation length establishes its final value at the lower Reynolds number when the larger separation is on the bottom wall than when the larger separation is on the free surface. In fact, for the symmetric geometry, only a single point at $Re_H = 1200$ seems to reattach earlier. To establish that the reattachment length did shorten as Re_H is reduced for the symmetric geometry, the second author repeated the experiments in a different water channel in Athens, Greece. Indeed, as Re_H is reduced X_R/H shortens. The value of Re_H when X_R/H first decreases is also lower for the case of the long separation onto the free surface when compared to the case of the long separation on the bottom wall. Similar behavior is also observed for asymmetric geometries plotted in Fig. 4. The length of the short stall is hardly affected by Reynolds number, though it appears to shorten slightly as the Reynolds number is increased. This pattern is a logical one since at low Reynolds number the flow pattern will be symmetric [2] and the reattachment length at this low Reynolds number will lie between the long and short stall lengths measured at the higher Reynolds number. From flow visualization it appeared as if the long stall was lengthened because the angle between the inlet flow and a normal to the inlet increases as the extent of the smaller separation decreases. The large effect of this angle on the reattachment distance of the long stall is similar to the sensitivity of the reattachment length for flows over sharp-edged bluff bodies to the tunnel blockage effect ([10], [11]). The effect of increasing Reynolds number on the length of the long stall is opposite to that observed for the single-sided sudden expansion ([12]).

Comparing the separation lengths when the long stall is on the bottom wall or the free surface, the reattachment distance X_R/H is 20 percent shorter when the long stall is on the free surface. Thus, although the observed flow patterns are qualitatively similar, the two flow patterns are not exact mirror images of each other as they are for the case of two solid walls [1]. The longer separation on the free surface is about 1.5H shorter than when the longer separation is on the bottom wall. It would be surprising if the flow patterns were identical mirror images of each other since the free surface constrains the flow field in a manner different from a solid wall. While both the free surface and the bottom wall restrict vertical motions, the no-slip boundary condition on the solid wall restricts streamwise and spanwise motions much more than a free surface. Because the lengths of the short stalls are also not identical, it is not possible to say that this 1.5H difference is caused by wall friction alone. It may be that the 1.5H difference in the length of the long stall is due to rather small changes in the length of the short stall and much less due to the effect of wall friction.

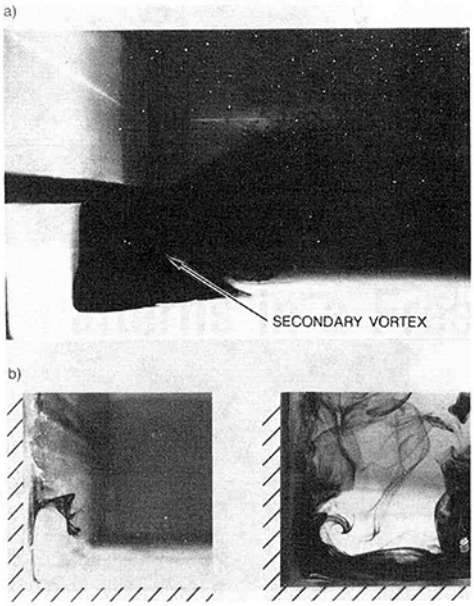

Fig. 5 Flow visualization in the separated zone. (*a*) secondary vortex beneath the long separation, (*b*) two views of the tertiary eddy in the corner between the inlet wall and the bottom wall.

The general features of the flow were visualized using dye at a Reynolds number of 2000 for both stable flow patterns. Figure 5(*a*) illustrates the rather large size of the secondary vortex rotating between the long stall and the corner which is 0.75H–1.0H in extent. The flow field in Fig. 5(*a*) was visualized by injecting dye into the secondary vortex and waiting about 30 seconds for the dye to diffuse. The dye was held in place by the reverse flow in the primary separation. The flow in this region showed lower levels of mixing than that in the primary vortex. The dye remained in the secondary vortex for a minute or more before being removed at the top of the secondary vortex near the slot inlet. It frequently appeared as if the fluid was being pulled directly from the secondary vortex into the free shear layer associated with the inlet slot. In this case the flow traveled almost vertically upward from the wall to the slot inlet without any associated motion in the upstream direction. A large intermittent vortex structure whose axis was perpendicular to the bottom wall was responsible for this motion. The average position of these transient structures was the time-mean position of border between the primary and secondary separation zones.

A third (tertiary) eddy rotating in the counterclockwise sense and about 2 cm in size was also observed (Fig. 5(*b*)). The existence of such a set of vortices of ever diminishing size was suggested by Moffat [13]. Proof of their existence in the laboratory is rare due to their small physical size compared to

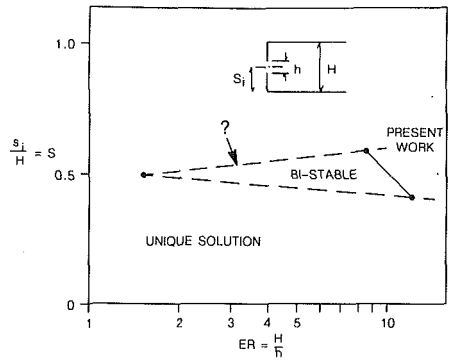

Fig. 6 Parameter space showing the region for bistable flow patterns

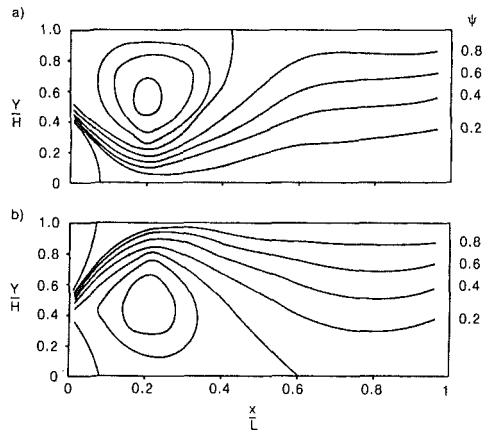

Fig. 7 Streamlines for H = 20 cm. (*a*) long separation on the free surface, (*b*) long separation on the bottom wall. Streamlines shown every 0.2 times the inlet mass flow.

scales measurable visually or by other means. Details of the corner geometry are also critical. Consideration of the size progression of the first three vortices (1.3m, 0.17m, 0.02m) suggests the fourth vortex should be about 2mm in diameter. Since the fillet radius of the inlet wall to the bottom wall is about 5mm in diameter, it is doubtful that this vortex would exist.

The secondary vortex shown in Fig. 5(*a*) also occurred when the long stall was on the free surface although it was only 1/2 to 1/3 the streamwise extent in this case. A tertiary vortex was not observed on the free surface.

To examine the effects of flow asymmetry on the bistable flow patterns, the flow depth was increased and decreased until only a single stable flow pattern was observed. This stable flow pattern always had the characteristic that the short stall was associated with the smaller of the two expansions, irrespective whether the flow boundary was the free surface or the bottom wall. Only one stable flow pattern was observed when $S < 0.37$ or $S > 0.59$. Two stable flow patterns existed for all depths between these values. Based on this, the parameter space of ER and S can be divided into regions where one or two stable flow patterns exist. In [1] only one flow pattern was observed for ER < 1.5 when S = 0.5, a parameter space such as Fig. 6 might result.The straight lines joining the present results and those of [1] for visual use to show that such a region must exist.

At the large values of ER investigated here, bistable flow existed for asymmetries as large as 10 percent on each side of S = 0.5. This suggests first that large tolerances can probably be used in fluidic devices similar in design to the geometry used here. Secondly, it suggests that the forces which govern the existence of the bistable flow field are not strongly dependent on wall position within a wide range. Since the flow is relatively insensitive to wall position, it seems reasonable that

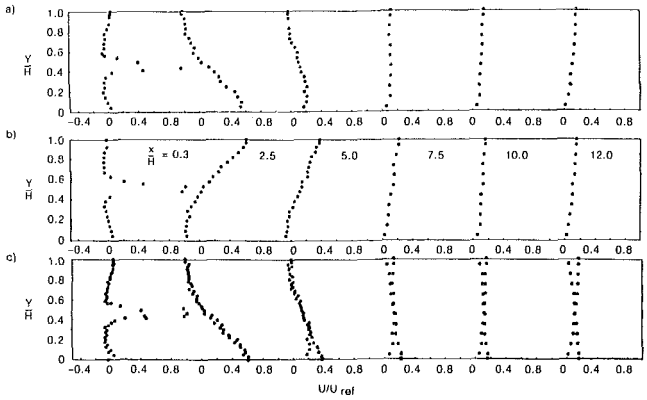

Fig. 8 Mean Velocity Profiles. Profiles shown at X/H = 0.3, 2.5, 5.0, 7.5, 10.0, 12.0 (*a*) long stall on the free surface, (*b*) long stall on the bottom wall, (*c*) comparison of (*a*) with the reflection of (*b*).

wall friction and other near wall processes play a minor role in establishing the separated flow pattern. Further experiments in this regard are discussed below.

To supplement the qualitative data just discussed, LDA profiles at streamwise locations of X/H = 0.3, 2.5, 5.0, 7.5, 10.0 and 12.0 were taken. One data set was taken with the long stall on the free surface and one with the long stall on the bottom wall. The bistable patterns were so stable that these experiments could run 10–18 hours without any change in the flow pattern. The streamlines which result from these data are shown in Fig. 7. The flow in the separation zones is much more asymmetric than might be expected from the geometry alone. The streamlines confirm the observations made with dye that the two stable flow patterns are not mirror images but nonetheless quite similar to each other. In both cases, there is rather strong streamline curvature associated with the reattaching streamline of the smaller separation bubble. From Fig. 7 the radius of curvature of this streamline can be estimated to be of order H. This value is five to ten times larger than the streamline curvature associated with the reattaching streamline of the single-sided sudden expansion or for the reattachment streamline of the larger stall. After reattachment the flow is almost uniform and even less than 0.5H from the outlet weir, the streamline pattern does not show any obvious signs of distortion. This is especially surprising because flow visualization shows evidence of a separation region in the corner between the outlet weir and the bottom wall.

The mean velocity profiles are shown in Fig. 8. In this figure, (*a*) represents measurements taken when the long stall is on the free surface, (*b*) represents measurements taken when the long stall is on the bottom wall and (*c*) is a comparison of (*a*) with the reflection (*b*) so that the long stall appears to be on the same side of the inlet for the two flow cases. Figure 8(*c*) compares directly the effect of the wall constraint on the flow structure.

When considering the data of Fig. 8, it is helpful to distinguish between three flow zones. In zone 1, X/H = 0.3 and 2.5, the profiles for the two flow cases are almost exactly mirror images of each other. At X/H = 0.3 the profile cuts through the small stall as well as the larger one and thus the mean velocity data indicate large separation regions on both sides of the slot inlet. The profile at X/H = 2.5 is roughly midway through the streamwise extent of the larger stall. At this streamwise location, the flow on the side associated with the large stall has strong back flow while the opposite side is flowing in the forward direction. The maximum value of the mean velocity in the reverse direction at X/H = 2.5 is about −0.2 times the inlet velocity. Nearly the same value observed for the single-sided expansion [14]. Although the profiles at these locations for the two cases show strong similarity, near the top and bottom of Fig. 8(*c*) there are some slight differences

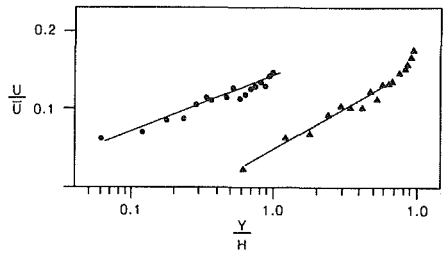

Fig. 9 Log plots of the velocity profiles in the recovery region • 200 cm; ▲ 241 cm; $\bar{U}$ is the depth average velocity in the tank

due to the "wall" constraint which forces the streamwise velocity at the wall to be zero for the case of a solid wall, while the mathematical formulation for the free surface constraint is approximately $dU/dy = 0$. This difference causes the mean velocity data to reach a peak near the bottom wall in Fig. 8(*a*) $X/H = 2.5$ while a peak does not exist near the free surface in Fig. 8(*b*) at the same streamwise location. At $X/H = 2.5$, the differences between the two cases are also confined to the "wall" region. When the long stall is on the bottom wall, there is forward flow near the wall indicating the existence of the secondary eddy observed visually. When the long stall is on the free surface, the time average velocity at the free surface is negative. This corresponds with the information supplied by flow visualization that the secondary vortex is much smaller when the long stall is on the free surface than when the long stall is on the bottom wall.

Zone 2, is illustrated by the profile at $X/H = 5.0$. At this location, when the long stall is on the free surface, reattachment is occurring, while $X/H = 5.0$ is well within the recirculation zone when the long stall is on the bottom wall. A comparison of the profiles show more extensive differences at this station. There is almost no backflow evident for the case of the long stall on the free surface, while strong backflow is evident when the long stall is on the bottom wall. Corresponding differences are also observed in the flow velocities on the opposite wall as is required by continuity.

Zone 3 is downstream of reattachment. In this zone, the flow relaxes back to turbulent open channel flow. Since the data in Figs. 8(*a*) and 8(*b*) are for the same Reynolds number, given a long enough development distance, the velocity profiles for the two cases would become identical. The trend toward this condition is observed in the data at $X/H = 7.5$, 10.0 and 12.0. Corresponding to this, the profiles cross each other at mid-depth in Fig. 8(*c*). The profiles of mean velocity when placed in log coordinates have well developed long regions as is shown in Fig. 9. The accuracy of the data was not high enough to observe the typical dip below the log-law which occurs in mean velocity data downstream of reattachment in the backward facing step flow [15]. The reason for the large scatter observed in this region is due to the extremely low flow velocities ($U = 1$ cm/s).

Streamwise turbulence intensities associated with the two flow patterns are shown in Fig. 10. This data can be interpreted in a manner similar to that of the mean velocity data. The observed scatter is considerably larger, however. Again, at $X/H = 0.3$ and 2.5, the profiles are almost mirror images of each other. At $X/H = 0.3$, there are much higher turbulence levels on the side with the short stall than on the side with the long stall. This is undoubtedly due to the fact that turbulence generation is largest near reattachment [16] and that the data on the side with the short stall are much closer to reattachment than the data taken on the side with the long stall. At $X/H = 2.5$, the turbulence intensity on the side associated with the small stall is lower than the level at $X/H = 0.3$ while the turbulence intensity on the side with the long stall has increased. The largest levels of turbulence intensity at this location are associated with the free shear layer. This would be expected from data taken on the single-sided expansion [9].

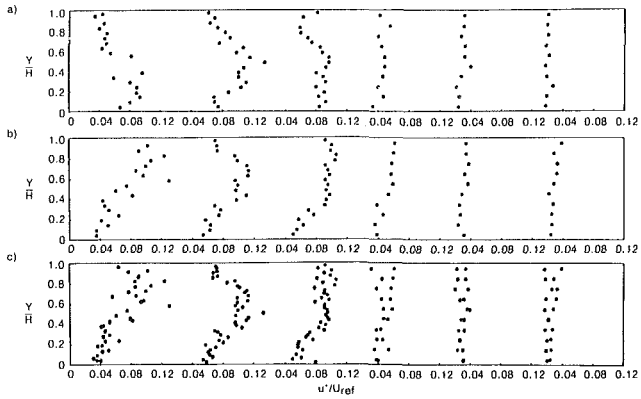

Fig. 10 Streamwise turbulence intensity profiles (see Fig. 8 for details)

At $X/H = 5.0$, the turbulence intensity on the side associated with the long stall is larger than the turbulence intensity on the side associated with the short stall. This is explained by the fact that on the side of the flow field associated with the long stall, turbulence intensities should be rising toward reattachment while on the opposite side they are relaxing from their levels at the reattachment point of the short stall. A comparison between the two flow states shows that differences in the turbulence levels are smaller than the uncertainty of the data.

Downstream of reattachment, the levels of streamwise turbulence intensity are decaying quite rapidly. Turbulence levels appear almost uniform at the last station. Since it would be expected that the turbulence levels near the bottom wall would be larger than those near the free surface, measurement uncertainty due to the low flow velocities certainly contributes to the uniform appearance of the profiles in this zone.

Discussion

An important question raised by the existence of two stable flow patterns for the same inlet and boundary conditions is: what factors influence the existence and nature of these two flow patterns? Nondimensional parameters which could affect the existence and nature of the flow patterns are: Re_H, ER, and S, inlet conditions and boundary conditions. Below a certain Reynolds number the bistable flow patterns cannot exist and that the flow patterns on each side of the inlet will be symmetric and independent of each other [2]. Here, above $Re_H = 2000$, further increases in Reynolds number did not alter the flow patterns observed.

Below this value, the length of the longer stall shortened, suggesting that for $Re_H < 500$, the flow pattern may become symmetric. In single sided sudden expansion when $Re_H < 500$, viscous forces dominate and the flow scales in a laminar fashion [17]. Combined, this suggests that strong viscous forces inhibit the bistable flow pattern.

The inlet conditions are likely to strongly influence the flow field. For the case of the single-sided sudden expansion at the same Re_H, the reattachment length is 30 percent shorter when the boundary layer upstream of the expansion is laminar than when the upstream boundary layer is turbulent [18]. It must be expected that the reattachment lengths for the short and long stall may change substantially if the upstream boundary layers in the slot are turbulent. However, the same bistable flow pattern was observed as is reported here for the case of laminar initial conditions as well as for turbulent initial conditions [1]. It can be concluded that the transition process is not responsible for the existence of the bistable flow patterns.

Further evidence that the initial conditions of the flow are not critical for the establishment of the bistable pattern was generated by placing wires and other obstacles asymmetrically in the nozzle region and observing that the flow pattern was not sensitive to such disturbances. Due to the strong acceler-

ation in the nozzle used and its damping effect on disturbances, it would be surprising if disturbances upstream of the inlet were important. Not surprisingly, the introduciton of blockage in the inlet did not alter the stability of the bistable states since Fig. 6 shows the bistable states relatively insensitive to S.

The constraint at the free surface and the bottom wall plays a relatively minor role in determining the stabilty and structure of the bistable flow patterns. The fact that one "wall" of the present experiment was not a solid wall but rather a free surface influenced the size of the two recirculation zones and influenced the mean velocity very near the "wall," but the bistable flow fields were found to exist whether one of the walls was a free surface or a solid wall. The middle 80 percent of the flow field at the stations $X/H = 0.3$ and 2.5 were mirror images of each other despite the different boundary constraints. It appears that wall friction is relatively unimportant in determining the structure of the present flow field. This same conclusion has been reached previously for the turbulent wall jet by comparing the structure of the wall jet when the "wall" is a free surface to the standard wall jet [19]. In the same study it was concluded that the most important property of the "wall" (irrespective of whether it is a free surface or solid) is the damping of the vertical fluctuations and not friction. By analogy this is probably also the case for the present experiment but measurements of the full Reynolds stress tensor would be required to verify this point.

At high Re_H, the major variables affecting the existence of the bistable flow pattern were ER and S. In [1], at small enough ER, bistable flow did not exist. At small ER, the shear layers on each side of the inlet are relatively far from each other and relatively close to a wall. At large ER, the opposite is the case. For strongly asymmetric geometries, one of the free shear layers is realtively closer to a surface than the other and the distance between the shear layers becomes a larger fraction of the distance to the nearest surface. These are all indications that it is an interaction of the free shear layers which is responsible for the existence of the bistable states. Since it has been shown that viscous forces are not responsible, most likely pressure forces are responsible for this interaction.

Further confirmation that it is the interaction of the free shear layers that leads to bistable flow was given by a series of dye experiments in which disturbances were added to the flow. As stated earlier, disturbances upstream of the inlet had no effect. One flow pattern could be changed to the other only when objects were oscillated in the free shear layers vertically on both sides of the inlet and in the horizontal region between the inlet and the location of reattachment of the short separation. Other disturbances which were unsuccessful in changing the flow pattern include placing 2-D metal bars of size $Y/H = 0.1$ in the recirculation zone, wooded blocks on the free surface, a $2'' \times 4''$ wood plank placed anywhere in the flow downstream of $X/H = 2$ and oscillated by hand.

Conclusions

Bistable flow patterns have been observed in a turbulent flow within a symmetric sudden expansion when one of the sides onto which the flow separates is a free surface. Within the separation region, the two flow fields are almost mirror images of each other, strongly asymmetric about the inlet even when the inlet geometry is symmetric and consist of a long stall on one side of the inlet, and a short stall on the opposite side. Flow visualization experiments and detailed laser-Doppler anemometry experiments were performed to examine the mean flow and turbulence structure of both bistable flow fields in detail. In addition to specific design information pertinent to the geometry studies here, general information on bistable flows and the role of wall friction in separated flow patterns could also be gained. The initial state of the flow was seemingly random when impulsively started, while the probability for the short stall to initially be on the free surface was much higher than 0.5 when the free surface level was raised slowly from the top edge of the inlet slot to the final symmetric geometry with the flow exiting the inlet slot. Once established, both flow patterns are stable to small disturbances and the flow pattern could be made to change from one stable state to the other are only by larger disturbances of the free shear layer. Disturbances upstream of the inlet, near the wall, the free surface or downstream of the separation were unsuccessful in changing the flow pattern. Flow history upstream was found to be unimportant in establishing the flow pattern and the process should not be confused with a hysteresis since each flow pattern was seemingly stable indefinitely.

From the experiments it can be concluded that the role of wall friction in establishing the overall flow pattern is relatively minor since the flows in the two bistable states are so similar despite the very different conditions imposed on the flow at a free surface and at a solid wall.

Acknowledgments

The project was sponsored by the German Government (Deutsch Forschungsgemeinschaft) through the SFB 210. The authors would like to thank Mr. D. Weier who performed some of the measurements reported here. The figures were prepared by A. Tridafillidi, B. Schwanhauser and the Illustrating Department at United Technologies Research Center. The first author was supported in the final stages of the write-up by UTRC.

References

1 Abbott, D. E., and Kline, S. J., 1962, "Experimental Investigation of Subsonic Turbulent Flow over Single and Double Backward Facing Steps," ASME *Journal of Basic Engineering*, Vol. 84, pp. 317-324.

2 Durst, F., Melling, A., and Whitelaw, J. H., 1974, "Low Reynolds Number Flow Over a Plane Symmetric Sudden Expansion," *JFM*, Vol. 64, Part 1, pp. 218-232.

3 Filetti, E. G., and Kays, W. M., 1967, "Heat Transfer in Separated Reattached and Redevelopment Regions Behind a Double Step at Entrance to a Flat Duct," ASME *Journal of Heat Transfer*, Vol. 89, pp. 163-167.

4 Brown, G. L., and Roshko, A., 1974, "On Density Effects and Large Structures in Turbulent Mixing Layers," *JFM*, Vol. 64, Part 4, pp. 775-816.

5 Adams, E. W., 1987, "A Comparison of Measured Near-Wall Velocity Profiles and Flow Visualization in a Separated Flow," *Proc. 3rd Int. Symposium on Laser Anemometry*, FED, Vol. 55, ASME, New York, N.Y.

6 Tropea, C. D., 1982, "Die Turbulente Stufenstroemung in Flachkanaelen und offenen Gerinnen," Ph.D. thesis, Univ. Karlsruhe, Report SFB 80/E/210.

7 Schmitt, F., and Scharna, H., 1986, "Eine neue Auswertesoftware fuer die LDA-Signalerfassung mit Transientenrecordern," Report 635, Inst. fuer Hydromechanik, Univ. Karlsruhe.

8 Stevenson, W. H., Thompson, H. D., and Craig, R. R., 1984, "Laser Velocimeter Measurements in Highly Turbulent Recirculating Flows," ASME JOURNAL OF FLUIDS ENGINEERING, Vol. 106, No. 2, pp. 173-180.

9 Adams, E. W., and Eaton, J. K., 1988, "An LDA Study of the Backward Facing Step Flow Including the Effects of Velocitiy Bias," ASME JOURNAL OF FLUIDS ENGINEERING, Vol. 110, No. 3, pp. 275-282.

10 Durst, F., and Rastogi, A. K., 1980, "Turbulent Flow Over Two-Dimensional Fences," *Turbulent Shear Flows II*, Springer-Verlag, NY, pp. 218-232.

11 Smits, A. J., 1981, "Sealing Parameters for a Time Averaged Separation Bubble," ASME JOURNAL OF FLUIDS ENGINEERING, Vol. 104, June, pp. 178-184.

12 Kottke, V., 1984, "Heat, Mass and Momentum Transfer in Separated Flows," *Int. Chen. Eng.*, Vol. 24, No. 1, Jan., pp. 1-11.

13 Moffatt, H. K., 1964, *JFM*, Vol. 18, p. 1.

14 Eaton, J. K., and Johnston, J. P., 1981, "A Review of Research on Subsonic Turbulent Flow Reattachment," *AIAA J.*, Vol. 19, No. 9, Sept., pp. 1093-1100.

15 Bradshaw, P., and Wong, F. Y. F., 1972, "The Reattachment and Relaxation of a Turbulent Shear Layer," *JFM*, Vol. 52, Part 1, pp. 113-135.

16 Pronchick, S. W., and Kline, S. J., 1983, "An Experimental Investigation of the Structure of a Turbulent Reattaching Flow Behind a Backward Facing Step," Report MD-42, Thermosciences Div., Mech. Eng. Dept., Stanford Univ., CA.

17 Acrivos, A., Leal, L. G., Snowden, D. D., and Pon, F., 1968, "Further Experiments on Steady Separated Flows Post Bluff Objects," *JFM*, Vol. 34, Part 1, pp. 25-48.

18 Adams, E. W., Johnston, J. P., and Eaton, J.K., 1984, "Experiments on the Structure of Turbulent Reattaching Flow," Report MD-43, Thermosciences Div., Department of Mech. Engrg., Stanford Univ., Stanford, CA.

19 Rodi, W., 1980, "Turbulence Models and Their Application in Hydraulics—A State of the Art Review," IAHR, Delft, The Netherlands.

Flow Over a Cylinder at a Plane Boundary—A Model Based Upon ($k-\epsilon$) Turbulence

T. Solberg
Norwegian Institute of Technology,
N-7034 Trondheim, Norway

K. J. Eidsvik
Norwegian Hydrotechnical Laboratory,
N-7034 Trondheim, Norway

A model for two-dimensional flows over a cylinder at a plane boundary is developed. The model, based upon a (k-ϵ) turbulence closure, is formulated in a curvilinear coordinate system based upon frictionless flow. A length scale modification in areas of adverse pressure gradient and recirculating flow appears to be more realistic than the standard (k-ϵ) model. The main features of the predicted flow do not depend critically upon the details of the grid or model, which means that a well defined solution is obtained. The solution appears to be reasonable and validated to the extent that the data permits.

Introduction

Flows over bluff bodies are associated with stagnation, separation, recirculation and non-stationary vortex shedding. All these aspects are represented in the flow around a cylinder. Analytic estimates are often addressing idealized small Reynolds number flows and/or the initial flow around impulsively started cylinders (Fornberg [1], Cebeci et al. [2], Phonc Loc and Bonard [3]). Aspects of approaching turbulence are discussed by Hunt [4]. Separation is reviewed by Simpson [5]. Estimates for engineering purposes are commonly based upon highly ad hoc models. For instance, are hydrodynamic forces estimated by Morison's equation, Fourier representations, or discrete vortex methods. Laboratory experience has established complicated relations between nondimensional numbers (Sarpkaya and Isacson [6]). Numerical calculations of turbulent flows around cylinders have been attempted by Majumdar and Rodi [7]. Several aspects of the flow are predicted reasonably accurate. However, the authors state that their stationary model is not satisfactory when unsteady vortex shedding is of importance. Separation is predicted some 10 degrees too late. The length of the separation wake is overpredicted. The drag coefficient is predicted too small.

Since the flow behind a cylinder at a plane boundary is characterized by a steady recirculating flow with minimal vortex shedding, it is probably simpler to model and verify than the flow around a free cylinder. If models for this flow could be verified to be realistic, a basis for addressing vortex shedding flows is also established. Experimental data are obtained by Bearman and Zdravkovich [8], Tsiolakis et al. [9] and Aiba and Tsuchida [10]. The approaching turbulent boundary layer and turbulent wake seem to be essential features of the flow. It therefore appears that a realistic turbulence model should be applied. Which candidate is sufficiently rich is difficult to judge. Experience, as summarized by Launder et al. [11], suggests that at least a two-equation dynamic turbulence closure is necessary for estimating recirculating flows. The most documented and commonly used (k-ϵ) turbulence closure, with a simple modification, is therefore chosen for the present study. The main features of the model predictions turn out to be realistic.

Contributed by the Fluids Engineering Division for publication in the JOURNAL OF FLUIDS ENGINEERING. Manuscript received by the Fluids Engineering Division June 26, 1987; revised manuscript received August 1988.

Model

Coordinate System. Separation over a smoothly curved surface is a main aspect of the present study. Hence, a boundary fitted coordinate system is essential. Such a system also simplifies the boundary conditions and enables an effective grid distribution. The orthogonal system chosen is based upon the velocity potential and stream function for a frictionless flow over the solution domain. For the present problem this transformation is (Milne-Thomson [12]):

$$\frac{2\hat{x}}{\pi D u_\infty} = \coth\frac{\pi D}{2x}. \tag{1}$$

Here D is the cylinder diameter and u_∞ is the free-stream velocity. The complex location in a cartesian coordinate system with origo at the contact point between the cylinder and the plane is $x = x_1 + ix_2$. To represent efficiently the largest flow gradients in the neighborhood of the plane and cylinder, the components of $\hat{x}$ are stretched: $\hat{x}_i = \hat{x}_i(\hat{x}_i)$. Equispaced $\hat{x}_i$-coordinates are shown in Fig. 1. Along the plane and on the cylinder it follows that $\hat{x}_2 = 0$. Far away from the cylinder the transformation becomes simply $\hat{x} = u_\infty x$. It is noted that the singularity at $x = 0$ introduces a significant cylinder support in the discrete representation. A transformation mapping the curve given by the plane and the cylinder into a straight line, must have a singularity at $x = 0$. The point $x = 0$ corresponds to two points in the transformed coordinate system $\hat{x}$. This singularity must be avoided by the grid, so that the cylinder must necessarily have a support. In the present case, it turns out that its size decreases slowly as the general grid size is reduced. However, since the velocity near $x = 0$ must be small,

the bulk flow around the cylinder is not expected to depend critically upon whether a cylinder support is present or not.

Differential Equations. Although the approaching flow is fully developed turbulent, it is expected that viscous effects are significant for the boundary layer development towards separation. It appears therefore that low Reynolds number turbulence models would be desirable. However, experience with such models applied to recirculating flows shows that they tend to converge slowly or even diverge (Chieng and Launder [13], Majumdar and Rodi [7]). Here the standard, high Reynolds number, (k-ϵ) turbulence model is applied over the whole flow domain. In an orthogonal coordinate system the conservation of mass, momentum, turbulent kinetic energy and turbulent dissipation can then be summarized in a general transport equation as shown by Raithby et al. [15]:

$$\frac{\partial \rho\phi}{\partial t}+\frac{1}{h_1h_2}\left[\frac{\partial}{\partial \hat{x}_1}h_2\left(\rho\hat{u}_1\phi-\frac{\Gamma_\phi}{h_1}\frac{\partial\phi}{\partial\hat{x}_1}\right)+\right.$$
$$\left.+\frac{\partial}{\partial\hat{x}_2}h_1\left(\rho\hat{u}_2\phi-\frac{\Gamma_\phi}{h_2}\frac{\partial\phi}{\partial\hat{x}_2}\right)\right]=\hat{S}_\phi \qquad (2)$$

The expected value density and velocity are ρ and (u_1, u_2) respectively. The metric tensor is $g_{ij}=h_i^2\delta_{ij}$. The diffusion coefficient, Γ_ϕ, and the source terms appropriate to each variable, $\hat{S}_\phi$, are given in Table 1.

Boundary Conditions. To simplify notations, the physical normal coordinate, n, which is parallel to $\hat{x}_2$, is introduced. The approaching turbulent boundary layer is assumed to be in local equilibrium. Hence

$$u_1(n)=\frac{u_*}{\kappa}\left[\ln\left(E\frac{nu_*}{\nu}\right)+w\left(\frac{n}{\delta}\right)\right], u_2(n)=0,$$

$$k(n)=C_\mu^{-1/2}\min[u_*^2, (l\partial u_1/\partial n)^2], \qquad (3)$$

$$\epsilon(n)=(C_\mu^{1/2}k)^{3/2}/l,$$

at $x_1=-12D$. Here u_* is the surface friction velocity, k is turbulent kinetic energy, and ϵ turbulent dissipation rate. A smooth surface roughness with $E=9.0$ is chosen. The wake function is approximated as $w(n/\delta)=(1+6\Pi)(n/\delta)^2-(1+4\Pi)(n/\delta)^3$, with $\Pi=0.5$ (Johnston [16]). The minimum operation on $k(n)$ is applied to avoid a kinetic energy maximum originating from this wake function. When the free-stream velocity $u_1(\delta)=u_\infty$ and the boundary-layer thickness δ are specified, the friction velocity is obtained from the equation $\kappa u_1(\delta)=u_*(\ln E\delta u_*/\nu+2\Pi)$. The length scale is specified as $l=\min(\kappa n, C_\mu\delta)$. At the lower boundary, including the cylinder, the usual equilibrium boundary layer conditions are applied (Launder et al. [11]).

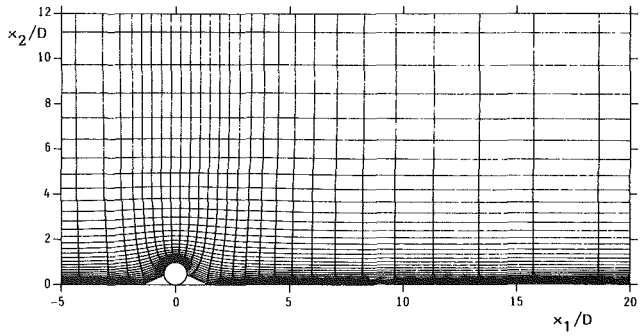

Fig. 1 Curvilinear grid based upon equation (1) and stretching away from the bottom boundary and cylinder. The illustrated grid is 32 × 32, while the grid used for the integration referred in Fig. 3, 4, 5, 6, 7, and 9 is 82 × 42.

$$u_*^2=(C_\mu^{1/2}k)^{1/2}u_1/u^+$$

$$\iint PdV=(\rho u_*^2u_1/n)\Delta V$$

$$\iint \epsilon dV=((C_\mu^{1/2}k)^{3/2}u^+/n)\Delta V \qquad (4)$$

$$\partial k/\partial n=0$$

$$\epsilon=(C_\mu^{1/2}k)^{3/2}/\kappa n,$$

at the grid point next to the wall. Here $u^+=1/\kappa\ln(En^+)$ and $n^+=(C_\mu^{1/2}k)^{1/2}n/\nu$. Since the standard $k-\epsilon$ model is realistic for fully developed turbulent flow, the first grid point should be located at a distance $n^+>11.63$. Near the cylinder top it turns out to drop below. In this case the laminar relation $u^+=n^+$ is applied. This implies that a high Reynolds number turbulence model is applied over a small area of low Reynolds number flow. Majumdar and Rodi [7] compare such a model with van Driest viscosity formulation to indicate that this may be acceptable. At the downstream and upper boundaries, the conditions are chosen as in equation (5).

$$\frac{\partial u_1}{\partial x_1}=\frac{\partial u_2}{\partial x_1}=\frac{\partial k}{\partial x_1}=\frac{\partial\epsilon}{\partial x_1}=0 \quad \text{at } x_1=24D$$
$$u_1=u_\infty, u_2=0 \quad \text{at } x_2=12D \qquad (5)$$
$$k=k_\infty, \epsilon=(C_\mu^{1/2}k_\infty)^{3/2}/C_\mu\delta.$$

Numerical Solution Procedure. The governing equations are solved by the finite volume method described by Raithby et al. [15]. The differential equations are integrated over control volumes defined by the grid. The finite difference equations are obtained using hybrid differences for the convective terms. A steady-state solution is achieved iteratively by under-relaxation. Hence, for a guessed (previous iteration) velocity

Nomenclature

C_μ, C_1, C_2 = model coefficients
c_f, c_p = surface stress- and pressure coefficients
D = cylinder diameter
E = coefficient
h_1^2, h_2^2 = components of metric tensor g_{ij}
k = mean turbulent kinetic energy
l, l_ϵ, l_k = turbulent length scales
n = normal coordinate
P = production of mean turbulent kinetic energy
p = mean pressure
S_ϕ = source term
t = time
$u=(u_1, u_2)$ = mean velocity
u_∞ = free-stream velocity
u_* = friction velocity
w = wake function
$x=(x_1, x_2)$ = orthogonal cartesian coordinate system
Γ_ϕ = effective diffusivity
δ = boundary-layer thickness
δ_{ij} = Kronecker delta function
ϵ = mean dissipation rate
θ = angle
κ = von Karman constant
μ = effective viscosity
ν = laminar viscosity
Π = coefficient in wake function
ρ = density
$\sigma_k, \sigma_\epsilon$ = Prandtl-Schmidt numbers
τ_{ij} = turbulent stress tensor
ϕ = scalar variable
-, ^ = refers to transformed coordinate systems

Table 1 The diffusion coefficients Γ_ϕ and the source terms $\hat{S}_\phi$ for the equations of motion. Stresses and production terms in Table 2

ϕ	Γ_ϕ	$\hat{S}_\phi$
1	0	0
$\hat{u}_1$	μ	$-\frac{1}{h_1}\frac{\partial p}{\partial \hat{x}_1}+\frac{1}{h_1 h_2}\left[\frac{\partial}{\partial \hat{x}_1}h_2\left(\hat{\tau}_{11}-\frac{\mu}{h_1}\frac{\partial \hat{u}_1}{\partial \hat{x}_1}\right)+\frac{\partial}{\partial \hat{x}_2}h_1\left(\hat{\tau}_{12}-\frac{\mu}{h_2}\frac{\partial \hat{u}_1}{\partial \hat{x}_2}\right)\right]+\frac{1}{h_1 h_2}\left[\frac{\partial h_2}{\partial \hat{x}_1}(\rho\hat{u}_2^2-\hat{\tau}_{22})-\frac{\partial h_1}{\partial \hat{x}_2}(\rho\hat{u}_1\hat{u}_2-\hat{\tau}_{12})\right]$
$\hat{u}_2$	μ	$-\frac{1}{h_2}\frac{\partial p}{\partial \hat{x}_2}+\frac{1}{h_1 h_2}\left[\frac{\partial}{\partial \hat{x}_1}h_2\left(\hat{\tau}_{12}-\frac{\mu}{h_1}\frac{\partial \hat{u}_2}{\partial \hat{x}_1}\right)+\frac{\partial}{\partial \hat{x}_2}h_1\left(\hat{\tau}_{22}-\frac{\mu}{h_2}\frac{\partial \hat{u}_1}{\partial \hat{x}_2}\right)\right]+\frac{1}{h_1 h_2}\left[\frac{\partial h_1}{\partial \hat{x}_2}(\rho\hat{u}_1^2-\hat{\tau}_{11})-\frac{\partial h_2}{\partial \hat{x}_1}(\rho\hat{u}_1\hat{u}_2-\hat{\tau}_{12})\right]$
k	μ/σ_k	$P-\rho\epsilon$
ϵ	μ/σ_ϵ	$C_1 P\frac{\epsilon}{k}-C_2\rho\frac{\epsilon^2}{k}$

and pressure field, the momentum equations are solved. The velocity and pressure fields are updated by the SIMPLE-algorithm (Patankar [17]) to enforce mass conservation. The equations for the scalar variables are solved next. The iteration is continued until the relative residuals summed over the solution domain are less than $5\cdot10^{-3}$ for each variable. This ensures that the relative mass imbalance in any control volume does not exceed 10^{-5}.

Model Specification and Modification. The physical coefficients are chosen traditionally as: $\sigma_k=1.0$, $\sigma_\epsilon=1.3$, $C_\mu=0.09$, $C_1=1.44$, $C_2=1.92$ and $\kappa=0.4$. The grid system is illustrated in Fig. 1.

It turns out that Rodi and Scheuerer's [14] inaccuracy of the standard $(k-\epsilon)$ model in adverse pressure gradient is confirmed. Both in the approaching boundary layer and in the recirculating area behind the cylinder the dissipation turns out, by subjective judgment, to be predicted too small and the kinetic energy too large. The turbulent length scale, $l_\epsilon=C_\mu^{3/4}k^{3/2}\epsilon^{-1}$, is therefore also predicted too large. The evidence from the present flow, together with previous experience [14], is considered certain enough for a modification of the standard $(k$-$\epsilon)$ model to account for adverse pressure gradient effects. Although physically plausible changes of the standard ϵ-equation have been suggested [11, 14], a parsimonious modification is chosen, namely to apply a one-equation model where the $(k$-$\epsilon)$ is inappropriate. Rodi and Scheuerer [14] find a one-equation model to be very accurate in adverse pressure gradient boundary layer flow. The length scale in the one-equation model is specified as $l_k=\kappa n_{\min}$, where $n_{\min}$ is the minimum distance to a boundary. The modification of the $(k-\epsilon)$ model is then given by choosing the minimum lengthscale and estimating the dissipation as in a one equation model when $l_k<l_\epsilon$.

Table 2 Stress and production terms

$$\hat{\tau}_{11}=2\mu\left(\frac{1}{h_1}\frac{\partial \hat{u}_1}{\partial \hat{x}_1}+\frac{\hat{u}_2}{h_1 h_2}\frac{\partial h_1}{\partial \hat{x}_2}\right)-\frac{2}{3}\rho k$$

$$\hat{\tau}_{22}=2\mu\left(\frac{1}{h_2}\frac{\partial \hat{u}_2}{\partial \hat{x}_2}+\frac{\hat{u}_1}{h_1 h_2}\frac{\partial h_2}{\partial \hat{x}_1}\right)-\frac{2}{3}\rho k$$

$$\hat{\tau}_{12}=\mu\left(\frac{h_2}{h_1}\frac{\partial}{\partial \hat{x}_1}\left(\frac{\hat{u}_2}{h_2}\right)+\frac{h_1}{h_2}\frac{\partial}{\partial \hat{x}_2}\left(\frac{\hat{u}_1}{h_1}\right)\right)$$

$$P=\mu\left[2\left(\frac{1}{h_1}\frac{\partial \hat{u}_1}{\partial \hat{x}_1}+\frac{\hat{u}_2}{h_1 h_2}\frac{\partial h_1}{\partial \hat{x}_2}\right)^2+2\left(\frac{1}{h_2}\frac{\partial \hat{u}_2}{\partial \hat{x}_2}+\frac{\hat{u}_1}{h_1 h_2}\frac{\partial h_2}{\partial \hat{x}_1}\right)^2+\left(\frac{h_2}{h_1}\frac{\partial}{\partial \hat{x}_1}\left(\frac{\hat{u}_2}{h_2}\right)+\frac{h_1}{h_2}\frac{\partial}{\partial \hat{x}_2}\left(\frac{\hat{u}_1}{h_1}\right)\right)^2\right]$$

$$l=\min(l_\epsilon, l_k). \tag{6}$$

Model Prediction. Figures 2 and 3 show predictions with the standard and modified model respectively. Both show similar predictions of the separation point and bulk properties of the wake. However, particularly in the recirculating area, given isocurves for both k and l are closer to the bottom for the standard model. The recirculation vortex is somewhat stronger and larger in the modified model. Since the adverse pressure deficiency of the standard model and the near bottom lengthscale l_k appear to be well documented, the modified model is considered to be most realistic. Its prediction is illustrated in Figs. 3, 4, 5, 6, and 7.

As the cylinder is approached the wall shear stress and the low level mean velocity decreases. A low level maximum of kinetic energy and length scale develops. A weak recirculation area in front of the cylinder is realistic and indicates that the cylinder support does not have an important influence upon the bulk flow. Along the cylinder front face the pressure drops and the mean velocity increases rapidly. The acceleration parameter, $-2^{-1}\nu u_\infty^{-1}(1-c_p)^{-3/2}h_1^{-1}\partial c_p/\partial \hat{x}_1$, is predicted to be ca $4\cdot10^{-5}$. This is significantly larger than the critical value for laminarization of $3\cdot10^{-6}$ (Launder et al. [11]). Also a convex wall curvature tends to stabilize and decrease turbulence [16]. This suggests that such a boundary layer could be laminarized. The present model, based upon fully developed turbulence, predicts that the surface stress increases rapidly over the cylinder front face. The low level turbulent kinetic energy is fairly constant. Over the cylinder top and backward face, separation is predicted, with approximately constant base pressure. Along the wall behind the cylinder, the pressure and shear stress increases. The longitudinal dimension of the wake region is approximately $x_1/D=8$, which is reasonable and much less than for a small Reynolds number wake (Fornberg [1]). The wake characteristic mean velocity defect has its maximum at $x_1/D\approx2$ while the characteristic kinetic energy maximum occurs at $x_1/D\approx4$.

The length scale variations also appear to be reasonable. Near the boundaries there is a linear increase of length scale in accordance with the $(k-\epsilon)$ model modification. Higher up, there is a length scale maximum both in front of the cylinder and in the recirculating area behind. Near the top of the boundary layer a somewhat peculiar length scale minimum is predicted. This area is associated with very small turbulent kinetic energy so that it is dynamically insignificant. However, as compared to Tsiolakis et al.'s [9] data, such a length scale minimum could also be realistic. Since the length scale minimum coincides systematically with convex flow curvature, it could be a result of this. In convex curvature, tur-

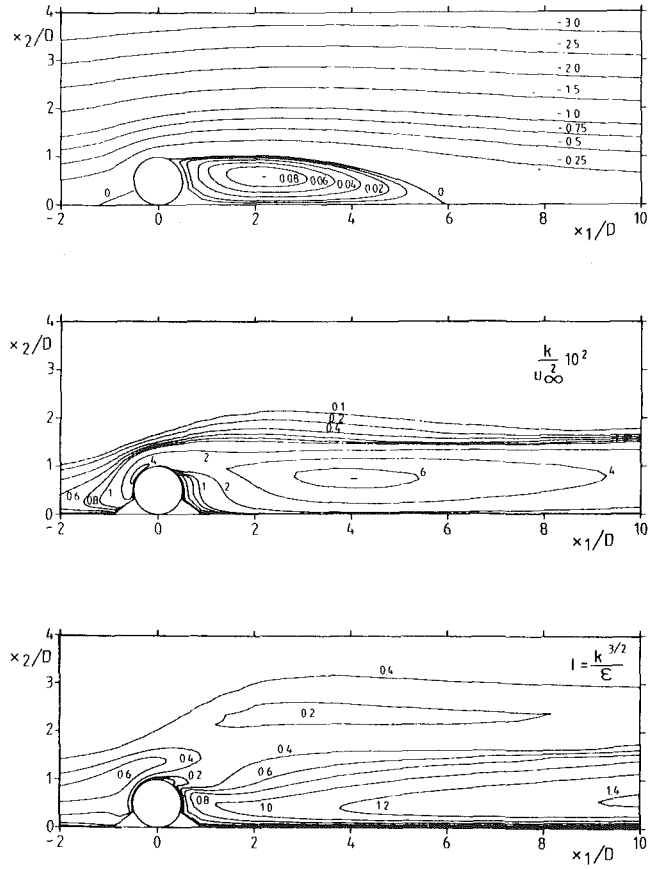

Fig. 2 Standard (k—ϵ) model. Isocurves for mean streamlines, kinetic energy and lengthscale. $Re = u_\infty D/\nu = 4.5 \cdot 10^4$, $\delta/D = 0.8$. Grid: 65 × 45.

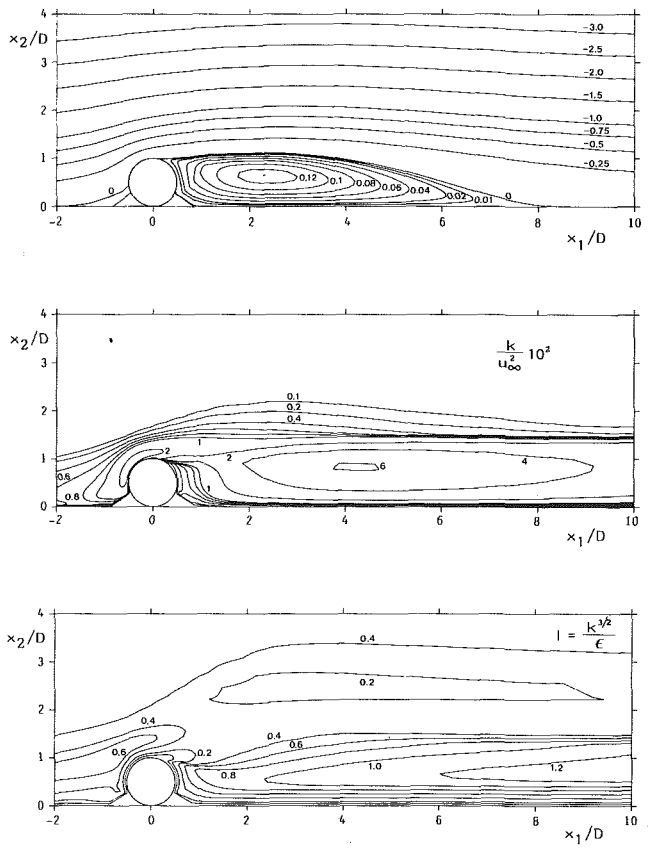

Fig. 3 Modified model. As in Fig. 2. Grid: 82 × 42.

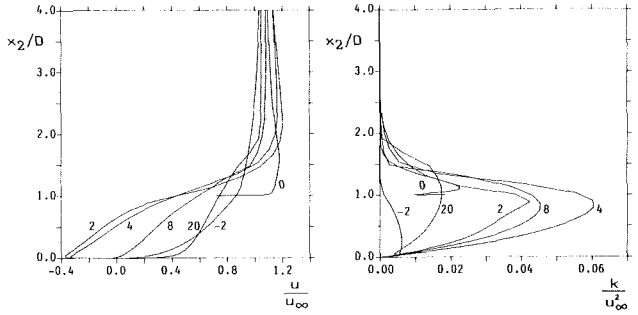

Fig. 4 Flow profiles at longitudinal coordinates $x_1/D = -2, 0, 2, 4, 8, 20$. Modified model.

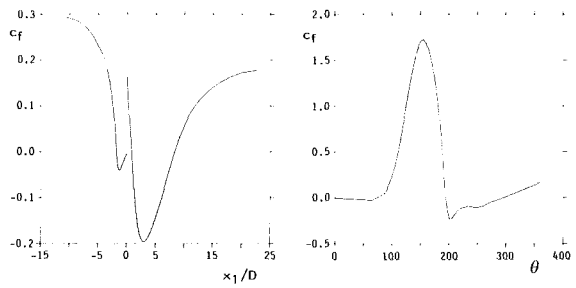

Fig. 5 Surface stress coefficient $c_f = 2\,\tau(0)\rho^{-1}\,u_\infty^{-2}$. Modified model.

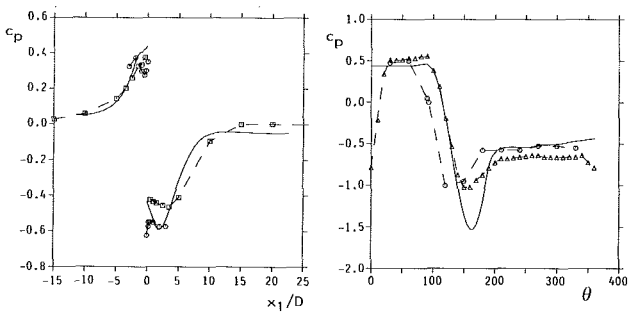

Fig. 6 Predicted and measured pressure coefficient, $c_p = (p - p_\infty)\rho^{-1}u_\infty^{-2}$ along the wall and cylinder. Modified model. 0: Bearman and Zdravkovich [8]. □: Tsiolakis et al. [9] Δ: Aiba and Tsuchida [10].

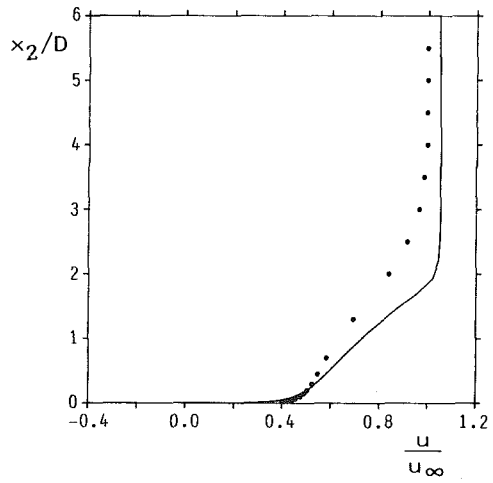

Fig. 7 Predicted and measured mean velocity profile at $x_1/D = 20$. Modified model. ●: Tsiolakis et al. [9].

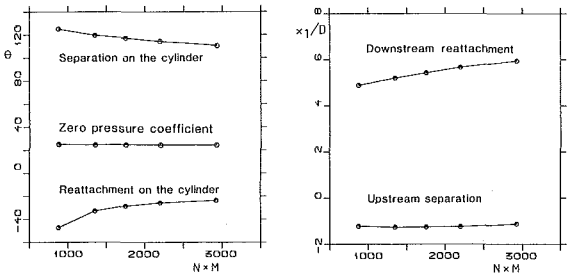

Fig. 8 Grid variations. Standard (k—ϵ) model. Grid: 35 × 25, 45 × 30, 50 × 35, 55 × 40 and 65 × 45.

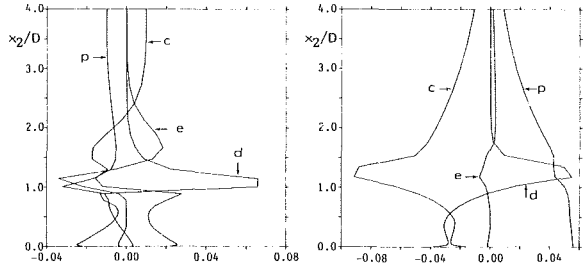

Fig. 9 Numerical imbalance of momentum equation. Modified model. Profiles at longitudinal coordinates $x_1/D = 2$ and 4, c-convection term, p-pressure gradient, d-diffusion term, e-imbalance. $Re = u_\infty D/\nu = 4.5 \cdot 10^4$, $\delta/D = 0.8$.

bulence tends to be damped [16]. According to the equation $l = C^{3/4} k^{3/2}/\epsilon$, l could then also tend to decrease in convex curvature flows.

At larger downstream distance, not shown, the maximum velocity defect, kinetic energy and length scale, appears to approach Schlichting's far wake self-similarity law $k^{1/2} \alpha (x_1/D)^{-1/2}$, $l \alpha (x_1 D)^{1/2}$.

Data Comparison

Experimental data are the main guide towards realistic modelling of turbulent flows. However, some aspects of a turbulence model will always be unrealistic and data comes from nonideal experiments. Small differences between predictions and data should therefore be accepted without rejecting general models that appear to give useful predictions of comparable flows.

The traditional measurement effort has mainly been directed towards two features: One is the estimation of resultant heat loss and hydrodynamical force in terms of drag and lift coefficients. The other feature is the relaxation of the boundary layer far behind the cylinder. We feel that prediction of such observations may not be sufficiently sensitive to the model for local flow around the cylinder. These data may therefore be nonoptimal for model validation. It appears that quantitative observations of the near cylinder flow field would be more model discriminant. The most relevant, simple observations known to us are Bearman and Zdravkovich's [8] and Aiba and Tsuchida's [10] pressure data, and Tsiolakis et al.'s [9] wake data. The experiments are characterized by the following experimental conditions respectively (Re, δ/D) = ($4.5 \cdot 10^4$, 0.8), ($3.1 \cdot 10^4$, 1.0), ($1.8 \cdot 10^4$, 2.6). The data come from flows with tripped turbulent boundary-layer inflow. However, as has been estimated, the flow could be laminarized over the front face of the cylinder. The model is valid for fully developed turbulent flow. With this in mind the experimental conditions referred above are considered to be almost identical, so simulations are only done with Bearman and Zdravkovich's [8] values. Model predictions and data are shown in Figures 6 and 7. From our point of view there is a remarkable similarity. Most aspects appear to be predicted realistically. Nevertheless, focusing upon the apparent differences:

Relative to Bearman and Zdravkovich's [8] data, the cylinder front reattachment, pressure minimum- and separation-points appear to be predicted some 20 degrees too late. This indicates that the experimental flow may have been laminarized over the cylinder. From their flow visualizations, it also looks like the experimental near wake is somewhat wider than predicted, and the mean streamlines above the cylinder and wake are more inclined away from the plane than predicted. The visualizations were from a nontripped flow where separation at the cylinder top most probably occurred from a laminar boundary layer. Such differences are therefore reasonable to expect (compare Fornberg's [1] laminar flow estimates).

Aiba and Tsuchida's [10] data come from an experiment with continuous pressure over the contact point between the cylinder and wall. It seems nonreasonable that this leakage could imply that the location of the front reattachment point was estimated too high. Relative to their data, the prediction of the front reattachment point therefore seems realistic. Their base pressure appears to be somewhat smaller than predicted.

The most significant difference between the data and predictions appears to be the magnitude of the minimum pressure near the top of the cylinder. The speed over the cylinder top is probably estimated too high. While the cylinder drag is predicted accurately, the lift is probably significantly overpredicted relative to both data sets.

Tsiolakis et al.'s [9] wake data and our predictions are illustrated in Fig. 7. Again there is good correspondence between data and predictions without model adjustment. The most evident difference appears to be that the predicted wake may be somewhat too narrow. Since Tsiolakis' et al. [9] experiment was done with an inflow boundary layer thickness $\delta/D = 2.6$, while the simulations are done for $\delta/D = 0.8$, such a difference is reasonable. This also indicates that numerical diffusion is not of a decisive character in the simulations.

Errors and Uncertainty

Grid variations are illustrated in Fig. 8. Central features of the flow, such as separation and reattachment locations appear to be insensitive to grid variations. The hybrid central/upwind differencing scheme applied may give significant numerical diffusion (cf. McGuirk et al. [18]). This is undesirable when the particular feature under study is turbulence. The magnitude of this error is estimated by the following scheme: From the estimated fields the different terms in the equations of motion are evaluated by a central difference scheme, which is accurate to second order. Possible imbalance in the equations of motion is interpreted as a measure of the effect of numerical diffusion. It turns out that over most of the computational domain the numerical diffusion is estimated to be small. However, as illustrated in Fig. 9, the numerical imbalance may be comparable to real physical effects near the upper boundary of the recirculating area. As expected, the numerical scheme is therefore not as accurate as is desirable in these (small) areas. Nevertheless, the analysis suggests that numerical errors are not decisive and that a numerically well conditioned result is obtained.

Parameter adjustments in models as rich as the present could almost certainly result in detailed data fit. However, a fit would also most probably be physically and statistically insignificant (compare Eidsvik [19]). This illusion should be avoided at all cost. Since generally useful incomplete models are sought, previous experience with comparable models applied to comparable flows should be assigned large significance. Parameters should be kept standard until massive evidence indicates a better alternative. The data comparison of the present model suggests that model prediction fits the data within the measurement error *without* parameter

adjustments. The apparent discrepancies suggest that better data are needed, so that comparisons can be focused toward them.

Concluding Remarks

A dynamical model for flows over a cylinder at a plane boundary is developed. The model, based upon a $(k-\epsilon)$ turbulence closure, is formulated in a curvilinear coordinate system based upon frictionless flow. A modification to a one-equation turbulence model in areas of adverse pressure gradient and recirculating flow appears to be more realistic than the standard $(k-\epsilon)$ model.

Near the upper boundary of the recirculation area there is significant numerical diffusion in the hybrid central/upwind differencing scheme. In spite of this, the main features of the predicted flow are insensitive to reasonable model and grid changes. This means that a well-defined prediction is obtained.

Data comparisons indicate that main features of the flow are accurately predicted without model adjustments, also separation and reattachment. However, there are indications that the pressure near the cylinder top may be significantly underpredicted. The apparent differences between prediction and data call for better experimental verification before their significance can be decided.

Acknowledgments

This study is funded by NAVF and SINTEF. The encouragement, computer program and computer time provided by Professor B. Magnussen are highly appreciated.

References

1 Fornberg, B., 1980, "A Numerical Study of Steady Viscous Flow Past a Circular Cylinder," *J. Fluid Mech.*, Vol. 98, pp. 819–855.

2 Cebeci, T., Stewardson, K., and Schimke, S. M., 1984, "Unsteady Boundary Layers Close to the Stagnation Region of Slender Bodies," *J. Fluid Mech.*, Vol. 147, pp. 315–332.

3 Phonc Loc, T., and Bonard, R., 1985, "Numerical Solution of the Early Stage of the Unsteady Viscous Flow Around a Circular Cylinder: a Comparison with Experimental Visualization and Measurements," *J. Fluid Mech.*, Vol. 100, pp. 83–111.

4 Hunt, J. C. R., 1973, "A Theory of Turbulent Flow Around Twodimensional Bluff Bodies," *J. Fluid Mech.*, Vol. 61, pp. 625–706.

5 Simpson, R. L., 1985, "Two-dimensional Turbulent Separated Flow," AGARD-AG-287, Vol. 1, 104 pp.

6 Sarpkaya, T., and Isacsson, M., 1981, *Mechanics of Wave Forces on Offshore Structures*, Van Nostrand Reinhold Co., New York, 651 pp.

7 Majumdar, S., and Rodi, W., 1985, "Numerical Calculations of Turbulent Flow Past Circular Cylinders," *Proc. 3rd Symposium on Numerical and Physical Aspects of Aerodynamical Flows*, Long Beach, Calif.

8 Bearman, P. W., and Zdravkovich, M. M., 1978, "Flow Around a Circular Cylinder Near a Plane Boundary," *J. Fluid Mech.*, Vol. 89, pp. 33–47.

9 Tsiolakis, E. P., Krause, E., and Müller, U. R., 1985, "Turbulent Boundary Layer Wake Interaction," *Turbulent Shear Flows*, Vol. 4, Springer-Verlag, 395 pp.

10 Aiba, S., and Tsuchida, H., 1985, "Heat Transfer around a Circular Cylinder near a Plane Boundary," *Trans. JSME*, Vol. 51-463, pp. 866–873.

11 Launder, B. E., Reynolds, W. C., and Rodi. W., 1985, *Turbulence models and their applications, Vol.2*, Collection de la direction des études et recherches d'electricité de France. Editions Eyrolles 61, Bd Saint – Germain Paris 5^e, 400 pp.

12 Milne-Thomson, L. M., 1986, *Theoretical Hydrodynamics*, MacMillan & Co., London, 743 pp.

13 Chieng, C. C., and Launder, B. E., 1980, "On the Calculation of Turbulent Heat Transport Downstream from an Abrupt Pipe Expansion," *Numerical Heat Transfer*, Vol. 3, pp. 189–207.

14 Rodi, W., and Scheuerer, G., 1986, "Scrutinizing the k-ϵ Turbulence Model Under Adverse Pressure Gradient Condition," ASME JOURNAL OF FLUIDS ENGINEERING Vol. 108, pp. 174–179.

15 Raithby, G. D., Galpin, P. F., Van Doormaal, J. P., 1986, "Prediction of Heat and Fluid Flow in Complex Geometries Using General Orthogonal Coordinates," *Numerical Heat Transfer*, Vol. 9, pp. 125–142.

16 Johnston, J. P., 1976, "Internal Flows," *Topics in Applied Physics. Turbulence.* Bradshaw, P., Ed. Springer-Verlag, pp. 109–170.

17 Patankar, S. V., 1980, *Numerical Heat Transfer and Fluid Flow*, McGraw-Hill, 197 pp.

18 McGuirk, J. J., Taylor, A. M. K. P., and Whitelaw, J. H., 1982, "The Assessment of Numerical Diffusion in Upwind Difference Calculations of Turbulent Recirculating Flows," *Turbulent Shear Flows 3*, Springer-Verlag, pp. 206–224.

19 Eidsvik, K. J., 1988, "Wind-Wave Generation of Ocean Current. On Model Identification," *IEEE, Journal of Oceanic Engineering*, Vol. 13, pp. 43–49.

Supplementary Boundary-Layer Approximations for Turbulent Flow

L. C. Thomas

S. M. F. Hasani

Mechanical Engineering Department,
King Fahd University of Petroleum & Minerals,
Dhahran, Saudi Arabia

Approximations for total stress $\bar{\tau}$ and mean velocity $\bar{u}$ are developed in this paper for transpired turbulent boundary layer flows. These supplementary boundary-layer approximations are tested for a wide range of near equilibrium flows and are incorporated into an inner law method for evaluating the mean wall shear stress $\bar{\tau}_0$. The testing of the proposed approximations for $\bar{\tau}$ and $\bar{u}$ indicates good agreement with well-documented data for moderate rates of blowing and suction and pressure gradient. These evaluations also reveal limitations in the familiar logarithmic law that has traditionally been used in the determination of wall shear stress for non-transpired boundary-layer flows. The calculations for $\bar{\tau}_0$ obtained by the inner law method developed in this paper are found to be consistent with results obtained by the modern Reynolds stress method for a broad range of near equilibrium conditions. However, the use of the proposed inner law method in evaluating the mean wall shear stress for early classic near equilibrium flow brings to question the reliability of the results for $\bar{\tau}_0$ reported for adverse pressure gradient flows in the 1968 Stanford Conference Proceedings.

Introduction

Standard boundary-layer approximations that pertain to the order of magnitude of the transport characteristics (i.e., $\bar{u}$, $\bar{v}$) and derivatives in transport characteristics within turbulent boundary layers are well known (Kays and Crawford, 1980; Schetz 1984; Schlichting, 1979; White, 1974). Because of approximate similarities that generally exist within boundary layers, these traditional boundary-layer approximations can be supplemented by approximations for the distributions in total stress for a broad range of boundary-layer flow applications. The Couette law is the best known boundary-layer approximation of this kind. Supplementary boundary-layer approximations such as this provide a basis for establishing useful approximations for distributions in the mean velocity u which can be used in numerical full field and integral solution methods. The objective of this paper is to develop and test practical approximations for total stress and mean velocity which are applicable across the entire flow field for transpired turbulent boundary-layer flows.

Formulation

Supplementry boundary-layer approximations are developed in this section for the distributions in total stress $\bar{\tau}$ and mean velocity $\bar{u}$ applicable to steady two-dimensional incompressible plane and axisymmetric wall-bounded flows.

Approximations for Total Stress. The distribution of total stress $\bar{\tau}(=\bar{\tau}_{xy}-\rho\ \overline{u'v'})$ across the boundary layer is represented by the momentum equation,

$$\rho\left(\bar{u}\frac{\partial\bar{u}}{\partial x}+\bar{v}\frac{\partial\bar{u}}{\partial y}\right)=\frac{\partial\bar{\tau}}{\partial y}-\frac{d\bar{P}}{dx} \tag{1}$$

or its integral form,

$$\bar{\tau}=\bar{\tau}_0+\frac{d\bar{P}}{dx}\,y+\rho\ \bar{v}_0\ \bar{u}+\frac{\rho}{r_0}\left[\int_0^y\frac{\partial}{\partial x}\,(r_0\bar{u}^2)\,dy\right.$$

$$\left.-\bar{u}\int_0^Y\frac{\partial}{\partial x}\,(r_0\bar{u})dy\right] \tag{2}$$

In the region near the wall, the axial gradient $\partial\bar{u}/\partial x$ is very small, such that the integral convective terms on the right-hand side of equation (2) can be neglected. With these integral terms assumed to be negligible, equation (2) reduces to the Couette flow approximation,

$$\bar{\tau}=\bar{\tau}_0+\frac{d\bar{P}}{dx}\,y+\rho\ \bar{v}_0\ \bar{u} \tag{3}$$

This equation takes the dimensionless form

$$\frac{\bar{\tau}}{\bar{\tau}_0}=1+\beta_\delta\xi+B_M U \tag{4a}$$

where $U=\bar{u}/U_\infty$, $\xi=y/\delta$, $\beta_\delta = d\bar{P}/dx\ \delta/\bar{\tau}_0$, and $B_M = \rho\ \bar{v}_0 U_\infty/\bar{\tau}_0$, or

$$\frac{\bar{\tau}}{\bar{\tau}_0}=1+P^+y^++v_o^+u^+ \tag{4b}$$

where $u^+ = \bar{u}/U^*$, $y^+ = yU^*/\nu$, $U^*=\sqrt{\bar{\tau}_0/\rho}$, $P^+ = \nu/U^*$ $1/\rho\ d\bar{P}/dx = \beta_\delta/\delta^+$ and $v_0^+ = \bar{v}_0/U^* = B_M/U_\infty^+$. Couette flow approximations of the form of equation (4) are commonly employed in numerical codes for calculating the distribution of transport characteristics in the vicinity of the wall.

Contributed by the Fluids Engineering Division for publication in the JOURNAL OF FLUIDS ENGINEERING. Manuscript received by the Fluids Engineering Division March 28, 1988; revised manuscript received January 1989.

The extent of the Couette flow region is dependent upon the significance of the integral convective terms appearing in equation (2). The Couette flow approximation can be employed over the inner 5 percent of the boundary layer ($0 \leq y/\delta \gtrsim 0.05$), except for situations involving strong acceleration and suction and large variations in radius of curvature r_0.

Attention is now turned to the region away from the wall where the effect of axial convection is significant. It is the convective effect that is responsible for bringing $\bar{\tau}$ into accord with the conditions that exist at the outer edge of the boundary layer. For developing boundary layers, the pertinent constraints at the outer edge are approximated by

$$\bar{\tau} = 0 \quad \text{and} \quad U = 1 \quad \text{at } y = \delta \qquad (5a,b)$$

$$\frac{\partial \bar{\tau}}{\partial y} = 0 \quad \text{and} \quad \frac{\partial U}{\partial y} = 0 \quad \text{at } y = \delta \qquad (5c,d)$$

and

$$\frac{\partial^i \bar{\tau}}{\partial y^i} = 0 \quad \text{and} \quad \frac{\partial^i U}{\partial y^i} = 0 \quad \text{at } y = \delta \qquad (5e,f)$$

for $i = 2, 3, 4, \ldots$. As has been indicated, $\bar{\tau}$ must satisfy the Couette flow approximation in the region near the wall. (By satisfying this equation, we are in effect satisfying the necessary constraints on $\bar{\tau}$ and $\partial\bar{\tau}/\partial y$ at $y = 0$.)

Rather than attempting to deal formally with the axial convective terms in equation (2), as would be done in the numerical field approach, the distribution in $\bar{\tau}$ across the boundary layer can be approximated in terms of δ and other parameters by analytic functions that satisfy the constraints near the wall and outer edge of the boundary layer.

Following the approach developed by Thomas and Amminger (1988) for laminar boundary-layer flow, $\bar{\tau}$ is approximated by an Nth order polynomial of the form

$$\frac{\bar{\tau}}{\bar{\tau}_0} = \sum_{n=0}^{N} a_n \xi^n + B_M U \qquad (6)$$

where the coefficients a_n are specified in accordance with the Couette equation and equations (5). The Couette law is satisfied as ξ becomes small by setting $a_0 = 1$ and $a_1 = \beta_\delta$, such that equation (6) becomes

$$\frac{\bar{\tau}}{\bar{\tau}_0} = 1 + \beta_\delta \xi + B_M U + \sum_{n=2}^{N} a_n \xi^n \qquad (7a)$$

or

$$\frac{\bar{\tau}}{\bar{\tau}_0} = 1 + P^+ y^+ + v_o^+ u^+ + \sum_{n=2}^{N} a_n \xi^n \qquad (7b)$$

Equation (7) can be combined with the primary and secondary constraints to obtain Nth order one-parameter or multiparameter approximations. For example, a practical 3rd order one-parameter approximation of this kind is given by

$$\frac{\bar{\tau}}{\bar{\tau}_0} = 1 + \beta_\delta \xi + B_M U - (3 + 2\,\beta_\delta + 3\,B_M)\xi^2 + (2 + \beta_\delta + 2\,B_M)\xi^3 \qquad (8)$$

which satisfies the Couette law, equation (4), and equations (5*a*) and (5*c*). Higher-order one-parameter approximations of this type are readily obtained by setting N equal to larger integer values and by satisfying higher-order constraints at the boundaries. However, this approach generally does not provide much improvement over equation (8). Alternatively, higher-order multiple-parameter approximations can be developed by specifying one or more higher-order coefficients in accordance with information that pertains to the distribution in the flow characteristics across the flow field, rather than at the boundaries. To illustrate, a 4th order two-parameter approximation is given by

$$\frac{\bar{\tau}}{\bar{\tau}_0} = 1 + \beta_\delta \xi + B_M U - (3 + 2\,\beta_\delta + 3\,B_M - a_4)\xi^2 + (2 + \beta_\delta + 2B_M - 2\,a_4)\xi^3 + a_4 \xi^4 \qquad (9)$$

Approximation for Mean Velocity $\bar{u}$. The mean velocity $\bar{u}$ can be expressed in terms of $\bar{\tau}$ and the mixing length l via the equation

$$\bar{\tau} = \mu \frac{\partial \bar{u}}{\partial y} + \rho l^2 \left(\frac{\partial \bar{u}}{\partial y}\right)^2 \qquad (10)$$

where $\bar{u} = 0$ at $y = 0$ and $\bar{u} = U_\infty$ at $y = \delta$. Equation (10) is integrated and expressed in terms of wall variables to obtain the familiar result

Nomenclature

a = damping parameter
a^+ = dimensionless damping parameter ($= aU^*/\nu$)
A_0 = constant in equation (1)
A_1 = constant in equation (1)
b = constant in equation (1)
B_M = blowing parameter ($= \rho\bar{v}_0 U_\infty/\bar{\tau}_0$)
c = constant in equation (1)
C = integration constant
C_0 = integration constant in equation (1)
d = constant in equation (1)
D = $1 - \exp(-y^+/a^+)$
F = blowing fraction ($= \bar{v}_0/U_\infty$)
f_x = friction factor $\left[\tau_0/\left(\frac{1}{2}\rho U_\infty^2\right)\right]$
l = mixing length
l^+ = dimensionless mixing length ($= lU^*/\nu$)
P^+ = dimensionless pressure gradient parameter [$= \nu/\rho U^{*3}\ (d\bar{P}/dx)$]
r_0 = radius of curvature
$\bar{u}$ = mean velocity in x-direction
u' = fluctuating velocity component in x-direction
U = dimensionless velocity ($= \bar{u}/U_\infty$)
U_∞ = free-stream velocity
U^* = friction velocity ($= \sqrt{\bar{\tau}_0/\rho}$)
u^+ = dimensionless mean velocity in x-direction ($= \bar{u}/U^*$)
U_∞^+ = dimensionless free-stream velocity ($= U_\infty/U^*$)
$\bar{v}$ = mean velocity in y-direction
v' = fluctuating velocity component in y-direction
$\bar{v}_0$ = mean transpiration velocity
v_0^+ = dimensionless mean transpiration velocity ($= \bar{v}_0/U^*$)
x = streamwise coordinate
y = vertical coordinate
y^+ = dimensional vertical coordinate in wall variable form ($= yU^*/\nu$)
α_0 = mixing length parameter for outer region
β_δ = $= \delta/\bar{\tau}_0(d\bar{P}/dx)$
δ = boundary-layer thickness
δ^+ = dimensionless boundary layer thickness ($= \delta U^*/\nu$)
κ = constant ($= 0.41$)
$\bar{\tau}$ = mean total shear stress
$\bar{\tau}_0$ = mean shear stress at wall
ρ = density
μ = viscosity
μ_t = turbulent viscosity
ν = kinematic viscosity
$-\rho\overline{u'v'}$ = turbulent shear stress (Reynolds stress)

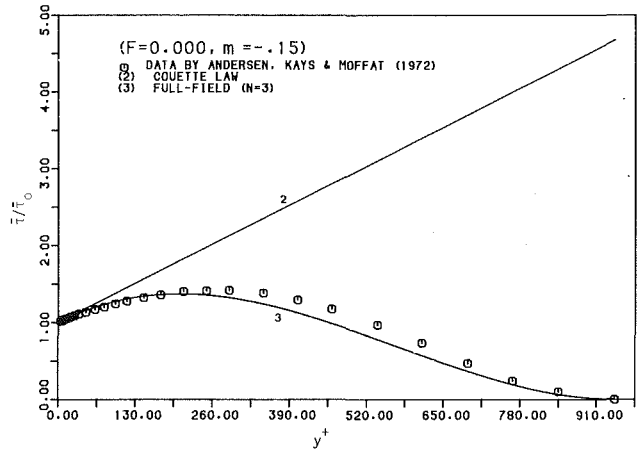

Fig. 1(*a*) Distribution in total stress $\bar{\tau}/\bar{\tau}_0$ at $x = 70$ in

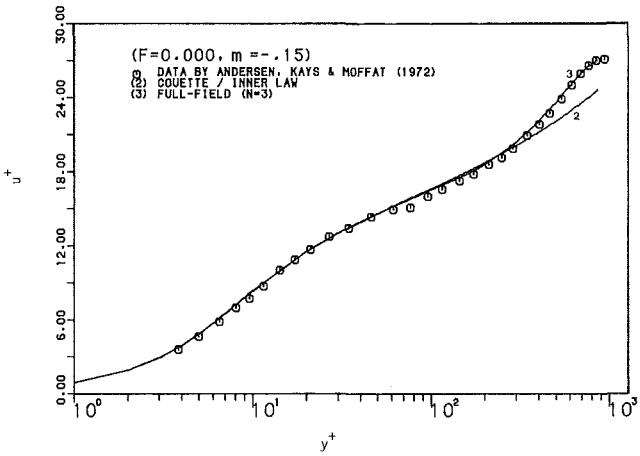

Fig. 1(*b*) Distribution in mean velocity u^+ at $x = 70$ in

Fig. 1 Experimental data and approximations for equilibrium boundary layer flow with mild adverse pressure gradient

$$u^+ = 2\int_0^{y^+} \frac{(\bar{\tau}/\bar{\tau}_0)\, dy^+}{1+\sqrt{1+4l^{+2}\bar{\tau}/\bar{\tau}_0}} \tag{11}$$

The mixing length for near equilibrium turbulent boundary layers with moderate pressure gradients and transpiration rates can be represented by (Anderson, Kays and Moffat, 1972, 1975; Kays and Moffat, 1975)

$$l^+ = \kappa y^+ \left[1-\exp\left(-\frac{y^+}{a^+}\right)\right] \qquad \text{inner region} \quad (12a)$$

$$l^+ = \alpha_0 \delta^+ \qquad \text{outer region} \quad (12b)$$

where $\kappa = 0.41$,

$$a^+ = \frac{25}{d[v_0^+ + bP^+/(1+cv_0^+)]+1} \tag{13}$$

with $b = 5.24$ and $c = 10$ for $P^+ \le 0$, $b = 2.9$ and $c = 0$ for $P^+ > 0$, $d = 7.1$ for $v_0^+ \ge 0$ and $d = 9$ for $v_0^+ < 0$, and

$$\alpha_0 = A_0\left(\frac{6000}{\mathrm{Re}_{\delta_2}}\right)^{1/8}\left(1-A_1\frac{\bar{v}_0}{U_\infty}\right) \quad \text{for } \mathrm{Re}_{\delta_2} \le 6000 \tag{14a}$$

$$= A_0\left(1-A_1\frac{\bar{v}_0}{U_\infty}\right) \quad \text{for } \mathrm{Re}_{\delta_2} \ge 6000 \tag{14b}$$

with $A_0 = 0.07$ and $A_1 = 67.5$.

With $\bar{\tau}$ and l represented by equations (6) and (12), equation (11) can be used to approximate the distribution in u^+ across the flow field. The limiting form of this approximation which is applicable to the intermediate region of the turbulent core takes the form

$$u^+ = \int \frac{(1+P^+y^+ + v_0^+ u^+)^{1/2}}{\kappa y^+}\, dy^+ + C \tag{15}$$

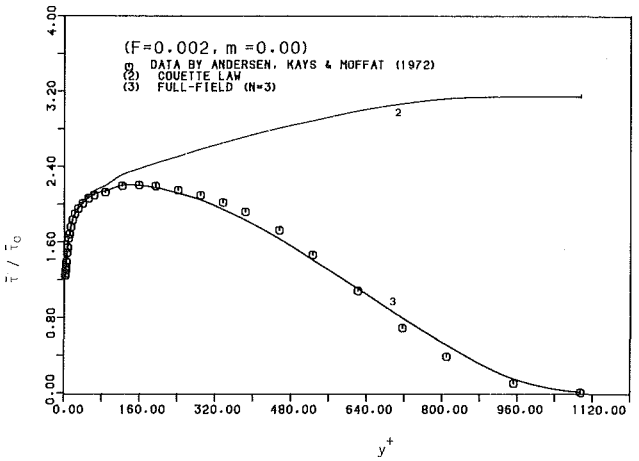

Fig. 2(*a*) Distribution in total stress $\bar{\tau}/\bar{\tau}_0$ at $x = 70$ in

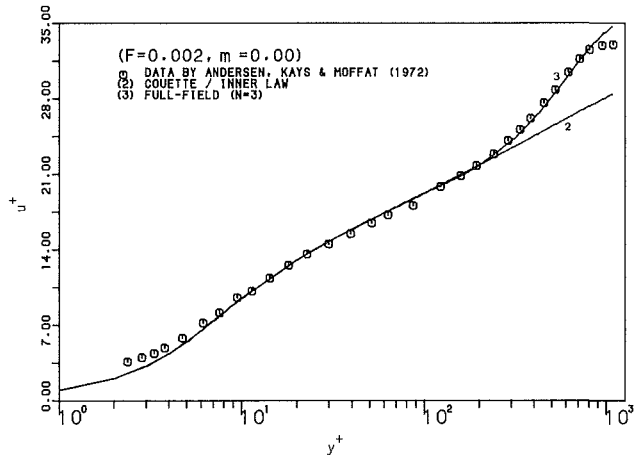

Fig. 2(*b*) Distribution in mean velocity u^+ at $x = 70$ in

Fig. 2 Experimental data and approximations for equilibrium boundary layer flow with moderate blowing and uniform free-stream velocity

where C is a function of P^+ and v_0^+. This equation reduces to the familiar log law,

$$u^+ = \frac{1}{\kappa}\ln y^+ + C_0 \tag{16}$$

for $P^+ = 0$ and $v_0^+ = 0$, where $\kappa = 0.41$ and $C_0 = 5.0$.

Evaluation

The boundary-layer approximations for $\bar{\tau}/\bar{\tau}_0$ and u^+ developed in this paper can be evaluated on the basis of experimental data for distributions in the total stress and mean velocity $\bar{u}$ associated with equilibrium and near equilibrium boundary layers with transpiration and pressure gradient.

The experimental measurements obtained at Stanford University (Anderson, Kays and Moffat, 1972, 1975; Kays and Moffat, 1975) for transpired boundary layers with mild to moderate pressure gradients are among the best documented data for equilibrium flows. These data were used as a standard for transpired flows at the 1981 Stanford Conference and will be relied upon as the primary frame of reference in the present study.

Distributions in Dimensionless Stress $\bar{\tau}/\bar{\tau}_0$ and Velocity u^+. The Couette law and the 3rd order one-parameter full field approximation for $\bar{\tau}/\bar{\tau}_0$ given by equations (4) and (8) are compared in Figs. 1(*a*), 2(*a*), and (3*a*) with experimental data for transpired turbulent flows. As expected, the Couette ap-

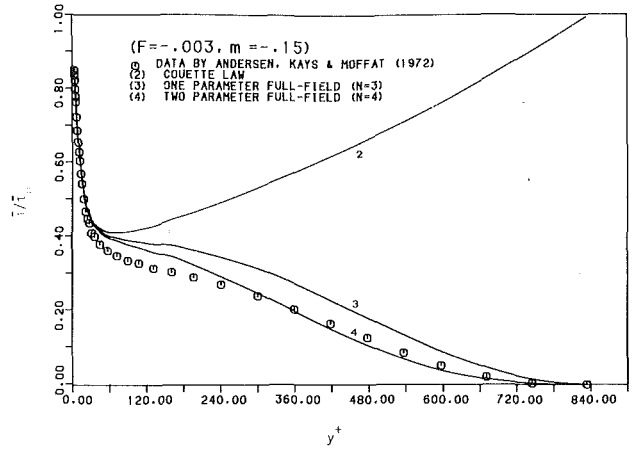

Fig. 3(*a*) Distribution in total stress $\tau/\bar{\tau}_0$ at $x = 70$ in

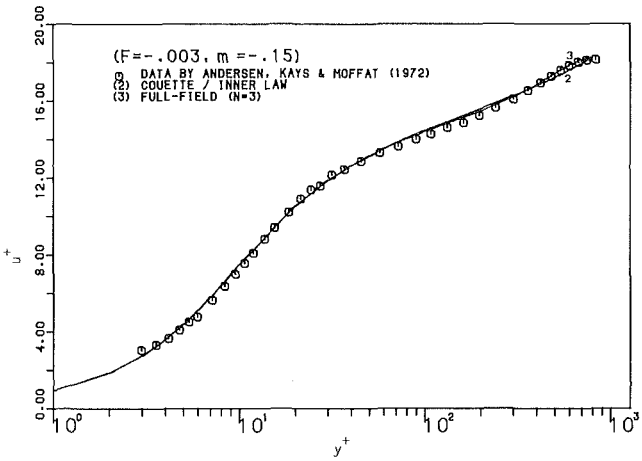

Fig. 3(*b*) Distribution in mean velocity u^+ at $x = 70$ in

Fig. 3 Experimental data and approximations for equilibrium boundary layer flow with moderate suction and mild adverse pressure gradient

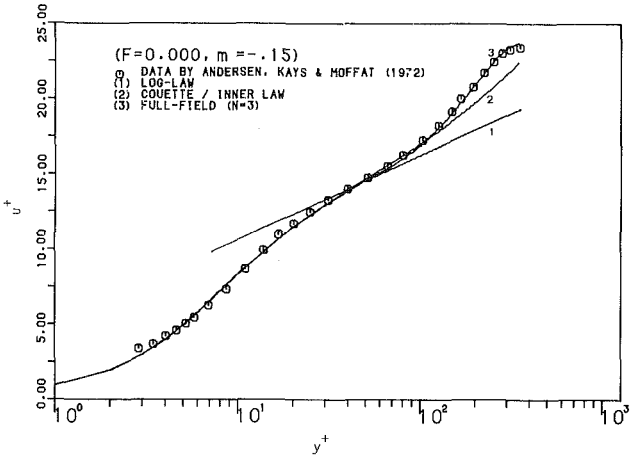

Fig. 4(*a*) Distribution in mean velocity at $x = 10$ in

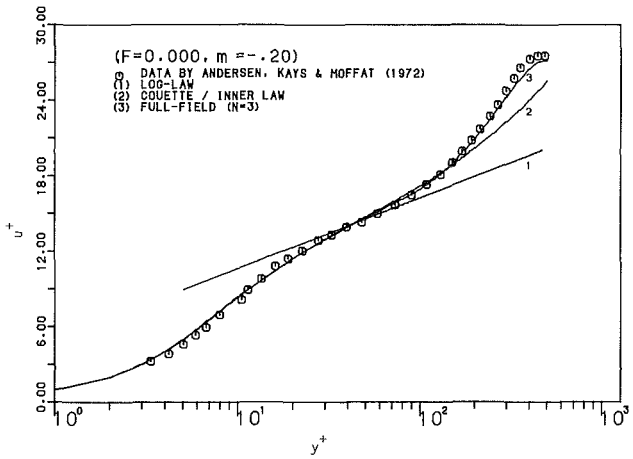

Fig. 4(*b*) Distribution in mean velocity at $x = 22$ in

Fig. 4 Experimental data and approximations for equilibrium boundary layer flows with mild adverse pressure gradient

proximation is observed to be applicable in the region near the wall ($y^+ \leq 30$; $\xi \leq 0.03$ to 0.07), but separates from the data in the turbulent core. These results also indicate that the 3rd order polynomial provides reasonable approximation for $\bar{\tau}/\bar{\tau}_0$ across the entire flow field, with the accuracy being somewhat poorer for suction than for blowing. Whereas modest improvements in the accuracy can be achieved in some cases by the use of higher-order one-parameter approximations, two-parameter approximations, although less practical, are more accurate. A 4th order two-parameter approximation for $\bar{\tau}/\bar{\tau}_0$ is shown in Fig. 3(*a*).

The distributions in u^+ obtained by use of the 3rd order approximation for $\bar{\tau}/\bar{\tau}_0$ are compared with experimental data in Figs. 1(*b*), 2(*b*), and 3(*b*). The calculations for u^+ obtained on the basis of this full field approximation are observed to be in excellent agreement with the data. In this connection, the use of higher order one- and two-parameter approximations for $\bar{\tau}/\bar{\tau}_0$ were found to provide no significant improvements in the quality of the approximation for u^+.

Figures 1(*b*), 2(*b*), and 3(*b*) also indicate that the Inner/Couette law provides a very reasonable first approximation for u^+ across the flow field, with the differences within the inner region ($\xi \leq 0.1$) being imperceptible. This close agreement is brought about by (i) the accuracy of the Couette and damping factor approximations near the wall ($\xi \lesssim 0.03$ to 0.07), the relatively smaller gradients du^+/dy^+ in the region immediately away from the wall, and (iii) compensating errors (i.e., over-predictions within the outer region) in equations (4) and (12).

The logarithmic law given by equation (16) with $\kappa = 0.41$ and $C_0 = 5.0$ has been employed to evaluate friction factors for nontranspired boundary-layer flows with pressure gradients (Coles and Hirst, 1968; East and Sawyer, 1966; White, 1974). The log-law is compared with the inner and full-field form of equation (11) and experimental data for moderate adverse pressure gradient flow in Figs. 4(*a*) and (*b*). Whereas the log-law intersects the data, it by no means provides a viable correlation over the intermediate region. The very noticeable difference between the log-law and the data shown in these figures brings to question the advisability of relying on the traditional Coles crossplot method for the evaluation of the friction factor for moderate to strong adverse pressure gradient flows. In this connection, use of the simple logarithmic law for boundary layer flows with moderate to strong adverse pressure gradients is incompatible with experimental indications and the widely accepted view that the mixing length within the inner region is characterized by equation (12*a*). Although the appropriateness (12*a*) has been challenged by East and Sawyer (1966), the measurement by Kays and associates are difficult to refute.

Application: Measurement of Wall Shear Stress

The experimental evaluation of wall shear stress for developing turbulent boundary-layer flows is very difficult because of uncertainties involved in velocity measurements close to the wall. The Reynolds stress approach developed at

Stanford University (Andersen, Kays and Moffat, 1972, 1975; Kays and Moffat, 1975) appears to be quite reliable, except near separation. This approach is based on the y-integral momentum equation, equation (2), which reduces to the following form near the wall where the convective integral terms are negligible:

$$\frac{f_x}{2}=\frac{-\overline{u'v'}}{U_\infty^2}-\frac{\nu}{U_\infty^2}\frac{\partial \bar{u}}{\partial y}+\frac{y}{U_\infty}\frac{dU_\infty}{dx}-\frac{\bar{u}\bar{v}_0}{U_\infty^2} \tag{17}$$

To establish the friction factor, equation (17) is combined with experimental measurements for $\bar{v}_0$, U_∞ and distributions in Reynolds stress $-\rho\overline{u'v'}$ and mean velocity $\bar{u}$ near the wall. The friction factor is selected such that the profile for $-\rho\overline{u'v'}/U_\infty^2$ computed from the above equation passes through the measured Reynolds stress just outside the wall region. However, since this method requires inputs for Reynolds stress, it cannot be applied to the important body of data for nontranspired equilibrium flows which were published between 1950 and 1965 by Clauser (1954), Wieghardt (1951), Bradshaw and Ferriss (1965), Ludwieg and Tillmann (1950), and others. In this connection, the significance of this early data was enhanced because of their use in the testing and rating of computational approaches by Patankar and Spalding (1967 *a*, *b*), Cebeci and Smith (1968), Bradshaw and Ferriss (1965, 1966), Alber (1968), Moses (1964, 1966), and many others at the 1968 Stanford Conference (Kline et al., 1968). The Coles crossplot method was used in the evaluation of $\bar{\tau}_0$ for nontranspired equilibrium and non-equilibrium flows at this landmark conference. However, because this method involves the use of the simple logarithmic law given by equation (16), the appropriateness of this approach for moderate to strong adverse pressure gradients is questionable.

To establish an alternative and more reliable approach to the evaluation of $\bar{\tau}_0$ for equilibrium boundary layers which is applicable to this early body of data as well as to more recent data for transpired flows, U^* will be inferred on the basis of comparisons of experimental data for the mean velocity $\bar{u}$, with the inner law calculations for u^+ obtained by the Couette approximation for $\bar{\tau}/\bar{\tau}_0$ and the damping factor approximation for mixing length l.

Using the Couette approximation for $\bar{\tau}$, the inner law for u^+ is put into the form

$$\bar{u}=\frac{2U^{*2}}{\nu}\int_0^{yU^*/\nu}\frac{1+y/U^{*2}(d\bar{P}/dx)+\bar{v}_0\bar{u}}{1+\sqrt{1+4(\kappa yDU^*/\nu)^2\,[1+y/U^{*2}(d\bar{P}/dx)+\bar{v}_0\bar{u}]}}\,dy \tag{18}$$

where $D=1-\exp\,[-yU^*/(\nu a^+)]$ and a^+ is given by equation (13) for equilibrium conditions. This equation can be used to calculate $\bar{\tau}_0$ by adjusting U^* such that the calculations for mean velocity $\bar{u}$ pass through the data in the region $(0.05 \le \xi \le 0.1)$, where the inner law is valid and the data can be expected to be reasonably accurate. The method is summarized as follows: (i) an initial value of U^* is assumed, (ii) P^+ and $v_0{}^+$ are computed, (iii) a^+ is computed by the use of equation (13), (iv) equation (11) is integrated numerically to obtain u^+ versus y^+ or u versus y, (*v*) the calculations for $\bar{u}$ are compared with the data in the region $0.05 \le \xi \le 0.1$, (vi) U^* is adjusted and steps (i)–(v) are repeated until agreement between the inner law and the data are within acceptable limits. As a final step, the adequacy of the Couette law is checked by com-

Table 1 Equilibrium flows

m	F	x (in.)	$f_x(1)$	$f_x(2)$	Percent difference
0.0	0.000	46	0.00362	0.00362	0.0
		70	0.00331	0.00336	−1.49
0.0	0.002	46	0.00205	0.00208	−1.44
		70	0.00184	0.00184	0.0
−0.15	0.000	46	0.00284	0.00290	−2.07
		70	0.00262	0.00272	−3.77
−0.15	0.001	46	0.00200	0.00204	−1.96
		70	0.00182	0.00182	0.0
−0.15	−0.001	46	0.00392	0.00392	0.0
		70	0.00374	0.00374	0.0
−0.20	0.000	46	0.00228	0.00228	0.0
		70	0.00219	0.00214	+2.34

Table 2 Mildly nonequilibrium flows

m	F	x (in.)	$f_x(1)$	$f_x(2)$	Percent difference
0.0	0.000	22	0.00404	0.00404	0.0
0.0	0.002	22	0.00256	0.00254	+0.79
0.0	0.00375	22	0.00150	0.00154	−2.60
		46	0.00107	0.00114	−6.54
		70	0.00091	0.00096	−5.21
−0.15	0.000	22	0.00324	0.00338	−4.14
−0.15	−0.001	22	0.00424	0.00424	0.0
−0.15	−0.00322	22	0.00680	0.00680	0.0
	−0.00287	46	0.00631	0.00620	+1.77
	−0.00268	70	0.00600	0.00586	+2.39
−0.20	0.000	22	0.00263	0.00258	+1.94

(1) Present method.
(2) Reynolds stress method (Andersen, Kays and Moffatt, 1972).

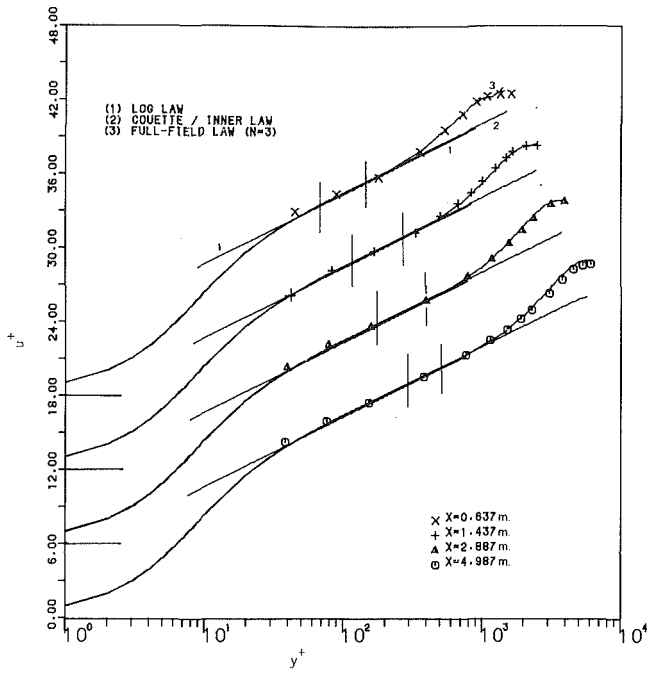

Fig. 5(*a*) Wieghardt (1951) zero pressure gradient

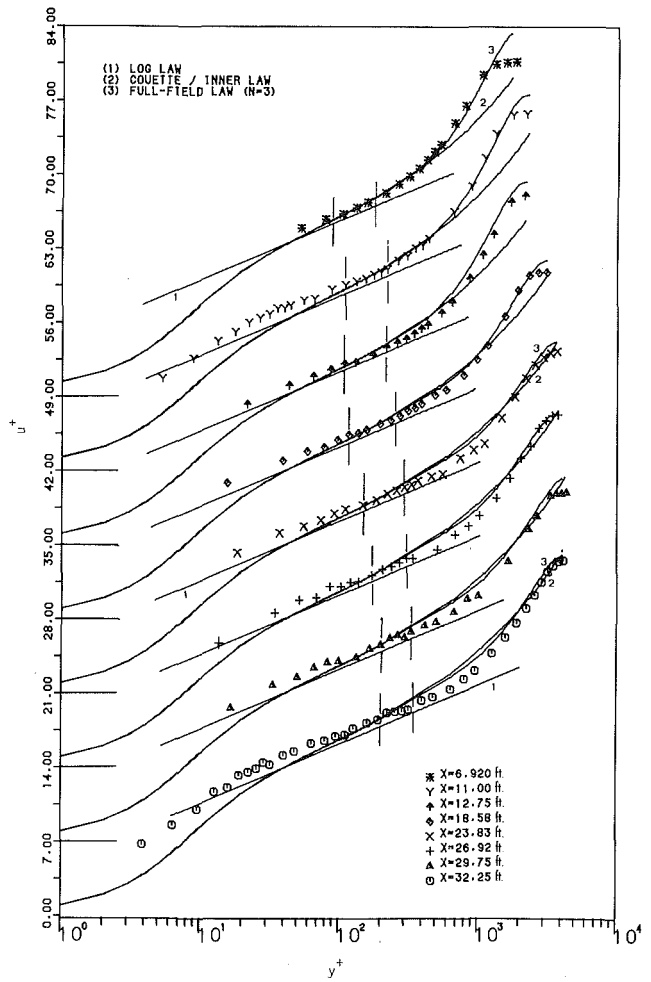

Fig. 5(*b*) Clauser I (1954) mild adverse pressure gradient

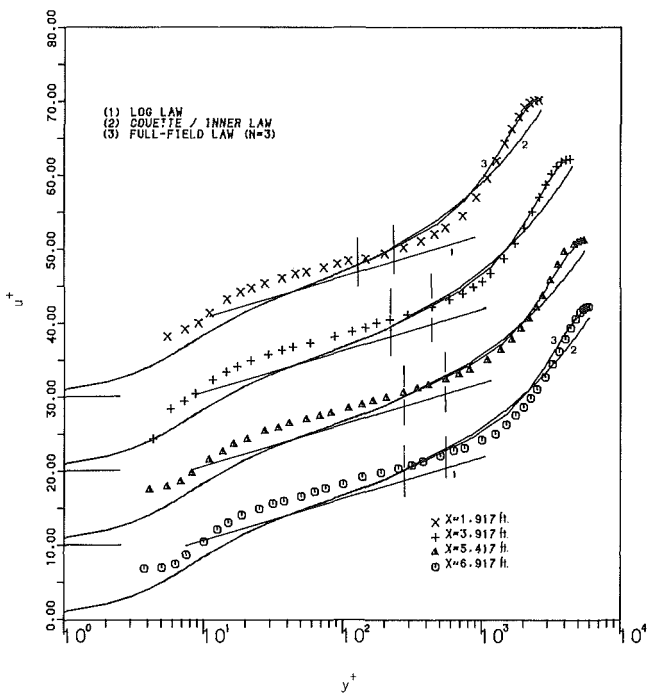

Fig. 5(*c*) Bradshaw and Ferriss (1965) moderate adverse pressure gradient

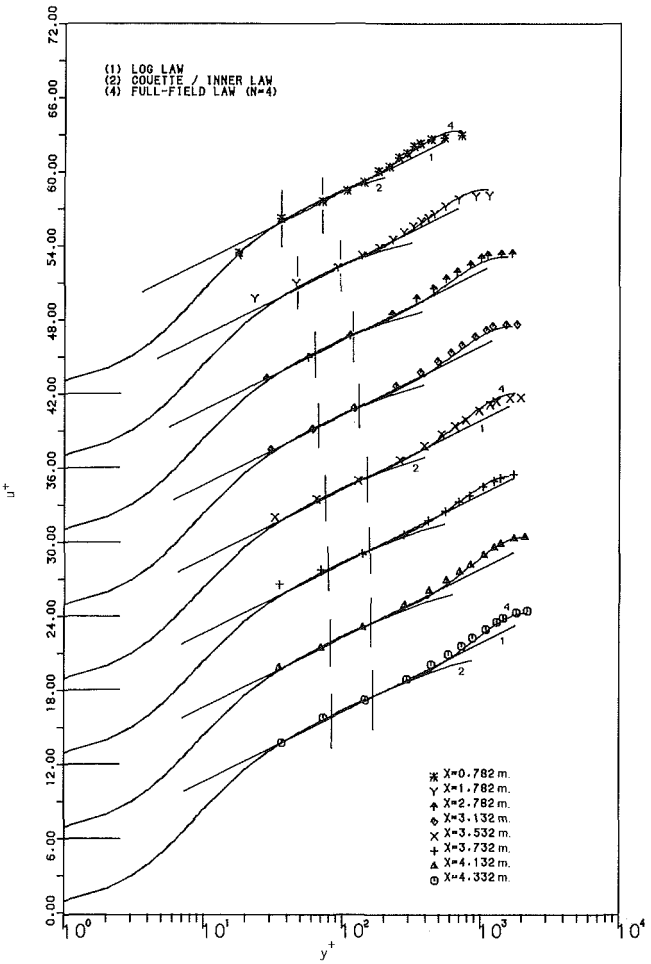

Fig. 5(*d*) Ludwieg and Tillmann (1950) moderate favorable pressure gradient

Fig. 5 Dimensionless velocity distributions

paring the resulting inner law calculations for u^+ with calculations obtained by use of the full-field inputs for $\bar{\tau}/\bar{\tau}_0$ and l.

To test the method, U^* has been calculated for the equilibrium flows of Andersen, Kays and Moffat (1972) for mild to moderate pressure gradients and rates of transpiration. The resulting calculations for friction factor f_x obtained by the use of equation (13) for a^+ are compared in Table 1 with values obtained by Andersen, Kays, and Moffat (1972) by means of the Reynolds stress method. The average absolute difference between the results of the two approaches is generally within about 1 percent. Hence, the proposed inner law method is judged to be compatible to the more sophisticated Reynolds stress approach for equilibrium conditions. Wall shear stress evaluations obtained by these two approaches are shown in Table 2 for mildly nonequilibrium conditions and fairly strong transpiration rates. Results of the two methods differ by an average of 2.3 percent. These larger differences are apparently due to limitations in the correlation for a^+.

The present inner law method has been used to evaluate the wall shear stress for the early nontranspired near equilibrium boundary-layer flows of Wieghardt (1951), Clauser (1954), Bradshaw and Ferriss (1965), and Ludwieg and Tillmann (1950). The resulting calculations for friction factor presented in Hasani (1987) indicate discrepancies relative to the Coles crossplot method of the order of 0 percent for the Wieghardt flow (zero pressure gradient), 5 to 6 percent for the Clauser I flow (mild adverse pressure gradient), 12 to 18 percent for the Bradshaw and Ferriss flow (moderate adverse pressure gradient), and 0 to 4 percent for the Ludwieg and Tillmann flow (moderate favorable pressure gradient). Inner law calculations for u^+ and y^+ made in connection with the evaluation of U^* by the present method using equation (11) are shown together with experimental data for u (expressed in terms of u^+) in Figs. 5(a–d). The traditional log-law given by equation (16) is also shown in these figures. The results indicate compatibility between Coles crossplot method and the present inner law method for mild adverse to favorable pressure gradients. However calculations for friction factor obtained by the present method fall significantly below results obtained by use of equation (16) for moderate to strong adverse pressure gradients. In connection with Figs. 5(a–d), it is observed that the experimental data in the wall region for these early nontranspired flows lie above the inner law calculations. Because of the universal nature of the distribution in u^+ versus y^+ within the wall region for nontranspired flow, discrepancies between data and calculations in this region can be attributed to experimental limitations in these early investigations.

Conclusion

Supplementary boundary-layer approximations have been developed in this paper for distributions in total stress $\bar{\tau}$ and velocity associated with incompressible transpired turbulent boundary layer flow, with emphasis on near equilibrium conditions. These boundary-layer approximations have been tested for a wide range of near equilibrium flows and have been incorporated into a method for evaluating the wall shear stress.

The resulting one- and two-parameter approximations for stress $\bar{\tau}$ are applicable across the entire boundary layer. These relations have been combined with standard inputs for mixing length to obtain approximations for the velocity distribution. Whereas the two-parameter approximations are more accurate, the practical one-parameter approximations generally prove to be quite adequate and provide a basis for the evaluation of wall shear stress and for the development of a reliable integral solution method for transpired turbulent boundary layer flow.

The testing of the boundary-layer approximations for $\bar{\tau}$ and u^+ indicate good agreement with well-documented data for moderate rates of blowing and suction and pressure gradient. These evaluations also reveal limitations in the familiar logarithic law that has traditionally been used in the evaluation of wall shear stress for nontranspired boundary-layer flows.

The method developed in this work for evaluating the wall shear stress features the use of the proposed boundary-layer approximations for $\bar{\tau}$ and u^+ within the inner region, which involves the specification of the damping parameter a^+ by the use of the correlations that are available in the literature for equilibrium boundary layers. The calculations for $\bar{\tau}_0$ obtained by this method have been found to be consistent with the results obtained by the modern Reynolds stress method for a wide range of near equilibrium conditions. The use of the method in evaluating the wall shear stress for the early classic near equilibrium flows with adverse pressure gradient published by Clauser and Bradshaw and Ferriss result in values of $\bar{\tau}_0$ that are significantly lower than the values reported on the basis of the standard Coles crossplot method. Based on indications concerning the applicability of the present method and the inadequacy of the simple logarithmic law established on the basis of the more recent body of data and the more comprehensive Reynolds stress method developed at Stanford University, it would appear that values of wall shear stress reported at the 1968 Stanford Conference are considerably high for these flows. These conclusions regarding equilibrium flows also bring to question the reliability of the results for $\bar{\tau}_0$ associated with nonequilibrium flows reported in the 1968 Stanford Conference Proceedings. In addition, the judgments concerning the performance of the various predictive methods must also be brought to question.

The present method can be employed for the evaluation of friction factors for nonequilibrium boundary layer flows provided reliable input for the parameter "a" is available. Although various methods of establishing "a" for near separating flows have been put forth in the literature, none have been verified and have gained wide acceptance.

Acknowledgment

The authors wish to acknowledge the support provided for this study by King Fahd University of Petroleum and Minerals.

References

Alber, I. E., 1968, "Investigations on Nonsimilar Turbulent Boundary Layer Development," Dynamic Science Report TR-A68-101.

Andersen, P. S., Kays, W. M., and Moffat, R. J., 1972, "The Turbulent Boundary Layer on a Porous Plate: An Experimental Study of the Fluid Mechanics for Adverse Free-Stream Pressure Gradients," Department of Mechanical Engineering, Stanford University, Stanford, Calif.

Andersen, P. S., Kays, W. M., and Moffat, R. J., 1975, *Journal of Fluid Mechanics*, Vol. 69, pp. 353–375.

Bradshaw, P., and Ferriss, D. H., 1965, "The Response of a Retarded Equilibrium Turbulent Boundary Layer to the Sudden Removal of Pressure Gradient," *NPL Aero Report*, 1145.

Bradshaw, P., and Ferriss, D. H., 1966, *NPL Aero Report* 1217.

Coles, D. E., and Hirst, E. A., 1968, "Computation of Turbulent Boundary Layers," *AFOSR-IFP-Stanford Conference Proc.*, Vol. 11, Department of Mechanical Engineering, Stanford University, Stanford, Calif.

Cebeci, T., and Smith, A. M. O., 1968, "A Finite-Difference Solution of the Incompressible Turbulent Boundary-Layer Equations by Eddy-Viscosity Concept," Douglas Aircraft Div. Report DAC 67130.

Clauser, F., 1954, "Turbulent Boundary Layers in Adverse Pressure Gradients," *Journal of Aeronautical Sciences,* Vol. 21, pp. 91–108.

East, L. F., and Sawyer, W. G., 1966, "An Investigation of the Structure of Equilibrium Turbulent Layers," *Journal of Sound and Vibration*, Vol. 3, p. 277.

Hasani, S. M. K., 1987, "The Use of Supplementary Boundary Layer Approximations in the Analysis of Turbulent Boundary Layer Flows," M. S. thesis, King Fahd University of Petroleum and Minerals, Dhahran, Saudi Arabia.

Herring, H. J., and Mellor, G. L., 1968, "A Method of Calculating Compressible Turbulent Boundary Layers," NASA Grant NGR 31-001-174.

Kays, W. M., and Crawford, M. E., 1980, *Convective Heat and Mass Transfer*, 2nd Ed., McGraw-Hill Inc., New York, NY.

Kays, W. M., and Moffat, R. J., 1975, *Studies in Convection*, 1, Academic Press, London, pp. 213–319.

Kline, S. J., Morkovin, M. V., Sovran, G., and Cockrell, D. J., 1968, "Computation of Turbulent Boundary Layers," *AFOSR-IFP-Stanford Conference Proc.*, Vol. 1, Department of Mechanical Engineering, Stanford University, Stanford, Calif.

Ludwieg, H., and Tillmann, W., 1950, "Investigations of the Wall Shearing Stress in Turbulent Boundary Layers," NACA 1285; Translated from *Ing. Arch.*, Vol. 17, 1949, pp. 288–299.

Moses, H. L., 1964, "The Behavior of Turbulent Boundary Layers in Adverse Pressure Gradients," Doctoral Dissertation, MIT Gas Turbine Report 73.

Moses, H. L., 1966, ASME Paper 66 WA/FE-14.

Patankar, S. V., and Spalding, D. B., 1967, "A Finite Difference Procedure for Solving the Equations of the Two-Dimensional Boundary Layer," *Int. Journal of Heat and Mass Transfer*, Vol. 10, pp. 1389–1412.

Patankar, S. V., Spalding, D. B., 1967, *Heat and Mass Transfer in Boundary Layers*, Morgan-Grampian, London.

Schetz, J. A., 1984, *Foundations of Boundary Layer Theory for Momentum, Heat, and Mass Transfer*, Prentice-Hall Inc., Englewood Cliffs, NJ.

Schlichting, H., 1979, *Boundary Layer Theory*, 7th Ed., McGraw-Hill, Inc., New York, NY.

Thomas, L. C., and Amminger, W. L., 1988, "A Practical One-Parameter Integral Method for Laminar Incompressible Boundary Layer Flow with Transpiration," ASME *Journal of Applied Mechanics*, Vol. 10, pp. 474–480.

White, F. M., 1974, *Viscous Fluid Flow*, McGraw-Hill, New York, NY.

Wieghardt, K., Tillmann, W., 1951, "On the Turbulent Friction Layer for Rising Pressure," NACA TM 1314; Translated from U&M Report 6617, 1944.

Experiments on Transition to Turbulence in a Constant-Acceleration Pipe Flow

P. J. Lefebvre
Naval Underwater Systems Center,
Newport, RI 02841

F. M. White
University of Rhode Island,
Kingston, RI 02881

Experiments were conducted to study transition to turbulence in pipe flows started from rest with a linear increase in mean velocity. The data were taken at the Unsteady Flow Loop Facility at the Naval Underwater System Center, using a 5-cm diameter pipe 30 meters long. Instrumentation included static pressure, wall pressure, and wall shear stress sensors, as well as a laser Doppler velocimeter and a transient flowmeter. A downstream control valve was programmed to produce nearly constant mean flow accelerations, a, from 2 to 12 m/s^2. In each of 37 runs, the time of transition to turbulence was the same throughout the pipe to within ±30 ms, indicating a global instability. As acceleration increased, the transition Reynolds number Re_D increased monotonically from 2×10^5 to 5×10^5. Other dimensionless transition parameters are also presented, the simplest and most effective of which is $T^* \approx 400 \pm 10$ percent for the present experiments, where $T^* = t_{tr}(a^2/\nu)^{1/3}$ and ν is kinematic viscosity.

Introduction

It is well known that a strong convective acceleration (highly favorable freestream pressure gradient) has a stabilizing effect on steady boundary layer flow. In laminar flow, acceleration will delay transition to turbulence. In turbulent flow, acceleration will thicken the viscous sublayer, damp the inner-layer turbulence, and, if sufficiently strong, induce a reversion toward laminar-flow conditions.

There are many studies of the relaminarization phenomenon, as reviewed by Narasimha and Sreenivasan (1979) and by Sreenivasan (1982). The latter makes a distinction between "laminarescent" flow, which occurs suddenly, and a "relaminarizing" flow, which occurs gradually with an ill-defined onset. A rough criterion for relaminarization is a critical value of the convective acceleration parameter

$$K = \frac{\nu}{U^2}\frac{dU}{dx} \tag{1}$$

where $U(x)$ is the freestream velocity. Jones and Launder (1972) suggest that a value $K \approx 3\times10^{-6}$ is usually sufficient to suppress turbulence in a boundary layer. However, Narasimha and Sreenivasan (1973) show that other details, such as the surface shear stress variation, can also influence the process. They point out that K is probably not a definitive criterion, since it does not include any parameters of the boundary layer itself.

In contrast to the wealth of work on convective (steady flow) acceleration, there has been much less published on the effect of transient acceleration or locally unsteady flows. Stettler and Hussain (1984) report on transition in periodic pipe flows, and Ramaprian (1984) reviews this subject. Leutheusser and Lan (1977), experimenting with start-up of flow in a pipe, showed that the transition Reynolds number may be delayed. In most such experiments, as in Kataoko et al. (1975), transition occurs after the acceleration has greatly decreased. A single data point relevant to the present experiment is given by Van der Sande et al. (1980), who opened a valve to generate flow with slowly decreasing acceleration in a 5-cm diameter water pipe. Transition to turbulence occurred at $t_{tr} = 4.2$ s, corresponding to a mean velocity of 1.15 m/s. The critical Reynolds number was $Re_D \approx 58{,}000$, far larger than the value of 2000 normally associated with steady transition.

Moss (1989), experimenting with accelerating pipe flow at low Reynolds numbers ($Re_D \leq 20{,}000$), gave no correlations but observed two different modes of transition: 1) a turbulent "slug" arising naturally in the boundary layer; and 2) a turbulent "puff" propagating downstream from the pipe inlet. Only mode #1, a global slug, was observed in the present study.

The purpose of this paper is to report data on transition to turbulence of pipe flows started from rest under conditions of nearly uniform acceleration. Two different parameters—a local acceleration and a local Reynolds number—will be shown to correlate the results with reasonable accuracy.

Experimental Procedure

The experiment was performed in the Unsteady Flow Loop Facility at the Naval Underwater Systems Center (NUSC), Newport, RI. The design and operation of this facility are described in detail by Lefebvre (1986).

The layout of the facility is shown in Fig. 1. A stainless-steel reservoir supplies a pump that delivers flow at variable rates to

Contributed by the Fluids Engineering Division of The American Society of Mechanical Engineers and presented at the Applied Mechanics, Bioengineering, and Fluids Engineering Conference, Cincinnati, Ohio, June 14-17, 1987. Revised manuscript received by the Fluids Engineering Division April 4, 1989.

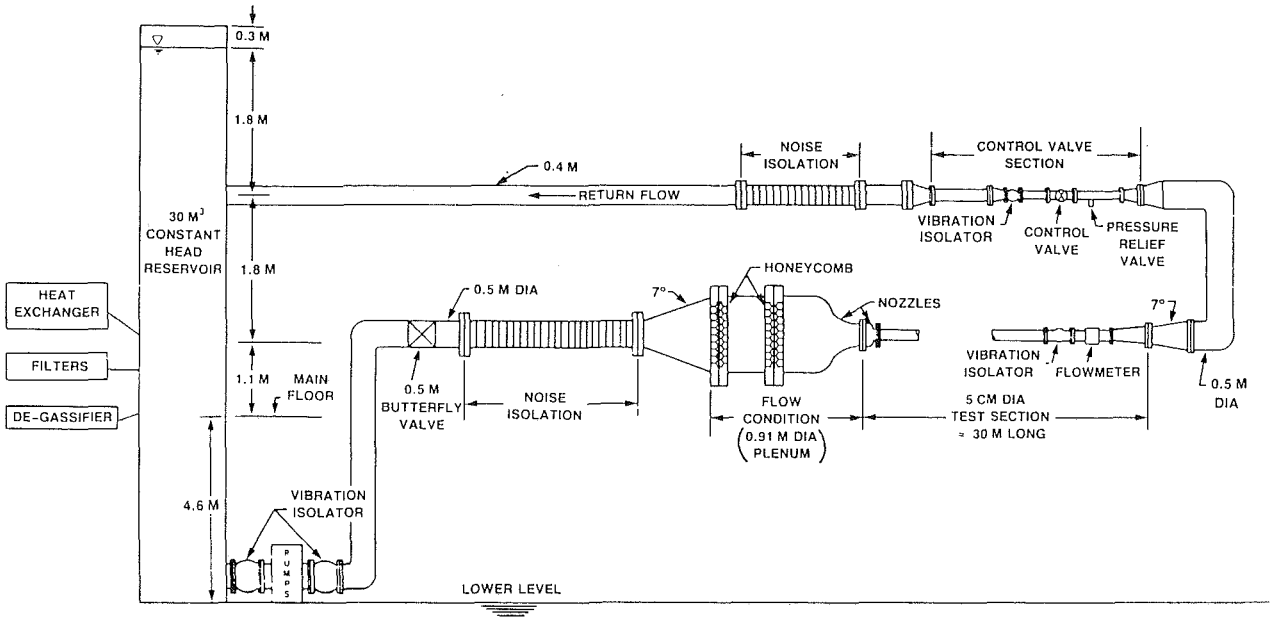

Fig. 1 Flow loop facility layout

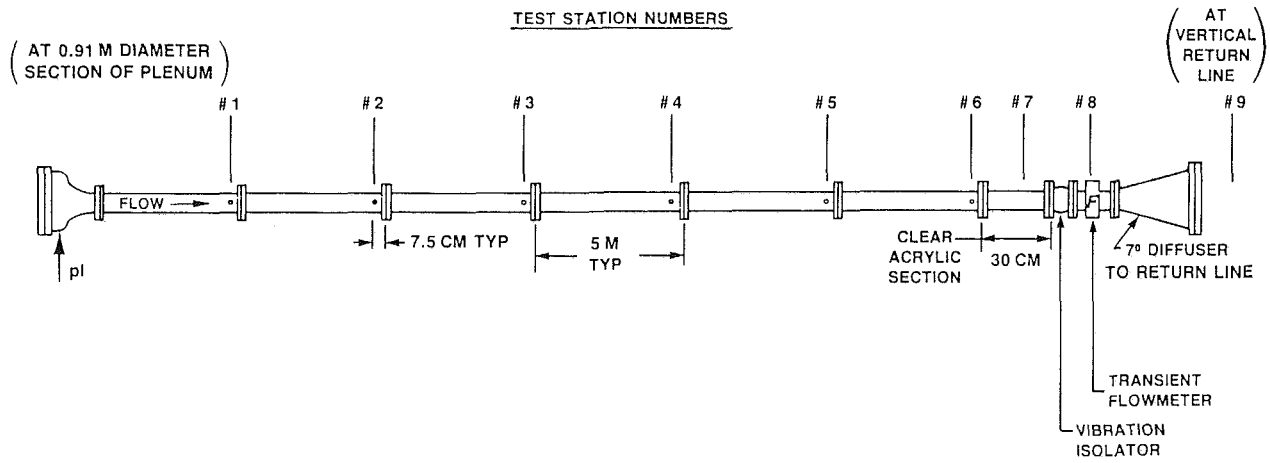

PHYSICAL SPECIFICATIONS
1. INSIDE DIAMETER = 5 ± .0025 CM
2. INSIDE SURFACE FINISH = 0.4 MICRONS
3. MATING AT FLANGES WITHIN 0.0025 CM
4. O-RING FACE SEAL AT FLANGES (NO HORIZONTAL GAP AT FLANGES)

STATION	INSTRUMENTATION
1–6	PRESSURE TAP/FLUSH PRESSURE SENSOR/SURFACE SHEAR STRESS SENSOR
7	LASER DOPPLER VELOCIMETER
8	TRANSIENT FLOWMETER
9	TEMPERATURE PROBE

Fig. 2 Five-cm diameter test section

Nomenclature

a = acceleration
D = pipe diameter
D^* = dimensionless diameter, equation (5)
K = relaminarization parameter, equation (1)
K_a = transition parameter, equation (6)
r = radial coordinate
R = pipe radius
Re_D = pipe Reynolds number, VD/ν
Re_δ = boundary layer Reynolds number, $V\delta/\nu$
t = time
t^* = dimensionless time, $\nu t/R^2$
T^* = transition parameter, equation (5)
u = axial velocity
u_f = Poiseuille maximum velocity, $R^2(-dp/dx)/4\mu$
V = instantaneous mean axial velocity
y = coordinate normal to pipe wall
δ = boundary layer thickness (99 percent)
δ^* = displacement thickness
θ = momentum thickness
μ = viscosity
ν = kinematic viscosity

Subscript

tr = at the transition point

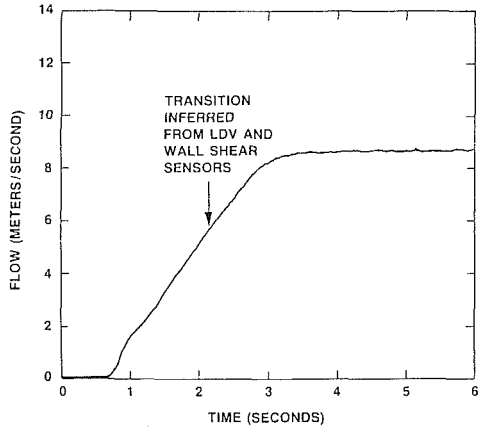

Fig. 3 Transient flowmeter output during a typical run ($a = 3.7$ m/s^2). (Uncertainty in flow = ± 1 percent, in time = ± 60 μs)

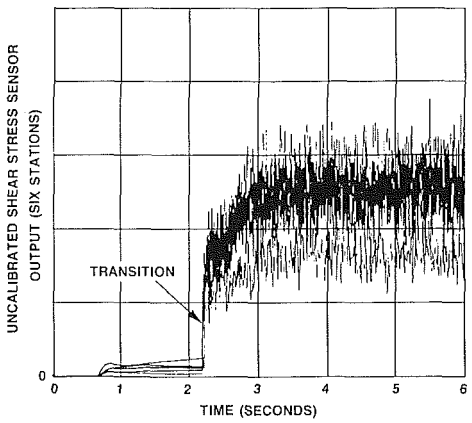

Fig. 4 Simultaneous transition of six surface shear stress sensors 5 meters apart ($a = 3.7$ m/s^2). (Uncertainty in time = ± 60 μs)

the test section. Vibration isolators, noise isolators, and flow straighteners are provided where appropriate. Control valves up to 30 centimeters in size may be installed downstream of the test section. The control valve is part of a unique feedback control system that provides programmed acceleration of the flow. Reservoir water is conditioned to maintain temperature within ±1°C, and filters remove particles as small as 0.5 microns. The test section flow rate is monitored to within ±1.0 percent of reading accuracy by a transient, electromagnetic flowmeter, whose details are described by Lefebvre and Durgin (1986).

As shown in Fig. 2, the test section is a 5-centimeter-diameter pipe with six measuring stations spaced approximately 5 meters apart. Each station has a static pressure tap, a flush-mounted wall pressure sensor, and a hot-film surface shear stress sensor. At the end of the test section is a clear acrylic section for laser Doppler velocimeter (LDV) measurements.

For these experiments, the control system was programmed to provide a constant acceleration from rest, leveling off to a final, steady, mean velocity of either 9 or 11 meters/second. Thirty-seven runs were made at mean-flow accelerations varying from 1.85 to 11.8 meters/second^2. Typical run duration was about 5 seconds. Transition to turbulence was monitored by both the LDV, focused at the centerline, and the six surface shear sensors. The hot-film surface shear stress sensors were uncalibrated because only the time of transition was being observed. Data were collected at a rate of 120 Hz on a MassComp MC500 digital data acquisition system.

Figure 3 shows the flowmeter output during a typical run. The arrow indicates the transition point as determined by the

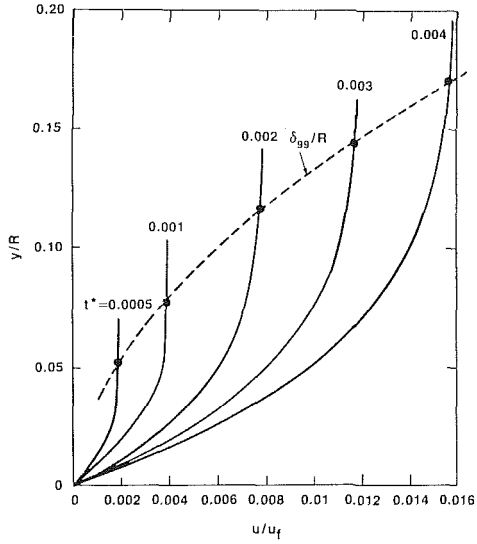

Fig. 5 Computed velocity profiles from equation (2)

LDV and the surface shear sensors. The flowmeter, being a volume-flow device, is not sensitive to transition and shows only a small oscillation after turbulence ensues.

As can be seen in Fig. 4, all six surface shear stress sensors show transition to turbulence at nearly the same time, indicating that the entire accelerating flow undergoes a kind of global instability. The LDV measurement (not shown) also indicated transition at the same time. Among these seven sensors, the maximum indicated deviation in transition time was 50 milliseconds, or about 3 percent of the total time to transition. It is concluded that pipe startup flow has a nearly unique transition time, independent of spatial position, at least for uniform accelerations.

Comparison With the Szymanski Laminar Solution

A classic analytic solution for startup of laminar pipe flow, caused by a suddenly applied pressure gradient, was given by Szymanski (1932). His solution for the unsteady velocity profiles u(r, t) is given by

$$\frac{u}{u_f} = 1 - r^{*2} - \sum_{n=1}^{\infty} \frac{8J_0(\lambda_n r^*)}{\lambda_n^3 J_1(\lambda_n)} \exp(-\lambda_n^2 t^*), \qquad (2)$$

where $r^* = r/R$, $t^* = \nu t/R^2$, and λ_n are the zeroes of the Bessel function J_0. The parameter $u_f = R^2(-dp/dx)/4\mu$ is the final maximum velocity corresponding to steady Poiseuille pipe flow. For t^* approaching unity, u approaches the Poiseuille flow; for small $t^* < 0.05$, the centerline velocity increases linearly with time, simulating a constant-acceleration startup.

For the experiments reported in this paper, the values of t^* at transition varied from 0.00105 to 0.0032. These values are small enough for Szymanski's solution to be a valid approximation of a constant acceleration. Therefore, equation (2) will be used to predict some laminar flow parameters for the proposed transition correlations.

Computed Boundary Layer Parameters

Equation (2) may be used to compute velocity profiles and other boundary layer parameters in this region of early startup, $t^* < 0.004$. Some plotted results are shown in Fig. 5. The 99 percent boundary layer thickness is shown as a dashed line and has the approximate mathematical form

$$\delta_{99\%} \approx 2.9(\nu t)^{1/2} \qquad (3)$$

In like manner the momentum and displacement thicknesses and shape factor are given by, approximately,

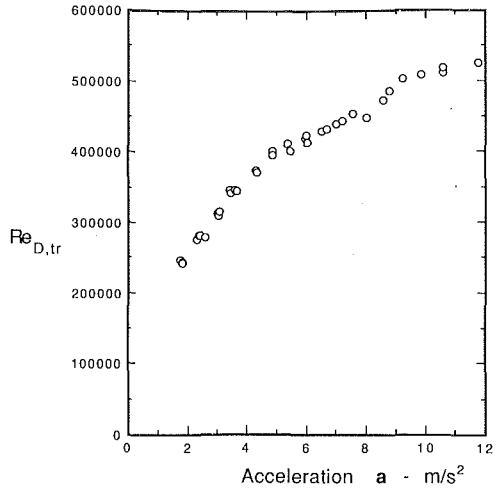

Fig. 6 Measured values of the pipe transition Reynolds number (Uncertainty in $Re_D = \pm 1.1$ percent, in $a = \pm 3$ percent)

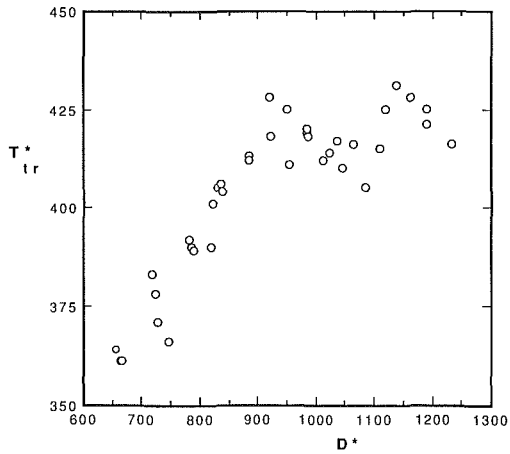

Fig. 7 Experimental transition times plotted according to equation (5). (Uncertainty in $T^* = \pm 2$ percent, in $D^* = \pm 1$ percent)

$$\theta \approx 0.35(\nu t)^{1/2}$$
$$\delta^* \approx 0.77(\nu t)^{1/2} \qquad (4)$$
$$H = \delta^*/\theta \approx 2.2$$

Because the Szymanski solution has no axial gradients, these parameters are functions of time only. At these early times, $t^* < 0.004$, viscous diffusion has not reached the centerline of the pipe. The maximum laminar boundary layer thickness at transition in the experiment was $\delta_{99\%} \approx 0.17\ R$.

Proposed Correlation Groups

In this study, the pipe walls were smooth, the first measurement station was 100 diameters downstream of the entrance, and care was taken to avoid external disturbances. Acceleration a was held constant for each run. Therefore, transition time was a function of only three parameters: $t_{tr} = fcn(D, \nu, a)$. Dimensional analysis yields the following correlation:

$$t_{tr}(a^2/\nu)^{1/3} = fcn[D(a/\nu^2)^{1/3}], \text{ or } T^* = fcn(D^*) \qquad (5)$$

Alternately, one could look at more traditional parameters: 1) Szymanski's time $t^* = \nu t/R^2$ from equation (2); 2) an alternate dimensionless time, (at^2_{tr}/D); 3) a local Reynolds number, Re_δ or Re_θ; 4) pipe Reynolds number Re_D; or 5) a "relaminarization" type grouping which used local rather than convective acceleration:

$$K_a = \frac{\nu a}{V^3} \qquad (6)$$

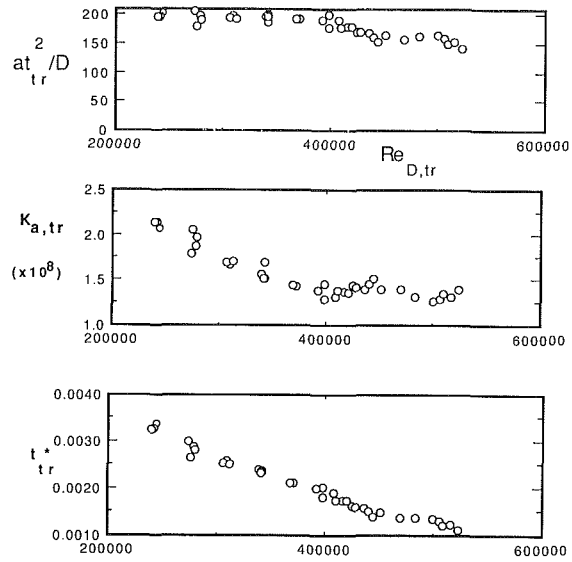

Fig. 8 Alternate presentations of the transition data. (Uncertainty in $at^2/D = \pm 3$ percent, in $K_a = \pm 5$ percent, in $t^* = \pm 2$ percent, in $Re_D = \pm 1.1$ percent)

Since $V = at$ for this case, these alternate parameters are not independent but rather are directly related to T^* and D^* from equation (5), as follows:

$$t^* = 4T^*/D^* \quad at^2/D = T^{*2}/D^* \quad Re_\delta = 2.9T^{*-3/2}$$
$$Re_\theta = 0.35T^{*-3/2} \quad Re_D = T^*D^* \quad K_a = T^{*-3}$$

Although equation (5) should be a satisfactory correlation—and is the best formulation in the writers' opinion—these alternate correlations will also be presented because of their familiarity and relevance to related transition problems. Note that K_a in the present experiment is a stronger parameter than K in relaminarization studies, since K_a is directly related to the boundary layer thicknesses.

Results

The experimental data consist of 37 values of transition time t_{tr} and mean velocity V_{tr} for accelerations a varying from 1.85 to 11.8 m/s^2. All other parameters can be computed using the known viscosity of water.

Figure 6 shows the measured values of transition Reynolds number Re_D which rises from 2.4 E5 to 5.2 E5, or two orders of magnitude higher than for steady flow, as acceleration increases.

Figure 7 shows the data plotted in the form of equation (5), which is the central result of this study. Thus dimensionless transition time T^* is almost constant, with a mean value of 404 and a standard deviation of 20. The vertical scale has been expanded to show a gradual increase with D^*. The increase is so small that we conclude that, for this range of accelerations, transition time is proportional to $(\nu/a^2)^{1/3}$, independent of the pipe diameter. This agrees with the observation that the boundary layer thickness at transition is much less than the pipe radius.

Figure 8 gives three alternate presentations of the data. In the top graph, (at^2_{tr}/D) is nearly constant, implying that transition time is approximately proportional to D/V_{tr}. One might conclude that the measured accelerations are "low" in the sense that transition is probably due not to inertial or acceleration effects but rather to the instability of the instantaneous velocity profiles.

The middle graph of Fig. 8 shows that K_a at transition is not constant but decreases gradually toward an asymptotic value

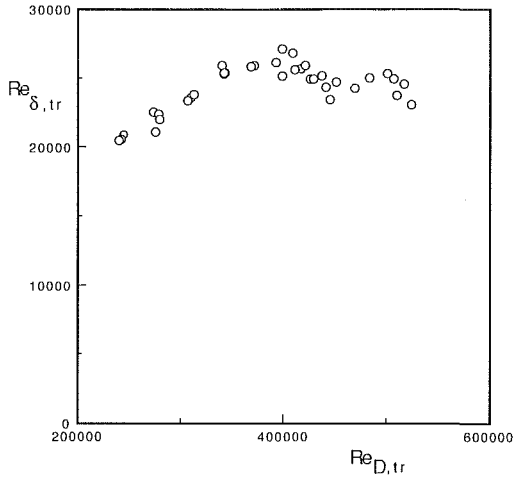

Fig. 9 The boundary layer thickness Reynolds number at transition (Uncertainty in $Re_\delta = \pm 10$ percent, in $Re_D = \pm 1.1$ percent)

of 1.2 E-8. This low value reinforces the idea that transition is due to "quasi-steady" velocity profile instability.

The bottom graph in Fig. 8 shows transition values of the Szymanski variable t^*, which are not constant but decrease montonically with Re_D. This particular presentation is not nearly as effective as Fig. 7.

Finally, Fig. 9 shows the boundary layer thickness Reynolds number at transition, which is approximately constant at $Re_{\delta,tr} \approx 24{,}000 \pm 15$ percent. Since momentum thickness $\theta = 0.121\ \delta$ from equation (4), a proportional result holds for $Re_{\theta,tr} \approx 2900 \pm 15$ percent.

In the limit of zero acceleration, one expects a steady transition value $Re_{D,tr} \approx 2000$, or $Re_{\delta,tr} \approx 1000$. Thus, if Figure 9 were extended toward lower accelerations (lower Re_D), we would expect the transition values to continually decrease toward the steady-state. This is substantiated by the single data point of Van der Sande (1980) for $a \approx 0.27$ m/s^2, for which $Re_{D,tr} \approx 58{,}000$, $T^*_{tr} \approx 180$, and $Re_{\delta,tr} \approx 7000$. It is clear that further data are needed, for accelerations less than 2 m/s^2, to verify this trend.

Conclusions

Experiments in the NUSC Unsteady Flow Loop Facility have generated 37 data points for transition to turbulence of pipe flow started from rest with a constant acceleration. All tests used fresh water in a 5-cm diameter smooth pipe 30 m long, with programmed accelerations ranging from 1.85 to 11.8 m/s^2. Transition was global, occurring at nearly the same time on all instruments. The pipe transition Reynolds number varied from 2.4 E5 to 5.2 E5 and increased approximately as $a^{1/3}$.

A transition-time correlation using the Szymanski variable t^* shows that t^*_{tr} decreases from 0.0032 to 0.00105 as Reynolds number increases.

Alternate correlations show that the parameters T^*, Re_δ, at^2/D, and K_a are all approximately constant at transition, with the recommended values

$$T^*_{tr} \approx 400 \pm 10\% \qquad Re_{\delta,tr} \approx 24000 \pm 15\%$$
$$at^2_{tr}/D \approx 180 \pm 20\% \qquad K_{a,tr} \approx 1.5\ E-8 \pm 35\%$$

These results imply that transition time is nearly independent of pipe diameter, but further experiments with different pipe sizes are needed to verify this hypothesis.

The results are not valid for a nonconstant acceleration, since V will no longer be proportional to a. It is recommended that experiments be performed with nonlinear transients $V(t)$ to study the transition process under more general conditions.

It is conjectured, on the basis of the steady-flow limit and a single result of Van der Sande (1980), that T^*_{tr} will decrease significantly as the acceleration drops below the lowest measured value of 1.85 m/s^2. Further experiments are needed in this range. Finally, extension of the theory of laminar-shear-flow instability to a constant-acceleration flow would be most welcome.

Acknowledgment

This project was supported by the Independent Research Program at the Naval Underwater Systems Center (NUSC), Newport, Rhode Island. The authors extend special appreciation to K. M. LaPointe of NUSC for his extensive assistance in each phase of the testing program.

References

Jones, W. P., and Launder, B. E., 1972, "Some Properties of Sink-Flow Turbulent Layers," *J. Fluid Mech.*, Vol. 56, Part 2, pp. 337–351.

Kataoko, K., Kawabata, T., and Miki, K., 1975, "The Start-up Response of Pipe Flow to a Step Change in Flow Rate," *J. Chem. Eng. Japan*, Vol. 8, No. 4, pp. 266–271.

Lefebvre, P. J., 1986, "Design and Evaluation of NUSC's Flow Loop Facility," Technical Document 6512, NUSC, Newport, RI, May 1.

Lefebvre, P. J., and Durgin, W. W., 1986, "A Transient Electromagnetic Flowmeter," *Proc. ASME Symp. on Measuring and Metering of Unsteady Flows*, Winter Annual Meeting, Anaheim, CA, pp. 7–10.

Leutheusser, H. J., and Lan, K. W., 1977, "Laminar-to-Turbulent Transition in Accelerated Motion," *Proc. 17th Cong. IAHR*, part A118, pp. 343–350.

Moss, E. A., 1989, The Identification of Two Distinct Laminar to Turbulent Transition Modes in Pipe Flows Accelerated from Rest," *Experiments in Fluids*, Vol. 7, pp. 271–274.

Narasimha, R., and Sreenivasan, K. R., 1973, "Relaminarization in Highly Accelerated Turbulent Boundary Layers," *J. Fluid Mech.*, Vol. 61, Part 3, pp. 417–447.

Narasimha, R., and Sreenivasan, K. R., 1979, "Relaminarization of Fluid Flows," *Advances in Applied Mechanics*, Vol. 19, pp. 221–309.

Ramaprian, B. R., 1984, "A Review of Experiments in Periodic Turbulent Pipe Flow," *Proc. ASME Symp. on Unsteady Turbulent Boundary Layers and Friction*, FED Vol. 12, Winter Annual Meeting, New Orleans, LA. pp. 1–16.

Sreenivasan, K. R., 1982, "Laminarescent, Relaminarizing, and Retransitional Flows," *Acta Mechanica*, Vol. 44, pp. 1–48.

Stettler, J. C., and Hussain, A. K. M. F., 1984, "On Transition of Pulsatile Pipe Flow," preprint paper, *IUTAM Symp. on Laminar-Turbulent Transition*, Novosibirsk, USSR, July 9–13.

Szymanski, P., 1932, "Some Exact Solutions of the Hydrodynamic Equations of a Viscous Fluid in the Case of a Cylindrical Tube," *J. Math. Pure et* Appliquées, Vol. 11, pp. 67–107.

Van der Sande, E., 1980, "Velocity Profiles in Accelerating Pipe Flows Starting from Rest," *Proc. 3rd Int. Conf. on Pressure Surges*, Canterbury, England, pp 1–14.

Warriner, D. K., and Pearson, J. T., 1984, "Laminarization Effects on the Dynamics of a Disk Levitated by Incompressible Fluid Flow," *Proc. ASME Symp. on Laminar-Turbulent Boundary Layers*, FED Vol. 11, New Orleans, LA, pp. 125–138.

M. H. Hamdan*
Graduate Student.

R. M. Barron
Professor, Director of FDRI.

Department of Mathematics & Statistics, and
Fluid Dynamics Research Institute,
University of Windsor,
Windsor, Ontario, Canada N9B 3P4

Shear-Driven Flow in a Porous Cavity

The shear-driven cavity flow is studied when the cavity is assumed to contain a porous material. A finite difference solution is obtained for the flow in a rectangular cavity for various cavity aspect ratios and permeability values. The effect of these parameters on the flow, and in particular on the development of corner eddies is illustrated.

1 Introduction

The shear-driven cavity flow has been the subject of numerous analytical and experimental investigations. The cavity model has usually been considered to study the effect of Reynolds number, Re, on the structure of the flow, the streamlines and the regions of viscous separation (cf. [1, 2, 3, 4]). It serves as a benchmark problem in the study of separated flows and the study of flows with closed streamlines as well as a means of testing numerical techniques and computational procedures used to obtain solutions to the full Navier-Stokes equations.

Of particular interest in the present study is the flow in a rectangular cavity when the enclosed domain is composed of a saturated porous medium. Depending on the type of the porous media and the flow considered, the differential equations governing fluid flow through porous media are the macroscopic equation of continuity and the macroscopic momentum equations, which are usually classified into two groups: momentum equations based on Darcy's law, which governs the fluid flow of the seepage type, and momentum equations that take into account the non-Darcian effects of inertia and/or viscous shear. In this second group is the well-known Brinkman's equation which accounts for the viscous shear effects. The mathematical form of these equations is discussed in section 2.

In the current work we consider the single phase flow through a saturated porous domain in the shape of a rectangular cavity consisting of three rigid walls while the top wall generates the fluid motion through a sliding motion in its own plane with a constant velocity. The cavity model is employed to determine and illustrate the regions of viscous separation in porous media and to study the effect of permeability on this separation. The effect of the cavity aspect ratio, ϵ = depth/width, on the flow characteristics is also illustrated. The idea of viscous separation in porous media may have direct impact on many physical applications, such as in the study of groundwater flow and in reservoir simulation. In this context, viscous separation hinders the main flow and results in an entrapment of some of the fluid which, therefore, remains unrecoverable. The numerical results obtained in this study illustrate that viscous separation in the medium considered occurs for relatively high permeability and thus it is postulated that when the flow is of the seepage type and is governed by Darcy's law, viscous separation might not occur.

Although the model considered does not take into account the effect of porous cavity walls, variations to this model might include the cases where the cavity inner domain is either porous or nonporous while the moving wall of the cavity is porous. Another alternative is to replace the moving wall with a porous, stationary wall with the flow generated in the cavity by an outer flow. This latter case is of particular importance in the study and design of porous airfoils and has been employed by Chen [5] in an attempt to reduce the shock wave drag.

The usual cavity slow flow when $\mathrm{Re}=0$ is well understood, and has been considered by many investigators (cf. Pan and Acrivos [3], Burgraff [2]). The viscous separation regions have been well defined and proven to be symmetric for all cavity aspect ratios considered [3]. The slower flow in a porous cavity is also symmetric with corner eddies which occupy smaller regions that diminish with lowering permeability.

2 Governing Equations

We consider the steady flow of an incompressible viscous fluid in a stationary and isotropic porous medium having constant permeability.

When the flow is of the seepage type, the equations governing the motion are given by the macroscopic equation of continuity and the momentum equations which take the form of Darcy's law, namely

continuity equation:

$$\nabla \cdot \mathbf{u} = 0 \tag{1}$$

momentum equations:

$$\mathbf{u} = -\frac{k}{\mu}\nabla p \tag{2}$$

where $\mathbf{u}$ is the Darcy velocity vector, p is the interstitial pressure, μ is the coefficient of viscosity, and k is the permeability.

Equation (2) represents Darcy's law in the absence of body forces. As implied by this equation, the type of flow considered is essentially irrotational and the viscous shearing action is seen to be negligible while the viscous damping effects (Darcy resistance) due to the porous matrix are retained. In

*Current Address: Assistant Professor, Department of Mathematics and Computer Science, Mount Allison University, Sackville, New Brunswick, Canada.

Contributed by the Fluids Engineering Division for publication in the JOURNAL OF FLUIDS ENGINEERING. Manuscript received by the Fluids Engineering Division March 20, 1988.

many physical applications, where the velocity ceases to be of the seepage type, viscous shear stresses which act on the fluid elements have to be accounted for and thus equation (2) has to be modified to better describe the flow phenomena and to account for the higher permeability associated with the flow. An equation that takes care of the above is that due to Brinkman [6]

$$\nabla p + \frac{\mu}{k}\mathbf{u} = \mu^* \nabla^2 \mathbf{u} \tag{3}$$

where μ^* is the effective viscosity of the fluid saturating the porous medium and μ is the viscosity of the fluid. These viscosity coefficients are, in general, different [7]. In this study we consider the ratio μ/μ^* to be arbitrary, but constant.

It should be noted that for large values of permeability, k, equation (3) reduces to the steady Navier-Stokes equations, in the absence of inertia, and reduces to Darcy's law, equation (2), for small values of k. It is thus expected that for small values of k the vorticity associated with the Brinkman-type flow will be small, since the Darcy flow is vorticity-free due to the potential nature of Darcy's law. In this context the Darcy flow regime can be recovered from that of Brinkman.

Considering the flow to be two-dimensional, eliminating the pressure from equation (3) and employing the continuity equation (1) yields the following streamfunction-vorticity formulation for the flow governed by Brinkman's model:

$$\frac{\partial^2 \xi}{\partial x^2} + \frac{\partial^2 \xi}{\partial y^2} = \frac{\beta}{k}\xi \tag{4}$$

$$\frac{\partial^2 \psi}{\partial x^2} + \frac{\partial^2 \psi}{\partial y^2} = -\xi \tag{5}$$

where ξ is the macroscopic vorticity, ψ is the macroscopic streamfunction and $\beta = \mu/\mu^*$.

The macroscopic streamfunction is defined in terms of the macroscopic velocity components by

$$u = \frac{\partial \psi}{\partial y}, \quad v = -\frac{\partial \psi}{\partial x} \tag{6}$$

where the macroscopic velocity components u and v are the horizontal and vertical components, respectively.

The solution to a specific boundary value problem can be obtained for $\psi(x,y)$ and $\xi(x,y)$ by solving equations (4) and (5). The velocity components can then be obtained through equation (6) and the pressure $p(x,y)$ can be obtained from the Laplace equation

$$\nabla^2 p = 0. \tag{7}$$

This equation is obtained by taking the divergence of equation (3) and employing equation (1), and is consistent with the work of Ooms et al. [8].

Although the Laplace equation for pressure governs the Darcy pressure, it is not surprising that the same type of pressure equation governs the Brinkman pressure in light of the fact that the two models overlap for small values of permeability. For larger permeability, the difference between the Darcy and Brinkman pressure is in the pressure boundary conditions and in the definition of the pressure gradients. As can be seen from equations (2) and (3), the Brinkman pressure gradients reduce to Darcy pressure gradients for small values of k.

3 The Cavity Model

The above streamfunction-vorticity formulation is used to study the steady rotational flow of a viscous incompressible fluid through the chosen type of porous medium in a rectangular cavity. Such motion is assumed to be generated by the steady sliding motion of the top wall of the cavity in its own plane with a constant velocity V_0 [2]. The cavity walls are assumed to be nonporous while the flow domain is assumed to consist of a porous material. The dimensionless form of the vorticity-streamfunction formulation is thus given by

$$\frac{\partial^2 \Omega}{\partial X^2} + \frac{\partial^2 \Omega}{\partial Y^2} = \frac{\beta}{K}\Omega \tag{8}$$

$$\frac{\partial^2 \Psi}{\partial X^2} + \frac{\partial^2 \Psi}{\partial Y^2} = -\Omega \tag{9}$$

and the dimensionless streamfunction is defined in terms of the dimensionless velocity components by

$$U = \frac{\partial \Psi}{\partial Y}, \quad V = -\frac{\partial \Psi}{\partial X}. \tag{10}$$

The above equations have been rendered dimensionless with respect to the cavity width L, and the moving wall velocity V_0, by using the following dimensionless variables:

$$X = x/L,\ Y = y/L,\ K = k/L^2,\ \Psi = \psi/V_0 L,\ \Omega = \xi L/V_0,$$
$$U = u/V_0, \text{ and } V = v/V_0.$$

The boundary conditions associated with the cavity and the flow considered are those given by [2], [3], and are expressed as

$$U = V = \Psi = \frac{\partial \Psi}{\partial X} = 0,\ \Omega = -\frac{\partial^2 \Psi}{\partial X^2} \text{ for } X = 0,\ 1 \text{ and } 0 \le Y < \epsilon \tag{11}$$

$$U = V = \Psi = \frac{\partial \Psi}{\partial Y} = 0,\ \Omega = -\frac{\partial^2 \Psi}{\partial Y^2} \text{ for } Y = 0 \text{ and } 0 \le X \le 1 \tag{12}$$

$$V = \Psi = 0 \text{ and } U = \frac{\partial \Psi}{\partial Y} = -1,\ \Omega = -\frac{\partial^2 \Psi}{\partial Y^2} \text{ for } Y = \epsilon \text{ and } 0 < X < 1 \tag{13}$$

where $\epsilon = \text{depth}/L$ is the cavity aspect ratio.

By contrast, the flow in a rectangular cavity at zero Reynolds number is governed by the coupled set of microscopic stream-function-vorticity equations

$$\frac{\partial^2 \Omega}{\partial X^2} + \frac{\partial^2 \Omega}{\partial Y^2} = \mathrm{Re}\left[\frac{\partial \Psi}{\partial Y}\frac{\partial \Omega}{\partial X} - \frac{\partial \Psi}{\partial X}\frac{\partial \Omega}{\partial Y}\right] = 0, \tag{14}$$

$$\frac{\partial^2 \Psi}{\partial X^2} + \frac{\partial^2 \Psi}{\partial Y^2} = -\Omega \tag{15}$$

where the Reynolds number is defined in terms of the moving

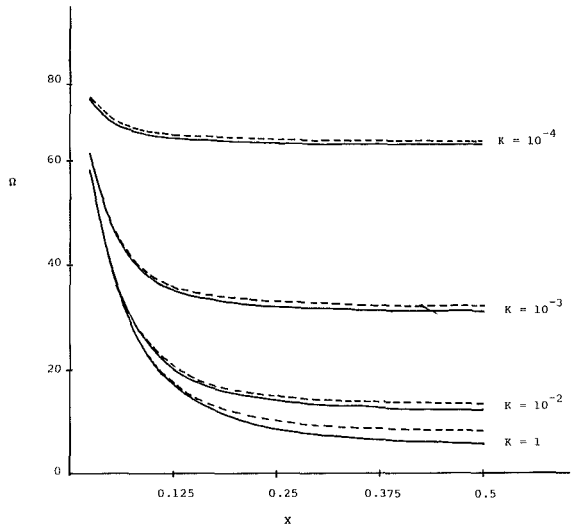

Fig. 1 Vorticity along the moving wall
— ϵ = 1.0, 1.5, 2.0
---- ϵ = 0.5

wall velocity V_0, the cavity width L, and the fluid viscosity μ^*, as $\mathrm{Re} = \rho L V_0 / \mu^*$.

The coupled equations (8) and (9) subject to the boundary conditions (11), (12), and (13) are approximated by central differences, using a uniform grid, and expressed in terms of tridiagonal matrices which are then inverted using the well-known tridiagonal solver (Thomas algorithm). The solution is iterated using the successive line over-relaxation (SLOR) scheme. It is worthwhile noting that the resulting matrices are diagonally dominant and the term β/K, in equation (8), enhances this diagonal dominance. The number of grid points used in the computation was adjusted as the aspect ratio varied so as to maintain step sizes of $\Delta X = \Delta Y = 0.025$. This choice of step sizes proved to be sufficient to illustrate the presence of secondary eddies. It should be noted that for the flow considered, step sizes $\Delta X = \Delta Y = 0.05$ also indicated the presence of secondary eddies but resulted in $\Psi = 0.09923$ at the vortex center, in the case of $\mathrm{Re} = 0$ and aspect ratio $\epsilon = 1$. The finer grid was thus adopted since it results in a streamfunction value at the vortex center that is closer to the value reported by Pan and Acrivos [3]. After a converged solution for Ψ and Ω is obtained, the velocity components are calculated using equation (10). Convergence is defined in terms of the following criterion:

$$|F_{i,j}^{n+1} - F_{i,j}^{n}| < 5 \times 10^{-5} \tag{16}$$

where n is the iteration level and $F_{i,j}$ stands for either $\Omega_{i,j}$, with (i,j) being the grid points in the flow domain and on the boundary, or $\Psi_{i,j}$, with (i,j) being the grid points in the flow domain.

For the sake of comparison, equations (14) and (15) were also solved by a similar method.

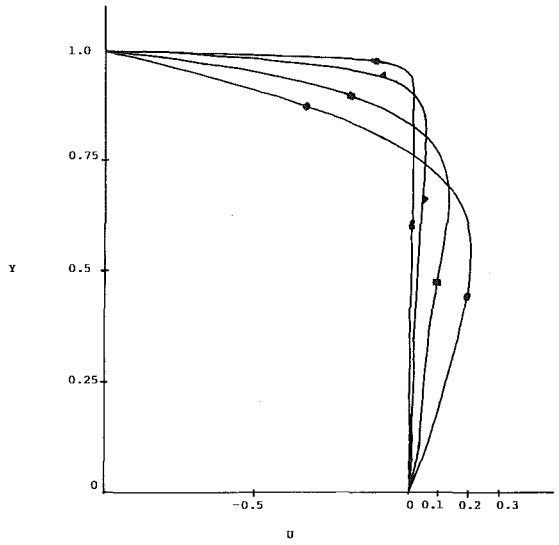

Fig. 2(a) Horizontal velocity component along vertical centerline of the cavity. $\epsilon = 1$, different permeability
- $K = 1$
- $K = 0.01$
- $K = 0.001$
- $K = 0.0001$

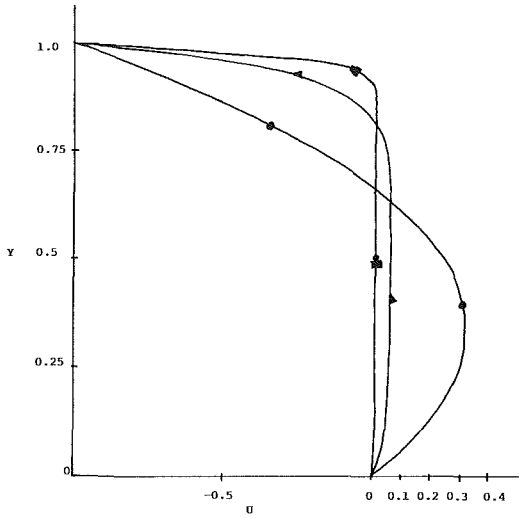

Fig. 2(b) Horizontal velocity component along vertical centerline of the cavity. $\epsilon = 0.5$ different K.
- $K = 1$
- $K = 0.001$
- $K = 0.0001$

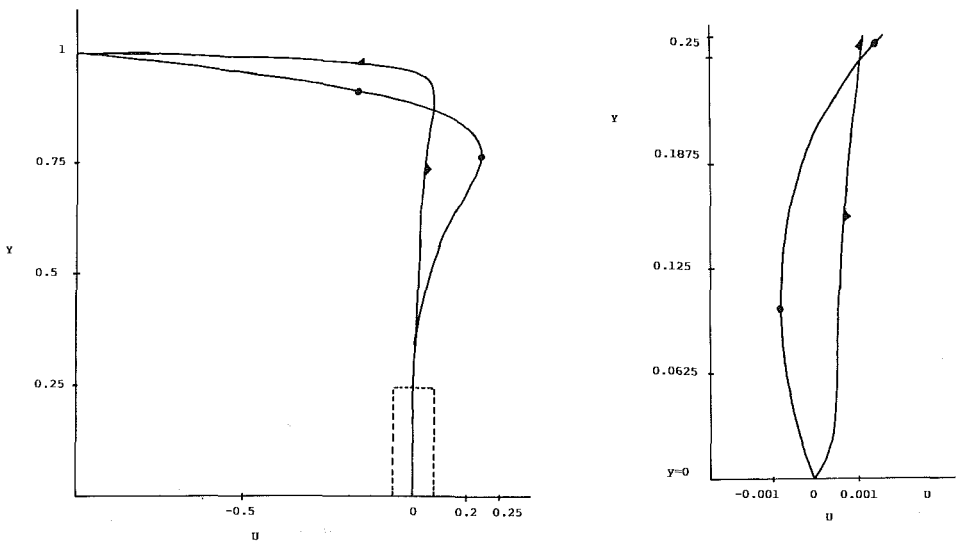

Fig. 2(c) Horizontal velocity components along vertical centerline of the cavity. $\epsilon = 2$, different K.
- $K = 1$
- $K = 0.001$

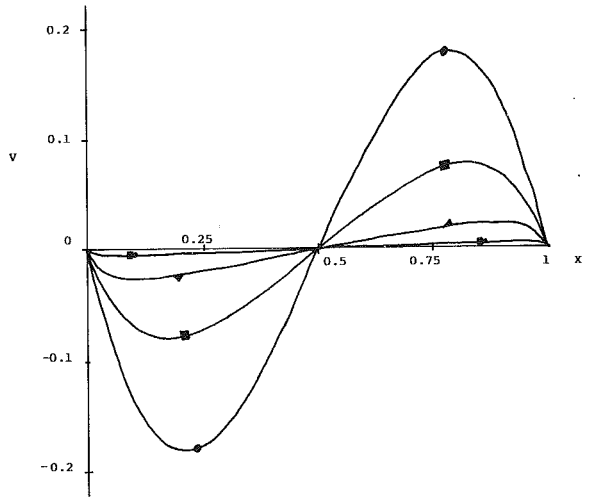

Fig. 3(*a*) Vertical velocity component along horizontal centerline of the cavity. $\epsilon = 1$, different K.
- $K = 1$
- $K = 0.01$
- $K = 0.001$
- $K = 0.0001$

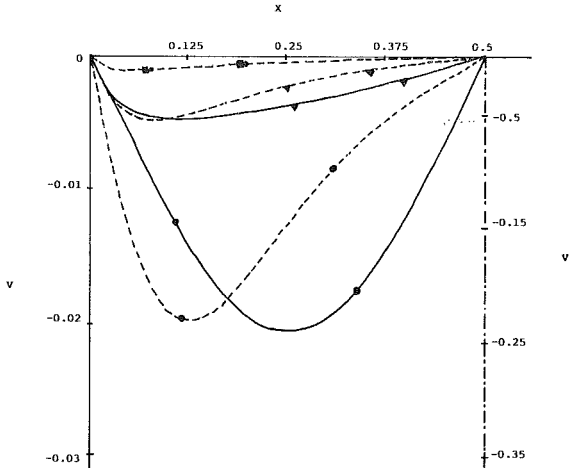

Fig. 3(*b*) Vertical velocity component along horizontal centerline of the cavity. $\epsilon = 0.5$, 2, different K.
- ---- $\epsilon = 0.5$
- — $\epsilon = 2$
- $K = 1$
- $K = 0.001$
- $K = 0.0001$

4 Results and Discussion

Without loss of generality, and for simplicity, the following discussion is based on the case of $\beta = 1$. Runs were made for the dimensionless permeability values $K = 10^{-4}$, 10^{-3}, 10^{-2}, and 1, and for cavity aspect ratios $\epsilon = 0.5$, 1, 1.5, and 2. Results are also obtained for the case of $\mathrm{Re} = 0$ to illustrate and emphasize the similarity with the results of $K = 1$. It is understood that when K approaches unity, the dimensional permeability approaches L^2 and the medium approaches the state of full conductivity, and thus the flow tends to the creeping flow at $\mathrm{Re} = 0$, provided that $L^2 \gg \delta^2$ where δ is the dimension of a repeating unit of the solid matrix.

4.1 Vorticity. Vorticity values along the moving wall are illustrated in Fig. 1 which, due to symmetry, is presented only for $0 < X \leq 0.5$. The increase in vorticity with decreasing permeability is clear and is due to the movement of the primary vortex center closer to the moving wall as the permeability decreases. For aspect ratios greater or equal to unity it is found that for a given permeability the numerical vorticity values at the moving wall do not change to within five decimal places. When $\epsilon = 0.5$, Fig. 1 also indicates the decrease in vorticity with increasing permeability and, for a given permeability, the increase in moving wall vorticity as ϵ is decreased. This is attributed to the higher velocity associated with the decrease in aspect ratio.

4.2 Velocity Profiles. Figures 2(*a*, *b*, *c*) present the profiles of the horizontal component of velocity along the vertical centerline of the cavity for different aspect ratios. All of these figures illustrate the reduction of the horizontal velocity component with decreasing permeability. At the lowest permeability the horizontal component of velocity along the vertical centerline is almost constant for the major part of the cavity height, for all aspect ratios, and is expected to reach a constant value, for each aspect ratio, with a further decrease in permeability.

The vertical velocity component along the horizontal centerline of the cavity is illustrated for different aspect ratios and different permeabilities in Figs. 3(*a*, *b*) and indicates the increase of this component with increasing permeability, for a given ϵ, and the decrease in this component with increasing ϵ.

4.3 Flow Development. The flow development for given aspect ratios and different permeability values is illustrated in Figs. 4(*a*, *b*, *c*, *d*).

As can be seen in Fig. 4(*a*), when $\epsilon = 1$ the streamlines tend to be closer to the upper wall as permeability is decreased. The secondary eddies for $\epsilon = 1$ are also shown in Fig. 4(*a*) to illustrate their presence for $K = 1$ and $K = 0.01$ and to compare them with the secondary eddies for $\mathrm{Re} = 0$. For lower permeability the secondary eddies did not appear. This could be attributed to the fact that either the flow is approaching the Darcy's flow where viscous separation does not occur or the computational grid is not fine enough. As the aspect ratio is decreased, the streamlines for lower permeability tend to span larger areas, as shown in Fig. 4(*b*). For all permeability values the streamlines tend to be flat and parallel to the lower and upper cavity walls over mid-portion of the cavity. The secondary eddies in this case have appeared for the low permeability value of 0.001, but not for $K = 0.0001$. For aspect ratios higher than unity, Figs. 4(*c*) and 4(*d*) illustrate the symmetric flow patterns for $\epsilon = 1.5$ and 2, respectively, which resemble, in the primary vortex region, the case of $\epsilon = 1$ for different permeability values. For $K = 1$, Fig. 4(*a*) illustrates the superposition of some of the primary streamlines for $\epsilon = 2$ on the corresponding streamlines for $\epsilon = 1$ to demonstrate the resemblance of the primary flow pattern. The secondary eddies for these aspect ratios of 1.5 and 2 are illustrated in Figs. 4(*c*) and 4(*d*), respectively, where these eddies were detected for $K = 1$, but not below this value. At this value of K the secondary eddies increase in size with increasing aspect ratio and at $\epsilon = 2$ a complete secondary vortex is formed.

4.4 Primary Vortex. As is well-known in the case of creeping flow, the flow pattern is symmetric with the vortex center occurring along the vertical centerline of the cavity at around three quarters of the cavity height, when $\epsilon = 1$. When the flow changes from slow to slower, as the medium permeability decreases, the location of the vortex center stays along the vertical centerline of the cavity but is seen to move towards the upper cavity wall, as illustrated in Table 1, for all aspect ratios tested. The value of the maximum streamfunction is found to decrease with decreasing permeability. This is accompanied by a decrease in the vorticity values, at the primary vortex center, for all aspect ratios. When the permeability is taken to be 10^{-4}, Table 1 shows that the

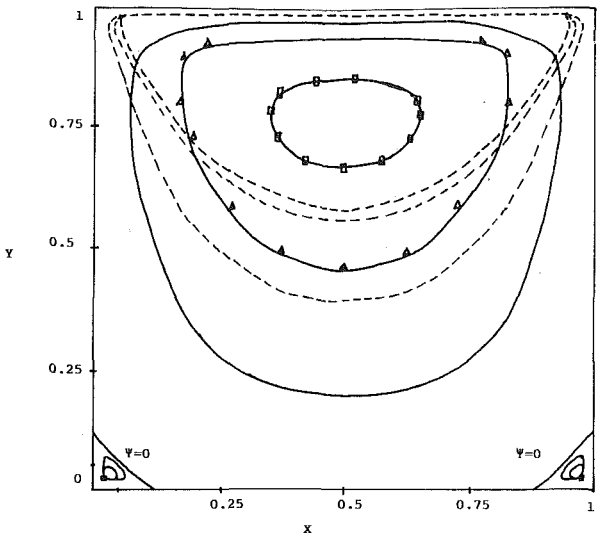

Fig. 4(*a*) Flow pattern for $\epsilon = 1$, different K and $\epsilon = 2$, $K = 1$.
Primary vortex:

----- $K = 0.001$, $\epsilon = 1$ } Inner streamline: $\Psi = 0.01$; Middle streamline: $\Psi = 0.009$; Outer streamline: $\Psi = 0.005$

— $K = 1$, $\epsilon = 1$ } Inner streamline: $\Psi = 0.09$; Middle streamline: $\Psi = 0.05$; Outer streamline: $\Psi = 0.01$

■ ■ $\epsilon = 2$, $K = 1$ } $\Psi = 0.09$

▲ ▲ $\epsilon = 2$, $K = 1$ } $\Psi = 0.005$

Secondary Eddies:
■ $K = 0.01$, $\epsilon = 1$, $\Psi = -.31 \times 10^{-6}$
Inner Secondary Loop
$\Psi = -.4 \times 10^{-5}$, $Re = 0$, $\epsilon = 1$
$\Psi = -.38 \times 10^{-5}$, $K = 1$, $\epsilon = 1$
Outer Secondary Loop
$\Psi = -.24 \times 10^{-5}$, $Re = 0$, $\epsilon = 1$
$\Psi = -.23 \times 10^{-5}$, $K = 1$, $\epsilon = 1$

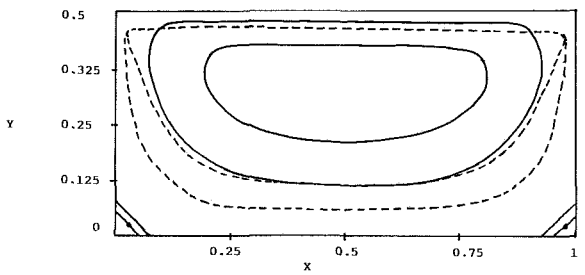

Fig. 4(*b*) Flow pattern for $\epsilon = 0.5$, different K.
Primary Vortex:
— $K = 1$; Inner streamline: $\Psi = 0.005$; Outer streamline: $\Psi = 0.002$
---- $K = 0.001$; Inner streamline: $\Psi = 0.005$; Outer streamline: $\Psi = 0.002$

Secondary Eddies:
● $\Psi = -.1 \times 10^{-5}$, $Re = 0$
$\Psi = -.98 \times 10^{-6}$, $K = 1$

— (outer): $\Psi = 0$, $K = 1$, $Re = 0$
— (inner): $\Psi = 0$, $K = 0.001$

streamfunction at the vortex center approaches the same constant value for all aspect ratios. In this case the vorticity values for different aspect ratios approach each other. This indicates that with a further reduction in the permeability the Brinkman's flow regime approaches that of Darcy's, and thus

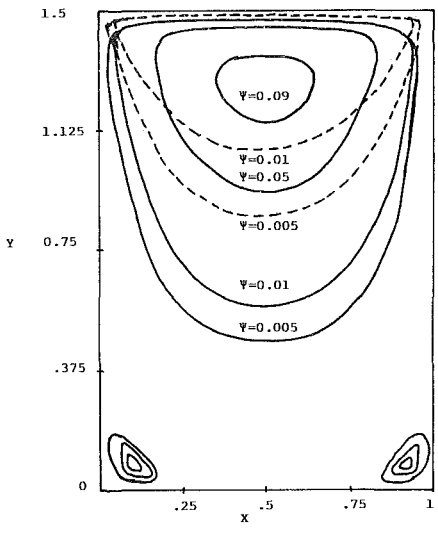

Fig. 4(*c*) Flow pattern for $\epsilon = 1.5$, different K.
Primary:
— $K = 1$
---- $K = 0.001$
Secondary (for $K = 1$)
Outer loop: $\Psi = -.13 \times 10^{-5}$
Middle loop: $\Psi = -.23 \times 10^{-5}$
Inner loop: $\Psi = -.4 \times 10^{-5}$

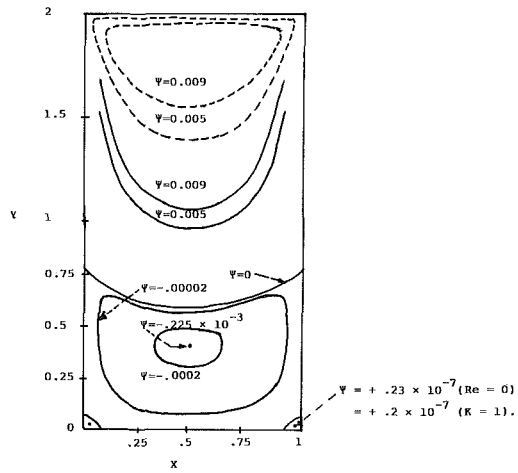

Fig. 4(*d*) Flow pattern for $\epsilon = 2$, different K.

— $K = 1$
---- $K = 0.001$

Table 1 Location (Y) and magnitude of largest Ψ. Ψ^*, Y^* indicate results of Pan and Acrivos [3]

	ϵ 0.5	1.0	1.5	2.0
Re = 0	$\Psi = 0.07278$	0.09982	0.10055	0.10055
	$\Psi^* = 0.073$	0.1	----	0.1
	$\Omega = 4.0341$	3.3307	3.3204	3.3206
	$Y = 0.325$	0.775	1.275	1.775
	$Y^* = 0.3372$	0.76	----	1.75
$K = 1$	$\Psi = 0.07243$	0.09887	0.09958	0.09958
	$\Omega = 4.0058$	3.2901	3.2801	3.28
	$Y = 0.325$	0.775	1.275	1.775
$K = 10^{-3}$	$\Psi = 0.02281$	0.02359	0.02362	0.02362
	$\Omega = 3.1313$	1.4303	1.4298	1.4298
	$Y = 0.425$	0.9	1.4	1.92
$K = 10^{-4}$	$\Psi = 0.00550$	0.00561	0.00561	0.00561
	$\Omega = 0.95999$	0.95757	0.95762	0.95767
	$Y = 0.45$	0.95	1.45	1.95

one expects the vorticity to diminish with a further decrease in permeability. When the permeability is 10^{-3} and higher, the values of streamfunction and vorticity essentially become independent of the aspect ratio $\epsilon \geq 1$, which is supportive of the argument that the creeping flow in the upper region of the cavity for aspect ratios greater that unity is similar to that when $\epsilon = 1$, [3]. Comparison of our results for $\mathrm{Re} = 0$ and the results of Pan and Acrivos [3] is given in Table 1 which indicates a slight discrepancy that may be due to the finer step size they employed.

5 Conclusions

The shear-driven flow in a rectangular porous cavity has been considered. Some of the key conclusions that describe the qualitative effects of lowering the permeability are as follows:

1 The primary vortex center is located along the vertical centerline of the cavity, and moves closer to the moving wall with decreasing permeability.

2 The decrease in permeability results in a reduction of the streamfunction value at the primary vortex center, and a decrease in vorticity there, for all aspect ratios tested.

3 Flow separation occurs in shallow cavities, $\epsilon < 1$, at high and intermediate permeabilities while for deep cavities, $\epsilon > 1$, the flow separation occurs at high values of permeability. In the case of square porous cavities secondary eddies develop for high values of permeability.

References

1 Benjamin, A. S., and Denny, V. E., "On the Convergence of Numerical Solutions for 2-D Flows in a Cavity at High Re," *J. Comput. Phys.*, Vol. 12, 1973, p. 348.

2 Burggraf, O. R., "Analytical and Numerical Studies of the Structure of Steady Separated Flows," *J. Fluid Mech.*, Vol. 24, Part 1, 1966, p. 113.

3 Pan, F., and Acrivos, A., "Steady Flows in Rectangular Cavities," *J. Fluid Mech.*, Vol. 28, Part 4, 1967, p. 643.

4 Schreiber, R., and Keller, H. B., "Driven Cavity Flows by Efficient Numerical Techniques," *J. Comput. Phys.*, Vol. 49, 1983, p. 310.

5 Chen, Chung-Lung, "Computation of Transonic Flow Over Porous Airfoils," Ph.D. dissertation, Dept. of Aerospace Engineering Sciences, Univ. of Colorado, 1986.

6 Brinkman, H. C., "A Calculation of the Viscous Force Exerted by a Flowing Fluid on a Dense Swarm of Particles," *Appl. Sci. Res.*, A1, 1947a, p. 27.

7 Williams, W. O., "Constitutive Equations for a Flow of an Incompressible Viscous Fluid Through a Porous Medium" *Quarterly of Appl. Mathematics*, Oct. 1978, p. 255.

8 Ooms, G., Mijnlieff, P. F., and Beckers, H. L., "Frictional Force Exerted by a Flowing Fluid on a Permeable Particle, with Particular Reference to Polymer Coils," *The Journal of Chem. Phys.*, Vol. 53, No. 11, 1970, p. 4123.

Transient Free Surface Shape in an Abruptly Rotating, Partially Filled Cylinder

Sangmin Choi
School of Mechanical Engineering,
Korea Institute of Technology,
Taejon, Korea

Jae Won Kim

Jae Min Hyun
Mem. ASME.

Department of Mechanical Engineering,
Korea Advanced Inst. Science
& Technology,
Seoul, Korea

An experimental investigation has been made to depict the transient free surface shape in spin-up from rest of a liquid in a partially filled cylinder. The rotational Reynolds number is large and the cylinder aspect ratio is 0(1). The experiments have been designed to validate the analytical model due to Homicz and Gerber, which is an extension of the model of Wedemeyer, Goller, and Ranov. An outline of this analytical model is given. The experimental setup and techniques are briefly described. The main emphasis is placed on presenting the experimental data of the free surface shape when the steady-state free surface intersects one or both of the endwall disks. The analytical predictions of the free surface shape are found to be in satisfactory agreement with the experimental measurements for all the possible free surface configurations. These explicit comparisons establish the practical usefulness of the analytical model; the model is capable of predicting the transient free surface shape during the spin-up phase of a liquid.

1 Introduction

Consider an axisymmetric closed container that is filled with a liquid. When the container impulsively starts rotating about its central axis from the motionless initial state, the subsequent transient flow of the liquid is termed "spin-up from rest" (Greenspan and Howard, 1963; Wedemeyer, 1964). This internal flow constitutes a problem of fundamental interest in unsteady rotating fluid dynamics. A proper understanding of this flow is essential to the stability analysis of liquid-filled projectiles and spin-stabilized liquid propellant rockets (Homicz and Gerber, 1987).

Modern studies of spin-up began with the classical paper by Greenspan and Howard (1963). They performed a linearized analysis of spin-up of a liquid in a circular cylinder. As is the case for the majority of applications, we take the characteristic rotational Reynolds number $\mathrm{Re} = \Omega R^2/\nu$ being large. Here, Ω is the angular frequency of the rotating container, R the radius of the container, and ν the kinematic viscosity of the fluid. Greenspan and Howard clearly established that the meridional flows are set up by the action of the pumping mechanism of the Ekman layers formed on the endwall disks. Therefore, the interior core substantially attains the solid-body rotation on a convective time scale $t_s = (H/R)\mathrm{Re}^{1/2}\,\Omega^{-1}$, which is an order of magnitude smaller than the diffusive time scale $t_D = \mathrm{Re}\Omega^{-1}$. Here, H denotes the height of the cylinder.

An elegant model was proposed by Wedemeyer (1964) to tackle the strongly nonlinear spin-up from rest. The major dynamic ingredients of Wedemeyer's model represented extensions of the basic model due to Greenspan and Howard (1963). The vital role of the Ekman layer pumping mechanism was recognized; several physically sound assumptions were taken, which yielded a simplified partial differential equation to describe the dominant azimuthal flow field. The results of Wedemeyer's model have been shown to depict the gross characteristic features of the flow evolution (e.g., see Watkins and Hussey, 1977). The significance of the meridional circulation was brought into focus in this model, and it was made possible to predict that the global flow achieved the steady state on a time scale t_s. The nonlinear model due to Wedemeyer (1964) has since occupied the center piece of analytical approaches in spin-up from rest. This model has been the subject of extensive verifications by laboratory experiments (Watkins and Hussey, 1977) and numerical simulations (Kitchens, 1980b, Hyun et al., 1983). Amplifications and modifications to this model have also been attempted (Weidman, 1976).

The aforementioned works are concerned with the case when the liquid completely fills the closed cylinder. A question naturally arises as to the process of spin-up from rest in a partially filled cylinder, i.e., a fluid system with a free surface. In certain situations of practical interest, the liquid fills only a part of the container. For these fluid systems, the positions of vents and inlets should be carefully designed to prevent spilling or obstruction of flow during the spin-up phase.

The above considerations warrant an accurate description of the transient shape of free surface during spin-up. Goller and Ranov (1968) developed a simplified computing scheme mainly based on the Wedemeyer model, which could account for the presence of a free surface. They incorporated a number of heuristically plausible assumptions in the numerical procedures to compute the transient shape of free surface. They subsequently presented the computed results for the free surface; these were found to be in good agreement with their

Contributed by the Fluids Engineering Division for publication in the JOURNAL OF FLUIDS ENGINEERING. Manuscript received by the Fluids Engineering Division May 17, 1988.

laboratory measurements. However, the model of Goller and Ranov was restricted to the cases when the free surface did not intersect either of the endwall disks. As succinctly portrayed by Gerber (1975), at a high angular frequency Ω, the free surface intersects one or both of the endwall disks, depending on the fill ratio and the cylinder aspect ratio.

Recently, Homicz and Gerber (1986) further refined the model due to Goller and Ranov (1968) in order to compute the free surface shape when the free surface intersects one or both of the endwall disks. Relying on physical insight, Homicz and Gerber (1986, 1987) invoked several assumptions which would lead to predicting the free surface shape with a modest amount of computing efforts. Numerical results were presented for the predicted free surface shapes; however, these results have not been validated in a quantitative sense. As remarked by Homicz and Gerber, due to the lack of laboratory experimental data in the literature, it has not been possible to verify their numerical solutions. The present paper addresses this point. We have carried out comprehensive and systematic laboratory experiments to describe the free surface shape in spin-up from rest. The purpose of this paper is to demonstrate the comparisons between the predicted results of the previous models (Goller and Ranov, 1968; Homicz and Gerber, 1986, 1987) and the measurement data of the transient free surface shape. Emphasis will be placed on the cases when the free surface intersects one or both of the endwall disks.

2 The Analytical Model

For the sake of completeness of the presentation, we shall briefly review the highlights of the analytical model due to Goller and Ranov (1968), and Homicz and Gerber (1986). The details are elaborated in the above publications.

At the initial state of rest, the liquid level is L. We shall adopt the cylindrical frame (r, θ, z) with corresponding velocity components (u, v, w). At $t = 0$, the cylindrical container abruptly begins to rotate about the central axis. For the situations of large Re $[= \Omega R^2/\nu]$, it has been well established that the "columnar" flow approximation is valid in the bulk of the interior region, i.e., u, v and the pressure p are functions of r and t only. Consequently, a simplified version of the momentum equation having v as the main unknown variable is obtained.

$$\frac{\partial V}{\partial t} + u\left(\frac{\partial V}{\partial r} + \frac{V}{r}\right) = \mathrm{Re}^{-1}\left(\frac{\partial^2 V}{\partial r^2} + \frac{\partial}{\partial r}\left(\frac{V}{r}\right)\right). \quad (1)$$

The above equation has been expressed in nondimensional form. The velocity components were made dimensionless by using ΩR, the time by Ω^{-1}, and the radial distance r was nondimensionalized by R.

In order to close the above system, the key step is to secure a functional relationship $u = f(v,r)$. Homicz and Gerber (1986) assumed that the radial motion in the core was made up by the contributions from the top and bottom Ekman layers and the free surface motion. For convenience, these can be written as

$$u = u_{\mathrm{TEL}} + u_{\mathrm{BEL}} + u_{\mathrm{FS}}, \quad (2)$$

in which u_{TEL} and u_{BEL} denote the contributions from the top and bottom Ekman layers and u_{FS} represents the contribution from the free surface. The crux of the model development by Homicz and Gerber (1986) is that, by incorporating intuitively satisfying physical assumptions, u_{TEL} and u_{BEL} can, respectively, be expressed as functions of v and r. Care has been taken to distinguish the various stages of the free surface shape, i.e., whether the free surface intersects neither, one or both of the endwall disks. The treatment of u_{FS} is essentially the same as that used in Goller and Ranov (1968). The idea is that, for the free surface motion, the flux across a radial surface at a given radial location should be balanced by the fluid volume change between the axis and that radial location.

As to u_{TEL} and u_{BEL} in equation (2), a slightly amended form of the classical results by Wedemeyer (1964) was utilized. The evaluation of the radial velocity component in the interior generated by the Ekman layer pumping mechanism has been well documented (Wedemeyer, 1964, Kitchens, 1980a), and this provides the basis for u_{TEL} and u_{BEL}. An important element in the model of Homicz and Gerber (1986) is that, when the free surface intersects one or both of the endwall disks, the contributions from u_{TEL} and/or u_{BEL} are zero for the "dry" portions of the endwall disks. These treatments are admittedly not entirely rigorous. However, the objective of the analytical model development at this phase is to describe, with reasonable accuracy, the gross features of the transient free surface shape. A somewhat heavy reliance on the phenomenological approaches can then be justified in this context.

In summary, the numerical results of this model had been shown to be in close agreement with the experimental data for the cases when the free surface intersected neither of the endwall disks (Goller and Ranov, 1968). In the present study, the free surface shape predicted by this model will again be subjected to verification by the comprehensive and systematic laboratory measurements; these verifications will encompass the cases when the free surface intersects neither, one or both of the endwall disks.

In order to conduct explicit validations, a numerical code was constructed following the calculation procedures elaboratored in Homicz and Gerber (1986, 1987).

3 The Experiment

A carefully controlled experimental program was undertaken to determine the free surface shape. The experimental apparatus consisted of a rotating turntable, a cylindrical container partially filled with a fluorescence-dye enhanced fluid, a slit beam generator, and photographic image recording devices along with a computer. Shown in Fig. 1 is a schematic of the turntable flow system, and Fig. 2 displays the overall experimental setup including the data recording and processing systems.

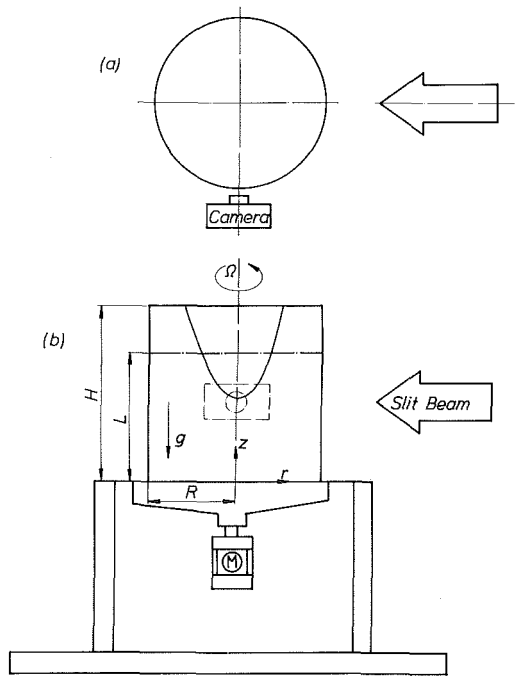

Fig. 1 Schematic of the rotating turntable system. *(a)* top view, *(b)* Front view.

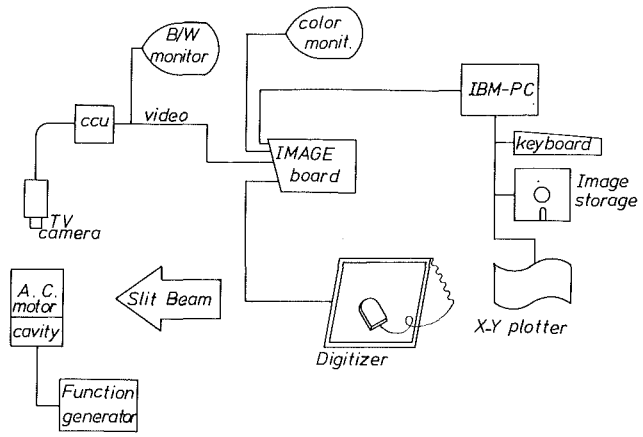

Fig. 2 Experimental apparatus. Main elements are a video camera, a cylindrical container on the top of the rotating turntable, a slit beam generator, a video monitor showing the processing image of free surface, and a computer.

The rotating turntable was built with a precision controlled AC servo motor. The rotational speed of the motor was controlled by adjusting the frequency of input signal from a function generator. The rotational speed was continuously checked by monitoring the signal from the servo motor as well as by using a digital tachometer. The turntable was capable of maintaining the rotational speed within ± 0.1 percent of the set value. The response time of the turntable to achieve a full-speed rotation by the impulsive start was less than 0.012 second (i.e., less than 0.1 revolution at the typical rotating speed of 400 rpm).

A cylindrical tank (inside diameter 94 mm and height 200 mm) was fabricated with plexiglass. The tank was equipped with a vertically movable top endwall disk to adjust the cylinder aspect ratio, H/R. The cylinder was securely coupled to the turntable to maintain the upright configuration and preclude the sloshing. The typical working fluid was water, with a minute amount of fluorescence dye (Butylaniline) dissolved. The appropriate concentration of the dye was determined by repeating the experiments until an optimum excitation lighting could be obtained. The diametrical cross section of the free surface was visualized by a planar light source. A slit beam generator, equipped with a 1500 Watt halogen lamp, a cylindrical lens and a pair of slits, was used to produce a slit beam of 300 mm height (with 1.0 to 2.0 mm in depth due to the finite width of the slit beam).

The cross-sectional plane was clearly visible with green color. Visual observations were performed along an axis perpendicular to the light source. Since the diametrical section was viewed across a cylindrical volume of fluid as well as the plexiglass sidewall, the radial distance from the center line had to be corrected in order to compensate for optical distortion (or lens effect). A simple geometric optic calculation, based on the difference in refractive indices of water to air, was found to be adequate; carefully calibrating the parabolical shapes of free surface at a fully stabilized solid body rotation of the fluid. This model was incorporated in subsequent quantification efforts of the cross-sectional image data. As the flow process evolves in time, different modes of reflections generated several optical illusions of the free surface shape. Special attention was paid to trace the correct view.

Optical images were captured and stored by two different means: a 35mm still camera and subsequent processings of the printed photographs using a digitizing tablet; and direct input by using a Vidicon camera (OPC type OTC 1510) and an image processing system (PC-vision plus by Imaging Technologies Inc.). Elaborate cross checkings of the two methods produced error-free input of the planar image into a digitized pixel data (512×512 resolution) with negligible spatial distortions. In order to secure the transient behavior of the free surface development, images were recorded typically at a 2 second interval.

4 Comparisons of the Results

A set of experiments is characterized by the following four dimensionless parameters: the Reynolds number, Re [$= \Omega R^2/\nu$]; the Froude number, Fr [$= (\Omega R)^2/gH$], where g is the gravity; the aspect ratio, H/R; the fill ratio, L/H. We selected the experimental conditions to cover the range of the parameter values adopted in the numerical results reported by Homicz and Gerber (1986), i.e., Re $\sim 10^5$, Fr ≤ 6.0. However, it was not entirely practical to carry out the experiments to encompass the whole ranges of the parameter values as were exemplified in Homicz and Gerber (1986). Some mismatches of the parameter values were due mainly to the fact that the working fluids used were not the same. In order to compare the present experimental data with the predictions of Homicz and Gerber, efficient numerical codes were written in accordance with the procedure reported in Homicz and Gerber; thus, the transient free surface shapes due to the model of Homicz and Gerber were calculated for the parameter values used in the present experiments.

First, we shall consider the situation in which the free surface intersects neither of the endwall disks. This case was dealt with by Goller and Ranov (1968) as part of the original developmental efforts of the analytical model. The present experimental measurements principally reproduced the free surface configuration depicted by Goller and Ranov (1968) over a wide range of the experimental parameter values. Goller and Ranov (1968) exhibited that the predictions of the analytical model were found to agree, with a high degree of accuracy, with the measurements. This earlier conclusion by Goller and Ranov (1968) has been confirmed by the present experiments. The computed free surface shape as well as the accompanying experimental data were documented well in Goller and Ranov (1968); therefore, we shall omit these results in the present paper.

We next turn to the case of large Fr such that the free surface intersects the top endwall disk. After the instant when the free surface reaches the outer radius of the top disk, only a part of the top disk is wetted. Homicz and Gerber (1986) introduced a new parameter, i.e., the radius of intersection with the top disk, $r_H(t)$, such that $u_{\mathrm{TEL}} = 0$ for $r \leq r_H(t)$. Consequently, the terms u_{FS} and u_{TEL} in equation (2) have to be modified to reflect the fact that $r_H(t)$ decreases with time as spin-up progresses. As pointed out by Homicz and Gerber (1987), no published investigations have addressed the nature of the boundary layer for this case. Effectively utilizing physically sound guidelines, Homicz and Gerber came up with heuristically plausible expressions for u_{TEL} (see equation (10) of Homicz and Gerber, 1986).

Figure 3 exemplifies the experimental data obtained for the transient free surface configuration when the steady state free surface intersects the top endwall disk. Also plotted in the figure are the numerical results calculated according to the analytical model of Homicz and Gerber (Fig. 3(*b*) of Homicz and Gerber shows the same flow configuration but at a slightly different Fr). Evidently, the global qualitative features are in satisfactory agreement with the measurements. The last instant shown indicates the steady state limit, which is consistent with the steady state configuration envisioned by Gerber (1975). As expected, this spin-up time scales with $(H/R)\mathrm{Re}^{1/2}\Omega^{-1}$. The encouraging comparisons displayed in Fig. 3 provide strong credence to the appropriateness of the approximate analytical model of Homicz and Gerber (1986), despite the use of the heuristic assumptions built into the model.

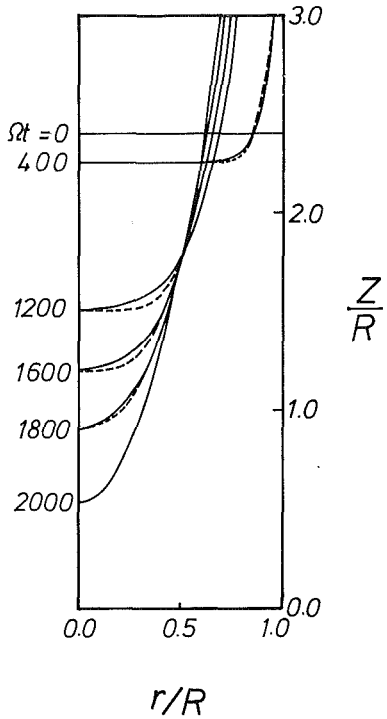

Fig. 3 Comparisons of the transient free surface shapes, Re = 1.172 × 10^5, Fr = 3.0, H/R = 3.0, and L/H = 0.8.
———, experiment; -------, numerical calculation based on the Homicz and Gerber model.
(Maximum uncertainty in z/R is ±0.02, and in r/R ±0.007)

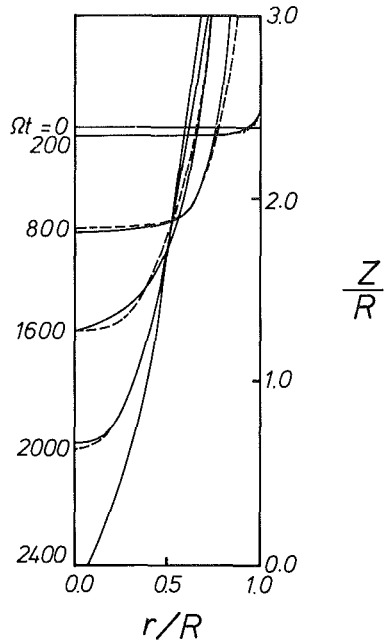

Fig. 4 Comparisons of the transient free surface shapes, Re = 1.172 × 10^5, Fr = 5.5, H/R = 3.0 and L/H = 0.8.
———, experiment; -------, numerical calculation based on the Homicz and Gerber model.
(Maximum uncertainty in z/R is ±0.02, and in r/R ±0.007)

A closer inspection of Fig. 3 reveals that the analytical model tends to underpredict the degree of spin-up as manifested in the shape of free surface. As time elapses, the radial location of the region of the apparent discrepancies between the predictions and the measurements moves toward the central axis. The discrepancies demonstrated in Fig. 3 could stem from a multitude of sources. Some of the inconsistencies and inaccuracies of the original Wedemeyer flow model, which forms the foundation of the analytical model of Homicz and Gerber, have been pointed out (Hyun et al., 1983). Part of the discrepancies could be attributed to the approximate modelling of u in equation (2). At the present stage of model verifications, it is not possible to accurately pinpoint the sources comprising the discrepancies. Perhaps, as suggested by Homicz and Gerber (1986), we may attempt to readjust the form of expression for u_{TEL} in the proposed analytical model. In view of the fact that the relative discrepancies are quite small in magnitude, it appears that a fine-tuning of the empirically adjustable constants κ_T and γ_T in the formulation of u_{TEL} (see equation (10) of Homicz and Gerber, 1986) could improve appreciably the analytical predictions.

Figure 4 illustrates the comparisons when the free surface intersects both of the endwall disks. The radius of intersection with the bottom disk is denoted by $r_0(t)$. Homicz and Gerber, by relying on a logic similar to the above, yielded an analytical expression for u_{BEL}, taking into account that $r_0(t) < 1$. Two adjustable constants were included in the formula. As evidenced in Fig. 4, the capabilities of the analytical model of capturing the overall features of the transient free surface shape are corroborated by the experimental data for this case as well.

5 Conclusion

The transient free surface shape predicted by the analytical model due to Homicz and Gerber (1986) has been shown to be consistent with the experimental data. The experiments have encompassed all possible free surface configurations, i.e., the cases when the free surface intersects neither, one or both of the endwall disks. The direct comparisons of the results have demonstrated that the analytical model is capable of predicting the transient free surface shape in spin-up from rest with reasonable accuracy. For further refinement of the model with a view toward quantitative improvements, full-scale numerical simulations of the Navier-Stokes equations will be of great usefulness.

Acknowledgment

The authors are grateful to the referees whose valuable comment led to substantial improvements in the paper. This work was supported in part by research grant from the Korea Science and Engineering Foundation.

References

Gerber, N., 1975, "Properties of Rigidly Rotating Liquids in Closed Partially Filled Cylinders," ASME *Journal of Applied Mechanics*, Vol. 97, pp. 734–735.

Goller, H., and Ranov, T., 1968, "Unsteady Rotating Flow in a Cylinder with a Free Surface," ASME *Journal of Basic Engineering*, Vol. 90, No. 4, pp. 445–454.

Greenspan, H. P., and Howard, L. N., 1963, "On a Time Dependent Motion of a Rotating Fluid," *Journal of Fluid Mechanics*, Vol. 17, Part 3, pp. 385–404.

Homicz, G. F., and Gerber, N., 1986, "Numerical Model for Fluid Spin-Up from Rest in a Partially Filled Cylinder," AIAA paper 86-1121, pp. 1–9.

Homicz, G. F., and Gerber, N., 1987, "Numerical Model for Fluid Spin-Up from Rest in a Partially Filled Cylinder," ASME JOURNAL OF FLUIDS ENGINEERING, Vol. 109, pp. 195–197.

Hyun, J. M., Leslie, F., Fowlis, W. W., and Warn-Varnas, A., 1983, "Numerical Solutions for Spin-Up from Rest in a Cylinder," *Journal of Fluid Mechanics*, Vol. 127, pp. 263–281.

Kitchens, C. W. Jr., 1980a, "Ekman Compatibility Conditions in Wedemeyer Spin-up Model," *Physics of Fluids*, Vol. 23, pp. 1062–1064.

Kitchens, C. W. Jr., 1980b, "Navier-Stokes equations for Spin-Up in a Filled Cylinder," *AIAA Journal*, Vol. 18, No. 8, pp. 929–934.

Watkins, W. B., and Hussey, R. G., 1977, "Spin-Up from Rest in a Cylinder," *Physics of Fluids*, Vol. 20, No. 10, pp. 1596–1604.

Wedemeyer, E. H., 1964, "The Unsteady Flow within a Spinning Cylinder," *Journal of Fluid Mechanics*, Vol. 20, Part 3, pp. 383–399.

Weidman, P. D., 1976, "On the Spin-Up and Spin-Down of a Rotating Fluid. Part I: Extending the Wedemeyer Model. Part II: Measurements and Stability," *Journal of Fluid Mechanics*, Vol. 77, pp. 685–735.

Asymmetrical Boundary Layer Separation at the Base of a Two Cylinder Geometry

M. T. Boyle
Assistant Professor of Mechanical Engineering,
University of Maine,
Orono, ME 04469-0110

L. S. Langston
Professor of Mechanical Engineering,
University of Connecticut,
Storrs, CT

This paper reports on the experimental description of the three-dimensional horseshoe vortex system occurring at the base of two cylinders mounted side by side on an endwall. The spacing between the two cylinders is adjusted to generate a family of viscous flows. Flow visualization performed in a water tunnel provides a qualitative understanding of the flow over a range of flow variables. A detailed wind tunnel experiment, provides a quantitative description of the flow at a single test condition. The flow is described by the use of a five-hole pressure probe and by cylinder and endwall surface static pressure measurements. At $Re_D = 2.5 \times 10^5$ the measurements show an asymmetrical primary vortex with a wide flat cross section. A small counter rotating vortex is found between the primary vortex and the cylinder leading edge.

Introduction

An important problem in fluid mechanics is the three-dimensional separation of a wall boundary layer in front of a right circular cylinder mounted on the wall. The fluid in the boundary layer that rolls up in front of or around the cylinder base is called a horseshoe or necklace vortex system. The term "system" is used because there is often more than a single vortex. In all that follows we are concerned with the region around the front half of a cylinder and not the wake region.

The right cylinder-endwall geometry is simple, yet the flow around it has many of the features (e.g., vortex motion, singular points, and skewed boundary layers) of more complicated fluid flows. It could be termed the "flat plate" of three-dimensional flows and has been the subject of many studies [1–5]. A recent experimental work by Eckerle and Langston [6] provides a detailed description of the vortex system around the base of a single cylinder for the case of a turbulent endwall boundary layer. Three-dimensional flows of this nature have a strong effect on endwall and cylinder surface heat transfer coefficients. This has obvious significance for heat transfer augmentation in heat exchanger design. Endwall and cylinder surface heat and mass transfer coefficients have been measured by a number of researchers [7–11].

The single cylinder produces a *symmetrical* horseshoe vortex system at its base. However, many three-dimensional boundary layer flows separate to form an *asymmetrical* horseshoe vortex system. A very common example of such an asymmetric flow is the boundary layer separation at the hub and tip junctions of turbine airfoils. Descriptions of the three-dimensional aerodynamics in turbine cascade passages are provided in references [12–14]. The vortex features of the flow contribute significantly to the viscous loss of the fluid as it moves through the turbine. On the cascade endwall surface the heat transfer coefficients are controlled by the three-dimensional flow [15–17].

The purpose of this paper is to propose a simple "flat plate" experiment for these asymmetrical horseshoe vortex systems. The geometry proposed is two right cylinders of equal diameter mounted side-by-side on an endwall as shown in Fig. 1. Far from the endwall the flow can be thought of as two-dimensional, a case that has been reported on by Bearman and Wadcock [18]. Close to the endwall a horseshoe vortex system forms around each cylinder, but because of the asymmetric static pressure field the horseshoe vortices are skewed, as shown in Fig. 1. The saddle points are displaced by the angle θ. (The case of $\theta = 0$ corresponds to a single cylinder). It

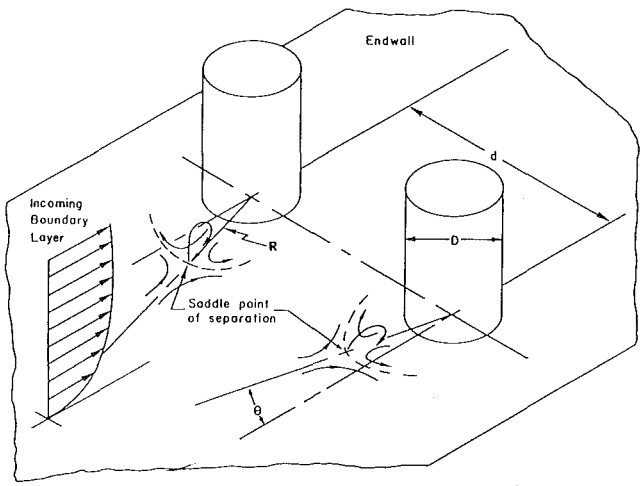

Fig. 1 Two cylinder geometry with asymmetric horseshoe vortex systems

Contributed by the Fluids Engineering Division for publication in the JOURNAL OF FLUIDS ENGINEERING. Manuscript received by the Fluids Engineering Division December 14, 1987.

can be reasoned that by varying the cylinder spacing (either d or d/D) the degree of asymmetry can be controlled, and many features of a more complicated flow (such as the turbine passage problem) can be modeled conveniently and comparatively inexpensively.

In this paper we report on an experimental study of the two cylinder geometry in order to document the three-dimensional flow near the endwall and upstream of the cylinder wakes. Studies were performed with laminar flow in a water tunnel (Re_D: 200–4000) to demonstrate the asymmetric behavior and to measure the effect of three length scales (δ, D, d) on saddle point position. Flow field measurements were then taken in a wind tunnel for a turbulent endwall boundary layer at $Re_D = 2.5 \times 10^5$ and $d/D = 1.5$.

In all of the tests, the use of a tunnel with sidewalls implies that a cascade of two cylinder elements was tested. The parallel tunnel walls approximate mid-streamlines between "image" cylinder pairs on either side of the two cylinder model.

Water Tunnel Experiment

Flow visualization experiments performed in a water tunnel provide a description of the qualities of the three-dimensional flow. In particular the effects of d, D, V, and δ on saddle point location (R, θ) are investigated for the two cylinder problem. The accuracy of the measurements made in the water tunnel is sufficient for a qualitative description of the flow over ranges of the above independent variables. The reader is referred to Boyle [19] for a detailed description of the experimental facility.

Flourscein dye and hydrogen bubbles were used to visualize the flow. Measurements were made with five cylinder diameters and three incoming velocities. The characteristics of the boundary layer developing on the fixed length of endwall can be directly correlated to V. The cylinder spacing was varied over the range from $d/D = 1.0$ (touching) to $d/D = 8.0$. Saddle point position was also measured with a single cylinder on the water tunnel centerline for each cylinder diameter. This corresponds to an infinite array of cylinders with a spacing equal to the test section width.

The results of the water tunnel investigation are divided into two subsets: those that produce a double asymmetric vortex system and those that produce a single symmetrical vortex system. As the cylinder spacing is descreased below a critical value of d/D, the three-dimensional flow near the endwall changes from one where a vortex system wraps around the base of each cylinder to one where a single large vortex system wraps around the base of both cylinders. For this larger system a single symmetrical saddle point of separation is located on the water tunnel centerline. This occurs for values of d/D as high as 2.0. For d/D below the critical value, R increases dramatically. This can be interpreted as the viscous boundary layer responding to the two cylinder geometry as though it were a single large object. Although the large single vortex system and the transition to it from the two smaller systems (as d/D decreases) is a very interesting viscous flow problem, this work focuses on the asymmetrical vortex system flow.

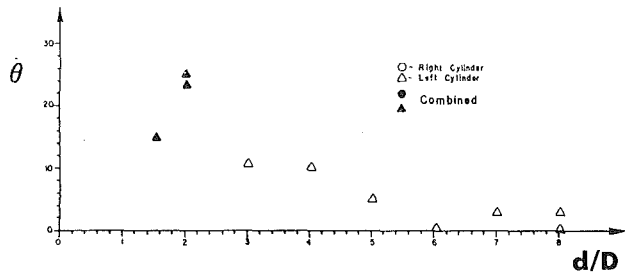

Fig. 2(a) Saddle point turning with cylinder spacing. $Re_D = 600$.

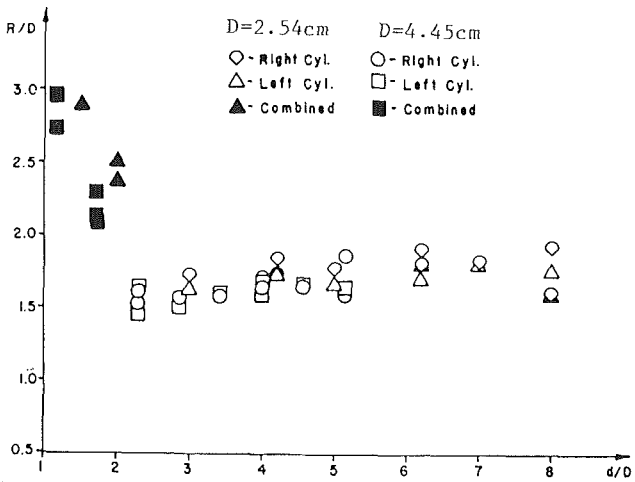

Fig. 2(b) Saddle point standoff distance with cylinder spacing, $Re_D = 600$ for 2.54 cm cylinder

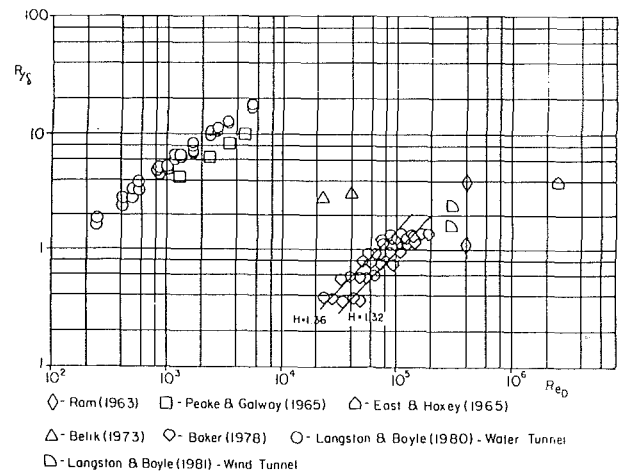

Fig. 2(c) Comparison of two cylinder data to the single cylinder data of others

As the two cylinders are moved closer together, the angular coordinate of the saddle point of separation, θ, increases. This is shown in Fig. 2(a) for data taken with $Re_D = 600$. Also, as

Nomenclature

CPS = $(P_s - P_s)/q_r$
CPT = $(P_{T_r} - P_T)/q_r$
d = spacing of cylinder axes
D = cylinder diameter
H = shape factor
P_s = static pressure
P_T = total pressure
P_{T_r} = reference total pressure
q = dynamic head
q_r = reference dynamic head
R = distance from cylinder center
Re_D = diameter Reynolds number
v = local velocity
V = reference velocity
W_i = uncertainty in i value
x,z = location in horizontal plane
y = location in traverse direction
yaw = flow angle in horizontal plane
δ = boundary layer thickness
θ = yaw
ϕ = flow pitch angle

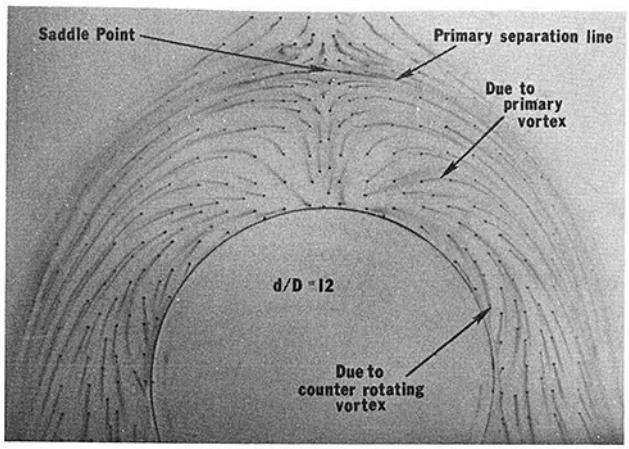

Fig. 3 Endwall flow visualization—single cylinder

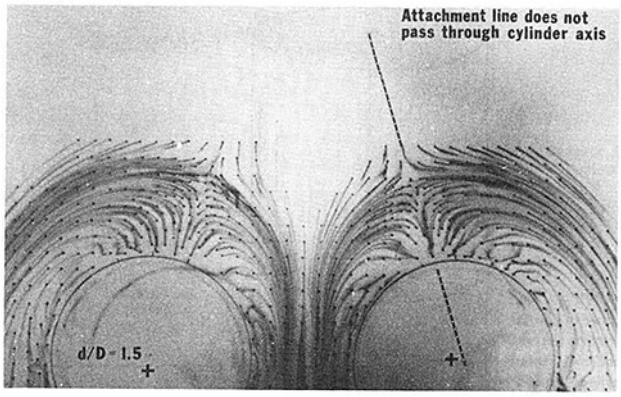

Fig. 4 Endwall flow visualization—$d/D = 1.5$

d/D decreases, the saddle point of separation turns around the base of each of the cylinders with little effect on the saddle point standoff distance, R. This is shown in the data of Fig. 2(b). Because of the insensitivity of R to d/D, we are able to compare the R data for the two cylinder problem to the data obtained from the single cylinder studies of other researchers. This comparison is made in Fig. 2(c) where the saddle point standoff distance data is plotted in the R/δ versus Re_D coordinate system. This coordinate system is especially revealing for the presentation of our water tunnel data, with the boundary layer characteristics coupled to V. A monotonically increasing function of R/δ with Re_D is shown. Baker's [1] data show the independent effect of the boundary layer shape factor.

Through the water tunnel investigation a knowledge of the variables that control three-dimensional separation and the impact of these variables on the location of the endwall saddle point is obtained. The water tunnel work establishes the two-cylinder experiment as an interesting and useful one for investigating the three-dimensional separation problem in general. The wind tunnel portion of this study provides some of the detailed characteristics of these flows at higher Reynolds number.

Wind Tunnel Experiment

Test Conditions, Instrumentation and Uncertainty. The flow is described by measurements made with a five-hole probe and with endwall and cylinder surface pressure measurements. The endwall and cylinder surface streamline topology is depicted by the use of the ink-dot visualization technique [20]. The two cylinder spacing corresponds to $d/D = 1.5$. The Reynolds number based on cylinder diameter is 2.5×10^5 and the incoming boundary layer characteristics are $\delta = 5.41$ cm, $H = 1.24$. Both δ and H were measured at the position of the model leading edge with the model removed.

The test section cross section is 0.305 m tall by 1.83 m wide. The maximum attainable test section velocity is 32 m/s. The two cylinders span the 0.305 m test section height and are centered in the test section. They are made from 15.88 cm diameter machined aluminum tubing. Static pressure taps are installed in the cylinder surfaces and in the surface of the test section ceiling. Each cylinder can be rotated about its axis to provide a detailed surface pressure map. The ceiling taps are located in a large aluminum disk which can also be rotated. A 48 port scanivalve was used with a Gould differential pressure tranducer for all pressure measurements. The pressure transducer was calibrated with a Betz micromanometer. An L.C. Smith probe positioner was used to move a five-hole probe across the test section span. A detailed description of the methodology used for probe positioning and alignment is given in Boyle [19]. A summary of the uncertainties of each of the variables measured with the five-hole probe is as follows:

W_q	= 0.0879 cm water	W_{CPS}	= 0.040
W_v	= 0.301 m/sec	W_ϕ	= 0.60 deg
W_{CPT}	= 0.0190	W_{yaw}	= 0.8 deg
W_x	= 0.038 cm	W_z	= 0.038 cm
W_y	= 0.051 cm		

For surface static pressure $W_{\mathrm{CPS}} = .009$.

The odds are 20 to 1 that the measured value lies within these uncertainties [21].

Surface Flow Visualization. Figures 3 and 4 show the ink-dot visualization on the floor for the single cylinder case and the $d/D = 1.5$ case. The effect of the asymmetrical vortex system is clearly displayed by the turning of the whole endwall pattern toward the neighboring cylinder. For both geometries, the primary separation line occurs on the endwall just upstream of the primary vortex and is shown by the convergence of streamlines along it. The effects of a small vortex rotating counter to the primary vortex is seen in the streaklines that turn toward the cylinder. Diverging streamlines in this region show the location of an attachment line on the endwall between the primary vortex and the counter rotating vortex. The features of this streamline topology are shown in the interpretive sketch of Fig. 5.

Figure 6 is a tracing of the cylinder surface streakline pattern for $d/D = 1.5$. The tracing is made from a number of experimental "runs" taken on portions of the vertically oriented surface. The mainstream stagnation and separation lines are clearly shown. The asymmetry in the angular location of each line can be seen in the figure. Downstream of the mainstream separation lines there is enough evidence of a line from which streamlines diverge to show an attachment line along the cylinder span. This topology indicates a vertically oriented vortex standing between the mainstream separation and the mainstream attachment. The downward sloping streaklines on the lower end of the cylinder surface, near stagnation, are due to the turning of the primary vortex. Near the endwall the effect of the counter rotating vortex is to cause streaklines to slope upward as one moves around the cylinder away from stagnation. The authors' interpretation of the streamline topology associated with these vortices is described by the use of Fig. 5. It should be noted that the effect of the counter rotating vortex is evident only at large values of θ; in the near stagnation region it is small and its effect is not observed. Therefore, the dotted line portion of Fig. 5 is hypothesized. The counter rotating vortex was only observed by the use of flow visualization.

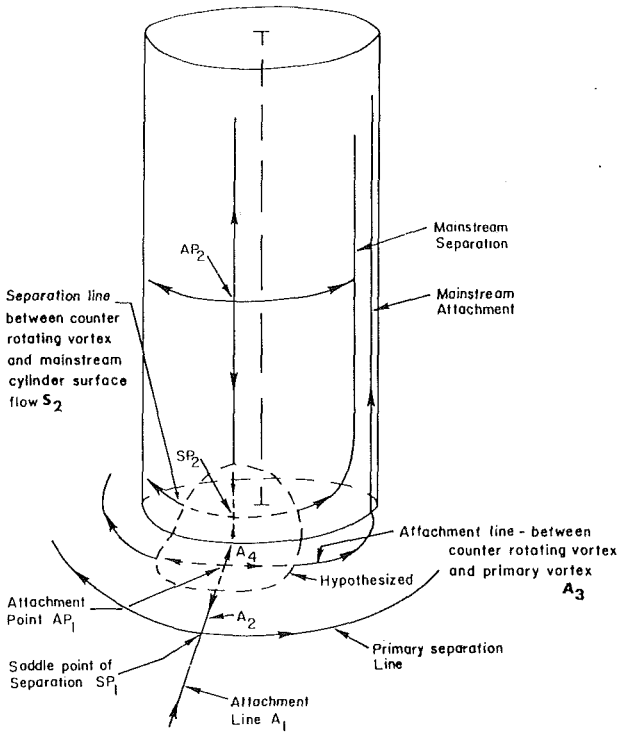

Fig. 5 Surface topology sketch based on flow visualization data

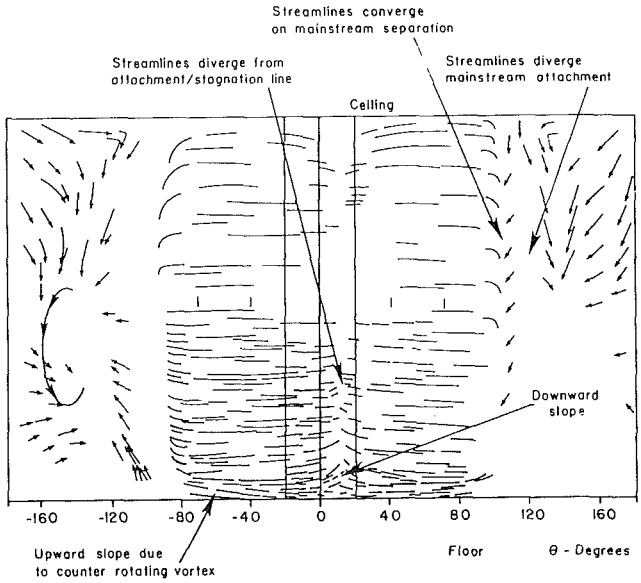

Fig. 6 Cylinder surface flow visualization

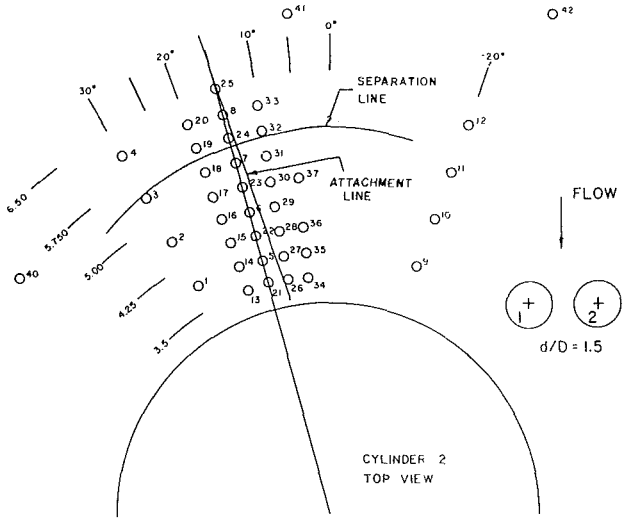

Fig. 7 Traverse locations

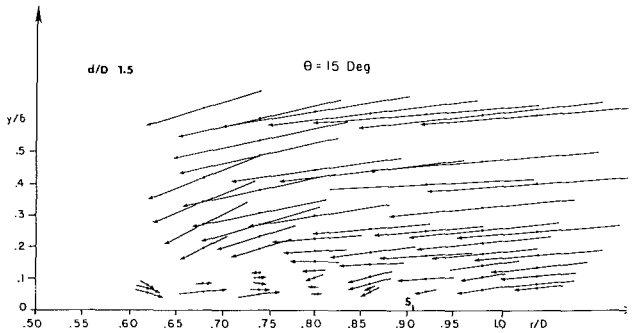

Fig. 8(a) Velocity vectors

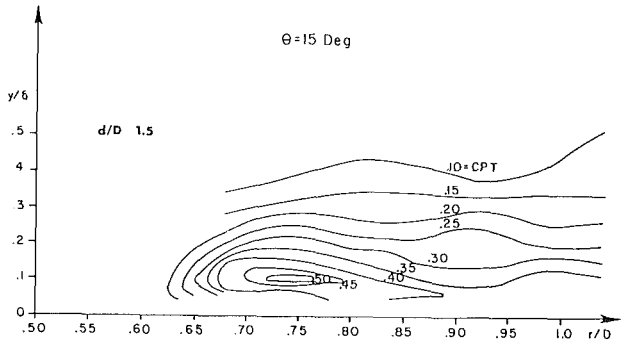

Fig. 8(b) Total pressure contours

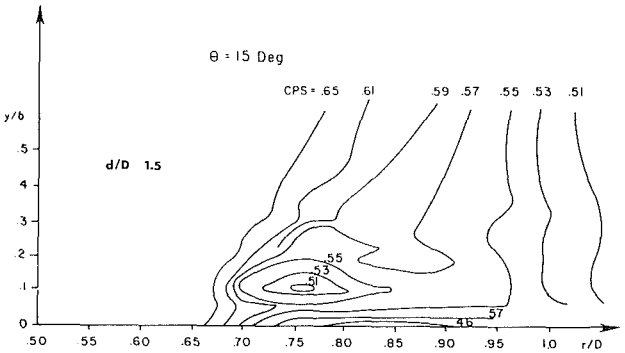

Fig. 8(c) Static pressure contours

Five-Hole Probe Measurements. Spanwise traverses were taken with a five-hole probe at the locations shown in Fig. 7. The probe is calibrated for use in the nulled mode and can measure pitch angles as large as 30 degrees. The cylinder diameter is 60 times larger than the probe diameter, so that probe interference is small. Figures 8(*a*), 8(*b*) and 8(*c*) show the velocity vector, total pressure coefficient, and static pressure coefficient data measured in the $\theta = 15$ degree plane. The velocity vectors are projected into the plane. The nondimensional ordinate y/δ is used to show the portion of the incoming boundary layer that participates in the primary vortex. The characteristics measured in the $\theta = 15$ degree plane are very similar to those measured by Eckerle and Langston [6] in the symmetry plane for the single cylinder problem. The position of the endwall separation line is shown in Fig. 8(*a*); this is obtained from the flow visualization. A vortex with a wide flat cross section is evident. The core of the vortex is located at approximately $y/\delta = 0.10$, $r/D = 0.74$. Viscous loss is at a maximum in the region of the vortex core and closed static

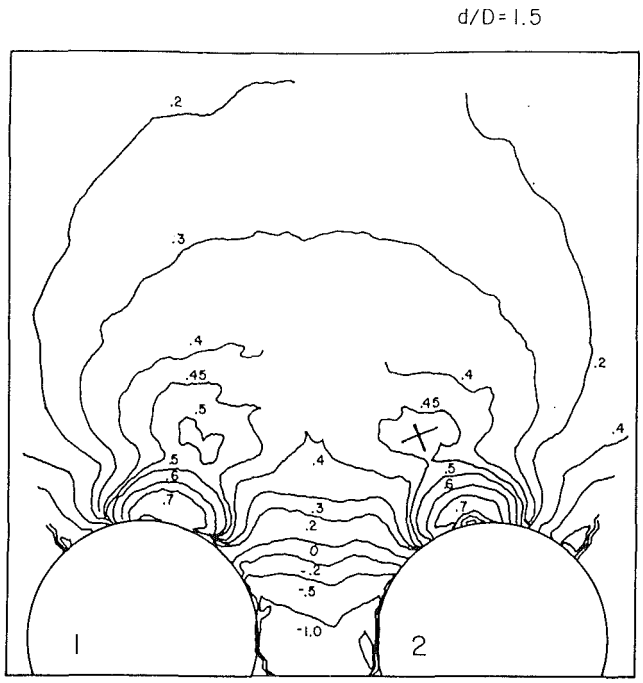

Fig. 9 Endwall static pressure—ceiling

pressure contours surround the core. Large velocity vectors are found in the reverse flow region. Enhanced heat transfer in this region [7–11] can be attributed to the high velocities.

The data used to evaluate CPS at $y=0$ in Fig. 8(*c*) is obtained from the static pressure distribution measured on the test section ceiling. Due to an asymmetrical wind tunnel inlet condition (top to bottom), caused by the placemat of the wind tunnel in the laboratory, the ceiling boundary layer is 25 percent thicker than the floor boundary layer. Flow visualization tests show that R is insensitive to small changes in δ at this Reynolds number. More experiments are required before we can be sure that this insensitivity extends to the surface static pressure measurements.

The three-dimensional five-hole probe measurements detail the aerodynamics in the region immediately surrounding the saddle point of separation. Although this flow is clearly asymmetrical, with fluid particles accelerating more rapidly between the two cylinders than around the outside of the model, the qualitative description is very similar to that for the basic single cylinder problem (reference [6]).

Endwall and Cylinder Surface Pressure. The endwall pressure distribution for the two cylinder geometry corresponding to $d/D=1.5$ is shown in Fig. 9. The measurements were made on the test section ceiling. The pressure is asymmetrical about the cylinder axis and symmetric about the wind tunnel centerline. Except for the asymmetries this distribution is very similar to that measured in front of a single cylinder [6]. In a large region surrounding the saddle point of separation the static pressure coefficient is fairly uniform, approximately 0.45–0.50. During the flow visualization work this was determined to be a region of low velocity. Baker's [1] work also shows a large region of nearly uniform pressure in the saddle point region. He attributes this to an unsteady vortex system. The measurements made for this two-cylinder geometry show a steady primary vortex.

At the saddle point location, the pressure gradient along the direction of the primary separation line is zero. The model derived by Langston and Wagner (22) shows this to be consistent with a symmetrical separation where the attachment line

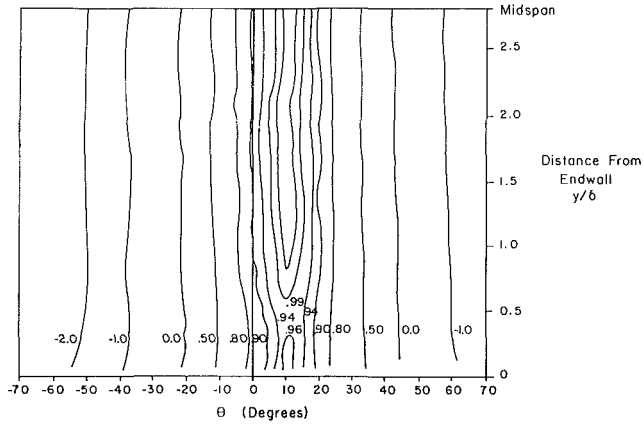

Fig. 10 Cylinder surface isobars—CPS

and the separation line meet normally. It can be seen in Fig. 4 that these lines meet normally. This means that although the overall flow is asymmetrical with respect to the cylinder and asymmetrical with respect to the attachment line, in the region very near the saddle point the flow is symmetrical about the attachment line. The asymmetrical pressure field generated in the potential flow region is not sufficient to generate an asymmetrical separation. Indeed one may ask if there is such a thing as an asymmetrical saddle point of separation.

Figure 10 is a plot of the isobars on the lower half of the cylinder surface. The stagnation line is at $\theta=11.0$ degrees. The three-dimensional flow affects the pressure distribution over approximately one boundary layer thickness of the cylinder height. A minimum in pressure occurs at $y/\delta=0.32$. Baker [1], Ram [2], and East and Hoxey [4] used this minimum and a minimum on the endwall attachment line to locate the primary vortex core. It is clear that this is not an accurate method for the wide flat vortex reported herein.

Conclusions

Water tunnel experiments performed at low Reynolds number establish the two cylinder model as a good geometry for the fundamental study of the asymmetrical horseshoe vortex problem. A family of three-dimensional viscous flows is easily generated by simply adjusting the cylinder spacing. For d/D over the critical value, that value of d/D where the vortex system changes from two asymmetric systems to a single large symmetric system, the water tunnel work shows R to be insensitive to d/D. R/δ increases with increasing Re_D or increasing H.

Wind tunnel measurements supply a quantitative description of the aerodynamics in the vortex flow region for a single, specific flow condition. The asymmetry of the flow is evident in the turning of the vortex system around the cylinder, the asymmetric endwall pressure distribution and the asymmetric cylinder surface pressure distribution. In spite of the asymmetrical static pressure field that drives the endwall flow, and the asymmetrical vortex system itself, the three-dimensional separation from the endwall is locally symmetric about the attachment line. Numerical schemes designed to predict horseshoe vortex flow systems can use the two cylinder model to verify accuracy before attempting more complicated flow geometries.

Acknowledgments

This work was supported by NASA Grant No. NSG3238 under the direction of L.J. Goldman of the NASA Lewis Research Center.

References

1 Baker, C. J., "Vortex Flow Around the Bases of Obstacles," A dissertation submitted in the University of Cambridge, Sept. 1988.

2 Ram, V. V., "Unteruchungen uber die Eckengrenschict an einem Kreiszylnder Mit Setenwand," Bericht 63/64, Instit for Stroungsmechanik, Technische Hochschule Braunschweig, pp 1–12, 1963.

3 Peake, D. J., and Galway, R. D., "The Three-Dimensional Separation of a Plane Incompressible Laminar Boundary Layer Produced by a Circular Cylinder Mounted Normal to a Flat Plate," High Speed Aerodynamics Section, NAE, NRC, Ottowa, Canada, 1965, pp. 1049–1080.

4 East, L. F., and Hoxey, R. D., "Low Speed Three-Dimensional Separation of a Plane Incompressible Boundary Layer Produced by a Circular Cylinder Mounted Normal to a Flat Plate," National Research Council Report, pp. 1–82, 1965.

5 Belik, L., "The Secondary Flow About Circular Cylinders Mounted Normal to a Flat Plate," *Aeronautical Quarterly*, Feb. 1983, pp. 47–54.

6 Eckerle, W. A., and Langston, L. S., "Horseshoe Vortex Formation Around a Cylinder," ASME *Journal of Turbomachinery*, Apr. 1987, pp. 278–285.

7 Ireland, P. T., and Jones, T. V., "Detailed Measurements of Heat Transfer on and Around a Pedestal in Fully Developed Passage Flow," Presented at the 8th International Heat Transfer Conference, San Francisco, 1986.

8 Goldstein, R. J., Chyu, M. K., and Hain, R. C., "Measurement of Local Mass Transfer on a Surface in the Region of a Protruding Cylinder with a Computer Controlled Data Acquisition System," *Int. J. of Heat and Mass Transfer*, Vol. 28, 1985, pp. 977–985.

9 Dresar, N. V., and Mayle, R. E., "Convection at the Base of a Cylinder with a Horseshoe Vortex," *Proceedings of the 8th International Heat Transfer Conference*, Vol. 3, San Francisco, 1986.

10 Sparrow, E. M., and Stahl, T. J., and Traub, P., "Heat Transfer Adjacent to the Attached End of a Cylinder in Crossflow," *Int. J. of Heat and Mass Transfer*, Vol. 27, 1984, pp. 233–242.

11 Goldstein, R. J. and Karni, J., "The Effect of a Wall Boundary on Local Mass Transfer, Vol. 106, 1984, pp. 260–362.

12 Langston, L. S., Nice, M. L., and Hooper, R. M., "Three-Dimensional Flow Within a Turbine Cascade Passage," ASME *Engineering for Gas Turbine and Power*, Vol. 99, Jan. 1977, pp. 21–28.

13 Yamamoto, A., "Prediction and Development of Secondary Flows and Losses Within Two Types of Straight Turbine Cascades," ASME *Journal of Turbomachinery*, Vol. 109, 1987, pp. 186–193.

14 Boyle, M. T., Simonds, M., and Poon, K., "A Comparison of Secondary Flow in a Vane Cascade and a Curved Duct," Presented at 1988 ASME Winter Annual Meeting, December 1988, Accepted for publication in ASME *Journal of Turbomachinery*.

15 Graziani, R. A., Blair, M. F., Taylor, J. R., and Mayle, R. E., "Experimental Study of Endwall and Airfoil Surface Heat Transfer in Large Scale Turbine Blade Cascade," ASME *Journal of Engineering for Power*, Vol. 102, Apr. 1980, pp. 257–267.

16 York, R. E., Hylton, L. D., and Mihek, M. S., "An Experimental Investigation of Endwall Heat Transfer and Aerodynamics in a Linear Vane Cascade," ASME *Journal of Engineering for Gas Turbine and Power*, Vol. 106, Jan. 1984, pp. 159–167.

17 Boyle, M. T., and Hoose, K. V., "Endwall Heat Transfer in a Vane Cascade Passage and in a Curved Duct," to be presented at the 1989 Inter. Gas Turbine Conference, Toronto, June 1989.

18 Bearman, P. W., and Wadcock, A. J., "The Interaction Between a Pair of Circular Cylinders Normal to a Stream," *J. of Fluid Mechanics*, Vol. 61, 1973, pp. 495–511.

19 Boyle, M. T., "Three-Dimensional Separation and Vortex Formation," A dissertation submitted to the University of Connecticut, 1984.

20 Langston, L. S., and Boyle, M. T., "A New Surface-Streamline Flow Visualization Technique," *J. of Fluid Mechanics*, Vol. 125, 1982, pp. 53–58.

21 Kline, S. J., and McClintock, F. A., "Describing Uncertainties in Single Sample Experiments," *Mechanical Engineering*, 1953, pp. 3–8.

22 Langston, L. S., and Wagner, C. A., "A Streamline Model for a Saddle Point of Separation, Univ. of Connecticut, Mechanical Engineering Technical Report, Oct. 1983.

Three-Dimensional Flow Pattern Upstream of a Surface-Mounted Rectangular Obstruction

K. Y. M. Lai
Research Associate.

A. H. Makomaski
Senior Research Officer.

Gas Dynamics Laboratory,
Division of Mechanical Engineering,
National Research Council of Canada,
Ottawa, Ontario K1A 0R6
Canada

A three-dimensional TEACH-like computer code is developed and employed to study the flow phenomena upstream of a rectangular obstruction placed in a two-dimensional turbulent boundary layer. Satisfactory comparison is obtained with the experimental results of Blair (1984, 1987). The general trends, regarding the dependence of vortex dimensions, wall static pressure distributions and saddle point positions on $Re = U_\infty \delta^*/\nu$ and on $D^* = D/\delta^*$, are similar to the experimental results for circular cylinders (Eckerle and Langston, 1986 and Baker, 1980). The position of the saddle point depends on the turbulence intensity in the primary vortex. The pressure coefficient at the foot of the obstruction depends solely on D^* if no corner vortex exists. This coefficient is reduced when a corner vortex is present. All the computed flow patterns are similar to the one-vortex model of Eckerle and Langston (1986). The four-vortex model reported by Baker (1980) and Hunt et al. (1978) cannot be found in any of the calculations.

1 Introduction

When a two-dimensional turbulent boundary layer approaches an obstruction mounted on a surface, a complicated three-dimensional flow pattern results, both in front and around the obstruction. Such a situation is encountered in axial-flow machinery at the roots of compressor and turbine blades, at the junction of wing and aircraft fuselage, around bridge piers in a river with the stream velocity varying with height and around tall buildings.

The phenomenon is associated with the nonuniformity of the stagnation pressure at the leading edge of the obstruction, caused by the approaching boundary layer on the surface on which the obstruction is mounted (Hawthorne, 1954). The pressure variation, and the consequent downward velocities along the obstruction, result in a complicated vortex pattern, which is responsible for the creation of a horseshoe vortex which later envelops the whole of the obstruction. The region ahead of an obstruction is, therefore, of great interest and importance in many practical flow situations.

In the past, mainly experimental studies of the flow phenomena were carried out at low speeds. The obstruction for which the largest body of fundamental data exists is the circular cylinder. The flow past a cylinder has been investigated, in chronological order, by Belik (1973), Baker (1980) and Eckerle and Langston (1986). The pertinent conditions and results are summarized in Table 1.

Following the work of Hunt et al. (1978), who applied topology to explain the vortex system existing in flows past surface-mounted obstructions, Baker (1980) adopted the four-vortex model shown in Fig. 1, utilized by a number of authors for other geometries as well, to represent the flow phenomena ahead of obstructions. The model is characterized by the two separation lines S_1 and S_2 and the two attachment lines A_1 and A_2. The alternative one-vortex model, recently proposed by Eckerle and Langston (1986), is shown in Fig. 2 and is characterized by one separation line S_1 and one attachment line A_2. The point S_1 is normally identified as the saddle point (shown in Fig. 3). The results shown in Table 1 seem to imply that as the Reynolds number (based on D) and/or the ratio

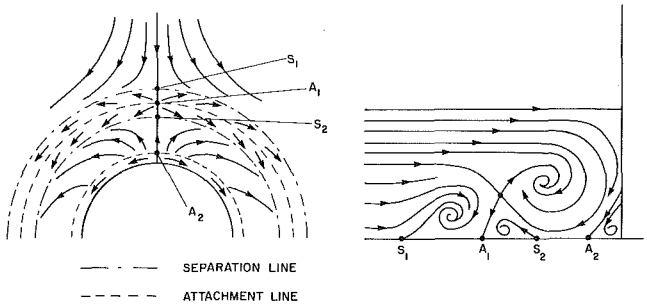

Fig. 1 The four-vortex model

Table 1 Results for circular cylinders

Reference	D/δ^*	$U_\infty D/\nu$	$U_\infty \delta^*/\nu^{(++)}$	Vortex Model
Baker (1980)	4 to 30	4×10^3 to 9×10^4	9.4×10^2 to 1.1×10^4	four-vortex model adopted
Eckerle and Langston (1986)	65	5.5×10^5	8.5×10^3	one-vortex model indicated

(++) Values deduced by the present authors.

Contributed by the Fluids Engineering Division for publicatoin in the JOURNAL OF FLUIDS ENGINEERING. Manuscript received by the Fluids Engineering Division March 11, 1988.

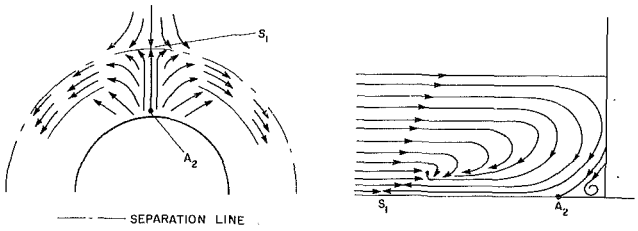

Fig. 2 The simple vortex model

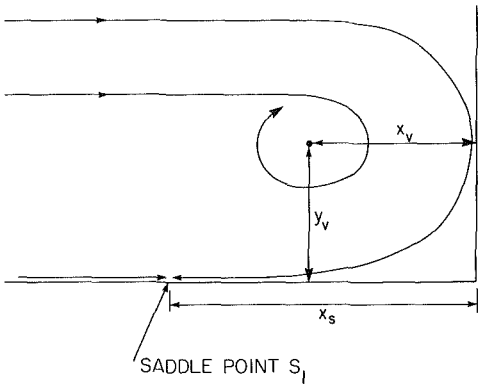

Fig. 3 Definition of vortex dimensions

D/δ^* increase, the vortex pattern changes from the assumed four-vortex configuration to the indicated one-vortex configuration.

Baker (1980) has shown by dimensional analysis and by experiments that the characteristics of the primary vortex, pressure distribution beneath the vortex system and boundary layer separation (saddle-point position) ahead of a long cylinder, depend mostly on the parameters $D^* = D/\delta^*$ and $\mathrm{Re} = U_\infty \delta^*/\nu$.

In an attempt to deepen the understanding of the nature of the vortex system, and to confirm whether both the above vortex models exist and whether their existence depends on either one or both of the parameters Re and D^*, numerical experiments are carried out. A suitable numerical procedure for calculating three-dimensional turbulent flows is developed and employed: (1) to study the vortex system generated and (2) to investigate the dependence of the vortex characteristics and the flow ahead of the obstruction on Re and D^*.

A series of five computations of two-dimensional turbulent boundary layer flows impinging on a rectangular obstruction has been carried out, with one of the computations approximately simulating the conditions studied by Blair (1984, 1987). The working conditions cover approximately the same range of $U_\infty D/\nu$ and D^* as for the cylinder (Baker, 1980), with D representing now the obstruction width. This range is chosen to enable comparisons with the detailed results of Baker (1980) and to determine whether the four-vortex model adopted is justified. Since the results of Baker (1980) indicate a weak dependence of the phenomena on Re, it is not considered necessary to cover Baker's range of Re completely. Thus no consideration was given to the numerical simulation at higher speeds. However, the range of D^* used in this work fully covers Baker's results.

2 Description of the Physical Model

A schematic diagram of the situation modelled is shown in Fig. 4. The dimensions of the rectangular domain bounded by the four walls are given in Table 2.

This arrangement is consistent with the wind tunnel test section described by Blair (1984). The rectangular obstruction, spanning the domain from top to bottom, is located along the centerline 0.27 m from the inlet plane abcd and is 0.152 m wide. According to Blair (1984), the inlet velocity U_∞ is 9.1 m/s and the turbulence intensity of the core flow I is 0.7 percent. The approaching boundary layer is fully turbulent and two-dimensional, and its thickness δ at the inlet plane is 0.0371 m. The flow is assumed to be steady and incompressible. Location of the inlet plane is such that the flow there is not significantly affected by the presence of the obstruction. Only a symmetrical quarter of the physical domain is used as a solution domain.

3 Mathematical Model

3.1 Governing Equations. The ensemble-mean equations of motion for steady-state, incompressible and turbulent flow can be written in Cartesian tensor notation as follows:

Continuity:
$$\frac{\partial \rho u_i}{\partial x_i} = 0 \qquad (1)$$

Nomenclature

C_p = pressure coefficient $= (p - p_\infty)/(\frac{1}{2}\rho U_\infty^2)$

C_{pe} = effective pressure coefficient
$$= \left[\left(p + \frac{2}{3}\rho k\right) - \left(p + \frac{2}{3}\rho k\right)_\infty\right] \Big/ \left(\frac{1}{2}\rho U_\infty^2\right)$$

C_1 = constant in turbulence model (= 1.44)

C_2 = constant in turbulence model (= 1.92)

C_μ = constant in turbulence model (= 0.09)

D = diameter of cylinder; width of rectangular obstruction (Fig. 4)

D^* = ratio D/δ^*

H = height of rectangular duct (Fig. 4)

I = turbulence intensity

k = turbulence kinetic energy

l_m = mixing length

L = length of rectangular duct (Fig. 4)

L_0 = length of rectangular obstruction (Fig. 4)

p = static pressure

p_∞ = free-stream static pressure

Re = Reynolds number defined by $U_\infty \delta^*/\nu$

u_i = velocity tensor

U_∞ = free-stream velocity in x-direction

W = width of rectangular duct (Fig. 4)

x, y, z = Cartesian coordinates (Fig. 4)

x_i = Cartesian coordinate tensor

x_s = distance of saddle point (Fig. 3)

x_v, y_v = distances of primary vortex (Fig. 3)

δ = boundary layer thickness

δ^* = displacement thickness

ϵ = rate of dissipation of turbulence energy

κ = von Karman constant(= 0.4187)

μ = dynamic viscosity

ν = kinematic viscosity

ρ = density

$\sigma_k, \sigma_\epsilon$ = Schmidt numbers for k and ϵ

τ = shear stress

Subscripts

eff = effective i.e., sum of laminar and turbulent

s = saddle point

t = turbulent

v = primary vortex center

∞ = free-stream conditions

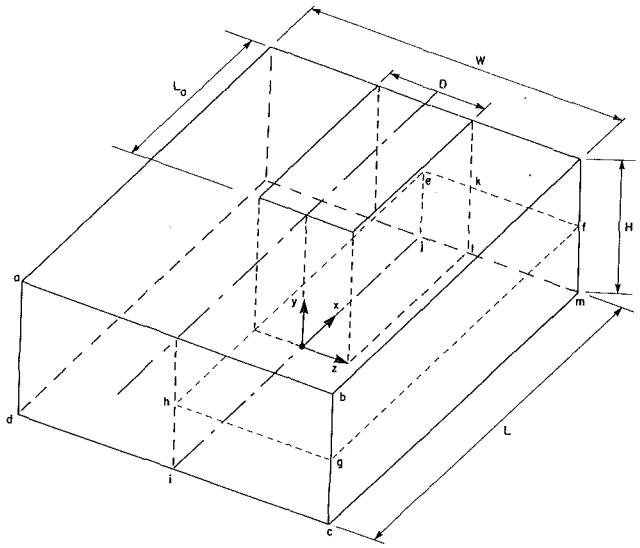

Fig. 4 Computational and physical domain

$$\text{Momentum:}\quad \frac{\partial}{\partial x_i}(\rho u_i u_j) = -\frac{\partial}{\partial x_j}\left(p + \frac{2}{3}\rho k\right) + \frac{\partial}{\partial x_i}\left\{\mu_{\text{eff}}\left[\frac{\partial u_j}{\partial x_i} + \frac{\partial u_i}{\partial x_j}\right]\right\} \tag{2}$$

Here the effective viscosity hypothesis has been used to represent the combined molecular and turbulent (Reynolds) stresses, where

$$\mu_{\text{eff}} = \mu + \mu_t \tag{3}$$

3.2 Turbulence Model. Following the practice of Launder and Spalding (1974), the turbulent viscosity is determined from the values of the turbulence kinetic energy k and its dissipation rate ϵ according to

$$\mu_t = \rho\, C_\mu \frac{k^2}{\epsilon} \tag{4}$$

The values of k and ϵ are determined from their own transport equations:

$$\frac{\partial}{\partial x_j}(\rho u_j k) = \frac{\partial}{\partial x_j}\left[\frac{\mu_{\text{eff}}}{\sigma_k}\frac{\partial k}{\partial x_j}\right] + G - \rho\epsilon \tag{5}$$

$$\frac{\partial}{\partial x_j}(\rho u_j \epsilon) = \frac{\partial}{\partial x_j}\left[\frac{\mu_{\text{eff}}}{\sigma_\epsilon}\frac{\partial \epsilon}{\partial x_j}\right] + [C_1 G - C_2 \rho\epsilon)\frac{\epsilon}{k} \tag{6}$$

$$G = \mu_t \frac{\partial u_i}{\partial x_j}\left[\frac{\partial u_i}{\partial x_j} + \frac{\partial u_j}{\partial x_i}\right] \tag{7}$$

The values of C_μ, C_1 and C_2 are given in the Nomenclature.

3.3 Boundary Conditions. With reference to Fig. 4, the solution domain is bounded by the horizontal planes hefg and ijmc with the obstruction volume excluded. The velocity component and gradients of all other variables perpendicular to the symmetry planes hefg and heji are set to zero.

At the outlet plane kfml, the distribution of velocity u is first estimated from the upstream value for the given outlet cell and then is adjusted to give the required total mass flow. Also, gradients of other variables along the main flow direction ($\partial/\partial x$) are assumed zero.

Close to the walls, including the obstruction walls, all the transport processes are modelled by using the wall function method (Launder and Spalding, 1974). This method is based on the one-dimensional Couette flow assumptions of constant shear stress and equilibrium of the production of k and its dissipation. The tangential velocity component is governed by the logarithmic law of the wall. No-slip and impermeable boundary conditions are also imposed along the walls.

Table 2 Geometrical parameters

H	0.2 m
W	0.5 m
L	0.52 m
L_0	0.25 m
D	0.152 m

At the calculational inlet plane hgci, a one-seventh power-law boundary layer profile for a smooth wall is imposed on the streamwise velocity. The cross-stream and transverse velocities are zero. The distributions of k and ϵ within the boundary layer are obtained by assuming local equilibrium and by using the mixing length hypothesis. Thus,

$$k = \tau/(\rho\, C_\mu^{1/2}), \quad \epsilon = \frac{\tau}{\rho}\frac{\partial u}{\partial y} \tag{8}$$

where $$\tau = \rho\, l_m^2\left[\frac{\partial u}{\partial y}\right]^2$$

and $$l_m = \min\,[\kappa y,\ C_\mu \delta] \tag{9}$$

The free-stream values of k and ϵ are evaluated from

$$k_\infty = 1.5\,(I\, U_\infty)^2 \tag{10}$$

and

$$\epsilon_\infty = k_\infty^{1.5}/\delta$$

4 Solution Procedure

The method adopted for solving equations (1), (2), (5) and (6) is similar to the TEACH-2E code (Gosman and Ideriah, 1976). The solution domain is discretized by the finite volume approach (Gosman and Ideriah, 1976). The discretized equations are formed by employing the hybrid central/upwind differencing scheme (Spalding, 1972). The sets of equations are solved by the SIMPLE algorithm (Patankar and Spalding, 1972). The solution of the equations is obtained by a block iteration procedure (Lai, 1987). Details of the numerical solution procedure are described elsewhere (Lai, 1987).

Computations are performed on a nonuniform grid, which comprises of $45 \times 24 \times 27$ interior grid points in the x, y, and z directions respectively. Under-relaxation factors of 0.25 for velocities and 0.5 for other variables are used. To achieve convergence, the number of iterations required is at least 600. The CPU time on the IBM 3090 computer is about 25 seconds per iteration.

The five cases studied are summarized in Table 3. Run 1 approximately simulates the conditions studied by Blair (1984). Figure 3 defines the various distances relating to the primary vortex. A discussion of grid dependence is given under "Effect of Grid Size."

5 Discussion of Results

5.1 Flow Pattern. Figures 5 and 6 show the orientation of the local velocities for Runs 1 to 5, respectively in the plane of symmetry and in the horizontal plane close to the endwall. Figure 7 shows the nondimensional planar velocity vectors, normalized by U_∞, for Run 4.

It is seen that for all the cases, a three-dimensional primary vortex is formed in the plane of symmetry. When the approaching boundary layer is in the region of adverse pressure gradient created by the obstruction, the layer starts to separate three-dimensionally. A part of the fluid, originally close to the endwall, climbs up along the shear layer originating at the saddle point S_1 (triangular symbols) defined in Fig. 3 and terminating in the region of formation of the primary vortex.

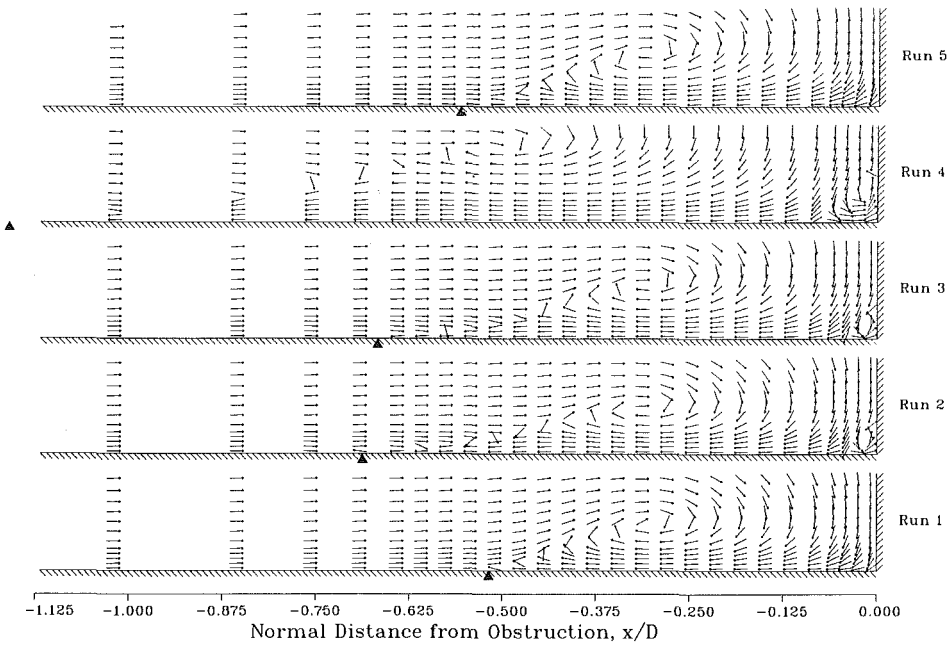

Fig. 5 Orientation of velocity vectors in the vertical plane of symmetry

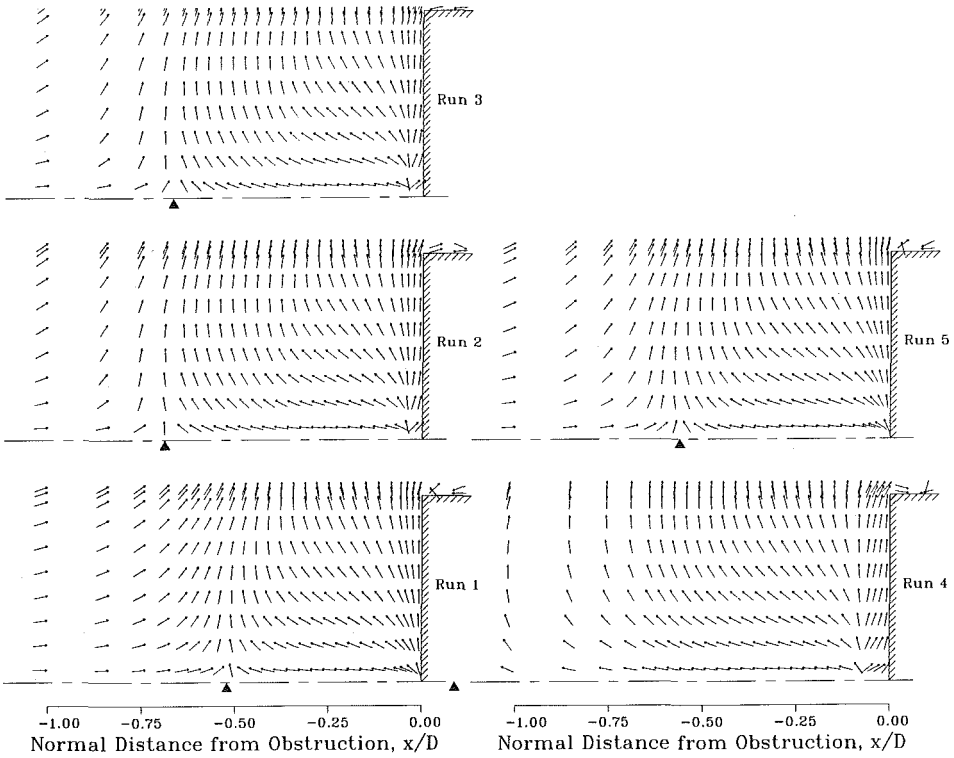

Fig. 6 Orientation of velocity vectors in the horizontal plane at $y/D = 3.29 \times 10^{-3}$

The part of the fluid farther away from the endwall passes over the vortex, approaches the obstruction, turns around the obstruction and passes tangentially around it. Some of this fluid is forced to move in the reverse direction toward S_1, is decelerated and deflected sideways as the result of blockage by the incoming flow. These results are similar to the results of Fig. 4 of Eckerle and Langston (1986).

It is noticed that at lower Re (Runs 2, 3 and 4), a corner vortex, indicated by the reversal of velocity vectors near the obstruction, occurs at the foot of the obstruction. This vortex disappears for Runs 1 and 5 and its size increases with the decrease of Reynolds number based on D. This behaviour is similar to the creation of corner eddies in cavity flows at lower Reynolds numbers as discussed by Nallasamy and Prasad (1977).

Figures 5 and 6 show the position of S_1. For lower Re, as the vortex stretches, the saddle point moves away from the obstruction. This fact is explainable by the lower shear stresses generated by smaller turbulent diffusion and small velocity gradients inside the boundary layer.

Figure 8 shows the contours of nondimensional turbulence kinetic energy, $k^* = k/(\frac{1}{2}U_\infty^2)$, in the vertical plane of sym-

metry. The high level of turbulence is clearly identified with the core of the primary vortex. Also it is observed that the thickness of the region below the primary vortex, which contains the values of k^* between 0 and 0.07, varies for the different runs. This thickness increases with the decrease of Re and with the movement of the saddle point away from the obstruction, indicating lower turbulent diffusion as discussed above. It is shown later that the high level of turbulence is accompanied by a change in the distribution of static pressure.

5.2 Pressure Distribution. Figure 9 shows the distribution of nondimensional static pressure, $C_p = (p - p_\infty)/(\frac{1}{2}\rho U_\infty^2)$, on the endwall in the plane of symmetry. It is seen that Runs 1 and 2 (both of the same D^* but of different Re) collapse to the same curve between the primary vortex and a point at about $x/D = -0.05$. At the obstruction, C_p for Run 1 approaches the value of 1, while for Run 2 pressure drops, indicating the existence of a corner vortex. Similarly, Runs 3 and 5 collapse to another curve, reaching lower values at the obstruction. These results confirm Baker's results for a cylinder (Baker, 1980), which indicate that C_p curves mainly depend on D^* and only slightly on Re. One also observes that for Run 4 (lowest value of D^* tested), C_p at the obstruction drops to a much lower value than for the other runs. This leads to another conclusion, namely, that C_p at the obstruction drops monotonically with the decrease of D^*.

The above results can be explained as follows (Baker, 1979). Inspection of Table 3 shows that as Re changes, the vertical position of the primary vortex y_v/D, defined in Fig. 3, changes insignificantly. Hence when D^* increases, which implies that the approaching boundary layer becomes thinner, the fluid flowing near the foot of the obstruction is expected to come from a region of higher nondimensional velocity u/U_∞, i.e. close to the free-stream value. Consequently, for the cases of higher Re and D^*, the static pressure near the obstruction is closer to the stagnation pressure of the free stream.

Comparison of Figs. 5 and 9 shows that for all the runs with better formed vortices, the pressure trough on the endwall is beneath the center of the primary vortex. Similar results were obtained for cylinders (Baker, 1980). Similarly to the result of Eckerle and Langston (1986), the saddle points occur in the region of the incident boundary layer with adverse pressure gradients, and not at the local pressure peaks.

In addition to Fig. 9, Fig. 10 shows the static pressure contours in the vertical plane of symmetry. The regions of low pressure are seen to be associated with the centers of the primary vortices. This is particularly clear for the two high Reynolds number flows (Runs 1 and 5). It is confirmed that uniform pressure exists near the inlet plane to the computational domain, as expected.

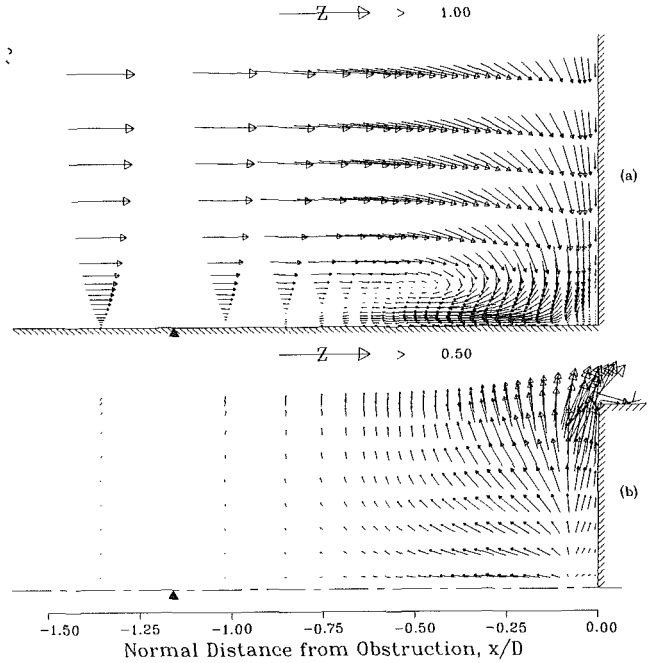

Fig. 7 Velocity vectors for Run 4: (a) the vertical plane of symmetry; (b) the horizontal plane at $y/D = 3.29 \times 10^{-3}$

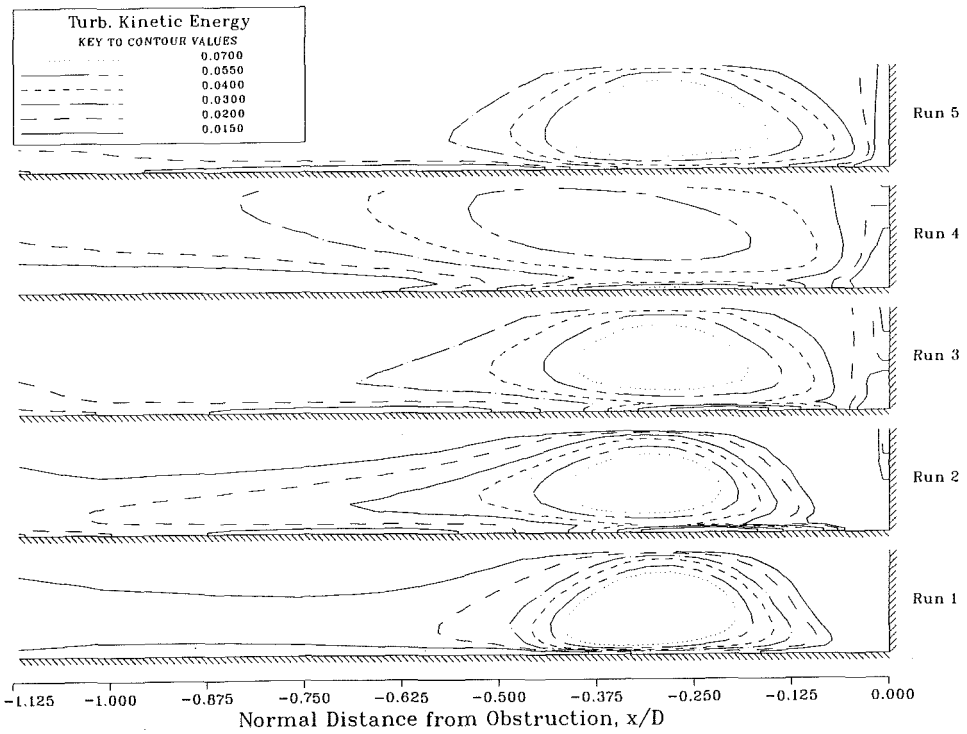

Fig. 8 Contours of turbulence kinetic energy in the vertical plane of symmetry

Table 3 Results of computations

Run No.	U_∞ m/s	D mm	δ^* mm	$D^* = \frac{D}{\delta^*}$	$\frac{U_\infty D}{\nu}$	$\mathrm{Re} = \frac{U_\infty \delta^*}{\nu}$	$\frac{x_s}{D}$	$\frac{x_v}{D}$	$\frac{y_v}{D}$
1	9.1	152	4.45	34.2	6.9×10^4	2.0×10^3	0.52	0.30	0.065
2	0.91	152	4.45	34.2	6.9×10^3	2.0×10^2	0.69	0.31	0.066
3	0.91	152	12.0	12.7	6.9×10^3	5.4×10^2	0.67	0.31	0.071
4	0.91	50	12.0	4.2	2.3×10^3	5.4×10^2	1.16	0.49	0.105
5	3.38	152	12.0	12.7	2.6×10^4	2.0×10^3	0.56	0.31	0.071

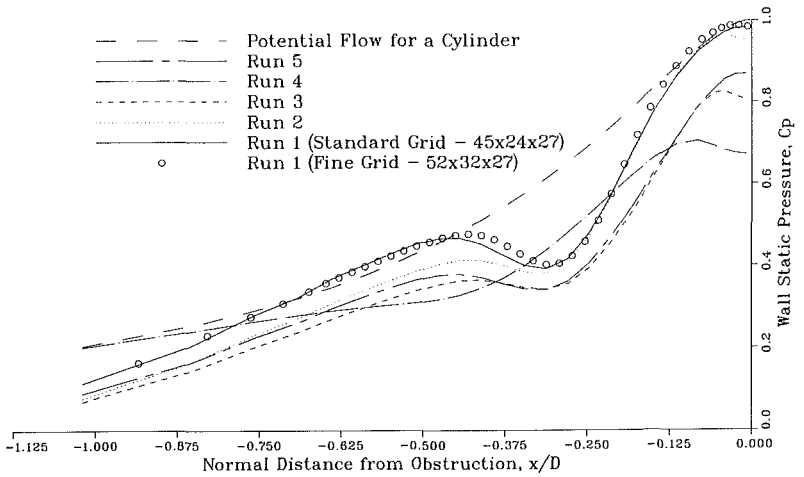

Fig. 9 Distribution of static pressure on the endwall in the vertical plane of symmetry

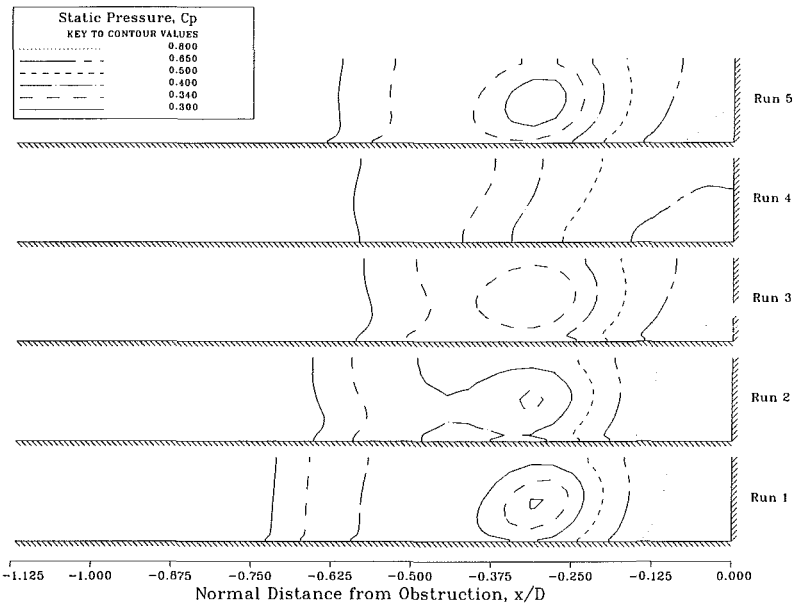

Fig. 10 Contours of static pressure in the vertical plane of symmetry

Figure 11 shows the pressure contours on the horizontal plane close to the endwall. It is verified that high pressure exists at the foot of the obstruction in the vertical plane of symmetry. The overall distributions are very similar to the experimental results of Eckerle and Langston (1986) and Vasilić-Melling (1977). The latter experimental results are for a flow over a cubical (rather than a tall) obstruction. Hence they are not suitable for a quantitative comparison with the present numerical results. As the general shapes of the distributions are very similar for Runs 1 and 2 and for Runs 3 and 5, the weak dependence of the phenomenon on Re (at least in this range of Re) is confirmed.

Figure 12 shows the contours of the effective pressure C_{pe} in the vertical plane of symmetry. This quantity is of interest to workers concerned with pressure measurements in turbulent flows. The figure demonstrates that for turbulent vortex flows, the change of effective pressure across the vortex is smaller than the change of static pressure. This is due to a compensatory effect of high turbulence in the region of low static pressure in the core of the vortex.

For general comparison, Fig. 9 also includes the potential flow solution for a circular cylinder. The best overall agreement at large distances from the obstruction is seen for Run 4 and this can be explained as follows. Figure 8 indicates that comparatively low turbulence levels existing for Run 4 imply lower losses in the reversed flow. The blockage effect of the obstruction for this run is small and there is no indication of the existence of a vortex core characterized by a region of low

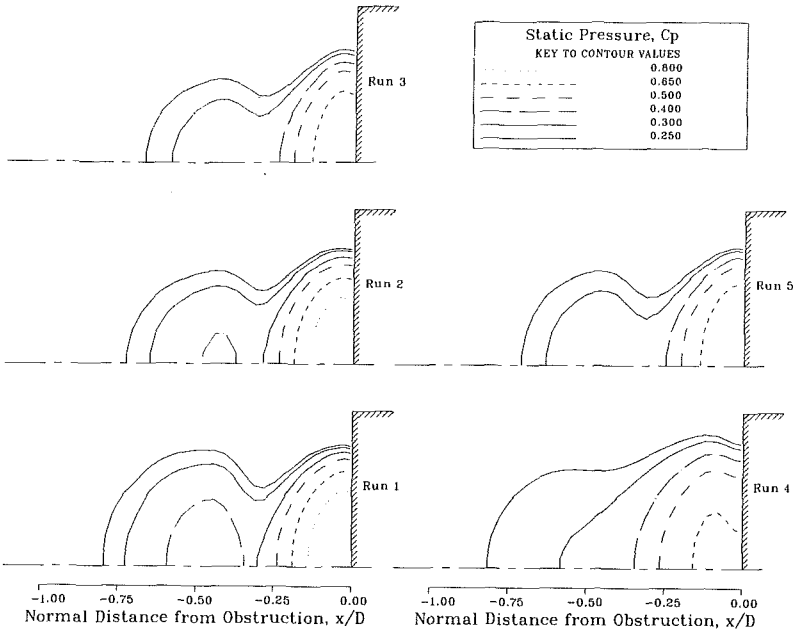

Fig. 11 Static pressure distribution in the horizontal plane at $y/D = 3.29 \times 10^{-3}$

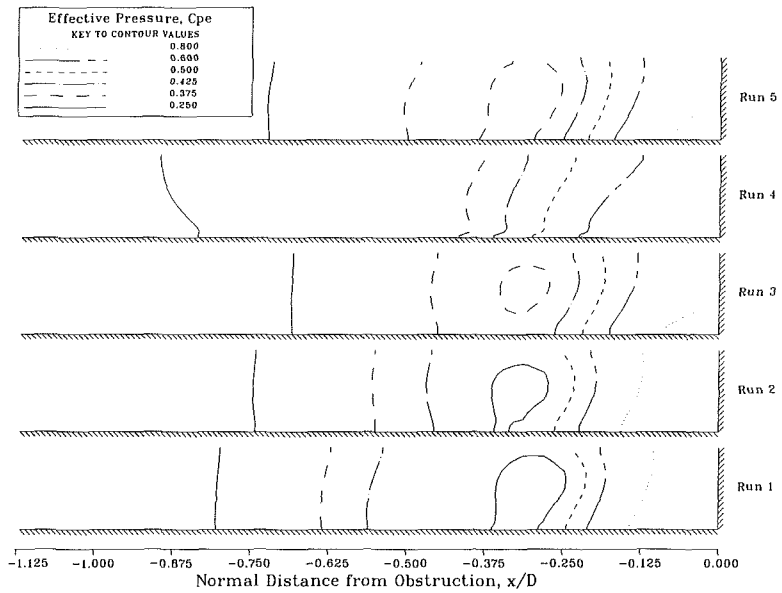

Fig. 12 Contours of effective pressure in the vertical plane of symmetry

pressure (Fig. 10). The flow for Run 4 can therefore be approximated by two parallel streams: the top stream away from the endwall moving toward the obstruction and the bottom stream close to the endwall moving toward the saddle point, which for Run 4 is much farther away from the obstruction. The reversed flow over the distance of $x/D = 1$ from the obstruction is subjected to smaller losses, and pressure on the endwall is more representative of the pressure at a large vertical distance from the endwall, which in turn is closer to the potential value.

5.3 Vortex Properties. Figure 3 defines x_s, the distance of the saddle point from the obstruction, and the distances of the primary vortex (x_v and y_v), used for the comparison of trends with the experimental results of Blair (1987) and Baker (1980). There is very little experimental data available for the rectangular obstruction. The computed values of x_s are deduced from the distributions of wall shear stresses.

The value of x_s/D for Run 1 can be compared with the results for a rectangular obstruction (Blair, 1987) and for a cylindrical obstruction (Baker, 1980). Thus Run 1 gives $x_s/D = 0.52$, while the analysis by the present authors of the flow visualization pattern (Blair, 1987) gives $x_s/D = 0.6 \pm 0.05$. Deduced from Fig. 10 of Baker (1980), the value of x_s/D is approximately 0.6, agreeing closely with the result of Blair (1987). This shows great similarity of results for the two geometries.

The dependence of the computed x_s/D on Re and D^* shows a similar behaviour to the results of Baker (1980). Thus at constant $\mathrm{Re} = 2.5 \times 10^3$ (Runs 1 and 5), x_s/D increases as D^* decreases. Similar behaviour is seen for constant $D^* = 34.2$ (Runs 1 and 2), x_s/D increasing as Re decreases. The latter behaviour is also seen for constant $D^* = 12.7$ (Runs 3 and 5). As discussed under "Flow Pattern," an increase in x_s/D occurs when the turbulence level below the primary vortex is lower (e.g. Run 4).

Table 3 shows that for all the runs at higher values of D^*, the values of x_v/D appear to depend only slightly on both Re and D^*. However, y_v/D depends on D^*: as D^* increases, y_v/D decreases. In addition, as D^* decreases, δ^* increases only in relation to D making the flow around the vortex "less potential." Hence a lower peak value of C_p exists, as demonstrated in Fig. 9.

In the present work there is no evidence of the existence of the four-vortex model of Hunt et al. (1978). The saddle point S_1 of Fig. 2 can be identified for all the results computed, and the attachment point A_2 can also be identified for Runs 2, 3 and 4. However, there is no evidence of the existence of points A_1 and S_2 of Fig. 1.

It is possible that due to numerical diffusion and the difficulty of modelling turbulence in recirculating flows, the present numerical algorithm may not be able to simulate properly the rather weak secondary vortices, which would exist in the four-vortex model, in addition to the main primary vortex. However, if points A_1 and S_2 were to exist, one would expect some qualitative indication of the change of flow direction associated with these points, but no such behaviour can be seen in Figs. 5 to 7. A possible explanation could be that the present computed results are for a steady flow, while the points A_1 and S_2, perceived in the experiment (Blair, 1984), could be a manifestation of the mobility of the saddle point S_1 due to an unsteady flow in the vicinity of the primary vortex as noted by Eckerle and Langston (1986) and Blair (1984). Another explanation could be that the flow investigated is turbulent rather than laminar. Baker (1979) has noted that multiple-vortex systems can be observed clearly for low Reynolds number laminar flows. In the present problem, the turbulent boundary layer generates much larger wall shear stresses, which may "annihilate" any small vortices close to the endwall.

It is concluded that the present numerical results for a steady turbulent flow can only be explained by the simple vortex model of Eckerle and Langston (1986). The flow pattern for Run 4 of Fig. 7 is almost identical to this simple model.

5.4 Effect of Grid Size. The above results are obtained with a grid $45\times24\times27$, which makes great demands on the available computing facilities. Nonetheless, some estimate of the adequacy of this grid (called "standard") is necessary.

A calculation to repeat Run 1 is carried out using a grid of $52\times32\times27$, which is near the limit of the available computing facilities, both in terms of memory (14 MB) and execution time (over 40 hours).

The grid is refined in the x and y directions in the region of the vortex. Thus, in the region $-0.658<x/D<0$ upstream of the obstruction, 22 cells are replaced by 35 cells, and in the region $0.0724>y/D>0$, 8 cells are replaced by 16 cells. In the x direction the extra precision upstream of the obstruction is obtained partly at the expense of reduced resolution downstream of the plane of the face of the obstruction.

It is found that the results for the two grids are very similar. Figure 9 shows that the difference between the standard and fine grid results is small. A small deviation occurs in the region of the adverse pressure gradient for the returning boundary layer (at $x/D\approx-0.375$). Similar agreement is obtained for the position of the saddle point, the fine grid result being slightly closer to the experimental value (standard grid $x_s/D=0.52$, fine grid $x_s/D=0.54$).

It is concluded that the adopted grid is adequate for the purposes of this paper.

6 Conclusions

1 A mathematical model and a numerical algorithm have been developed and successfully applied to study flows ahead of a rectangular obstruction placed in a turbulent boundary layer. The numerical results confirm the trends for circular cylinders and agree quantitatively with the limited experimental data for a rectangular obstruction.

2 It is shown that the general flow characteristics for cylinders and rectangular obstructions are similar.

3 The numerical results indicate only one primary vortex together with a corner vortex at lower Re. The usually accepted four-vortex model (Hunt et al., 1978) is not observed.

4 The horizontal position of the primary vortex is practically independent of Re and D^*. However, the vertical position of this vortex depends on D^*, and x_s/D depends on both Re and D^*.

5 The position of the saddle point appears to depend on the level of turbulence near the endwall in the vicinity of the primary vortex. This point moves closer to the obstruction as the turbulence level increases.

6 The endwall static pressure coefficient, C_P, depends mainly on D^* and only slightly on Re. In addition, a further modification in C_P occurs when a corner vortex exists.

7 There is a definite need for further experimental work on rectangular obstructions.

Acknowledgments

The authors are grateful to Dr. R. G. Williamson for valuable comments on this work and to Professor Martha Salcudean for permission to use the code TEMA, on which the present code is based.

References

Baker, C. J., 1979, "The Laminar Horseshoe Vortex," *Journal of Fluid Mechanics*, Vol. 95, Part 2, pp. 347–367.

Baker, C. J., 1980, "The Turbulent Horseshoe Vortex," *Journal of Wind Engineering and Industrial Aerodynamics*, Vol. 6, Nos. 1 and 2, pp. 9–23.

Belik, L., 1973, "The Secondary Flow About Circular Cylinders Mounted Normal to a Flat Plate," *The Aeronautical Quarterly*, Vol. 24, No. 1, pp. 47–54.

Blair, M. F., 1984, "Heat Transfer in the Vicinity of a Large-Scale Obstruction in a Turbulent Boundary Layer," AIAA Paper No. 84-1723.

Blair, M. F., 1987, Private communication.

Eckerle, W. A., and Langston, L. S., 1986, "Horseshoe Vortex Formation Around a Cylinder," ASME Paper No. 86-GT-246.

Gosman, A. D., and Ideriah, F. D. K., 1976, "TEACH-2E: A General Computer Programme for Two-Dimensional Turbulent Recirculating Flows," Internal Report, Department of Mechanical Engineering, Imperial College, University of London, U.K.

Hawthorne, W. R., 1954, "The Secondary Flow About Struts and Airfoils," *Journal of the Aeronautical Sciences*, Vol. 21, No. 9, pp. 588–609.

Hunt, J. C. R., Abell, C. J., Peterka, J. A., and Woo, H., 1978, "Kinematic Studies of the Flows Around Free or Surface-Mounted Obstacles; Applying Topology to Flow Visualizaton," *Journal of Fluid Mechanics*, Vol. 86, pp. 179–200.

Lai, K. Y. M., 1987, "TURCOM: A Computer Code for the Calculation of Transient, Multi-Dimensional, Turbulent, Multi-Component Chemically Reactive Fluid Flows, Part 1: Turbulent, Isothermal and Incompressible Flow," NRC Technical Report TR-GD-011.

Launder, B. E., and Spalding, D. B., 1974, "The Numerical Computation of Turbulent Flows," *Computer Methods in Applied Mechanics and Engineering*, Vol. 3, pp. 269–289.

Nallasamy, M., and Prasad, K. K., 1977, "On Cavity Flow at High Reynolds Numbers," *Journal of Fluid Mechanics*, Vol. 79, Part 2, pp. 391–414.

Patankar, S. V., and Spalding, D. B., 1972, "A Calculation Procedure for Heat, Mass and Momentum Transfer in Three-Dimensional Parabolic Flows," *International Journal of Heat and Mass Transfer*, Vol. 15, pp. 1787–1806.

Spalding, D. B., 1972, "A Novel Finite-Difference Formulation for Differential Equations Involving Both First and Second Derivatives," *International Journal for Numerical Methods in Engineering*, Vol. 4, pp. 551–559.

Vasilić-Melling, D., 1977, "Three-Dimensional Turbulent Flow Past Rectangular Bluff Bodies," Ph.D. thesis, Imperial College, University of London, U.K., (also Report No. HTS/77/10).

Boundary Layer Measurements at an Internal Free Surface in a Partially Filled Horizontal and Rapidly-Rotating Container

T. J. Singler
Assistant Professor of Mechanical Engineering,
State University of New York at Binghamton,
Binghamton, NY 13901

Steady flow in a partially filled horizontal circular cylinder rotating rapidly about its symmetry axis is investigated experimentally. Radial boundary layer profiles of the azimuthal velocity in the neighborhood of the internal free surface are reported for a range of inverse Froude numbers and for two types of free surfaces. Results indicate good agreement with an existing theory.

Introduction

The problem of flow in a partially filled rotating cylindrical container has been investigated in a number of diverse contexts. Ruschak and Scriven (1976) studied rimming flow as a model for industrial processes such as spin casting of plastics, cream separation, and liquid degassing. Cooper (1979) explored the potential of rotating liquid metal free surfaces in connection with liners for imploding plasmas. The flow about a rotating buoyant core was analyzed by Greenspan (1976) as a possible model to explain the generation of secondary vortices about the main funnel of a tornado. Sedney (1985) discussed the problem of spin-up/spin-down of partially filled rotating containers in the larger context of aerodynamic stability of liquid-filled spin-stabilized projectiles. In still another context, Hendricks and Morton (1979) examined the problem of vibration in partially filled rotors.

A liquid partially filling a cylindrical container rotating about its symmetry axis which is perpendicular to the direction of gravity can exist in a number of flow states. Depending on the region of parameter space (rotation rate, void fraction, viscosity, etc.), the possible flow states include: a steady laminar annular flow with a well defined internal free surface; a stable oscillatory flow in which the internal free surface supports waves; an unsteady vortical flow in which there appears to be an aperiodic shedding of line vortices from the internal free surface; and a highly turbulent flow which precedes aircore formation and follows aircore collapse. This last flow shares a small part of parameter space with the steady annular flow in a metastable region. Gans and Yalisove (1982) provide a stability map delineating these flow states. The steady annular flow state is contiguous to all other flow regimes. It is the simplest of the various flows and has been studied the most intensively. Understanding it seems essential to the development of insight into some of the other more complex flows.

The laminar state occurs when the container rotation rate is sufficiently rapid that centrifugal forces dominate the flow and the liquid assumes an annular shape bounding an aircore of cylindrical form (see Fig. 1). An interesting variation of this flow occurs when a rigid buoyant float (with a length just less than that of the container) is placed in the container and the remaining container volume is filled with liquid; the float is not constrained and is free to move about in the container. For sufficiently high rotation rates the float axis aligns itself parallel to the container axis and an annular flow configuration obtains which appear exactly like that of the aircore case. The flow in either case may be regarded as a perturbed rigid body rotation. Despite their similarities, however, a qualitative and quantitative difference exists between the two cases which derives from the differences in the boundary conditions at the free interface: for the case of the aircore the appropriate boundary condition is that of vanishing shear while that for the rigid float is a no-slip condition. The resulting velocity field differences are mainly manifest in the boundary layer region adjacent to the free interface. The boundary layer structure at this interface is tiered and the lowest order layer is an Ekman layer.

Phillips (1960) first studied the flow in a horizontal partially filled cylinder in rapid rotation about its symmetry axis. Considering the aircore case, he used an inviscid two-dimensional (2-D) linear model pivoted about a state of rigid rotation. His results showed the lowest order correction to rigid rotation to be singly periodic in the azimuthal coordinate θ with magnitude $0(\epsilon)$, where $\epsilon = g/\Omega^2 a$. He also predicted that the core was displaced from the rotation axis by a distance $0(\epsilon)$ in the direction of gravity. Subsequent models were more complex. Greenspan (1976) considered the rigid float case using a 2-D, viscous, and weakly nonlinear model. He found boundary layers on the core and container boundaries and predicted a retrograde rotation of the float. The absolute rotation of the float is prograde; however, observed from a frame rotating with the container, the float rotates with a sense opposite to that of the container. Gans (1977, 1979) considered both aircore and rigid float cases using a viscous, weakly nonlinear, but 3-D model. The added dimension allowed for Stewartson layers on the core and container sidewalls, the

Contributed by the Fluids Engineering Division for publication in the JOURNAL OF FLUIDS ENGINEERING. Manuscript received by the Fluids Engineering Division May 13, 1988.

$E^{1/4}$-layer of which contributed negligibly to the aircore retrograde rotation but dominated that for the rigid float. Thus Gans' prediction for retrograde rotation of the float conflicted with that of Greenspan. His measurements of float retrograde rotation showed very good agreement with his own theoretical prediction while differing significantly from Greenspan's. Whiting (1978) verified the existence of the Stewartson layers on the aircore boundary. He measured aircore displacement and retrograde rotation and verified Phillips' prediction for the former. His measurements of retrograde rotation, however, disagreed sharply with Gans' (1977) theoretical prediction for the aircore, differing by as much as a factor or seven and falling between predictions for the rigid float and aircore; all his experiments were performed using aqueous glycerol solutions. Motivated by the situation of the data between the two theories, both Whiting (1978) and Gans and Yalisove (1982) suggested the discrepancies were due to nonideal behavior of the aircore free surface. Presumably they were alluding to the well-known ability of absorbed surface active impurities to alter the behavior of a fluid interface through changes in the interfacial rheological properties, the most important of which are the surface dilatational elasticity and surface shear viscosity. Large values for these properties can produce an interface with rigid-like characteristics (Quinn and Scriven (1970)). Gans and Yalisove measured the azimuthal component of velocity in water for the aircore case and found good agreement with Phillips' inviscid prediction but their apparatus was not sensitive enough to resolve the boundary layers.

This paper reports measurements of the absolute azimuthal velocity in the core boundary layer. Two types of cores are investigated, the aircore and rigid float, in order to study the boundary layer flow for limiting forms of interfacial behavior. A brief outline of the relevant theory is given in the following section. Description of the apparatus and experimental procedures is given in the subsequent section, followed by presentation and discussion of results.

Theoretical Background

Let Ω, a, g, ρ, and ν represent the container rotation rate, container inside radius, gravitational acceleration, fluid density, and kinematic viscosity. If a, Ωa, and $\rho\Omega^2 a^2$ are taken as typical values of position, velocity, and pressure, the dimensionless equations of steady motion for an incompressible fluid may be written

$$\mathbf{V}\cdot\nabla\mathbf{V}+\nabla P-\mathrm{E}\nabla^2\mathbf{V}=\epsilon\hat{\mathbf{g}} \tag{1}$$

$$\nabla\cdot\mathbf{V}=0 \tag{2}$$

where $\mathbf{V}$ and P are the absolute velocity and pressure, $\hat{\mathbf{g}}$ is a unit vector in the direction of gravity, $\mathrm{E}=\nu/\Omega a^2$ is the Ekman number, and $\epsilon=g/\Omega^2 a$ is the inverse Froude number. An additional dimensionless parameter, $c=R_c/a$, where R_c is the core radius, characterizes the size of the core (for the case of the aircore which is not perfectly circular, R_c may be thought of as the radius of a cylinder formed from the void fraction volume, with a length equal to that of the container). Both ϵ and E are assumed small compared to one. Solutions to the set of equations (1) and (2) must satisfy the appropriate boundary conditions. On all container walls, a no-slip condition is required. At the core boundary, a set of conditions must be satisfied which depend on the nature of the interface under consideration. For the aircore case, the conditions to be satisfied are the usual kinematic condition, zero shear stress, and continuity of pressure across the surface (surface tension effects are neglected). For the float case, the conditions are no-slip, zero net force on the float, and zero net torque on the float (the latter two conditions follow from the assumption of steady flow).

Equations (1) and (2) with $\epsilon=0$ admit a rigid rotation solution. For sufficiently small ϵ, the term $\epsilon\hat{\mathbf{g}}$ forces small departures of the flow from rigid rotation. It is natural then to express each dependent variable as the sum of a rigid component and a perturbation which may be written as an expansion in powers of the parameter ϵ:

$$\mathbf{V}=\frac{\Omega\times\mathbf{r}}{\Omega a}+\sum_{i=1}^{\infty}\epsilon^i\mathbf{v}_i \tag{3}$$

$$P=P_0+\frac{1}{2}(r^2-c^2)+\sum_{i=1}^{\infty}\epsilon^i p_i \tag{4}$$

Nomenclature

a = container radius (m)
A_1, A_2, B_1, B_2 = parameters in interior solution
$\tilde{A}, \tilde{B}$ = parameters in boundary layer solution
c = ratio of core radius to container radius, R_c/a
E = Ekman number, $\nu/\Omega a^2$
f = digital Doppler frequency
g = acceleration of gravity (m/s^2)
$\hat{\mathbf{g}}$ = unit vector in direction of gravity
k = LDV calibration constant
K_1, K_2 = parameters in data curve fit
P = absolute pressure
P_0 = interfacial pressure
p = perturbation pressure
$\mathbf{r}$ = position vector (m)
r = dimensionless radius, $|\mathbf{r}|/a$
R = boundary layer coordinate, $(c-r)/(2\mathrm{E})^{1/2}$
R_c = core radius (m)
$\mathbf{v}$ = perturbation velocity
$\mathbf{V}$ = absolute velocity vector
V = absolute azimuthal velocity
v = perturbation azimuthal velocity
$\hat{z}$ = unit vector in direction of rotation
ϵ = inverse Froude number, $g/\Omega^2 a$
ν = kinematic viscosity (m^2/s)
ρ = density (kg/m^3)
θ = azimuthal coordinate
Ω = rotation rate (vector quantity boldface) (s^{-1})

Subscripts

1 = first-order perturbation solutions
2 = second-order perturbation solutions

Symbols

$\hat{}$ = interior quantity
$\tilde{}$ = boundary layer quantity

Substitution of equations (3) and (4) into (1) and (2) and grouping in like-powers of ϵ leads to an ordered sequence of linear problems for the $\mathbf{v}_i$ and p_i the first two of which are

$$0(\epsilon): \quad \mathbf{v}_{1,\theta} + 2\hat{\mathbf{z}} \times \mathbf{v}_1 + \nabla p_1 - \mathrm{E}\nabla^2 \mathbf{v}_1 = \hat{\mathbf{g}} \tag{5}$$

$$\nabla \cdot \mathbf{v}_1 = 0 \tag{6}$$

$$0(\epsilon^2): \quad \mathbf{v}_{2,\theta} + 2\hat{\mathbf{z}} \times \mathbf{v}_2 + \nabla p_2 - \mathrm{E}\nabla^2 \mathbf{v}_2 = -\mathbf{v}_1 \cdot \nabla \mathbf{v}_1 \tag{7}$$

$$\nabla \cdot \mathbf{v}_2 = 0 \tag{8}$$

where the subscript θ in the first terms of (5) and (7) denotes the derivative with respect to θ of the components of the $\mathbf{v}_i$ only and $\hat{\mathbf{z}}$ is a unit vector in the direction of rotation. In the $r-\theta$ coordinate system, the components of the $\hat{\mathbf{g}}$ are singly periodic in θ. As $\hat{\mathbf{g}}$ is the only inhomogeneity in the $0(\epsilon)$ problem, it follows that $\mathbf{v}_1$ and p_1 are singly-periodic. The interaction of $\mathbf{v}_1$ with itself leads to both a rectified and doubly periodic forcing term in (7). Consequently $\mathbf{v}_2$ and p_2 have both axisymmetric and doubly periodic dependencies. The axisymmetric aximuthal component of $\mathbf{v}_2$ divided by the nominal core radius gives the lowest order contribution to the retrograde rotation; consistent with the discussion in the Introduction, the component of $\mathbf{v}_2$ is negative for both aircore and float cases.

A salient analytical difficulty in the problem arises from the non-concentricity of the radial boundaries (see Fig. 1). Various approaches have been used to overcome this difficulty. Phillips (1960) and Ruschak and Scriven (1976) used a coordinate system centered in the container and described the core boundary using a Taylor series about $r=c$. Greenspan used a bilinear transformation to map the two boundaries concentric. Gans (1977, 1979) resolved the problem by using two coordinate systems, one centered with respect to each radial boundary and by solving the equations of motion subject to appropriate boundary conditions in each system; he then matched the two sets of solutions at a point remote from either boundary. The measurements reported herein were all made in the neighborhood of the core; consequently Gans' results in core coordinates are a natural choice for comparison. Gans found solutions for the $\mathbf{v}_i$ and p_i in (3) and (4) of the form

$$\mathbf{v}_i = \hat{\mathbf{v}}_i + \tilde{\mathbf{v}}_i, \; p_i = \hat{p}_i + \tilde{p}_i \tag{9}$$

where caret quantities describe the flow away from the boundaries and tilde quantities correct the interior solutions at the boundaries. The general form of his linear $(0(\epsilon))$ perturbation solutions are identical for both aircore and float cases. In particular the azimuthal component of $\mathbf{v}_1$ in core coordinates far from the container endwalls is

$$v_1 = \hat{v}_1 + \tilde{v}_1 \tag{10}$$

where

$$\hat{v}_1 = \left[A_1 - \frac{B_1}{3r^2}\right]\sin\theta + \left[A_2 - \frac{B_2}{3r^2}\right]\cos\theta \tag{11}$$

$$\tilde{v}_1 = \exp R[\tilde{A}\cos(R+\theta) + \tilde{B}\sin(R+\theta)], \tag{12}$$

and

$$R = \frac{c-r}{(2\mathrm{E})^{1/2}}$$

For the expressions for the constants in (11) and (12), the reader is referred to Gans (1977, 1979). His solutions are valid for the range of parameter space given by

$$0 < \mathrm{E}^{1/2} \ll \epsilon \ll \mathrm{E}^{1/4} \ll c < 1. \tag{13}$$

Gans derives only the axisymmetric solutions at $0(\epsilon^2)$, presumably because the doubly-periodic solutions do not influence the retrograde rotation (like the singly periodic solution, their azimuthal average is zero). The axisymmetric solutions will not be included in the theoretical plots which follow.

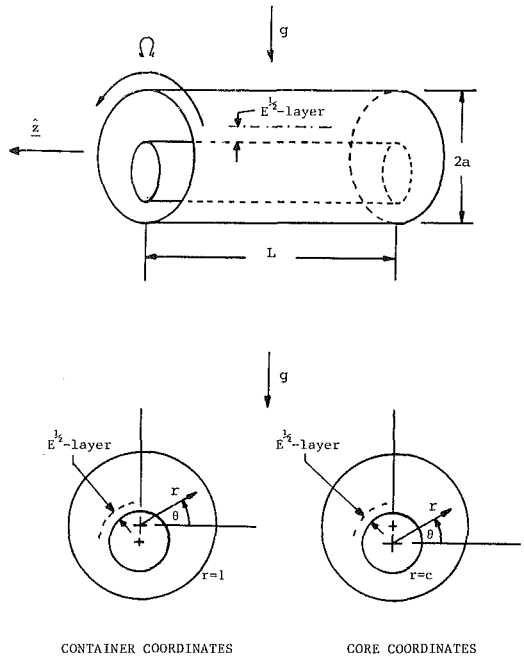

Fig. 1 Views of the experiment

Experimental Methods

The experimental container had a length of 1.969×10^{-1} m and an inside diameter of 1.575×10^{-1}m. The main body of the container was fabricated from stainless steel tubing and the endwalls were made of ordinary glass, machined parallel to within 2.54×10^{-5} m. There were two tapped holes with threaded plugs and O-ring seals for purposes of adding and withdrawing liquid. The main hole was located on the axial midpoint of the container sidewall; a smaller secondary hole was located in the sidewall adjacent to one of the endwalls for the purpose of removing small bubbles. The inside ends of the plugs were machined to conform with the container wall. The container was supported externally by bearings which were mounted in bearing pillows secured to the top of a milling machine turret. The container was belt driven by a motor, was dynamically spun-balanced, and rotated with a diametral concentricity of better than 2.54×10^{-5}m. The rotation rate of the container was regulated by controlling the speed of the motor. A light intercept-photodiode assembly optically encoded the container rotation rate, generating an electrical pulse train which was used to compute the rotation period using software in a MC6800 microprocessor $(\mu-P)$. The measured period was compared to a desired period stored in the $\mu-P$ which updated a reference voltage via digital circuitry to a modified commercial speed controller that drove the motor. This closed loop control maintained a container rotation rate accuracy of ±0.10 rad/sec over the range $41.89-73.30$ rad/s.

A laser Doppler velocimeter (LDV), configured in the dual beam forward scatter mode, was mounted as an integral unit to the milling machine carriage, thus permitting three-dimensional orthogonal positioning of the probe volume with respect to the container and alleviating the need to refocus the receiving optics after repositioning of the probe (see Figs. 2 and 3). The LDV was aligned to measure the azimuthal component of the flow. The dimensions of the probe volume were calculated from the LDV optical parameters to be 1.6789×10^{-4}m, 1.6968×10^{-4}m, and 1.1624×10^{-3}m, in the radial, azimuthal, and axial directions of the container, respectively. The analog signal from the photomultiplier was processed by a DISA 55L20 frequency tracker which provided an analog voltage proportional to Doppler frequency. This

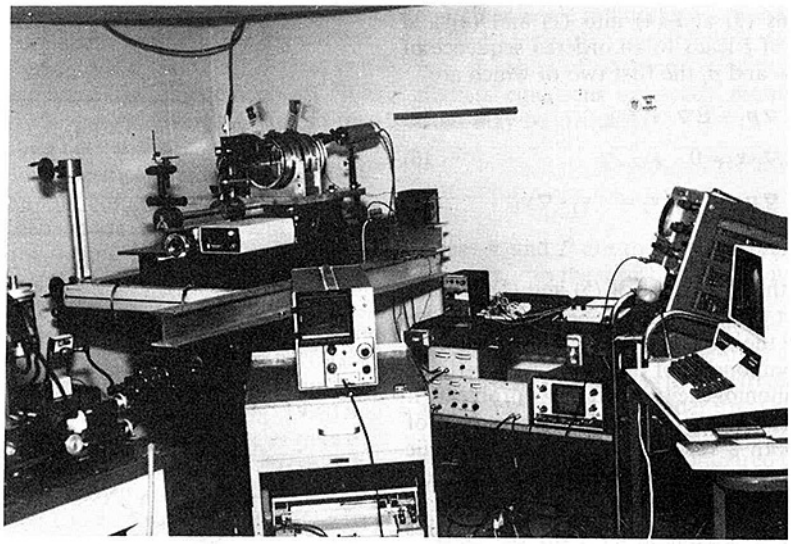

Fig. 2 Photograph of the measurement platform and velocimeter system

TOP VIEW OF LDV SYSTEM

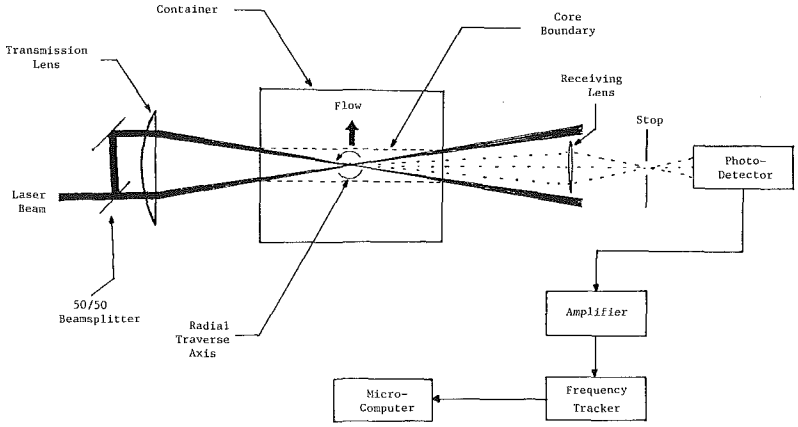

Fig. 3 Schematic of laser doppler velocimeter system showing principal optical components relative to the experimental container, and signal processing

voltage was digitized and the digital number stored in memory on a microcomputer. The data acquisition process was controlled by an assembly language routine accessed from Basic. To construct a single frequency datum point, 2000 samples were acquired over a time interval of several hundred rotation periods. The frequency was taken to be the average of the samples: precision indices of the mean were very small, typically less than 0.05 percent.

The test liquids used were aqueous glycerol solutions, 87 percent by weight of glycerol, (prepared from laboratory-grade glycerol and doubly distilled water), and a 100 cSt silicone oil. Their viscosity-temperature responses were measured using an Ubbelohde-type viscometer and constant temperature bath. The temperature of the liquid in the cylinder was measured before and after data runs and the viscosity was taken to be the viscosity at the average temperature; the temperature rise during any experiment never exceeded 1°C. Test liquids with viscosity values of approximately 100 cSt were chosen to make the Ekman ($E^{1/2}$) boundary layers thick enough to resolve experimentally while not allowing the sidewall $E^{1/4}$-layers on the core and container boundaries to overlap. Aluminum oxide ($\sim 3\mu$m dia) was used as a scattering agent for the silicone oil; the aqueous glycerol solutions required no seeding. The fidelity of seeding particles as Lagrangian tracers was poorest for the aluminum oxide seeding in silicone oil. An estimate of centrifugation velocities, based on equilibrium between centrifugal buoyancy and Stoke's drag, was 3×10^{-6} m/s, a value less than the predicted $0(\epsilon)$ radial velocities. Centrifugation of scattering centers was easily reversed, however, by occasionally letting the core collapse between data runs and allowing the fluid to mix.

Both the container origin and a calibration constant for the conversion of (digital) Doppler frequency to flow velocity were determined using a single procedure. The frequency f as a function of radius (measured from an arbitrary datum not necessarily corresponding to the container center) was measured with the container completely filled with liquid and rotating at a constant angular velocity. Calibration runs were performed for at least those rotation rates for which partially filled data was then taken. Consistent with the assumption of a rigid body rotation, the calibration profiles were well approximated by straight lines of the form $f = K_1 r + K_2$. Extrapolation of the calibration curves to the value $f = 0$ yielded values for $r = -K_2/K_1$ corresponding to the center of the container (extrapolation was required because the tracker was incapable of tracking to zero frequency). The center was taken

to be the average over all such values. Knowledge of the center position allowed calculation of rigid rotation velocity values for each calibration point. Under the assumption that velocity was linearly proportional to frequency, $V=kf$, the ratio of the velocity to frequency at any point gave a value for the calibration constant k. The calibration constant for any experiment was taken as the average over all calibration points. The relative uncertainty of k determined in this fashion was less than 8×10^{-4} for all experiments, while the container origin was determined to within 7.62×10^{-5}m (0.003 in.). Calibration profiles were repeated after an experiment as a check for instrumentation drift and carriage position errors.

Data for the partially filled container were taken for a single dimensionless core radius of $c=0.3$. The azimuthal component of velocity was measured along the radius corresponding to $\theta=\pi/2$ at a fixed axial position 7.64×10^{-2}m from the endplate nearest the transmission optics. Several axial traverses were performed at fixed radius and established that the LDV system could not detect second order axial (z) dependence of the azimuthal velocity. The traverses were initiated with the probe at the container endwall nearest the transmission optics. The focal length of the transmission optics was too short to allow endwall-to-endwall transverses but provided access to approximately one half of the container. The axial position or the probe was determined using ray tracing with an estimated accuracy of 1×10^{-3}m. The azimuthal velocity exhibited a z-dependence only in the $0(\epsilon)$ endwall Ekman layer; the axial depth of this layer was typically less than 5×10^{-3}m from the endwall. Further motion of the probe towards the interior of the container showed the azimuthal velocity to be independent of z. The findings of Gans and Yalisove (1982) were consistent with this observation, and also demonstrated the singly periodic θ-dependence of the flow. The particular choice of $\theta=\theta/2$ for radial traverses was made because it is the most interesting from the perspective of the flow stability, which is briefly discussed in the following section. The majority of data points were taken inside three e-folds of the predicted Ekman boundary layer on the core. Measurements were made for both the aircore and rigid float cases. The float was carefully machined from plexiglass tubing and had a length and outside diameter of 1.565×10^{-1}m and 4.724×10^{-2}m, respectively. It was sealed at the ends and had an effective density ρ_F of 1.526×10^{2} kg/m^3. For aircore data runs, a volume of liquid corresponding to $c=0.3$ was withdrawn from a full cylinder.

A set of measurements was performed to determine whether surface rheology could have a measurable effect on the flow behavior near the aircore. A measurable change in the aircore boundary layer profile was sought in response to an imposed change in the surface rheology. The latter change was effected by the addition of a commercial surfactant, Triton X405, to the bulk liquid; the surfactant was soluble in the glycerol solution. Aircore boundary layer profiles were recorded for an aqueous glycerol solution for a series of rotation rates. The same liquid was then contaminated by addition (0.01 wt. percent) of surfactant and boundary layer profiles of the contaminated solution were repeated for the same rotation rates. Measurements of the surface rheological parameters were not possible. Such measurements require a very specialized apparatus (Quinn and Scriven (1970), Scott (1979)), However, differences in static surface tension measurements were used as qualitative evidence that adsorption of contaminant molecules changed the values of the surface rheological properties for the static air-glycerol interface. The assumption was made that some change in the properties persisted in the dynamic interface of the aircore. The surface tension was measured using a ring tensiometer before and after the addition of surfactant; the respective values were 61.4 dynes/cm and 47.55 dynes/cm. The addition of surfactant had no measurable effect on the viscosity of the bulk fluid. A control experiment was performed using silicone oil to model an ideal (uncontaminated) free surface. Silicon oils are virtually immune to surface active contamination by the types of organic contaminants present in typical nonclean laboratory environments.

The parameter order-of-magnitude requirements (13) for the validity of Gans' theory were nominally satisfied though not always in the strictest asymptotic sense.

Results and Discussion

Radial profiles of the absolute azimuthal velocity, further normalized by c, are shown in Figs. 4 and 5 for the rigid float and aircore cases, respectively. The solid lines represent Gans' theory given by (3), after division by c, to $0(\epsilon)$. The theoretical curves in Fig. 4 include corrections of the rigid float theory for nonzero mass of the float; this requires that the value of ϵ be reduced by the factor $(\rho-\rho_F)/\rho$. The truncated ordinates in all

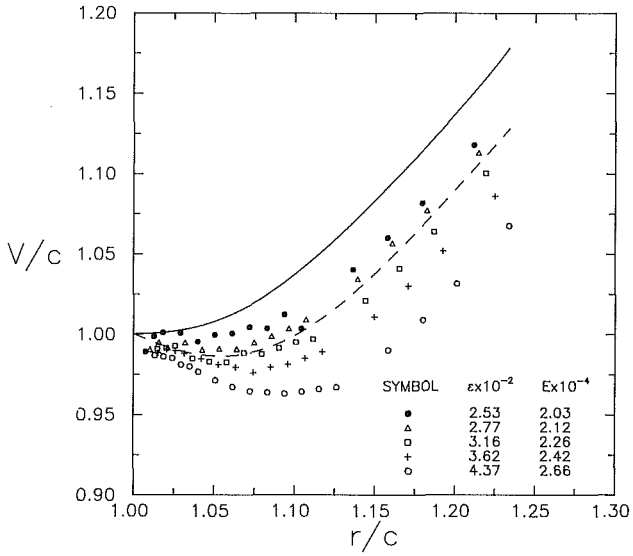

Fig. 4 Absolute azimuthal velocity profiles for the rigid float for different inverse Froude and numbers. Solid and dashed lines are Gans' (1979) theoretical predictions: ● (_____); ○ (----). (The estimated uncertainties in *v/c* and *r/c* are both 0.007 at (20:1) odds.)

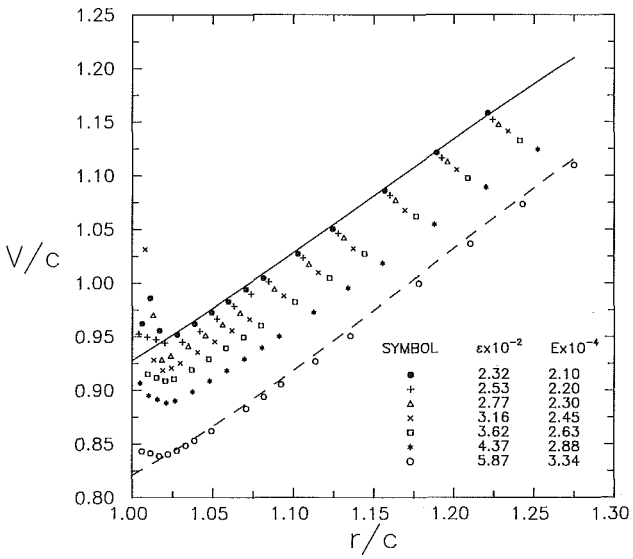

Fig.5 Absolute azimuthal velocity profiles for the aircore for different inverse Froude and Ekman numbers. Solid and dashed lines are Gans' (1977) theoretical predictions: ● (_____); ○ (----). (The estimated uncertainties in *v/c* and *r/c* are both 0.009 at (20:1) odds.)

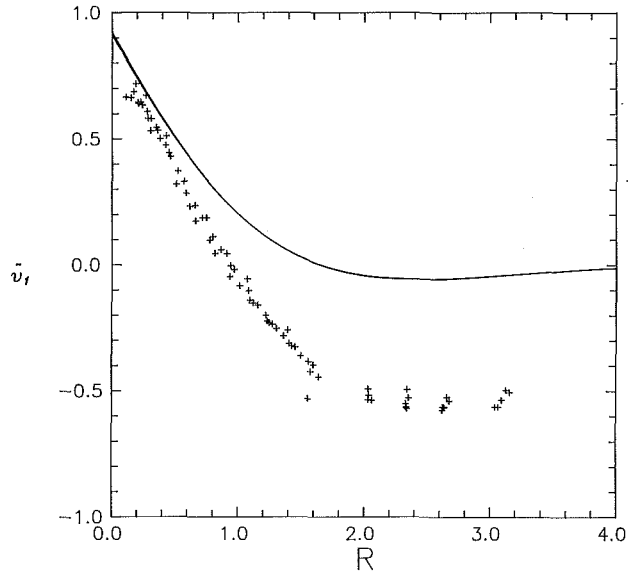

Fig. 6(*a*)

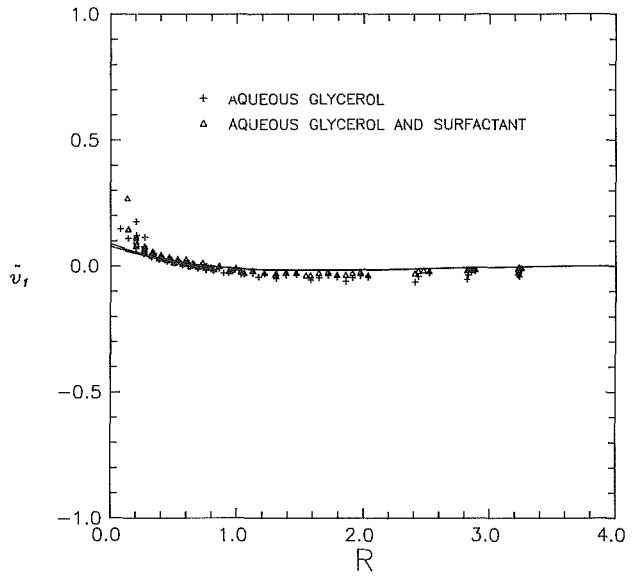

Fig. 6(*c*)

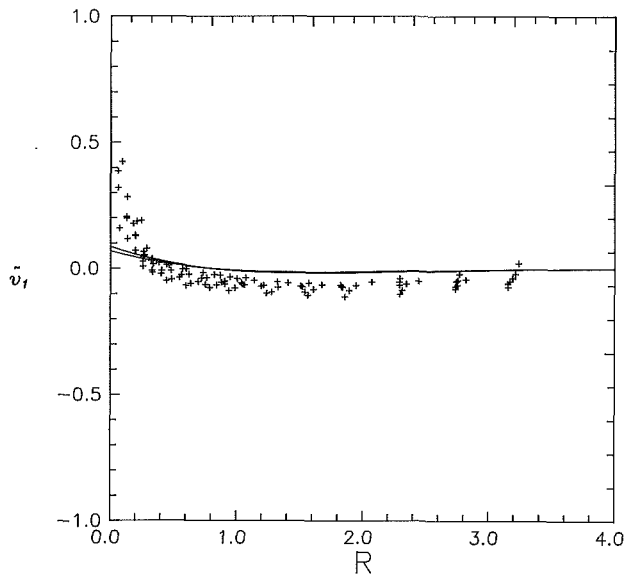

Fig. 6(*b*)

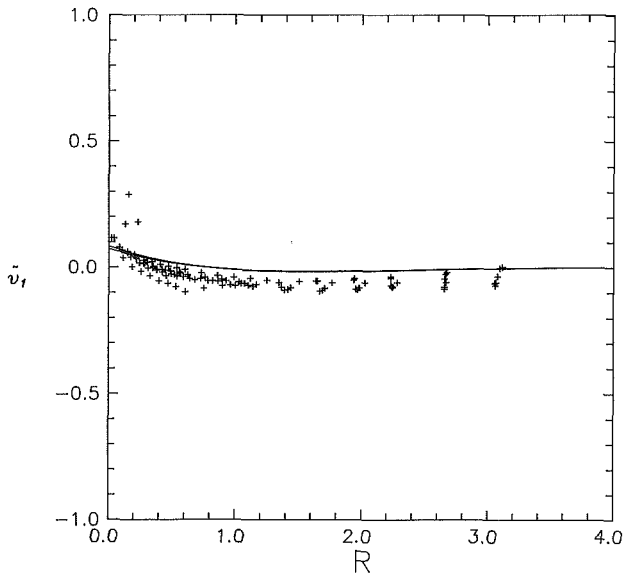

Fig. 6(*d*)

Fig. 6 Boundary layer velocities versus boundary layer coordinate: (*a*) rigid floats; (*b*) aircore, aqueous glycerol; (*c*) aircore, aqueous glycerol/aqueous glycerol and surfactant; (*d*) aircore, silicone oil. (The estimated uncertainties in $\bar{v}$, and R are 0.05 and 0.1, respectively, at (20:1) odds.)

the plots exaggerate the magnitudes of the discrepancies. Points with the largest discrepancies in Figs. 4 and 5 are within 5 and 1 percent, respectively, of the theoretical predictions. The data for both cases fall below the theoretical line; this same trend appears in Gans and Yalisove (1982). It is surprising to find the largest discrepencies associated with the rigid float and not the aircore. Based on the retrograde rotation measurements discussed above, the opposite result would seem more likely. However agreement close to the core boundary is quite good for the rigid float; it is the interior flow where the largest discrepancies arise. There is a systematic departure with radius of the data from theory. The discrepancy appears to assume some constant value in the interior, a value which clearly correlates with ϵ. The next order correction in the theory would be $0(\epsilon^2)$; terms of this magnitude would not account for the interior discrepancies, nor would experimental error. The small discrepancies near the core in Fig. 4, however, are not inconsistent with a retrograde rotation of the float and are of the same order of magnitude as an $0(\epsilon^2)$ correction. The dispersion of the data very near the core in Fig. 5 is probably anomalous. Flare is a well-known characteristic of LDV signals near phase boundaries. The flare is worse for some rotation rates than for others as the aircore interface is sensitive to structural vibrations in the apparatus. A similar problem did not arise for the rigid float data because the float was less sensitive to vibration and because the float had a diffuse exterior finish which was capable of scattering light.

The boundary layer behavior is most clearly presented by forming the $0(\epsilon)$ boundary layer correction, $\tilde{v}_1$. From equation (3), the absolute azimuthal velocity to $0(\epsilon)$ is

$$V = r + \epsilon(\hat{v}_1 + \tilde{v}_1).$$

Experimental values for $\tilde{v}_1$ can be formed from a given normalized velocity measurement by subtracting off the rigid

rotation component r, dividing by ϵ, and subtracting the interior velocity $\hat{v}_1$ as given by (11). Comparisons of the experimental $\tilde{v}_1$ and the theoretical $\tilde{v}_1$ as given by (12) are shown in Fig. 6. Figures 6(*a*) and 6(*b*) are the same data as Figs. 4 and 5, recast in boundary layer form. The expression for $\tilde{v}_1$ in (12) depends on E. Each theoretical curve in Fig. 6 is actually the overlay of two curves corresponding to the extreme values of E for a given experiment; the two curves are so close as to appear almost indistinct. The data for the rigid float compare well with theory very near the core but progressively deviate from theory away from the core boundary. This parallels the behavior of the absolute velocity profiles in Fig. 4. The data in Fig. 6(*a*) suggest a smaller boundary layer scale than that predicted by theory. Aircore boundary layer functions (Figs. 6(*b*)-6(*d*)) show better agreement. The disparity with theory near the core boundary is most pronounced in Fig. 6(*b*). The rise in $\tilde{v}_1$ near the interface resembles the behavior for the rigid surface in Fig. 6(*a*), perhaps suggesting that the aircore interface is supporting a finite shear stress. However the scale is much sharper than the bounday layer scale established by the rigid surface data. This seems to strengthen the assumption that the rise in $\tilde{v}_1$ at the core was anomalous. That the flare is worse in Fig. 6(*b*) than in Figs. 6(*c*) and 6(*d*) is likely attributable to the fact that the cylinder was rebalanced between the experiments of Figs. 6(*b*) and 6(*c*) and consequently there was probably less surface wave motion forced by mechanical vibrations in the experiments of Figs. 6(*c*) and 6(*d*). The data from the latter experiments bear on the issue of surface rheological effects on the boundary layer flow. Figure 6(*c*) shows a superposition of the data for aqueous glycerol and aqueous glycerol contaminated with surfactant. There are no discernable differences between the two data sets. The boundary layer behavior for silicone oil (which was assumed to form an ideal free surface at the core) shown in Fig. 6(*d*) is qualitatively identical to the preceding figure. It seems fair to infer, then, that it is unlikely that surface rheological effects can measurably alter the character of the aircore boundary layer flow. This of course conflicts with the speculations of both Whiting (1978) and Gans and Yalisove (1982).

A few remarks may be made regarding the stability of the steady annular flow for which both Phillips and Greenspan developed stability criteria. Phillips' was an inviscid criterion for the aircore based on a balance between centrifugal and buoyancy forces at the interface at the critical azimuth of $\theta = \pi/2$. His result is actually an absolute stability limit, the actual instability usually occurring for much higher rotation rates than predicted due to the existence of large amplitude centrifugal waves on the interface. The onset of the oscillatory flow regime is retarded by the action of viscosity; the role of viscosity as a parameter in the overall stability map has not yet been qualitatively assessed. Greenspan's criterion was a viscous criterion for the rigid float flow based on the onset of vortex shedding from the core. He took as the onset of separation the initial appearance of a stagnation point in the interior flow at the outer edge of the core boundary layer. In his conclusion, he categorizes the core instability as a type of shear layer instability, and speculates that the complex process leading to aircore collapse is explicable in terms of a slight variant of the mechanism responsible for rigid float instability. His analysis seems directed at the case for small c. Figure 4 gives conditional qualitative support of Greenspan's instability postulation. As the rotation rate decreases (ϵ increases), the boundary layer thickens and the velocity becomes nonmonatonic with increasing radius and a well forms in the velocity profile. It appears possible that for very small c, the depth of the velocity well would be equal in magnitude to the rigid body rotation and subsequently a stagnation point could form. In terms of the theory, it is tempting to say that a stagnation point would form when the $0(\epsilon)$ corrections become of the same magnitude as the rigid rotation component. However, one suspects that nonuniformities would arise in the asymptotic expansions before such a balance could occur. It does seem very unlikely that a stagnation point could form for any but very small values of c. Furthermore, Greenspan's speculation that a similar instability mechanism is responsible for the aircore instability is not supported by the data. There is no suggestion of a developing nonmonatonic behavior in Fig. 5 by either data or theory.

Conclusions

Boundary layer profiles of the aximuthal velocity were recorded at an internal free surface in a rotating flow. Two types of free surfaces were investigated. Aircore velocity profiles were within 1 percent of theory in both the boundary layer and interior. Rigid float profiles were within 5 percent of the theoretical predictions with the largest discrepancies occurring in the interior flow. The rigid float data also exhibited a sharper boundary layer scale than was predicted. Experiments to assess possible surface rheological effects on the aircore boundary layer behavior, while not rigorous enough to be conclusive, suggested that surface contamination of the aircore interface had no measurable $0(\epsilon)$ effect on the boundary layer profile. Rigid surface boundary layer profiles display nonmonatonic behavior with increasing radius in a way that qualitatively supports Greenspan's stability hypothesis for very small values of c but which suggest his hypothesis is inappropriate for moderate and large c as well as for the aircore flows.

References

1 Cooper, A., "Formation of a Viscous Boundary Layer on the Free Surface of an Imploding Rotating Liquid Cylinder," *Journal Fluid Mechanics*, Vol. 93, July 1979, pp. 305–317.

2 Gans, R. F., "On Steady Flow in a Partially-Filled Rotating Cylinder," *Journal Fluid Mechanics*, Vol. 82, Sept. 1977, pp. 415–427.

3 Gans, R. F., "On the Flow Around a Buoyant Cylinder Within a Rapidly Rotating Horizontal Cylindrical Container," *Journal Fluid Mechanics*, Vol. 93, Aug. 1979, pp. 529–548.

4 Gans, R. F., and Yalisove, S. M., "Observations and Measurements of Flow in a Partially-Filled Horizontally Rotating Cylinder," *Journal Fluids Engineering*, Vol. 104, Sept. 1982, pp. 363–366.

5 Greenspan, H. P., "On a Rotational Flow Distributed by Gravity," *Journal Fluid Mechanics*, Vol. 74, March 1976, pp. 335–351.

6 Hendricks, S. L., and Morton, J. B., "Stability of a Rotor Partially-Filled with a Viscous Incompressible Fluid," ASME *Journal of Applied Mechanics*, Vol. 46, Dec. 1979, pp. 913–918.

7 Phillips, O. M., "Centrifugal Waves," *Journal Fluid Mechanics*, Vol. 7, March 1960, pp. 340–352.

8 Quinn, J. A., and Scriven, L. E., "Interfacial Phenomena," Fourteenth Advanced Seminar, American Institute of Chemical Engineers, 1970.

9 Rushak, K. J., and Scriven, L. E., "Rimming Flow of a Liquid in a Rotating Horizontal Cylinder," *Journal Fluid Mechanics*, Vol. 76, July 1976, pp. 113–125.

10 Scott, J. C., "The Preparation of Clean Water Surfaces for Fluid Mechanics," *Surface Contamination: Genesis, Detection, and Control*, Vol. 1, Plenum, (ed., K. L. Mittal), 1979, pp. 477–497.

11 Sedney, R., "Some Rotating Fluid Problems in Ballistics," *Mathematics Applied to Fluid Mechanics and Stability*, Proceedings of a conference dedicated to Richard D. DiPrima, SIAM, Troy, NY, Sept. 1985, pp. 87–109.

12 Whiting, R. D., "An Experimental Study of Steady Flow in a Partially-Filled Rotating Cylinder," Ph.D. dissertation, University of Rochester, Dept. of Mech. and Aerospace Sci., Jan. 1978.

M. Stieglmeier

C. Tropea

Lehrstuhl für Strömungsmechanik,
Universität Erlangen-Nurnberg,
Erlangen, Federal Republic of Germany

N. Weiser

W. Nitsche

Institut für Luft -und Raumfahrt,
Technische Universität Berlin,
Berlin, Federal Republic of Germany

Experimental Investigation of the Flow Through Axisymmetric Expansions

This study examines the flow field in three axisymmetric expansions having diffuser half-angles of 14, 18, and 90 deg, respectively. Velocity measurements were performed at a Reynolds number of $Re = 1.56 \times 10^4$ using a single component LDA operated in forward scatter. The test facility was refractive index matched, allowing measurement of the velocities $\bar{U}$, $\bar{V}$, $\bar{W}$, $\overline{u^2}$, $\overline{v^2}$, $\overline{w^2}$, $\overline{uv}$ and $\overline{uw}$ upstream of, and throughout the entire recirculation region. The results indicate that the diffuser geometry influences the separated shear layer appreciably over the entire length of the diffuser section. The production of turbulence immediately after separation is much higher in the case of the 14 and 18 deg diffuser compared to the 90 deg expansion, leading to higher diffusion rates in the separated shear layer, and hence earlier reattachment of the shear layer.

Introduction

The flow through axisymmetric expansions is one of the most commonplace examples of turbulent, separated flow fields in practical engineering situations. Wide-angle diffuser geometries appear in a variety of monitor and control devices in piping systems, while the 90 deg diffuser, or sudden expansion, is typical of piping junctions or weld ribs. The sudden expansion is also a common geometry in combustion chambers, acting as a flame stabilizer or simply as a sudden dump diffuser. Although this interest in the flow has led to a significant number of experimental and numerical investigations of the flow field and its influence on heat and mass transfer coefficients, there exists a lack of detailed knowledge about turbulence properties, especially in the recirculation regions of the flow. This can be attributed undoubtedly to the difficulties in operating an LDA in axisymmetric flow geometries due to refractive effects of the containment wall. The present study presents velocity data for three diffuser geometries of half-angles 14, 18, and 90 deg. The results provide insight into the influence of the diffuser geometry on the turbulence structure, and comparisons are made with other separated flows in simple geometries. In addition, the measurements presented here are detailed enough to be of value for verification and development of numerical codes and turbulence models.

The velocity field in wide-angle diffusers is dominated largely by the separation of the flow from the diffuser wall and by the resulting recirculation region, the extent of which has in the past been determined using a variety of measurement techniques. Back and Roschke [2] used dye injection to determine the mean reattachment length of the flow dowstream of an abrupt circular expansion as a function of Reynolds number. The results allow the flow to be classified into three ranges according to Reynolds number: a laminar range in which the mean reattachment length continually increases with Reynolds number; a transitional range with a large decrease of reattachment length; and a turbulent range in which the mean reattachment length remains independent of Reynolds number. This is a common behavior for a large variety of separated flows, for example the plane backstep (Armaly et al., 1983), and is likely applicable to axisymmetric diffusers, although no such data exist for diffusers of variable angle.

Earlier investigations of the flow through axisymmetric expansions were hindered by the lack of suitable measuring techniques for recirculating flows. Chaturvedi (1963) used pitot tubes and hot wires to obtain the mean and fluctuating flow fields respectively for diffusers with half-angles of 15, 30, 45, and 90 deg. Although the accuracy of these measurements is questionable in the recirculating regions, he did find notable differences in the turbulence structure outside of the recirculation region between diffusers with half-angles of 15 deg and diffusers with the half-angles 30, 45, and 90 deg. On the basis of head loss measurements and corrected hot-wire measurements the turbulence production and diffusion is expected to be largely independent of diffuser angle above values of 32 deg.

More recent investigations of axisymmetric expansions have employed the laser Doppler anemometer for velocity measurements. These include studies by Freeman (1975), Moon and Rudinger (1977), Durrett et al. (1984), Khezzar et al. (1985) and Szczepura (1985) which are summarized together with various other investigations in Table 1. All authors employing LDA have, however, encountered difficulties in obtaining some of the velocity components or measuring in the near wall regions, due to the refraction of the laser beams on the cylindrical surfaces of the test section. Several authors used a partial compensation by enclosing the test section in a water filled, plane-walled container, and Dur-

Contributed by the Fluids Engineering Division for publication in the JOURNAL OF FLUIDS ENGINEERING. Manuscript received by the Fluids Engineering Division July 22, 1988.

Table 1 Experimental investigations of flow through axisymmetric expansions

Author	Diffuser half-angle	Re No.	D_2/D_1	Measuring techniques	Measured quantities
Chaturvedi (1963)	15, 30, 45, 90 deg	200,000	2.0	Pitot static HWA tufts	U, p, pw $\overline{u^2}$, $\overline{v^2}$, $\overline{w^2}$, $\overline{uv}$ x_R
Back, Roschke (1972)	90 deg	20-4200	2.6	dye injection	x_R
Moon, Rudinger (1977)	90 deg	280,000	1.4	LDA visualization	$\bar{U}$ x_R
Freeman (1978)	90 deg (nozzle)	30,000		LDA	$\bar{U}$, u^2
Ha Ming, Chassaing (1979)	90 deg	72,000	2.0	HWA	$\bar{U}$ $\overline{u^2}$, $\overline{v^2}$, $\overline{w^2}$, $\overline{uv}$
Durret et al. (1984)	90 deg	84,000	1.9 2.7	LDA	$\bar{U}$,$\bar{V}$ $\overline{u^2}$, $\overline{v^2}$, $\overline{uv}$
Khezzar et al. (1985)	90 deg	40,000	1.75	LDA visualization	$\bar{U}$, $\bar{V}$, $\overline{u^2}$, $\overline{v^2}$, $\overline{uv}$ x_R
Szczepura (1985)	90 deg	200,000	1.94	LDA (2 comp.)	$\bar{U}$, $\bar{V}$, $\bar{W}$, $\overline{u^2}$, $\overline{v^2}$, $\overline{w^2}$ $\overline{uv}$, $\overline{uw}$, $\overline{u^3}$, $\overline{v^3}$, $\overline{w^3}$ $\overline{uw^2}$, $\overline{u^2w}$, $\overline{uv^2}$, $\overline{u^2v}$
Weiser, Nitsche (1987, 1988)	6, 10, 14, 18, 22.5, 45, 90 deg	10,000-70,000	1.6	HWA sublayer fence piezo foils	$\bar{U}$, $\bar{V}$, $\overline{u^2}$, $\overline{v^2}$, $\overline{uv}$ τ_w, x_R p_w, p_w'
Present work (1989)	14, 18, 90 deg	15,600	1.6	LDA	$\bar{U}$, $\bar{V}$, $\bar{W}$, $\overline{u^2}$, $\overline{v^2}$, $\overline{w^2}$ $\overline{uv}$, $\overline{uw}$, x_R, $E(f)$

rett et al. (1984) presented a novel correction lens for compensation of the refractive effects. In the present study this difficulty has been overcome by fully matching the refractive index of the working fluid with that of the containment glass, thus allowing all desired velocity components to be measured. The summary in Table 1 also indicates that no study performed with LDA has investigated the effect of diffuser half-angle on the turbulence structure, and therefore this is one of the major contributions of the present work.

Experimental Description

Flow Facility. Experiments were conducted in the vertically mounted refractive index matched test facility pictured in Fig. 1. The flow was drawn from a constant head tank through a nozzle and flow straighteners into an inlet pipe of diameter 50 mm (D_1). A trip wire was placed immediately downstream of the inlet nozzle to insure a fully developed turbulent pipe flow at the inlet to the test section 30 diameters downstream.

The test section consisted of interchangeable diffuser sections having half-angles of 14, 18, or 90 deg. The downstream diameter was 80 mm (D_2), resulting in a diameter ratio D_2/D_1 of 1.6 and an area ratio of 2.56. The maximum achievable Reynolds number based on the mean flow velocity was

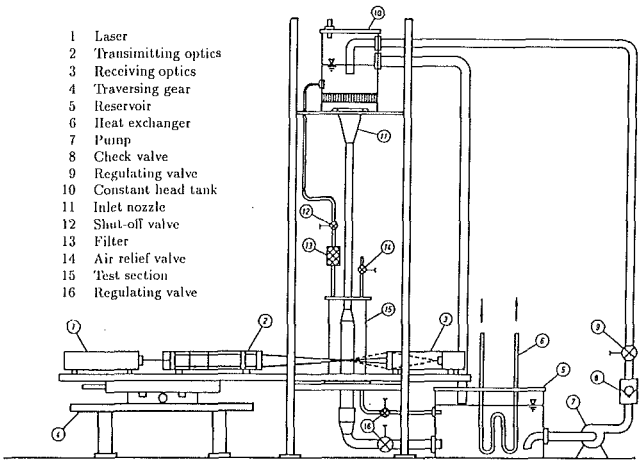

Fig. 1 Diagram of experimental apparatus

$\mathrm{Re} = 1.56 \times 10^4$. The centerline velocity upstream of the diffuser, U_0, was used as a normalizing velocity in the presentation of results and was equal to 2.51 m/s for all diffuser geometries.

The test section was encased in an outer, square-sided con-

Nomenclature

D_1 = inlet pipe diameter
D_2 = outlet pipe diameter
$E(f)$ = frequency spectrum
f = frequency
h = $(D_2 - D_1)/2$ height of expansion
k = $(\overline{u^2} + \overline{v^2} + \overline{w^2})/2$: turbulent kinetic energy
p_w = wall static pressure
R = local pipe radius
Re = Reynolds number based on mean bulk velocity
U, V, W = axial, radial and azimuthal velocities
U_m = bulk mean velocity
U_0 = maximum upstream velocity
x, r, θ = axial, radial, and azimuthal coordinates
x_R = position of mean reattachment
α = diffuser half-angle
Λ = vorticity thickness
θ_c = integral time scale
$\rho_{uu}(\tau)$ = autocovariance coefficient

tainment vessel extending 100mm upstream and 600mm downstream of the diffuser inlet. The volume between the test section and the outer containment was filled with the working fluid, which was selected to have a refractive index equal to that of the containment glass. Thus the test section pipe was mechanically present but optically transparent, facilitating the use of the laser Doppler anemometer for velocity measurements. The match of refractive indices was achieved by mixing two diesel oils with different refractive indexes in proportions suitable to yield the desired index of refraction. Since the refractive index is dependent on temperature, a heat exchanger was incorporated into the test loop to regulate the temperature to within $\pm 0.5°C$. Further details of all aspects of the experimental facility are described by Wieser and Nitsche (1987, 1988).

Laser Doppler Anemometer. The LDA was a one-component, forward scatter system operating with a He-Ne laser. The natural redish colour of the diesel oil prevented the originally planned Ar-Ion laser from being used, since the increased absorption led to local heating of the fluid and resulted in severe beam divergence. The focal length of 250 mm resulted in a measuring control volume with a diameter of $200\mu m$ and a length of 2 mm. A single Bragg cell with downmixing was used to provide a net frequency shift of 1 MHz, allowing measurements to be made in the reverse flow direction up to 100 percent of the inlet flow velocity.

The LDA system was mounted on a traversing table outfitted with precision measuring gauges, which insured a high relative positioning accuracy. The absolute positioning of the measuring volume was determined by traversing into the wall boundaries and detecting the shift frequency. The absolute positioning accuracy in three directions are estimated to be: $z - \pm 100\mu m$; $r(\perp$ to optical axis$) - \pm 100\mu m$; r ($\parallel$to optical axis$) - \pm 1$mm. The radial positioning parallel to the optical axis was less accurate due to the 2 mm length of the control volume.

As indicated in Fig. 2, either the tangential (W) or the radial (V) component of velocity could be measured depending on the positioning of the measuring control volume on either of two perpendicular diameters. A 90 deg rotation of the optics from their orientation in Fig. 2 allowed the axial component (U) to be measured. By performing additional velocity measurements at $\pm 45°$ orientations about the optical axis, the stress components $\overline{u^2}$, $\overline{v^2}$, $\overline{w^2}$, $\overline{uv}$, and $\overline{uw}$ could also be obtained. The redundant measurement of $\bar{U}$ (from the ± 45 deg measurement) agreed with the directly measured $\bar{U}$-profile to within 1 percent over the entire pipe diameter at all planes which were examined. Further results from which the accuracy of the velocity measurements can be estimated are presented in the following section.

The LDA signals were processed using a frequency counter (Dantec 55L90) operated in the fixed cycle mode with a 5/8 comparison (1.5 percent). The digital output was sampled at regular time intervals of 0.01 s, with data rates ranging between 0.4 and 3 kHz. This mode of sampling, together with an ensemble mean estimator, has been shown by Tropea (1987) and Adrian and Yao (1987) to yield bias-free estimates of the mean velocity and frequency spectra at all levels of turbulence, provided that the particle arrival rate is sufficiently high. Typically, the data density must be such that a minimum 5 to 10 particles per integral time scale are available, a condition which was met in the present experiment. The data was collected and processed in a personal computer (HP Vectra) using a high speed parallel interface especially designed for LDA measurements as described by Tropea and Struthers (1987).

Experimental Results

Preliminary measurements were performed to verify the axial symmetry of the flow field. Typical deviations of the mean and RMS velocity measured parallel and perpendicular to the LDA optical axis can be seen in Fig. 3. Subsequent measurements presented in this paper have been obtained by traversing perpendicular to the optical access to take advantage of the higher positioning accuracy. A small swirl component of up to 6 percent of $\bar{U}$ was observed immediately next to the wall at the diffuser inlet. Otherwise the swirl was less than 1 percent of the inlet velocity at all measurement planes and therefore this component of the mean velocity is not presented in the results below. The volume flow rate was computed at all axial measurement planes by integrating the axial velocity profiles across the pipe radius. Deviations from the inlet volume flow rate remained less the 5 percent for all diffuser models. These deviations did not correlate with particular measurement planes and can be attributed to the cumulative effects of errors present in positioning, test section precision, long-time stability of the flow, statistical uncertainty and in the residual bias of the mean velocity estimators used. The various measurement uncertainties associated with this experiment are summarized in Table 2.

The measured radial velocity component was compared

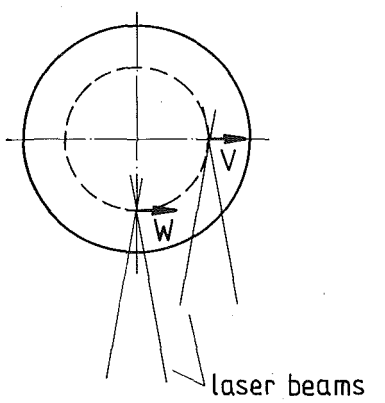

Fig. 2 Orientation of laser-Doppler anemometer

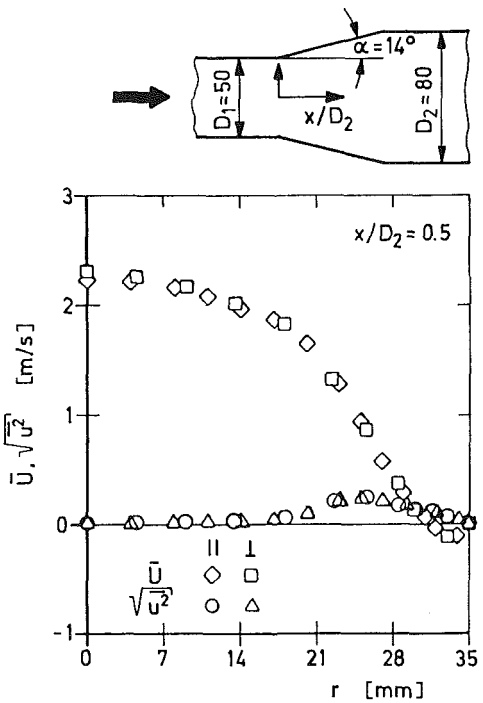

Fig. 3 Example of the axial symmetry of the flow

Table 2 Summary of uncertainty errors

Quantity	Fixed error		Variable error
	Major source	Max. value	
x, r	absolute positioning	±0.1 mm	±0.010 mm
$\bar{U}$, $\bar{V}/U_0$			
Outer Flow ($Tu<10\%$)	test section precision	±1.0%	±0.3%
Separated region ($Tu>20\%$)	statistical velocity bias	$\pm(Tu)^2\times 100\%$	$\pm Tu\times 4.5\%$
$\overline{u^2}$, $\overline{v^2}$, $\overline{w^2}$	mcv gradient	±.004 m/s	<1%
$\overline{uv}$, $\overline{uw}$	broadening		

Notes: $Tu=\sqrt{\overline{u^2}}/\bar{U}$ (local), % refers to measured value
$N=2000$, $\alpha=0.05$, $t_{2000:0.025}\approx 2$, $\chi^2_{2000:0.05}=0.005$

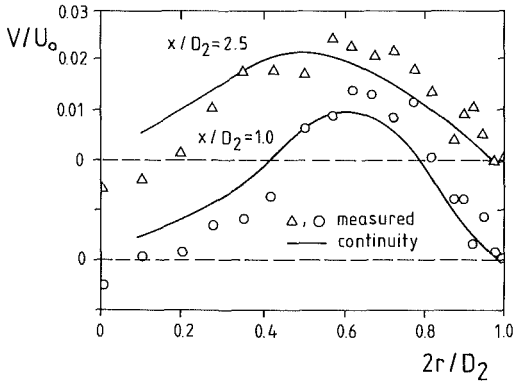

Fig. 4 Comparison of measured and computed radial velocity component for the sudden expansion geometry

with the radial velocity obtained by integrating the continuity equation from the centerline to the wall. Two such comparisons are illustrated in Fig. 4 for measurement planes before and after the mean reattachment position. The agreement is very good considering the absolute magnitude of this velocity component.

The measured flow fields are presented in Figs. 5–7, showing two mean velocity components, three normal stress components and two shear stress components for the three diffuser models. Comparisons were made for the sudden expansion geometry with measurements performed by Weiser and Nitsche (1987) using a hot-wire anemometer in an air-flow rig having the same flow geometry. The agreement is excellent for the mean velocity components on the measurement planes common to both investigations. The turbulence quantities measured in the present study using an LDA were, however, consistently about 30 percent higher than the HWA data of Weiser and Nitsche (1987), except for $\overline{v^2}$, which was up to 100 percent higher.

The W-momentum equation indicates that the shear stress component $\overline{uw}$ should be equal to zero, thus these results serve as a check on the measurement accuracy and on the axisymmetry of the flow. The value of $\overline{uw}/U_m^2$ in general does not exceed 0.2 percent, except for a few points at the diffuser inlet which reach values of 0.8 percent. This is most probably related to the mean swirl measured at the same positions.

The normal stresses presented in Figs. 5–7 allow an evaluation of the commonly used approximation, $k=3(\overline{u^2}+\overline{v^2})/4$, for the turbulent kinetic energy. This expression is used frequently when only two of the normal stresses have been experimentally determined, but a comparison to $k=\frac{1}{2}(u^2+v^2+w^2)$, as used in the $k-\epsilon$ turbulence model, is required. The approximation assumes that the missing component $\overline{w^2}$, lies midway between $\overline{u^2}$ and $\overline{v^2}$. For these geometries the present results show that this is, in general, an overestimation of k. In most instances $\overline{w^2}$ is about equal to $\overline{v^2}$. This is in contrast to similar measurements performed in plane geometries (Moss et al., 1979, Dimaczek et al., 1988), in which $\overline{w^2}$ indeed lies about midway between $\overline{u^2}$ and $\overline{v^2}$.

The corresponding reattachment lengths, as computed by extrapolating the $\bar{U}=0$ line to the wall, were $x_R/D_2=1.26$, 1.49 and 1.87 for the 14, 18, and 90 deg diffusers respectively. Figure 8 summarizes the measured reattachment lengths, normalized using the "step height," $h=(D_2-D_1)/2$, for various diffuser geometries and Reynolds numbers. Several different techniques were used to measure the mean reattachment lengths shown in this diagram, including flow visualization and measurement of the wall shear stress. This diagram confirms previous studies showing that for $\alpha>15-16$ deg the recirculation region increases with increasing diffuser half-angle. The influence of Reynolds number and/or area ratio appears to be secondary, and no systematic dependence on either of these parameters can be recognized from this diagram.

Low frequency unsteadiness of the flow velocity has been observed by several authors in various separated flow geometries (e.g., Eaton and Johnston, 1981, Driver et al., 1987), and was also observed in the flow visualization studies of the present flow. The observed nondimensional frequencies of $fh/U_0=0.07$ (Eaton and Johnston, 1981), or $fx_R/U_0=.5-.8$ (Mabey, 1972) are well below those of turbulent flow fluctuations and correspond in the present study to frequencies of the order of 5–15 Hz. To investigate this aspect of the flow, measurements of the power spectral density of the U-velocity fluctuations were carried out at a matrix of positions outside of, and within the recirculation region. Figure 9 presents spectra measured at various radii at a downstream position of $x=120$mm ($x/x_R\approx 0.8$) in the 90 deg diffuser geometry. This figure typifies the results obtained in different diffusers, indicating that while the reattachment point was unsteady, there was no dominant frequency observed in the expected range at any position in the flow. It appears that the unsteady behavior takes on a more random character in the axisymmetric flow geometry. This observation supports the hypothesis of Ruderich and Fernholz (1986) that a higher degree of periodic unsteadiness may be associated with smaller blockage effects, or in this case with lower downstream to upstream area ratios. The differences between the spectra at various radial positions reflect the change of the $\overline{u^2}$ velocity component, which is equal to the area under the spectral curves.

The autocorrelation function ρ_{uu} of the velocity fluctuations was computed from the measured spectra, using the inverse Fourier transform. Results of these computations are shown for the case of the sudden expansion at a streamwise position of $x/x_R=0.8$ in Fig. 10. The integral time scale, as

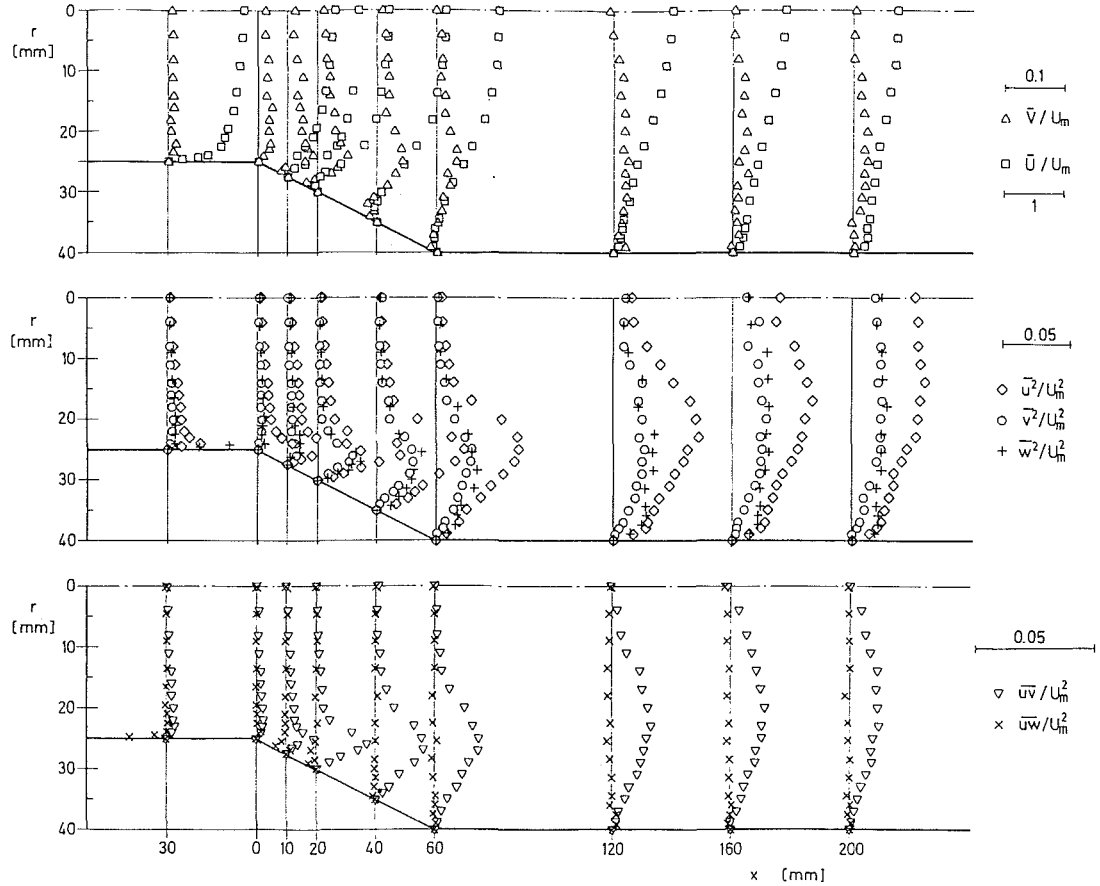

Fig. 5 Velocity profiles for 14 deg diffuser

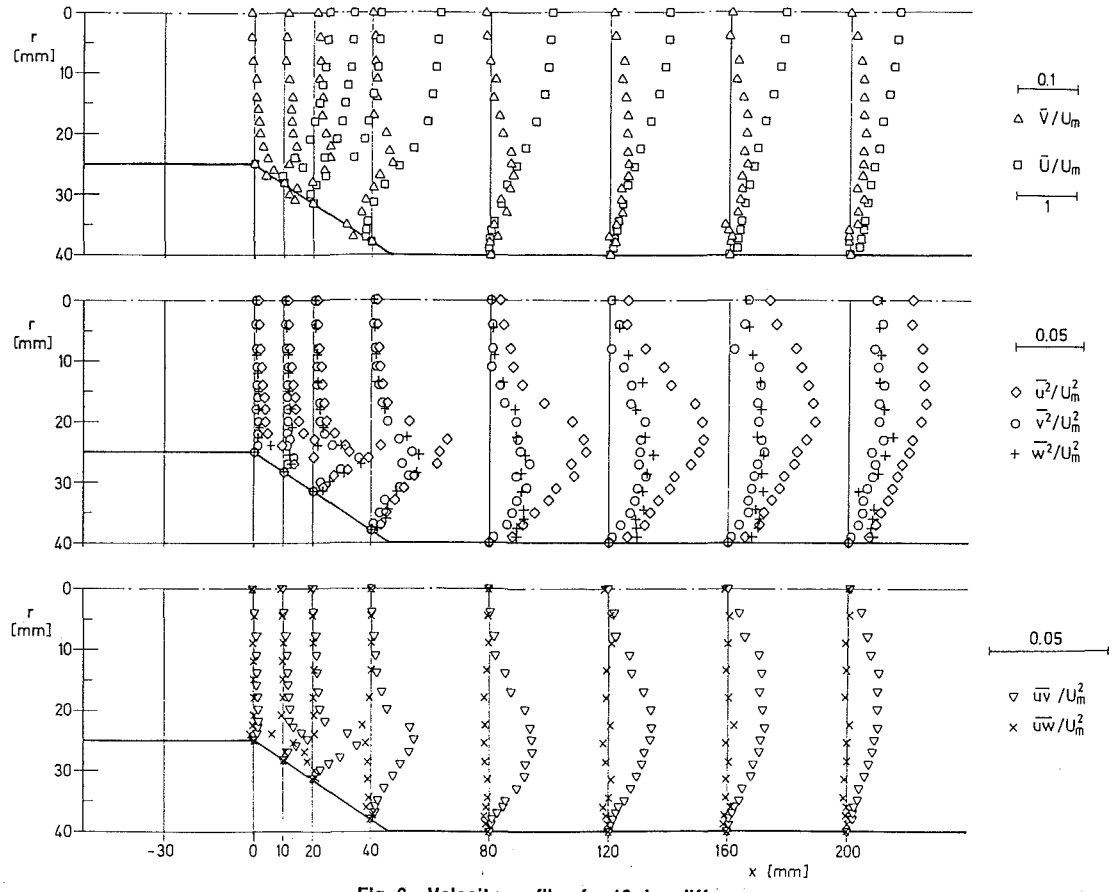

Fig. 6 Velocity profiles for 18 deg diffuser

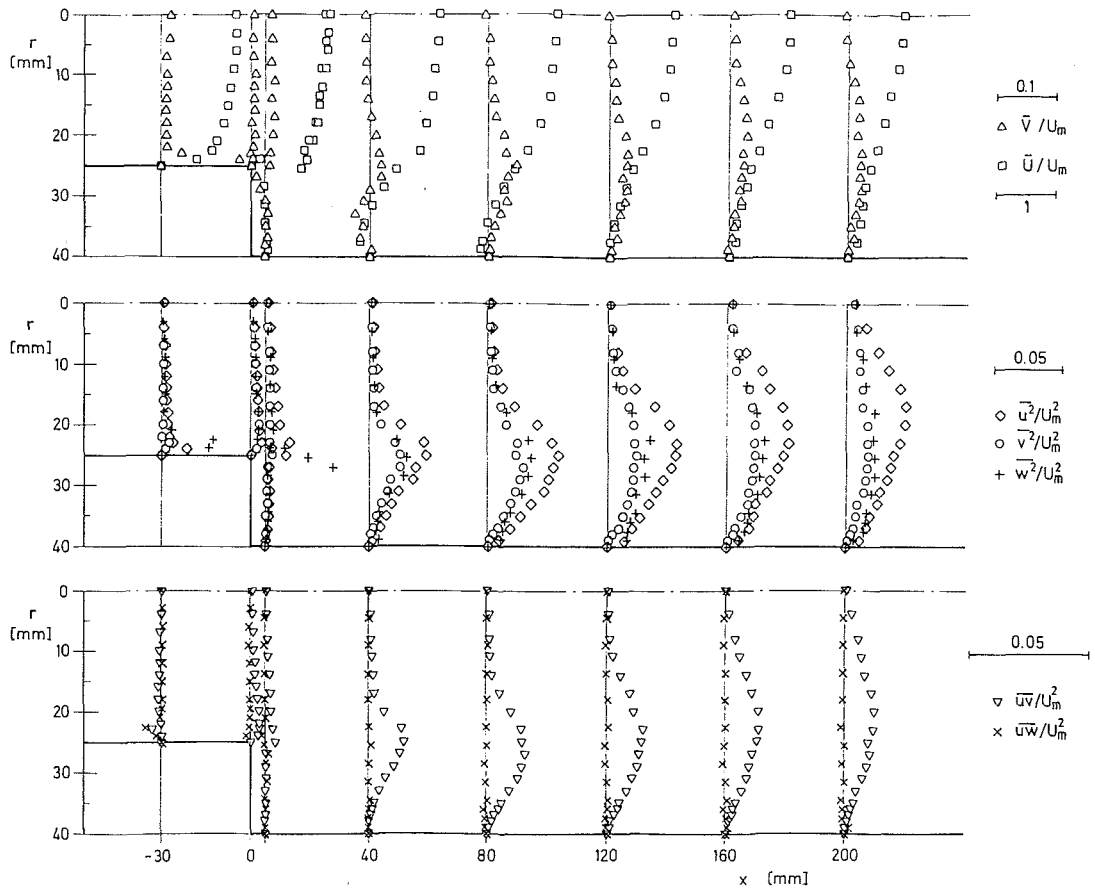

Fig. 7 Velocity profiles for 90 deg diffuser

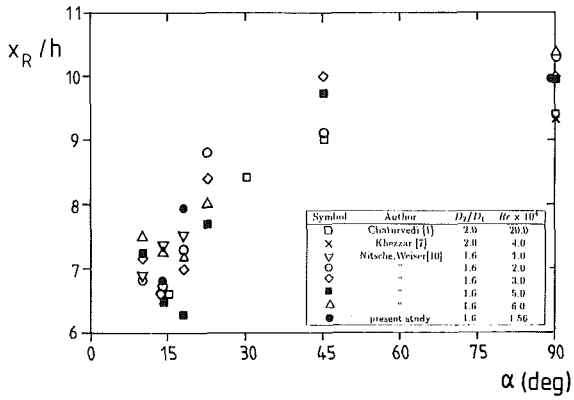

Fig. 8 Summary of measured reattachment lengths for various diffuser half-angles

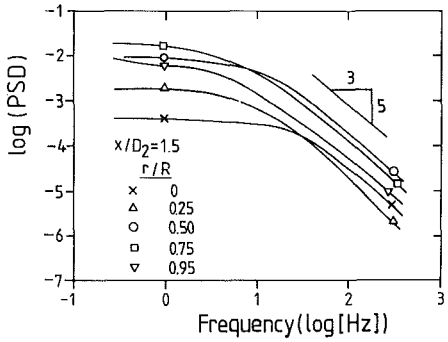

Fig. 9 Power spectral density of U-velocity fluctuations at $x/D_2 = 1.5$ in the 90 deg diffuser

computed by integrating $\rho_{uu}(\tau)$ up to the first zero crossing is also given in this figure. This time scale increases by a factor of approximately 5 between the core flow and the recirculation region, which confirms the fact that the necessary measurement time increases significantly within the recirculation region to maintain comparable levels of measurement accuracy.

Discussion of Results and Conclusions

All three diffuser geometries show separation of the flow at the edge of the expansion inlet and a mean reattachment at some point downstream of the diffuser section. This is not completely in agreement with investigations of Weiser and Nitsche (1987, 1988), which show the separation occurring in

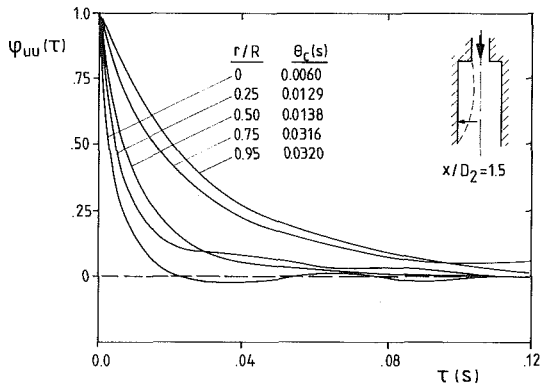

Fig. 10 Autocorrelation function and integral time scale, θ_c, of U-velocity fluctuations in the sudden expansion geometry

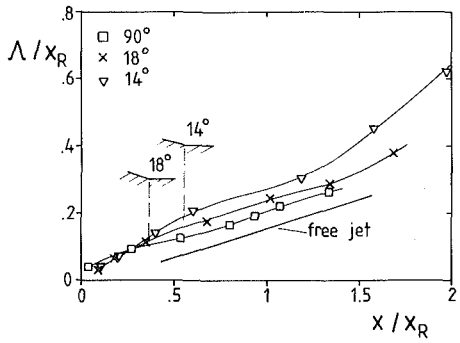

Fig. 11 Growth of vorticity thickness (free jet data has arbitrary virtual origin)

the diverging section of the diffuser for half-angles of 18 and 22.5 deg. The upstream turbulence level was approximately 4 percent in both studies, therefore the only distinguishing difference in experimental conditions is the presence of a low swirl at the diffuser inlet in the present study. No other experimental data is presently available which can resolve this question, however it appears that the point of separation for diffuser angles in this range is sensitive to the presence of swirl. Numerical computations of this flow performed by the authors using a finite differencing scheme with a $k-\epsilon$ turbulence model also predict a separation point of the flow in the diverging section of the diffuser inlet for the 14 and 18 deg diffuser geometries. Note that this apparent fixing of the separation point at the expansion inlet at low swirl numbers is contrary to the effect observed at high swirl numbers. At high swirl numbers (>0.4), the induced radial pressure gradient forces the flow to remain attached throughout the diverging section, as discussed in detail by Habib and Whitelaw (1982).

The growth of the separated shear layers, as measured by the increase of the vorticity thickness, Λ:

$$\Lambda = U_0 / \left| \frac{dU}{dr} \right|_{max} \tag{1}$$

is shown in Fig. 11, normalized by x_R and plotted against x/x_R. The 14 and 18 deg diffusers show an initial rapid increase of Λ, which is sustained until the end of the diffuser section, at which point the slope of Λ takes on the value observed for the 90 deg diffuser. In the region immediately before and after reattachment the spread rate appears to be independent of the diffuser angle and in fact agrees well with results obtained by Husain and Hussain (1979) in the far field of an axisymmetric mixing layer. After reattachment ($x/x_R > 1.3$) the growth of vorticity thickness again increases more rapidly, a behavior which is in good agreement with similar measurements performed in various plane and axisymmetric separated flows and summarized in Castro and Haque (1987).

The results presented in Fig. 11 show that the separated shear layer is influenced considerably by the proximity of the diffuser wall, at least for diffuser half-angles up to 18 deg. Although the radial velocity gradient is somewhat larger immediately after separation in the case of the 14 and 18 deg diffuser, over most of the recirculation region it is lower than in the 90 deg diffuser case.

The maximum values achieved by the normal stress components and the uv shear stress are shown in Fig. 12, normalized with U_0^2 and plotted against x/x_R. Also included in these diagrams are the maximum values of k, which follow the maximum values of $\overline{u^2}$ closely for all diffusers studied. The stress components rise more rapidly after separation for the 14 and 18 deg diffusers than for the 90 deg diffuser. The $\overline{v^2}$ and $\overline{w^2}$ maxima reach comparable values for all diffusers, however the maximum value of $\overline{u^2}$ and k are lower for the 90 deg diffuser. This suggests that the production of turbulent kinetic energy, as given by

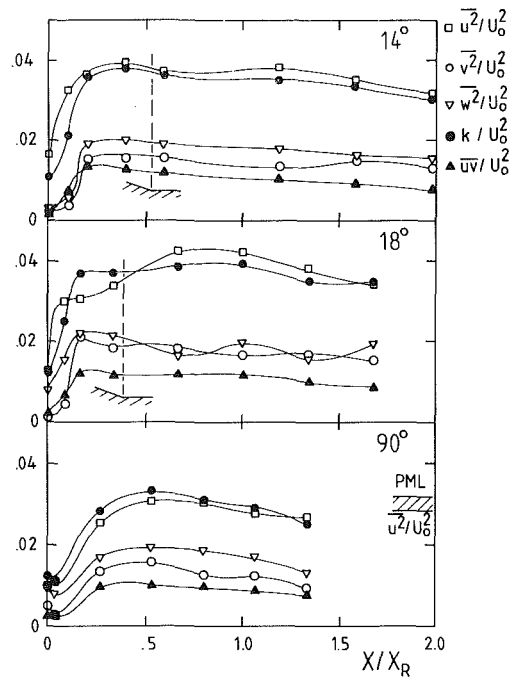

Fig. 12 Maximum values of Reynolds stresses and comparison to plane mixing layer (PML)

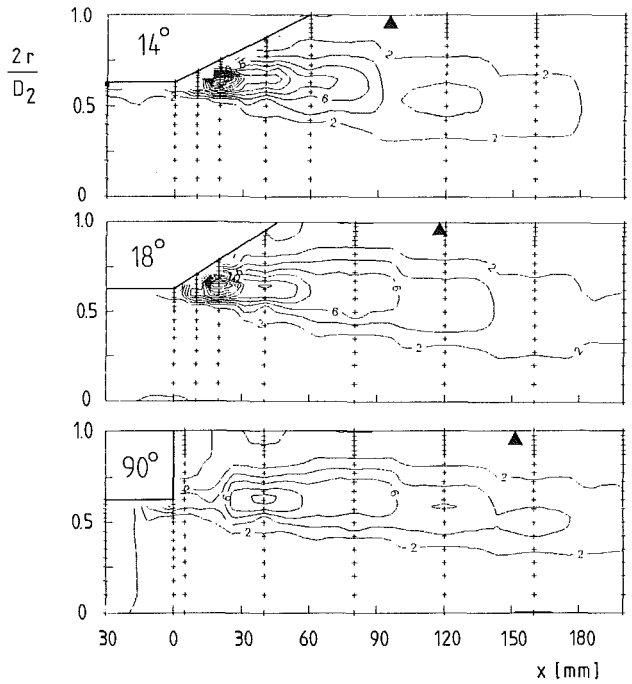

Fig. 13 Contour plots of production of turbulent kinetic energy ($\times 10^3 h/U_0^3$, ▲ mean reattachment)

$$P = \overline{uv}\left(\frac{\partial \bar{U}}{\partial r} + \frac{\partial \bar{V}}{\partial x}\right) + \overline{u^2}\frac{\partial \bar{V}}{\partial x} + \overline{v^2}\frac{\partial \bar{V}}{\partial r} + \overline{w^2}\frac{\bar{V}}{r} \tag{2}$$

is larger for the 14 and 18 deg diffusers.

Evaluation of equation (2) showed that it depended almost entirely on the product of uv and $\partial \bar{U}/\partial r$ and only this term was used in subsequent computations. Figure 13 presents contour plots of the production term for the three diffuser models, on which the actual measurement positions have also been indicated. The radial dimension has been scaled by the factor 2 for clarity. The production of turbulent kinetic energy

reaches values in the 14 and 18 deg diffusers which are up to 3 times larger than those in the 90 deg diffuser. This is due primarily to higher values of the shear stress uv immediately after separation and to a much lesser extent to a higher value of the radial velocity gradient. This localized region of high production extends downstream only about half the geometric length of the diffuser section. Beyond this region the radial velocity gradient is seen to increase with diffuser half-angle (Fig. 11), whereas the shear stress decreases with increasing diffuser half-angle. Thus the production of turbulent kinetic energy becomes approximately independent of the diffuser geometry in this region.

The data presented in Figs. 11–13 allow some general conclusions to be drawn about the effect of the diffuser wall on the flow field. Directly after separation the proximity of the wall in the 14 and 18 deg diffusers leads to high velocity gradients and a high production of turbulence. This is immediately reflected in a spread rate of the separated shear layer which exceeds the value observed for the 90 deg expansion. This initial rapid diffusion of the separated shear layer in the 14 and 18 deg diffuser leads to an earlier mean reattachment of the flow, but also to lower radial velocity gradients throughout most of the subsequent recirculation region. Thus the production of turbulence also decreases downstream of this entrance region of the diffuser, and the spread rate of the shear layer decreases to a value comparable with the 90 deg diffuser. The higher levels of normal stresses and shear stresses observed for the 14 and 18 deg diffusers are, however, sustained throughout the entire diffuser section and beyond the point of mean reattachment.

This description of the flow is not in complete agreement with the observations of Chaturvedi (1963). Although he reports a higher initial spreading rate of the shear layer in a 15 deg diffuser than in the 30, 45, or 90 deg diffusers, he also shows lower values of turbulence production for the 15 deg diffuser. This may however, be a problem of measurement resolution, since his first measurement plane was half way through the diffuser section. A second conclusion of Chaturvedi's, that the diffuser geometry influences the flow field for diffuser half-angle less than 32 deg, is substantiated by the present experiments.

Acknowledgments

The present work was a cooperative effort between the Lehrstuhl für Strömungsmechanik, Erlangen and the Institut für Luft- und Raumfahrt, Berlin. Partial funding from the Deutsche Forschungsgemeinschaft (Tro 194/3-3, Ha 532/19-3) is gratefully acknowledged, as are several fruitful discussions with Dr. R. Sellens. The data presented in this paper are available in ASCII format on PC/XT/AT compatible media.

References

1 Adrian, R. J., and Yao, C. S., 1987, "Power Spectra of Fluid Velocities Measured by Laser Doppler Velocimetry," *Exp. in Fluids*, Vol. 5, pp. 17–28.

2 Armaly, B. F., Durst, F., Pereira, J. C. F., and Schönung B., 1983, "Experimental and Theoretical Investigation of Backward-Facing Step Flow," *Journal of Fluid Mech.*, Vol. 127, p. 473.

3 Castro, I. P., and Haque, A., 1987, "The Structure of a Turbulent Shear Layer Bounding a Separation Region," *Journal of Fluid Mech.*, Vol. 179, pp. 439–468.

4 Chaturvedi, M. C., 1963, "Flow Characteristics of Axisymmetric Expansions," *Proc. of the ASCE, J. of Hydr. Division*, pp. 61–92.

5 Dimaczek, G., Tropea, C., and Wang, A. B., 1988, "Turbulent Flow Over Two-Dimensional, Surface-Mounted Obstacles: Plane and Axisymmetric Geometries," *Proc. 2nd European Turb. Conf.*, Berlin.

6 Driver, D. M., Seegmiller, H. L., and Marvin, J. G., 1987, "Time-Dependent Behavior of a Reattaching Shear Layer," *AIAA Journal*, Vol. 25, No. 7, pp. 914–919.

7 Durrett, R. P., Stevensen, W. H., and Thompson, H. D., 1984, "LDV Measurements Near the Step in an Axisymmetric Sudden Expansion Air Flow," *Proc. 2nd Int. Symp. of Appl. of Laser Anemom. to Fluid Mech.*, Lisbon, 1984.

8 Eaton, J., and Johnston, J., 1981, "Low Frequency Unsteadiness of a Reattaching Turbulent Shear Layer," *Proc. of 3rd Int. Symp. on Turbulent Shear Flows*, Davis, CA.

9 Freeman, A. R., 1975, "Laser Anemometer Measurements in the Recirculating Region Downstream of a Sudden Pipe Expansion," *Proc. LDA Symposium*, Copenhagen.

10 Habib, M. A., and Whitelaw, J. H., 1982, "The Calculation of Turbulent Flow in Wide-Angle Diffusers," *Num. Heat Trans.*, Vol. 5, pp. 145–164.

11 Ha Ming H., and Chassaing, D., 1979, "Perturbations of Turbulent Pipe Flow," *Turbulent Shear Flows I*, eds. F. Durst, B. E. Launder, F. W. Schmidt, J. H. Whitelaw, Springer-Verlag, pp. 178–197.

12 Husain, Z. D., and Hussain, A. K. M. F., 1979, "Axisymmetric Mixing Layer: Influence of the Initial and Boundary Conditions," *AIAA Journal*, Vol. 17, No. 1, pp. 48–55.

13 Khezzar, L., Whitelaw, J. H., and Yianneskis, M., 1985, "An Experimental Study of Round Sudden Expansion Flows," *Proc. 5th Symp. on Tur. Shear Flows*, Cornell University, pp. 5–25.

14 Mabey, D., 1972, "Analysis and Correlation of Data on Pressure Fluctuations in Separated Flow," *Journal of Aircraft*, Vol. 9, pp. 642–645.

15 Moon, L. F., and Rudinger, G., 1977, "Velocity Distribution in an Abruptly Expanding Circular Duct," ASME JOURNAL OF FLUIDS ENGINEERING, pp. 226–230.

16 Moss, W. D., Baker, S., and Bradbury, L. J. S., 1979, "Measurements of Mean Velocity and Reynolds Stresses in Some Regions of Recirculating Flow," *Turbulent Shear Flows*, ed. Durst, Launder, Schmidt, Whitelaw, Springer-Verlag, Berlin.

17 Ruderich, R., and Fernholz, H. H., 1986, "An Experimental Investigation of a Turbulent Shear Flow with Separation, Reverse Flow, and Reattachment," *Journal of Fluid Mech.*, Vol. 163, pp. 283–322.

18 Szczepura, R. T., 1985, "Flow Characteristics of an Axisymmetric Sudden Pipe Expansion: Results Obtained from the Turbulence Studies Rig, Part I: Mean and Turbulence Velocity Results," Report TPRD/B/0702/N85, Central Electricity Generating Board, Berkeley Nuclear Laboratories, England.

19 Tropea, C., "Turbulence-Induced Spectral Bias in Laser Anemometry," *AIAA Journal*, Vol. 25, No. 2.

20 Tropea, C., and Struthers, D., 1987, "Microprocessor Based On-Line Measurement System for LDA," Paper 29, *Proc. of Use of Computers in Laser Velocimetry*, ISL, Saint Louis.

21 Weiser, N., and Nitsche, W., 1987, "Experimentelle und numerische Untersuchungen zur abgelösten Strömung an einer Rohrstufe mit variablem Öffnungswinkel," ILR-Mitteilung 177, Institut für Luft- und Raumfahrt, Berlin.

22 Weiser, N., and Nitsche, W., 1988, "Zur rotationssymmetrischen Innenströmung mit Ablösung" ILR-Mitteilung 193, Institut für Luft- und Raumfahrt, Berlin.

Turbulent Boundary Layer Development in the Presence of Small Isolated Two-Dimensional Surface Discontinuities

D. J. Cockrell
Senior Lecturer,
Department of Engineering,
University of Leicester,
Leicester, Great Britain

H. H. Nigim
Assistant Professor,
Faculty of Engineering,
Bir Zeit University,
West Bank,
via Israel

M. A. Alhusein
Assistant Professor,
Department of Engineering,
Mu'tah University,
Mu'tah,
Al-Karak, Jordan

Discontinuities in surfaces over which fluids flow can occur in a variety of situations. One of contemporary engineering significance is that which arises on aircraft wings, where the wing forms a junction with an auxiliary lifting surface. Such discontinuities are often two-dimensional and may well be small, lying within the logarithmic regions of the turbulent boundary layers in which they are immersed. In this paper such surface discontinuities are idealized into shapes whose drag coefficients, when they have been isolated from their surrounding surfaces, have been previously determined and tabulated. By making appropriate assumptions about the boundary layer characteristics in the vicinity of the discontinuities and then adopting appropriate integral boundary layer prediction techniques, methods are developed for continuing the boundary layer prediction process across them and then downstream of them. These computations compare well with experimental results, even for comparatively large discontinuities and the technique is recommended for use in a predictive role.

Introduction

It can be very difficult to avoid the introduction of small discontinuities into the finished surfaces of aircraft. For example, Fig. 1 indicates how two-dimensional surface discontinuities are introduced at the locations at which the leading-edge slats and the trailing-edge flaps retract into the main aerofoil. Although these may be small in height in comparison with the local boundary layer thickness their presence can result in significant drag increments.

Young and Paterson [1] explain that these increments arise from a combination of four interacting phenomena:

(i) pressure forces which act on the surface protuberances themselves;

(ii) changes in the local surface shear forces both immediately in front of and behind the surface protuberances;

(iii) modifications which occur to the development of the boundary layer downstream;

(iv) flow separation which occurs immediately upstream and downstream of the protuberances.

Since all of these phenomena are influenced by the free-stream pressure gradient the drag increments are dependent on the local surface configuration. Once the drag has been quantified, then with care during manufacture and in maintenance these increments could be minimized, if it could be shown to be cost-effective to do so. Hence it is desirable to make a detailed appreciation of the detriment to aerodynamic performance which these surface discontinuities can cause.

In this paper, only the consequences of two-dimensional surface discontinuities which are formed in effectively incompressible flows are considered, two-dimensional discon-

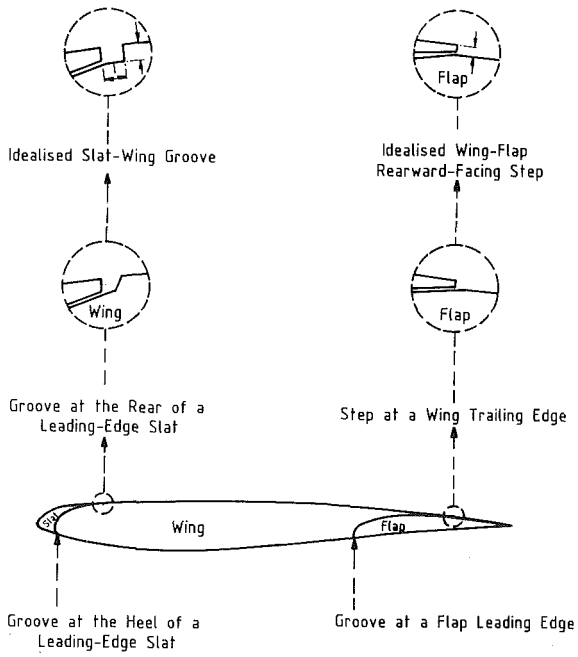

Fig. 1 Two-dimensional surface discontinuities on aircraft wings

Contributed by the Fluids Engineering Division for publication in the JOURNAL OF FLUIDS ENGINEERING. Manuscript received by the Fluids Engineering Division August 28, 1988.

tinuities being those which do not vary over the span of the relevant surfaces. Small surface discontinuities are chosen and these give rise to weak perturbations in the flow downstream. Following Bradshaw and Wong [2], "weak perturbations" implies that although velocity scales and length scales in the downstream turbulent boundary layer may be altered by their presence, no significant changes take place to the dimensionless properties of the turbulence structure. For such a state of affairs to occur the height h of such small two-dimensional surface discontinuities relative to the undisturbed local boundary layer thickness δ_0 must be such that $h/\delta_0 << 1.0$. To meet these requirements it is anticipated that such discontinuities will lie within the logarithmic region of the turbulent boundary layers in which they are immersed.

When determining the total drag increment which results from these small surface discontinuities, it is sufficient to model the discontinuity as if there were at its location a step function increment in the boundary layer integral characteristics. Both immediately upstream and immediately downstream of the discontinuity the flow may separate from the surface, the lengths of the resulting separation regions being functions of the discontinuity shape and its size. Behind the downstream separation region a redeveloping boundary layer reattaches to the surface. In the prediction procedure which is described here both the separation region downstream of the discontinuity and the redeveloping boundary layer which follows it are modelled.

By employing an appropriate integral turbulent boundary layer prediction technique, the consequential increase in boundary layer thickness downstream, the surface shear forces and the propensity for the flow to separate are determined. Although the method is applicable to virtually any integral boundary layer prediction program, the authors have used a lag-entrainment technique which was developed in the United Kingdom after the 1968 Stanford Boundary Layer Conference by Green, Weeks and Brooman [3].

Drag Coefficients for Isolated Two-Dimensional Surface Discontinuities

Values of the drag coefficient for isolated two-dimensional surface discontinuities must be determined experimentally. Although data are sparse they can be found in appropriate sources such as those which Young and Paterson have summarized. Many of the relevant experiments were performed at zero free stream pressure gradient, notably by Gaudet and Winter [4]. Where these discontinuities are sufficiently small compared with the local boundary layer thickness for their drag D to be considered independent of free stream conditions, then:

$$D = f(\text{discontinuity shape}; h; u_\tau; \rho; \mu) \quad (1)$$

where u_τ is the friction velocity of the local surface undisturbed by any discontinuity, while ρ and μ signify the density and the viscosity of the fluid. It then follows that:

$$\frac{D}{\rho u_\tau^2 h} = \frac{C_D}{c_f} = f(\text{discontinuity shape}; h^+) \quad (2)$$

where the drag coefficient for the surface discontinuity $C_D = D/(\frac{1}{2}\rho U^2 h)$, C_f is the skin friction coefficient for the surface location in the absence of the discontinuity and h^+ is the dimensionless discontinuity height:

$$h^+ = \frac{h u_\tau}{v} \quad (3)$$

and the relationship for drag given in equation (2) is independent of the pressure in the free stream. There is good experimental evidence for writing this relationship, at a given free-stream Mach number, in the form:

$$\frac{C_D}{c_f} = A \log h^+ + B \quad (4)$$

Experimental values for A and B have been obtained from reference [1] and have been given in Table 1 for certain surface discontinuity geometries in an incompressible free stream. These values are strongly dependent on discontinuity shape, tabulated values applying to discontinuities which have unchamfered geometries.

Whatever the free-stream pressure gradient may be, the drag coefficient C_D for a small isolated two-dimensional surface discontinuity of height h is related to the step increment in

Table 1 Drag coefficients for idealized discrete two-dimensional surface discontinuities in incompressible flows

Discontinuity shape		A	B	Source
Rearward-facing step	h	16	−6	Gaudet and Winter [5]; Wieghardt [6]; Pallister [7]
Forward-facing step	h	60	−80	Gaudet and Winter; Wieghardt; Pallister
Square ridge	h	150	−190	Gaudet and Winter; Wieghardt
Spanwise slot	h	2	−2	Gaudet and Winter

Nomenclature

C_D = isolated discontinuity drag coefficient
c_f = skin friction coefficient at the location in the absence of a surface discontinuity
$H = \delta^*/\theta$ = boundary layer shape factor
$\bar{H} = (\delta - \delta^*)$ = boundary layer entrainment shape factor
h = discontinuity height
$h^+ = hu_\tau/v$ = dimensionless discontinuity height
L = dissipation length scale in the boundary layer
U = local free stream velocity
u = local velocity in the boundary layer at height y from the surface
u_τ = friction velocity
x = streamwise distance
x_R = boundary layer reattachment location
δ = boundary layer physical thickness
δ^* = boundary layer displacement thickness
v = kinematic viscosity
θ = boundary layer momentum thickness
τ_{max} = maximum shear stress in the boundary layer

Subscripts

D = in the developing boundary layer
eq = in an equilibrium boundary layer
0 = at a discontinuity location
R = close to flow reattachment
T = at the location at which the momentum thickness increment is required
1,2 = immediately upstream and downstream of the discontinuity, respectively

the boundary layer momentum thickness $\Delta\theta_0$ which it causes, by:

$$C_D = 2\Delta\theta_0/h. \tag{5}$$

Techniques for Predicting Boundary Layer Characteristics Downstream of Surface Discontinuities

From Table 1, or from some other discontinuity drag coefficient data source e.g., Heorner [8], together with equation (5) the increase in the boundary layer momentum thickness caused by a two-dimensional discontinuity of known geometry on a surface for which in its absence the local boundary layer characteristics are known, can be directly determined. This local effect at the surface discontinuity location results in boundary layer thickening downstream with a consequent variation of both the skin friction and of flow separation tendencies. These effects can be determined through application of an appropriate boundary layer prediction technique.

A simple method of predicting the downstream boundary layer growth is by the use of the magnification factor prediction concept, which Nash and Bradshaw [9] published some twenty years ago. By assuming that over the surface downstream of the discontinuity the boundary layer shape factor H remains constant and equal to 1.5, an expression is obtained for the downstream boundary layer momentum thickness increment $\Delta\theta_T$ in terms of the step increment across the discontinuity, $\Delta\theta_0$:

$$\frac{\Delta\theta_T}{\Delta\theta_0} = \left[\frac{\theta_0}{\theta_T}\right]^{0.2} \left[\frac{U_0}{U_T}\right]^{4.2} \tag{6}$$

where U denotes the free-stream velocity and the subscripts $_0$ and $_T$ imply the discontinuity location and that of the line downstream perpendicular to the flow at which the momentum thickness increment is required. Since, together with equation (5), $\Delta\theta_T/\Delta\theta_0$ gives the drag coefficient of the discontinuity inclusive of its associated surface, this ratio is sometimes referred to as the surface magnification factor.

For present purposes, maintaining the shape factor downstream of the discontinuity equal to 1.5 is unsatisfactory, particulary when the surface under consideration is close to the aerofoil trailing edge, where the free stream pressure gradient is usually strongly adverse. A more appropriate integral boundary layer prediction technique would be one which established the variation which occurs downstream of the discontinuity in the boundary layer shape factor. So that this can be done it is first necessary to determine the step change in one other parameter which occurs across the discontinuity. The boundary layer displacement thickness δ^* is selected.

The Displacement Thickness Datum Downstream of the Discontinuity

Since the flow usually separates from the upper surface of a given discontinuity the new shear layer which grows immediately downstream will possess properties which emanate from this separation region. To determine the downstream displacement thickness, allowance must therefore be made for the physical height of the discontinuity. For example, if the discontinuity were a forward-facing step of height h, the new shear layer which begins to develop downstream does so with its origin at a height $+h$ relative to the upstream boundary layer. Similarly, if it were a rearward-facing step of height h, the origin for the boundary layer downstream would be at a height $-h$ relative to that upstream.

Computing Displacement Thickness Increments Across Surface Discontinuities

Two different techniques are described for determining the boundary layer displacement thickness increment which occurs at the small surface discontinuity location. To this downstream displacement thickness the physical height of the discontinuity may need to be added or subtracted, as explained above.

In the first technique it is assumed that the mass flow within the boundary layer immediately downstream of the discontinuity is equal to that immediately upstream that is, the boundary layer mass flow thickness $(\delta - \delta^*)$ immediately downstream is equal to that immediately upstream. Since the entrainment shape factor $\bar{H}$ is defined by:

$$\bar{H} = (\delta - \delta^*)/\theta \tag{7}$$

then the entrainment shape factor $\bar{H}_2$ immediately downstream of the discontinuity will be given in terms of its value upstream $\bar{H}_1$ by:

$$\bar{H}_2 = \bar{H}_1[\theta_0/(\theta_0 + \Delta\theta_0)]. \tag{8}$$

As $\Delta\theta_0$ is given by equation (5) and Table 1, $\bar{H}_2$ is determined. If it can be expressed in terms of the boundary layer shape factor H_2 the displacement thickness immediately downstream of the discontinuity is found.

In a turbulent boundary layer on a smooth surface an appropriate relationship for $\bar{H}$ in terms of H has been developed by Gaudet [10] in the form:

$$\left(\frac{2+\beta}{4-\beta}\right)\frac{\bar{H}}{H} = \frac{3}{2}\,\frac{H}{H-\beta} - 1 \tag{9}$$

where β is a function of Reynolds number and is given by the expression:

$$\beta = \frac{1}{1 - \left(\dfrac{0.68}{\log R_\theta - 1}\right)^{1.75}} \tag{10}$$

Equation (9) gives two different values for the shape factor H_2 in terms of the entrainment shape factor $\bar{H}_2$. The one nearest in value to the shape factor H_1 immediately upstream of the discontinuity is normally chosen.

An alternative assumption from which the boundary layer displacement thickness increment across a small surface discontinuity could be determined is that the discontinuity's presence does not appreciably alter the boundary layer shape factor, so that H_2 is equal to H_1, immediately upstream of the discontinuity. By applying Gaudet's expressions to the boundary layer formed both upstream and downstream of the discontinuity it is seen that little change occurs to the entrainment shape factor across the discontinuity so that the increase in boundary layer thickness $\Delta\delta$ is given approximately by:

$$\Delta\delta \simeq (\delta_1/\delta_1^*)\Delta\delta^*. \tag{11}$$

This value can be compared with that obtained when making the preferred assumption, that the boundary layer mass flow thickness is conserved across the discontinuity, when:

$$\Delta\delta = \Delta\delta^*. \tag{12}$$

It will be shown that conservation of mass thickness gives results which best accord with experimental determinations.

The Separating Region and the Redeveloping Boundary Layer Downstream

The lengths of the flow separation regions immediately in front of and immediately behind the surface discontinuity are functions of its height h and they can become extensive. In this model no attempt has been made to model the region immediately upstream. Although there are disparities in published data concerning the relationship between the length of the downstream region and the discontinuity height, relation-

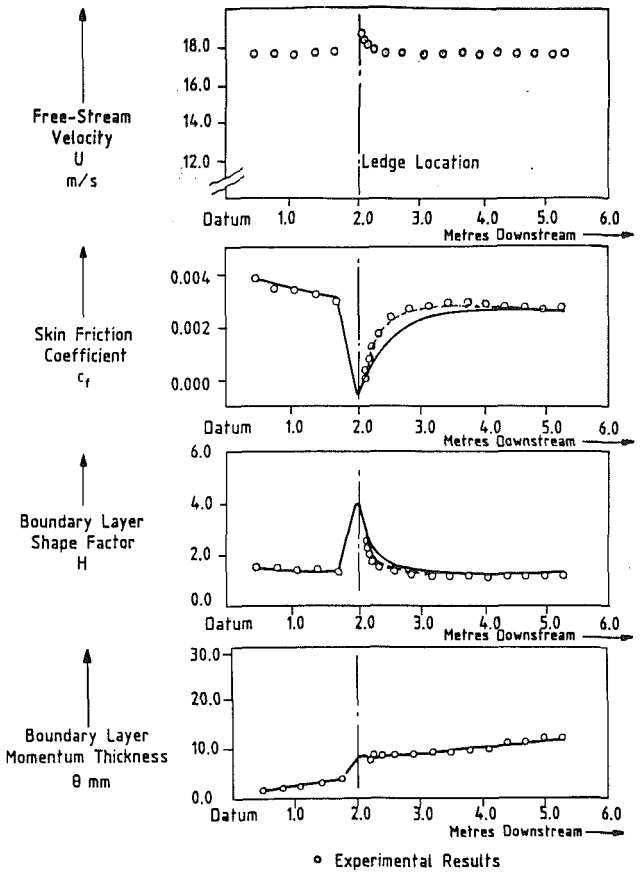

Fig. 2 Prediction of the flow characteristics upstream and downstream of Tillmann's 12.0 mm two-dimensional ledge

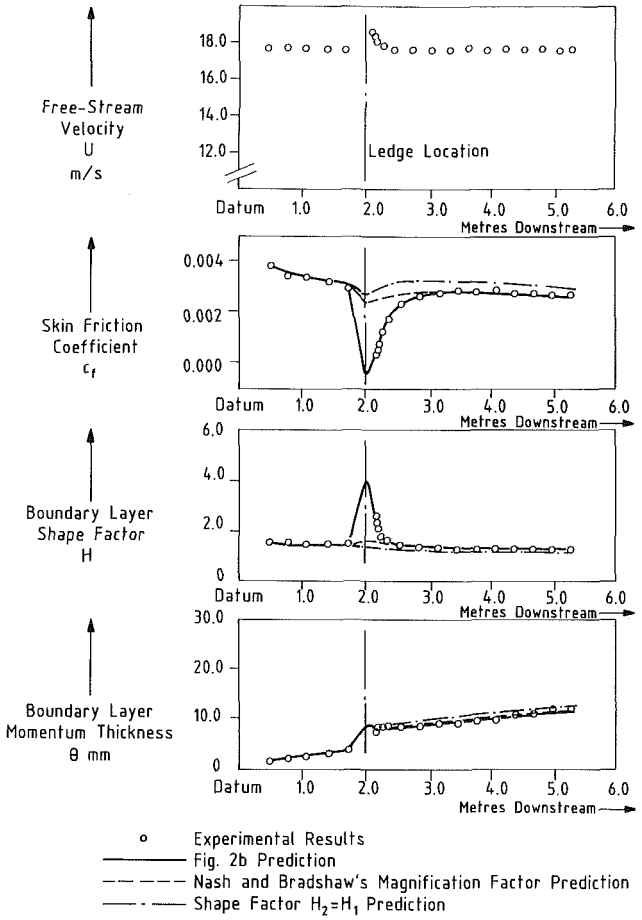

Fig. 3 Effect of prediction technique on the determination of flow characteristics upstream and downstream of Tillmann's ledge

ships both by Tillmann [11] and by Bradshaw and Wong [2] have been adopted here, so that independently of any free stream pressure gradient, the distance from the location of the discontinuity to flow reattachment has been assumed to equal $13h$ with small square ridge discontinuities and $6h$ with rearward-facing steps.

Green, Weeks, and Brooman's lag-entrainment boundary layer prediction technique permits modifications to be made to the values of the boundary layer dissipation length scale L and the maximum shear stress $\tau_{\max}$. For the reattaching subboundary layer downstream of the separation region caused by the discontinuity, modifications are made to these two flow properties. Whereas in an equilibrium boundary layer the dissipation length is a constant proportion of the local boundary layer thickness, at flow reattachment it is only some 80 percent of this value. It then grows exponentially as the developing subboundary layer increases in height. As an appropriate expression for the dissipation length L in this subboundary layer, Bradshaw and Wong therefore proposed:

$$\frac{L}{\delta}=0.095\left[1-0.3\ \exp\left\{-\left(\frac{x-x_R}{80\ h}\right)\right\}\right] \tag{13}$$

where h is the surface discontinuity height and the streamwise distance x is equal to x_R at flow reattachment, increasing with distance thereafter. With this relationship the dissipation length scale L equals 0.067 δ at flow reattachment and increases exponentially as the boundary layer recovers from the discontinuity-induced flow separation.

Kim, Kline, and Johnston [12] showed that in a redeveloping boundary layer the maximum value of the shear stress is some eight times its corresponding value in an equilibrium boundary layer. As an expression for the maximum shear stress in the redeveloping region $(\tau_{\max})_D$ they proposed:

$$(\tau_{\max})_D=(\tau_{\max})_{\text{eq}}\left[1+\left(\frac{(\tau_{\max})_R-(\tau_{\max})_{\text{eq}}}{(\tau_{\max})_{\text{eq}}}\right)\exp\left\{-1.25\left(\frac{x-x_R}{x_R}\right)^2\right\}\right] \tag{14}$$

where the subscripts eq and R, respectively, imply the values obtained in an equilibrium boundary layer and in a separated boundary layer which is close to reattachment. In experiments performed by Moss and Baker [13] $(\tau_{\max})_R$ was found to be equal to $(0.072)^1/_2\rho U^2$ for the reattached region downstream of a square-ridge discontinuities, $(0.060)^1/_2\rho U^2$ when the surface discontinuity was a forward-facing step and $(0.020)^1/_2\rho U^2$ when it was rearward-facing step.

Both equations (13) and (14) were developed from experiments which were performed in a zero pressure gradient. In the absence of any more appropriate experimental data these expressions have been assumed to be independent of the free stream pressure gradient.

Comparison With Experimental Results

Among the best measurements which have been made immediately downstream of a surface discontinuity are those which Tillmann [11] published in 1945 for the zero free-stream pressure gradient flow behind a two-dimensional 12 mm square ledge immersed in a 40 mm thick boundary layer and these are shown in Fig. 2. In the figures the free-stream velocity distributions shown are those in the presence of the surface discontinuities. In Figs. 2 and 3 the experimental values shown for the skin friction coefficients are those which Coles [14] reappraised for the 1968 Stanford Boundary Layer Conference.

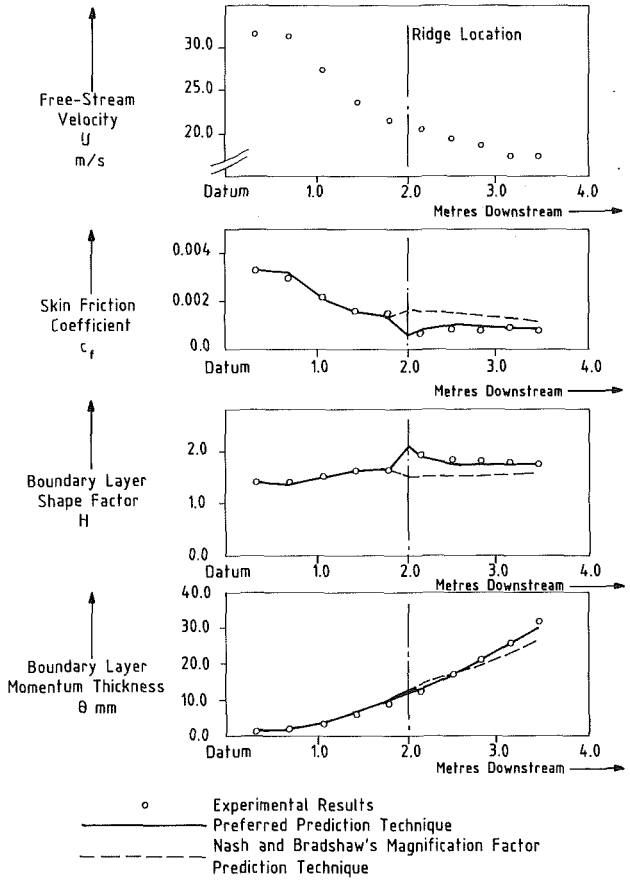

Fig. 4 Prediction of the flow characteristics upstream and downstream of Nigim's 6.35 mm square ridge in a strongly adverse free-stream pressure gradient

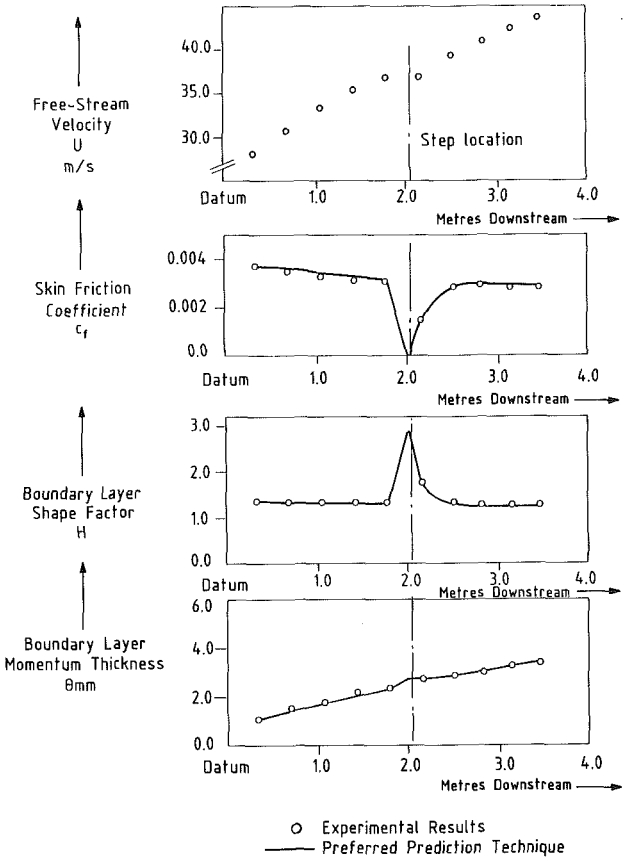

Fig. 5 Prediction of the flow characteristics upstream and downstream of Higazy's 4.0 mm rearward-facing step in a favorable free-stream pressure gradient

At 1.51 meters upstream of the ledge Tillmann's initial measurements of the skin friction coefficient c_f, the boundary layer shape factor H and its momentum thickness θ, together with the free-stream velocity U were fed in as the inputs to the integral lag-entrainment boundary layer prediction technique. The drag of the ledge is estimated from the boundary layer momentum thickness increment which Tillmann obtained at its location. Using this value, together with the corresponding displacement thickness increment given by assuming no change occurs in the boundary layer mass flow thickness across the ledge and that the boundary layer downstream of the ledge grows from a height equal to that of the ledge, the lag-entrainment prediction technique gives results shown in Fig. 2 for the flow downstream of the ledge discontinuity.

When equations (13) and (14) are used to model the downstream separation region and the redeveloping boundary layer much better predictions are obtained and these results accord very well with the measurements which Tillmann made.

In the reverse flow region which occurs when the flow separates downstream of a surface discontinuity negative values of skin friction coefficient are predicted. These agree with experimental measurements which Westphal, Eaton and Johnston [15] have made in the separation region downstream of a step.

In Fig. 3 the same experimental and predicted characteristics for flow over a ridge in a zero free-stream pressure gradient are compared with those predicted from Nash and Bradshaw's magnification factor technique and also when the boundary layer shape factor is assumed to be unchanged across the discontinuity, so that $H_2 = H_1$. In the region immediately downstream of the ledge only the preferred unchanging mass flow thickness method, incorporating equations (13) and (14), gives results which match with the experimental results. However, as the distance downstream of the discontinuity is increased the results obtained from all three prediction techniques become comparable and then they all accord well with the measured values.

Nigim [16] introduced discrete, square-sectioned, two-dimensional surface discontinuities on to an otherwise smooth surface subjected to a strongly adverse free-stream pressure gradient. The graphs in Fig. 4 show the effects on the boundary layer downstream of a 6.35 mm square ridge discontinuity situated 2.02 meters downstream from the origin. Predictions indicate that the Nash and Bradshaw magnification factor technique, which assumes that the shape factor downstream of the ridge is constant and equal to 1.5, is much less satisfactory than the preferred unchanging mass flow thickness method, together with equations (13) and (14). In situations in which the boundary layer shape factor greatly exceeds 1.5, the magnification factor technique has little to commend it.

Treating a small two-dimensional surface discontinuity as the cause of a step increment in boundary layer thickness parameters is a satisfactory procedure regardless of either the discontinuity shape or the nature of the free stream. For example, Higazy [17] has obtained experimental data for the effect of rearward-facing steps on boundary layer growth in a variety of free-stream pressure gradients. In Fig. 5 experimental characteristics which he obtained are shown in a favorable free-stream pressure gradient for boundary layer growth downstream of a 4 mm high rearward-facing step located on a smooth surface 2.1 meters downstream of the origin. Computed characteristics, based on the preferred constant mass flow thickness across the discontinuity prediction technique

are seen to compare well with the experimental results. As shown in Fig. 3, the alternative techniques do not predict the experimental characteristics well immediately downstream of the discontinuity.

Small Surface Discontinuities

Although the success of the technique is dependent on the height of the surface discontinuities being small in comparison with the local boundary thickness, there is considerable latitude in determining at what discontinuity height the technique ceases to be effective. As a conservative estimate their heights should be sufficiently small to permit these discontinuities to lie within the inner region of the boundary layer. The extent of this region is pressure gradient dependent, limiting the dimensionless discontinuity height h^+ to about 500 in a very strongly adverse pressure gradient but permitting h^+ to extend to 2000 or 3000 when the free-stream pressure gradient is favorable.

Stagnation of the local velocity within the boundary layer will occur at the discontinuity surface. This process may be partial or complete stagnation, depending on the discontinuity shape, hence the arbitrary values of the coefficients A and B in equation (4). However, the form of this relationship is a direct consequence of the stagnation process. Writing the drag D of the discontinuity in terms of the pressure distribution $(p-p_0)$ which is developed over it as:

$$D=\int_0^h (p-p_0)\mathrm{d}y \tag{15}$$

then for a given discontinuity the drag can be expressed in terms of local velocity stagnation by:

$$D=\int_0^h \left(\frac{1}{2}\rho u^2\right)dy \tag{16}$$

and if it is within the inner region of the boundary layer in which:

$$\frac{u}{u_\tau}=f\left(\frac{yu_\tau}{v}\right) \tag{17}$$

Then

$$\frac{\mathrm{D}}{\frac{1}{2}\rho u_\tau^2}=\int_0^h \left(\frac{u}{u_\tau}\right)^2 dy=F\left(\frac{hu_\tau}{v}\right)=F(h^+) \tag{18}$$

which is equation (2).

The experimentally-determined relationship in equation (4) applies to a wide range of two-dimensional surface discontinuity shapes. If a given discontinuity has a dimensionless height h^+ which does not greatly exceed the stated limits, then over much of the discontinuity surface stagnation of the inner boundary layer will still take place and Higazy [17] has shown that the form of equation (4) is still applicable. Where discontinuities such as grooves extend into the surface over which the fluid flows rather than form excrescences on the surface, the dimensionless discontinuity height h^+ could well exceed the limits quoted without the form of relationship in equation (4) becoming inapplicable.

Conclusions

A preferred technique for predicting the growth of the boundary layer downstream of small two-dimensional surface discontinuities, where small is defined as lying within the logarithmic boundary layer region, is presented. This technique is based on modelling the discontinuity as if it were the source of step changes in appropriate integral boundary layer characteristics and considering that at the discontinuity no change occurs in the boundary layer mass flow thickness. Though the flow separation region immediately upstream of the discontinuity is not modelled the effects of the separation region downstream and the consequent redeveloping boundary layer are included in the model.

Computations compare well with experimental results and will do so even when the heights of the discontinuities are sufficiently large for them to protrude beyond the logarithmic region of the boundary layer.

References

1 Young, A. D., and Paterson, J. H., Aircraft Excrescence Drag. AGARDograph 264, 1981.

2 Bradshaw, P., and Wong, F. Y. F., "The Attachment and Relaxation of a Turbulent Shear Layer," *Journal of Fluid Mechanics*, Vol. 52, 1972, pp. 113–135.

3 Green, J. E., Weeks, D. J., and Brooman, J. W. F., "Prediction of Turbulent Boundary Layers and Wakes in Compressible Flow by a Lag-entrainment Method," U.K. Aero. Res. Council R.&M. 3791, 1973.

4 Gaudet, L., and Winter, K. G., "Measurements of the Drag of Some Characteristic Aircraft Excrescences Immersed in Turbulent Boundary Layers," Paper 4, Aerodynamic Drag Conference Proceedings AGARD-CP-124, Izmir,Turkey, Apr. 1973.

5 Gaudet, L., and Winter, K. G., "Measurements of the Drag of Some Characteristic Aircraft Excrescences Immersed in Turbulent Boundary Layers," U.K. Royal Aircraft Establishment Tech. Memo., 1538, 1973.

6 Wieghardt, K., "Increase in Turbulent Skin Friction Caused by Surface Irregularities," U.K. Ministry of Aircraft Production Reports and Translations 103 (Translation of FB 1563, ZWB, 1942), 1946.

7 Pallister, K. C., "Wind Tunnel Measurements of the Transonic Drag of Excrescences Immersed in a Turbulent Boundary Layer," U.K. Aircraft Research Association Report 37, 1974.

8 Hoerner, S. F., *Fluid Dynamic Drag*, Published by the Author, 1958.

9 Nash, J. F., and Bradshaw, P. J., "The Magnification of Roughness Drag by Pressure Gradient," *J. Roy. Aer. Soc.*, Vol. 71, 1967, pp. 44–46.

10 Gaudet, L., "Integral Boundary-Layer Parameter Relationships and a Skin-Friction Law Derived from a Velocity Profile Family for Two-Dimensional Incompressible Flow," U.K. Royal Aircraft Establishment Tech. Memo. Aero 2080, 1986.

11 Tillmann, W., "Investigations of Some Peculiarities of Turbulent Boundary Layers on Plates," U.&.M. 6627, 1945, translated as British Rep. & Transl. CGD-497, MAP-VG 34-T, 1946.

12 Kim, J., Kline, S. J., and Johnston, J. P., "Investigation of a Reattaching Turbulent Shear Layer: Flow Over a Backward-Facing Step," ASME JOURNAL OF FLUIDS ENGINEERING, Vol. 102, Sept. 1980, pp. 302–308.

13 Moss, W. D., and Baker, S., "Re-Circulating Flows Associated with Two-Dimensional Steps," *Aeronautical Quarterly*, Vol. 31, Aug. 1980, pp. 151–172.

14 Coles, D. E., "A Young Person's Guide to the Data," Vol. II of the *Proceedings, Computation of Turbulent Boundary Layers Conference—1968*, edited by D. E. Coles and E. A. Hirst, Thermosciences Division, Stanford University, 1968.

15 Westphal, R. V., Eaton, J. K., and Johnston, J. P., "A New Probe for the Measurement of Velocity and Wall Shear Stress in Unsteady, Reversing Flow," ASME JOURNAL OF FLUIDS ENGINEERING, Vol. 103, Sept. 1981, pp. 478–482.

16 Nigim, H. H., "Effects of Small Isolated Roughness Elements on Turbulent Boundary Layers," Ph.D. thesis, Univ. of Leicester, 1981.

17 Higazy, M. G. A. F. I., "Influence of Isolated Backward-Facing Steps on Boundary Layers," Ph.D. thesis, Univ. of Leicester, 1986.

Impulse Response Method for Frequency-Dependent Pipeline Transients

Lisheng Suo
Graduate Research Assistant.

E. B. Wylie
Professor.
Fellow ASME

Department of Civil Engineering,
The University of Michigan,
Ann Arbor, MI 48109

An effective numerical method is presented to compute transients in piping systems in which frequency-dependent parameters influence the response. Frequency-dependent friction is utilized as the parameter-of-concern herein, however, the procedure can accommodate other factors such as frequency-dependent wavespeed equally well. The method, a variation in the impulse response method, is developed from the frequency response analysis and incorporates the fast Fourier transform. Examples are included showing the application of the method in computing both classic waterhammer and transients in pipes with frequency-dependent friction. Computed results agree very well with those from the standard method of characteristics and with physical experiments.

Introduction

Recorded fluid transients in actual systems sometimes differ from those computed by conventional methods utilizing the classic waterhammer theory. One of the primary reasons for this lack of agreement is that frequency-dependent factors in the actual systems, such as the frequency-dependent friction and wavespeed, are ignored in the classic theory. The frequency dependence may be caused by the viscosity of fluids, the viscoelastic behavior of fluids and pipe wall materials, the acoustic radiation of elastic energy as may occur in rock tunnels, or other influences. In this paper a numerical method is introduced as a different and attractive approach to deal with frequency dependence. It offers capabilities for analysis of a broader class of problems than currently can be handled by other methods.

A great effort has been contributed to the transient response of fluid lines with frequency-dependent friction since the early '60s and several methods and solutions are available in the literature. Based on the classic linear theory, Brown [2] derived the propagation operator and characteristic impedance, which fully describe the effect of the frequency-dependent viscosity on the propagation of acoustic waves in fluid transmission lines, and provided an analysis of impulse and step transient decay in lines. Brown and Nelson [3] further presented solutions of step responses in liquid lines and showed the application of the solution in simple transient analysis. Oldenburger and Goodson [12] developed the finite product technique to simplify the evaluation of transfer functions and the computation of transients. Holmboe and Rouleau [10] performed experiments to display the effect of viscous shear on transients in liquid lines and confirmed Brown's theoretical results. Karam and Leonard [11] developed a time-domain model, which utilized the convolution of a simple theoretical impulse response in a semi-infinite line with an arbitrary but known input wave to obtain the transient response in a finite fluid line. Zielke [18] derived an expression relating the viscous shear in transient laminar flow to both the velocity and the rate of velocity change, and, by use of a modified method of characteristics (MOC), computed the transient in a pipeline with frequency-dependent friction. Trikha [14] presented an approximate weighting function to replace the one in Zielke's expression, which offered the advantage of not requiring the storage of the entire flow history.

Although it is well known that the nonlinearity of pipe wall materials and dynamic effects of pipe walls may result in frequency-dependent wavespeeds, there has not been much research in this environment. Fanelli [7] showed theoretically that the dynamic effect of the rock mass surrounding a rock-bored penstock led to a complex-valued and frequency-dependent Young's modulus or wavespeed, which would make the waves propagating in the penstock dispersive. Fanelli, Angelico, and Escobar [8] reported an experimental confirmation of the transfer matrix method applied to a laboratory perspex pipeline. The calibrated wavespeed in the pipeline was frequency-dependent and of complex value as a consequence of the hysteretic and dynamic behavior of perspex. Franke and Seyler [9] adopted a frequency-dependent wavespeed and a separate frequency-dependent damping factor to compute hydraulic transients in viscoelastic pipes. The impulse response method was utilized instead of the standard MOC, however the treatment was not entirely satisfactory due to the use of lumped inertia, the consideration of separate friction effects, and the treatment of boundary conditions.

Because of the high effectiveness of the fast Fourier transform (FFT) algorithm, the Fourier transform method has been recently used in fluid transient analyses, however, mostly for linearized systems and harmonic analyses. Its unique feature of relating the system behavior in both the time domain and the frequency domain makes the method extremely suitable in dealing with problems of frequency dependence. Tsang et al. [15, 16] used the FFT method to predict the

Contributed by the Fluids Engineering Division for publication in the JOURNAL OF FLUIDS ENGINEERING. Manuscript received by the Fluids Engineering Division March 28, 1988.

dynamic behavior of air transimission lines subjected to an impulse, step or arbitrary excitation. The calculation procedure was considered relatively simple, while the numerical results showed good agreement with experimental measurements. Clifton [6] presented examples to illustrate the computation of transient responses of hydraulic systems with the FFT techniques. These examples took into account the interaction between elastic waterhammer, distributed friction losses and linearized control elements such as an orifice, a governed turbine, etc.

An effective numerical method is proposed herein to compute transients in complex systems with various frequency-dependent factors. The method, abbreviated to "IMPREM" since it is a variation in the IMPulse REsponse Method, is developed from the frequency response analysis and incorporates the FFT technique. The basic equations and the development of IMPREM are first presented along with a brief description of the numerical scheme. Examples are then included to show the application of IMPREM in computing both the classic waterhammer and transients in pipes with frequency-dependent friction. Comparisons of computed results with those from the standard MOC and with physical experiments show good agreement. The method also holds for systems with frequency-dependent wavespeeds and examples can be found in reference [13].

Basic Equations

The simplified one-dimensional momentum and continuity equations for turbulent unsteady pipe flow read [17]

$$\frac{\partial p}{\partial x}+\rho\frac{\partial v}{\partial t}+\rho g\sin\alpha+\frac{\rho f}{2D}v^2=0 \tag{1}$$

$$\frac{\partial p}{\partial t}+\rho a^2\frac{\partial v}{\partial x}=0 \tag{2}$$

Application of equations (1) and (2) to a single pipe segment, with the assumption of sinusoidal waves and linearized friction, shows that the complex-valued variations of pressure head H and flow Q at two sections x far apart along the pipe are related by the transfer matrix

$$\begin{Bmatrix} H \\ Q \end{Bmatrix}_D = \begin{bmatrix} \cosh\gamma x & -Z_C\sinh\gamma x \\ -\dfrac{1}{Z_C}\sinh\gamma x & \cosh\gamma x \end{bmatrix} \begin{Bmatrix} H \\ Q \end{Bmatrix}_U \tag{3}$$

where subscripts D and U refer to downstream and upstream sections, respectively. Propagation constant γ and characteristic impedance Z_C are defined by

$$\gamma=\sqrt{Cs(Ls+R)} \tag{4}$$

$$Z_C=\frac{\gamma}{Cs} \tag{5}$$

with

$$C=\frac{gA}{a^2};\quad L=\frac{1}{gA};\quad R=\frac{f\bar{q}}{gDA^2}.$$

For laminar flow and assuming a constant, or steady, friction factor, resistance parameter R is defined as

$$R=\frac{32\nu}{gAD^2}$$

With consideration of frequency-dependent friction, the above transfer matrix, equation (3), still holds as long as terms γx and Z_C are replaced by the appropriate propagation operator [2]

$$\Gamma(s)=\frac{sx}{a}\left[1-\frac{2J_1(ir\sqrt{s/\nu})}{ir\sqrt{s/\nu}J_0(ir\sqrt{s/\nu})}\right]^{-1/2} \tag{6}$$

and characteristic impedance

Nomenclature

a = waterhammer wavespeed
A = cross-sectional area of pipe
b,c = see equations (26) to (29)
C = gA/a^2, capacitance
C_d = valve discharge coefficient
D = diameter of pipe
f = Darcy-Weisbach friction factor
g = gravitational acceleration
$h(t)$ = pressure head
$\Delta h(t)$ = head variation
H = complex-valued head variation
i = $\sqrt{-1}$
J_0,J_1 = the first type Bessel functions
l = length of pipe
L = $1/gA$, inertance
N = number of samples in FFT
p = pressure
$\Delta p(t)$ = pressure pulse entering the pipe
$\Delta p_x(t)$ = pressure response at section x to $\Delta p(t)$
$\Delta P(\omega)$ = Fourier transform of $\Delta p(t)$
$q(t)$ = flow rate
$\bar{q}$ = mean flow rate
$\Delta q(t)$ = flow variation
Q = complex-valued flow variation
r = radius of pipe
$r_{xp}(t)$ = pressure response at section x to a pressure impulse at upstream end
$r_{Dh}(t)$ = head response at downstream valve to a flow impulse at valve
$r_{xh}(t)$ = head response at section x upstream to a flow impulse at valve
$r_{xq}(t)$ = flow response at section x upstream to a flow impulse at valve
R = resistance parameter
s = $\sigma+i\omega$, Laplace variable
t = time
Δt = time sampling rate
T = half-period of discrete function in time domain
v = velocity
x = distance along pipe
Z_C = characteristic impedance for pipe with constant friction factor
$Z(s)$ = characteristic impedance for pipe with frequency-dependent friction
α = angle between pipeline and horizontal level
γ = propagation constant
$\Gamma(s)$ = propagation operator
$\delta(t)$ = Dirac-Delta function or impulse function
ν = kinematic viscosity of liquid
ρ = density of liquid
τ = time variable in convolution, dimensionless valve opening
ω = frequency, rad/s
$\Delta\omega$ = frequency sampling rate
Ω = half-period of discrete function in frequency domain

Subscripts

D = downstream section
r = reference state
t = at time t
U = upstream section
x = section x away from disturbance
0 = initial state

$$Z(s)=\frac{a}{gA}\left[1-\frac{2J_1(ir\sqrt{s/\nu})}{ir\sqrt{s/\nu}J_0(ir\sqrt{s/\nu})}\right]^{-1/2} \tag{7}$$

For pipes with frequency-dependent wavespeeds, all the equations are valid but wavespeed a becomes a function of frequency.

In the frequency response analysis, Laplace variable s is replaced by $i\omega$.

Impulse Response Method

The principal concepts and general equations of IMPREM are developed herein and illustrated in two typical cases: (1) propagation of a pressure pulse in a long pipe, and (2) waterhammer in a reservoir-pipe-valve (R-P-V) system induced by the motion of a downstream valve.

The Fourier integral of the Dirac-Delta function, or the impulse function, reads [1]

$$\delta(t)=\frac{1}{2\pi}\int_{-\infty}^{\infty}e^{i\omega t}d\omega=\frac{1}{\pi}\int_0^{\infty}\cos\omega t d\omega \tag{8}$$

which implies that an impulse may be considered as the summation of an infinite number of sinusoidal exciters with identical moduli, $d\omega/\pi$, but with different frequencies, ω, continuously varying from 0 to ∞.

Suppose a pressure impulse is imposed at the entrance of a pipe. As shown by equation (8), the impulse consists of an infinite number of exciters. In particular, the pressure response at the section x downstream from the entrance to the exciter of frequency ω may be obtained from equation (3) with the frequency response analysis [5, 17], which is

$$\mathbf{Re}\left[\frac{1}{\pi}(\cosh\gamma x-\sinh\gamma x)e^{i\omega t}d\omega\right]=\mathbf{Re}\left[\frac{1}{\pi}e^{-\gamma x}e^{i\omega t}d\omega\right] \tag{9}$$

where **Re** represents the "real part of." Notice that the relation $H_U/Q_U(=Z_U)=Z_C$ for an infinitely long pipe has been inserted in the equation. Thus, for case 1, the physical response at section x to the pressure impulse at the entrance can be expressed as

$$r_{xp}(t)=\int_0^{\infty}\mathbf{Re}\left[\frac{1}{\pi}e^{-\gamma x}e^{i\omega t}\right]d\omega=\frac{1}{\pi}\mathbf{Re}\left[\int_0^{\infty}e^{-\gamma x}e^{i\omega t}d\omega\right] \tag{10}$$

Similarly, if a discharge impulse is imposed at the downstream valve of the R-P-V system, the physical pressure-head response at the valve, and the pressure-head and flow response at section x upstream from the valve, to the discharge impulse are, respectively:

$$r_{Dh}(t)=\frac{1}{\pi}\mathbf{Re}\left[\int_0^{\infty}(-Z_C\tanh\gamma l)e^{i\omega t}d\omega\right] \tag{11}$$

$$r_{xh}(t)=\frac{1}{\pi}\mathbf{Re}\left[\int_0^{\infty}Z_C(\sinh\gamma x-\cosh\gamma x\ \tanh\gamma l)e^{i\omega t}d\omega\right] \tag{12}$$

$$r_{xq}(t)=\frac{1}{\pi}\mathbf{Re}\left[\int_0^{\infty}(\cosh\gamma x-\sinh\gamma x\ \tanh\gamma l)e^{i\omega t}d\omega\right] \tag{13}$$

The reservoir boundary condition, $H_U=0$, is included in these equations. Hereafter, the functions of frequency in the integrands are defined as the transfer functions, while the functions of time on the left-hand sides of equations (10) to (13) are called the response functions. Equations (10) to (13) also indicate that the transfer function and the response function are a Fourier transform pair.

Assume that, in case 1, the pressure pulse entering the pipe is $\Delta p(t)$. This pulse may be decomposed to a series of impulses of different amplitudes. The pressure response at section x to each of the impulses may be obtained from equation (10). Superimposing these responses results in the corresponding response to the pressure pulse, $\Delta p(t)$. The above procedure is carried out by convolving response function $r_{xp}(t)$ with pressure pulse $\Delta p(t)$. That is

$$\Delta p_x(t)=\int_0^t r_{xp}(t-\tau)\Delta p(\tau)d\tau \tag{14}$$

Similarly, denoting the discharge variation at the valve in case 2 by $\Delta q_D(t)$, the pressure-head change at the valve, and the pressure-head and discharge changes at section x, are

$$\Delta h_D(t)=\int_0^t r_{Dh}(t-\tau)\Delta q_D(\tau)d\tau \tag{15}$$

$$\Delta h_x(t)=\int_0^t r_{xh}(t-\tau)\Delta q_D(\tau)d\tau \tag{16}$$

$$\Delta q_x(t)=\int_0^t r_{xq}(t-\tau)\Delta q_D(\tau)d\tau \tag{17}$$

Boundary conditions are as follows. In case 1, in addition to $H_U/Q_U=Z_C$ included in the transfer function, the pressure pulse, $\Delta p(t)$, is assumed to be known *a priori*. Equation (14) yields the pressure response at any section along the pipe. In case 2, besides $H_U=0$ implied in the transfer functions, the valve boundary condition has to be introduced:

$$q_D(t)=(C_dA)_t\sqrt{2gh_D(t)} \tag{18}$$

where $q_D(t)=q_{D0}+\Delta q_D(t)$ and $h_D(t)=h_{D0}+\Delta h_D(t)$ with subscript 0 referring to the known initial value. $(C_dA)_t$ is assumed to be prespecified. Thus, both the discharge and pressure-head variation at the valve, $\Delta q_D(t)$ and $\Delta h_D(t)$, can be solved for simultaneously from equations (15) and (18). Notice that the linearization of the valve boundary condition, which is required in all the conventional frequency response analyses, is not necessary in IMPREM. Having found $\Delta q_D(t)$, the pressure-head and discharge transients at any section in the pipe, $\Delta h_x(t)$ and $\Delta q_x(t)$, are computed from equations (16) and (17).

Numerical Schemes

Two alternative approaches may be used to manipulate the above equations numerically: (1) use the inverse FFT to evaluate the response function, then convolve the response function with the pressure pulse or discharge variation directly; (2) use FFT to find the Fourier transform of the pressure pulse, case 1 for instance, denoted by $\Delta P(\omega)$, then obtain product $e^{-\gamma x}\times\Delta P(\omega)$, and finally perform the inverse FFT of the product, resulting in the desired convolution, $r_{xp}(t)*\Delta p(t)$. The latter is based on the convolution theorem, which states that convolution $r_{xp}(t)*\Delta p(t)$ and product $e^{-\gamma x}\times\Delta P(\omega)$ are a Fourier transform pair. IMPREM uses the former approach for the following reasons:

1. For a given system, the response function is unique and needs to be evaluated only once. Using either different pressure pulses or different valve motions in the convolution procedure yields corresponding transients. In addition, only the transient during a short time period after it starts is likely to be of interest and of importance. In other words, the upper limit of the convolution integral, t, is small in each of equations (14) to (17). Therefore, the first approach appears simpler and more efficient.
2. The nonlinear valve boundary condition is directly utilized in case 2. The discharge variation at the valve is itself an unknown and its Fourier transform cannot be found until it has been computed—the second approach is actually unavailable in this case.

The discrete FFT with the Cooley-Turkey base-2 algorithm is adopted to compute the response function, i.e., the inverse Fourier transform of the transfer function. This can be done because of the relation [1]

$$\int_{-\infty}^{\infty} F(\omega)e^{i\omega t}d\omega = \left[\int_{-\infty}^{\infty} F^*(\omega)e^{-i\omega t}d\omega\right]^* \tag{19}$$

where superscript * expresses "the conjugate of." Since the impulse response must be real, the final conjugation operation outside the square brackets may be omitted. When performing the FFT, the real and imaginary parts of a conjugated transfer function are extended to the negative frequency range as an even and an odd function, respectively, resulting in a real response function. Therefore, all the **Re**'s in equations (10) to (13) are unnecessary.

According to the theory of FFT, the discrete response function and discrete transfer function, each of N samples, are a pair of periodic functions with periods in the time and frequency domain being $2T$ and 2Ω, respectively. The following relations hold:

$$N = 2^n \tag{20}$$

$$\Delta\omega = \frac{2\Omega}{N} \tag{21}$$

$$\Delta t = \frac{\pi}{\Omega} = \frac{2T}{N} \tag{22}$$

Equation (22) implies the Nyquist sampling rule. In computation, choose Ω equal to, or an integer multiple of, the period of the transfer function, if the transfer function itself is a periodic function in the frequency domain, or as big as possible to reduce the truncation error. $2T$ should be big enough so that the response function dies out within the period to avoid the aliasing error. Various computer codes to perform FFT are available in the literature; the program in reference [4] is directly used in this study.

When applying the discrete convolution, equation (15) may be written as

$$\Delta h_D(t) = \int_0^{t-\Delta t} r_{Dh}(t-\tau)\Delta q_D(\tau)d\tau + \int_{t-\Delta t}^{t} r_{Dh}(t-\tau)\Delta q_D(\tau)d\tau = \Delta h'_D + r_{Dh}(0)\Delta q_D(t)\Delta t \tag{23}$$

Notice that at each time step $\Delta h'_D$ is known. For a given reference state, for example the initial steady state in the case of closing a valve, or the final steady state in the case of opening a valve, the valve boundary condition reads

$$q_{Dr} = (C_dA)_r\sqrt{2gh_{Dr}} \tag{24}$$

with subscript r referring to the reference state. From equations (23), (18) and (24),

$$\Delta q_D(t)^2 + \left(2q_{D0} - \frac{\tau^2 q_{Dr}^2 r_{Dh}(0)\Delta t}{h_{Dr}}\right)\Delta q_D(t) + q_{D0}^2 - \frac{\tau^2 q_{Dr}^2(h_{D0}+\Delta h'_D)}{h_{Dr}} = 0 \tag{25}$$

where $\tau = (C_dA)_t/(C_dA)_r$. The solution of equation (25) is

$$\Delta q_D(t) = -b \pm \sqrt{b^2 - c} \tag{26}$$

in which,

$$b = q_{D0} - \frac{\tau^2 q_{Dr}^2 r_{Dh}(0)\Delta t}{2h_{Dr}} \tag{27}$$

$$c = q_{D0}^2 - \frac{\tau^2 q_{Dr}^2(h_{D0}+\Delta h'_D)}{h_{Dr}} \tag{28}$$

In the case when the valve is opening, $\Delta q_D(t) > 0$, while in the case when the valve is closing, $|\Delta q_D(t)| < q_{D0}$. Both require the plus sign in equation (26). Therefore,

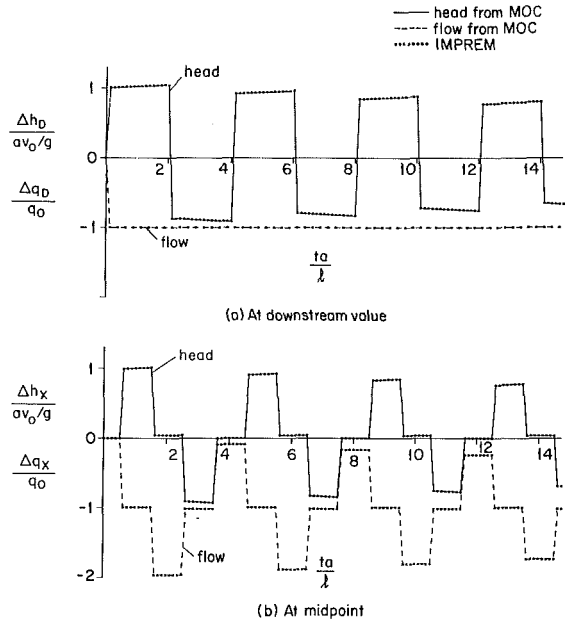

Fig. 1 Waterhammer due to a sudden valve closure. Constant friction factor.

$$\Delta q_D(t) = -b + \sqrt{b^2 - c} \tag{29}$$

Computational Examples

Two groups of computational examples utilizing IMPREM are given below, both referring to the physical data from Holmboe's experiments [10]. The first group analyzes the hydraulic transients in a system with a constant, linear friction factor. The computed results by use of IMPREM are compared with those from the standard MOC to show the method's validity, accuracy and ability to simulate a nonlinear boundary. The second group deals with transients in a system with frequency-dependent friction. The numerical results from IMPREM agree with the experimental data very well.

Transients in a System With a Constant Friction Factor. The data from Holmboe's waterhammer experiment are used and repeated here: a laminar flow occurs in a simple pipe of length $l = 118$ ft (35.97 m) and diameter $D = 1$ in (2.54 cm). Initial steady velocity $v_0 = 0.42$ ft/s (0.128 m/s), constant wavespeed $a = 4343$ ft/s (1323.7 m/s), and kinematic viscosity of the liquid $\nu = 4.27 \times 10^{-4}$ ft^2/s (3.97×10^{-5} m^2/s). The pipe is connected to a reservoir of constant head at the upstream end and to a control valve at the downstream end.

Assuming a constant friction factor, the waterhammer due to a sudden valve closure is computed, and the normalized head and flow variations (divided by av_0/g and q_0, respectively) at the downstream valve and at the pipe midpoint are plotted in Fig. 1. The results from both IMPREM and MOC are almost identical, indicating the validity and accuracy of IMPREM. The waterhammer due to a slow valve closure is shown in Fig. 2, in which the nonlinear behavior of the valve has been included in both methods. Again the two methods produce the same results. In the example, the frequency range is truncated at $\Omega = 925$ rad/s, resulting in a discrete time step $\Delta t = 0.0034$ s. Number of samples $N = 2048$ is chosen in FFT, and a required transient time duration 0.4 s (less than 6 percent of the period $2T = 6.96$ s) is specified in the convolution.

Transients in Systems With Frequency-Dependent Friction. Two computational examples are presented here, which correspond to Holmboe's pulse propagation experiment and to his waterhammer experiment [10].

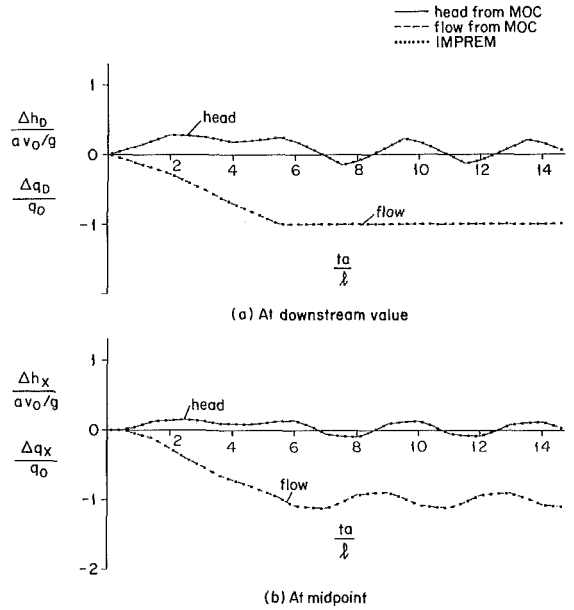

Fig. 2 Waterhammer due to a slow valve closure. Constant friction factor.

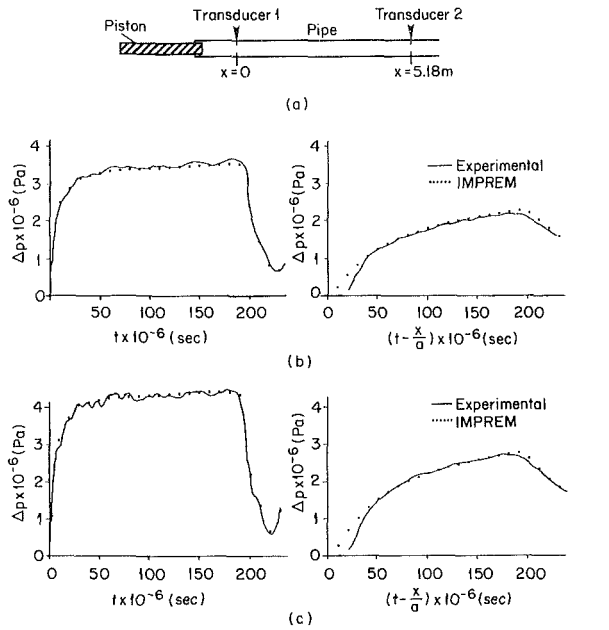

Fig. 3 Propagation of pressure pulse. Input at $x=0$ on the left Response at $x=5.18$ m on the right. Data from reference [10]. Frequency-dependent friction.

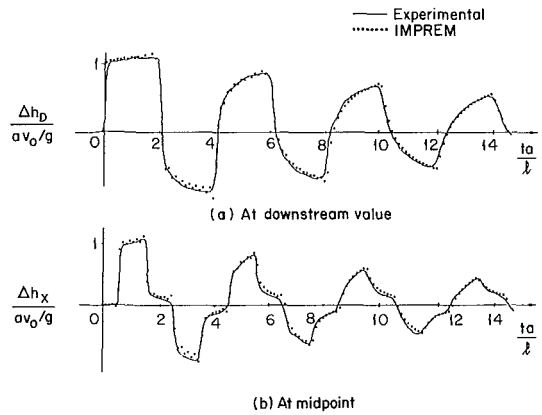

Fig. 4 Waterhammer due to a sudden valve closure. Data from reference [10]. Frequency-dependent friction.

Figure 3(a) shows schematically the setup for the pulse propagation experiment. The system parameters are: diameter of the pipe $D=0.6$ in. (1.52 cm), distance between the two transducers along the pipe $x=17$ ft (5.18 m), constant wavespeed $a=4720$ ft/s (1438.7 m/s), and kinematic viscosity of the liquid $\nu=3.64\times10^{-3}$ ft^2/s (3.38×10^{-4}m^2/s). The motion of the piston mounted at the upstream end of the pipe generates the input pressure pulse, intended to be a square wave but actually is not known exactly. Being more physical, the pulse recorded by the first transducer in the experiment is used in the computational example as the known input pulse. It is sampled at equal time intervals of 10 μs to conduct the discrete convolution. Since the pulse consists of high frequency components, a very wide truncated frequency range $\Omega=\pi\times10^5$ rad/s is required when computing the impulse response by FFT. However, a small number of samples, 512 or more, is adequate for the present case, in which no reflection is involved. The pressure pulse at the second transducer is then computed with IMPREM and compared with the recorded one. Two experimental runs with different amplitudes of the pressure pulses, 510 psi (3.52 MPa) and 630 psi (4.35 MPa), are simulated, as shown in Figs. 3(b) and 3(c). A good agreement between the numerical and experimental results is found except for the wave fronts. The discrepancy might be due to (1) the sampling of the input pulse in the computation, which makes the wave front mild, and (2) the effect of the precursor, likely to be presented in the experiment as indicated by Holmboe and Rouleau but ignored in this computation. The fact that the precursor steepens the wave front can also be noticed in Fig. 3 in reference [10].

In the final example of a waterhammer computation, the same data as listed for the first group of examples are used except that the frequency-dependent friction is considered and the number of samples, N, is reduced to 1024. The transients due to a sudden valve closure are computed with IMPREM and compared with the experimental measurements as shown in Fig. 4. Excellent agreement can be observed.

Summary

The numerical method proposed in this paper presents an attractive alternative to analysis techniques currently in use for pipeline fluid transients. The method can treat various frequency-dependent factors easily, simulate nonlinear behavior of the boundary at the disturbance, and analyze any complex system containing elements that can be treated by the standard impedance method or transfer matrix method. For this class of problems the method is shown to be robust, and capable of predicting physical system response with accuracy.

Acknowledgment

This is a part of the thesis submitted by the first author to The University of Michigan in partial fulfillment of the requirements for the Ph.D. degree. Financial aid from the National Science Foundation under Grant No. MSM-8709564 is greatly appreciated.

References

1 Brigham, E. O., *The Fast Fourier Transform*, Prentice-Hall, Inc., Englewood Cliffs, New Jersey, 1974.

2 Brown, F. T., "The Transient Response of Fluid Lines," ASME *Journal of Basic Engineering*, Vol. 84, Dec. 1962, pp. 547–553.

3 Brown, F. T., and Nelson, S. E., "Step Responses of Liquid Lines with Frequency-Dependent Effects of Viscosity," ASME *Journal of Basic Engineering*, Vol. 87, June 1965, pp. 504–510.

4 Burrus, C. S., and Parks, T. W., *DFT/FFT and Convolution Algorithms. Theory and Implementation*, A Wiley-Interscience Publication, John Wiley & Sons, 1985.

5 Chaudhry, M. H., *Applied Hydraulic Transients*, 2nd Edition, Van Nostrand Reinhold Co., 1987.

6 Clifton, L. M., "Fast Fourier Transform Techniques for the Computation

of Hydraulic System Transients," *Forum on Unsteady Flow—1986*, The Winter Annual Meeting of ASME, Anaheim, Calif., Dec. 1986, pp. 10–12.

7 Fanelli, M., "Hydraulic Resonance in Rock-Bored Penstocks," *Water Power*, Sept. 1973, pp. 342–346.

8 Fanelli, M., Angelico, G., and Escobar, P., "Comprehensive Experimental Confirmation of Transfer Matrix Theory for Uniform Pipelines under Steady Pulsating Conditions," *Proc. 4th Int. Conf. on Pressure Surges*, Bath, England, BHRA, Fluid Eng., Paper J1, Sept. 1983.

9 Franke, P.-G., and Seyler, F., "Computation of Unsteady Pipe Flow with Respect to Visco-elastic Material Properties," *Journal of Hydraulic Research*, IAHR, Vol. 21, No. 5, 1983, pp. 345–353.

10 Holmboe, E. L., and Rouleau, W. T., "The Effect of Viscous Shear on Transients in Liquid Lines," ASME *Journal of Basic Engineering*, Vol. 89, Mar. 1967, pp. 174–180.

11 Karam, J. T., Jr., and Leonard, R. G., "A Simple Yet Theoretically Based Time Domain Model for Fluid Transmission Line Systems," ASME JOURNAL OF FLUIDS ENGINEERING, Vol. 95, No. 4, Dec. 1973, pp. 498–504.

12 Oldenburger, R., and Goodson, R. E., "Simplification of Hydraulic Line Dynamics by Use of Infinite Products," ASME *Journal of Basic Engineering*, Vol. 86, Mar. 1964, pp. 1–10.

13 Suo, L., "Hydraulic Transients in Rock-Bored Tunnels," *Ph.D. dissertation*, The University of Michigan, Ann Arbor, MI, 1988.

14 Trikha, A. K., "An Efficient Method for Simulating Frequency-Dependent Friction in Transient Liquid Flow," ASME JOURNAL OF FLUIDS ENGINEERING, Vol. 97, No. 1, Mar. 1975, pp. 97–105.

15 Tsang, S. H. L., "Periodic Air Flow in Volume-Loaded Tubes by the Fast Fourier Transform Method," Forum on Unsteady Flow—1986, The Winter Annual Meeting of ASME, Anaheim, California, Dec. 1986, pp. 13–15.

16 Tsang, S. H. L., Benson, M. W. and Granberg, R. H., "The Open and Blocked Distributed Air Transmission Lines by the Fast Fourier Transform Methods," ASME *Journal of Dynamic Systems, Measurement, and Control*, Vol. 107, Sept. 1985, pp. 213–219.

17 Wylie, E. B., and Streeter, V. L., *Fluid Transients*, McGraw-Hill, New York, NY., 1978, Republished FEB Press, Ann Arbor, MI, 1983.

18 Zielke, W., "Frequency-Dependent Friction in Transient Pipe Flow," ASME *Journal of Basic Engineering*, Vol. 90, March 1968, pp. 109–115.

J. C. Bruggeman[1]
Research Assistant.

A Hirschberg
Associate Professor.

M. E. H. van Dongen
Associate Professor.

A. P. J. Wijnands
Senior Technician.

Department of Physics,
Eindhoven University of Technology,
5600 MB Eindhoven, The Netherlands

J. Gorter
Senior Scientist,
Research Laboratory of N.V. Nederlandse Gasunie
9700 MA Groningen, The Netherlands

Flow Induced Pulsations in Gas Transport Systems: Analysis of the Influence of Closed Side Branches

A theoretical analysis is presented of the low frequency aero-acoustic behavior of closed side branches along a gas transport pipe. The theory predicts the hydrodynamic conditions for moderate and strong pulsations. A model is proposed which predicts the order of magnitude of the power generated by the aero-acoustic source. The theoretical analysis leads to the design of spoilers which reduce the pulsation level by 30 to 40 dB. The results obtained by theoretical analysis and model experiments (Reynolds number 10^6) have been confirmed in full scale tests (Reynolds number 10^8).

1 Introduction

Pressure pulsations of high amplitude ($p' = 2.5$ bar for a dynamic pressure $\frac{1}{2}\rho U_0^2 = 0.24$ bar and a total pressure $p_0 = 60$ bar) have been observed in a compressor station of the Dutch gas transport system. The ratio of acoustic velocity amplitude to steady flow velocity was 0.4. The flow was characterized by a low Mach number ($M = 0.07$) and high Reynolds number ($Re = 10^8$). The pulsation frequency was 10 Hz, corresponding to a Strouhal number $Sr_D = 0.32$, based on pipe diameter D and steady flow velocity U_0. Other, lower amplitude, resonances were observed for Sr_D ranging from 0.13 to 2 (Fig. 1) The frequencies were well below cutoff frequency for propagation of nonplanar waves in the ducts (0.3 m $< D <$ 1.0 m). The pulsations occurred in configurations in which closed side branches were present, due to the shut down of compressors. In many cases the frequency f corresponded with an acoustic wavelength λ such that the side branch length was equal to $\lambda/4$. As pulsations occurred above a critical flow velocity, the problem was solved reducing U_0 by means of a byass. In view of severity of the pulsations and the cost of the ad hoc solution, a program was initiated to investigate the phenomena, clarify the role of side branches, and explore the possibilities of predicting and preventing pulsations.

The basic geometry is a T-joint of a main pipe and a side branch of approximately equal dimensions (Fig. 2). Studies on the aero-acoustics of pipelines with side branches are scarce [1, 2]. The problem is to some extent similar to that of self sustained oscillations in flows past cavities [1, 3, 4] in mufflers [5], or in organ-pipes [6, 7]. These flows have been studied extensively. A theoretical model for the flow in a T-joint has been developed, based on these studies and on our experiments in pipes with a square cross section. Preliminary results have been presented in an earlier paper [8]. In the present paper, a more systematic discussion is presented (section 2), based on the concept of vortex sound [9, 10]. Details of the formal theory, which have to be omitted due to space limitations can be found in [11]. An extensive series of experiments in a 1/10 scale model of a pipe system with pipes of circular

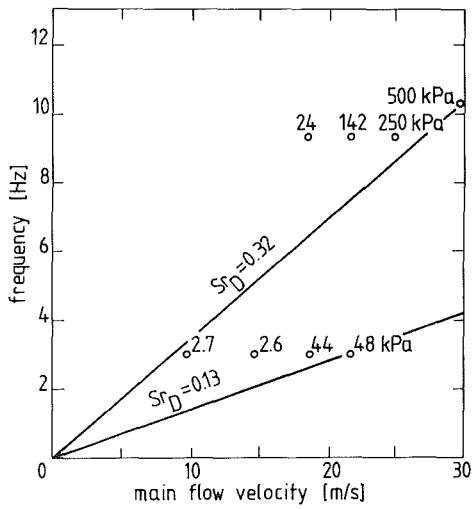

Fig. 1 Pulsations measured at the closed end of a side branch in the pipe system of a compressor station (accuracy: pressure amplitude ± 5 percent, main flow velocity ± 0.1 m/s, frequency ± 0.05 Hz)

[1] Present address: TNO-Institute of Applied Physics (TPD), 2600 AD Delft, The Netherlands.

Contributed by the Fluids Engineering Division for publication in the JOURNAL OF FLUIDS ENGINEERING. Manuscript received by the Fluids Engineering Division January 15, 1987; revised manuscript received September 20, 1988.

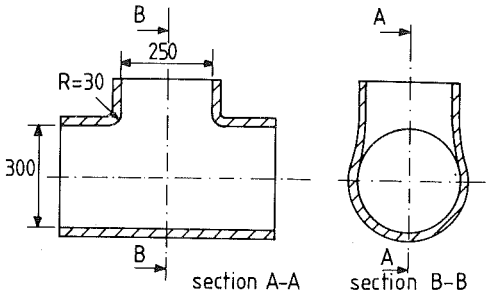

Fig. 2 Geometry of a T-joint used in large scale gas transport systems (dimensions in mm)

cross section (pipe diameter 3 cm, static pressure 1 to 16 bar), in a setup with pipes of square cross section (pipe width 6 cm, atmospheric pressure) and in a full scale setup (pipe diameter 30 cm, static pressure 60 bar) will be described elsewhere, [12, 13]. The experimental data, which are relevant to the modeling of the flow in a T-joint, are summarized in section 3 of the present paper.

The unstable shear layer, separating the main flow in a T-joint from the stagnant gas in the closed side branch, is the aero-acoustic source which drives a resonant acoustic field in pipe sub-systems with small acoustic losses. The acoustic field in return, controls the hydrodynamic (vortical) perturbations of the flow in the T-joint. It turns out that this interaction takes place predominantly at the upstream edge. Hence, the character of the flow in the T-joint depends strongly on the ratio of unsteady to steady flow velocity: $p'/\rho c U_0$, where p', ρ, c, and U_0 are unsteady pressure amplitude at a velocity node (in many cases the closed end of the side branch), density, velocity of sound and steady flow velocity respectively. On the basis of this parameter three cases can be distinguished. In the case of *small amplitudes* ($p'/\rho c U_0 < 10^{-3}$) the growth of the hydrodynamic velocity disturbances of the shear layer may be described with linearized stability theory up to a point one hydrodynamic wavelength downstream of the point where the shear layer is excited. As stressed by Michalke [14], due to the large amplification factor over the first wavelength (500) further downstream the growth of shear layer disturbances usually saturates, because of nonlinear effects. In the case of *moderate pulsation* amplitudes ($10^{-3} < p'/\rho c U_0 < 10^{-1}$, sections 2.1–2.6), only the behavior of the first part of the shear layer may be described with linearized stability theory. In the *large amplitude* case ($p'/\rho c U_0 = 0(1)$, section 2.7), the dynamics of the flow in the T-joint are essentially nonlinear. It appears that the amplitude of flow induced pulsations in pipes with closed side branches is either moderate or large, according to these definitions. Examples of pipe system geometries are discussed in which moderate or large pulsation amplitudes may be expected (sections 2.6 2.7).

2 Model of Aero-Acoustic Sources

2.1 Resonance Process. Flow induced pulsations in a pipe with a closed side branch are the result of the interaction between the shear layer and the acoustic field. From our experiments [8, 11, 12, 13] it appears that the resonance process proceeds as follows:

- The sound field excites the shear layer at the upstream edge of the T-joint.
- Instability of the shear layer results in the formation of coherent vortex structures.
- Interaction of the nonstationary vorticity with the sound field results in a transfer of energy from the flow to the acoustic field.
- The acoustic properties of the system determine the amplitude and the phase of the feedback at the upstream edge.

The coherent vortex structures which are formed in a self excited shear layer have a two dimensional character [15–17]. We therefore will assume for our theoretical analysis a two dimensional flow.

2.2 Shear Layer Instability and Vortex Shedding. For a thin shear layer ($f\theta/U_0 \ll 1$), the excitation of the shear layer by the acoustic field is described by an unsteady Kutta condition at the upstream edge, i.e., the effect of viscosity on the flow is taken into account by requiring a finite flow velocity at the edge. At high Reynolds numbers and small or moderate pulsation amplitudes this leads to the assumption of tangential separation of the flow at the edge, parallel to the main pipe axis [3]. This allows an estimate of the magnitude of the hydrodynamic perturbation of the shear layer at the upstream edge for a given acoustic field. For small amplitudes linearized stability theory for inviscid quasi parallel free shear layers may be used to estimate the influence of the steady flow velocity profile on the growth of the perturbation [14, 18, 19]. This theory predicts that growth will only occur when the Strouhal number Sr_θ based on the initial momentum thickness of the

Nomenclature

B = stagnation enthalpy (m^2/s^2)
c = velocity of sound (m/s)
D = pipe diameter (m)
E = acoustic energy density (N/m^2)
f = frequency (Hz)
$G(\mathbf{x}, t; \mathbf{y}, \tau)$ = Green function ($m^{-1}s^{-1}$)
$H(t-\tau)$ = Heavyside function
H = pipe width (m)
H_0 = characteristic pipe width (m)
I = acoustic energy flux vector ($Nm^{-1}s^{-1}$)
$k = \omega L_0/c$ = nondimensional frequency
$\mathbf{i}, \mathbf{j}, \mathbf{k}$ = unit direction vectors of x, y, z coordinate system
L = side branch length (m)
L_0 = characteristic pipe length (m)
$\mathrm{M} = U_0/c$ = Mach number
n = integer
p' = unsteady pressure (Pa)
p_0 = absolute pressure in settling chamber (bar)
p_n = mode of the orthonormal set $\{p_n\}$ ($m^{-3/2}$)
P = acoustic power (Watt)
q = amplitude of acoustic flux per unit of pipe width (m^2/s)
R = edge radius
$\mathrm{Re} = U_0 D/\nu$ = Reynolds number
S = boundary surface (m^2)
$\mathrm{Sr}_x = fx/U_0$ = Strouhal number based on length x, where $x = D$ or H
time (s)
$T = 1/f$ = oscillation period (s)
T = large time interval (s)
U = steady flow velocity (m/s)
U_0 = cross section and time averaged

shear layer θ_s and steady flow velocity U_0 satisfies the condition

$$\mathrm{Sr}_\theta < 0.04 \tag{1}$$

This condition explains the limited range of Sr_D values found in cavity resonances [1, 3]. A spoiler placed upstream of the cavity increases θ_s. In the small amplitude case condition 1 predicts a reduction of pulsations by means of an upstream spoiler, as observed experimentally by several investigators [1, 3, 4]. In our experiments [8, 11, 12, 13], even for moderate pulsations ($10^{-3} < p'/\rho c U_0 < 10^{-1}$), the initial magnitude of the hydrodynamic perturbation of the shear layer is quite large. As a result the exponential growth of the perturbation predicted by linearized theory is only observed in a small region close to the upstream edge. The shear layer vorticity soon concentrates into structures which can be described as discrete vortices. This saturation of the growth of the shear layer disturbances is, of course, not described by linearized theory. In the extreme case of large pulsation amplitudes, i.e., $p'/\rho c U_0 = 0(1)$, condition (1) is expected to be of no use. For large values of Sr_D, more than one vortex will be present in the T-joint. Coalescence of vortices, which is a prominent feature of free shear layers [20], is not expected when the number of vortices in the shear layer is less than 6. The discrete vortex character of excited shear layers will be used to formulate a simple model for the flow in a T-joint for moderate pulsation amplitudes.

2.3 Shear Layer Model for Moderate Amplitudes. Similar to the modeling of the flute by Howe [10] and of the Helmholtz resonator by Nelson [15, 16], we assume that a line vortex is shed periodically from the upstream edge. We promise a very simple ad hoc model which is justified by experimental verification reported elsewhere [9, 11, 12]. The path of the vortex is determined by the main flow, the acoustic perturbation, the images of the vortex in the walls and the presence of other vortices. For the sake of simplicity, we assume that the line vortex travels at a constant velocity U_c parallel to the axis of the main pipe. U_c is proportional to U_0 and expected to be close to $U_0/2$. The circulation of the vortex increases with a constant rate: $\Gamma = U_0^2 t/2$, until it reaches the value corresponding to the concentrated circulation of one hydrodynamic wavelength of the shear layer disturbance: $\Gamma = U_0^2/2f$. At that moment a new vortex is shed at the upstream edge of the T-joint. It is assumed that the acoustic velocity field in the T-joint triggers the formation of the new vortex. This leads to the assumption that a discrete vortex starts to develop at the moment at which the direction of the acoustic velocity at the upstream edge of the T-joint changes from side branch outwards to side branch inwards. This model of the shear layer behavior at moderate amplitudes will be used as an aero-acoustic source model in calculations of the amplitude and frequency of flow-induced pulsations. The modeling of the acoustic properties of a pipe system is discussed in the next section.

2.4 Acoustic Modeling of Pipe System for Low Frequencies

2.4.1 Convected Wave Equation. For moderate pulsation amplitudes the acoustic field in a pipe system with compact vorticity inhomogeneities and a low Mach number, homentropic and irrotational steady flow can be described with a convected wave equation:

$$\left\{\frac{1}{c^2}\left(\frac{\partial}{\partial t} + \mathbf{U}\cdot\nabla\right)^2 - \nabla^2\right\} B' = \nabla\cdot(\mathbf{w}\times\mathbf{v}), \tag{2}$$

where B' is the fluctuating part of the stagnation enthalpy:

$$B' = \frac{p'}{\rho} + \mathbf{U}\cdot\mathbf{u}, \tag{3}$$

and $\mathbf{U}$, $\mathbf{u}$, and $\mathbf{w}$ are, respectively, irrotational steady flow, acoustic velocity ($\nabla\times\mathbf{u} = 0$), and vorticity, where

$$\mathbf{w} = \nabla\times\mathbf{v}. \tag{4}$$

$\mathbf{v}$ is, in the general case, the sum of steady velocity, acoustic velocity and solenoidal unsteady velocity.

It was shown by Howe [10], that it is more convenient to use B' in combination with $\mathbf{u}$, rather than p' and $\mathbf{u}$, as acoustic variables when a low Mach number, nonuniform steady flow is present.

$\mathbf{u}$ and B' are related by the momentum equation:

$$\frac{\partial \mathbf{u}}{\partial t} = -\nabla B'. \tag{5}$$

The aero-acoustic source model for moderate amplitudes, presented in the previous section takes the form:

$$\nabla\cdot(\mathbf{w}\times\mathbf{v}) = \nabla\cdot\{-\mathbf{k}\times\mathbf{i}\}\delta(\mathbf{x} - \mathbf{i}\,U_0 t)\,\frac{U_0^2 t}{2}\,U_c. \tag{6}$$

Hence, although $\mathbf{w}$ and $\mathbf{v}$ are in general a function of pulsation amplitude, in the previous section we have proposed a source model for moderate amplitudes with a source strength which is a function of the steady flow velocity only. The acoustic prop-

Nomenclature (cont.)

velocity in main pipe = steady flow velocity in main pipe (m/s)
U_c = convective velocity of vortex (m/s)
$\mathbf{u}$ = acoustic velocity (m/s)
$\mathbf{v}$ = local flow velocity (m/s)
V = integration volume (m^3)
$\mathbf{w} = \mathrm{rot}\,\mathbf{v}$ = local vorticity of the flow (s^{-1})
$\mathbf{x}$, $\mathbf{y}$ = position vectors
x, y, z = coordinates in Cartesian system, x axis parallel to axis of main pipe
x = distance from upstream edge (m)
α_n = amplitude of mode n ($m^{5/2}s^{-2}$)
Γ = circulation (m^2/s)
$\delta(\mathbf{x} - \mathbf{i}\,U_0 t)$ = 2 D delta function (m^{-2})
$\epsilon = H_0/L_0$ = small parameter in low frequency approximation
ν = kinematic viscosity (m^2/s)
ρ = density (kg/m^3)
θ = momentum thickness (m)
θ_s = initial shear layer momentum thickness (m)
λ = acoustic wavelength (m)
τ = time (s)
$\omega = 2\pi f$ = angular frequency (s^{-1})

Indices

c = critical or convective
max = value at resonance
n = mode number
rms = root mean square
0 = characteristic or steady part

Superscripts

$'$ = unsteady part
$*$ = complex adjoint

Other Symbols

$\langle\,\rangle$ = time average

erties of the pipe system, which we have to know in order to solve equation (2), are, for low frequencies and a low Mach number steady flow, determined by the lengths of the pipe sections, the impedance boundary conditions at the terminations of the pipe system and by the steady flow Mach number.

2.4.2 Low Frequency Approximation. An approximate solution for the acoustic field in a pipe system with a T-joint has been obtained with the "method of matched asymptotic expansions" (MMAE), using the ratio of characteristic duct width H_0 to duct length L_0 as a small parameter:

$$\epsilon = H_0/L_0 \ll 1. \tag{7}$$

Since we are interested in the case of a nondimensional frequency k of order unity:

$$k = \omega_0 L_0/c = 0(1), \tag{8}$$

ϵ is proportional to the ratio of duct width to acoustic wavelength. Since $k\epsilon \ll 1$, only plane waves have to be taken into account in the straight duct sections. To leading order in ϵ, the acoustic velocity in a T-joint can be described with an incompressible irrotational flow. In this approximation one can use the powerful methods of complex analysis for the calculation of local values of $\mathbf{u}$ [11, 21]. Finally, the unknown constants in the solution for the T-joint and the solutions for the straight duct sections are determined by using Van Dyke's matching principle [22]. This yields a solution to leading order in ϵ for the complete pipe system. From now on B' and $\mathbf{u}$ denote the low frequency approximations of the fluctuating part of the stagnation enthalpy and acoustic velocity.

2.4.3 Formal Solution. A formal solution to the convected wave equation was obtained with Green's theorem [11]. This yields an integral equation relating B' to the source distribution and boundary conditions:

$$B'(\mathbf{x}, t) = \int_{-T}^{T} \int_V G \, \nabla_y \cdot (\mathbf{w} \times \mathbf{v}) d\mathbf{y} \, d\tau$$

$$+ \int_{-T}^{T} \int_S (G \nabla_y B' - B' \nabla_y G) \cdot \mathbf{n} \, dS(\mathbf{y}) \, d\tau. \tag{9}$$

The low frequency Green's function $G = G(\mathbf{x}, t; \mathbf{y}, \tau)$ was obtained with a modal expansion [11]:

$$G = \sum_n \frac{{c_0}^2 H(t-\tau) p_n(\mathbf{x}) p_n^*(\mathbf{y}) \sin[\omega_n (t-\tau)]}{\omega_n} \tag{10}$$

The low frequency modes $p_n \sin(\omega_n t)$ are free vibrations of the pipe system for loss free boundary conditions. They can be calculated with MMAE. This yields for every mode the corresponding velocity distribution in each T-joint of the pipe system.

It is assumed that for pipe systems with small or negligible radiation losses and for the aero-acoustic source in the present problem, the solution of equation (9) will be a quasi periodic function of time with a slowly varying amplitude. In that case one can expand B' and $\mathbf{u}$ in the low frequency modes of the pipe system:

$$B_n = \alpha_n p_n \sin \omega_n t, \tag{11a}$$

$$\mathbf{u}_n = \frac{\alpha_n}{\omega_n} \nabla p_n \left\{ \cos \omega_n t - \frac{\dot{\alpha}_n}{\alpha_n \omega_n} \sin \omega_n t \right\}, \tag{11b}$$

and use the method of averaging to find an approximate solution to equation (9) (see reference [11]):

$$\frac{\rho_0}{{c_0}^2} \alpha_n^* \dot{\alpha}_n = -\rho_0 \int_V <(\mathbf{w} \times \mathbf{v}) \cdot \mathbf{u}_n^*> d\mathbf{y}$$

$$-\rho_0 \int_S <B_n^* \mathbf{u}_n> \cdot \mathbf{n} \, dS(\mathbf{y}), \tag{12}$$

where * and $<>$ denote a complex adjoint and an average over the oscillation period respectively. Often, a single mode gives a reasonable description of the acoustic field.

2.5 Acoustic Energy Balance. The definition of acoustic energy in situations with steady flow is still a subject of debate as indicated by Myers [23]. We propose to define the total acoustic energy per mode in the pipe system as:

$$E_n = \frac{\rho_0}{{c_0}^2} \alpha_n \alpha_n^* \sin^2 \omega_n t, \tag{13}$$

since for this quantity an energy balance can be derived by taking the sum of equation (12) and its complex adjoint:

$$1/2 \frac{\rho_0}{c0^2} (\alpha_n^* \dot{\alpha}_n + \alpha_n \dot{\alpha}_n^*) = -\rho_0 \int_V < \frac{\mathbf{u} + \mathbf{u}^*}{2} \cdot (\mathbf{w} \times \mathbf{v}) > d\mathbf{y}$$

$$-\rho_0 \int_S < \frac{B_n^* \mathbf{u}_n + B_n \mathbf{u}_n^*}{2} > \cdot \mathbf{n} \, dS(\mathbf{y}). \tag{14}$$

This is equivalent to

$$< \frac{\partial E_n}{\partial t} > = <P_n> - \int_S <\mathbf{I}_n> \cdot \mathbf{n} \, d\, S(\mathbf{y}), \tag{15}$$

where P_n and $\mathbf{I}_n$ denote the power of the aero-acoustic source for mode n and the acoustic intensity of mode n, respectively:

$$P_n = -\rho_0 \int_V 1/2(\mathbf{u}_n + \mathbf{u}_n^*) \cdot (\mathbf{w} \times \mathbf{v}) d\mathbf{y}, \tag{16a}$$

$$\mathbf{I}_n = 1/2\{B_n^* \mathbf{u}_n + B_n \mathbf{u}_n^*\}. \tag{16b}$$

For the case of a stationary acoustic field, equations (15, 16 *a* and *b*) are similar to the expression for acoustic energy absorption by vortical flows, given by Howe [24, 25], which is often used in studies of sound generation by low Mach number flows [8, 17]. Please note that the Green function employed by Howe assumes either a compact pipe system or free field conditions. The present derivation is somewhat more general as it is valid for noncompact pipe systems.

Equation (16*a*) can be used to calculate the power of the aero-acoustic source. As $(\mathbf{w} \times \mathbf{v})$ in the source model for moderate pulsations is independent of the amplitude of the acoustic field, equations (15, 16 *a* and *b*) show that in that case the power generated by the source is directly proportional to the pulsation amplitude, while the radiation losses through the terminations of the pipe system are proportional to the pulsation amplitude squared. Hence, the pulsation amplitude stabilizes at a moderate value, determined by the assumed amplitude independent impedance boundary conditions at the terminations of the pipe system.

2.6 Resonance. Optimum power transfer from the dipole sound source $\nabla \cdot (\mathbf{w} \times \mathbf{v})$ to the acoustic field occurs when the source is located in an acoustic velocity maximum, i.e., in a pressure node of the standing wave pattern. This partially explains why strong pulsations often occur when the side branch length L is equal to a quarter of the acoustic wavelength or:

$$L(n + 1/2)\lambda/2; n = 0, 1, 2, \ldots\ldots \tag{17}$$

when (17) is satisfied there is a pressure node at the T-joint. Furthermore, a side branch of length L satisfying this condition is an excellent reflector for low frequency sound waves. Hence, the condition of optimum sound production coincides with minimum radiation losses. A pipe section of length 2L, terminated by a side branch of length L at the upstream side and by an unflanged pipe end at the downstream side is therefore a system with small radiation losses for frequencies satisfying equation (17). A pipe section of length 2L terminated by two side branches of length L is a pipe system with negligible radiation losses for the same frequencies.

We now consider the hydrodynamic condition for resonance in three limiting cases where the acoustic flux in one of the side branches of a T-joint vanishes. For the single side

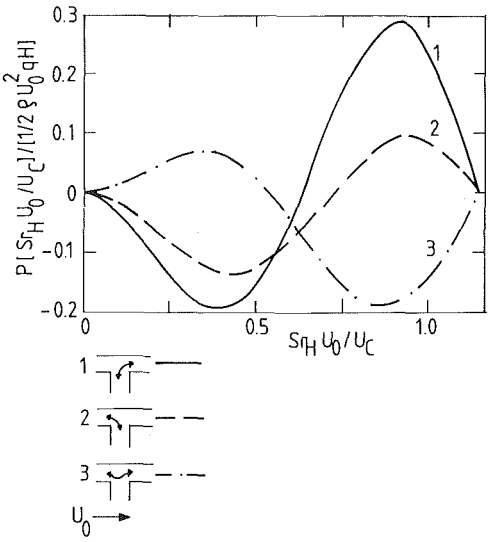

Fig. 3 Acoustic power as a function of nondimensional frequency, calculated with single vortex source model for moderate amplitudes

branch system described above, the mode with the lowest frequency corresponds to an acoustic velocity distribution with zero flux in the upstream branch of the T-joint (first limiting case, see Fig. 3). For the fundamental mode of the double side branch system, the same spatial distribution of **u** is found in the first (upstream) T-joint, while in the second T-joint the acoustic flux in the downstream branch is zero (second limiting case). A third limiting case is obtained for a T-joint with vanishing acoustic flux in the side branch. This situation occurs for a short side branch ($L/\lambda \ll 1$). As the acoustic flux in one of the branches is vanishing, the acoustic fluxes in the two other branches are equal in each of the three cases. The amplitude q of this flux is assumed to be known. For each case, the time averaged source power P, calculated with equation (16*a*) is shown in Fig. 3 as a function of the nondimensional frequency $Sr_H U_0/U_c$. This parameter reflects the variation of steady flow velocity since the frequency is determined by the mode considered, H is determined by the geometry, and the ratio of U_0 to U_c is assumed to be a constant. For moderate amplitudes equation (6) was used as the model for the source **wxv**, while the low frequency acoustic velocity distribution at the position of the vortex was calculated with potential flow theory (section 2.4.2). For the cases in which the flux into the side branch is not vanishing (cases 1 and 2 in Fig. 3), the theory predicts a negative value of P for low values of $Sr_H U_0/U_c$. This is due to the fact that the vortex has left the T-joint before the acoustic velocity changes sign. In the first half of a period of the acoustic oscillation, the vortex absorbs acoustic energy. For higher values of $Sr_H U_0/U_c$, this absorption is compensated by the sound production which occurs when the vortex approaches the downstream edge of the T-joint in the second half of the period. The maximum power P is found near $Sr_H U_0/U_c = 1$. In the case of vanishing acoustic flux into the upstream pipe segment, the maximum of P is higher than in the case of vanishing acoustic flux into the downstream pipe segment. This is explained by the fact that in the first case the acoustic velocity near the upstream edge (where absorption occurs) is lower than near the downstream edge (where production occurs), while in the second case the situation is reversed [11].

Particularly interesting is the third case of no acoustic flux into the side branch. This results in acoustic velocities of equal magnitude near upstream and downstream edges, with components in the direction of the side branch of opposite sign. A positive value of the time averaged acoustic power P, is obtained when the vortex reaches the downstream edge before the acoustic velocity changes sign.

This explains that P is now positive at high velocities (low Sr_H, Fig. 3 case 3). A maximum for P is predicted for $Sr_H U_0/U_c = 0.3$. Figure 3 only shows the results obtained for small values of $Sr_H U_0/U_c$ which corresponds to low frequencies for a given U_0. Resonance at higher frequencies is expected for:

$$Sr_H U_0/U_c = (n+1) \text{ and } (n+1/3);\ n = 0, 1, 2, \ldots . \quad (18)$$

Increasing radiation and friction losses at higher frequenices will, however, limit the Strouhal number observed in experiments to low values of n.

2.7 Source Behavior at Large Pulsation Amplitudes. As we stated earlier (section 2.5), when losses due to radiation and friction are dominant, our aero-acoustic source model (section 2.3) yields a finite pulsation amplitude because the power generated by the source is directly proportional to $|\mathbf{u}|$ while losses are proportional to $|\mathbf{u}|^2$. In full scale gas transport systems however, friction losses are very small while in pipe configurations such as the double side branch system discussed in section 2.6, radiation losses are negligible for certain frequencies. In such cases the amplitude of the pulsations is determined by a nonlinear dependence of the source strength $\nabla \cdot (\mathbf{w} x \mathbf{v})$ on the acoustic field which occurs at high amplitudes. The constant strength model of the aero-acoustic source proposed above is not valid for these conditions. The amplitude limiting mechanism has been explained by Howe [25] and is referred to in the literature as "vortex damping" [26]. For high amplitude pulsations we have to settle for an approximation to zeroth order in M in order to keep the wave operator linear. Hence, convective terms in equations (2, 3, 5) and (11–14) have to be dropped [11]. However, the expression for the source power, equation (16*a*), still holds. From equation (16*a*) we see that because **w** and **v** depend on **u** at high amplitudes, the power extracted from the acoustic field by vortex shedding at the upstream edge increases with approximately a third power of $|\mathbf{u}|$. When the vortex approaches the downstream edge, **w** is expected to depend less strongly on **u** so that the power generated increases only with approximately a second power of $|\mathbf{u}|$. This implies that for a given mode and for a given radius of the edges of the T-joint, above a critical amplitude $(p'/\rho c U_0)_c$, the flow will absorb acoustic energy, while below $(p'/\rho c U_0)_c$ energy will be produced. In absence of losses this critical amplitude $(p'/\rho c U_0)_c$ is the only possible stationary amplitude of pulsations. For rounded edges $(p'/\rho c U_0)_c$ is expected to be of order unity.

For a sharp upstream edge in combination with a rounded downstream edge a lower value of $(p'/\rho c U_0)_c$ is expected because the local acoustic velocity increases with decreasing radius which results in enhanced sound absorption.

$(p'/\rho c U_0)_c$ is expected to be mainly determined by the geometry of the edges of the T-joints for given acoustic velocity distribution and hydrodynamic resonance condition (Sr_H). We therefore expect that the ratio of pulsation amplitude to dynamic pressure will be inversely proportional to the Mach number:

$$(p'/\tfrac{1}{2}\rho U_0^2)_c = (2/M)(p'/\rho c U_0)_c. \quad (19)$$

This idea was checked with a numerical simulation. In contrast to the moderate amplitude case, the rate of vorticity shedding is now estimated by assuming an unsteady Kutta condition at the upstream edge. The path of the vortex is calculated with potential flow theory, taking into account the steady flow, the acoustic velocity distribution and the effect of the vortex shed in the previous period. Simulation of a double side branch system confirms the existence of a critical amplitude $(p'/\rho c U_0)_c$ at which absorption and sound production by the vortices balance each other. This simulation predicts an amplitude $(p'/\rho c U_0)_c = 0.34$ for $Sr_H = 0.5$, for sharp edges.

3 Comparison of Theoretical Predictions With Experimental Data

3.1 Setups. Experimental data were obtained in two scale model pipe systems and in a full scale setup. Data obtained in the first model pipe system were used to check the modeling of the flow in a T-joint. This setup is made of pipes with a square cross section. The basic pipe system is a resonator consisting of a pipe section terminated by a closed branch at the upstream side and by an unflanged pipe end at the downstream side. In some experiments a second side branch was used as a downstream termination. Adjustable side branch lengths allow for variations of the pipe system geometry. A T-joint with windows makes the flow accessible for visualization and laser doppler anemometry. The second model pipe system consists of pipes with a circular cross section. Again, single and double side branch pipe systems were investigated. The shape of T-joints in this setup is similar to the shape of T-joints in full size gas transport piping (Fig. 2). Data obtained in this setup were used to check the aero-acoustic calculations which were presented in section 2. By operating the setup at total pressures from 1–16 bar, an extrapolation was made to the situation of negligible friction, which occurs in large scale gas transport systems. Complete descriptions of the model pipe system are given in [11, 12], along with a detailed account of the data. Some preliminary experimental results were presented in [8]. In the following, a summary is presented of the data obtained in the model pipe systems, for comparison with the theoretical predictions of section 2. In addition, the theoretical predictions are compared with some of the data obtained in the pipe system of a compressor station (field data, see introduction) and with data obtained in a full scale setup [13].

3.2 Model Pipe System With Pipes of Square Cross Section. Flow visualization experiments and laser doppler velocity measurements show that the coherent vortex structures in the flow in a T-joint have a two-dimensional character. This justifies the two-dimensional modeling of the flow in a T-joint, at least for pipes with a square cross section. Furthermore, for small and moderate amplitudes the predicted tangential separation of the flow at the upstream edge of the T-joint, parallel to the main pipe axis, is confirmed. At moderate and large pulsation amplitudes a concentration of the vorticity shed at the upstream edge into discrete vortices is observed. From the flow visualization pictures, the convective velocity U_c of the vortices appears to be constant and equal to (0.40 ± 0.02) times the steady flow velocity U_0. A discrete vortex is formed at the upstream edge at the moment of minimum pressure at the end of the side branch. This corresponds to the moment at which the acoustic velocity at the upstream edge of the T-joint turns into the side branch.

Point measurements of the steady and unsteady velocity of the flow in a T-joint with laser doppler anemometry show good agreement with the predictions of the model for moderate amplitudes, when the convective velocity U_c found from visualization is used for the theory. Point measurements of unsteady velocity and unsteady pressure in the single side branch and double side branch pipe configurations discussed in section 2.6, agree within the experimental accuracy (2 percent) with single mode descriptions of the acoustic field. In these pipe configurations pulsations appear at the frequencies predicted by the resonance condition for acoustic waves, equation (17). The spatial distributions of the acoustic velocity in the T-joints of these pipe systems are equal to cases 1 and 2 of Fig. 3 (section 2.6). The same spatial distribution of the acoustic velocity was found in the first (upstream) T-joint of the double side branch system. The spatial distribution of acoustic velocity in the second T-joint of the double side branch system is equal to case 2 of Fig. 3 (section 2.6). Flow induced pulsations occur in these configurations at ratios of frequency and steady flow velocity equal to $\mathrm{Sr}_H = (0.4 \pm 0.02)(n+1)$, where H is the side branch width. Since $U_c/U_0 = 0.4$ was found for the ratio of convective velocity of the vortex U_c and steady flow velocity U_0, the resonance condition for the shear layer disturbance of equation (18), for the acoustic velocity distributions corresponding to cases 1 and 2 of Fig. 3, is confirmed. At moderate amplitudes, the power of the aero-acoustic source appears to be directly proportional to the pulsation amplitude, as predicted in section 2.6. The source strength, calculated from the data [12], is a factor 3 lower than the magnitude predicted by the theoretical model.

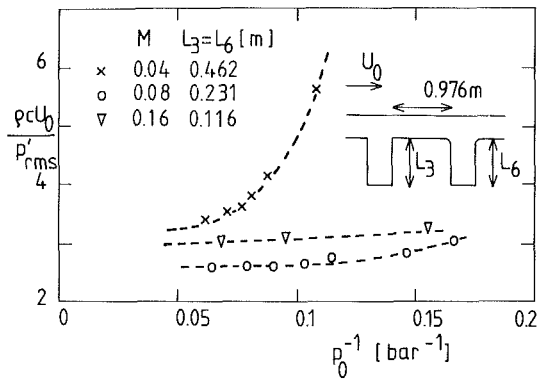

Fig. 4 Effect of main flow Mach number on nondimensional amplitude $p'_{rms}/\rho c U_0$ in the limit of zero friction. Double side branch setup with circular pipe cross section (accuracy: pressure amplitude ± 5 percent, absolute pressure ± 0.05 bar)

3.3 Model Pipe System With Pipes of Circular Cross Section. The experimental data obtained in the scale model pipe system with pipes of circular cross section, at moderate pulsation amplitudes, agree with the predictions of hydrodynamic resonance conditions equation (18), when the side branch width H is replaced by the averaged width of the side branch $(\pi D/4)$. This justifies the two-dimensional modeling of the flow in T-joints, for pipes with circular cross section. These data for the moderate pulsation amplitude case were obtained in a single side branch pipe system, operated at atmospheric pressure. For these conditions the strength of the aero-acoustic source, calculated from the data, agrees within a factor 5 with the magnitude predicted by the theoretical model. The data confirm the theoretical prediction for the influence of losses due to radiation and friction on the pulsation amplitude.

Data obtained in a well tuned double side branch pipe system, operated at a total pressure of 1–16 bar, were used for an extrapolation to the case of negligible losses due to radiation and friction (Fig. 4). In the limit of zero friction a finite pulsation amplitude is found:

$$(p'/\rho c U_0)_c = (0.6 \pm 0.1) \text{ for } 0.05 < \mathrm{M} < 0.3,$$

for T-joints with rounded edges. This confirms the concept of a critical amplitude $(p'/\rho c U_0)_c$, independent of the steady flow Mach number M, proposed in section 2.7, equation (19). The data for the critical amplitude are in order of magnitude agreement with the results of the numerical simulation (section 2.7). The maximum amplitude of flow induced pulsations in our experiments exceeds the maximum value obtained by Hill and Greene [27] with a whistler nozzle by a factor 2.

A considerably lower maximum pulsation amplitude $-(p'/\rho c U_0)_c = 0.1-$ was found when the rounded upstream edge in the second T-joint was replaced by a square (sharp) edge. This confirms the idea of enhanced sound absorption by vortex shedding when the acoustic velocity at the upstream

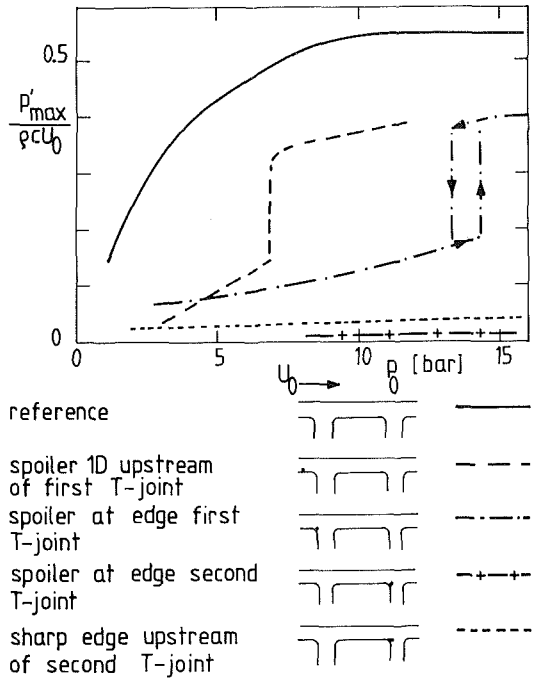

Fig. 5 Influence of total pressure p_0 on the performance of spoilers and sharp edges (accuracy: pressure amplitude ±5 percent, absolute pressure ±0.05 bar)

edge of a T-joint is increased. More sound absorption can be obtained when the acoustic velocity at the upstream edge of the second T-joint is further increased with a flat plate, placed over the edge to form a 1/10D long trailing edge (Fig. 5). A further decrease of $(p'/\rho c U_0)_c$ is achieved with a spoiler instead of the plate (Fig. 5). This results in a decrease of the pulsation level by 30–40 dB compared to the pipe system with rounded edges in both T-joints. Although spoilers placed one diameter upstream of side branches proved to work well in a model pipe system operated at atmospheric pressure, pulsations were not suppressed at higher total pressure (16 bar). This is contrary to the favorable experience with spoilers upstream of cavities, reported in the literature [3, 4]. This effect is attributed to the nonlinear character of the flow near the upstream edge in the present low Mach number problem. Details of the geometry of the spoilers may be found in [12, 13].

3.4 Full Scale Experiments. Scale model experiments and theory for a single and a double side branch system explain the field data on Sr_D obtained by Gasunie in a complex pipe system (Fig. 1). In particular the very low value $Sr_D = 0.13$ observed by Gasunie is predicted by the theory. The highest level of pulsations observed, $p'/\rho c U_0 = 0.4$ for $Sr_D = 0.32$ is, however, lower than the one obtained in scale models $(p'/\rho C U_0)_c = 0.6$. Further, the question arose if spoilers tested in scale models ($Re = 10^6$) would give the same performance at full scale ($Re = 10^8$). For these reasons a full scale experiment was carried out with a double side branch setup. Details of experimental procedure and data are reported elsewhere [13]. In the full scale setup a maximum pulsation level $p'/\rho c U_0 = 0.3$ was obtained for $Sr_D = 0.32$. The pulsation level appeared to be determined by losses due to coupling to structural vibrations. By changing the stiffness of the setup we could influence the pulsation level significantly. The difference between high pressure scale model and field data is therefore expected to be mainly due to a difference in structural rigidity for the scale model and full scale pipe systems.

The full scale test confirmed the excellent performance in scale models at 16 bar total pressure of our newly designed spoilers (40 dB reduction of the pulsation level). The spoilers of classical design, placed upstream of the T-joints, did not reduce the pulsation level significantly.

4 Conclusions

4.1 Aero-Acoustic Source. A theoretical analysis, based on the concept of vortex sound of Powell and Howe, has been presented for the low frequency aero-acoustic behavior of closed side branches at low Mach and high Reynolds numbers. The theory is based on the assumption of periodic shedding of line vortices from the upstream edge of the T-shaped junction of the main pipe and a side branch (T-joint). In our theory a single vortex is shed at the moment when the acoustic velocity at the upstream edge of the T-joints turns into the side branch. The vortex is assumed to accumulate all vorticity shed at the upstream edge. At moderate pulsation amplitudes $(10^{-3} < p'/\rho c U_0 < 10^{-1})$ the rate of vorticity shedding is assumed to be $U_0^2/2$, its value in a stationary flow. The path of the vortex is assumed to be parallel to the axis of the main pipe and the convective velocity U_c of the vortex is assumed to be constant. For high amplitudes $(p'/\rho c U_0 = 0(1))$, the rate of vorticity shedding is estimated by assuming an unsteady Kutta condition at the upstream edge. In this case the path of the vortex is calculated on the basis of potential flow theory. The power transferred from the vortex to the acoustic field is calculated with a single mode approximation of the acoustic velocity distribution.

4.2 Moderate Amplitudes. A detailed study of the flow pattern, using laser doppler anemometry, flow visualization and local pressure measurements, confirms the theory and yields a value of $U_c = 0.4\ U_0$ for moderate pulsation amplitudes. The theory correctly predicts the hydrodynamic conditions ($Sr_H = 0.4\ (n+1)$ or $Sr_H = 0.4\ (n+1/3)$; $n = 0, 1, 2, \ldots$) for resonance found in scale model experiments and field data. The theory explains why pulsations often have a frequency corresponding to a wavelength such that $L = (n + \frac{1}{2})\ \lambda/2$, where L is the side branch length.

The constant source strength, implied by the theoretical source model for moderate amplitudes, is confirmed by the data. The aero-acoustic source strength, obtained from measurements with variable radiation and friction losses, agrees within a factor 5 with the theoretical value.

4.3 Large Amplitudes. Experiment and theory show that very large pulsation amplitudes $p'/\rho c U_0 = 0.6$ can be obtained in a pipe system with two side branches of length L placed a distance of 2L apart, when T-joints with the geometry typical for large scale gas transport pipelines are used. This resonator, formed by two acoustic reflectors, is a simple illustration of what can happen in a pipe system with multiple side branches. The critical parameter which determines the pulsations level in the double side branch pipe system is the radius of curvature of the upstream edge of the second (downstream) T-joint. In the T-joints used in gas transport systems the edges are rounded with a typical radius of curvature $R = 0(D/10)$. In the limit of vanishing losses due to radiation and friction, replacing these rounded edges by sharp ones reduces the pulsation level $(p'/\rho c U_0)_c$ by a factor of 6. The pulsation level appears to be independent of the Mach and Reynolds number. The existence of such a critical amplitude independnet of the steady flow Mach number is predicted by theory and confirmed by our experiments. The effect of a sharp edge, as explained by the theory, is an increased initial absorption of acoustic energy when the vortex is shed, due to the increase of the amplitude of the local acoustic velocity with decreasing radius of curvature of the edge. Note that other authors recommend rounding of edges to suppress pulsations [28].

4.4 Spoilers. The large amplitude behavior described above leads to the design of spoilers to reduce pulsation levels.

Efficient spoilers reducing pulsation levels by 30–40 dB have been obtained. Spoilers of classical design which are supposed to reduce the puslation level by increasing the momentum thickness of the shear layer separating the main flow from the stagnant gas in the side branch, appear to be ineffective in the limit of negligible radiation and friction losses.

4.5 Full Scale Experiments. The results of theory and scale model experiments were confirmed, not only by the field data (Fig. 1) but also by full scale experiments.

Acknowledgments

The project was initiated by J. Smid, G. Vossers, and L. Poldervaart. Technical support was provided in particular by A. Huisman, E. van Voorthuizen, and J. Willems. A large number of students have contributed to the research, in particular C. de Jong, J. Brouwers, J. L. Rouvroye, P. Jutte, N. Smits, and and A. Jack.

References

1 Rockwell, D., and Naudascher, E., "Self-Sustaining Oscillations of Flow past Cavities," ASME JOURNAL OF FLUIDS ENGINEERING, Vol. 100, June 1978, pp. 152–165.

2 Ingard, U., and Singhal, V. K., "Flow Exictation and Coupling of Acoustic Modes of a Side-Branch Cavity in a Duct," *J. Acoustic. Soc. Am.*, Vol. 60, Nov. 1976, pp. 1213–1215.

3 Rockwell, D., "Oscillations of Impinging Shear Layers," *AIAA Journal*, Vol. 21, May 1983, pp. 645–664.

4 Shaw, L. L., "Suppression of Aerodynamically Induced Cavity Pressure Oscillations," *J. Acoustic. Soc. Am.*, Vol. 66, Sept. 1979, pp. 880–884.

5 Davies, P. O. A. L., "Flow Acoustic Coupling in Ducts," *J. of Sound and Vibration*, Vol. 77, 1981, pp. 191–209.

6 Fletcher, N. H., "Air Flow and Sound Generation in Musical Wind Instruments," *Ann. Rev. Fluid. Mech.*, Vol. 11, 1979, pp. 124–126.

7 McIntyre, M. E., Schumacher, R. T., and Woodhouse, J., "On the Oscillations of Musical Instruments," *J. Acoustic. Soc. Am.*, Vol. 74, Nov. 1983, pp. 1325–1345.

8 Bruggeman, J. C., Wijnands, A. P. J., and Gorter, J., "Self-Sustained Low Frequency Resonance in Low Mach Number Gas Flow through Pipelines with Side Branch Cavities: a Semi-Empirical Model," paper No. AIAA-861924, AIAA 10th Aero-Acoustics Conf., July 9–11, 1986, Seattle, Washington.

9 Powell, A., "Theory of Vortex Sound," *J. Acoustic. Soc. Am.*, Vol. 36, Jan. 1964, pp. 177–195.

10 Howe, M. S., "Contributions to the Theory of Aerodynamic Sound, with Application to Excess Jet Noise and the Theory of the Flute," *J. Fluid Mech.*, Vol. 71, 1975, pp. 625–673.

11 Bruggeman, J. C., "Flow Induced Pulsations in Pipe Systems," Thesis, Eindhoven University of Technology, 1987.

12 Bruggeman, J. C., Hirschberg, A., Van Dongen, M. E. H., Wijnands, A. P. J., Gorter, J., "Self-Sustained Aero-acoustic Pulsations in Gas Transport Systems, Part 1: Scale Model Experiments on the Influence of Closed Side Branches," submitted to *J. Sound and Vibration*, 1989.

13 Gorter, J., Hirschberg, A., Wijnands, A. P. J., and Bruggeman, J. C., "Flow Induced Pulsations in Gas Transport Systems," to be presented at Int. Gas Research Conf., November 6–9 1989, Tokyo.

14 Michalke, A., "On Spatially Growing Disturbances in an Inviscid Shear Layer," *J. Fluid Mech.*, Vol. 23, 1965, pp. 521–544.

15 Nelson, P. A., Halliwell, N. A., and Doak, P. E., "Fluid Dynamics of a Flow Excited Resonance, Part I: Experiment," *J. of Sound and Vibration*, Vol. 78, 1981, pp. 15–38.

16 Nelson, P. A., Halliwell, N. A., and Doak, P. E., "Fluid Dynamics of a Flow Excited Resonance, Part II: Flow Acoustic Interaction," *J. of Sound and Vibration*, Vol. 91, 1983, pp. 375–402.

17 Stokes, A. N., and Welsh, M. C., "Flow Resonant Sound Interaction in a Duct Containing a Plate, II: Square Leading Edge," *J. of Sound and Vibration*, Vol. 104, 1986, pp. 55–73.

18 Elder, S. A., "Forced Oscillations of a Separated Shear Layer with Application to Cavity Flow-Tone Effects," *J. Acoustic. Soc. Am.*, Vol. 67, Mar. 1980, pp. 774–781.

19 Milchalke, A., "The Influence of the Vorticity Distribution on the Inviscid Instability of a Free Shear Layer," *Fluid Dynamics Trans.*, Vol. 4, 1969, pp. 751–760.

20 Ho, Chih-Ming, and Huang, Lein-Saing, "Subharmonics and Vortex Merging in a Mixing Layer," *J. Fluid Mech.*, Vol. 119, 1982, pp. 443–473.

21 Bruggeman, J. C., "The Propagation of Low Frequency Sound in a Two-dimensional Duct System with T-joints and Right Angle Bends: Theory and Experiment," *J. Acoustic. Soc. Am.*, Vol. 82, Sept. 1987, pp. 1045–1051.

22 Van Dyke, M., *Perturbation Methods in Fluid Mechanics*, Academic Press, 1964.

23 Myers, M. K., "An Exact Energy Corrolary for Homentropic Flow," *J. of Sound and Vibration*, Vol. 109, Sept. 1986, pp. 277–284.

24 Howe, M. S., "On the Absorption of Sound by Turbulence and Other Hydrodynamic Flows," *J. of Applied Mathematics*, Vol. 32, 1984, pp. 187–209.

25 Howe, M. S., "The Dissipation of Sound at an Edge," *J. of Sound and Vibration*, Vol. 70, 1980, pp. 407–411.

26 Bechert, D. W., "Sound Absorption Caused by Vorticity Shedding, Demonstrated with a Jet Flow," *J. of Sound and Vibration*, Vol. 70, 1980, pp. 389–405.

27 Hill, W. G., and Greene, P. R., "Increased Turbulent Jet Mixing Rates Obtained by Self-Excited Acoustic Oscillations," ASME JOURNAL OF FLUIDS ENGINEERING, Vol. 99, Sept. 1977, pp. 520–525.

28 Baldwin, R. M., and Simonns, H. R., "Flow Induced Vibration in Safety Relieve Valves," ASME *Journal of Pressure Vessel Technology*, Vol. 108, Aug. 1986, pp. 267–272.

Y. Zhuang

J. D. Wilson

E. P. Lozowski

University of Alberta, Edmonton, Alberta, Canada T6G 2H4

A Trajectory-Simulation Model for Heavy Particle Motion in Turbulent Flow

For many purposes it is useful to be able to mimic the paths of heavy particles in a turbulent flow. This paper gives a simple procedure by which this may be achieved, provided particle spin is not important and under the restriction that the ratio of particle to fluid density exceeds about 1000. The procedure is related to the models of Faeth (1986) and Hunt and Nalpanis (1985). Simulation of the experiments of Snyder and Lumley (1971) yielded acceptable agreement with the observed rate of heavy particle dispersion.

1 Introduction

In this paper we present a new method for the simulation of heavy particle trajectories in a turbulent flow. The method could be applied to calculate, for example, the drift of aerial spray or the distribution of fuel droplets within a combustion chamber (please note, however, that to date the method has been tested against observations only for the case of nearly homogeneous turbulence). The superiority of the Lagrangian approach to turbulent dispersion has been evident since it was developed by Taylor (1921). With the advent of accessible computing power it has become possible to mimic turbulent dispersion by calculating a large number of random trajectories from the source to the point of interest. This is the Lagrangian stochastic (or trajectory-simulation) method.

The fundamental advantage of the Lagrangian approach is that it correctly predicts the rate of dispersion in the near field of a source, whereas all attempts to close the heirarchy of Eulerian conservation equations have yielded solutions which are seriously in error close to the source. Thus if first-order closure (K-theory) is adopted, the eddy diffusivity (K) can be shown to depend not only upon the characteristics of the turbulence but also upon the time of travel (or distance) from the source. (Csanady, 1973; Batchelor, 1949).

Correct treatment of the near field is crucial in simulation of turbulent transport within crops or forests, and the adaptation of the Lagrangian stochastic method to this type of problem has lead to rapid development of supporting theory (see Durbin, 1983; van Dop et al., 1985; Thomson, 1984 and 1987; Sawford, 1986; Pope, 1987; Sawford and Guest, 1988). While some fundamental problems remain it is well established (e.g., Wilson et al., 1981) that the trajectory-simulation method can give accurate predictions for complex dispersion problems given only a crude knowledge of the flow field—the mean velocity, the velocity-fluctuation variances, and the autocorrelation timescale.

In the case of heavy particle dispersion, the trajectory-simulation method has a further advantage over other methods in that it is easy to include time-dependent processes such as droplet size reduction due to evaporation. However it is more difficult to calculate a heavy particle path than a fluid element path, because the velocity sequence driving the heavy particle is neither a fluid Lagrangian nor an Eulerian sequence. Therefore one must encapsulate both the temporal and the spatial correlation of the fluid velocity field rather than just the Lagrangian temporal correlation.

There are two approaches to the calculation of heavy particle trajectories. The first option is to calculate both the particle velocity u_{pi} and the fluid velocity u_i in the immediate vicinity of the particle, these velocities being linked by the equation of motion of the particle. The core of the problem then lies in determination of the fluid forcing velocity u_i. The work by Hunt and Nalpanis (1985) and Faeth (1986) falls into this category, as does the model we present. The alternative option is to establish the heavy particle velocity statistics (velocity variance and autocorrelation timescale). Given these statistics one may apply Taylor's analytical result, or, in the case of inhomogeneous turbulence, carry out a trajectory simulation. The recent work by Walklate (1987; see also comments by Wilson and Zhuang, 1988) belongs to this category.

Section 2 describes the new model, and section (3) presents simulations of the heavy particle dispersion experiments of Snyder and Lumley (1971).

2 Formulation of New Model

Provided the ratio ρ_p/ρ of particle density to fluid density is large ($>10^3$) the equation of motion for a rigid nonrotating spherical particle may be written (Schlicting 1968, Hjelmfelt and Mockros 1966):

$$du_{pi}/dt = F(u_i - u_{pi}) - g_i \tag{1}$$

Here the total instantaneous fluid velocity $u_i(t)$ may be decomposed into a mean and fluctuation $u_i(t) = U_i + u_i'(t)$, and g_i is the gravitational acceleration vector. F, whose reciprocal is the particle acceleration timescale, is given by:

$$F = (3/4)\, C_d\, \rho/\, (d\rho_p)\, |u_i - u_{pi}| \tag{2}$$

Contributed by the Fluids Engineering Division for publication in the JOURNAL OF FLUIDS ENGINEERING. Manuscript received by the Fluids Engineering Division February 16, 1988.

where d is the particle diameter and C_d is a drag coefficient

$$C_d = 24(1 + 3R_e/16)/R_e \tag{3}$$

Equation (1) is valid only for $R_e \lesssim 5$, where R_e is the slip Reynolds number:

$$R_e = d\,|u_i - u_{pi}|/\nu \tag{4}$$

Here ν is the kinematic viscosity of the fluid. Equation (1) is a nonlinear stochastic equation which may be integrated numerically to determine the heavy particle trajectory provided one can determine an appropriate (stochastic) sequence of values for the driving fluid velocity at discrete times $t^{(k)}$.

In our model, as in that of Faeth (1986), the driving fluid velocity undergoes abrupt, random changes as the particle encounters new eddies. Between these changes, while the particle passes through a given eddy, the driving fluid velocity remains correlated along the particle path but not, as in Faeth's model, constant.

When the particle encounters a new eddy we mark as the "star" the fluid element surrounding the particle at that instant (see Fig. 1). The particle is considered to stay within the present eddy until its separation from the star exceeds a chosen lengthscale L. To monitor this separation R, i.e., the passage from one eddy to the next, we calculate the trajectories of both the particle and the star.

We need correlated time series for the star velocity u_{*i}' and the driving fluid element velocity u_i'. These we generate using the Markov chains:

$$q_{*i}^{(k+1)} = \alpha_{*i} q_{*i}^{(k)} + \mu_{*i}^{(k+1)} \tag{5a}$$

$$q_i^{(k+1)} = \alpha_i q_i^{(k)} + \mu_i^{(k+1)} \tag{5b}$$

where the q's are dimensionless quantities which are scaled to obtain the velocity fluctuations

$$u_{*i}'^{(k)} = \sigma_i q_{*i}^{(k)} \tag{6a}$$

$$u_i'^{(k)} = \sigma_i q_i^{(k)} \tag{6b}$$

The summation convention does not apply in equations (5, 6) and σ_i is the velocity standard deviation. In the Markov chain equations (5*a*, *b*) the α's control the correlation between consecutive values of the velocity fluctuation. The μ's are random variations. To ensure unit variance for the q's the μ's must have the form

$$\mu^{(k)} = \sqrt{1 - \alpha^2}\ \gamma^{(k)} \tag{7}$$

where the γ's are random numbers having zero mean and unit variance. $\gamma_1^{(k)}$, $\gamma_2^{(k)}$, and $\gamma_3^{(k)}$ are independent of each other and of their values at any other time.

Each time the heavy particle encounters a new eddy and a new star is marked, say at time $t^{(0)}$, the Markov chains are reset

$$q_{*i}^{(0)} = q_i^{(0)} = \gamma_i^{(0)} \tag{8}$$

so that at that instant the driving fluid element and the star, being coincident, have equal velocities. The total velocities are obtained from the fluctuations by adding the mean. It remains to specify the α's.

For the star trajectories we require a fluid Lagrangian series, and the choice

$$\alpha_{*i} = \exp[-\Delta t/T_L] \tag{9a}$$

is conventional; here T_L is the Lagrangian integral timescale.

In the case of the time series for the driving fluid velocity we use the simple expression

$$\alpha_i = \exp[-\Delta t/T_L - |\Delta r_i|/L_g] \tag{9b}$$

where L_g is the lateral integral lengthscale and Δr_i is the separation between the previous and the present driving fluid element, i.e., the separation between the driving fluid element at the previous time $t^{(k)}$ and at the present time $t^{(k+1)}$. The reasoning behind equation (9*b*) is simple. Figure 1 identifies

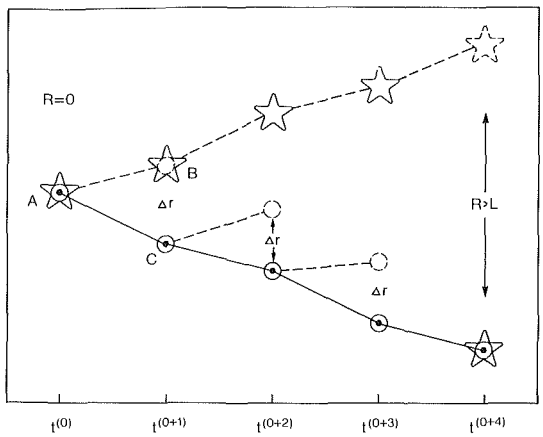

Fig. 1 Defining sketch for trajectory calculations showing the discretized path of a heavy particle (•) which is slipping downwards relative to the fluid around it. For clarity motion is shown only in the vertical direction. At each location (○) denotes the driving fluid element and (☆) the "star," a special fluid element identifying the eddy within which the particle now lies. A dashed image (○, ☆) implies that the element is not tracked beyond its present location. R is the separation between the particle and the star, and Δr is the separation between the particle and that fluid element which, at the previous time, was the driving fluid element.
At time $t^{(0)}$ the particle has entered a new eddy and the star is marked. At $t^{(0+1)}$ $\Delta r = R < L$, where L is the eddy lengthscale. At $t^{(0+2)}$ and $t^{(0+3)}$ $\Delta r < R < L$. At $t^{(0+4)}$ the particle has departed the eddy, i.e., $R > L$, and entered a new one. The new star is marked.

the heavy particle and the star, both at the location A at the instant the particle enters a new eddy. In the succeeding timestep Δt the star moves to B and the heavy particle to C. Provided the separation R between the particle and the star does not exceed the lengthscale L we consider the driving fluid velocity to be correlated with its previous value. We specify the correlation coefficient over interval Δt to be the product of the Lagrangian correlation coefficient along the (previous driving element) path AB and the Eulerian spatial correlation coefficient for the separation BC between the previous and the new driving element.

The timestep has been specified as

$$\Delta t = 0.1 \text{ minimum } (\tau_p, T_L) \tag{10}$$

where τ_p is the particle time constant. A discussion of the choice of the timestep for Lagrangian stochastic models is given by Wilson and Zhuang (1989). Our criterion (10) ensures that the choice of a smaller timestep will not affect the outcome of a simulation. Earlier simulations by Hunt and Nalpanis (1985) did not in all cases satisfy this necessary limitation on the timestep and may have yielded simulations whose agreement with experiment is misleading. The lengthscale L has been specified as

$$L = CL_g \tag{11}$$

A single value for C is to be used for all particle sizes. We found that the specification $C = 1.5$ gave best agreement with the Snyder and Lumley data.

Our model differs from that of Faeth (1986) primarily in our treatment of the driving fluid velocity as varying within each eddy. In Faeth's model the driving velocity was constant within an eddy and changed randomly (without correlation) when either the separation between the particle and the (constant-velocity) star exceeded a specified lengthscale or when a specified time had elapsed since the last fluid velocity choice. Faeth had available two adjustable constants and indicated that the model yielded simulations in good agreement with the Snyder and Lumley data.

3 Comparison With Observations

Snyder and Lumley (1971; hereafter SL) measured the

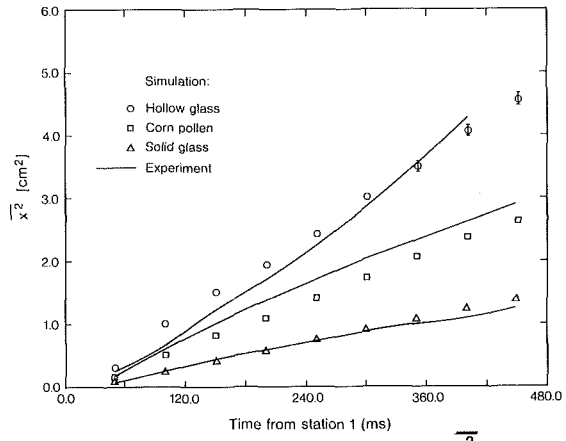

Fig. 2 Mean square heavy particle displacement $\overline{x^2}$ in the cross-stream direction as a function of time. Comparison of simulations with the experimental data of Snyder and Lumley (1971). Symbols give model solutions for:
- o **Hollow glass $\tau_p = 1.7$ millis.**
- □ **Corn pollen $\tau_p = 20.0$ millis.**
- △ **Solid glass $\tau_p = 45.0$ millis.**

Error bars give +/− the standard error of the mean.

dispersion of several types of particles which were injected into the decaying turbulence downstream from a grid in a wind tunnel. In addition to the particle dispersion data, comprehensive fluid velocity statistics were measured. The mean stream direction (x_3) was vertical. In our simulation we have included the variation of the velocity statistics along the stream. The streamwise and cross-stream fluid velocity variances are given by SL equations (9, 10). In decaying grid turbulence the timescale is expected to vary linearly with the streamwise coordinate, and from SL Fig. 14 we inferred that:

$$T_L = 0.1(x_3/M - 14)/(73 - 14) \tag{12}$$

where $M = 0.0254$m is the grid mesh length and $x_3/M = 14$ is our choice for the virtual origin of the decay. The transverse lengthscale was specified as:

$$L_g = T_L/\sigma \tag{13}$$

where σ is the transverse velocity standard deviation.

Density ratios ρ_p/ρ for the particles released by SL ranged from 8900 for solid glass down to 260 for hollow glass. The value $\rho_p/\rho = 260$ for hollow glass violates the restriction $\rho_p/\rho > 1000$ placed on the particle equation of motion (1). However if we estimate a typical value of the Stokes number

$$N_s = \sqrt{\nu/2\pi f d^2} \tag{14}$$

by setting the frequency $f = 1/T_L$ we obtain, for the hollow glass beads of the SL experiment, $N_s \sim 10$. At such a value for N_s (and even at values corresponding to a tenfold increase in frequency) it can be shown (Hjelmfelt and Mockros, 1966) that equation (1) is a very good approximation.

For each particle type released by SL we performed 10 simulations, in each of which we calculated 200 trajectories on an IBM PC-AT. Calculation of 2000 trajectories took approximately 2 hours using a "C" language program. During the simulations the slip Reynolds number was monitored. For the lightest particles, hollow glass ($\rho_p/\rho = 260$), R_e averaged 0.2. For the solid glass particles ($\rho_p/\rho = 8900$), R_e averaged 2.5.

Figure 2 shows the observed and calculated values for the mean-square transverse particle displacement as a function of time. The error bars shown +/− one standard error. The agreement between the observed and simulated spread is satisfactory.

4 Conclusion

We believe our model to be an improvement over earlier work. The temporal variation of the driving velocity is more realistic (we think) than is the case for Faeth's (1986) model; furthermore our model contains only 1 optimisable constant. We obtained a satisfactory simulation of the spread of Snyder and Lumley's lightest particles using an appropriate value for the timestep, whereas we believe the timestep used by Hunt and Nalpanis (1985) was unjustifiably large.

The generality of our method is limited by neglect of particle spin and other terms in the equation of motion. At one extreme, particles which are both small ($d <$ Kolmogorov lengthscale) and light ($\rho_p \leq \rho$) can legitimately be treated as fluid elements. At the other extreme, a small and very massive particle, our model is limited only by the restriction on the slip Reynolds number and an alternative formulation of the acceleration timescale (1/F) could be substituted.

References

Batchelor, G. K., 1949, "Diffusion in a Field of Homogeneous Turbulence," *Australian J. Sci. Res.*, Vol. 2, pp. 437–450.

Csanady, G. T., 1973, *Turbulent Diffusion in the Environment*, D. Reidel Publ. Co., Dordrecht, ISBN 90 277 0261 6.

Durbin, P. A., 1983, NASA Reference Publication, No. 1103.

Faeth, G. M., 1986, "Turbulence/Drop Interactions in Sprays," AIAA paper, No. 86-0136.

Hunt, J. C. R., and Nalpanis, P., 1985, "Saltating and Suspended Particles, Over Flat and Sloping Surface. 1. Modelling Concepts," *Proceedings of the International Workshop on Physics of Blown Sand*," Arhuis, Denmrak, Vol. I.

Hjelmfelt, A. T., and Mockros, L. F., 1966, "Motion of Discrete Particles in a Turbulent Fluid," *Appl. Sci. Res.*, Vol. 16, pp. 149–161.

Pope, S. B., 1987, "Consistency Conditions for Random-Walk Models of Turbulent Dispersion," *Phys. Fluids*, Vol. 30, No. 8, pp. 2374–2379.

Sawford, B. L., 1986, "Generalized Random Forcing in Random-Walk Turbulent Dispersion Models," *Phys. Fluids*, Vol. 29, No. 11, pp. 3582–3585.

Sawford, B. L., and Guest, F. M., 1988, "Uniqueness and Universality of Lagrangian Stochastic Models of Turbulent Dispersion," *American Meteorol. Soc. Eighth Symposium on Turbulence and Diffusion*, pp. 96–99.

Schlicting, H., 1968, *Boundary-Layer Theory*, McGraw-Hill.

Snyder, W. H., and Lumley, J. L., 1971, "Some Measurements of Particle Velocity Autocorrelation Functions in a Turbulent Flow," *J. Fluid Mech.*, Vol. 48, pp. 41–71.

Taylor, G. I., 1921, "Diffusion by Continuous Movements," *Proc. London Math. Soc.*, Vol. 20, pp. 196–211.

Thomson, D. J., 1984, "Random Walk Modelling of Diffusion in Inhomogeneous Turbulence," *Quart. J. Roy. Meteor. Soc.*, Vol. 110, pp. 1107–1120.

Thomson, D. J., 1987, "Criteria for the Selection of Stochastic Models of Particle Trajectories in Turbulent Flows," *J. Fluid Mech.*, Vol. 110, pp. 529–556.

Walklate, P. J., 1987, "A Random-Walk Model for Dispersion of Heavy Particles in Turbulent Flow," *Boundary-Layer Meteorology*, Vol. 39, pp. 175–190.

Wilson, J. D., Thurtell, G. W., and Kidd, G. E., 1981, "Numerical Simulation of Particle Trajectories in Inhomogeneous Turbulence, III: Comparison of Predictions with Experimental Data for the Atmospheric Surface Layer," *Boundary-Layer Meteorology*, Vol. 21, pp. 443–463.

Wilson, J. D., Lozowski, E. P., and Zhuang, Y., 1988, "Comments on a Relationship Between Fluid and Immersed-Particle Velocity Fluctuations Proposed by Walklate (1987)," *Boundary-Layer Meteorology*, Vol. 43, pp. 93–98.

Wilson, J. D., and Zhuang, Y., 1989, "Restriction on the Timestep to be Used in Stochastic Lagrangian Models of Turbulent Dispersion," *Boundary-Layer Meteorology* (in press).

Van Dop, H., Nieuwstadt, F. T. M., and Hunt, J. C. R., 1985, "Random Walk Models for Particle Displacements in Inhomogeneous Unsteady Turbulent Flows," *Phys. Fluid*, Vol. 28, No. 6, pp. 1639–1653.

H. Higuchi[1]

R. E. A. Arndt

M. F. Rogers[2]

St. Anthony Falls Hydraulic Laboratory,
University of Minnesota,
Minneapolis, MN 55414

Characteristics of Tip Vortex Cavitation Noise

Tip vortex cavitation noise was experimentally investigated utilizing hydrofoils with an elliptic planform. The noise was monitored by an array of hydrophones. A variety of cavitating conditions were studied, including inception, fully developed vortex cavitation, and surface cavitation. An analysis of noise source distribution indicated that sound at cavitation inception is radiated from either just downstream of the vortex roll-up region or right at the tip of the hydrofoil where the vortex cavity intially develops.

Introduction

Cavitation noise associated with tip vortices trailing from a marine propeller or hydrofoils is of practical importance. In addition, cavitation noise provides an excellent diagnostic tool to study the mechanisms of cavitation phenomena in a variety of applications. Surface cavitation noise has received the most attention in the past. Only a few papers in the open literature have specifically addressed tip vortex cavitation noise. For this reason, as recently pointed out by Strasberg (1986), the exact mechanism of noise generation due to a cavitating tip vortex is not, as yet, fully understood. Decades ago, Harrison (quoted by Strasberg (1986)) attempted to locate the sound source by traversing a hydrophone parallel to a cavitating tip vortex. Barker (1975) measured the time-averaged noise spectra of tip vortex cavitation and compared them with those of surface cavitation noise on a two-dimensional foil. He concluded that tip vortex cavitation has a lower noise level primarily because of its gaseous nature. Arakeri et al. (1986), however, analyzed tip vortex inception data taken at the St. Anthony Falls Hydraulic Laboratory and concluded that a significant tension effect exists just before inception. Data reported by Barker, unfortunately, are limited in scope and in spite of interesting qualitative discussions, no inception noise or time dependent measurements were reported. Latorre (1982) hypothesized that tip vortex cavitation noise is due to two types of mechanisms: bubble growth and the filling of a fully developed vortex cavity. This is a somewhat surprising result since cavitation noise is usually associated with collapsing bubbles. Latorre's hypothesis has not, as yet, been verified by other workers.

In their study of vortex cavitation noise radiating from marine propellers, Sponagle and Leggat (1984) employed a pressure gradient hydrophone in the near field and correlated the signal with that from a hydrophone in the far field. By traversing the near field pressure gradient phone along the wake, they determined the axial distribution of the source strength for three different blade designs. The propeller designed to generate only tip vortex cavitation by having blade loading skewed towards the tips, produced inception noise downstream of the propeller. Two other blade designs with more typical circulation distributions produced noise near the propeller plane. The reason for these differences in sound source location could not be determined. In a follow-on study of fully developed tip vortex cavitation, Leggat and Sponagle (1985) concluded that the maximum noise corresponds to the downstream region of the closure of a developed cavity. This is in contrast to the experimental conditions reported on herein where an extremely stable tip vortex cavity core is present and persists beyond the entire test section (>15 chord lengths). Barker's (1975) work was carried out under similar conditions. Unfortunately not enough data were presented in Leggat and Sponagle's paper (ibid) to make comparisons with data collected from stationary hydrofoils. Ligneul et al. (1983) also performed an analytical and experimental study of propeller tip vortex cavitation. They observed a uniform increase of approximately 10 dB in the spectral level in the frequency range 2 to 10 KHz. Nonetheless, one has to be careful in relating tip vortex cavitation from a stationary hydrofoil to that from a rotating propeller, since centrifugally induced secondary flows may alter the tip vortex development (Arndt, 1976).

In order to gain further information on the mechanism of sound generation, an experimental investigation was initiated to characterize the various types of cavitation noise associated with tip vortex cavitation. It is to be noted that early works on the subject suffer from limited instrument capabilities. In the present investigation, tip vortex cavitation noise was also compared with surface cavitation noise. For this purpose, two types of hydrofoil sections were tested. A cambered foil was designed to induce tip vortex cavitation prior to the occurrence of surface cavitation and a hydrofoil of symmetric section was designed to have surface cavitation in the absence of tip vortex cavitation. This enables one to study the noise characteristics of surface cavitation and tip vortex cavitation separately and in combination. Distinctly different noise characteristics were observed for each type of cavitation. As discussed subsequently, the inception sound source location within the tip vortex was estimated with an array of hydrophones. The time delay

[1]Presently at Dept. of Mechanical and Aerospace Engineering, Syracuse University, Syracuse, NY 13244.

[2]Presently at Harza Engineering Company, Chicago, Ill. 60606.

Contributed by the Fluids Engineering Division and presented at the International Symposium on Cavitation and Multiphase Flow Noise, Winter Annual Meeting, Anaheim, Calif., December 7-12, 1986 of THE AMERICAN SOCIETY OF MECHANICAL ENGINEERS. Manuscript received by the Fluids Engineering Division October 20, 1987.

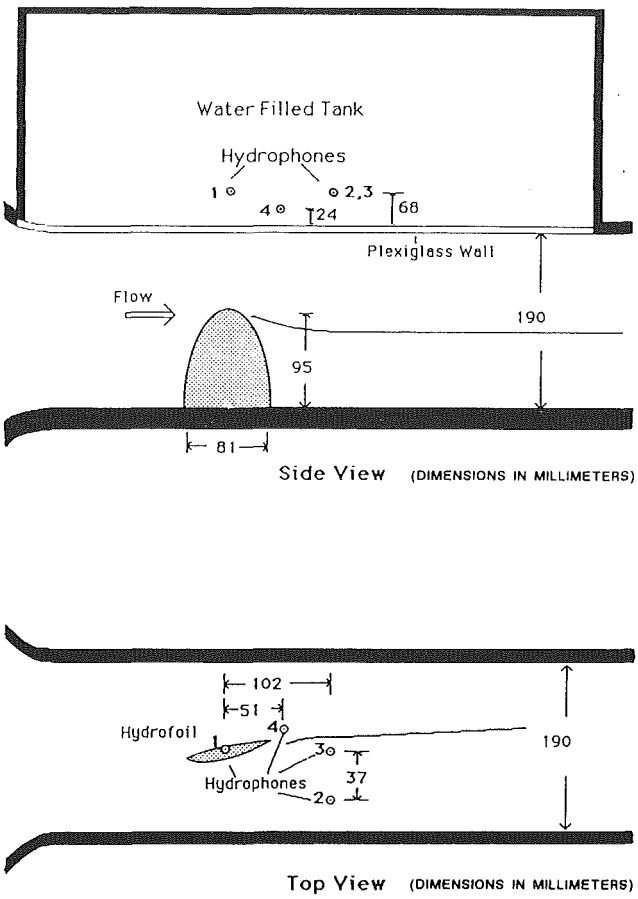

Fig. 1 Experimental setup

technique, used in interpreting the data, was limited to observations of cavitation inception.

Experimental Procedures

(a) Experimental Setup. The experiment was conducted in a high speed water tunnel having a 1250 mm long test section that was 190 mm square in cross section. The experimental set up is shown schematically in Fig. 1. The roof of the test section is made of plexiglass which was 5 mm in thickness. It is almost acoustically transparent and is contoured to minimize the axial pressure gradient in the test section.

A hydrofoil with an elliptical planform of aspect ratio of 3.0 and a NACA 66_2–415 cross section with an $a=0.8$ mean line was used for tip vortex cavitation studies. The half span of the foil was 95 mm and the base chord was 81 mm. As mentioned above, this hydrofoil was designed to produce tip vortex cavitation in the absence of surface cavitation. In order to compare the noise from tip vortex cavitation and surface cavitation, another foil with the same planform but with a symmetric NACA 66-012 cross section was also tested. Due to a relatively sharp low pressure region near the leading edge at finite angle of attack, this foil induced surface cavitation at cavitation numbers considerably higher than the inception indices for tip vortex cavitation.

The acoustic signature was monitored by four Brüel and Kjær (B&K) model 8103 hydrophones with Ithaco model 144L preamplifiers positioned in a water filled chamber separated from the test section by an almost acoustically transparent wall. (A similar setup was used by Barker (1975)). The positioning of the hydrophones is also shown in Fig. 1. Both the pressure fluctuations due to the turbulent boundary layer on the test section wall (see Narayan and Plunkett, 1985) and the water tunnel background noise were measured to be insignificantly low compared to the cavitation noise. On the other hand, the test section was found to be highly reverberant and this effect had to be taken into account as discussed later. The free stream turbulence level was measured to be less than 0.18 percent (Killen, 1988).

The signals from the individual hydrophones were simultaneously digitized at 2 MHz per channel by a Nicolet model 4094 four-channel digital oscilloscope with a disk drive. The data were stored on disks and were analyzed in an on-line HP9836A micro computer. The digital oscilloscope was preset to capture the single noise events corresponding to either cavitation inception or continuous cavitation noise. An HP digital wave form analysis program which includes a standard fast Fourier transform routine and a Levinson autoregressive smoothing routine was used with minor modifications.

Acoustic data collection was concurrent with video observation. Thus, various types of noise signals could be correlated with different types of cavitation phenomena.

(b) Calibration of the Hydrophone Array. The hydrophones were first calibrated in a large water tank where an acoustic free field could be simulated. Using an ITC-1002 spherical projector, high frequency (typically 60 KHz sine wave) tone bursts were generated and were measured by the four B&K hydrophones as mentioned above. Each hydrophone in the array was placed in the same relative positions as utilized in the water tunnel. In order to calibrate both the hydrophone array and the acoustic characteristics of the water tunnel itself, the projector was next placed in the test section in place of the hydrofoil. By triggering the digital oscilloscope by the projector pulse, the output from the individual hydrophones were simultaneously digitized. The initial pulses in these traces were the projector output itself via direct path which had the same waveform as the near field measurement of the projector signal. The subsequent pulses reflected by the tunnel walls were clearly identified. These were in qualitative agreement with a computer simulation of tunnel reverberation discussed later. The speed of sound was calculated and the sound source identification program was tested during the calibration.

Given the experimental setup, measurements are considered to have been in the acoustic near field up to 20 KHz. As will be shown, however, the spectra of the various cavitation noise signals extend over a much higher frequency range. Furthermore, unlike traditional methods of spectral measurements, e.g., by Barker (1976) and Arakeri and Iyer (1986), individual noise traces were digitally captured and an FFT was performed on these traces, significantly eliminating ambiguities of the sound wave transmission pattern. Differences in the present instantaneous, individual noise traces were rather

Nomenclature

a = mean line designation
C = base chord
C_g = dissolved gas content
Re = Reynolds number based on the free stream velocity and the base chord
x,y,z = tunnel coordinates (see Fig. 1)
α = angle of attack
α_0 = angle of zero lift
σ = cavitation number

dramatic as shown in the results section, and are considered to be accurate within the uncertainty cited.

(c) Inception Sound Source Identification. Cavitation inception was detected both visually and acoustically. The inception was marked by a distinct burst of noise in the flow field. By pretriggering the A/D converter with the hydrophone signal itself, individual traces of instantaneous pressure time traces at four different locations could be recorded. By measuring the time delay of arrival among the four hydrophones, the sound source location can be estimated by a triangulation method. The three time delays among four time traces define three two-dimensional manifolds. The intersection of these manifolds is the location of the noise source. Time delays among the initial pulses on the traces were measured with a cursor on the digital oscilloscope. A cross-correlation technique applied to the pressure traces of the initial pulses produced essentially the same time delay information as those obtained directly from the traces. Given three time delays among four hydrophones as inputs, implicit simultaneous equations for the three coordinates of the sound source were solved iteratively.

As noted earlier, the pressure traces indicate that a significant amount of reverberation is present. By limiting the source location analysis to the direct signals from single events prior to the reflection from the tunnel walls, the effects of reverberation can be minimized. The present method of sound source identification, unfortunately, is not applicable to the noise signal from more developed cavitation. Once a steady two phase flow is established, path identification of a continuous sound source can be treated with a time averaged cross correlation technique (see, for example, Fisher et al., 1977). The present paper does not address this issue.

The four hydrophones were placed so that the separation between each hydrophone was maximized, with the constraint that direct radiation from the noise sources arrives at each hydrophone in advance of the arrival of any reflected pulses. As will be discussed later, the vertical separation of the hydrophones was compromised by the geometry of the water-filled chamber above the test section.

During the calibration of the hydrophone array, it was found that the results for the source location were sensitive to several parameters including the hydrophone coordinates, in particular the z-direction offset of hydrophone No. 4 (see Fig. 1), and the speed of sound. The speed of sound was corrected for measured water temperature, but the pressure and the gas content also influence the speed of sound and hence the accuracy of the analysis. The free stream velocity was not taken into account since it was less than 1 percent of the speed of sound. (The sound speed was determined during the calibration procedure). In addition, there were measurable effects due to the finite size of the sensing element, even though the frequency response of the hydrophone was adequate. As an example, the time of arrival of hydrophone No. 2 was perturbed slightly in the data analysis program. A 0.5 micro second variation which is the limit of resolution of the digital oscilloscope used, resulted in variations of 12 mm in the x-coordinate, 12 mm in the y-coordinate and 19 mm in the z-coordinate. The 0.5 microsecond resolution was improved somewhat by polynomial curve fitting the traces near their peak. The z-coordinate was most susceptible to error, though the error in z-coordinate did not influence as much the accuracy in other coordinates. The z-coordinate corresponding to the tip vortex trajectory as made visible by a cavitating core could be used as an alternative check on the sound source location procedure.

Uncertainties in other measurements presented here are shown together with the results.

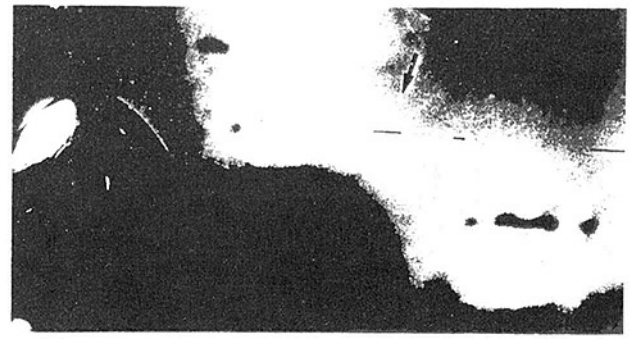

(a)

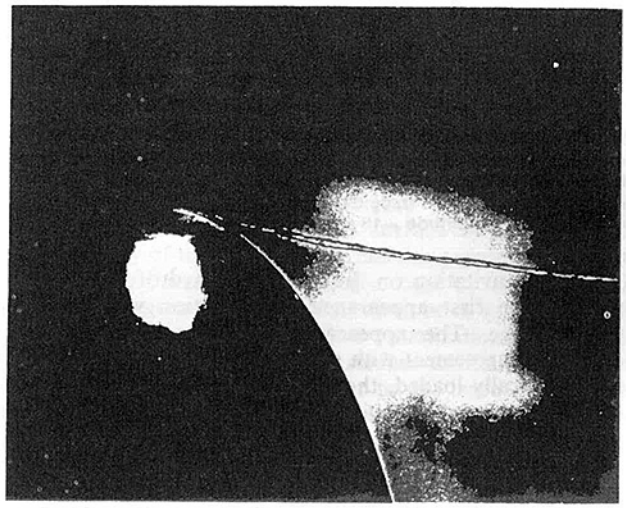

(b)

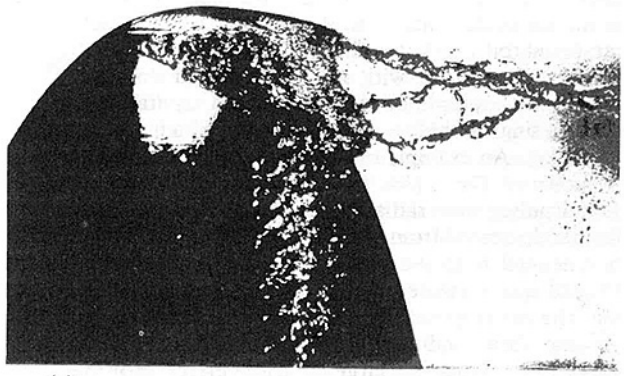

(c)

Fig. 2 Various types of tip vortex cavitation. (a) Inception ($\sigma = 1.4$, $\alpha - \alpha_0 = 2.4$ deg, $Re = 6.1 \times 10^5$); (b) Continuous tip vortex cavity ($\sigma = 1.15$, $\alpha - \alpha_0 = 9.5$ deg, $Re = 5.3 \times 10^5$); (c) Tip vortex cavitation with surface cavitation ($\sigma = 0.43$, $\alpha - \alpha_0 = 11.5$ deg, $Re = 5.3 \times 10^5$).

Results and Discussion

(a) Cavitation Inception and Development. Different types of cavitation phenomena were observed and recorded on still photos and on video tapes. Reynolds number (free-stream velocity), angle of attack, dissolved gas content, and the test section pressure were varied. The functional dependence of cavitation inception index on these parameters was reported separately (Higuchi, et al., 1986).

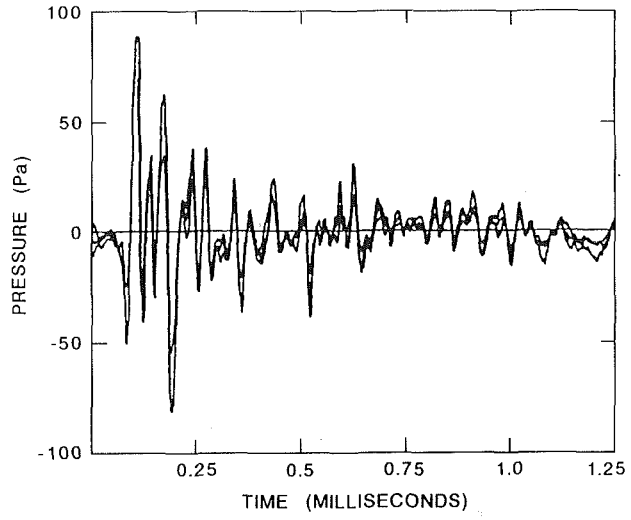

Fig. 3 Time trace of surface cavitation inception. Symmetric foil, $\sigma = 2.0$, $\alpha = 6$ deg.
(Three cavitation events are superposed.)
(Resolution of the time trace data: 0.5 μs,
Uncertainty in amplitude ±18 percent over 4Hz-150KHz.)

Surface cavitation on the symmetric hydrofoil was as expected. The first appearance of cavitation was along the leading edge. The appearance of the cavitation was in qualitative agreement with the assumption that the hydrofoil was elliptically loaded, though a more careful study showed three-dimensional behavior of the foil boundary layer with separation (Higuchi et al., 1987).

The inception of tip vortex cavitation occurred either as an unsteady appearance of a single bubble within one or two chord lengths from the tip or a continuous cavity suddenly appearing from about the same position which subsequently attached itself to the tip. In some cases, a fully-developed cavity appeared to develop right at the tip. However, a careful analysis of the video tapes in the latter cases indicated that the inception actually occurred as a continuous cavity some distance downstream of the foil which rapidly attached itself to the tip of the foil. Typical cavitation phenomena with the cambered foil are shown in Fig. 2. Figures 2(b) and 2(c) were taken with a strobe with a 5 microsecond duration. Figure 2(a) is an example of the intermittent cavitation inception where a single bubble is captured on the film in the vortex roll-up region. An example of the developed tip vortex cavitation is shown in Fig. 2(b). In either case of inception, distinct sound pulses were radiated. As the test section pressure was further decreased from the point shown in Fig. 2(b), the cavity extended over the entire tip region, which subsequently formed into a twisted ribbon shape. Barker (1975) reported that the cavity gradually thickened into a ribbon structure if constant flow conditions were maintained for several minutes. He attributed this to a large diffusion effect. However, in the present test at various gas contents, various phenomena persisted over a long period until the flow conditions such as the angle of attack were changed. The noise level decreased with the appearance of a fully developed cavity and remained low with decreasing cavitation number until a cavity covered a portion of the tip of the hydrofoil. Further decrease in pressure (cavitation number) beyond this point resulted in surface cavitation noise of considerably increased intensity. As shown in Fig. 2(c), surface cavitation is observed in the region where trailing edge boundary layer separation was predicted and observed in oil film visualization studies (Higuchi et al., 1987). At higher angles of attack, the tip vortex cavitation began to be accompanied by leading edge cavitation in the area between the leading edge separation and reattachment shown in the oil film visualization study.

(b) Typical Noise Traces.

Surface Cavitation on a Symmetric Foil. Pressure traces of surface cavitation inception are shown in Fig. 3. (These particular traces had been measured with a Gould CS131 hydrophone. Corresponding spectra will be discussed later.) As the multiple traces in the figure indicate, the noise signals due to inception are very repeatable indicating a localized and repeatable inception point. This was supported by high speed photography which indicated that surface cavitation was limited to the first quarter chord of the hydrofoil. The reverberation of the tunnel results in multiple pulses (echoes) for a single cavitation event. By ensemble averaging the noise traces on the digital oscilloscope, the pulse shape of a single bubble event could be obtained and mathematically modeled (Higuchi and Arndt, 1985). The modeled waveform was similar to that reported by Harrison (1952). A simple acoustic model of the reverberant water channel was utilized to quantify the reverbation in a computer simulation. From the ensemble averaged traces, an analytical expression for the single pulse was obtained. The simulated single pulse had a relatively broad spectral peak near 20 KHz, above which the spectra decayed gradually with increasing frequency. As mentioned earlier, the measurements were considered to be in the acoustic near field up to 20KHz. Hence the method is limited to sharp pulses having Fourier transforms essentially in a high frequency range. The measured time traces substantiated this assumption. The reflection by the test section walls was modeled by a sound source and its images. The ray acoustics approximation was applied to spherical sound waves with radial attenuation. The test section was defined as a 190 mm $\times$ 570 mm rectangle surrounded by hard surfaces with appropriate resistive acoustic impedance. As stated earlier, inception of surface cavitation was limited to a localized region of the hydrofoil. Using this as the location of a cavitation source, a simulated waveform with reverberation was computed from a mathematical representation of the single pulse. The computed time trace modeled the actual data very well (Higuchi and Arndt, 1985).

Tip Vortex Cavitation Inception. Different types of pressure traces were noted during tip vortex cavitation inception. Representative pressure traces captured at the hydrophone location No. 3 (see Fig. 1) are shown in Fig. 4. Typical inception data exhibited moderately damped, very regular low frequency oscillations starting with a negative pressure pulse (see Fig. 4(a)). Note the minimal background noise of the flow recorded in this figure prior to the cavitation inception. These oscillations were observed either when the intermittent short cavitation bubble becomes visible within one or two chord lengths downstream in the tip vortex, or when a continuous cavity appears at a similar axial position and moves upstream and attaches itself to the foil tip. These low frequency oscillations of different frequencies and different amount of damping were observed at various gas contents, Reynolds numbers, and angles of attack. The frequency of oscillation varied from 2.5 KHz to 6 KHz depending on test conditions. In many cases, particularly at low angles of attack, cavitation inception had the appearance of elongated bubbles, presumably the result of discrete portions of the vortex core intermittently cavitating as shown in Fig. 2(a). The observed frequencies are too low to be associated with cavitation bubble collapse (see e.g., Fitzpatrick and Strasberg, 1956). Although the natural frequency of such elongated bubbles is unknown, the observed noise frequency range is comparable to the natural frequencies of spherical bubbles of equivalent volume as observed. One problem with this hypothesis as a cause of the noise, however, is that this type of noise was observed over a wide range of gas content, and there was no discernible relationship between frequency and gas content. Another difficulty is that the pressure amplitude of these oscillations far ex-

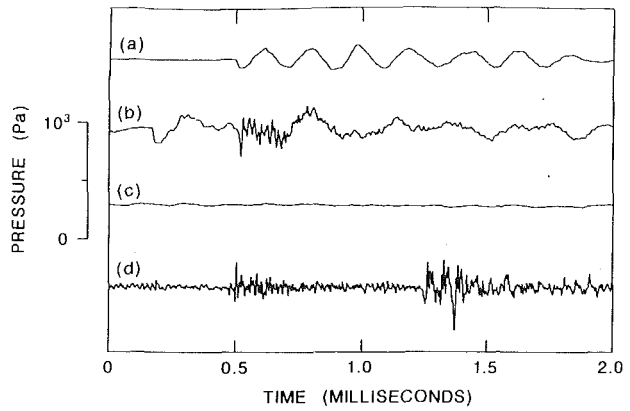

Fig. 4 Time traces of tip vortex cavitation ($C_g = 12.5$ ppm). Cambered foil, hydrophone location No. 3.
(Resolution of the time trace data: 0.5 μs., Uncertainty in amplitude ± 25 percent over 0.1Hz-140KHz.)

(a) Inception ($\sigma = 3.97$, $\alpha - \alpha_0 = 12.5$ deg, Re $= 9.5 \times 10^5$); (b) Inception ($\sigma = 3.53$, $\sigma = \alpha_0 = 13.5$ deg, Re $= 9.5 \times 10^5$); (c) Continuous tip vortex cavity; ($\sigma = 3.29$, $\alpha - \alpha_0 = 15.5$ deg, Re $= 9.1 \times 10^5$); (d) Tip vortex cavitation with surface cavitation ($\sigma = 0.88$, $\alpha - \alpha_0 = 9.5$ deg, Re $= 9.3 \times 10^5$).

ceeded that expected from simple gas bubble oscillations. In other cases, a high speed video showed that a leading edge of the detached continuous cavity oscillated axially. Further analysis of a cylindrical cavity is needed to more accurately describe the source of the low frequency noise.

Other inception data had a similar frequency pressure pulse at the onset but it was followed by a series of high frequency oscillations. These sharp pulses were observed when the cavitation index was lowered rather rapidly. Under such circumstances a steady cavity core appears suddenly. Figure 4(b) corresponds to such a case, which displays a negative transient pressure due to this cavity formation. It is believed that the high frequency noise is generated when the continuous cavity rapidly moves upstream and attaches itself to the tip of the hydrofoil. Pressure traces from four hydrophones revealed that the pulse was generated at or very close to the tip of the foil.

From the available noise data and visual records, it was not possible to identify the existence of a Reynolds number effect or gas content effect on the inception pressure signals in spite of their strong influence on the cavitation inception number.

Continuous Tip Vortex Cavitation. Once continuous tip vortex cavitation occurs, the noise level decreases markedly as shown in Fig. 4(c). As the pressure is further decreased, the cavity radius increases and the foil tip starts to cavitate. The sound level significantly increases with the onset of a surface cavity.

Prior to the onset of the surface cavitation, and within a very narrow band of cavitation number and at a moderately high angle of attack ($\approx 10 \pm 2$ degrees), a discrete tone was generated in the frequency range 340-900 Hz. Holding free stream velocity constant, the frequency of the tone varied continuously within a certain range with cavitation number, a higher pitch corresponding to higher cavitation number and smaller cavity core radius. Limited data indicate that the frequency varied almost linearly with velocity at constant cavitation number. This phenomenon was apparently associated with cavitation on the suction side of the tip and the braided structure of the vortex cavity. Under strobscopic illumination, it was observed that the tip cavity pulsated and the braided structure rotated in synchronism with the emitted tone. At first it was conjectured that the phenomon was due to a flow induced vibration of the foil since the resonance frequency of

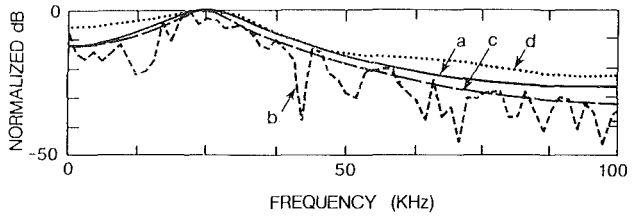

Fig. 5 Power spectral density of surface cavitation noise and reverberation effect.
(Uncertainty in magnitude ± 5 db, in frequency ± 1.5 KHz.)

(a) A simulated single pulse (from Higuchi and Arndt, 1985); (b) A simulated pulse with reflections (FFT); (c) A simulated pulse with reflections (Levinson AR, 4th order); (d) Cavitation inception data (see Fig. 3).

the foil was determined to be about 400Hz. The fact that the tonal frequency varied continuously with both free stream velocity and cavitation number discounts this theory. The actual mechanism for noise generation in this regime remains to be investigated.

Tip Vortex Cavitation With Surface Cavitation. As the cavitation index is further lowered, surface cavitation appears in the vicinity of the region where laminar separation and turbulent reattachement occur. As discussed by Higuchi et al. (1987), this region has been observed to be in agreement with theoretical prediction and the flow visualization studies. The pressure trace corresponding to surface cavitation inception had a sharp pressure pulse similar to the trace on the symmetric foil shown in Fig. 3. The noise level increases, mainly in the high frequency range, as shown in Fig. 4(d). Although there were amplitude variations among the traces from each hydrophone, the traces are shown here without a distance correction since the noise source location is the unknown to be found (see Fig. 1). Again, the variation of gas content in the range 4.5 ppm to 12.5 ppm had no observable effect on the pressure traces.

(c) Acoustic Spectra.

Reverberation Effect and Surface Cavitation Inception. The effect of tunnel reverberation was studied for the cases of surface cavitation inception. Time-averaged spectra as taken by Barker (1975) and to a lesser degree by Arakeri and Iyer (1986) are subject to large errors due to reverberation. In the present study, the individual pulses were recognizable in the signal and Fourier analysis was performed on these individual pulses. As noted earlier, the wave form of a single bubble collapse in the free field was obtained by ensemble averaging the surface cavitation inception data. Using this wave form, single bubble noise in the presence of reflections from the walls could be simulated numerically. The computed effect of reverberation on the power spectrum is shown in Fig. 5, where the power spectrum of a simulated single bubble collapse is compared to the power spectrum of a simulated pulse with reflections. The spectrum obtained by a standard fast Fourier transform routine exhibits a large amount of raggedness due to wave cancellation by multiple reflections. Levinson autoregressive modeling is a suitable smoothing technique for spectral estimation in this case. The result of fourth order autoregressive modeling is shown in the figure. Note that the spectrum of the reverberant signal matches very closely that of the original free field pulse when the spectra are normalized to maximum amplitudes. The amplitude of the reverberant spectrum was approximately 7dB higher than that of the free field in this example, and appears to scale with the number of reflections from each individual pulse. The measured spectrum of cavitation noise is also shown in Fig. 5(d). The agreement between the measured and simulated data is satisfying. The general shape of the spectrum

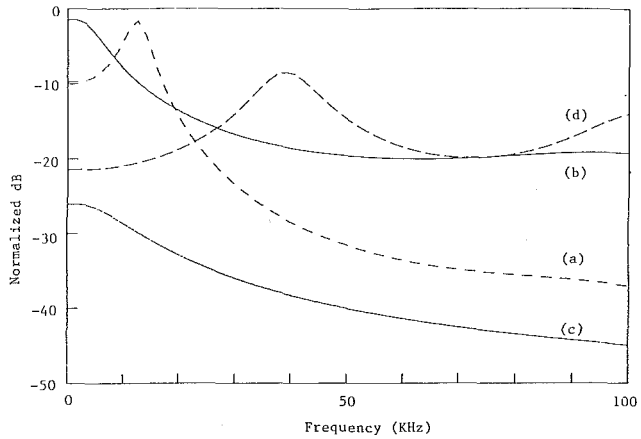

Fig. 6 Power spectral density of tip vortex cavitation noise (Normalization: 190 dB re 1 $\mu Pa^2/Hz$). (Uncertainty in magnitude ± 5db, in frequency ± 0.1 KHZ.)

(a) Inception ($\sigma = 3.97$, $\alpha - \alpha_0 = 12.5$ deg, Re $= 9.5 \times 10^5$); (b) inception ($\sigma = 3.53$, $\sigma - \alpha_0 = 13.5$ deg, Re $= 9.5 \times 10^5$); (c) Continuous tip vortex cavity; ($\sigma = 3.29$, $\alpha - \alpha_0 = 15.5$ deg, Re $= 9.1 \times 10^5$); (d) Tip vortex cavitation with surface cavitation ($\sigma = 0.88$, $\alpha - \alpha_0 = 9.5$ deg, Re $= 9.3 \times 10^5$).

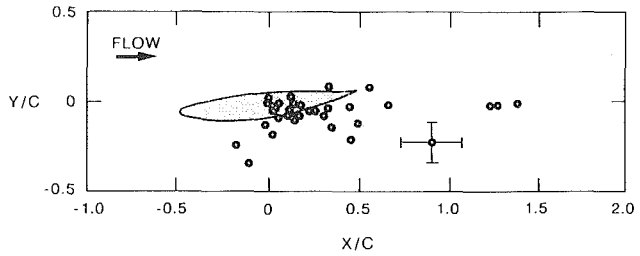

Fig. 7 Sound source locations of tip cavitation inception (various angles of attack and free stream velocities)

remained unchanged and was similar to Fitzpatrick and Strasberg's (1956) theoretical spectrum for a single bubble, although the present spectrum showed a faster decay rate with frequency. The conclusion from these studies is that, for localized cavitation noise sources, the effects of reverberation on the measured spectrum is only on the amplitude. The relative shape remains unchanged.

Arakeri and Iyer (1986) conducted a study of cavitation noise in which the rate of cavitation events could be carefully controlled by an electrolytic nuclei seeding technique. Though they did not measure individual noise pulses, they found that the time averaged spectrum of the noise from multiple cavitation implosions retains the shape of the theoretical single bubble spectrum, which is in accordance with an analysis by Morozov (1969). The amplitude scales with the rate of cavitation events and it was also noted that the mutual interaction among bubbles is negligible. This is consistent with our present computer simulation of the single bubble collapse accompanied by reflected waves. Naturally, a more sophisticated simulation could be performed, but with all the limitations of a simple model, the agreement is satisfactory. Moreover, the model demonstrates the physical phenomenon of reverberation quite adequately. The important point is that cavitation noise can be studied in a highly reverberant water tunnel provided that the time traces can be analyzed individually rather in a time-averaged fashion. Furthermore it should be noted that in the present experiment the initial peaks in the individual noise traces are unaffected by reverberation, and in addition, the differences in individual traces from different cavitation phenomena are rather dramatic (see Figs. 3 and 4).

Spectra of Tip Vortex Cavitation. Acoustic spectra of tip vortex cavitation at different stages of development are presented in Fig. 6. (Smoothing of the FFT was made with a 15th order Levinson AR method to retain details of the power spectra). As mentioned earlier, two types of acoustic signals were noted during tip vortex cavitation inception. The power spectrum shown in Fig. 6(a) corresponds to inception when there is a low frequency regular oscillation (Fig. 4(a)). A dominant peak is evident at low frequency, and the spectrum drops off rapidly. The power spectrum shown in Fig. 6(b) corresponds to inception accompanied by high frequency noise (see Fig. 4(b)). The spectrum exhibited a strong low frequency component and a gradual decrease of spectrum level above 100KHz. The visual observations at these test conditions indicate that the moderately large high frequency component may be caused by the impingement of the tip vortex cavity on the surface of the foil, as noted earlier. In spite of some similarity in spectra, it is felt that the surface cavitation is not the source of noise in this case. As shown in Figs. 6(c) and 4(c), the noise level decreases abruptly as a steady tip vortex cavitation develops to form a well defined cavity core trailing from the tip of the foil (see e.g., Fig. 2(b))). As noted earlier, a distinct tone, with a sharp spectral peak, is generated within a very narrow range of the cavitation number. This noise appears to occur only when the tip vortex cavity has a braided structure. The frequency of the tone is variable with both velocity and cavitation number. Tonal frequencies in the range of 340 Hz to 900 Hz have been observed. The pitch decreases and then finally vanishes at lower cavitation numbers. When surface cavitation appears, the noise level increases dramatically, especially in the higher frequency bands as shown in Fig. 6(d). The power spectrum of the combined tip vortex and surface cavitation is very similar to the spectrum of continuous surface cavitation alone (not shown) on the symmetric foil. Thus it can be assumed that, when it occurs, surface cavitation is the dominant noise source. It is of interest to note that although the spectrum of the noise due to tip vortex and surface cavitation in combination exhibited a decay rate similar to Fitzpatrick and Strasberg's (1956) theoretical value, the spectrum of tip vortex cavitation noise alone displayed a significantly steeper decay rate with frequency. This indicates that distinctly different noise generation mechanisms are associated with tip vortex cavitation noise. This point requires further clarification with future research.

(d) Inception Sound Source Location. The present results for sound source location should be viewed within the limitations of the measurement technique. As stated previously, a short tone burst of 60 KHz was used for calibration. Because the initial peak point in each transmitted waveform was identified, the statement of valid frequency range did not have to be made in detail, unlike time-averaged measurements. For the localization procedure, an attempt was made to identify the direct arrival of the initial pulse (or recognizable initial wave form), and the accuracy was limited only by the frequency response of the system and the A/D converter, and possibly by the broadening of the pulse crest through the fluid medium. Naturally, the sharper the peak of the waveform, the more accurately the arrival time could be obtained. The same argument applies when delay times were obtained using a digital cross-correlation technique. In addition, the localization analysis was also carried out assuming an infinite line source rather than a point source. When selected data were reevaluated, a consistent solution to the line source equations could not be achieved even when a solution as a point source existed. This implies that the point source assumption was still the best approximation to the events measured presently. There was a significant number of cases, however, where the

satisfactory convergence of solution was not achieved, and sound sources of finite length remain to be investigated.

Typical results on inception noise are shown in Fig. 7 without identifying individual test conditions for each point since no definite trend due to different parameters was seen. In spite of the scatter in the data, the present results indicate that the noise sources are concentrated very close to the hydrofoil tip, either within one or two chord lengths downstream from the tip within the vortex roll-up region, or within the immediate neighborhood of the foil tip corresponding to the upstream end of the continuous cavity. These observations were in good agreement with the visual observation recorded on a video tape. Though it may be said that the present results only verified what has been already speculated in the past concerning the location of the sound source, the direct measurements of the individual noise source location have not been reported in the open literature prior to the present experiment. Naturally the accuracy of the experimentation must be improved in the future.

As noted earlier, the present method could, in principle, be extended to the case of continuous cavitation noise using time-averaged cross-correlation techniques. However, such an extension is hampered by the low noise level of the continuous developed cavity and tunnel reverberation effects, as well as the strong sources of noise created by surface cavitation at the lower cavitation numbers.

Conclusions

The findings from the present investigation are summarized below.

Several different types of cavitation inception noise signatures were noted. Tip vortex cavitation inception was observed to be either the sudden appearance of a continuous cavity, or the intermittent appearance of an elongated bubble extending axially over a relatively small portion of the tip vortex which primarily occurred at low angles of attack. The transient noise signal due to the former type of inception consisted initially of a negative pressure pulse implying the sudden occurrence of a cylindrical cavity. The initial pulse was followed by either a relatively low frequency, moderately damped oscillations or high frequency, strongly damped pulses in the noise signature. The latter high frequency oscillations were nominally observed at sudden inception at lower cavitation numbers. Further study including a high speed motion picture analysis is required to identify the noise source associated with the movement of the tip vortex cavity at its inception.

A hydrophone array was utilized to identify the noise source location. In spite of limitations on spatial resolution and repeatability, the results of this study gave physical evidence that cavitation inception noise sources are concentrated in the vortex rollup region, less than one or two chord lengths from the tip of the hydrofoil.

The noise intensity associated with fully developed tip vortex cavitation is significantly lower than inception noise. At high angle of attack, and under special circumstances, a very strong, low pitch tone occurs. The frequency of the tone varied with cavity core radius and free stream velocity, discounting the thought that this might be a flow induced vibration of the hydrofoil itself. Although no conclusive statement could be made from the present set of data, it was speculated that the oscillation of the twisted ribbon type cavity is responsible for this tone.

If surface cavitation occurs, it is the dominant noise source, overwhelming any type of vortex caviation noise. Surface cavitation in the absence of tip vortex cavitation was examined with a hydrofoil having a symmetric foil section. Well-defined noise pulses were observed, which correspond to individual bubble implosions on the hydrofoil surface. The noise sources were concentrated in a narrow region on the foil.

Although these tests were carried out in a highly reverberant water tunnel, experiments and computer simulations demonstrated that the shape of the measured spectra of the inception noise was unaffected.

Acknowledgment

This study was supported by the Office of Naval Research. The authors acknowledge many valuable comments made by reviewers.

References

Arndt, R. E. A., 1976, "Cavitation on Model Propellers with Boundary Layer Trips," *Cavitation and Polyphase Flow Forum*, ASME, N.Y., pp. 30–32.

Arakeri, V. H., and Iyer, R. N., 1986, "A New Technique in Cavitation Noise Research," *Proceedings of International Symposium on Cavitation*, Vol. 1, ed. by H. Murai, Sendai, Japan, pp. 299–304.

Arakeri, V. H., Higuchi, H., and Arndt, R. E. A., 1986, "Analysis of Recent Tip Vortex Cavitation Inception Data," *Proceedings of the American Towing Tank Conference*.

Barker, S. J., 1975, "Measurements of Radiated Noise in the Caltech High-Speed Water Tunnel, Part II: Radiated Noise from Cavitating Hydrofoils," Final Report on ONR Contract "Hydrodynam. Radiated Noise," GALCIT

Fisher, M. J., Harper-Bourne, M., and Glegg, S. A. L., 1977, "Jet Engine Noise Source Location: The Polar Correlation Technique," *Journal of Sound and Vibration*, Vol. 51, No. 1, pp. 23–54.

Fitzpatrick, H. M., and Strasberg,, M., 1956, "Hydrodynamic Sources of Sound," *1st Symposium on Naval Hydrodynamics*, F. S. Sherman (ed.) Publication 515, National Academy of Sciences, pp. 241–280, Washington, D. C.

Harrison, M., 1952, "An Experimental Study of Single Bubble Cavitation Noise," *J. Acous. Soc. of Am.*, Vol. 24, No. 6, pp. 776–783.

Higuchi, H., and Arndt, R. E. A., 1985, "Reverberation Effects on Cavitation Noise," *Cavitation and Multiphase Flow Forum*, edited by J. W. Hoyt and O. Furuya, FED-Vol. 23, ASME, N.Y., pp. 21–24.

Higuchi, H., Jiang, S. H., Rogers, M. F., and Arndt, R. E. A., 1986, "Cavitation Inception in Trailing Vortex From a Hydrofoil," *Symposium 1986, International Association for Hydraulic Research, Section on Hydraulic Machinery Equipment and Cavitation*, Montreal, Canada.

Higuchi, H., Quadrelli, J. C., and Farell, C., 1987, "Vortex Roll-Up from an Elliptic Wing at Moderately Low Reynolds Numbers," *AIAA Journal*, Vol. 25, No. 12, pp. 1537–1542.

Killen, J., 1988, private communication.

Latorre, R., 1982, "TVC Noise Envelope-An Approach to Tip Vortex Cavitation Noise Scaling," *Journal of Ship Research*, Vol. 26, No. 1, pp. 65–75.

Leggat, L. J., and Sponagle, N. C., 1985, "The Study of Propeller Cavitation Noise Using Cross Correlation Methods," ASME JOURNAL OF FLUIDS ENGINEERING, Vol. 107, pp. 127–133.

Ligneul, P., Crance, C., and Bovis, A., 1983, "Tip Vortex Cavitation Noise of a Screw Propeller: Theory and Experiments," *I. Mech. E.*, Vol. C225, pp. 289–297.

Morozov, V. P., 1969, "Cavitation Noise as a Train of Sound Pulses Generated at Random Times," *Soviet Physics-Acoustics*, Vol. 14, No. 3.

Narayan, N., and Plunkett, R., 1985, "Pressure Cross Spectra in Turbulent Boundary Layers in Water," *Shear Flow-Structure Interaction Phenomena*, NCA-Vol. 1, ASME.

Rogers, M. F., 1988, "Experiments in Tip Vortex Cavitation and Associated Noise," M.S. thesis, University of Minnesota, Minneapolis, Minn.

Sponagle, N. C., and Leggat, L. J., 1984, "The Spacial Distribution of Acoustic Sources at Propeller Vortex Cavitation Inception," *International Symposium on Cavitation Inception*, FED-Vol. 16, ASME, N.Y.

Strasberg, M., 1986, "Hydrodynamic Cavitation Noise," Keynote Lecture presented at the *International Symposium on Cavitation and Multiphase Flow Noise*, ASME Winter Annual Meeting, Anaheim, Calif.

The Damage Capacity of Cavitating Flow From Pulse Height Analysis

S. A. Fry
Department of Mechanical Engineering,
Polytechnic South West,
Plymouth, U.K.

Digital pulse amplitude acquisition systems are reviewed and an analogue pulse height analyser (PHA) is described. Cavitation experiments are reported in which pressure pulses in the liquid (water) are picked up by a flush mounted pressure transducer and measured using the PHA. Tests were carried out on two cavitation sources: a 60 deg symmetric wedge and a circular cylinder. Despite generating similar r.m.s. noise levels the wedge is 21 times as damaging as the circular cylinder at peak noise flow conditions (at $V=16$ m/s). By imposing thresholds on the spectra parameters it had been possible to find a linear calibration beween noise and erosion applicable to both cavitation sources over a range of flow velocities. A good correlation between cavitation noise and erosion was found by simply measuring the number of pulses above a suitable threshold.

I Introduction

The problems of cavitation damage are well-known to hydraulic engineers. However, for economic considerations hydraulic machines are often run with a limited amount of cavitation present. Under these conditions it would be very useful if noise could be used as a guide to the severity of the erosion. It has therefore long been hoped to find a relation between cavitation noise and erosion of the form

$$\psi = k\phi$$

where ψ is some measure of erosion (perhaps mass loss rate MLR or mean depth of penetration rate MDPR)

k is the calibration coefficient

and ϕ is some quantifiable characteristic of cavitation noise.

In most of the work to date the noise has been quantified by taking r.m.s. measurements in various frequency ranges. Such measurements can be useful for indicating the outset of cavitation, but have proven to be of limited value in quantifying the damage potential of the flow with developed cavitation. Although it has been shown that potential damage zones may be indicated by positions of high r.m.s. noise [1], relationships of the above form have only been established for specific flow geometrics. For instance, in reference [2] a good correlation was established between MLR and r.m.s., but for different shapes of body under similar flow conditions and in the same flow circuit the calibration varied as much as 200:1.

Recently measurements of the peak amplitudes of the bubble collapse noise have been taken to provide a more direct indication of cavitation intensity [3–6]. However, it is important to distinguish between the intensity of the flow and its damage capacity. All bubble collapses contribute to the cavitation intensity, but only those with high enough collapse energy provide a damage threat. Cavitation intensity is a feature of the flow which may be quantified by measuring pulse spectra [3 and 5], but no indication of damage capacity can be given without reference to the material to suffer damage.

In reference [7] Selim reports damage to 99.0 percent pure aluminum sidewall specimens resulting from cavitation from two sources: a 60 deg symmetric wedge and a circular cylinder, each spanning the test section with 50 percent blockage. It was found that for the same flow velocity at the throat the peak damage MLR was 21.4 times greater for the wedge than for the circular cylinder. The fact that the wedge is so much more damaging is of considerable interest, especially since corresponding values of r.m.s. noise are similar for both sources. This problem was taken as the starting point for the present work. Clearly, if it is hoped that noise measurement will ever be used as a guide to the severity of erosion, some statistical characteristic of the noise must be identified which varies in a similar manner to erosion i.e., some parameter whose value is approximately 20 times as great for the 60 deg wedge as for the circular cylinder under the above peak damage flow conditions. The search for such a noise parameter by measuring pulse height spectra is described in this report.

II Methods of Pulse Height Measurement

A. Cavitation Noise Signal. Examples of cavitation noise were obtained for the 60 deg symmetric wedge cavitating at peak noise flow conditions ($\sigma=4.61$) and an upstream velocity V of 18 m/s. The noise signal was picked up by a high frequency pressure transducer (Kistler 603B) flush-mounted into the test section wall 15 mm downstream of the base of the wedge. The signal was passed through a charge amplifier and examples were recorded by a digital storage oscilloscope. Many samples were recorded under the same flow conditions but using different sampling rates. The effect of sampling rate is shown in Figs. 1(a) and 1(b) which show cavitation noise sampled at intervals of 0.5 μ and 5.0 μs, respectively.

Decreasing the sampling rate by an order of magnitude has the effect of stretching the recorded pulse width by an order of magnitude. More seriously, it also has the effect of ap-

Contributed by the Fluids Engineering Division for publication in the JOURNAL OF FLUIDS ENGINEERING. Manuscript received by the Fluids Engineering Division November 23, 1987.

preciably reducing the measured amplitude of the noise pulse. It was concluded that cavitation noise could be measured with reasonable accuracy when sampled digitally every 0.5 μs. A sampling rate of 5.0 μs is inadequate because this results in the measured signal being distorted, invalidating subsequent analysis.

B. Review of Digital Techniques for Pulse Height Measurement. To date digital methods of measuring pulse peak amplitudes have suffered from inherent limitations. Two digital methods were used in reference [4].

Method 1. Points were sampled every 14 μs and stored in the computer memory. Afterwards the peaks in the recorded signal could be analyzed and the spectrum displayed. However, this sampling frequency is inadequate for the phenomenon of cavitation. As pointed out above, a sampling period of 0.5 μs is required.

Method 2. Pulse peaks were detected by an analogue device and only the peak amplitudes stored in the computer memory. This considerably reduces the memory requirements, but the peak detector ADC takes about 14 μs, resulting in a "dead time" i.e., peaks that occur within 14 μs of each other are missed.

C. Pulse Height Analyzer (PHA). After considering the above limitations of digital methods the author decided to investigate the possibility of acquiring cavitation pulse peak data using analogue methods. From Fig. 1(a) it was decided that the PHA must be capable of recording peak amplitudes in 14 amplitude ranges accurately down to the following limits of pulse width and spacing:

Specification; minimum pulse width
= 0.5 μs (at 1.0 μs spacing)
minimum pulse spacing
= 0.5 μs (at 1.0 μs width)

NOTES:

(1) It is more meaningful to set the specification in the time domain than in the frequency domain.
(2) It is not sufficient that the PHA should record peaks accurately down to the above limits. It is also necessary that the PHA should be "well behaved" when these limits are exceeded, i.e., under no signal conditions should the PHA record false extra peaks.

A PHA operating on analogue principles has been designed and developed which achieves the above specification. Also, on a square wave the PHA measures correctly down to a period of 1.3 μs (0.77 MHz). Since the PHA is an analogue device operating on-line it does not suffer from memory size limitations so that long sampling periods may be achieved. On the prototype the sampling period can be set from 0.1 s to 999.9 s in 0.1 s intervals. In addition, the PHA incorporates an overcounter which counts the number of peaks of amplitude greater than the range of the unit.

III Experimental Facilities

A. The Cavitation Tunnel. A considerable amount of experimental work has been carried out by Selim [7], including extensive MLR measurements on both cavitation source and sidewall specimens. Tests in the present investigation were carried out using a test section with dimensions (20 mm × 40 mm) and flow passage geometry the same as that used by Selim so that noise results could be compared with his MLR results.

The water is circulated by a fixed speed 19 kW centrifugal pump while a bypass control provides variable flow velocity through the test section. The tunnel pressure is varied independently by a pneumatic controller over a range of 0-10 bar, the control air being isolated from the water by a flexible stainless steel bellows. The test section incorporates a movable inner duct to facilitate noise measurements at different distances downstream of the cavitation source, see Fig. 2. A perspex window at the top of the test section allows cavity development to be observed while experiments are in progress.

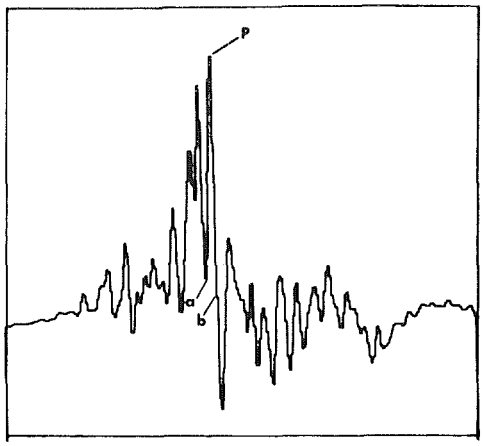

Fig. 1(a) Noise signal sampled digitally every 0.5 μs Pulse width (ab) = 2.5 μs

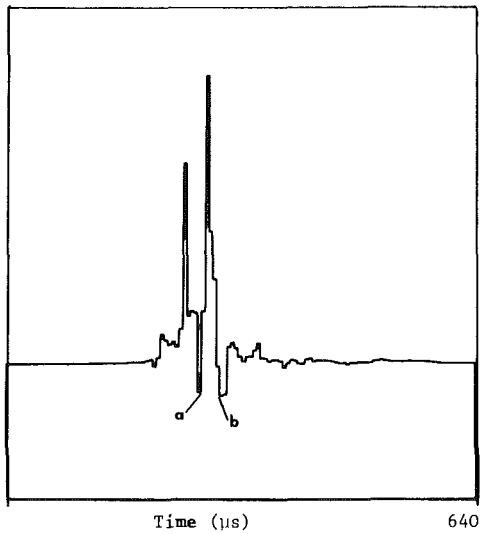

Fig. 1(b) Noise signal sampled digitally every 5.0 μs Pulse width (ab) = 25 μs

Fig. 1 Digital samples of cavity collapse noise signature measured 15 mm downstream of a cavitating 60 deg symmetric wedge. Peak noise flow conditions (σ = 4.61) at an upstream flow velocity of 18 m/s

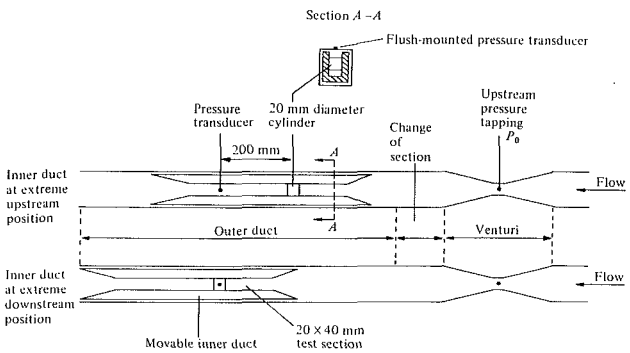

Fig. 2 Schematic diagram of movable duct test section (plan view)

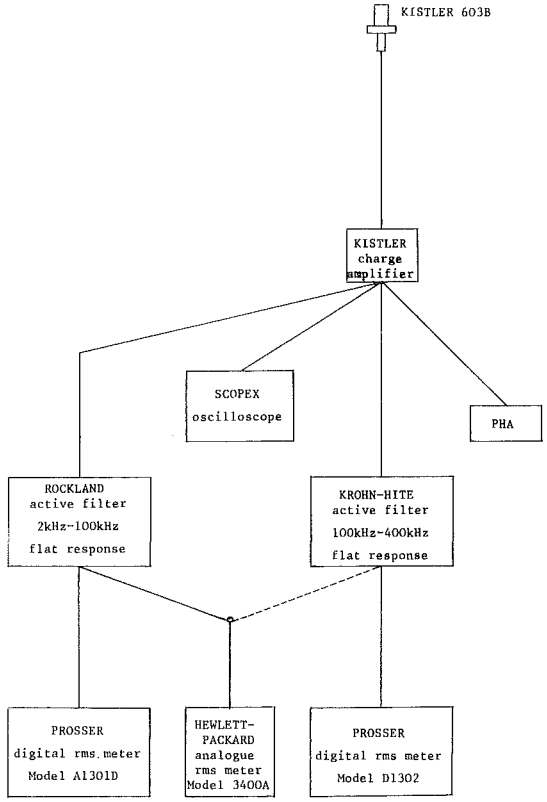

Fig. 3 Schematic diagram of noise instrumentation

Further details of this test section may be found in reference [1]. The tunnel flow velocity was determined from measurements across the venturi upstream of the movable duct assembly. The pressure inside the test section was calculated from pressure measurements taken at the throat of the venturi. Tests were carried out using two cavitation sources: one was a 60 deg symmetric wedge (20 mm base) with one apex pointing directly into the flow, and the other was a circular cylinder (20 mm diameter).

B. Noise Instrumentation. The noise measuring instrumentation is shown schematically in Fig. 3. The cavitation noise was picked up by a pressure transducer mounted in a special plastic adaptor to isolate it from high frequency accelerations (e.g., noise conducted through the perspex window). The signal from the transducer was amplified by a Kistler charge amplifier (Type 5001). The amplified signal was then passed directly to the PHA and monitored on a Scopex oscilloscope (Model 14D-10). Peaks were counted in 14 amplitude ranges each of 4 bar width.

The r.m.s. content of the noise signal was measured in two frequency ranges by Prosser digital r.m.s. voltmeters. The 2 kHz high-pass frequency was chosen to eliminate the considerable energy at the vortex shedding frequencies (see reference [8]).

C. Uncertainty Estimates. It is important to distinguish between variables which are adjusted to give the desired experimental conditions (e.g., sigma) and variables which are measured at those conditions (e.g., noise measurements) since the latter are subject to the statistical variation of the phenomenon. The uncertainty interval for sigma will depend only upon the systematic and random errors of the measuring devices used (estimated to be ± 0.01 at 20:1 odds). However, uncertainty estimates for noise measurements must also include estimates for the random variability of the noise.

Uncertainties for r.m.s. pressure (in low and high frequency ranges) and for n_i are estimated to be ± 10 percent at 20:1 odds. This results from the high level of random variability of the noise rather than uncertainty associated with the measuring instrumentation. In particular, considerable testing of the PHA has resulted in a high level of confidence in the accuracy of this instrument.

IV Test Procedure

Preliminary tests were carried out to identify the maximum noise to be measured. The gain of the charge amplifier was adjusted so that an acceptable number of peaks were obtained by the overcounter. This gain was then used for all experiments. It is most important not to vary the gain since it affects both the minimum threshold and the bandwidth of the PHA. The PHA and digital r.m.s. voltmeters were set to measure over a 10 second time period.

A. Test (a). Noise Measurements at Different Distances Downstream of the Source. Peak noise flow conditions were established at $V = 16$ m/s with the inner duct in the upstream position so that the pressure transducer was 200 mm downstream of the source. The inner duct was traversed and noise measurements taken at various positions along the duct until the source was situated directly beneath the pressure transducer.

The position at which the noise was at a maximum was found from Test (a), and the transducer was held at this distance downstream of the source for Tests (b) and (c).

B. Test (b). Noise Measurements Under Varying Cavitation Conditions. In these experiments the inner duct remained fixed at the maximum noise position and noise measurements were taken over a range of cavitation conditions. The upstream flow velocity was held constant at $V = 16$ m/s and the cavitation number (σ) was decreased by lowering the tunnel pressure.

C. Test (c). Noise Measurements at Different Flow Velocities. The inner duct was set to the maximum noise position. Peak noise conditions were established at upstream velocities of $V = 10$, 12, 14, 16, and 18 m/s and noise measurements taken.

V Results

All tests were carried out using tap water at ambient temperature. The tunnel was run under intense cavitating conditions and any air from the water bled off to achieve equilibrium air content before each test. Results are presented in terms of the cavitation number σ based on free stream flow conditions in the 20 mm $\times$ 40 mm test section upstream of the cavitation source.

A. Interpretation of Measured Pulse Height Spectra. Before presenting the results it is necessary to consider how to interpret the measured peak spectra as the measured spectra alone (without interpretation) are of limited value.

Consider the results of Test (b) for the circular cylinder. The r.m.s. of the cavitation noise was measured 10 mm downstream of the cylinder throat at 28 different values of σ. The familiar noise/cavitation number characteristic is shown in Fig. 4, exhibiting peak noise at test point 16. The shape of the characteristic is very similar to that obtained previously (reference [1]). At every test point measurements were also taken with the PHA to produce a pulse peak amplitude spectra corresponding to that point. An inset graph in Fig. 4 shows the pulse height spectra corresponding to 4 test points. The number of counts per second are shown on a logarithmic scale because this number increases considerably as the cavitation conditions become more intense. Increasing cavitation intensity not only results in many more peaks being measured at the

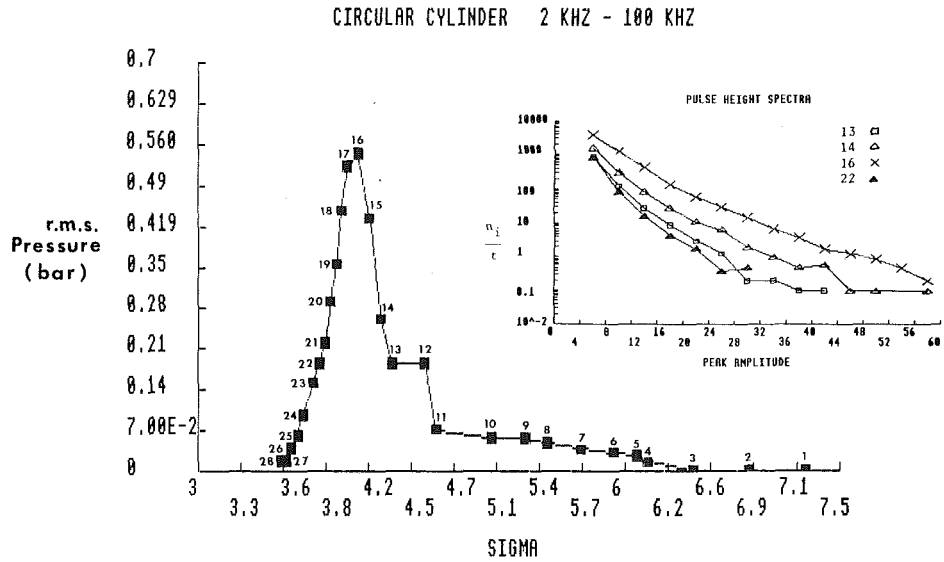

Fig. 4 Noise cavitation number characteristic for circular cylinder with pulse height spectra (inset)

low amplitude part of the spectrum, but also higher amplitude peak appear, i.e., there is a general increase in the fullness of the spectrum under more intense cavitation conditions, the spectrum being most full at test point 16. At lower cavitation numbers the cavitation noise is reduced and peak amplitude spectra decrease.

The above results show that there is some qualitative agreement between r.m.s noise and pulse height spectra. However, in order to carry out any kind of quantitative analysis some way must be found to assess the cavitation intensity of the measured spectrum.

B. Pulse Height Spectrum Parameters. It would be convenient if a single value could be attributed to a pulse height spectrum to indicate its collapse intensity. The simplest value is obtained by counting the event rate, i.e., the total number of peaks per second in all amplitude ranges. Total peak count T1 is given by

$$T1 = \frac{1}{t}\sum_{i=1}^{15} n_i \tag{2}$$

where n_i = number of counts in amplitude range i.
t = sampling period

The above definition is simple, but it makes no distinction between high amplitude and low amplitude pulses. An indication of cavitation intensity is obtained by summing the number of events in each amplitude range multipled by the mean amplitude of that range. Cavitation intensity I1 is given by

$$I1 = \frac{1}{t}\sum_{i=1}^{15} n_i a_i \tag{3}$$

where a_i = mean amplitude of amplitude range i
(The upper limit range 14 is used for a_{15})

It follows that the average peak amplitude A1 is given by

$$A1 = \frac{I1}{T1} \tag{4}$$

A further definition proprotional to the acoustic power of the pulses is obtained by summing the number of events with the squares of their amplitudes:

$$S1 = \frac{1}{t}\sum_{i=1}^{15} n_i a_i^2 \tag{5}$$

Definitions similar to S1 have already been used successfully by Kirejczyk and De to measure cavitation intensity.

By attributing a single value to each peak spectrum it is possible to plot these values againt cavitation number to produce a characteristic like the r.m.s. characteristic shown in Fig. 4. Test results are presented in terms of these four basic spectra parameters.

C. Results of Test (a) Noise Measurements at Different Distances Downstream of the Cavitation Source (at Peak Noise Flow Conditions). Although the shape of the downstream noise characteristics may be of interest, the main objective of Test (a) is to identify the position along the duct where the noise is at a maximum. For the circular cylinder both the event rate T1 and the cavitation intensity I1 were found to have their greatest values 10 mm downstream of the throat. Similarly, for the 60 deg wedge T1 and I1 again have maximum values at the same position along the duct (15 mm downstream of the throat of the wedge). Positions of 10 mm and 15 mm downstream of the throat were therefore used for the circular cylinder and the 60 deg wedge, respectively, in Tests (b) and (c).

D. Results of Test (b) Noise Measurements at Different Values of Cavitation Number (at Maximum Noise Position and Constant Upstream Velocity of V = 16m/s). The difficulty in accounting for the considerable difference in erosion rates for the 60 deg symmetric wedge and the circular cylinder by noise measurements has already been mentioned. To focus on this difference test results are presented for both sources together. Results of the circular cylinder are shown by squares while those for the 60 deg symmetric wedge are shown by solid triangles.

Figure 5 shows the effect of cavitation conditions upon the r.m.s. noise in the frequency range 2 kHz—100 kHz for both sources. It can be seen that peak noise conditions are reached earlier (at higher value of σ) for the wedge because of its increased flow blockage. For the same geometric blockage (50 percent) the wedge presents a greater blockage to the flow than the circular cylinder. It can also be seen that higher values of r.m.s. noise are measured for the wedge than for the circular cylinder. However, the ratio of the noise is far less than the erosion ratio of 21 measured by Selim (reference [7]). Similar results were obtained for r.m.s. measurements in the higher frequency range (100 kHz–400 kHz) as shown in Fig. 6.

Now let us turn to the pulse height spectra results. The effect of cavitation conditions upon the total event rate is shown in Fig. 7. It is clear that merely counting the total number of

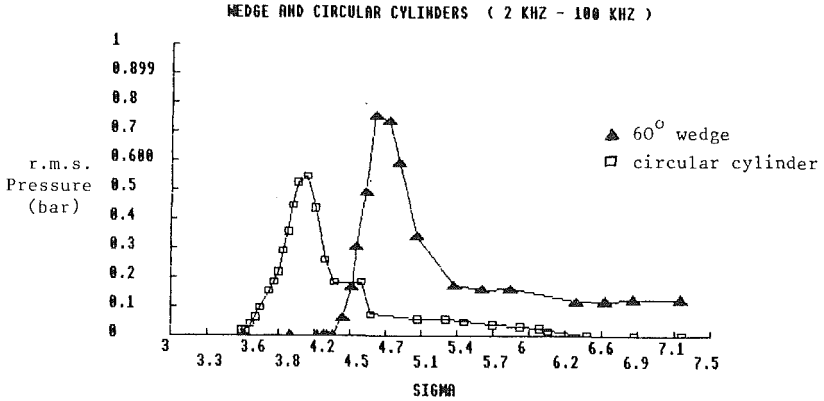

Fig. 5 Comparison of noise cavitation number characteristics for wedge and circular cylinders in low frequency range (2 kHz–100 kHz)

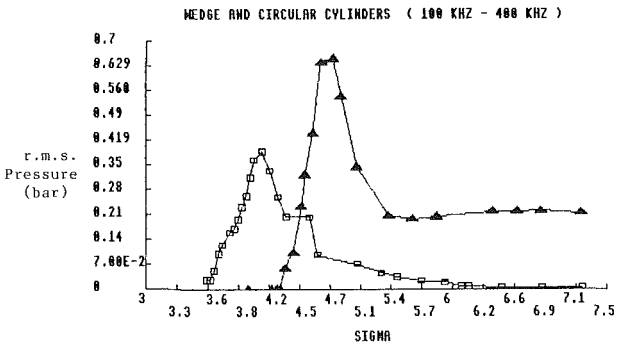

Fig. 6 Comparison of noise cavitation number characteristics for wedge and circular cylinders in high frequency range (100 kHz–400 kHz)

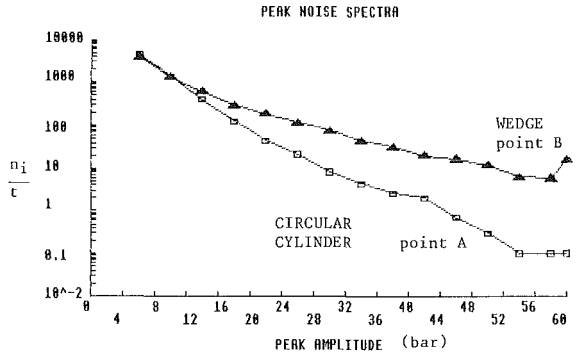

Fig. 8 Pulse height spectra for 60 deg wedge and circular cylinder at peak noise flow conditions, corresponding to points A and B on Fig. 7

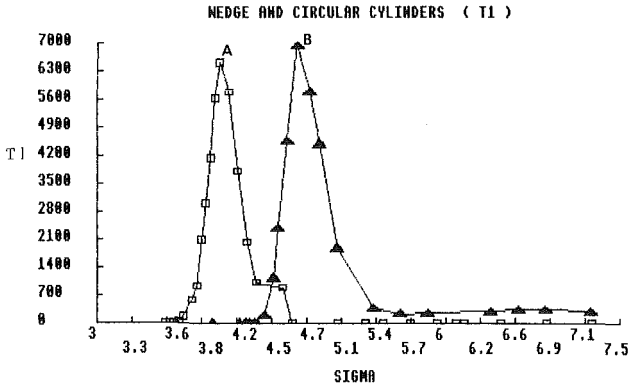

Fig. 7 Pressure pulse event rate (in all amplitude ranges) versus cavitation number for wedge and circular cylinders

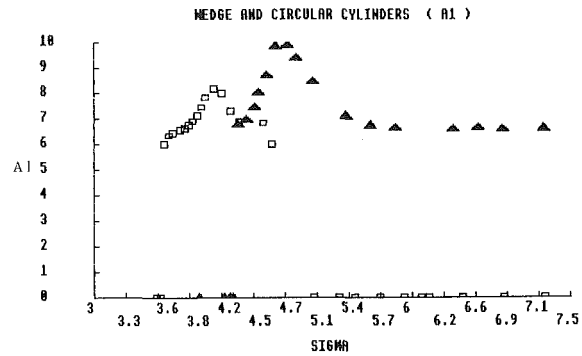

Fig. 9 Average peak amplitude (in all amplitude ranges) versus cavitation numbers for wedge and circular cylinders

pulses fails completely to distinguish between the two sources. However, the reason for this may be seen when the raw spectral data is examined. Figure 8 shows the peak noise spectra for each source corresponding to points A and B of Fig. 7. It is at once clear from Fig. 8 that the total number of counts is similar for the two sources despite the fact that there are more high energy pulses in the case of the wedge, i.e., the value of T1 is completely dominated by the high number of low energy pulses. We would, therefore, expect the average pulse height to be greater for the wedge, and this is shown to be the case in Fig. 9. It then follows that the cavitation intensity must also be greater for the wedge, and this also is shown in Fig. 10. The difference between the noise measurements for the two sources is, therefore, greater when measuring I1 than when measuring T1. This difference becomes even greater when measuring S1 (see Fig. 11) since more emphasis is placed on the higher energy pulses. However, even measuring S1 the noise ratio does not approximate to Selim's erosion ratio of 21.

It should be noted that the above pulse spectra parameters provide information about the condition of the fluid at the point of measurement only. Collapse pressures suffer attenuation between their point of collapse and the point of measurement, and this would have to be taken into account to obtain the true dynamic intensity of cavitation. Kirejczyk has carried out a considerable amount of work on the evaluation of cavitation intensity and four methods are reviewed in reference [5]: pressure pulses, ultrasonic waves in walls, vibration accelerations and hydroacoustic noise. However, in the present paper we are concerned with the damage capacity of the flow rather than its intensity. The damage capacity of the flow will depend upon the material properties of the material to suffer damage. For example, all bubble collapses contribute to S1, but only a proportion will have sufficient energy to

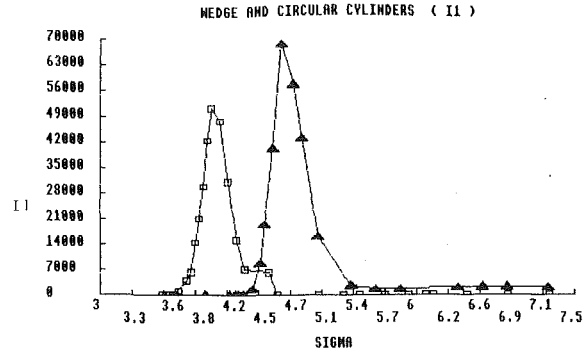

Fig. 10 Cavitation intensity (in all amplitude ranges) versus cavitation number for wedge and circular cylinders

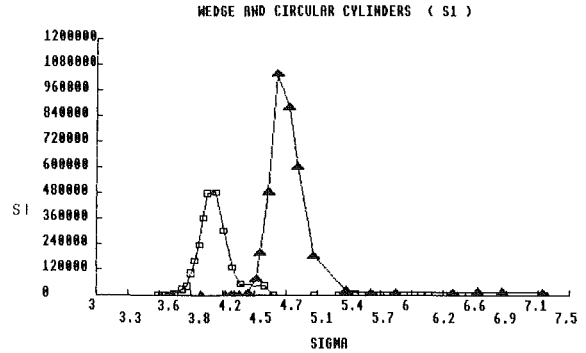

Fig. 11 S1 versus cavitation number for wedge and circular cylinders

cause any damage. It has been shown that below a certain collapse pulse amplitude no damage results [6]. It is therefore important to distinguish between collapses with sufficient energy to cause damage and those that cannot cause damage. One method is to impose some pulse amplitude threshold below which no damage should occur.

E. Spectra Parameters With Thresholds. In the search for a noise parameter which might indicate the damage capacity of the flow it was decided to investigate the effect of imposing thresholds on the four basic spectra parameters. However, choosing a suitable threshold is no simple matter. The choice is complicated by several factors including:

(1) The transducer is located in the perspex window remote from the collapse zone.
(2) Even if the transducer were located in the damage zone its signal would require considerable compensation since its output corresponds to the average pressure acting over the transducer surface whereas a microjet acts on a much smaller area.
(3) Selecting the correct stress threshold for different materials under these dynamic loading conditions may not be straightforward.

Because of the above complications it was decided to impose thresholds at each level in turn. This approach has the additional advantage that the effect of increasing thresholds can be investigated for the different spectra parameters.

F. Effect of Threshold on Spectra Parameters. We know the erosion ratio (60 deg wedge/circular cylinder) to be 21 from peak noise flow conditions at approximately V = 16 m/s [7]. From the corresponding pulse height spectra shown in Fig. 8 it can be seen that the difference between the measured spectra becomes greater for higher energy pulses. The ratio of the spectra parameters for the two sources may, therefore, be expected to increase as progressively higher thresholds are imposed. This is indeed found to be the case for T, I, and S ratios as shown in Table 1. Since T and I ratios increase similarly it follows that A [= I/T] ratios are insensitive to threshold and cannot distinguish between the two sources. Values calculated for threshold levels higher than level 11 are unreliable since an insufficient number of counts were recorded above this level. It may be noted that differences between spectra parameters T, I, and S become less significant at higher thresholds. Also, it is clear that imposing different thresholds serves to distinguish between sources far more readily than using different spectra parameters at a given threshold.

Most important, it is possible to find a threshold (level 8) where the noise ratio for the two sources matches their erosion ratio. This is significant because this is the first time noise measurements have been taken which match the erosion rates produced by the 60 deg wedge and circular cylinder sources. It is worth mentioning that the r.m.s. noise measurements taken in the same tests produced ratios of only 1.5 and 1.8 in the frequency ranges of 2 kHz–100 kHz and 100 kHz–400 kHz, respectively. Similarly, acoustic power (α r.m.s.^{2}) gave ratios of only 2.1 and 3.2 in these frequency ranges. These results are summarized in Table 2.

It is of interest to present the results of test (b) using the spectra parameters evaluated above the threshold level 8. Values of T8 are presented from both sources in Fig. 12. Here the results of test (b) appear quite different from those presented earlier in terms of r.m.s. noise (Figs. 5 and 6). Inspection of Fig. 12 shows the damage capacity of the flow to be much greater for the wedge, reflecting the true situation. Similarly, the damage capacity of the two cavitating flow becomes quite obvious when the noise measurements are presented in terms of I8 and S8 as shown in Figs. 13 and 14, respectively.

Finding noise parameters which exhibit a similar ratio to

Table 1 Pulse height spectra ratio (wedge/circular cylinder) for different thresholds. Peak noise flow conditions at V = 16 m/s.

Threshold level	T	I	S
1 (all counts)	1.2	1.4	2.3
2	1.6	2.0	3.0
3	2.6	3.2	4.4
4	4.2	5.1	6.7
5	6.5	8.0	9.5
6	9.4	10.9	13.0
7	14.7	15.9	17.9
8	17.9	19.4	21.5
9	23.9	24.5	27.1
10	27.8	30.8	32.8
11	30.0	32.2	35.7
12	74.0	77.8	86.0
13	130.0	125.0	126.0
14	95.0	92.0	94.0

Table 2 Comparison of noise ratios (60 deg wedge/circular cylinders) with erosion ratios for peak noise flow conditions at V = 16 m/s

Selim's erosion ratio	r.m.s. noise ratio		acoustic power ratio		spectra ratio (level 8)		
	2kHz–100kHz	100kHz–400kHz	2kHz–100kHz	100kHz–400kHz	T	I	S
21.4	1.5	1.8	2.1	3.2	17.9	19.4	21.5

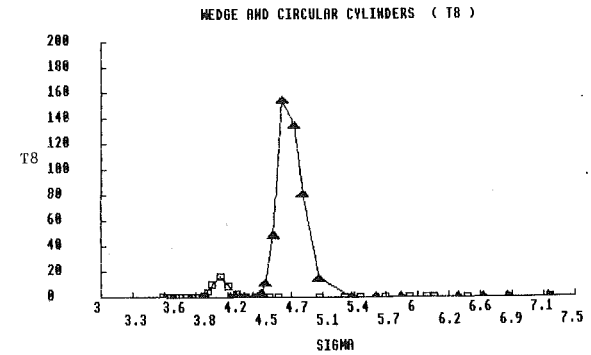

Fig. 12 Pressure pulse event rate (in amplitude ranges 8 and above) versus caviation number for wedge and circular cylinders

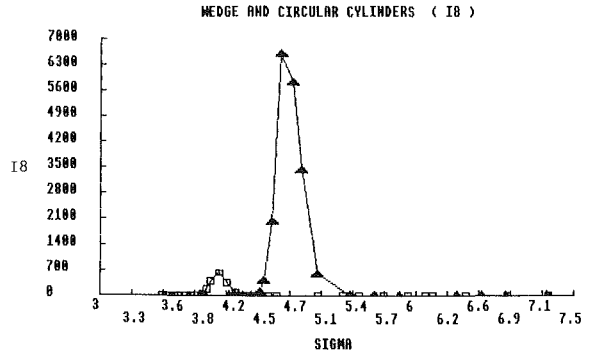

Fig. 13 Cavitation intensity (in amplitude ranges 8 and above) versus cavitation number for wedge and circular cylinders

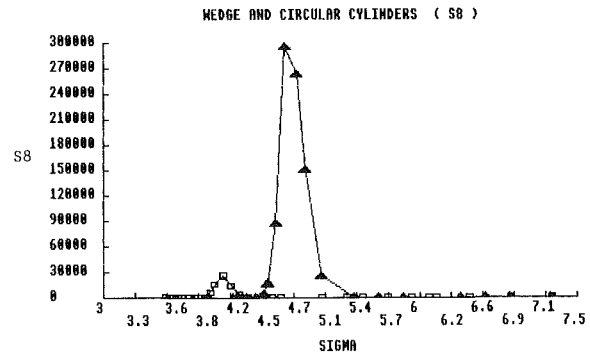

Fig. 14 S8 versus cavitation number for wedge and circular cylinders

Selim's erosion ratio at V = 16 m/s is most encouraging, but it still remains to be shown that these parameters are useful at other flow velocities. This is considered in the following section.

G. Results of Test (c). Noise Measurement at Different Flow Velocities (at Peak Noise Flow Conditions and at Maximum Noise Position). If the noise parameters T8, I8, and S8 are to be useful in indicating the damage capacity of the flow at different flow velocities they must vary in a similar way to erosion with flow velocity. In reference [7] Selim found that the erosion rates obey a velocity power law of the type MLR αV^n, with a greater velocity index for the circular cylinder ($n = 7.1$) than for the 60 deg wedge ($n = 5.8$).

It has already been shown that r.m.s. noise varies with some power of velocity (references [1, 2, 7, and 9]). The present results are in agreement with these earlier studies, and, in addition, it was found that the pulse height spectra parameters also obeyed a velocity power law. The velocity index was calculated for the spectra parameters T, I and S at each threshold level, and these results are summarized in Table 3 for the two cavitation sources.

Table 3 Velocity index for pulse height spectra parameters at different thresholds. Peak noise flow conditions.

Table 3(a) Velocity index for circular cylinder cavitation source

Threshold level	T	I	S
1	4.3	4.7	5.3
2	6.0	6.2	6.5
3	7.1	7.1	7.3
4	7.3	7.4	7.6
5	7.5	7.6	7.8
6	7.4	7.7	8.0
	No pulses above amplitude range 7 for tests at 10 m/s		

Table 3(b) Velocity index for 60 deg symmetric wedge cavitation source

Threshold level	T	I	S
1	3.0	3.5	4.2
2	3.7	4.0	4.6
3	4.1	4.4	4.9
4	4.5	4.8	5.3
5	4.9	5.2	5.6
6	5.4	5.7	6.0
7	5.9	6.1	6.4
8	6.3	6.6	6.8
9	6.7	6.9	7.1
10	7.8	7.8	7.9
11	8.0	8.1	8.2
12	8.4	8.4	8.4
13	8.6	8.6	8.6
14	8.5	8.6	8.6

Some general trends can be identified for both sources. At any given threshold level the velocity index increases when we change parameters from T to I; and again when we change from I to S. Also, for each spectra parameter the velocity index increases with increasing threshold. This second observation is in agreement with the De's earlier experiments [4] where pulse measurements were reported for three threshold levels. As De points out, this is consistent with known erosion results [10] where the damage velocity exponent was found to increase with material hardness.

Unfortunately, it was impossible to calculate the velocity index at level 8 for the circular cylinder because this source failed to produce any pulse counts at this level for peak noise flow conditions at the lowest flow velocity tested (10 m/s). However, examining the velocity index values for levels, 4, 5, and 6 suggests that the velocity index at level 8 would not be far removed from Selim's velocity index for erosion (7.1). However, it was possible to calculate the velocity index at level 8 for the symmetric wedge source. Values of 6.3, 6.6 and 6.8 were obtained for T, I, and S, respectively. Again, it is encouraging that these values are reasonably close to Selim's value of 5.8 for the erosion velocity index for this source.

The velocity index for the r.m.s. noise measurements were also calculated for comparison. These results are summarized in Table 4. It may be concluded that the spectra parameters provide a good indication of cavitation damage for 60 deg wedge and circular cylinders over the range of velocities tested (10 m/s to 18 m/s upstream velocity).

VI Discussion

A linear calibration between cavitation noise and erosion has been successfully achieved by imposing a suitable threshold on the measured pressure pulse spectra. However, choosing the correct threshold level is complicated by a number of factors. Even if the material threshold is known it is difficult to take sound attenuation into account correctly when measuring pressure pulses in the fluid. Such

Table 4 Comparison of velocity index for noise parameters and sidewall erosion

Table 4(a) Comparisons for circular cylinder

Selim's erosion ratio	r.m.s. noise index		acoustic power index		spectra index (level 6)		
	2kHz–100kHz	100kHz–400kHz	2kHz–100kHz	100kHz–400kHz	T	I	S
7.1	3.0	2.2	6.0	4.4	7.4	7.7	8.0

Table 4(b) Comparisons for 60 deg symmetric wedge

Selim's erosion ratio	r.m.s. noise index		acoustic power index		spectra index (level 8)		
	2kHz–100kHz	100kHz–400kHz	2kHz–100kHz	100kHz–400kHz	T	I	S
5.8	2.2	1.9	4.4	3.8	6.3	6.6	6.8

measurements provide the most direct information about the state of the fluid at the point of measurement, but it is known [1] that such measurements are very sensitive to transducer position. A more representation measure of the damage capacity of the cavitating flow might be achieved by measuring the resulting excitation of the constraining walls since these measurements are less sensitive to transducer position. In his tests on a mixed flow pump [5] Kirejczyk found the ultrasonic pulse spectrum in the pump casing remained in a direct relationship with the dynamic intensity of cavitation. It may, therefore, be hoped that such measurement might also provide an indication of flow damage capacity with some threshold imposed. This threshold should then be relatively insensitive to transducer position.

It is not suggested that the damage capacity of other cavitating flows might be indicated by imposing the threshold appropriate to the present tests. Rather, this investigation has shown that imposing thresholds on pulse amplitude spectra can provide a useful indication of the damage capacity of cavitation flow. It is hoped that further work using this approach will lead to an improved general correlation between cavitation noise and erosion.

VII Conclusion

Measurements of r.m.s. noise can be useful for qualitative assessment of cavitation such as detecting cavitation inception, but are of limited value for quantitative erosion prediction in developed cavitation. The latter is better determined from bubble collapse pulse amplitude spectra. However, it is difficult to measure cavitation pulses accurately, and the sampling frequency has been too low in digital data acquisition systems used to date. An analogue instrument called a pulse height analyzer has been designed to provide spectral data in cavitating flows. In conjunction with a flush-mounted pressure transducer, the pulse height analyzer has been used to measure pressure pulses in the fluid resulting from 60 deg wedge and circular cylinder cavitation sources. All bubble collapses contribute to the dynamic cavitation intensity, but only those with sufficient energy to cause damage contribute to the damage capacity of the flow. By imposing thresholds on the different pulse spectra parameters it has been possible to distinguish between the high energy (damaging) pulses from the 60 deg wedge and the lower energy (less damaging) pulses from the circular cylinder. In this way an indication of the damage capacity of the flow has been obtained.

For peak noise flow conditions at an upstream velocity of 16 m/s the wedge produces 21 times as much damage at the circular cylinder. This compares favorably with values 18, 19, and 22 for pulse spectra parameters T8, I8, and S8 respectively. In the same tests r.m.s measurements in frequency ranges 2 kHz–100 kHz and 100 kHz–400 kHz could achieve values of only 1.5 and 1.8 respectively.

Further, these spectra noise parameters were found to have similar velocity indices to that for erosion, indicating that the above correlation was not merely a fortuitous result at the flow velocity tested, but rather that it should apply over a reasonable flow range. Velocity indices from the spectra parameters increased with increasing threshold consistent with material hardness considerations.

Although more complicated noise spectra parameters were investigated it appears that a good correlation between cavitation noise and erosion might be achieved by simply measuring the number of pulses above a suitable threshold.

Pressure pulse amplitude measurements can vary considerably depending on the position in the fluid at which they are measured. A step closer to the long term objective of developing a cavitation damage meter might be to investigate spectral data for ultrasonic pulses in the constraining wall. Investigations with different flow geometries and different materials are also desired.

Acknowledgments

This work was supported by Procurement Executive, Ministry of Defence for a contract with A.R.E. (Holton Heath).

References

1 Hutton, S. P., and Fry, S. A., "Correlation of Cavitation Noise and Erosion," *Proceedings 2nd International Conference on Cavitation*, Edinburgh, Sept. 1983, pp. 269–276.

2 Selim, S. M. A., and Hutton, S. P., "Hydrodynamic Similitude for Cavitation Erosion," *Proceedings Conference on Cavitation Erosion in Fluid Systems*, ASME, 1981, pp. 15–25.

3 Kirejczyk, J., "The Energy Flux of Cavitating Flow," *Proceedings 6th Conference on Fluid Machinery*, Budapest, 1979.

4 De, M. K., and Hammitt, F. G., "New Method for Monitoring and Correlating Cavitation Noise to Erosion Capability," ASME JOURNAL OF FLUIDS ENGINEERING, Vol. 104, Dec. 1982, pp. 434–442.

5 Kirejczyk, J., "Cavitation Signs in Rotadynamic Pump," *Proceedings 2nd International Conference on Cavitation*, Edinburgh, Sept. 1983, pp. 115–121.

6 Steller, K. J., "On Prediction of Durability of Structural Materials Subjected to Cavitation," *Proceedings 2nd International Conference on Cavitation*, Edinburgh, Sept. 1983, pp. 251–258.

7 Selim, S. M. A., "Cavitation Erosion in Fluid Flow," Ph.D. thesis Department of Mechanical Engineering, Southampton University, 1981.

8 Fry, S. A., "Investigating Cavity/Wake Dynamics for a Circular Cylinder by Measuring Noise Spectra," *Journal of Fluid Mechanics*, May 1984.

9 Ramamurthy, A. S., and Bhaskaran, P., "Velocity Exponent for Erosion and Noise due to Cavitation," ASME JOURNAL OF FLUIDS ENGINEERING, Vol. 101, 1979, pp. 69–75.

10 Wood, G. M., Knudson, L. K., and Hammitt, F. G., "Cavitation Damage Studies with Rotating Disk in Water," ASME *Journal of Basic Engineering*, Vol. 89, No. 1, 1967, pp. 98–110.